FINAL REPORT

2012 UINTAH BASIN WINTER OZONE & AIR QUALITY STUDY

GENERAL EDITORS
SETH LYMAN AND HOWARD SHORTHILL, UTAH STATE UNIVERSITY

STUDY COORDINATION
UTAH DEPARTMENT OF ENVIRONMENTAL QUALITY

CONTRIBUTING ORGANIZATIONS (ALPHABETICALLY)

- ALPINE GEOPHYSICS
- BUREAU OF LAND MANAGEMENT
- COLORADO STATE UNIVERSITY
- ENVIRON
- ENVIRONMENTAL PROTECTION AGENCY
- NATIONAL OCEANIC AND ATMOSPHERIC ADMINISTRATION
- UNIVERSITY OF CALIFORNIA, BERKELEY
- UNIVERSITY OF CALIFORNIA, LOS ANGELES
- UNIVERSITY OF COLORADO, BOULDER
- UNIVERSITY OF WASHINGTON
- UNIVERSITY OF WYOMING
- UTAH DEPARTMENT OF ENVIRONMENTAL QUALITY
- UTAH STATE UNIVERSITY
- WESTERN ENERGY ALLIANCE

FUNDING ENTITIES (ALPHABETICALLY)

- BUREAU OF LAND MANAGEMENT
- DEPARTMENT OF ENERGY
- DUCHESNE COUNTY
- ENVIRONMENTAL PROTECTION AGENCY
- MR. MARC BINGHAM
- NATIONAL OCEANIC AND ATMOSPHERIC ADMINISTRATION
- NATIONAL SCIENCE FOUNDATION
- UINTAH COUNTY
- UINTAH IMPACT MITIGATION SPECIAL SERVICE DISTRICT
- UTAH DEPARTMENT OF ENVIRONMENTAL QUALITY
- UTAH SCHOOL AND INSTITUTIONAL TRUST LANDS ADMINISTRATION
- WESTERN ENERGY ALLIANCE (THROUGH MEMBERS ANADARKO PETROLEUM CORP., BILL BARRETT CORP., BERRY PETROLEUM CO., EOG RESOURCES, GASCO ENERGY INC., NEWFIELD EXPLORATION CO., QEP RESOURCES, AND XTO ENERGY INC.)

DOCUMENT NUMBER: CRD13-320.32
REVISION: PUBLIC RELEASE
DATE: FEBRUARY 01, 2013

TABLE OF CONTENTS

CHAPTER IV: EMISSIONS INVENTORY REPORT

CHAPTER V (PART A): SOURCE CHARACTERIZATION, ATTRIBUTION, AND OZONE DISTRIBUTION IN THE UINTAH BASIN USING THE NOAA MOBILE LABORATORY

CHAPTER V (PART B): TETHERED OZONESONDE MEASUREMENTS IN THE UINTAH BASIN

SYNOPSIS OF RESULTS

Till Stoeckenius[1], Dennis McNally[2], Seth Lyman[3], and Howard Shorthill[3]

[1]ENVIRON International Corporation

[2]Alpine Geophysics Corporation

[3] Bingham Entrepreneurship & Energy Research Center, Utah State University

EXECUTIVE SUMMARY

Background

In 2008, the United States Environmental Protection Agency (EPA) established a National Ambient Air Quality Standard (NAAQS) for ozone of 75 parts per billion (ppb), a regulatory number that is obtained by averaging over a three-year period, the annual fourth-highest daily maximum eight-hour ozone concentration. During winter 2009-10 and again during winter 2010-11, some eight-hour ozone concentration averages in the Uintah Basin of northeastern Utah were observed to exceed 75 ppb. A study conducted by Utah State University during winter 2010-11 showed that ozone concentrations were lower in areas on the periphery of and contiguous to the Uintah Basin than they were within, with the highest concentrations tending to occur at lower elevations near the Basin's center.

Since 2005, periods of high ozone have also been observed during some winters in the Upper Green River Basin (UGRB) of southwestern Wyoming. Several studies in both basins have determined that winter ozone formation requires (1) snow cover to increase available sunlight that drives ozone-forming photochemical reactions and (2) strong temperature inversions to decrease atmospheric mixing and allow ozone and its precursors to accumulate in a shallow layer of the atmosphere near the ground. Both basins contain extensive oil and gas development, and emissions from oil and gas operations have been implicated as a major source of ozone precursors in the UGRB.

While ozone is known to form during the complex, non-linear reactions of two principal precursors called volatile organic compounds (VOC) and nitrogen oxides (NO_x), understanding the relationship between changes in precursor emissions and the resulting changes in ozone concentrations is a significant challenge of ozone pollution management. The 2011-12 Uintah Basin Ozone Study (UBOS 2011-12), a comprehensive field measurement campaign, was launched to gain a better understanding of the factors contributing to elevated wintertime ozone in the Basin. This campaign was designed to (1) continue a long-term record of atmospheric chemistry and meteorology; (2) identify emissions sources; (3) understand the meteorological and chemical processes active in ozone production, including the possibility of unique photochemical mechanisms that contribute to elevated winter concentrations; and (4) provide information that leads to the development of effective mitigation strategies.

Findings

Unlike the previous two winters, ozone concentrations during UBOS 2011-12 were well below the NAAQS, peaking at an eight-hour average of 63 ppb, and snow cover and multi-day temperature inversions were virtually absent. Yet despite these differences, much valuable and useful data about ozone precursor emissions and atmospheric chemistry were collected. This document synthesizes the results reported by the UBOS 2011-12 teams. Key findings are summarized below:

- As in the UGRB, snow cover is a key element of high ozone episodes. (These episodes are also associated with light wind and strong, shallow temperature inversions that trap a pool of cold air underneath warmer air, limit atmospheric mixing, and trap ozone and its precursors close to the ground, allowing concentrations to build.) Snow cover promotes ozone formation in at least two ways. First, since it reflects sunlight, snow cover limits daytime heating of the earth's surface, thus keeping air cool near the surface and promoting temperature inversions. Second, the total amount of solar radiation passing through the atmosphere and available to drive chemical reactions responsible for ozone formation is nearly doubled as the snow cover reflects the incoming sunlight. Snow cover may also promote heterogeneous chemical reactions that enhance ozone formation.

- Analysis of historical weather data indicates that conditions conducive to ozone formation in the Uintah Basin occur on at least some days during about half of all winter seasons, and ozone levels characteristic of a severe ozone season, such as those measured in winter 2010-11, can be expected to occur approximately in one of every four seasons. Median ozone concentrations in 2012, a year with little snow cover and no persistent inversions, were 28-46 ppb.

- Neither the 2010-11 nor the 2011-12 study was designed specifically to quantify the contribution of pollutants from external sources to ozone episodes within the Basin, but available data suggest that such transport is not likely to represent a major contribution to peak ozone events. These lines of evidence include (1) higher concentrations of VOC and NO_x within the Basin than without, (2) correlations of VOC and NO_x concentrations with proximity to known sources, (3) meteorological conditions during ozone production episodes not conducive to transport from outside the Basin, and (4) VOC speciation (i.e., the mix of different VOC in the atmosphere) in the Basin characteristic of oil and gas operations, not of upwind urban sources.

- An emissions inventory developed for the study indicates that oil and gas operations were responsible for 98-99% of VOC (range of estimates) and 57-61% of NO_x emitted from sources within the Basin that were considered in the inventory. Some sources were not included in the inventory due to lack of available information (e.g., hydrocarbon seepage from soils and emissions from produced water disposal ponds and from plugged and abandoned wells). Among sources considered in the study, the Bonanza Power Plant emitted 33-36% of NO_x within the Basin during the study. More study is needed, however, to determine whether the Bonanza Plant's stack height limits its contribution to surface winter ozone production. Industrial operations change rapidly, and many gaps exist in current inventories. A new, comprehensive inventory effort is needed to model and effectively manage air quality in the Basin

- NO_x and VOC emission plumes can occur at different heights, with VOC emissions concentrated near ground level and some NO_x emissions being injected further aloft. These vertical gradients in NO_x and VOC may impact ozone formation and present challenges for modeling.

- Current understanding of the chemistry of ozone formation in polluted environments is based largely on summertime ozone episodes occurring in large urban areas; comparatively little is known about winter ozone formation. UGRB studies suggest the existence of chemical reactions unique to winter ozone formation. Three reaction pathways that may contribute to winter ozone production and deserve further investigation were identified by UBOS 2011-12: (1) sunlight-induced production of nitrous acid (HONO) from NO_2 on snow or particle surfaces, (2) alkene production on snow surfaces, and (3) nitryl chloride formation. Further field studies

during winter ozone episodes will be required to determine whether these reaction pathways merit inclusion in regulatory air quality models.

- Surface airflow during the light winds characteristic of conditions conducive to ozone formation is heavily influenced by the Uintah Basin's complex topography. Recirculating air patterns in the UGRB have been shown to concentrate pollutants and contribute to ozone production. More study is needed to understand how complex surface flows in the Uintah Basin influence ozone production and transport.

Recommendations

Mitigation

Determination of a comprehensive strategy for mitigating winter ozone issues in the Uintah Basin will require the development of meteorological and photochemical models that accurately simulate winter ozone production. Three-dimensional photochemical models can evaluate the sensitivity of ozone concentrations to changes in precursor emissions and predict the effects of emissions control strategies. Ambient measurements are essential to inform and validate the emissions inventories and models that will help determine mitigation strategies.

- Because models specific to winter ozone formation in the Uintah Basin have not been developed, information sufficient to determine the level of emission reductions that could eventually be required to achieve ozone-reduction objectives is not available. Furthermore, it is not known at this time if ozone levels in the Basin will be more effectively mitigated by NO_x or VOC controls, or if the control requirements may vary across the Basin. Under some conditions, reductions in NO_x emissions can actually result in increased ozone concentrations.

- The study team's current best estimate is that VOC controls will reduce ozone production, but the overall effectiveness of this strategy is unknown. Reductions in emissions of aromatic VOC (e.g., Benzene, Toluene, etc.) could be particularly effective since they are not only a direct health concern but also more active in ozone production than many other VOC. It is not known whether or to what extent NO_x emissions controls would be effective.

- Newly promulgated National Emission Standards for Hazardous Air Pollutants and New Source Performance Standards specific to the oil and gas industry will likely reduce emissions of VOC from a number of sources including glycol dehydrators (large source of aromatics), and may increase emissions of NO_x due to the requirement that emitted VOC be flared. Some of these standards only apply to new or modified sources.

- A voluntary "ozone action day" program similar to that implemented in the UGRB may be a cost-effective way to reduce peak ozone concentrations. Such a program would encourage limitation of industrial operations and public exposure to polluted air on days when high ozone is anticipated.

Future Studies

While data collected and analyses performed to date have provided much useful information, additional measurements (particularly during winter ozone episodes), analyses, and models are needed to guide air quality management plans and to develop more comprehensive mitigation strategies. Specific recommendations include:

- Additional field measurements during ozone episodes at sites across the Basin that characterize horizontal, vertical, and temporal characteristics of winter ozone formation and explore the possibility of chemical reactions unique to winter ozone episodes.
- Continued development of a Basin-specific emissions inventory that includes reconciliation with ambient measurements.
- Development of validated meteorological and photochemical models specific to winter ozone episodes in the Uintah Basin that include winter ozone formation simulations and lead to Basin-specific ozone mitigation strategies.

INTRODUCTION

Background

The Uintah Basin lies in the northeast corner of Utah and is bounded on the north by the Uinta Mountains, on the south by the Tavaputs Plateau, on the west by the Wasatch Range, and on the east by elevated terrain separating it from the Piceance Basin in Colorado. The Green River runs through the Basin from northeast to southwest, exiting through Desolation Canyon. The lowest point in the Basin is near Ouray and is approximately 4800 feet above sea level. Significant topographical variation on the order of tens to hundreds of vertical feet exists within the Basin.

Duchesne and Uintah Counties make up essentially the entire Basin. The Uintah and Ouray Indian Reservation covers a significant portion of the Basin (Figure 1). EPA and the Ute Tribe have jurisdiction over air quality management on the reservation, while the State of Utah manages air quality in other areas.

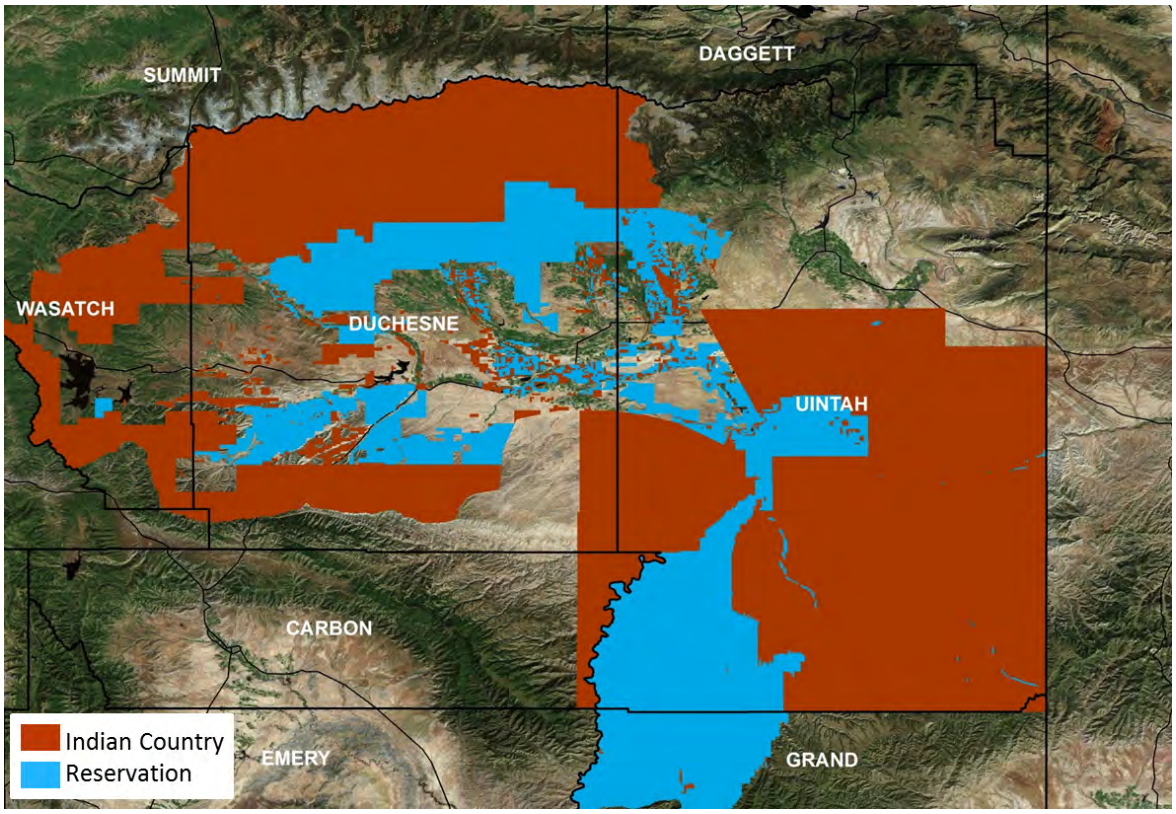

Figure 1. Uintah Basin and surrounding region with county boundaries (Utah only) and tribal areas.

The Basin is mostly rural and has a population of about 50,000 concentrated primarily in three towns (Duchesne, Roosevelt, and Vernal) that lie along the east-west State Highway 40 corridor (Figure 2). The economy of the Basin is driven by energy production from vast petroleum resources. Oil and gas production (approximately 8,000 wells; Chapter 4) is concentrated in sparsely populated areas in the south (Question C). A 500-megawatt coal-fired power plant (Bonanza) operates in the Basin. Agricultural production includes cattle, alfalfa, corn, potatoes, and other crops.

Air quality monitoring in the Basin began in 2006 when the Utah Department of Environmental Quality (UDEQ) installed monitors in Vernal to measure fine particulate matter ($PM_{2.5}$), ozone, and NO_x. Data were collected from February 2006 through December 2007. Eight-hour ozone averages as high as 81 ppb were found in the summer. No exceedances of the eight-hour standard for ozone were noted during winter. Two additional studies were conducted during the winters of 2007-08 and 2008-09, but these focused on $PM_{2.5}$, since no elevated winter ozone values had been observed in 2006-07.

In the spring of 2009, monitoring sites at Ouray and Red Wash in the oil and gas production area of the Basin were established as part of a consent decree. These sites were instrumented to measure $PM_{2.5}$, NO_x, ozone, and meteorological parameters year-round. In contrast with the relatively low ozone values of winter 2006-07, winter 2009-10 experienced ozone concentrations in exceedance of the standard. The highest eight-hour average was 124 ppb, while the fourth highest eight-hour value was 117 ppb (median eight-hour daily maximum was 67 ppb).

Utah State University (USU) conducted a study in the winter of 2010-11 to confirm the presence of elevated winter ozone concentrations, map the spatial extent of elevated ozone levels, and investigate

the meteorological and chemical conditions associated with the phenomenon (Martin et al., 2011). The 2010-11 USU study showed that ozone values were elevated throughout the Basin during several multi-day inversion episodes, with the highest concentrations tending to occur at lower elevations in the center of the Basin. The highest eight-hour ozone value measured at Ouray was 139 ppb (fourth highest eight-hour value of 116 ppb; median eight-hour daily maximum of 69 ppb). Elevated ozone was only observed in the presence of snow-covered ground and strong temperature inversions.

2011-12 Uintah Basin Ozone Study

A field campaign involving multiple investigators and measurement approaches was mounted in the winter of 2011-12 to gain a more complete understanding of factors contributing to elevated wintertime ozone in the Basin. UBOS 2011-12 consisted of six components, as listed in Table 1. Figure 2 shows a map of measurement sites used during the study.

Table 1. Report Chapters and principal research groups.

CHAPTER	RESEARCH GROUP
1. Long-Term Monitoring for Ozone and Key Precursor Species	Utah State University and Utah Department of Environmental Quality
2. Distributed Monitoring of Ozone, Precursors, and Meteorology	Utah State University and Utah Department of Environmental Quality
3. Intensive Measurements at the Horse Pool Site	NOAA Chemical Sciences Division and others
4. Emissions Inventory Report	Utah State University
5A. Source Characterization, Attribution, and Ozone Distribution in the Uintah Basin using the NOAA Mobile Laboratory **5B.** Tethered Ozonesonde Measurements in the Uintah Basin	NOAA Earth System Research Laboratory and others
6. Continuous Vertical Profiling of Meteorological Variables, Ozone, Nitrogen Oxides, Methane, and Total Hydrocarbons	University of Colorado, Boulder
7. The Potential for Ozone Production in the Uintah Basin: A Climatological Analysis	Utah State University

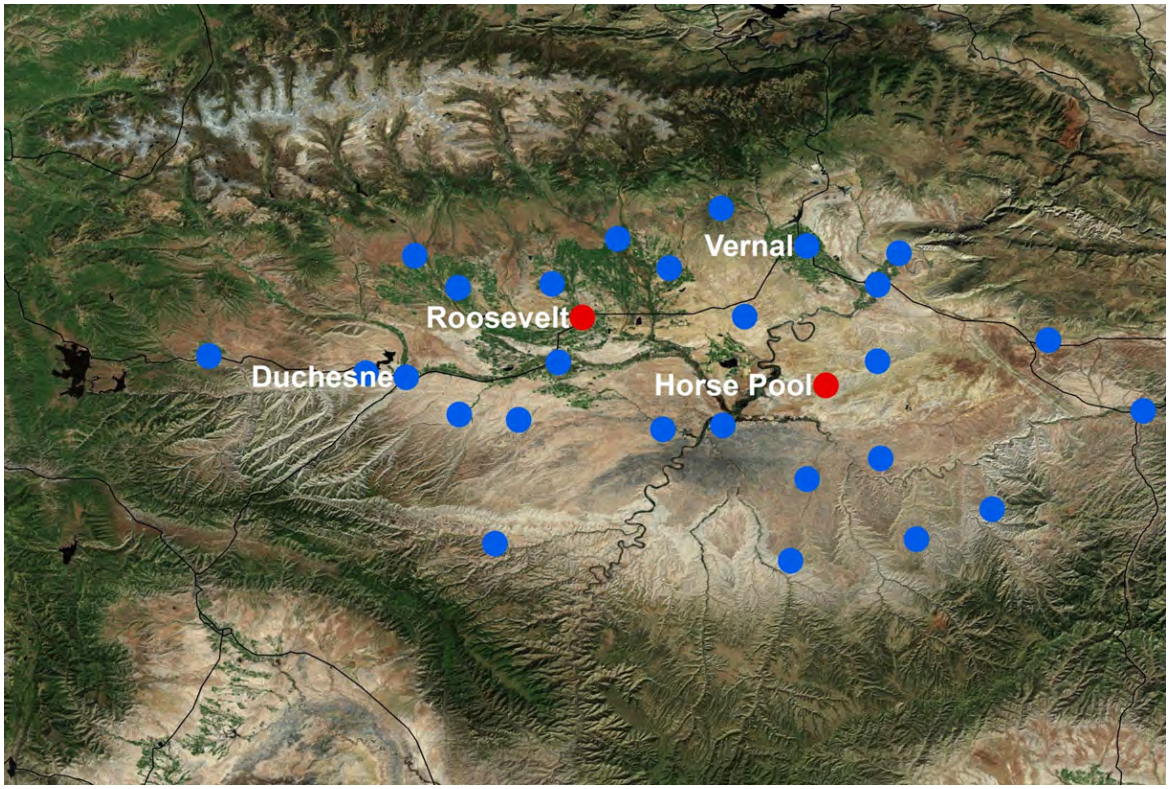

Figure 2. UBOS 2011-12 sites. Long-term sites from Chapter 1 are shown in red; all others in blue. Cities and the Horse Pool site are labeled.

Study management and coordination was provided by the Utah Division of Environmental Quality with support from the Bureau of Land Management. An oversight team and science steering committee directed the study. The oversight team consisted of representatives from Utah Department of Environmental Quality, Western Energy Alliance, Uintah Impact Mitigation Special Service District, Bureau of Land Management, and US Environmental Protection Agency. The science steering committee consisted of representatives from US Environmental Protection Agency; Western Energy Alliance; National Oceanic and Atmospheric Administration; University of Colorado, Boulder; Utah State University; and Utah Department of Environmental Quality.

A list of all entities involved in the study is given on the title page.

Study Report

Each participating research group reported its individual methods, results, conclusions, etc. These reports are included as chapters in this document (Table 1). A summary of winter ozone studies in the UGRB of southwestern Wyoming was also prepared in conjunction with this study and is available separately (Hall et al., 2012).

Utah State University and contracted representatives of Alpine Geophysics and ENVIRON International were tasked with preparing a final report that synthesizes and presents study findings. This sections, "Synopsis of Results," has been written as a series of responses to a set of key questions focused on the study objectives as listed below. For each response, a brief background discussion explaining the

significance of the question is provided, followed by a set of findings that answers the question in different ways. Each response concludes with a summary of the main points of the findings.

Questions are grouped by subject area as follows:

A. Physical Characteristics and Meteorology

- **A.1** What are the key characteristics of meteorological conditions associated with ozone exceedances in the Basin?
- **A.2** Was the difference between ozone concentrations in 2011-12 and previous winters a result of changes in meteorology or precursor emissions?
- **A.3** What is the climatological frequency of meteorological conditions that are conducive to ozone formation in the Uintah Basin?
- **A.4** What role does transport of ozone or ozone precursors into the Basin play in generating elevated ozone concentrations?
- **A.5** What similarities and differences are there between the Uintah Basin and the Upper Green River Basin in Wyoming?
- **A.6** Does significant vertical stratification of precursors occur? If so, what role does this play in ozone formation?

B. Atmospheric Chemistry of Ozone Formation

- **B.1** Do pathways for ozone production exist that are unique to wintertime ozone events?
- **B.2** Do VOC speciation and reactivity in the Basin have unique characteristics that contribute to wintertime ozone production?

C. Sources of Ozone Precursor Emissions

What are the primary sources of ozone precursor emissions in the Basin?

D. Mitigation Strategies

What possible mitigation strategies should be considered for adoption in the Uintah Basin?

E. Additional Information Needs and Modeling Issues

- **E.1** What special challenges does the Basin pose for meteorological modeling?
- **E.2** Can the formulation of existing 1-D box and more complex transport and chemical models represent the observed phenomena in the Basin? If not, what are the most urgent needs for improving model representation?
- **E.3** What are the main issues regarding winter ozone formation that should be the focus of future studies?

PART A: PHYSICAL CHARACTERISTICS AND METEOROLOGY

Question A.1

What are the key characteristics of meteorological conditions associated with ozone exceedances in the Basin?

Background

While meteorological conditions during the 2011-12 Uintah Basin Ozone Study were not conducive to the formation of ozone levels in excess of the EPA 75 ppb eight-hour standard, information about the key meteorological conditions associated with winter ozone episodes is available from data collected in previous years and from data collected in the UGRB, a basin with similar characteristics and similar winter ozone issues (Question A.5). Studies in the UGRB indicate that ozone episodes occur under clear skies during strong temperature inversions and in the presence of extensive snow cover (ENVIRON, 2008; Schnell et al., 2009; Stoeckenius and Ma, 2010). Comparisons of data collected during different winter seasons in which snow cover was and was not present indicate that snow cover is the key requirement for ozone formation. Box modeling of winter ozone events in the UGRB indicate that the high albedo of the snow is one of the key drivers of ozone formation (Nopmongcol et al., 2010; Carter and Seinfeld, 2012). In addition, it is hypothesized that snow cover promotes retention of the strong nocturnal surface inversion during the day, thus trapping pollutants near the surface and increasing ozone precursor concentrations and ozone production rates. Martin et al. (2011) found that similar conditions are required for ozone formation in the Uintah Basin.

Findings

Finding A.1.1: Snow cover and strong inversions with low mixed layer heights are required for formation of elevated winter ozone concentrations in the Uintah Basin. Meteorological conditions during the 2011-12 UBOS period differed from those in the previous two winters in that snow cover was not present, daytime temperature inversions were rare, and no exeedances of the ozone NAAQS were observed.

In all cases, ozone exceedances in the Uintah Basin have occurred during cold pool events when stagnant weather conditions combined with extensive snow cover resulted in an extremely shallow temperature inversion which trapped pollutants near the surface (mixed layer heights of 20-80 m were measured by Martin et al., 2011, during ozone-producing conditions).

In contrast to the 2009-10 and 2010-11 seasons, snow cover was nearly absent during the UBOS 2011-12 period, little local ozone production was observed (Chapter 3), and daytime ozone maxima were consistently below the NAAQS (Chapter 2). A comparison of hourly ozone concentrations for January – March 2011 with the same period in 2012 shows the marked difference between these two years (Figure 3). Several multi-day periods of elevated ozone concentrations were observed in winter 2010-11, and eight-hour average ozone concentrations at Ouray reached a maximum of 139 ppb (with 25 exceedances of the eight-hour standard). Median ozone values for all sites in 2010-11 ranged from 34-52 ppb. In contrast, the highest eight-hour average ozone value during the 2011-12 study was 63 ppb, and median values at sites ranged from 28-46 ppb.

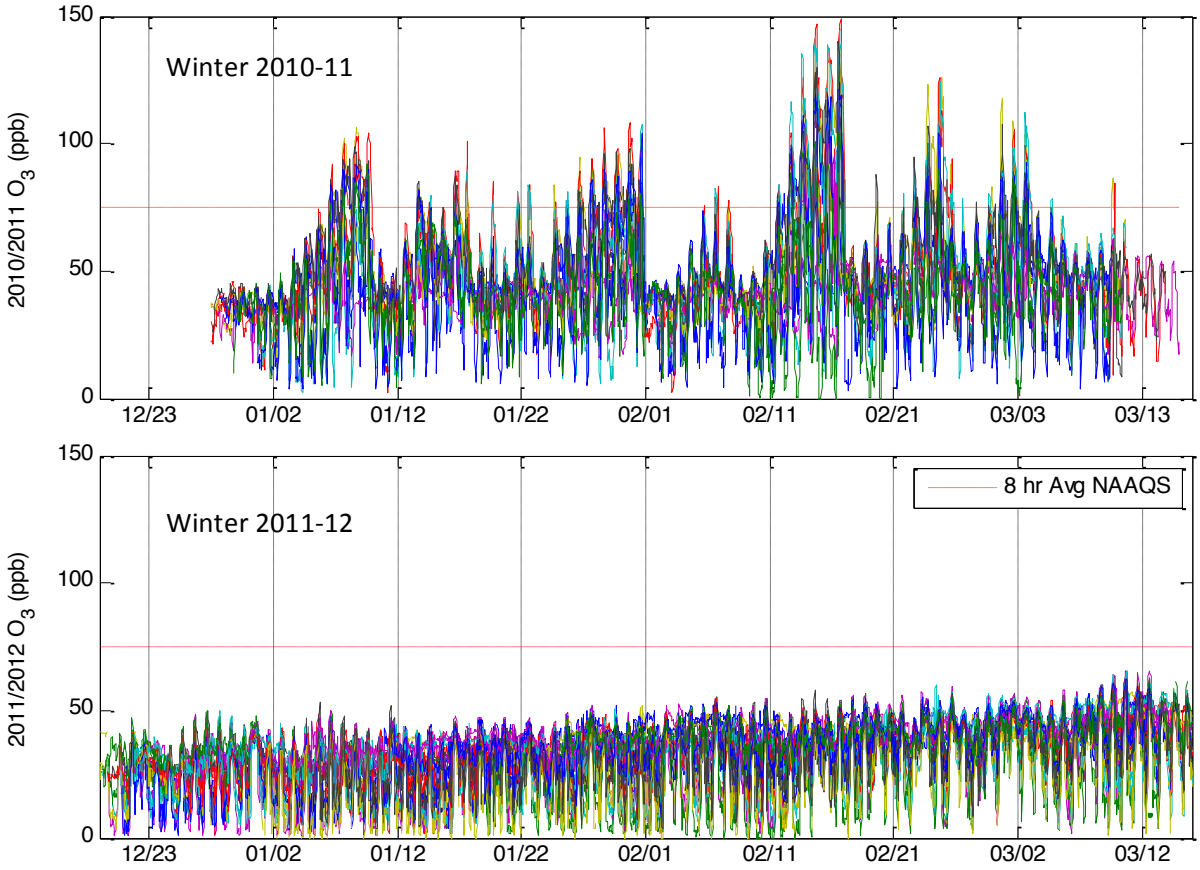

Figure 3. Comparison of hourly average surface ozone concentrations at multiple monitoring sites in the Uintah Basin for Jan.-Mar. 2011 (top) and 2012 (bottom); see Figure 2 for monitoring site locations.

In Chapter 7, Mansfield and Hall construct pseudo-vertical temperature profiles by examining surface temperature readings from stations located at different altitudes within and along the edge of the Uintah Basin. This analysis shows inversion conditions that occurred during 2011 were not present in 2012. Mansfield and Hall also construct a statistical model of ozone and meteorological data from 2009-2012 that confirms the role of temperature inversions and snow depth in ozone formation.

The statistical model developed in Chapter 7 shows that years with snow cover tend to have more daytime temperature inversions, giving weight to the hypothesis that snow cover enhances inversion formation by reflecting incoming solar energy and limiting surface heating. The statistical model also shows the influence of overnight carryover of ozone and ozone precursors: longer, multi-day periods with inversions and snow cover were characterized by higher ozone levels than shorter periods. Table 2, adapted from Chapter 7, demonstrates the association between snow cover and ozone.

Table 2. Highest wintertime ozone concentrations (eight-hour average) and number of exceedances of the eight-hour standard at Ouray for each year for which data are available. Also included is the number of days during which snow depth exceeded 50 mm.

Year	Highest 8-hr Value (ppb)	Number of Ozone Exceedances	Days with Snow Depth > 50 mm
2009-10	124	36	94
2010-11	139	25	81
2011-12	63	0	0

Finding A.1.2: Elevated ozone episodes occur most frequently during February.

Chapter 7 shows that while average snow depth and the frequency and strength of temperature inversions in the Basin peak in January, elevated ozone episodes are most common in February (based on the limited observational record), due to what Mansfield and Hall hypothesize is the rapid decrease in noon solar zenith angles following the winter solstice. The angle between the noon sun and vertical is usually too large (i.e., incoming solar radiation is not adequately abundant) to drive strong photochemical reactions until February. Exceptions can occur, however: an eight-hour ozone value of 101 ppb was recorded at Ouray on 23 Dec. 2009. While solar zenith angles continue to decrease until the summer solstice in June, snow typically melts in March, thereby ending the winter ozone season. A similar seasonal effect was noted in the UGRB by Stoeckenius and Ma (2010).

Conclusion

Snow cover is a necessary condition for formation of winter ozone episodes. Snow cover increases solar radiation and the propensity for inversions, two additional important conditions for winter ozone formation. Elevated ozone episodes are most common in February when the noon solar zenith angle has decreased sufficiently from its winter solstice maximum.

Question A.2

Was the difference between ozone concentrations in 2011-12 and previous winters a result of changes in meteorology or precursor emissions?

Background

Day-to-day variations in ozone concentrations in most urban air basins have been shown to be dominated by meteorological factors (e.g., Solomon et al., 2000; NRC, 1991). Day-to-day variations in emissions from oil and gas operations and other significant ozone precursor sources in the Uintah Basin are expected to be small (with some important exceptions such as drilling and well completions, pipeline venting, etc.) and, as in the more extensively studied urban air basins, day-to-day variations in ozone concentrations in the Basin are likely to be driven more by meteorological conditions than by changes in emissions.

Emissions from some oil and gas production activities (including drilling and completions, heaters, venting, and other processes) can vary on larger time scales (seasonal, annual) in

response to market forces, regulation, weather, etc., potentially creating fluctuations in precursor emissions and leading to variations in ozone levels.

Since ozone formation is a result of non-linear chemical reactions among precursors, reductions or increases in precursor emissions do not necessarily lead to proportionate reductions or increases in ozone concentrations. The effects of changes in precursor emissions, therefore, will need to be evaluated with a photochemical model to determine how emission changes affect ozone concentrations.

Findings

Finding A.2.1*: *Low ozone concentrations in 2011-12 relative to previous years were not accompanied by a decrease in oil and gas production activities. Meteorological measurements and analyses indicate that differences in the ozone concentrations observed in 2009-10, 2010-11, and 2011-12 were mostly due to differences in meteorological conditions.

Ozone precursor emissions inventories showing differences in the 2009-10, 2010-11, and 2011-12 winter seasons currently are not available. However, drilling and production data from the Utah Division of Oil, Gas, and Mining (Utah DOGM, 2012) suggest that activity in the Uintah Basin increased between 2009 and 2012 (Figure 4). Furthermore, no significant new emission control measures were introduced during this period. It is unlikely, therefore, that overall emissions would have decreased so significantly as to account for the lower ozone observed in 2011-12 compared to 2010-11. Differences in ozone concentrations among the 2009-10, 2010-11, and 2011-12 winter seasons were accurately simulated in Chapter 7 by a statistical model that included several meteorological parameters but did not incorporate changes in precursor emissions.

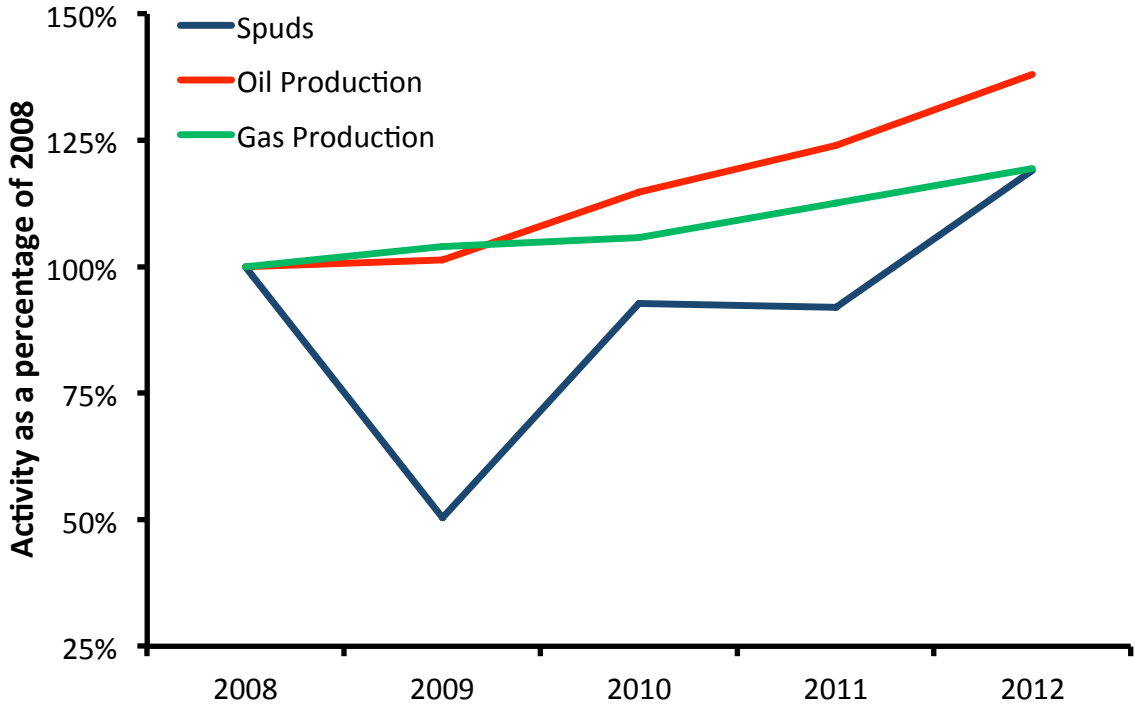

Figure 4. Recent annual drilling and production activity trend in the Uintah Basin (Uintah and Duchesne Counties) as a percentage of production in 2008 (Utah DOGM, 2012). 2012 spud counts (indicating number of wells where drilling was started) were extrapolated from Jan.-Aug. data, and 2012 production statistics were extrapolated based on Jan.-May data.

Conclusions

Meteorological conditions are the primary driving factor behind recent inter-annual variations in Uintah Basin ozone concentrations, though ozone production does in fact depend on precursor concentrations in addition to meteorology. UBOS 2011-12 results show that the strong inter-annual variability in wintertime meteorological conditions obscures relatively small changes in emissions, but large changes in emissions would be likely to have discernable impacts on winter ozone formation.

Question A.3

What is the climatological frequency of meteorological conditions that are conducive to ozone formation in the Uintah Basin?

Background

Ozone concentrations in excess of the NAAQS were observed in the Uintah Basin during the winters of 2009-10 and 2010-11, but concentrations were much lower in 2011-12. These inter-annual fluctuations have been demonstrated to be caused mostly by variations in the frequency and severity of meteorological conditions favorable to ozone formation (Questions A.1 and A.2). A similar situation exists in the UGRB as illustrated in Figure 5: ozone exceedances are observed

in some years but concentrations remain well below the NAAQS in others. The frequency of meteorological conditions conducive to ozone formation plays a crucial role in determining the attainment status of the Basin. Estimates of the frequency of conditions conducive to ozone formation are also useful in planning future field studies.

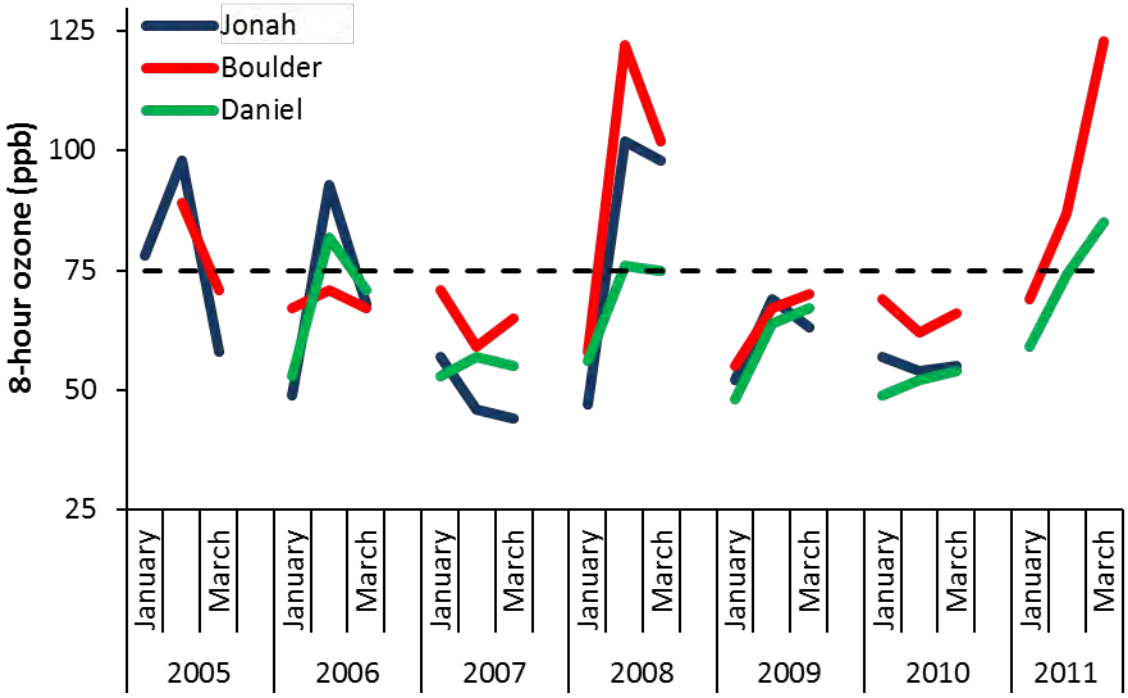

Figure 5. Monthly maximum eight-hour average ozone concentrations during the winter ozone season at monitoring sites in the UGRB. The dashed black line indicates 75 ppb.

Findings

Finding A.3.1*: *Conditions conducive to ozone formation likely occur on at least some days during about half of all winter seasons, and ozone levels characteristic of a severe ozone season (similar to winter 2010-11) can be expected to occur 27% of the time, assuming no change in precursor emissions.

Mansfield and Hall (Chapter 7) analyzed meteorological conditions in the Uintah Basin over a 63-year period (1950 – 2012) and estimated the historical frequency of meteorological conditions conducive to formation of elevated ozone levels. They developed a quadratic regression model that predicts the daily maximum eight-hour average ozone concentration at Ouray (which usually experiences higher ozone than other sites in the Basin during ozone episodes) based on key meteorological parameters including but not limited to snow depth, low level temperature lapse rate, and surface temperature at 1,400 m asl. The model was fitted to data from three consecutive mid-December to mid-March winter seasons starting with the 2009-10 season (the first season for which ozone data were available at Ouray). Model predictions of daily maximum ozone concentrations were then examined for the full 63-year meteorological data set to determine the predicted frequency of conditions associated with elevated ozone concentrations. Results of this analysis showed that, assuming emission levels equivalent to the average levels occurring during the 2009-10, 2010-11 and 2011-12 winter seasons, 27% of the

past 63 winter seasons are estimated to have had conditions at least as conducive to formation of high ozone as 2010-11. Forty-four percent of years were estimated to be compliant with the ozone NAAQS. It must be noted, however, that these results are based on observations of the correlations between ozone and meteorological conditions over just three winter seasons. Estimated frequencies of conditions conducive or not conducive to ozone episodes may change as more data are collected.

Conclusions

Based on the limited data currently available, meteorological conditions conducive to ozone concentrations exceeding 75 ppb occur in approximately half of all winter seasons. Seasons at least as extreme as the elevated ozone conditions of 2010-11 are likely to occur in 27% of years.

Question A.4

What role does transport of ozone or ozone precursors into the Basin play in generating elevated ozone concentrations?

Background

Determining the relative contributions of sources located outside of the Basin to ozone episodes in the Basin is a fundamentally important step in designing an appropriate control strategy. Studies conducted to date do not focus specifically on the question of transport of ozone and precursors in the Uintah Basin, but they do provide information about the influence of transport processes on in-Basin ozone concentrations.

Regional background ozone measured at remote locations in the intermountain West have been reported by Vingarzan (2004) to range from 37 to 47 ppb (range of annual medians for Yellowstone and Rocky Mountain National Parks) and by Brodin et al. (2010) to range from 27 to 50 ppb (10th to 90th percentile range for wintertime near Boulder, Colorado). Ozonesonde data collected well above the surface inversion during January-March in the UGRB showed concentrations ranging between 55 and 65 ppb (ENVIRON, 2008). In the absence of local production, ozone within the Uintah Basin is expected to be transported from global and regional sources, and concentrations are expected to fall within the range of these background values.

In evaluating the significance of the role of transported ozone in local ozone production episodes, it is important to keep in mind that local ozone production does not simply add to the pre-existing background ozone. Instead, local precursor emissions and resulting reaction products interact with transported ozone and ozone precursors in complex ways. The contribution of background pollutants to ozone episodes within the Basin can best be evaluated using a photochemical model that accurately simulates winter ozone formation. Modeling tools such as Ozone Source Apportionment Technology (OSAT; CAMx, 2012) and sensitivity analyses (for example, the higher-order direct decoupled method; Hakami et al., 2003; Cohan et al., 2005) can then be used to evaluate the contributions of transported species to ozone production in the Basin.

Findings

Finding A.4.1*: *Under the well mixed atmospheric conditions characteristic of the UBOS 2011-12 period, afternoon maximum one-hour average ozone measurements made at locations along the edge of the Basin were not significantly different from those made in the Basin interior, and were usually within the range of background concentrations reported for the region.

Ozone concentrations exceeding the eight-hour standard were not observed during the UBOS 2011-12 period, so direct observational evidence of transport under elevated ozone conditions was not obtained. Daytime maximum ozone levels were nearly uniform throughout the Basin in 2011-12, in marked contrast to conditions during 2010-11 (Chapter 2; Figure 6). Median ozone concentrations during winter 2011-12 ranged from 28-46 ppb for sites within the Uintah Basin and 41-46 for sites on the Basin Rim (Chapter 2), within the range of background ozone in the region. Chemical evidence showed that a limited amount of photochemistry and ozone production did occur (Chapter 3). Significant nighttime surface ozone depletion affected ozone concentrations in the center of the Basin and in population centers (Chapters 2 and 3).

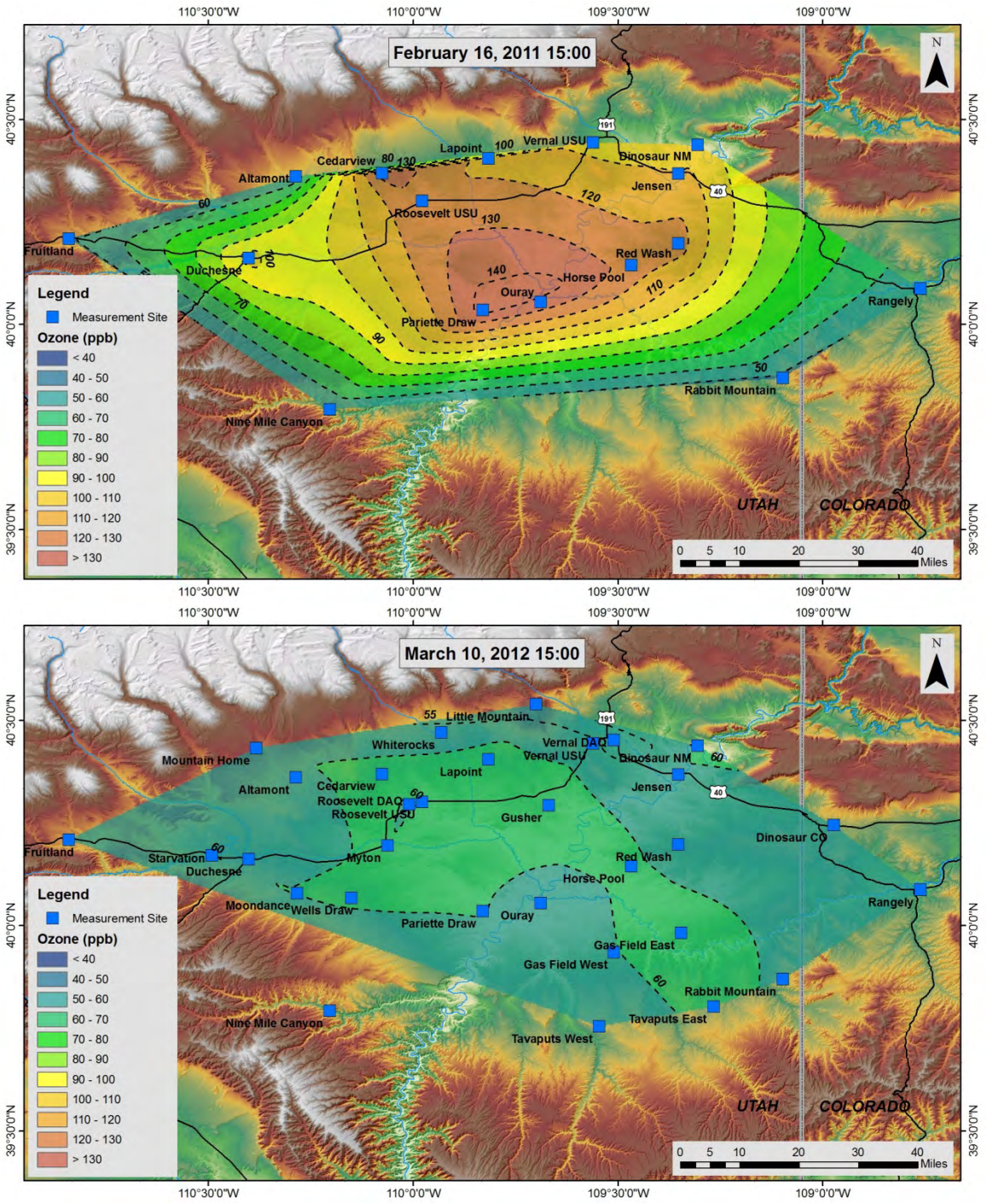

Figure 6. Highest 1-hour average ozone concentrations in the Basin during the 2011 study on 16 Feb. 2011 at 15:00 (top) and the 2012 study on 10 Mar. 2012 at 15:00 (bottom) (Chapter 2). Color scale intervals are the same for both panels. Contour lines are 10 ppb for 2011 map, 5 ppb for 2012 map.

Monitoring data from elevated ozone periods in winter 2010-11 showed that ozone at monitoring sites along the margins of the Basin were near background levels and much below levels in the Basin interior (Figure 6). This observation, together with light winds, rapid decrease

in ozone with elevation, and very low mixing heights observed during the 2010-11 episodes is consistent with a limited influence of transport on increases in ozone above typical background levels. Stoeckenius and Ma (2010) reached a similar conclusion for the UGRB.

Finding A.4.2: Data collected to date do not support a major role for precursor emissions transport on wintertime ozone production in the Basin. Strong evidence exists that most NO_x and VOC in the Basin are derived from local sources.

Detailed analyses of the relationships between pollutant levels within the Basin and levels in air masses entering the Basin were not conducted as part of UBOS 2011-12; however, passive monitoring of weekly average NO_x and $C_6 – C_{11}$ VOC showed no elevated values at sites located on the edges of the Basin. Passive VOC monitoring showed values at the margins of the Basin were much less than at the center of the Basin where oil and gas wells are concentrated, suggesting that sources within the Basin contributed significantly to in-Basin air quality during the study period (Chapter 2).

While precursor measurements at locations along the Basin margins were not available from the 2010-11 ozone episode periods, the lack of any nearby precursor sources and the isolation of the surface air mass within the Basin from the surrounding region under the strong, shallow inversions characteristic of episode events strongly suggest that precursor transport is not an important factor (Martin et al., 2011).

Average diurnal profiles of NO_x at Roosevelt and Red Wash show peaks that coincide with times of expected peak traffic periods (Chapter 1; Figure 7). The sharp morning peak and lower afternoon peak at Roosevelt (which are somewhat modified at Red Wash) are typical of more urban or traffic-impacted areas. The afternoon peaks in these urban profiles are likely lower for several reasons such as greater atmospheric mixing during the late afternoon and a broader afternoon peak in traffic as compared to the morning. The NO_x profiles at Ouray and Horse Pool exhibit a mid-day peak that coincides with a mid-day peak in traffic from a road 26 m north of the Horse Pool monitoring site (Chapter 1). The gradual overnight NO_x buildup at Ouray and Horse Pool suggests that more constant NO_x sources are also impacting these two sites. The remote Rabbit Mountain site has a flat profile consistent with a lack of any on-road source influence. These results suggest that on-road mobile sources are a driver of diurnal changes in NO_x concentrations at some locations in the Basin.

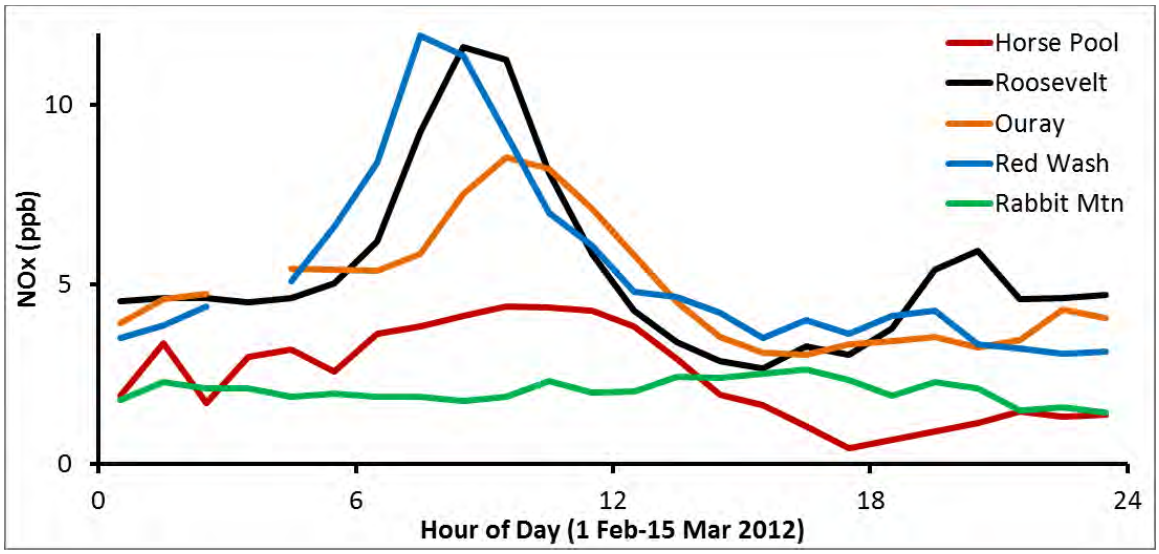

Figure 7. Average diurnal profiles of NO_x at five monitoring sites in the Basin (Chapter 1).

Passive VOC monitoring at multiple locations in the Basin showed that the concentration of heavier (C_6-C_{11}) VOC were highest in the oil and gas producing areas and were correlated with the number of wells located within 6 km of the monitoring site (Chapter 2). VOC composition also varied by location, with aromatics and cycloalkanes more abundant in gas producing areas than in oil producing areas. Data from the NOAA mobile lab showed significant methane enhancement above background levels and strong correlations of methane with alkanes (Chapter 5). The mobile lab also showed high concentrations of VOC downwind of known oil and gas-related sources. Methane data from multiple sites indicate that areas with high concentrations of gas wells (Ouray and Horse Pool) exhibited the highest methane concentrations (Chapter 1), consistent with methane data collected during the winter of 2010-11 (Martin et al., 2011).

Conclusions

While studies conducted to date did not specifically focus on the question of transport of ozone and precursors in the Uintah Basin, currently available evidence suggests that transported material is not likely to represent a major contribution to peak ozone events in the Basin. Additional data collection and analyses are needed to obtain a quantitative estimate of the contribution of transported material to Basin air quality.

Question A.5

What similarities and differences are there between the Uintah Basin and the Upper Green River Basin in Wyoming?

Background

This question is relevant to understanding the factors associated with Uintah Basin ozone episodes. A significant amount of data collection and analysis has been conducted in the UGRB, and results from the UGRB studies can help inform future work in the Uintah Basin.

Findings

Finding A.5.1*: *Winter ozone episodes in the Uintah Basin and UGRB share many key characteristics and data collected in either location are likely to be informative of factors associated with episodes in both basins.

Both the Uintah Basin and the UGRB are arid basins surrounded by higher terrain and located in sparsely populated portions of the Green River drainage (Figure 8) roughly 250 km apart that share a similar climate. The UGRB is about 600 m higher in elevation. The Uintah Basin is approximately 27,700 km^2; the UGRB is 18,700 km^2. Both basins experience elevated ozone concentrations during winter cold pool events that can last up to several days. Both basins contain intensive oil and gas exploration and production activity. However, oil production is greater in the Uintah Basin while gas production dominates the UGRB (see Figure 9). The Uintah Basin contains about 8000 active wells (Chapter 4), the UGRB about 5500 (WOGCC, 2012).

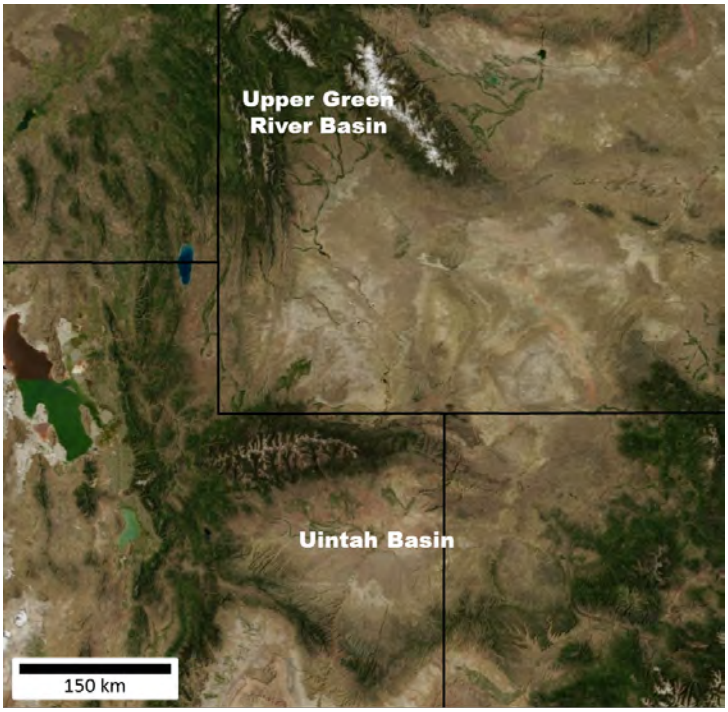

Figure 8. The Uintah and Upper Green River basins.

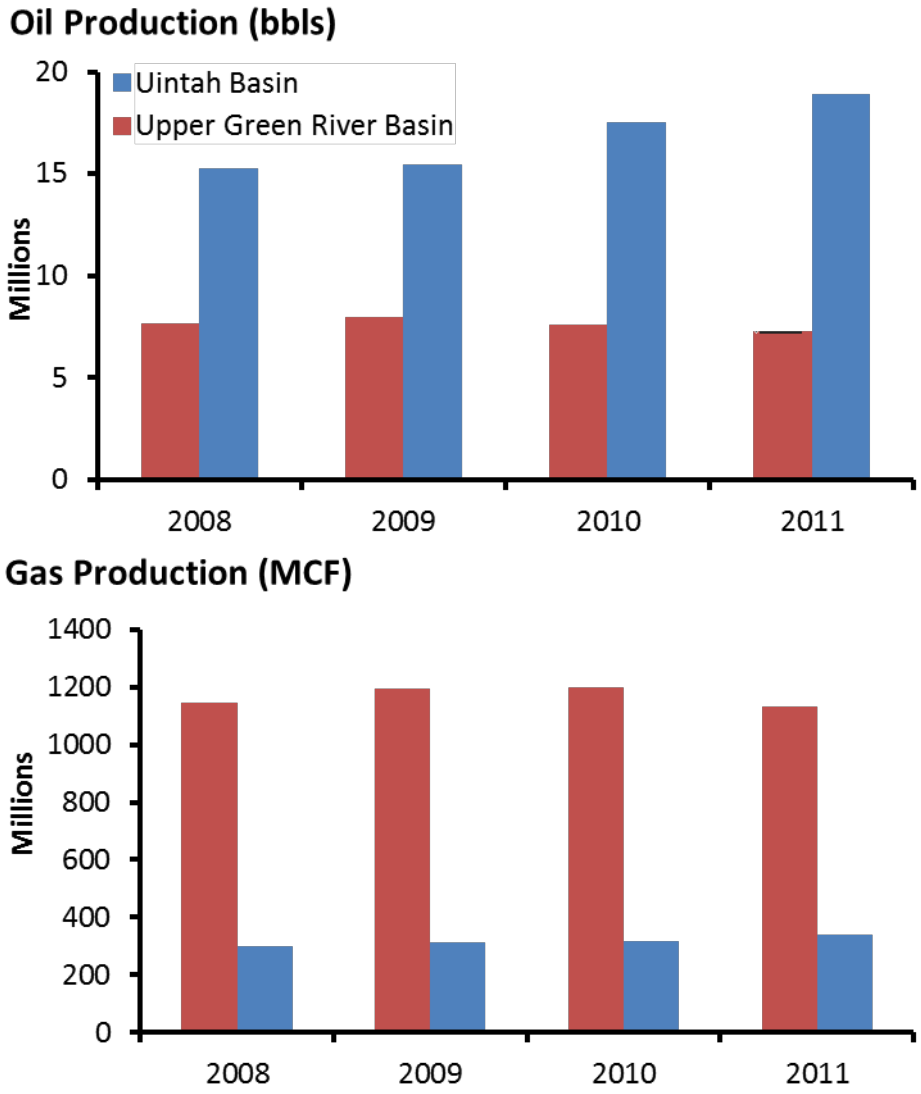

Figure 9. Annual oil and gas production in the Uintah Basin (Duchesne and Uintah counties; Utah DOGM, 2012) and the Upper Green River Basin (Sublette County; WOGCC, 2012).

A 2011 winter-specific emissions inventory for oil and gas activity in the UGRB reported 1914 tons of NO_x and 25,525 tons of VOC per month (WDEQ, 2012). Chapter 4 estimates 1100-1300 tons of NO_x and 9300 tons of VOC per month were emitted in the Uintah Basin in winter 2011-12. The UGRB inventory omits gas plants and on-road mobile sources, while these are 6-7% of NO_x and <1% of VOC in the Uintah Basin inventory, respectively. Emission densities of 0.1 tons of NO_x and 1.4 tons of VOC per km^2 in the UGRB, and 0.04 tons of NO_x and 0.3 tons of VOC per km^2 in the Uintah Basin are indicated.

Populations in both basins are concentrated in small towns. Uintah and Duchesne counties have a combined population of 51,195 (1.8 people per km^2), while the population of Sublette County, Wyoming is 10,247 (0.5 people per km^2; from 2010 Census).

A review of field measurements, data analyses, and modeling results for the UGRB is available (Hall et al., 2012). These analyses clearly confirm the association of winter ozone episodes with snow cover, strong inversions, and light winds. Elevated ozone concentrations have not been observed in the UGRB in the absence of snow cover. Data collected during the 2011 winter ozone episodes in the Uintah Basin (Martin et al., 2011) show that meteorological conditions during those events were very similar to those observed during UGRB ozone events. Similar to the UGRB, data collected during UBOS 2011-12 showed little local ozone production in the absence of snow cover.

Given the overall similarities of climate, emission sources, and winter ozone episode characteristics of the two air basins, collection and analysis of field study data in either basin can provide valuable information that is applicable to both.

Finding A.5.2*: *The Uintah Basin has some unique characteristics that require further study in order to design an effective ozone control strategy specifically for the Basin.

Some details of ozone production in the Uintah Basin are likely to be different from the UGRB. A 500-Megawatt coal-fired power plant, for example, is located within the Uintah Basin precisely where elevated ozone has been observed, but the only large power plants near the UGRB are well south of the area that has been shown to be involved in ozone production (WDEQ, 2009). No data are currently available with which to assess the contribution, if any, of power plant emissions to ozone exceedances in the Uintah Basin. Data collected during UBOS 2011-12 at the Horse Pool site include an event on 4 February 2012 that appears to be the impact of a plume from a nearby source with significant sulfur emissions (Chapter 3). Analysis of data from this event suggests that the plume is most likely from the Bonanza plant; however, this plume impact occurred under well-mixed conditions, not under the stable stratification associated with elevated ozone episodes. The extent to which the elevated Bonanza plume interacts with air close to the surface during ozone episodes is not known.

Given the greater amount of oil production in the Uintah Basin, VOC speciation and VOC/NO_x ratios are likely to differ between the two basins. Chapter 2 shows that the mix of VOC in oil-producing areas of the Uintah Basin is different than in gas-producing areas, perhaps leading to differences in the reactivity of VOC in each area.

NO_x emission sources and distribution are different for the two basins. Chapter 2 shows less NO_x in oil-producing than in gas-producing areas. The Uintah Basin has a higher population (and associated urban and traffic emissions) than the UGRB; monitoring showed higher NO_x at Vernal than any other monitored locations in the Basin, likely due to urban sources.

ENVIRON (2008) showed that ozone episodes in the UGRB are associated with recirculation of pollutants driven by a diurnal nighttime drainage and daytime upslope flow pattern. Similar detailed measurements and analysis of surface flow patterns during Uintah Basin ozone events have not been performed. The topography of the Uintah Basin is more complex than that of the UGRB, and wind patterns in the Basin can be very complex (Martin et al., 2011; Chapters 2 and 3; Question E.1). Further analysis of surface flow patterns in the Uintah Basin is needed.

Conclusions

Sufficient similarities between the Uintah Basin and the UGRB exist to merit continued analysis of the more extensive data set currently available for the UGRB to provide useful information

about ozone formation in the Uintah Basin. Surface air flow and the mix of precursor emissions in the Uintah Basin, however, are different from the UGRB, and the design of emission control strategies for the Uintah Basin cannot rely solely on studies from the UGRB.

Question A.6

Does significant vertical stratification of precursors occur? If so, what role does stratification play in ozone formation?

Background

VOC emissions in oil and gas production operations are expected to be released closer to the surface and to be less thermally buoyant than NO_x emissions. While NO_x emissions almost entirely are from fuel combustion and are released at heights ranging from near surface (e.g., heaters and boilers, on- and off-road vehicles) to small- or medium-sized stacks (e.g., compressor stations) to tall stacks (e.g., power plants), a large portion of VOC emissions are released from well sites or equipment at the same temperature as the surrounding air (Chapter 4). It is therefore reasonable to hypothesize a potential for vertical stratification of VOC and NO_x under the stable atmospheric conditions characteristic of ozone episodes. The resulting vertical gradients in VOC/NO_x ratios would produce vertical variations in ozone production and destruction rates and ozone responses to emission control strategies. For example, ozone formation during the morning hours may proceed more rapidly at locations and elevations with optimal VOC/NO_x ratios, and these rapidly formed ozone plumes could later impact monitoring stations. Knowledge of such vertical stratifications is needed to fully explain and accurately model the pattern of ozone and precursors observed over surface monitoring networks and the impacts of alternative emission control strategies.

Findings

Finding A.6.1*: *Vertical stratification of ozone precursors was observed at Horse Pool.

Measurements of NO_x and speciated VOC at five levels between the surface and 135 m at Horse Pool showed NO_x plumes impacting the site at various times and different elevations, even during relatively well-mixed conditions (Chapter 6; Figure 10). These observations are consistent with impacts at this site from nearby NO_x sources with varying effective plume heights. In contrast, VOC measurements showed that VOC such as ethane are more abundant near the surface and indicate a larger influence from sources near the surface (Figure 11). These results are limited to one location, and the degree to which they might apply to other locations in the Basin is not known.

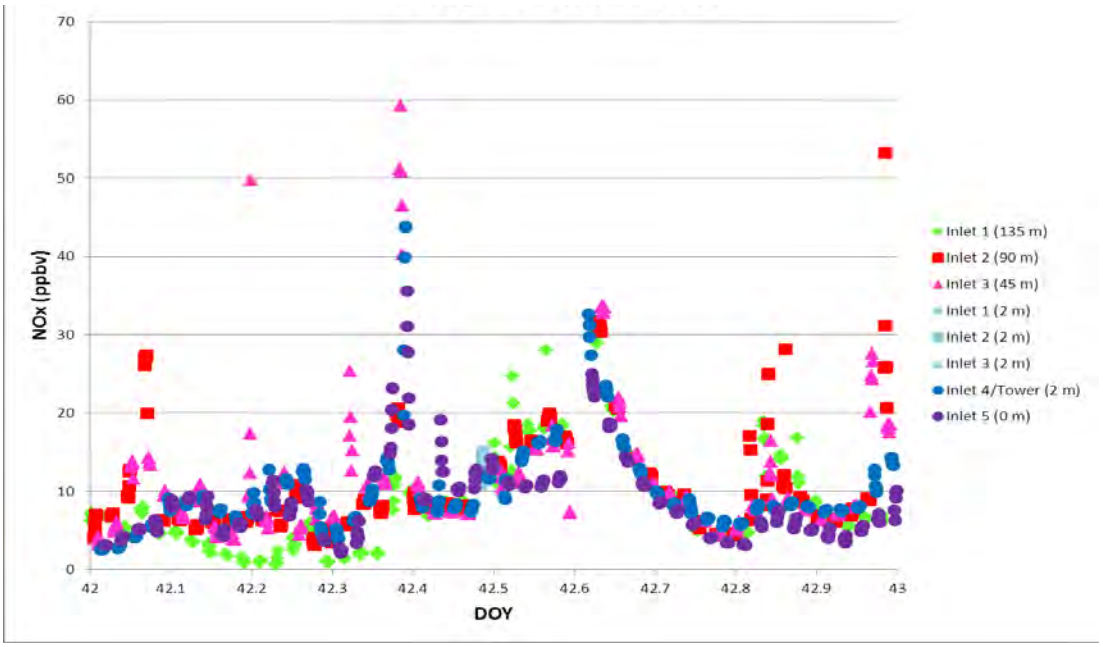

Figure 10. NO_x at different heights at Horse Pool on 11 Feb. 2012 (Chapter 6).

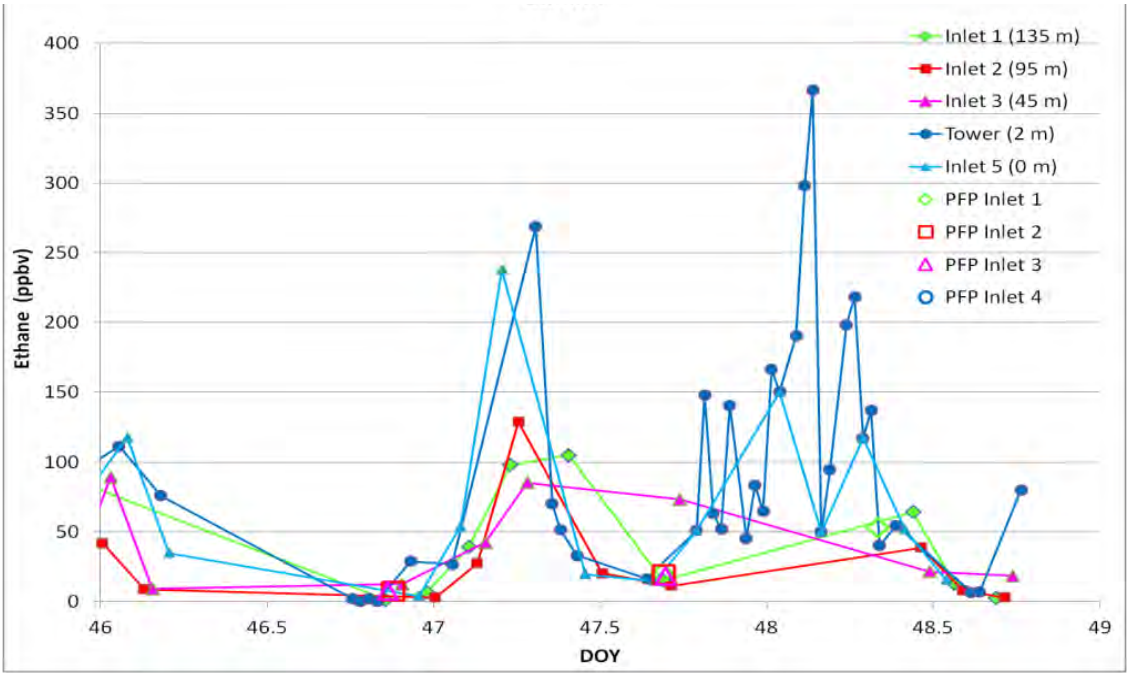

Figure 11. Ethane at different heights at Horse Pool on 15-18 Feb. 2012 (Chapter 6).

Most of the UBOS 2011-12 data were collected during periods without temperature inversions, and the vertical precursor stratifications noted above have the potential to be more prominent under conditions conducive to ozone formation, possibly resulting in daytime vertical ozone gradients.

Finding A.6.2*: *Under the well-mixed daytime conditions characteristic of the 2012 study period, ozone concentrations did not exhibit daytime vertical stratification. Ozone loss near the surface was evident at night.

Vertical ozone data collected at Ouray (Chapter 5; Figure 12) and other sites (Chapters 2, 3, 5, and 6) showed a temporal pattern wherein ozone concentrations were mostly uniform with height during the day, and loss of ozone, likely due to deposition and reaction of ozone with NO_x, was observed during the night under more stable conditions.

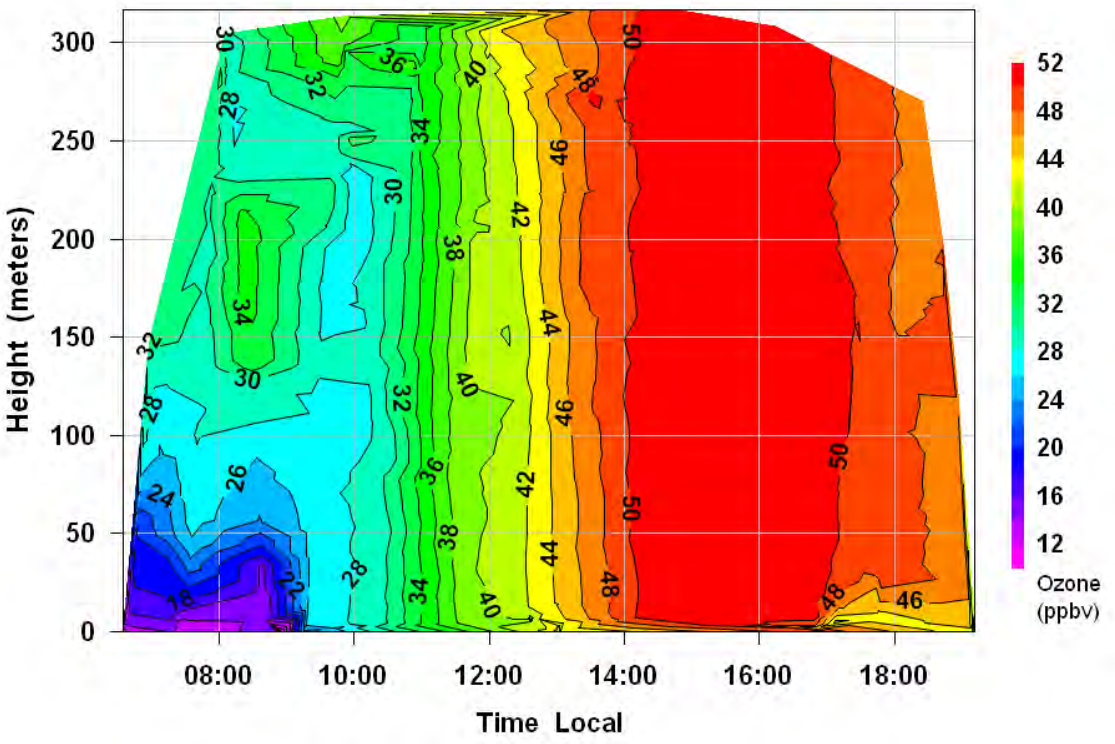

Figure 12. Time-height cross-section of ozone concentrations at Ouray interpolated from 20 ozonesonde profiles collected from sunrise to sunset on 17 Feb. 2012 (Chapter 5).

Conclusions

Despite the well-mixed daytime conditions encountered during UBOS 2011-12, some evidence of NO_x plumes above the surface and a prevalence of near-surface VOC sources impacting the Horse Pool site were observed. These data suggest that at least transient vertical gradients in VOC/NO_x ratios and ozone formation rates may exist under episode conditions. Similar measurements under conditions conducive to ozone formation are needed.

PART B: ATMOSPHERIC CHEMISTRY OF OZONE FORMATION

Question B.1

Do pathways for ozone production exist that are unique to wintertime ozone events?

Background

Our current understanding of ozone formation processes in polluted environments is based mostly on summertime ozone episodes occurring in large urban areas. Comparatively little is known about winter ozone formation in rural areas where the emissions budget is heavily influenced by oil and gas exploration and production activities (Chapter 4). Studies of winter ozone episodes in the UGRB have shown that these winter episodes are associated with snow cover and very stable "cold pool" atmospheric conditions and that ozone formation under these conditions is largely driven by the strong actinic UV flux resulting from the high albedo of the snow surface and the elevated concentrations of precursor pollutants trapped under the low level temperature inversion. Analyses of field study data and photochemical box modeling studies performed to date (ENVIRON, 2008; Schnell et al., 2009; Nopmongcol et al., 2010; Martin et al., 2011; Carter and Seinfeld, 2012) suggest that these two factors are key to the production of elevated winter ozone concentrations. In this respect, winter episodes are no different from summer episodes: both require a high UV flux, stable atmospheric conditions, and adequate concentrations of precursors.

Winter conditions in the Uintah Basin and UGRB nevertheless differ from urban summer conditions with respect to temperature, VOC composition, and the presence of a snow surface. In general, low winter temperatures decrease chemical reaction rates, though the effect of temperature on some reaction rates is not fully understood (Chapter 7; Martin et al., 2011; Carter and Seinfeld, 2012). Low temperature also limits water vapor mixing ratios; for example, the water vapor mixing ratio at 0°C, 50% humidity, and atmospheric pressure of 850 mbar is 2 g/kg, compared to more than 15 g/kg at 30°C and 50% humidity. A major pathway for the production of OH radicals in summer urban ozone episodes is photolysis of ozone followed by reaction of the freed oxygen atom with water vapor. Less water vapor in the atmosphere limits OH production from that pathway.

Analyses of data from pristine remote environments (Greenland and Antarctica) have identified sources of alkenes and NO_x within snow that appear to evolve via heterogeneous photochemistry (Swanson et al., 2002; Helmig et al., 2007). As pointed out by Stoeckenius and Ma (2010), however, the amounts of ozone precursors measured in these studies are far less than those found in areas with intensive oil and gas production such as the Uintah Basin or the UGRB, so drawing direct conclusions from this work is difficult. Nevertheless, heterogeneous reactions on snow surfaces could contribute to winter ozone formation. For example, elevated mid-day HONO concentrations over snow have been observed in the UGRB (ENVIRON, 2010; Rappenglueck, 2010) and are consistent with a hypothesized mechanism of formation of HONO from NO_x on the snow surface in the presence of sunlight. Sensitivity calculations performed by Carter and Seinfeld (2012) demonstrate that daytime heterogeneous HONO production may be sufficient to influence peak ozone concentrations under VOC limited conditions. The prevalence of VOC limited conditions in the Uintah Basin is not known.

Findings

Finding B.1.1: While conditions conducive to ozone formation were not observed during UBOS 2011-12, information about radical sources during this period may have applicability to ozone formation episodes.

Photolysis of ozone was a minor contributor to radical production during UBOS 2011-12, in contrast to typical summertime ozone production conditions (Chapter 3). Cl atoms derived from nitryl chloride were as important a radical source as ozone photolysis. However, the most likely chloride source is the soil, which is covered with snow during winter ozone episodes, so the significance of nitryl chloride photolysis on winter ozone production is not known. Mean concentrations of HONO were much lower than in urban areas in summertime. However, HONO was still a significant source of OH radicals during the study (Chapter 3).

Formaldehyde was a significant radical source during UBOS 2011-12 (Chapter 3). Formaldehyde concentrations were lower on average than values measured in Houston and Pasadena (Chapter 3). Formaldehyde at Horse Pool usually correlated with methanol (Figure 13) and this correlation was not related to the time of day, suggesting the formaldehyde is present as an impurity in the liquid methanol used as an antifreeze in oil and gas operations (Chapter 3; chemical analysis of methanol used in the Uintah Basin is needed). In some cases, formaldehyde spikes were not correlated with methanol but were correlated with CO, suggesting that these spikes were associated with fuel combustion (Chapter 3). Analysis by the University of Wyoming showed that formaldehyde, acetone, and organic aerosol mass were temporally related, indicating a photochemical source for formaldehyde (Chapter 3), and formaldehyde did experience diurnal cycling, with higher concentrations in daytime, providing more evidence for a photochemical source (Chapter 1).

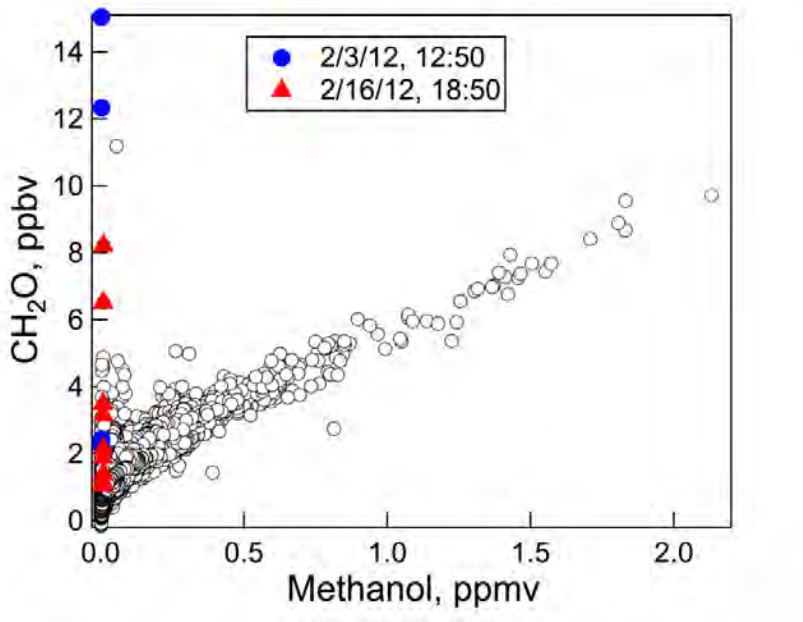

Figure 13. Correlation of formaldehyde and methanol at Horse Pool, with two unusual plumes denoted in blue (2/3 12:50) and red (2/16, 18:50) (Chapter 3).

Conclusions

Relative contributions of different radical sources to ozone production are likely different for wintertime ozone episodes in the Uintah Basin than for typical summertime cases in urban areas. Because conditions conducive to ozone formation did not exist during winter 2011-12, further work to determine radical sources and heterogeneous chemical mechanisms is needed.

Question B.2

Do VOC speciation and reactivity in the Basin have unique characteristics that contribute to wintertime ozone production?

Background

Data collected in the UGRB show that VOC emissions in oil and gas producing regions are strongly influenced by natural gas. Natural gas VOC speciation is heavily weighted towards light alkanes, making it markedly different from VOC mixtures typically encountered in large urban areas (ENVIRON 2008, 2010; Stoeckenius and Ma, 2010). Due to the widely differing reactivities of individual VOC species, variations in VOC composition can have significant impacts on ozone formation and the relative efficacy of VOC and NO_x control strategies. A thorough understanding of VOC speciation in the Uintah Basin and of the reactivities of VOC species under winter ozone episode conditions is an important prerequisite to the design of effective ozone control strategies.

Findings

Finding B.2.1*: *Observed hydrocarbon species abundances at most locations sampled in the Uintah Basin differ significantly from those found in large urban areas but are similar to those found in other western U.S. oil and gas production regions.

Methane levels in the Uintah Basin averaged 2.7 +/- 0.3 ppm, above observed background levels of 1.7 – 1.8 ppm (Chapter 1). Data from 2011 indicate average methane of 1.7 +/- 0.2 ppm at Vernal and 2.8 +/- 0.6 at Red Wash (Martin et al., 2011). Similarly elevated methane levels have been observed in the Upper Green River Basin (ENVIRON, 2008) and the Denver–Julesburg Basin (Petron et al., 2012).

Speciated VOC data collected during UBOS 2011-12 were heavily weighted towards light alkanes, similar to other areas with significant oil and gas production and different from most urban areas (Chapter 3). For example, mixing ratios of alkanes, and to a lesser extent, benzene, toluene and m,p-xylene, are higher in the Horse Pool data than in samples from the summertime Pasadena area, where alkenes and oxygenated compounds (except methanol) are more abundant (Figure 14).

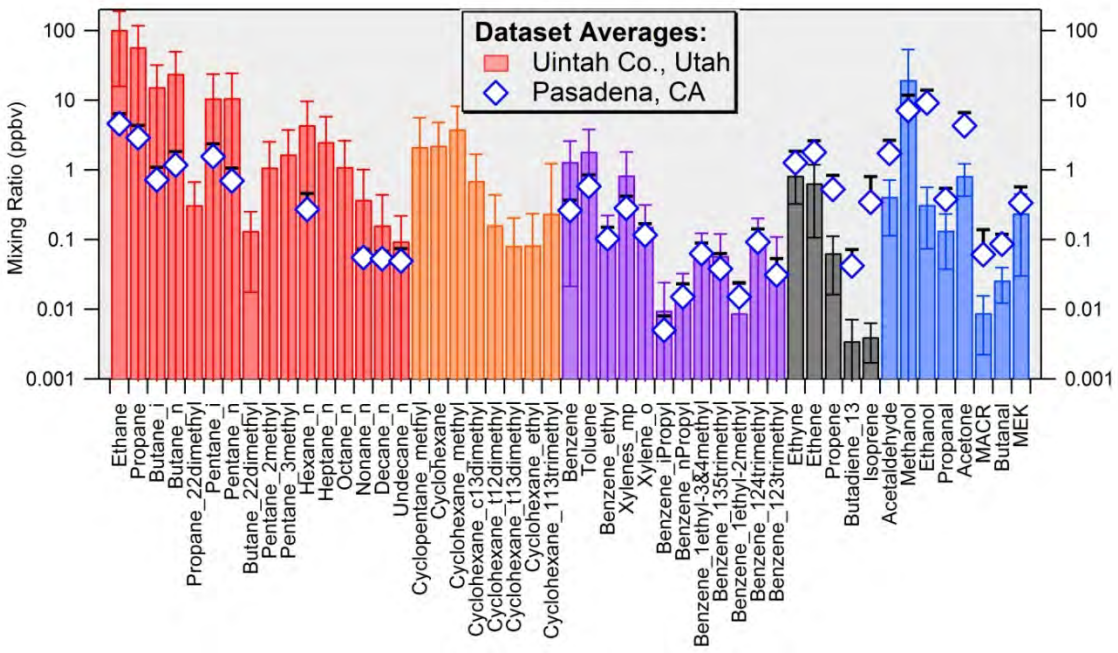

Figure 14. Mean mixing ratios collected during 15 January-29 February at Horse Pool and during May-June 2010 at Pasadena, California (Chapter 3).

Concentrations of iso-pentane and n-pentane were much higher at Horse Pool than in the Pasadena samples and are more similar to samples collected by NOAA researchers in Weld County, Colorado, in the Wattenberg Gas Field (Figure 15; Chapter 3). In addition, ratios of iso- to n-pentane at Horse Pool were significantly lower than in the Pasadena samples. Authors of Chapter 3 point out that the Horse Pool and Weld County ratios are similar to iso- to n-pentane ratios found in Wattenberg gas composition analyses whereas the Pasadena ratio is similar to that of light duty vehicle exhaust. Detailed gas composition analyses for the Uintah Basin are needed to validate these findings, and comparisons with VOC speciation in the UGRB are needed.

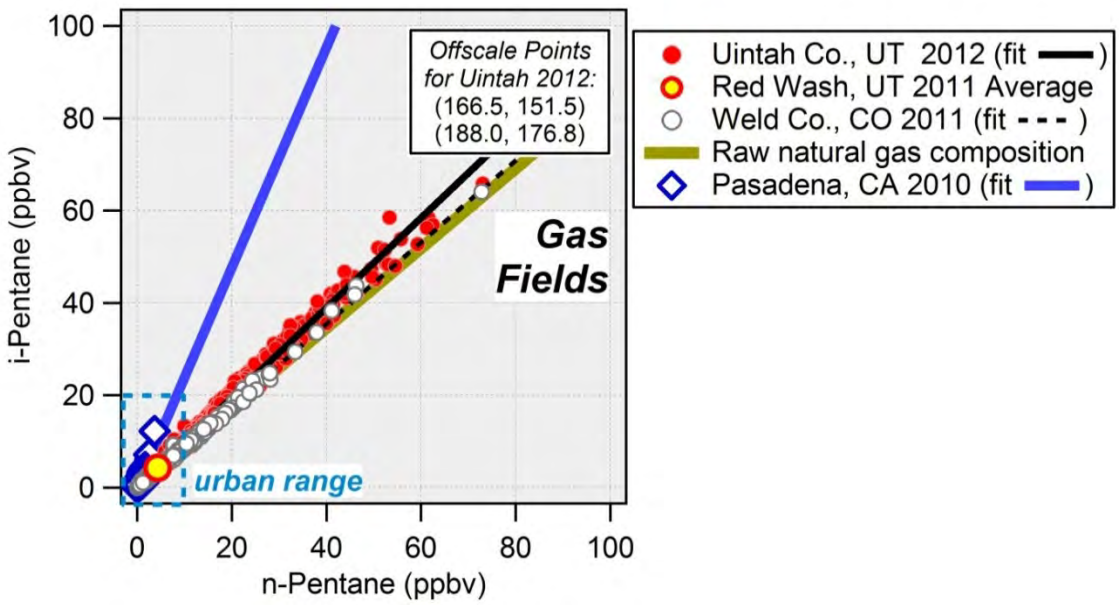

Figure 15. Iso-pentane to n-pentane ratios from data collected during 15 Jan.-29 Feb. at Horse Pool, during 21-25 Feb. 2011 at Red Wash, during 2011 in Weld Co., CO and during May-June 2010 in Pasadena, CA (Chapter 3).

Speciated VOC data from the Roosevelt site, which is more populated and located further away from the main concentration of gas wells, suggest a mixed influence of urban (mostly light duty vehicles) sources and oil and gas emissions (Chapter 1). Light alkanes were the most abundant species found in the Roosevelt samples, but alkenes were not detectable. Linear regression fits produced a benzene/toluene slope of 0.33 at Roosevelt, lower than the 0.80 slope found at Horse Pool and more representative of a typical urban source mix. Similarly, the benzene/o-xylene slope at Roosevelt (3.06) was lower and more representative of gasoline engine emissions than the 7.49 slope observed at Horse Pool. On the other hand, butane at Roosevelt was found to be more enriched relative to toluene than would be expected in a mobile source-dominated urban area, and an even greater enrichment occurred at Horse Pool.

VOC sampling at a variety of locations with the NOAA mobile laboratory (Chapter 5) showed that ethane and heavier alkanes were well correlated with methane across most samples, indicating a common source. Sampling downwind of certain sources, including a well completion operation with an open pond to retain fluid used in hydraulic fracturing, found elevated levels of reactive aromatics. Emission rates from ponds that retain used fracturing fluid are not known, and the prevalence of the practice of retaining fracturing fluid in open pits in the Uintah Basin is not known with certainty. New Source Performance Standards recently promulgated by EPA are expected to decrease emissions during gas well completions due to required separation and capture of gas and condensate from returned fracturing fluid (EPA, 2012).

Passive VOC sampling showed that VOC speciation is different in oil producing areas than in gas producing areas of the Basin (Chapter 2). These speciation differences could impact VOC reactivity and the effectiveness of NO_x versus VOC controls in mitigating winter ozone issues in different areas of the Basin.

Finding B.2.2: Elevated levels of alkenes were not observed during UBOS 2011-12.

Alkenes are known to be among the most reactive VOC and can, therefore, play an important role in ozone formation. The NOAA mobile laboratory measured and reported speciated hydrocarbon mixing ratios, including alkenes, from discrete air samples collected throughout a major portion of the Basin (Chapter 5). The median ethene measurement was less than 0.1 ppb, and the median propene and 1-butene concentrations were measured to be approximately 0.05 ppb. Alkenes are not known to be a significant component of raw natural gas, and direct emissions of alkenes from non-combustion oil and gas processes are expected to be low.

Sorbent tube VOC samples collected at Red Wash in February 2011 contained elevated acetylene (a.k.a. ethyne), ethene, propene, and isoprene (Martin et al., 2011). The source of the elevated values in the 2011 data is unclear, though it may be the result of uncertainties in sampling or laboratory analysis procedures. Isoprene in particular is expected to be low during winter in the Uintah Basin (Sakulyanontvittaya et al., 2012). Further measurements of alkenes in ozone producing conditions are needed. Many of the VOC canister samples collected in the Upper Green River Basin have been reported to contain light alkenes, though mostly at relatively low concentrations (ENVIRON, 2008, 2010).

Conclusions

Data collected during the UBOS 2011-12 measurement campaign indicate that VOC speciation, particularly outside of urban areas, appears to be dominated by oil and gas-related emissions; light alkanes, therefore, make up a larger portion of VOC in the Basin than is the case in urban areas. VOC speciation, however, is not uniform throughout the Basin.

PART C: SOURCES OF OZONE PRECURSOR EMISSIONS

Question C

What are the sources of ozone precursor emissions in the Basin?

Background

Ozone precursor emissions in the Uintah Basin are associated with a variety of sources. Anthropogenic emissions consist of typical urban (residential, commercial, and light industrial) source emissions associated with the approximately 50,000 residents, agricultural activities, a 500-Megawatt coal-fired electric generation unit, phosphate and gilsonite mining, and oil and gas extraction activities. Mining activities, calculated to account for less than 1% of NO_x and VOC emissions, were excluded from the inventory. Ancillary activity at the Bonanza plant (coal and waste handling, etc.) was not estimated, but emissions are expected to be low relative to Basin's emissions as a whole. Oil and gas-related emission sources include gas plants, compressors, well site sources (drill rigs, frac pumps, pump jacks, tanks, dehydrators, fugitives, et al.), pipelines, on-road and non-road mobile sources, produced water evaporation ponds, reserve pits, and so on (Figure 16). Non-anthropogenic emissions in the Basin include biogenic emissions of isoprene and other VOC and natural hydrocarbon seeps.

A complete and accurate emissions inventory is vital to the development of an ozone control strategy and is an essential part of regulatory photochemical modeling.

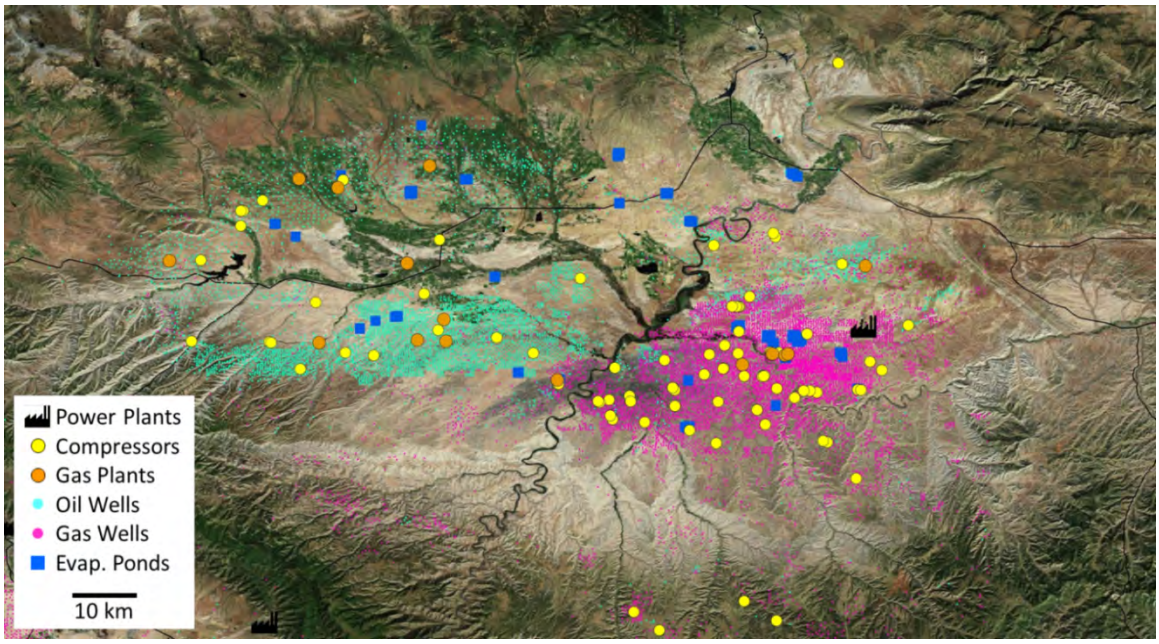

Figure 16. Locations of some oil and gas-related emissions sources in the Uintah Basin (the location of coal-fired power plants are also shown).

Findings

Finding C.1: Oil and gas-related sources are responsible for the majority of NO_x and VOC emissions in the Uintah Basin.

An emissions inventory for winter 2011-12 in the Uintah Basin was produced in Chapter 4 (Table 3). Some sources were not considered in this inventory, as explained in Chapter 4. Oil and gas-related emissions were based on WRAP Phase III projections (WRAP, 2012), with a number of updates, additions, and changes. The inventory shows that oil and gas emissions account for 98-99% of VOC emissions in the Basin (assuming parity between VOC and non-methane hydrocarbons [NMHC] since the percentage of NMHC that is ethane, which is required for calculation of VOC from NMHC, is unknown) and 58-62% of NO_x emissions (range of estimates). The Bonanza Power Plant accounts for 31-35% of NO_x emissions, the largest single NO_x source and source category in the inventory. Glycol dehydrators are the largest VOC source category. These are known to emit aromatic compounds that are especially reactive in ozone production, but new and existing glycol dehydrators will be regulated under new rules recently announced by EPA, which may reduce emissions from dehydrators in the Basin (EPA, 2012; Question D). The largest oil and gas-related source category for NO_x is compressor stations (20-23% of total NO_x emissions). Drill rigs, workover rigs, and fracking processes account for 11-19% of NO_x emissions (based on industry survey).

Table 3. Uintah Basin emissions estimates by category for February, in tons per month (Chapter 4). Some sources and estimates provided emissions of organic compounds as VOC, while some used non-methane hydrocarbons (NMHC). VOC usually excludes ethane, while ethane is included in NMHC. The percentage of NMHC that is ethane is not known for many sources, so conversion of NMHC to VOC is not possible at this time. Methane estimates for many oil and gas operations were not made.

SOURCE CATEGORY	VOC	METHANE	NMHC	NO_X
OIL & GAS EMISSIONS				
• **Glycol dehydrators**	2200†			13†
• **Heaters**				110†
• **Drill rigs**		0.39•	4.0•	330† or 156•
• **Workover rigs**		0.018•	0.18•	13† or 6.9•
• **Fracking processes**		0.055•	0.56•	22•
• **Pneumatic devices**	1850†			
• **Fugitives**	240†			
• **Venting processes**	180†			
• **Condensate tanks**	1700†			
• **Oil tanks**	1600†			
• **Pneumatic pumps**	1000†			
• **Compressor engines**◈	9†			47†
• **Artificial lift engines**	75†			240†
• **Other**	240†			13†
• **Compressor Stations**	130			390
• **Gas Plants**	25			14
• **Evap. ponds, land farms**[2]	0			0
• **Pipeline fugitive emissions**[5]		72	3.8	
TOTAL OIL & GAS	**9200**		**8.5**	**1000 to 1200**[3]
NON OIL & GAS EMISSIONS				
• **Bonanza Power Plant**				610
• **Mobile sources**[6]		4.4	68	106
• **Biogenic/Agricultural**		420		
• **Home Heating**		49	22	2.2
• **Land Fills**		37		
• **Natural Hydrocarbon Seeps**[5]		500*	25*	
TOTAL NON OIL & GAS		**510 to 1000**[4]	**90 to 120**[4]	**720**
GRAND TOTAL	**9200**		**98 to 130**[4]	**1700 to 1900**[3]

◈ Non-centralized.
† Estimates taken directly from WRAP 2012 projections.
• Estimates based on 2012 industry survey.
* Poorly constrained estimate (tightest bounds at this time put value between 30 and 30,000 tons/month).
[2] Data insufficient to estimate emissions for all ponds in winter conditions.
[3] Lower value results if the 2012 industry survey replaces WRAP projections.
[4] Lower value results if the contribution of natural seepage is omitted.
[5] Assumes 95/5 split in CH_4/NMHC percentages (Rice, et al, 1992).
[6] Likely does not include a complete accounting of mobile sources related to the oil and gas industry.

Because of multiple regulatory jurisdictions (see Introduction), it can be difficult to obtain accurate inventories of oil and gas facilities in the Uintah Basin. Emissions estimates for compressor stations and gas plants in Chapter 4 were not taken from the WRAP Phase III inventory but were instead based on a new list of facilities derived from state, local, federal, and private documents. This is likely to be the most accurate count of compressors and gas plants conducted for the Basin to date. Equipment and practices in the oil and gas industry are constantly updated, but the WRAP Phase III data on which much of the Chapter 4 inventory is based are more than six years old. A new, comprehensive inventory for the Uintah Basin is needed.

Natural and biogenic sources of VOC can be difficult to estimate. Chapter 4 assumes no emissions of VOC from biogenic sources, but a new study by Sakulyanontvittaya et al. (2012) provides a more detailed analysis and estimate of wintertime biogenic emissions for the region. Sakulyanontvittaya et al. estimate Basin-wide isoprene emissions of 0.0-0.2 tons per day in January, compared to 59-89 tons per day in July. It is anticipated that biogenic emissions of other VOC are likewise low in the Basin during winter. Chapter 4 estimates that methane emissions from cattle amount to 14 tons per day (methane likely plays only a minor role in ozone production in the Basin; Chapter 3). Estimates of emissions of methane and other hydrocarbons from natural (and anthropogenically enhanced) seepage are poorly constrained, and values in Table 3 should be used cautiously (Chapter 4).

Finding C.2: More analysis is needed to determine whether ambient measurements corroborate emissions inventories.

Chapter 2 shows that differences in NO_x and VOC concentrations between oil and gas producing areas of Duchesne and Uintah Counties agree with differences in emissions reported in the WRAP Phase III inventory (WRAP, 2012). Measurements by several investigators showed associations between known emissions sources and ambient concentrations (Question A.4; Chapters 1, 2, 3, 5, and 6). However, attempts to quantitatively evaluate NO_x and VOC emission sources, or to assess the accuracy of current inventories in a quantitative way, were not conducted as part of UBOS 2011-12.

Quality assurance of emissions inventories via reconciliation with ambient air quality data is an important component of air quality management. In addition to further analyses of UBOS 2011-12 data, new studies are needed to provide results that can be used to acquire quantitative information concerning emissions.

Conclusions

Oil and gas dominate Uintah Basin emissions inventories, though other significant sources exist. Further work to refine emissions estimates and verify inventories against ambient measurements is needed.

PART D: MITIGATION STRATEGIES

Question D

What possible mitigation strategies should be considered for adoption in the Uintah Basin?

Background

Current data is insufficient to determine the level of control that could eventually be required to achieve ozone-reduction objectives. Furthermore, it is not known at this time whether winter ozone problems in the Basin will be more effectively mitigated by NO_x or VOC controls, nor is it known whether control requirements will need to vary across the Basin. NO_x emissions reductions under VOC limited conditions can result in increases in ozone (Nopmongcol et al. 2010; Carter and Seinfeld 2012). VOC emission reductions, on the other hand, do not typically lead to an increase in ozone formation. Determination of whether the Basin (or different sections of it) is NO_x or VOC limited is critical to developing an effective, efficient mitigation strategy. To acquire this knowledge, measurements that coincide with conditions conducive to ozone formation, along with further analysis and modeling, will be required.

Carter and Seinfeld (2012) conducted box modeling for winter ozone episodes in the UGRB, including an analysis of whether ozone production was sensitive to NO_x or VOC controls. They found that ozone concentrations were VOC sensitive in three out of the four cases studied. Box models of a site in Boulder showed NO_x sensitivity in 2008, but VOC sensitivity in 2011. VOC/NO_x ratios and VOC speciation and reactivity may be significantly different in the two basins, so extrapolation of these findings to the Uintah Basin would be inappropriate. Carter and Seinfeld suggest, "determination of emission controls for the UGRB will require careful attention to the geographical distribution of both VOC and NO_x emissions and meteorology," and they note that 3D photochemical modeling will ultimately be required to understand the issue comprehensively. Similar attention and work will likely be required to determine whether winter ozone production in the Uintah Basin is sensitive to NO_x or VOC controls.

VOC emissions reductions are anticipated over the next several years due to new EPA rules, particularly the New Source Performance Standards for the oil and gas industry (EPA, 2012). Some of these standards became mandatory in 2012, and some will be phased in over the next three years. These standards target VOC emissions from oil and gas operations and are likely to reduce emissions from well completion activity, storage tanks, some well-site equipment, and compressors in the Basin, though they only cover new or modified sources. Also, EPA's new National Emission Standards for Hazardous Air Pollutants will limit emissions of aromatic compounds and other VOC from new and existing glycol dehydrators. These standards exclude some VOC sources, including but not limited to produced water disposal facilities, oil well completions, pipeline venting, and portions of the transmission segment of the oil and gas industry. For the most part these rules cover new sources only. They do not target NO_x emissions from the oil and gas industry and may increase NO_x in the Basin because of the requirement to flare emissions from storage tanks and other sources.

Any additional control programs implemented in the Basin could be mandatory or voluntary. Episodic control programs specific to conditions conducive to ozone formation could be considered. Traditionally, full-time emission control measures have been used to address air quality management needs, but episodic control could potentially be an effective air quality management tool in the Uintah Basin. This viewpoint is supported by the fact that winter ozone episodes in the Basin are highly episodic, occur only under very specific meteorological conditions that typically only last a few days at a time, and are relatively infrequent. Ozone concentrations in the intervening periods are near background levels, and other pollutants are generally well below EPA standards.

Voluntary episodic control programs in the form of "ozone action days," during which residents and businesses are urged to reduce driving and other emissions-generating activities when meteorological conditions favor ozone formation, are common in large metropolitan areas. A voluntary episodic emission control program has been instituted by the Wyoming Department of Environmental Quality in connection with ozone mitigation efforts in the UGRB (Hall et al., 2012). It is not known, however, whether episodic controls would be adequate to mitigate air quality concerns in the Uintah Basin.

Ultimately, a validated photochemical model that simulates winter ozone formation will be needed to fully understand and quantify the effectiveness of mitigation strategies and to tailor an emissions reduction program that is appropriate for the Uintah Basin. This modeling framework will rely on the data collected from studies in the Basin to provide meteorological and emissions inventory inputs, boundary conditions, and validation of ozone and precursor concentrations estimated by the model. This modeling effort is in the beginning stages.

Findings

Finding D.1: The study team's best current estimate is that VOC controls will reduce ozone production, but the overall effectiveness of this strategy is unknown.

Options to lower VOC emissions include:

- Reduce emissions from large sources of aromatic VOC since these are highly reactive with respect to ozone formation.
    - Elevated concentrations of aromatics were observed downwind of a well completion operation (Chapter 5). The influence this source category has on overall ozone production in the Basin is not known; however, New Source Performance Standards will reduce emissions of aromatics and other organic compounds from well completion operations since they require separation and capture of gas and condensate from water received from the well during completion (EPA, 2012).
    - Glycol dehydrators constitute another large source category for aromatics. Emissions from new and existing glycol dehydrators will be regulated by recently promulgated National Emission Standards for Hazardous Air Pollutants (EPA, 2012).
- Deploy other VOC-reduction strategies such as green completions, low bleed pneumatics, tank controls, and liquid collection systems controls where economically feasible. EPA's New Source Performance Standards require controls for some of these source categories, but only for new or modified equipment.

Finding D.2: Scientific data collected to date are insufficient to assess the degree to which NO_x reductions will be effective in reducing peak ozone concentrations.

Data collected in Chapter 5 suggest that some engines may be operating inefficiently (significant primary NO_2 emissions were observed) and that air quality benefits may be realized via more efficient operation of pump jack engines and other equipment. Engine emissions tests in the UGRB in 2011 found that many engines were operating inefficiently due to maintenance and operational problems (Dietrich, 2011; Hall et al., 2012). Proper maintenance and operation of engines may reduce NO_x emissions.

Finding D.3: A voluntary "ozone action day" program that encourages reductions in ozone precursor emissions and reductions in public exposure to elevated ozone concentrations during unfavorable weather conditions is a potentially useful mitigation tool.

Implementation of a voluntary "ozone action day" program modeled after similar programs in Wyoming (Hall et al., 2012) and elsewhere may provide public health benefits by reducing ozone exposure. These programs rely on forecasts of unfavorable weather conditions, typically with 24- to 72-hour lead times, that trigger a set of public outreach activities designed to alert businesses and the public of the ozone episode forecast and encourage actions that reduce both emissions and ozone exposures. Recommended actions might include temporarily delaying well completions until conditions improve, reducing other oil and gas field work as much as possible, reducing driving, avoiding outdoor activities, and so on. Data from UBOS 2011-12 do not specifically address questions regarding the potential efficacy of episodic controls.

UDEQ already issues three-day forecasts for air quality in the Uintah Basin. These forecasts are publicly available at http://www.airquality.utah.gov/aqp/vl.html and could be used as the basis for an episodic control program.

Conclusions

It is not known whether VOC or NO_x emission controls in the Basin would be most effective, but reductions in VOC are unlikely to increase ozone production and may provide a significant benefit. A voluntary ozone action day program could reduce ozone and protect public health during ozone events. New EPA rules are likely to reduce emissions of VOC, including reactive aromatics.

PART E: ADDITIONAL INFORMATION NEEDS AND MODELING ISSUES

Question E.1

What special challenges does the Uintah Basin pose for meteorological modeling?

Background

The Uintah Basin is broad (approximately 100 by 150 km) with numerous topographic features (on the order of tens to hundreds of meters) through a majority of the area. During the elevated ozone periods in winter 2010-11, the region had relatively light winds (Martin et al., 2011). Light wind conditions in complex terrain often feature thermally driven mountain-valley wind systems associated with diurnal surface heating and cooling cycles. These wind systems tend to blow up-valley or upslope during the day and downslope or down-valley (a.k.a. drainage flow) at night (Banta and Cotton, 1981). At a given time of day, the local winds blow from a preferred direction for several hours, and these diurnal patterns are often visible in multiday averages or composites.

The daytime component of local winds in winter often may not be well developed due to low solar angles and short day lengths, resulting in weak surface heating, weak forcing, and local winds that may be difficult to detect (Vergeiner and Dreiseitl, 1987). It is as yet unknown whether a discernible diurnal pattern in low-level winds in the Uintah Basin under winter ozone episode conditions exists. If diurnal upslope-downslope flows do exist, they may enhance ozone

production by recirculating pollutants and their reaction products, as has been observed in the UGRB (Stoeckenius and Ma, 2010).

During the 2010-11 measurement campaign, ozone concentrations were found to vary considerably across the Basin. This variability could be in part due to the uneven distribution of sources in the Basin and/or topographical and meteorological phenomena, including atmospheric transport over the complex terrain. The highest concentrations of ozone were measured at the lowest-elevation sites (Martin et al., 2011), which could be explained by drainage flows; however, elevated concentrations have been observed at higher-elevation sites on the far western edge of the UGRB in association with afternoon upslope flows (MSI, 2011), and at Whiterocks in the Uintah Basin in 2011 at an elevation of more than 6000 feet.

Meteorological models that will likely be used to support air quality modeling in the Basin were developed primarily for weather forecasting. Much of the research on and evaluation of these models has focused on their ability to replicate weather phenomena important to forecasting (i.e., frontal passage movement, hurricane track, cyclogenesis). Fewer development resources have been spent on the applicability of models for simulating the important features for weakly forced flows under inversion conditions. It is important that particular attention be given to meteorological model development and validation for winter air quality modeling in the Basin.

Findings

Finding E.1.1: Very different wind processes were identified during strong and weak wind conditions during UBOS 2011-12.

During UBOS 2011-12, strong-wind periods at Horse Pool were generally dominated by large-scale meteorological systems, as is typical of wintertime conditions in mid-latitude locations (Chapter 3). Under these conditions, near-surface winds are driven by stronger winds aloft, as illustrated in Figure 17. During weak-wind periods, the effects of local forcing become evident if the forcing is strong enough. Figure 18 shows the evolution of wind profiles on a day when such forcing is clear. On this day the nighttime winds had a distinct easterly component, while daytime winds were from the west up to several hundred meters above ground level. This diurnal pattern was observable at Horse Pool on most light-wind days during the 2011-12 study, and in composites of all days when the winds aloft were light (< 4 m/s), showing easterly flow draining toward the Green River at night and westerly upslope flow during daytime hours.

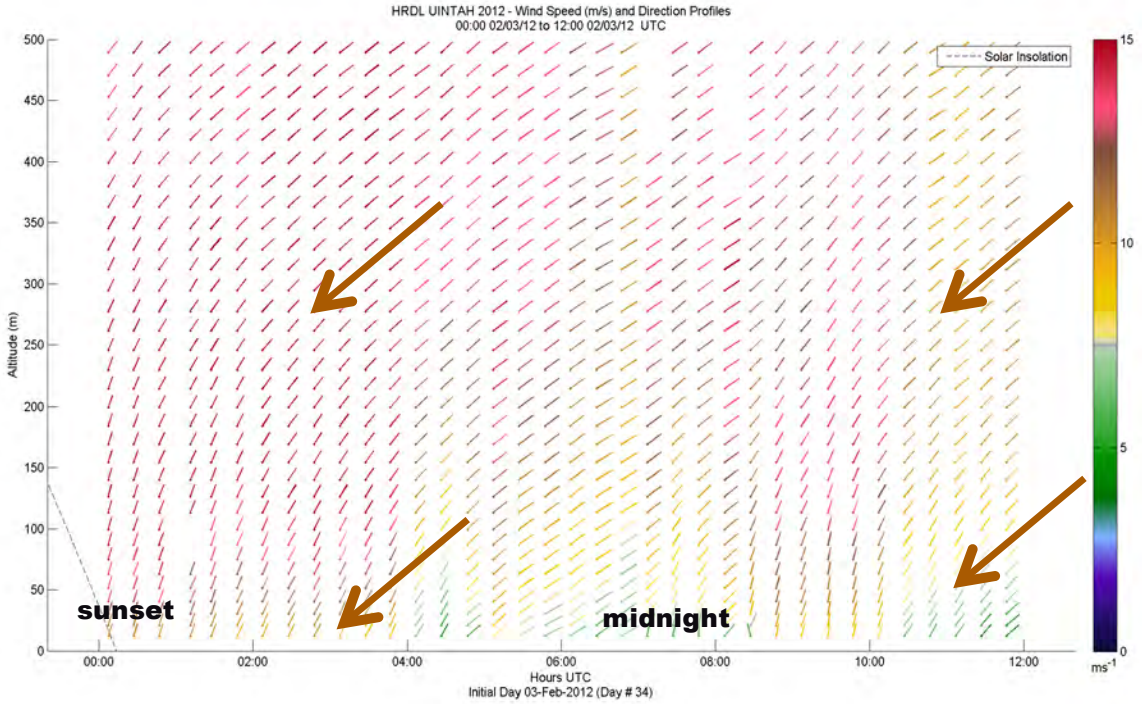

Figure 17. Profiles of 20-min wind speed and direction for 0000-1200 UTC on 3 Feb. 2012 at Horse Pool, showing strong northeasterly flow at 500 m above ground, extending down to the surface (Chapter 3). Wind barbs indicate direction from which winds were blowing, and color coding of barbs indicates wind speed as shown on color bar. Horizontal axis is time (UTC, which is 7 hr ahead of MST), and vertical axis is height above ground (m).

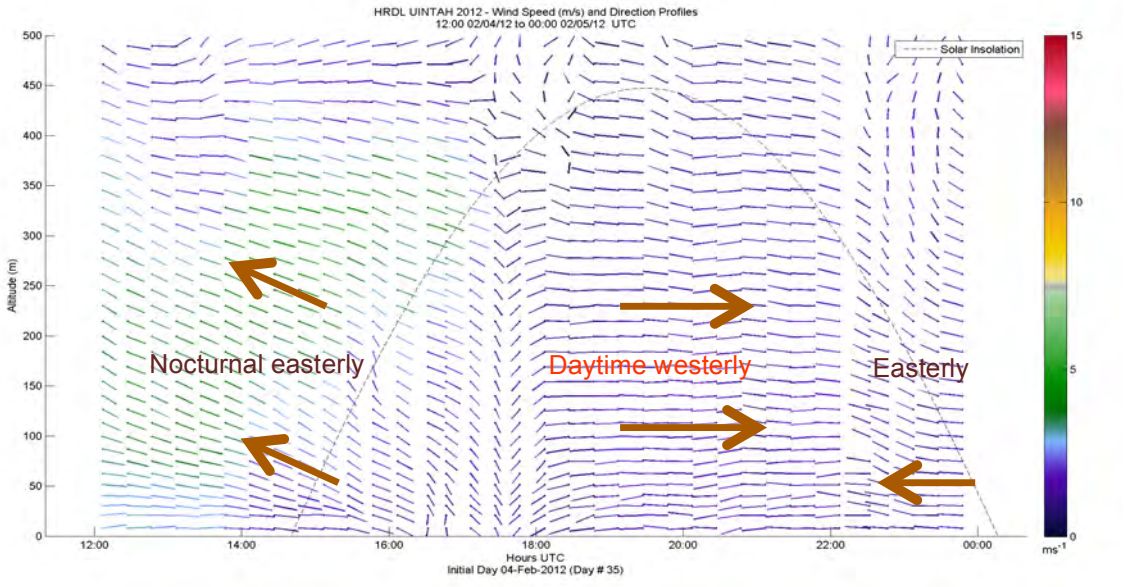

Figure 18. Profiles of 20-min wind speed and direction from 1200 UTC on 4 Feb to 0000 UTC on 5 Feb. 2012 at Horse Pool, showing diurnal cycle of winds below 500 m (Chapter 3). Dotted black curve is clear-sky solar flux, indicating daylight hours. Wind barbs and axes are as in Figure 17.

Finding E.1.2*: *Measurements showed significant variation of winds across the Basin and with time of day.

Figure 19 shows average day and night wind vectors at 14 meteorological stations around the Uintah Basin during February 2012 (Chapter 2). These results show that day and night mean wind directions were not consistent across the Basin, even among some sites that are in relatively close proximity. Most of the sites exhibit upslope/downslope flow that leads to near-180 degree shifts in wind direction between night and day. The directions of the day-night flows are not consistent at different sites and appear to be directed by local terrain; thus, the complex topography of the Basin likely leads to complex surface flows that transport ozone and its precursors around the Basin. This spatial heterogeneity may be magnified during inversion conditions conducive to ozone formation. Because of the complex topography of the Basin and its influence on surface flow and, by extension, pollutant transport, it will be critical for any modeling efforts of ozone formation to include high resolution simulations of topography and meteorology.

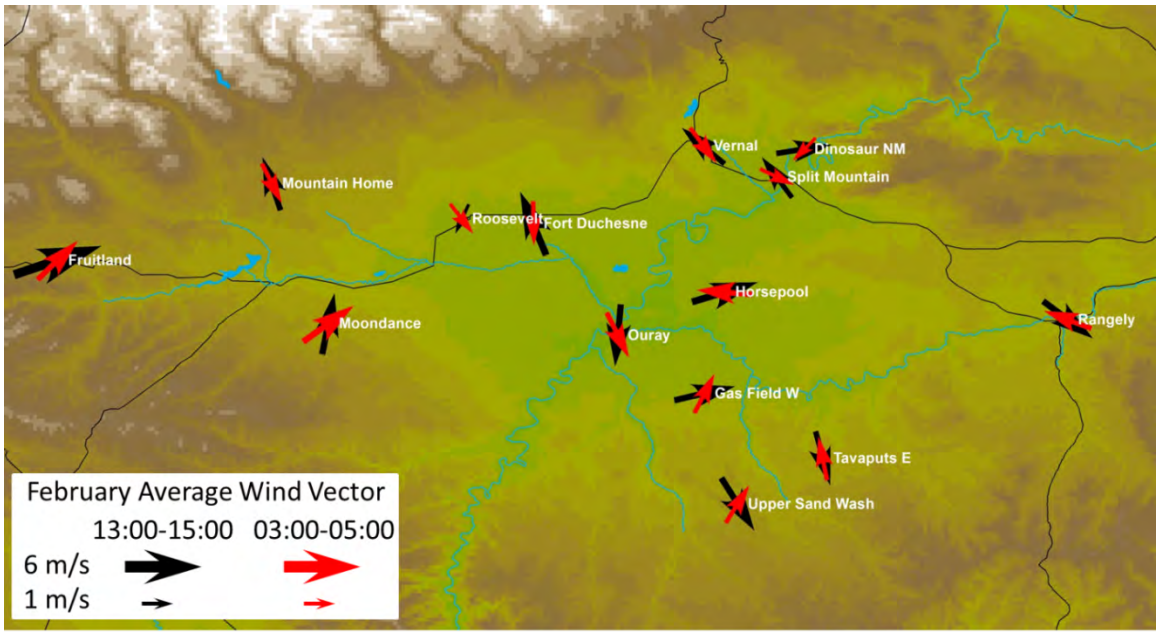

Figure 19. Mean day and night wind vectors at 14 meteorological stations around the Uintah Basin during Feb. 2012 (Chapter 2). The black arrows indicate monthly mean wind direction from 13:00 to 15:00 local time, and red arrows indicated monthly mean wind direction from 03:00 to 05:00 local time. The size of the arrow is proportional to the mean wind speeds for each time period.

Conclusions

During elevated ozone periods it is likely that air transport will be dominated by shallow, highly variable, locally driven flow patterns. How these surface flows affect ozone production and distribution is still unknown. It is critical that a meteorological model be configured to capture these local scale flow features and that sufficient observational data are available with which to validate the model predictions.

Question E.2

Can the formulation of existing 1-D box and more complex transport and chemical models represent the observed phenomena in the Basin? If not, what are the most urgent measurement needs for improving model representation?

Background

Three-dimensional photochemical modeling is the most advanced tool available for 1) understanding details of the ozone formation process, 2) evaluating ozone sensitivities to changes in precursor emissions, and 3) predicting the effects of emissions control strategies. One-dimensional photochemical box models are useful tools for evaluating chemical mechanisms and performing sensitivity analyses. For model simulations to be useful, however, they must faithfully reproduce key mechanisms of ozone formation and transport operating in the Uintah Basin. Merely demonstrating that a model is able to accurately reproduce the observed temporal and spatial distribution of ozone is not sufficient, as this does not ensure that ozone sensitivities to changes in precursor emissions will also be accurately predicted. Modelers typically refer to this problem as "getting the right answer for the wrong reason." Models must be carefully validated and verified against ambient measurements of ozone, precursors, and meteorological parameters.

In contrast to urban summertime ozone episodes for which all existing photochemical models used in regulatory applications were originally developed and evaluated, relatively little is known about winter ozone episodes in air basins in which emissions are dominated by oil and gas sources. Research is needed, therefore, to fully evaluate the applicability of existing models to winter ozone events and to identify any necessary modifications to model formulation.

Findings

Finding E.2.1: Data analyses and box modeling simulations of ozone episodes in the UGRB suggest that current chemical mechanisms may need to be modified to account for 1) potential daytime HONO formation and 2) temperature effects on chemical reaction rates.

Box modeling of ozone formation in the UGRB by Carter and Seinfeld (2012) and Nopmongcol et al. (2010) showed that existing chemical mechanisms (SAPRC-07 and CB05, respectively) generate peak ozone levels on par with observed values. However, sensitivity analyses performed by Carter and Seinfeld identified significant differences in VOC reactivities between the winter conditions in the UGRB and standard summer urban conditions. They also showed that the potential daytime production of HONO from NO_2 via heterogeneous reactions on the snow surface could contribute significantly to ozone production under some conditions.

Carter and Seinfeld (2012) also found significant spatial and temporal heterogeneity in chemical conditions across the UGRB. While a similar analysis of VOC versus NO_x sensitivity and VOC reactivities for winter conditions has not been performed in the Uintah Basin, it is not unreasonable to expect that similar spatial and temporal heterogeneity is present, given the similarities between the two basins, and given the complex topography (Question E.1) and spatial variability in emission source types in the Basin (Question A.4).

As indicated by Martin et al. (2011), existing chemical mechanisms that were developed and evaluated against data representative of summer urban conditions may not fully account for the effects of cold winter temperatures on reaction rates and the relative distributions of reaction products. Carter and Seinfeld (2012) also noted that the temperature sensitivities of some reaction mechanisms have not been fully evaluated. Chapter 7 shows that winter ozone production is temperature dependent. While results from these studies suggest that overall reactivity is lower under colder temperatures, quantitative research in this area is needed.

Finding E.2.2: Field measurements in ozone-producing conditions are needed to fully evaluate meteorological and photochemical models for Uintah Basin winter ozone episodes.

As noted above, UBOS 2011-12 did not encounter any elevated ozone episodes, and since ozone episode conditions are chemically and meteorologically distinct from non-episode conditions, data from the study will be less useful for model evaluation. Observations of ozone, precursors, reaction products, and meteorology under episode conditions are needed to support modeling in the Basin.

Analyses of 2010-11 ozone episodes presented by Martin et al. (2011) show that wind flow patterns in the Basin are extremely complex under ozone episode conditions. Winter cold pool events are challenging to simulate, and the ability of currently available meteorological models to reproduce these features remains mostly untested. Data needed to evaluate a meteorological model of the Basin include vertical profiles of winds and temperatures at multiple locations and surface meteorological parameters over an extensive network.

Data needed to evaluate a photochemical model for the Basin include continuous surface air quality measurements of ozone and key ozone precursors including, minimally, speciated VOC and NO_x. These measurements are needed at spatially representative sites that are also characteristic of different chemical environments (e.g., populated versus remote, oil producing versus gas producing).

Vertical profile measurements of ozone and precursors are also needed to understand transport behavior aloft. Additionally, CO and methane measurements can help identify emissions sources, and SO_2 measurements can help trace the plume impacts of coal-fired power plants. Measurements of speciated particulate matter can help characterize the sources and fate of VOC, NO_x, and other potentially relevant emissions sources such as wood burning stoves. Detailed measurements of key nitrogen species and VOC similar to those reported in Chapter 3 need to be repeated under episode conditions to develop a reasonable understanding of the radical budget that the photochemical model must be able to reproduce in order to accurately predict ozone sensitivity to changes in precursor emissions. Deposition rates of ozone and other key species on snow are also uncertain and measurements are needed to constrain deposition velocities for these compounds.

Conclusions

Further research is needed for development and validation of meteorological and photochemical models of winter ozone episodes in the Uintah Basin.

Question E.3

What are the main issues regarding winter ozone formation that should be the focus of future studies?

Background

Ozone levels recorded during UBOS 2011-12 were well below the ozone NAAQS. As a result, the study team was not able to perform measurements representative of conditions during which significant ozone formation occurs. While the data collected in the study have proven extremely useful, additional measurements under ozone episode conditions are needed to address key uncertainties such as the major components of the radical budget, the structure and characteristics of inversion meteorology, the sensitivity of ozone to VOC composition and changes in VOC and NO_x concentrations, and the vertical and horizontal distribution of ozone and precursors. Meteorological and photochemical modeling and further inventory development are also needed to identify the most effective mitigation strategies for reducing winter ozone.

Findings

Finding E.3.1: Continued study of winter ozone formation in the Uintah Basin is needed to develop effective mitigation strategies.

Continuing study goals include the following:

- Characterization of the horizontal spatial variability in ambient ozone, VOC, and NO_x concentrations during ozone episodes. These data are necessary to evaluate ozone sensitivity to VOC and NO_x in different areas within the Basin and to characterize emissions and transport across the Basin.
- Continued development of a Basin-wide emissions inventory that includes temporal and spatial distribution and speciation of VOC and NO_x and integrates gridded and activity-specific information from current inventories. Three categories of emissions inventory research exist:
    - Bottom up estimates using activity data and equipment emissions factors,
    - Top down estimates using ambient concentrations and modeling, and
    - Emissions estimates of specific source categories using measurements and modeling.
- Evaluation of the importance of snow photochemistry and radical sources (especially nitryl chloride, formaldehyde, and HONO). This data will address the potential for unique aspects of winter ozone chemistry to affect the sensitivity of ozone to VOC and NO_x. Of particular importance is resolving the apparently contradictory measurements of alkene abundances between the 2010-11 and 2011-12 studies and determining the contribution of alkenes to the radical budget and VOC reactivity.
- Characterization of NO_x emissions transport within and above the inversion layer. Transport of NO_x emissions above the inversion layer will affect VOC/NO_x ratios within

the inversion layer and could change the relative effectiveness of VOC and NO_x emissions mitigation.

- Characterization of inversion height and winds. These data are necessary for modeling Basin meteorology and ozone and for evaluating the transport and dispersion of emissions.

- Development of photochemical model simulations to evaluate the comparative effectiveness and to quantify the needed levels of VOC and NO_x mitigations. Modeling and measurement studies that are designed and implemented together and that build on each other's findings can be especially useful.

- Quantification of day-specific background ozone levels during elevated ozone episodes. These data are needed to accurately estimate the amount of ozone formed locally in the Basin compared to ozone transported into the Basin.

- Evaluation of trends in ozone, VOC, and NO_x ambient levels over multiple years.

REFERENCES

Banta, R. and Cotton, W. R.: Analysis of the structure of local wind systems in a broad mountain basin, J. App. Meteorol., 20, 1255-1266, 1981.

Brodin, M., Helmig, D., and Oltmans, S.: Seasonal ozone behavior along an elevation gradient in the Colorado Front Range mountains, Atmos. Environ., 44, 5305-5315, 2010.

CAMx user's guide v5.40: http://www.camx.com/files/camxusersguide_v5-40.aspx, last access: 2012.

Carter, W.P. and Seinfeld, J.H.: Winter ozone formation and VOC incremental reactivities in the Upper Green River Basin of Wyoming, Atmos. Environ., 50, 255-266, 2012.

Cohan, D. S., Hakami, A., Hu, Y., and Russell, A. G.: Nonlinear response of ozone to emissions: source apportionment and sensitivity analysis, Environ. Sci. Technol., 39, 6739-6748, 2005.

Dietrich, S. A.: WDEQ/AQD 2011 engine emissions study summary report, Wyoming Department of Environmental Quality, available at: http://deq.state.wy.us/aqd/Special%20Purpose%20Studies/WDEQ.AQD_2011_Engine_Emissions_Study.pdf, 2011.

ENVIRON: 2008 Upper Green River winter ozone study, ENVIRON International Corporation, available at http://deq.state.wy.us/aqd/downloads/AirMonitor/FinalReport10-08.pdf, 2008.

ENVIRON: 2009 Upper Green River winter ozone study, ENVIRON International Corporation, available at http://deq.state.wy.us/aqd/downloads/AirMonitor/Wint09_Final_3-2010_a0.pdf, 2010.

EPA oil and natural gas air pollution standards: http://www.epa.gov/airquality/oilandgas/, last access: 2012.

Hakami, A., Odman, M. T., and Russell, A. G.: High-order, direct sensitivity analysis of multidimensional air quality models, Environ. Sci. Technol., 37, 2442-2452, 2003.

Hall, C., Mansfield, M., Shorthill, H., Lyman, S.: Upper Green River Basin winter ozone: summary of public information about the Wyoming phenomenon, Utah State University Office of Commercialization and Regional Development, CRD/12-275B, 2012.

Helmig, D., Ganzeveld, L., Butler, T., and Oltmans, S. J.: The role of ozone atmosphere-snow gas exchange on polar, boundary-layer tropospheric ozone – a review and sensitivity analysis, Atmos. Chem. Phys., 7, 15-30, 2007.

Martin, R., Moore, K., Mansfield, M., Hill, S., Harper, K., and Shorthill, H.: Final report: Uintah Basin winter ozone and air quality study, December 2010 – March 2011. Energy Dynamics Laboratory, Utah State University Research Foundation, EDL/11-039, 2011.

MSI: 2011 Upper Green River winter ozone study, Meteorological Solutions, Inc., available at http://deq.state.wy.us/aqd/downloads/AirMonitor/Final_UGWOS_2011_Ozone_Study_Report_Text_and_Appendices.pdf, 2011.

Nopmongcol, O., Yarwood, G., and Stoeckenius, T.: 2008 winter ozone box model study. ENVIRON International Corporation, available at http://deq.state.wy.us/aqd/Ozone/Appendix%20A_BoxModel_WY_RevFinal.pdf, 2010.

NRC (National Research Council): Rethinking the Ozone Problem in Regional and Urban Air Pollution, National Academy Press, Washington, DC., 1991.

Pétron, G., et al., Hydrocarbon emissions characterization in the Colorado Front Range: A pilot study, J. Geophys. Res., 117, D04304, doi:10.1029/2011JD016360, 2012.

Rappenglueck, B., 2010. WDEQ UGWOS 2010 HONO Measurements, Appendix D in Final Report: 2010 Upper Green River Ozone Study. Meteorological Solutions, Inc., available at http://deq.state.wy.us/aqd/downloads/AirMonitor/Final%20Report_2010%20Upper%20Green%20River%20Ozone%20Study.pdf, 2010.

Sakulyanontvittaya, T., Yarwood, G., and Guenther, A., 2012. Improved biogenic emission inventories across the West: Final report. ENVIRON International Corporation, available at http://www.wrapair2.org/pdf/WGA_BiogEmisInv_FinalReport_March20_2012.pdf, 2012.

Schnell, R. C., Oltmans, S. J., Neely, R. R., Endres, M. S., Molenar, J. V. and White, A. B.:. Rapid photochemical production of ozone at high concentrations in a rural site during winter, Nature Geosci., DOI 10.1038/NGEO415, 2009.

Solomon, P., Cowling, E., Hidy, G., and Furiness, C.: Comparison of scientific findings from major ozone field studies in North America and Europe, Atmos. Environ., 34, 1885-1920, 2000.

Stoeckenius, T., and Ma, L.: A conceptual model of winter ozone episodes in southwest Wyoming. ENVIRON International Corporation, available at http://deq.state.wy.us/AQD/Ozone%20Conceptual%20Model%20Report_Sublette%20County.asp, 2010.

Swanson, A. L., Blake, N. J., Dibb, J. E., Albert, M. R., Blake, D. R., and Rowland, F. S.: Photochemically induced production of CH_3BR, CH_3I, C_2H_5I, ethene, and propene within surface snow at Summit, Greenland, Atmos. Environ., 36, 2671-2682, 2002.

Utah DOGM (Division of Oil, Gas, and Mining): http://oilgas.ogm.utah.gov/, last access: 2012.

Vergeiner, I., and E. Dreiseitl, 1987. Valley winds and slope winds—observations and elementary thoughts. Meteorol. Atmos. Phys. 36, 264-286.

Vingarzan, R.: A review of surface ozone background levels and trends, Atmos. Environ., 38, 3431-3442, 2004.

WDEQ: Technical support document I for recommended 8-hour ozone designation for the Upper Green River Basin, WY. Wyoming Department of Environmental Quality, Air Quality Division, available at: http://deq.state.wy.us/AQD/Ozone%20Nonattainment%20Information.asp, 2009.

WDEQ (Wyoming Department of Environmental Quality) Actual Emissions: http://deq.state.wy.us/aqd/Actual%20Emissions.asp, last access: 2012.

WOGCC (Wyoming Oil and Gas Conservation Commission): http://wogcc.state.wy.us/, last access: 2012.

WRAP (Western Regional Air Partnership): http://www.wrapair2.org/PhaseIII.aspx, last access: 2012.

CHAPTER I

LONG-TERM MONITORING FOR OZONE & KEY PRECURSOR SPECIES

Seth Lyman[1], Randy Martin[2], Scott Hill[3], Kori Moore[4], and Howard Shorthill[1]

[1]Bingham Entrepreneurship & Energy Research Center, Utah State University, Vernal, UT.

[2]Utah Water Research Laboratory, Utah State University, Logan, UT.

[3]Carbon Energy Innovations Center, Utah State University Eastern, Price, UT.

[4]Space Dynamics Laboratory, Utah State University Research Foundation, Logan, UT.

*Bowen Call, Neal Olson, and others at the Utah Department of Environmental Quality participated in establishing sites and collecting essential data.

INTRODUCTION

High wintertime ozone has only been observed in the Uintah Basin in the presence of heavy snow cover, strong ground-based inversions, and adequate concentrations of ozone precursors, particularly volatile organic compounds (VOC) and oxides of nitrogen (NO_x) (ENVIRON, 2010; Martin et al., 2011; Schnell et al., 2009). Observations further indicate significant year-to-year variability in Basin wintertime meteorology (see Chapter 7), and variability in precursor emissions is expected (see Chapter 4). Understanding of these phenomena is increasing, but significant gaps still exist, particularly with regards to the temporal and spatial variability in the conditions conducive to ozone formation.

Measurements of ozone, ozone precursors, and meteorological parameters over multiple years in the Basin are critical to understanding not only the complex interactions that produce ozone but also the effects of inter-annual variability. These data will be useful for verification of research and regulatory models that simulate ozone production in the Basin and for determination of suitable mitigation strategies. As precursor reduction strategies are implemented, long-term measurements will also verify the effectiveness of mitigation.

Permanent monitoring stations were established at Roosevelt, Utah, and at Horse Pool (an oil industry injection site in central Uintah County, Utah, to measure meteorological parameters and concentrations of ozone and precursors. The stations were operated during winter 2011-12 and will continue to operate in subsequent years to establish trends in measured parameters and to analyze factors that influence winter ozone production in the Uintah Basin.

Though work continues and further analyses are underway, this chapter describes and analyzes data collected during winter 2011-12 at the Roosevelt and Horse Pool sites. Support of this work was provided by the Uintah Impact Mitigation Special Service District, Mark and Debbie Bingham, the Utah Department of Environmental Quality, and the United States Department of Energy.

METHODS

Site Descriptions

The Roosevelt station resides at 40.2942, -110.0090 (~ 400 South 1000 West), near Constitution Park in Roosevelt, Utah, a population center moderately distant from concentrated areas of oil and gas development. The Horse Pool station is located at 40.1437, -109.4672, an area of intensive oil and gas extraction in southeast Uintah Basin. Figure 1-1 shows site photographs.

Instruments at each site were calibrated, audited, and serviced according to manufacturer and EPA protocols. Parallel instrumentation and capability afforded meaningful site comparisons. Data from other sites, including those operated by the Utah Department of Environmental Quality, Enefit, and Golder Associates, were also used.

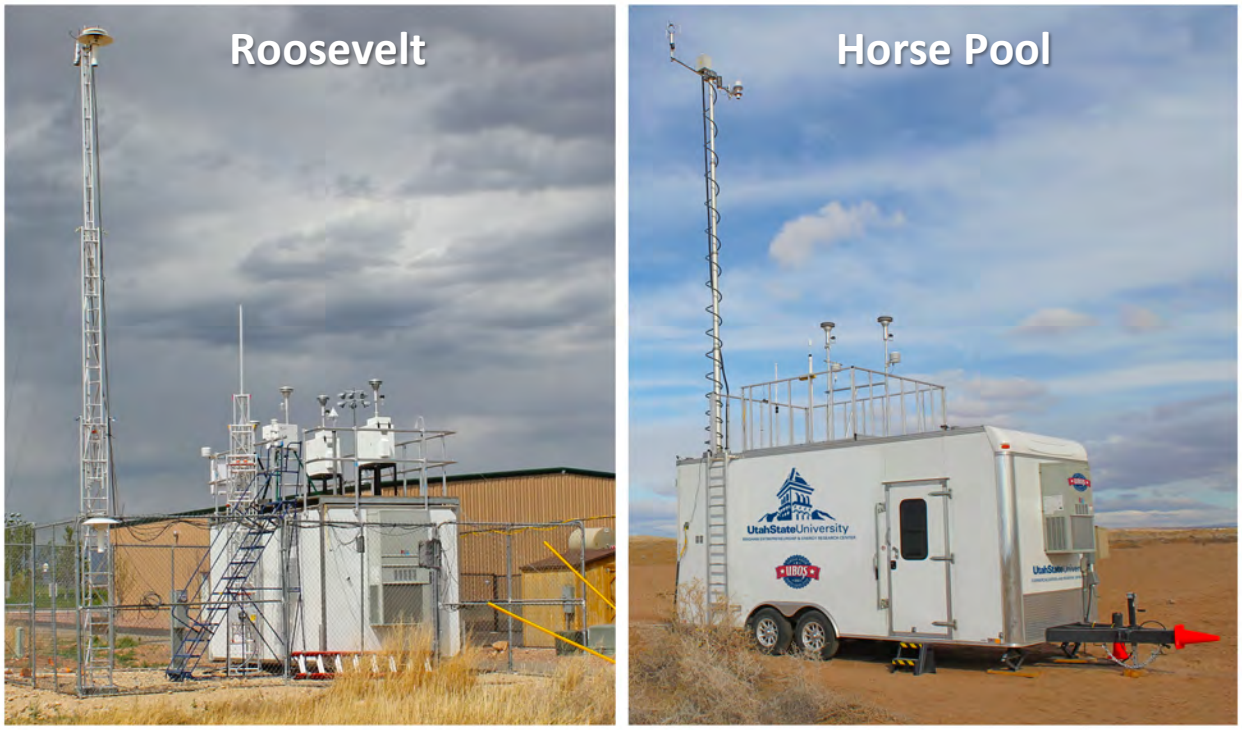

Figure 1-1. Mobile monitoring laboratories sited at Roosevelt and Horse Pool.

Ozone

Ozone was monitored using a Teledyne-API Model 400 analyzer at Roosevelt and an Ecotech Model 9810 analyzer at Horse Pool. The analyzers were calibrated using NIST-traceable ozone standards.

Oxides of Nitrogen

At both sites, measurements of NO, NO_2, and NO_x (NO + NO_2) were made using a photolytic NO_2 reducer to derive "true" NO_2. NO_y (sum of NO_x and other reactive nitrogen species, including HNO_3, HONO, PAN, particulate nitrates, etc.) was measured by converting all reactive nitrogen to NO with a catalytic molybdenum converter and analyzing the products as NO. NO_x and NO_y at Roosevelt were measured via a modified Thermo Model 42c analyzer with an Air Quality Design NO_{xy} converter. NO_x and NO_y at Horse

Pool were measured with an Ecotech 9841 analyzer (modified with photolytic NO_2 converter) and an Ecotech 9843 analyzer, respectively. Analyzers were calibrated using NIST-traceable NO standards.

Hydrocarbons

Roosevelt Site

At the Roosevelt site, non-methane hydrocarbons (NMHC) concentrations were measured using evacuated six-liter stainless steel Summa canisters that collected one-hour integrated whole air samples for commercial laboratory analysis (Ace Labs, Inc.). A real-time gas chromatograph was originally planned for the site, but the manufacturer was unable to supply a working instrument in time for the study. Canister samples were collected from 14-24 February 2012 from the roof of the sampling trailer at about four meters above ground level. Samples were collected each day at 1:00-2:00, 7:30-8:30, 13:00-14:00, and 18:00-19:00 Mountain Standard Time (MST). Samples were analyzed by gas chromatography/mass spectrometry for acetaldehyde, acetone, formaldehyde, and hydrocarbons (3-12 carbon atoms).

Vendor quantification of the identified spectra was accomplished using compound-specific calibration standards. Additionally, the vendor performed two blank canister analyses (no compounds found) and performed duplicate analyses on two separate samples (no significant differences found).

Methane grab samples at the Roosevelt site were manually collected into 30 mL glass vials with TFE septa from the rooftop of the sampling trailer from 14-24 February 2012. Samples were analyzed at the Utah Water Research Laboratory (UWRL) using a gas chromatography-flame ionization system. Methane vials, for the greater part, were collected at the start and end of each canister collection period, and intermittently throughout the daily sampling periods. Methane grab samples also were collected at several other locations throughout the Basin (Altamont, Moondance, Ouray, Pariette Draw, Red Wash, and Wells Draw).

Horse Pool Site

At Horse Pool, ambient methane and total NMHC concentrations were measured using a Chromatotech gas chromatograph that collected 30-second ambient air samples every five minutes. The system used an external zero air generator and either bottled or generated hydrogen, and was calibrated before and during the sampling period.

NMHC concentrations are reported in ppb-C3 (parts per billion in C3 [propane] equivalents). Since the detector response for a given compound is dependent on the number of carbon atoms in that compound, the system reports the number of carbon atoms in a sample, not the number of hydrocarbon molecules in the sample. For convenience, this output is scaled to the detector response for propane.

Carbonyl compounds were collected at Horse Pool and subsequently analyzed following the protocols outlined in EPA Compendium Method TO-11A (EPA, 1999). The samples were collected four times per day over two-hour periods (0:30-2:30, 7:00-9:00, 12:30-14:30, and 17:30-19:30) using a Tisch Environmental Model 423 3-Channel Carbonyl sampler and commercial dinitrophenylhydrazine (DNPH)-coated cartridges (Supelco, LpDNPH S10L). The Tisch system was calibrated prior to field deployment and sampled at a nominal flow rate of 1.0 L min^{-1}. To guard against unwanted ozone interferences, KI scrubbers preceded each of the

DNPH cartridges. These scrubbers were replaced weekly. Field blanks were taken once per day, and laboratory blanks and spiked samples were also analyzed. Samples were analyzed by high performance liquid chromatography at the UWRL. Commercial standards were used for peak identification and quantification.

Particulate Matter

Particulate matter was monitored at the Roosevelt and Horse Pool sites using both real-time (hourly averaged) and filter-based (daily integrated) samplers. At Horse Pool, both PM_{10} (particulate matter less than 10 µm in diameter) and $PM_{2.5}$ (particulate matter less than 2.5 µm in diameter) were monitored using hourly samplers; however, at Roosevelt, only $PM_{2.5}$ was monitored on an hourly basis. All hourly samples were made with MetOne BAM-1020 analyzers. Similar data from the UDEQ sampling station in Vernal were also included in the analysis.

Filter-based samplers were used to collect particulate matter for compositional analysis at the Roosevelt site. Three collocated $PM_{2.5}$ samplers were used 14-24 February 2012 at Roosevelt: two Anderson RAAS $PM_{2.5}$ systems and a BGI PQ200 system. The samplers' 23-hour sample period, from 12:30 to 11:30, left one hour each day for filter exchange. The samplers operated at an average flow rate of 16.7 Lpm and collected particulate matter on a 47 mm filter. Prior to the field deployment, each monitor's flow control system was calibrated using a certified transfer standard. At Horse Pool, measurements of chemical composition were collected by NOAA.

The Interagency Monitoring of Protected Visual Environments (IMPROVE) network has demonstrated that most fine particulate matter is composed primarily of crustal (elemental) species, organic carbon, elemental carbon (black, soot), ammonium sulfate, and ammonium nitrate (IMPROVE, 2011). These material classifications were targeted for identification.

Two pre-conditioned and pre-weighed 47 mm Teflon (TFE) membrane filters were used for gravimetric (total mass), ionic (soluble compounds), and X-ray fluorescence (elemental composition) analyses. In addition, one pre-conditioned 47 mm quartz filter was used for organic and elemental carbon analyses. The TFE filters were pre- and post-conditioned by storage at room temperature in a silica gel desiccator for a minimum of 24 hours. After conditioning, the filters were weighed using a Mettler MT5 microbalance on successive days until a consistency of ±2.5 µg was obtained for at least three consecutive weighings. Prior to and after exposure, quartz filters were kept in separate foil-covered petri dishes and stored in a lab refrigerator (≤4°C).

Ion chromatography analysis at the UWRL quantified the soluble ionic species of collected particulate matter. Soluble ions were extracted from filter samples by sonicating in de-ionized water for 10 minutes. Immediately following final extraction, half the extract was removed and spiked with HCl to fix the ammonium (NH_4^+) for cation analysis. The remaining extract was left untreated for anion analysis. Extracts were passed through a 0.2 µm nylon filter, and a Dionex ICS 3000 ion chromatograph was used to determine cation (AS-11 HC column) and anion (CS12A column) concentrations. Anion calibrations included fluoride, chloride, nitrate, nitrite, and sulfate. Cation calibrations included sodium, ammonium, potassium, magnesium and calcium. De-ionized water and quality control samples were checked prior to analysis and rechecked approximately every ten samples. Field and lab blanks of both filter types were collected and analyzed. Duplicate analyses were performed on no less than 10% of the samples.

After obtaining consistent mass determination, one TFE filter from each run was analyzed for $PM_{2.5}$-bound elemental composition via X-ray fluorescence (XRF) by a commercial laboratory (CHESTER LabNet, Tigard, OR) following EPA IO-3.3 protocol. Target elements included Na, Mg, Al, Si, P, S, Cl, K,

Ca, Ti, V, Cr, Mn, Fe, Co, Ni, Cu, Zn, Ga, Ge, As, Se, Br, Rb, Sr, Y, Zr, Mo, Pd, Ag, Cd, In, Sn, Sb, Ba, La, Hg, and Pb. As was the case with similar samples from the 2011 study, most of the target elements were observed, but not all were at levels statistically above the reported limits of detection.

Organic and elemental carbons in filter samples were determined by a commercial laboratory (Sunset Laboratory, Tigard, OR). As described by Birch and Cary (1996), filters were exposed to an oxygen-free, helium atmosphere and heated through a stepped series to approximately 700°C to vaporize organic carbon. The gas-phase carbon was transferred to an oxidizer oven where it was converted to carbon dioxide, followed by methanization and quantification via flame ionization detection. The remaining filter sample was then heated to 850°C, vaporizing the remaining elemental carbon and quantifying the elemental carbon concentrations following the same procedure as the organic carbon concentrations. The reported organic carbon concentrations were increased by the recommended multiplier of 1.7 to account for the non-carbon components of the organic compounds' mass (Malm and Hand, 2007).

Meteorology

Temperature at 2 and 10 m, pressure, wind speed and direction, relative humidity, precipitation, and snow depth were measured at Horse Pool and Roosevelt. Kipp and Zonen CNR4 net radiometers measured incoming and outgoing solar radiation at short (300-2800 nm) and long (4500-42000 nm) wavelengths at both sites. UVA and UVB radiometers were used to measure incoming and outgoing UV radiation at Horse Pool. Surface reflectance (i.e., albedo) was calculated from the difference between incoming and outgoing radiation.

Traffic

A motion-activated camera was installed adjacent to Wonsits Valley Road near the Horse Pool site. Images from this camera were compiled to determine traffic patterns.

RESULTS AND DISCUSSION

Ozone

Ozone data from Roosevelt, Horse Pool, and all other study sites are discussed in Study Component 2**.**

Oxides of Nitrogen

Concentrations of NO_x were variable on short time scales at both Roosevelt and Horse Pool, reflecting the influence of local sources on these sites (Figure 1-2). In Figure 1-2, differences between the sites at the lowest NO_x concentrations may be due in part to differences in instrument calibration and instrument performance near detection limits. Figure 1-3 shows the diurnal trend in NO_x at Horse Pool, Roosevelt, Ouray, Red Wash, and Rabbit Mountain, and Table 1-1 shows average concentrations of NO_x and other criteria pollutants at Horse Pool and Roosevelt.

NO_x and NO_y at Roosevelt showed a pronounced peak in the morning, likely due to NO_x emissions from vehicles during rush hour. The site exhibited a less pronounced peak during the afternoon rush hour period, likely because of increased atmospheric mixing that diluted emitted NO_x.

NO_x and NO_y at Horse Pool exhibited a slow nightly build-up that continued until midday. The lowest concentrations were observed in the late afternoon when atmospheric mixing was greatest. Maximum NO_x were observed at the time of greatest vehicle activity on Wonsits Valley Road, which is 26 m north

of the Horse Pool site (Figure 1-4). Vehicle traffic on Wonsits Valley Road did not follow a typical rush-hour pattern but instead peaked at midday, consistent with the diurnal pattern of NO_x at Horse Pool and indicating the influence of mobile source emissions on ambient NO_x in this oil and gas producing area. It is likely that traffic patterns on other roads in the area are similar to Wonsits Valley Road and that the average diurnal pattern of NO_x is influenced by traffic on all area roads.

NO_x at Ouray followed a diurnal pattern similar to that at Horse Pool. Since the Red Wash site is near a major highway with heavy traffic and is closer to population centers, peak traffic likely occurs earlier in the day, which would explain the earlier NO_x peak at that site. Rabbit Mountain, a remote site with little anthropogenic activity, had little NO_x and no pronounced diurnal pattern.

Were Horse Pool, Ouray, and Red Wash influenced primarily by stationary rather than mobile sources, diurnal profiles would show a buildup of NO_x at night and lowest NO_x at midday due to enhanced atmospheric mixing and dilution during the daylight hours. Instead, the match between traffic patterns and NO_x at these sites argues that mobile sources have a large influence in NO_x concentrations in oil and gas producing areas of the Uintah Basin.

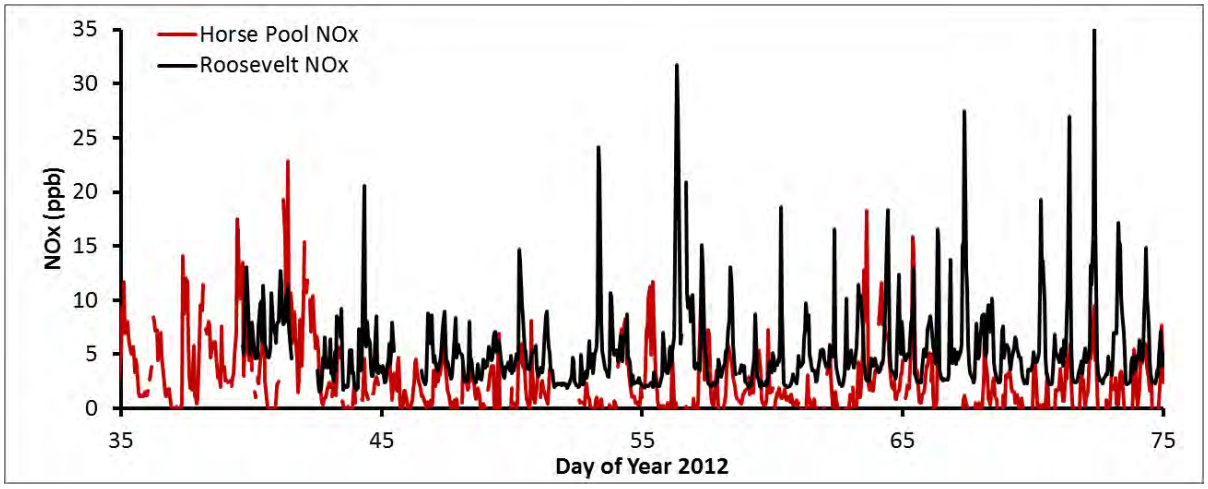

Figure 1-2. Time series of NO_x at Horse Pool and Roosevelt, winter 2012.

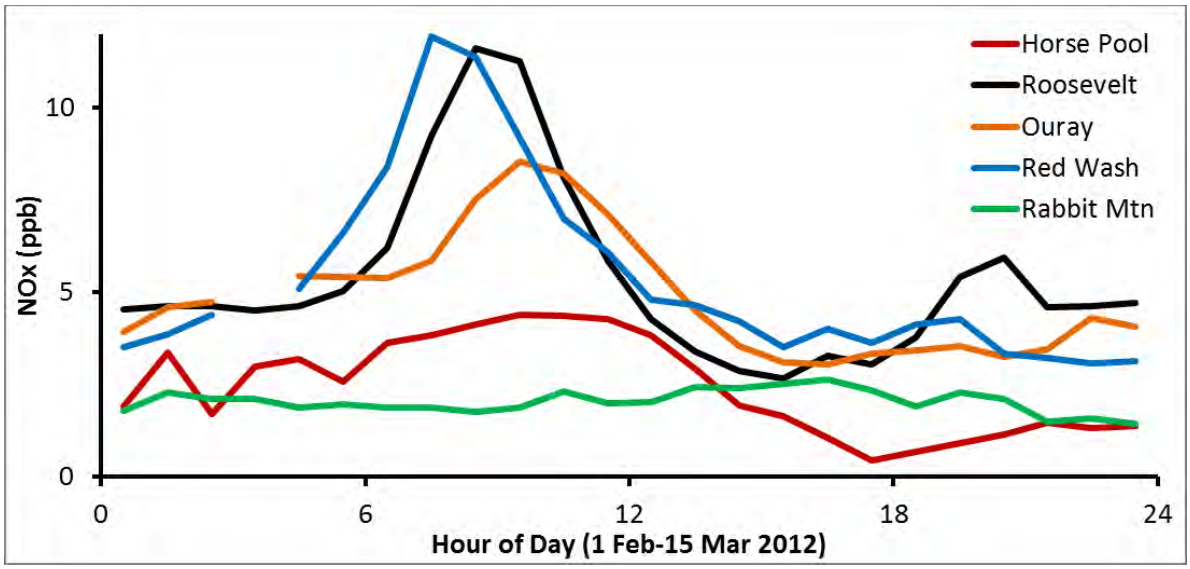

Figure 1-3. Diurnal hourly mean NO_x concentrations at several sites in the Uintah Basin (see Chapter 2).

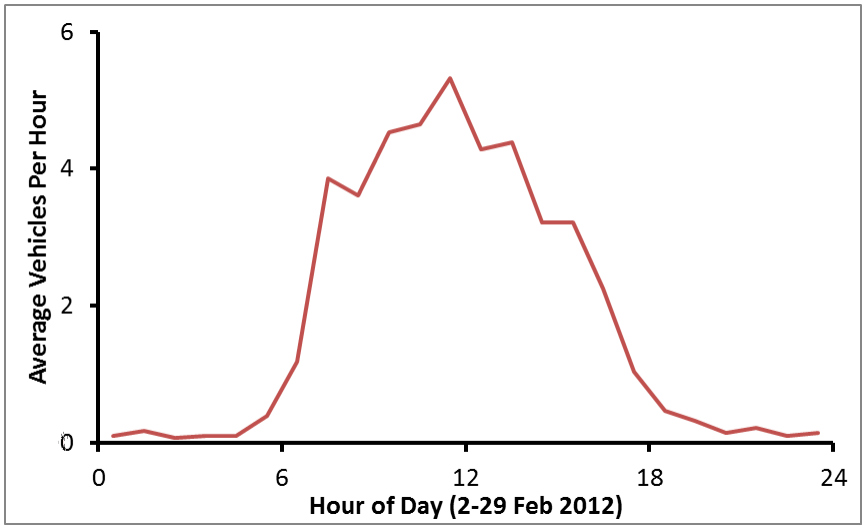

Figure 1-4. Average number of vehicles on Wonsits Valley Road (26 m north of Horse Pool site).

Table 1-1. Statistical summary of one-hour average criteria pollutant and meteorological data at Horse Pool and Roosevelt sites. "N.D." indicates a value below the detection limit of the instrument. "N/A" indicates a measurement that was not collected at that site.

	Horse Pool					Roosevelt				
Measurement	**Overall Average**	**13-15:00 Average**	**Standard Deviation**	**Max.**	**Min.**	**Overall Average**	**13-15:00 Average**	**Standard Deviation**	**Max.**	**Min.**
Ozone (ppb)	38.1	46.5	10.1	62.4	8.9	35.5	44.4	10.3	55.0	6.6
NO (ppb)	N.D.	N.D.	1.3	10.7	N.D.	N.D.	N.D.	0.8	6.2	N.D.
NO_2 (ppb)	2.8	1.6	2.7	19.6	N.D.	5.2	2.7	2.6	14.4	1.4
NO_x (ppb)	2.4	1.8	3.3	22.9	N.D.	5.4	2.8	3.8	35.5	1.5
NO_y (ppb)	4.1	3.2	4.4	27.3	N.D.	6.5	4.3	3.9	34.7	2.6
CO (ppm)	N.D.	N.D.	0.1	0.2	N.D.	N.D.	N.D.	0.2	0.5	N.D.
CO_2 (ppm)	399	399	4	410	392	N/A	N/A	N/A	N/A	N/A
SO_2 (ppb)	N.D.	N.D.	0.3	1.5	N.D.	N/A	N/A	N/A	N/A	N/A
H_2S (ppb)	N.D.	N.D.	0.3	1.1	N.D.	N/A	N/A	N/A	N/A	N/A
$PM_{2.5}$ (µg/m3)	4	4	4	38	N.D.	5	6	3	30	N.D.
Temp (°C)	2.6	6.6	5.6	19.9	-8.6	-1.0	3.9	4.4	13.9	-10.7
RH (%)	49	36	21	98	12	58	46	16	91	17
Wind (m/s)	2.9	3.9	2.3	14.1	0.5	2.3	3.2	2.2	15.8	0.0

Figure 1-5 shows average NO_x concentrations as a function of wind direction for Horse Pool, Red Wash, Ouray, and Rabbit Mountain. At Horse Pool and Red Wash, NO_x tended to be higher when wind came from the southeast. NO_x at Ouray tended to be highest when wind was from the east and southeast, while NO_x at Rabbit Mountain were highest when wind was from the northwest. In general, higher NO_x tended to come from areas of known stationary and mobile NO_x sources (i.e., oil, gas, and power production areas).

A separate study that included 10 weeks of passive and active NO_x measurements around the southeast Uintah Basin was conducted from March through June 2012 to provide more information about the spatial distribution of NO_x in this area. Also, an analysis that utilizes high spatial resolution air trajectories to determine the influence of individual sources and source areas on ambient NO_x in the Basin is underway. Results of these studies are not included in this document.

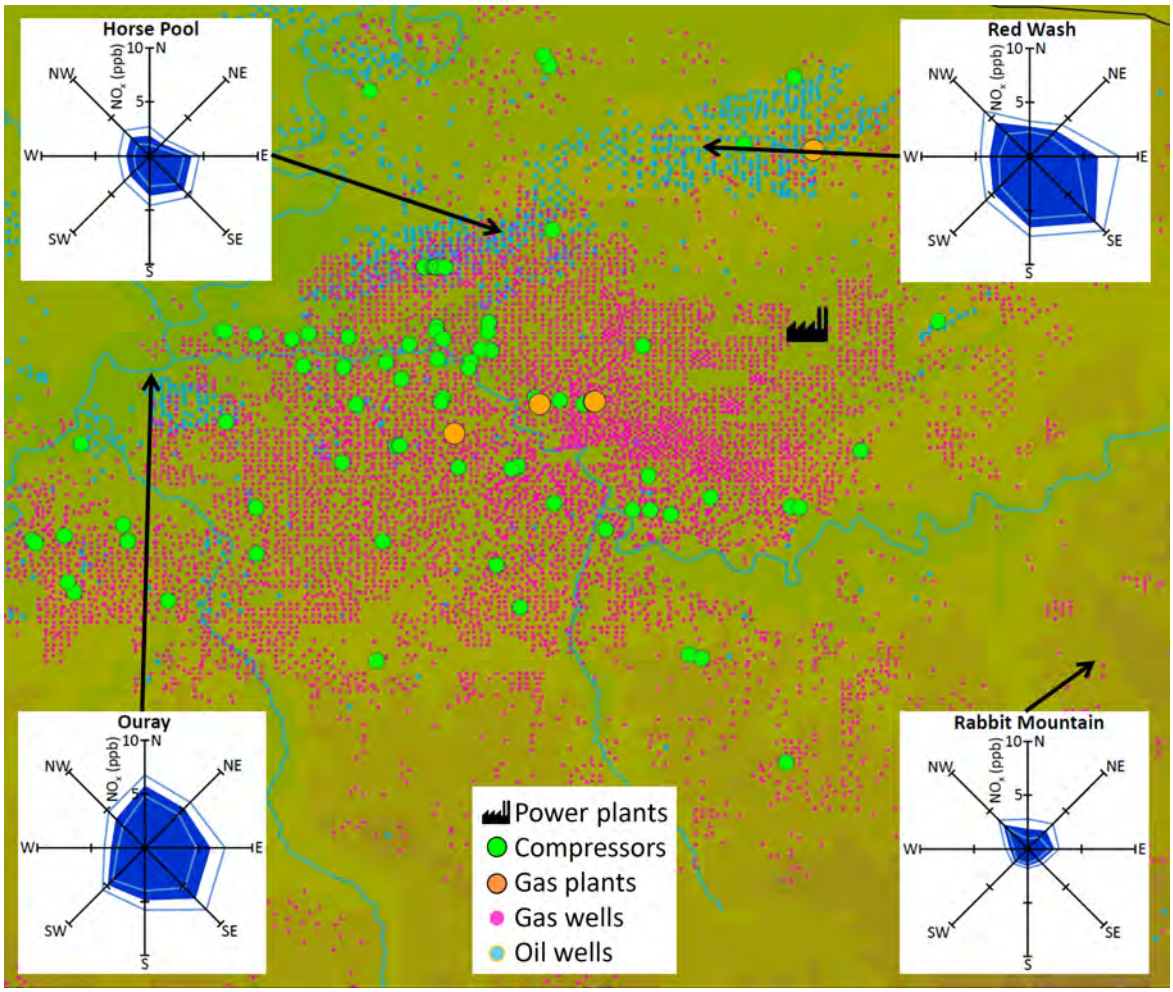

Figure 1-5. Potential NO_x sources in the southeast Uintah Basin, along with wind rose plots of NO_x concentrations at Horse Pool, Red Wash, Ouray, and Rabbit Mountain. The dark blue shape indicates the mean NO_x concentration when wind direction was from different sectors. The light blue lines represent 95% confidence intervals around the mean. Arrows point to the location of each site.

Since NO_y is the sum of NO_x and other reactive nitrogen compounds, subtraction of NO_x from NO_y (termed NO_z) gives the concentration of reactive nitrogen compounds in the atmosphere. These compounds are typically formed from chemical processing of NO_x. NO_z at Horse Pool was highest at night, consistent with measurements of individual reactive nitrogen compounds collected by NOAA at the site. The measurements indicate a relatively strong role for nighttime nitrogen chemistry at the site. A secondary peak in NO_z at Horse Pool at midday was likely due to photochemical processing of nitrogen species at the site (Roussel et al., 1996).

The different pattern emerged at Roosevelt where NO_z was lowest at night and highest in early afternoon. These data show that atmospheric chemistry is not uniform across the Uintah Basin, and nighttime nitrogen species (some of which can be daytime radical sources) may be less prevalent in populated areas than in oil and gas producing areas.

Since the difference between NO_y and NO_x is a measure of the compounds produced by chemical processing of NO_x, the ratio NO_x/NO_y can be used as an indicator of the amount of chemical processing

that has occurred at a given site. Higher NO_x/NO_y values indicate proximity to NO_x sources and/or less chemical processing. NO_x/NO_y was 0.74 ± 0.28 at Horse Pool and 0.78 ± 0.11 at Roosevelt, indicating very little active chemistry at either site (Aneja et al., 1996)

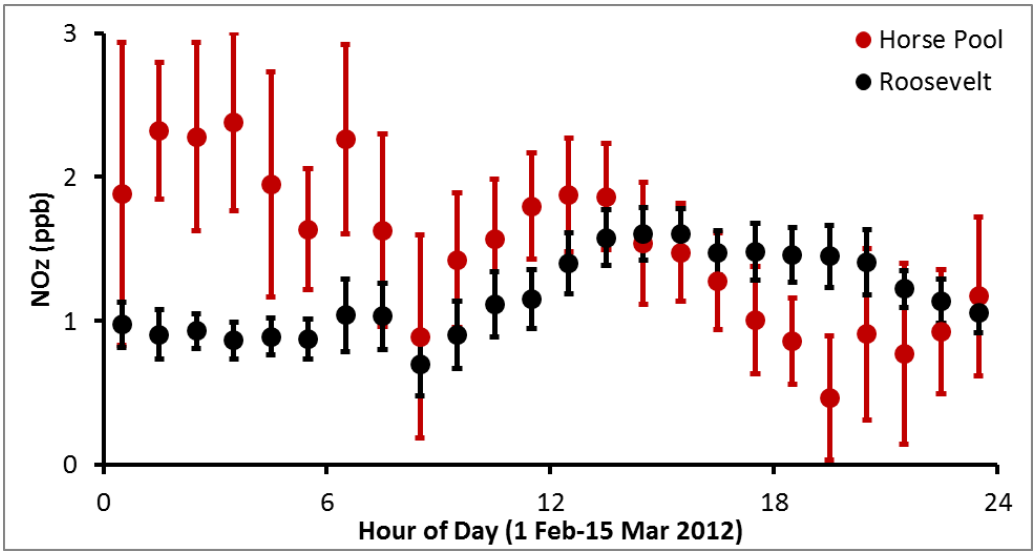

Figure 1-6. Diurnal NO_z (NO_y minus NO_x) at Horse Pool and Roosevelt. Circles represent means, and whiskers represent 95% confidence intervals.

Carbon Monoxide and Sulfur Dioxide

Average CO and SO_2 concentrations at Horse Pool and Roosevelt were less than detection limits and few spikes above this threshold were observed.

Methane and Total NMHC

Methane concentrations at sites remote from sources are typically in the range of 1.7-1.8 ppm (Finlayson-Pitts and Pitts, 2000). Figure 1-7 shows a time series for all methane samples for the 2012 winter test period at locations throughout the Uintah Basin. The gas chromatograph that produced these data, on occasion, poorly integrated methane peaks, leading to low or zero methane values. Zero values have been eliminated from the dataset, but values below the global background methane concentration are visible in the dataset, and these values may be artificially low.

Horse Pool experienced frequent values well above the tropospheric average (Figure 1-7). Figure 1-8 shows that maximum concentrations typically occurred during early morning (pre-sunrise) hours when atmospheric mixing was lowest, while minimum concentrations usually occurred in late afternoon when atmospheric mixing was greatest. In contrast to NO_x diurnal profiles, these data indicate that sources of methane and NMHC are likely more constant and stationary.

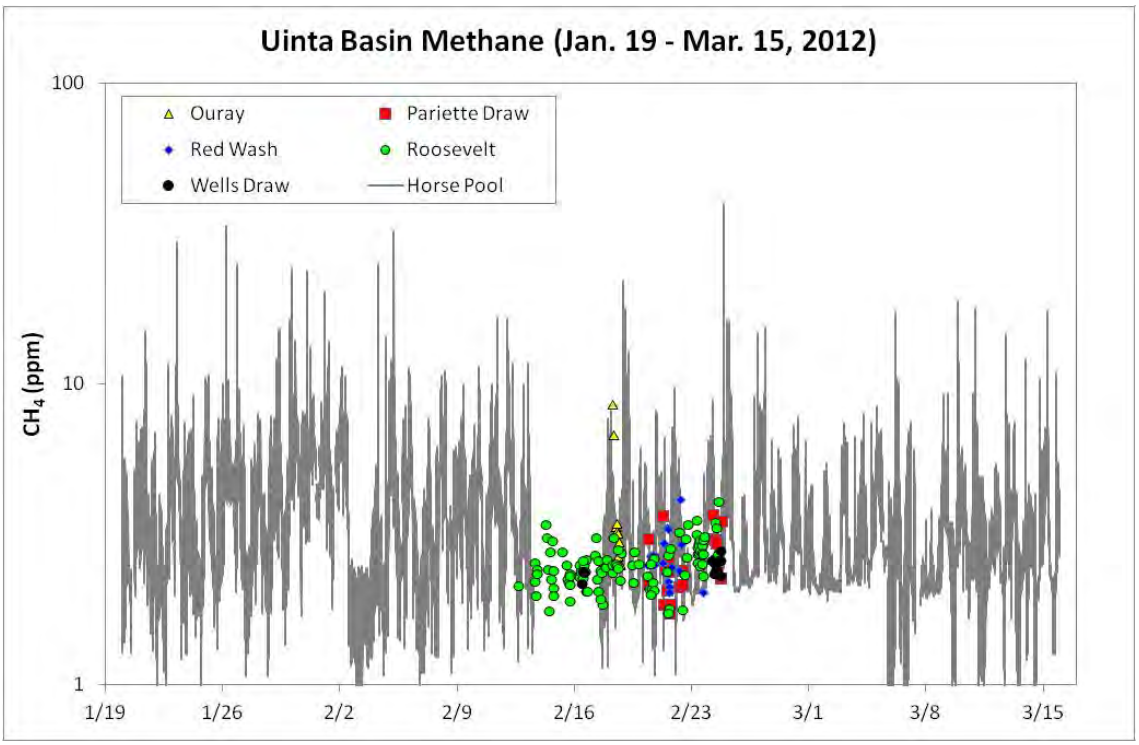

Figure 1-7. Ambient methane time series for automated analyzer at Horse Pool, along with grab samples from other sites, Jan.-Mar. 2012. Methane concentrations at sites remote from sources tend to be 1.7-1.8 ppm (Finlayson-Pitts and Pitts, 2000).

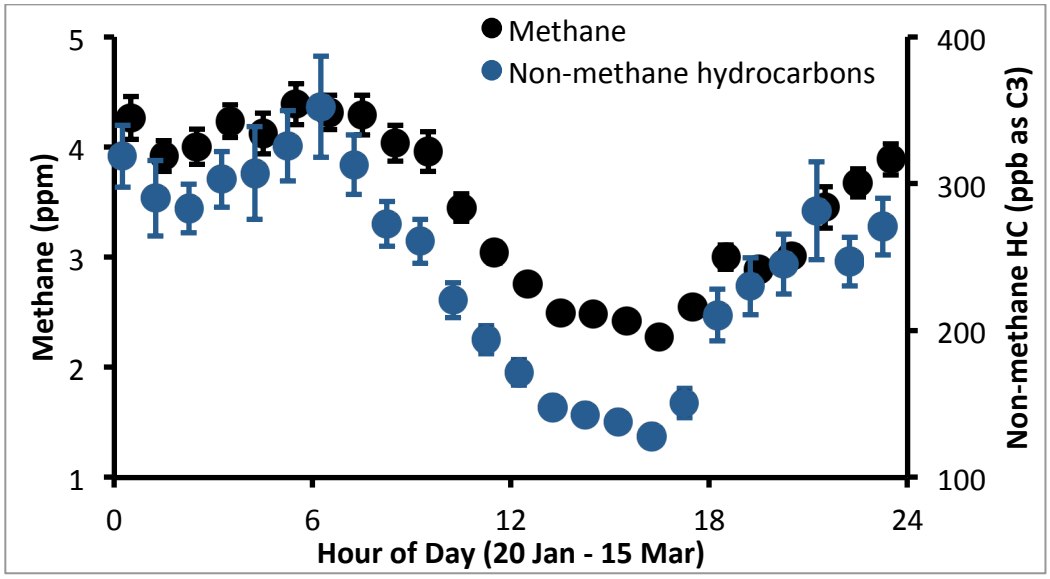

Figure 1-8. Diurnal methane and NMHC concentrations at Horse Pool. Circles represent hourly means, and whiskers represent 95% confidence intervals.

Figure 1-9 shows that the Horse Pool location experienced more variable ambient methane concentrations than other sites. This difference could be at least partly due to the fact that this site had a much larger dataset than the others. Ouray, despite a limited number of sample collections (n=10), was found to have the highest average methane concentration (3.92 ppm). The Basin-wide average methane concentration for the data shown in Figure 1-9 was 2.7 ± 0.3 ppm, 1.5 times the tropospheric background value.

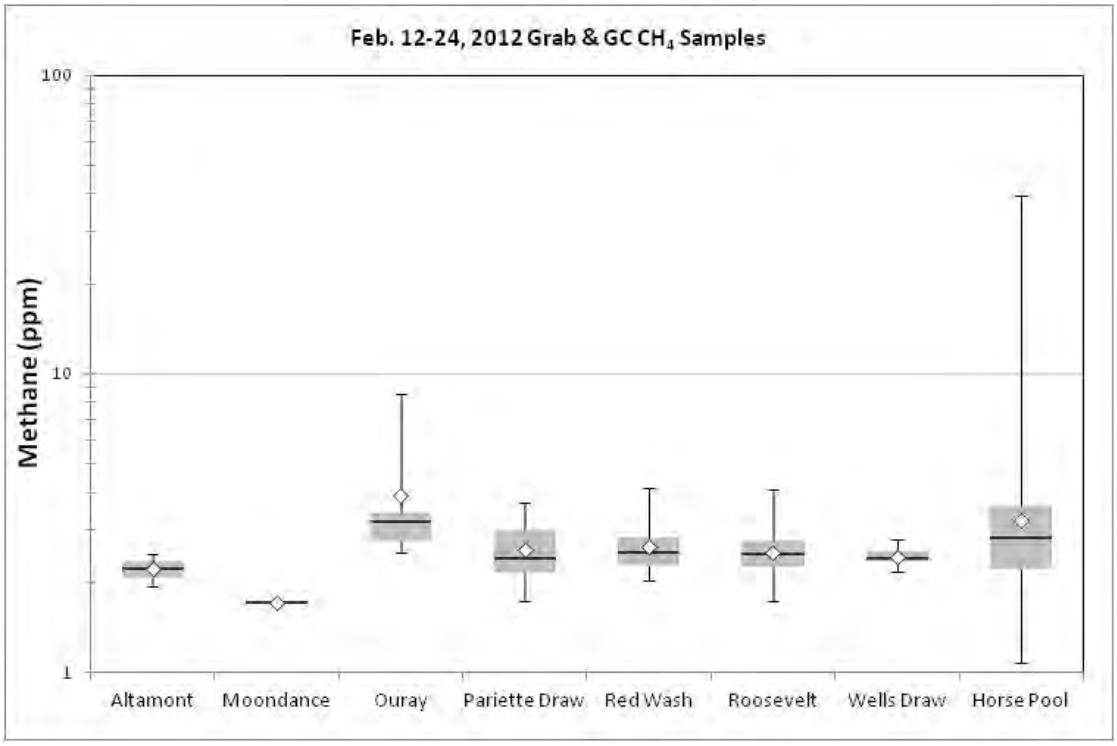

Figure 1-9. Box-whisker plot of methane concentrations at several sites, 12-24 Feb. 2012. Centerlines represent means, white diamonds represent medians, top and bottom edges of grey boxes represent 25th and 75th percentiles, and whiskers represent the maximum and minimum concentrations.

Methane concentrations measured in this study compare favorably with values observed in February 2011 (Martin et al., 2011) when Vernal methane averaged 1.7 ± 0.2 ppm and Red Wash averaged 2.8 ± 0.6 ppm. Other investigators measured methane in the Basin during winter 2011-12 and reported similar, and at times higher, methane concentrations at Horse Pool and other sites within oil and gas production areas.

NMHC concentrations were lower (243 ± 4.1 ppb as C3) than the methane concentrations over the study period. The diurnal behavior of the NMHC was similar to methane, with maximums occurring during the early morning hours (Figure 1-8).

Figure 1-10 shows a plot of methane vs. nonmethane hydrocarbons. Two non-methane/methane signatures are apparent: one with a non-methane/methane slope of approximately 0.185 and another with a slope of about 0.08. The higher slope was dominant when wind blew from the northwest, though air that came from other directions also showed some evidence of this signature.

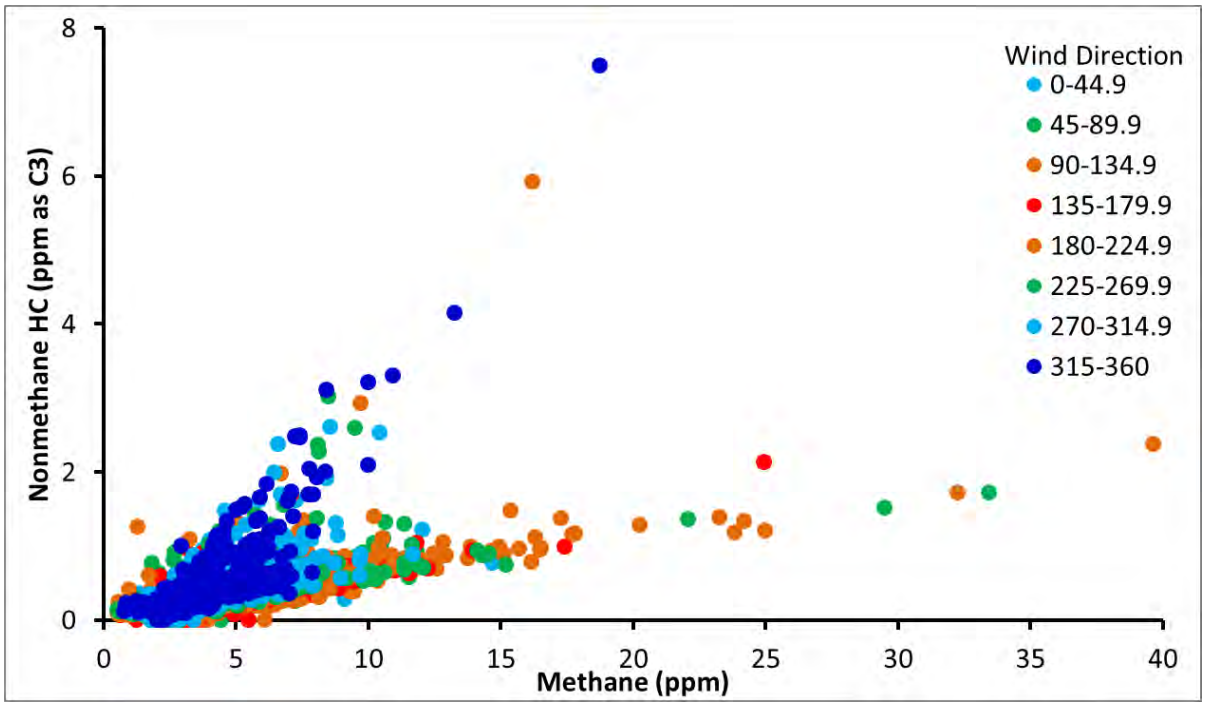

Figure 1-10. NMHC vs. methane at Horse Pool. Points are colored by wind direction at time of data collection. Cooler colors indicate wind from the northwest, and warmer colors indicate wind from the opposite direction.

Further investigation of these two different regimes, which likely indicate different source types, was pursued on 21 February 2012 by manual collection of Tedlar bag grab samples at different locations surrounding the Horse Pool site. Samples were taken by facing upwind and repeatedly filling and evacuating a 100 mL gas-tight syringe into a clean Tedlar bag until at least 1.5 L had been obtained. The bags were then analyzed in triplicate on the methane-nonmethane hydrocarbon analyzer at Horse Pool.

The non-methane:methane concentration ratio in Tedlar bag samples showed spatial variability in the area around Horse Pool (Figure 1-11; the concentration ratio is related to, but distinct from, the slope of the linear regression relationships discussed above). Samples near Ouray and Pelican Lake had similar methane concentrations to other samples, but had almost 75% higher NMHC concentrations (data not shown), resulting in higher non-methane:methane ratios. While the spatial distribution of non-methane:methane ratios does not exactly correspond with the wind sector with highest slope in Figure 1-10, it does indicate that different areas of the Basin have different source signatures. NOAA investigators identified higher order (>C6) hydrocarbons as a potential source of the increased NMHC in air at Horse Pool that came from the northwest (J. Gilman, personal communication). The source of the additional hydrocarbons is unclear. Figure 1-11 shows little oil and gas activity in the area with higher non-methane:methane ratios; however, the ratio of oil wells to gas wells is higher in this area and throughout the area northwest of Horse Pool, which may lead to fewer methane emissions relative to emissions of heavier hydrocarbons.

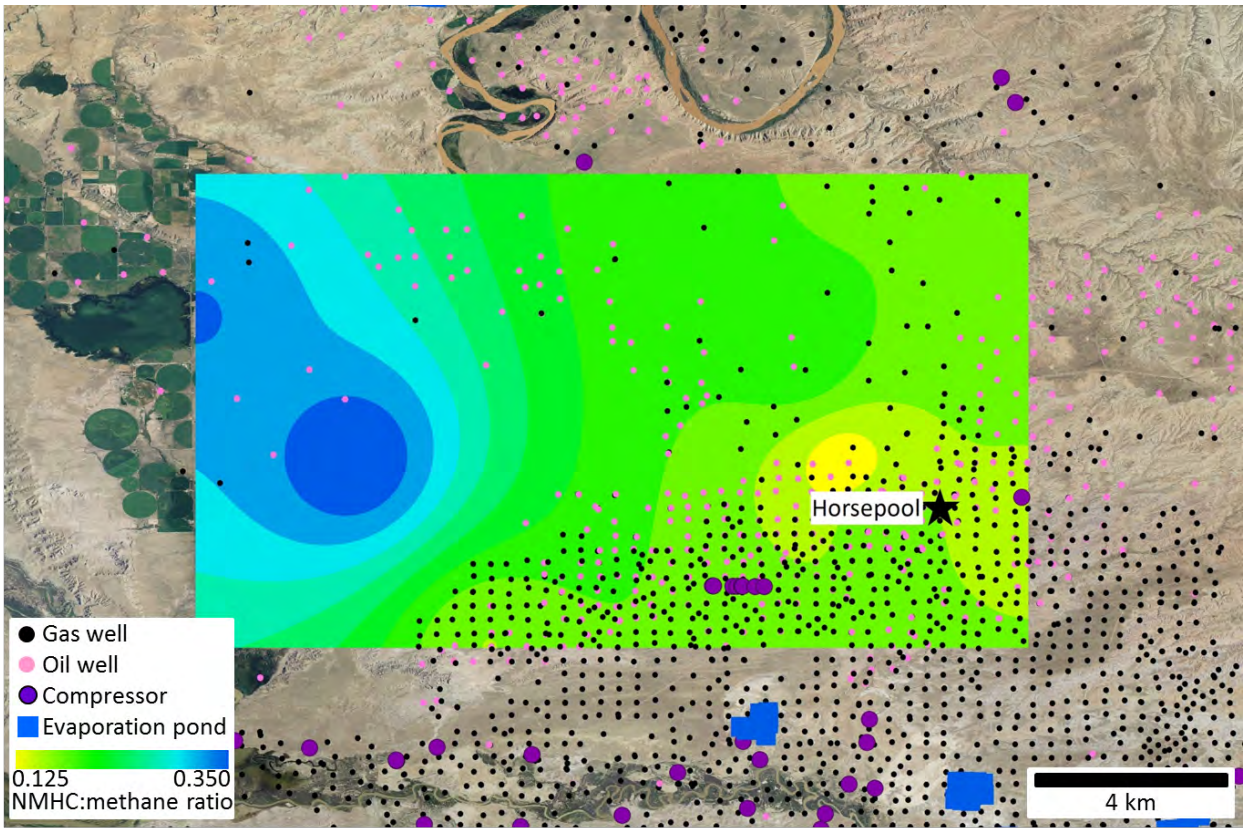

Figure 1-11. Non-methane:methane ratios in air samples near Horse Pool, 21 Feb. 2012.

Speciated NMHC at Roosevelt

Hydrocarbons in canister samples at Roosevelt were dominated by alkanes, especially lighter alkanes and methylcyclohexane (Figure 1-12). Benzene, toluene, and xylenes were low, and C8 and larger aromatics were rarely observed. A number of branched and cyclic alkanes were frequently observed. No alkenes were observed. Lighter straight-chain alkanes were more abundant than heavier straight-chain alkanes (Figure 1-13). Alkane concentrations were more abundant during the night and morning than during midday and early evening (Figure 1-13), and other hydrocarbons followed this same trend (data not shown). This diurnal trend is similar to the observed trend for methane and NMHC at Horse Pool (Figure 1-8).

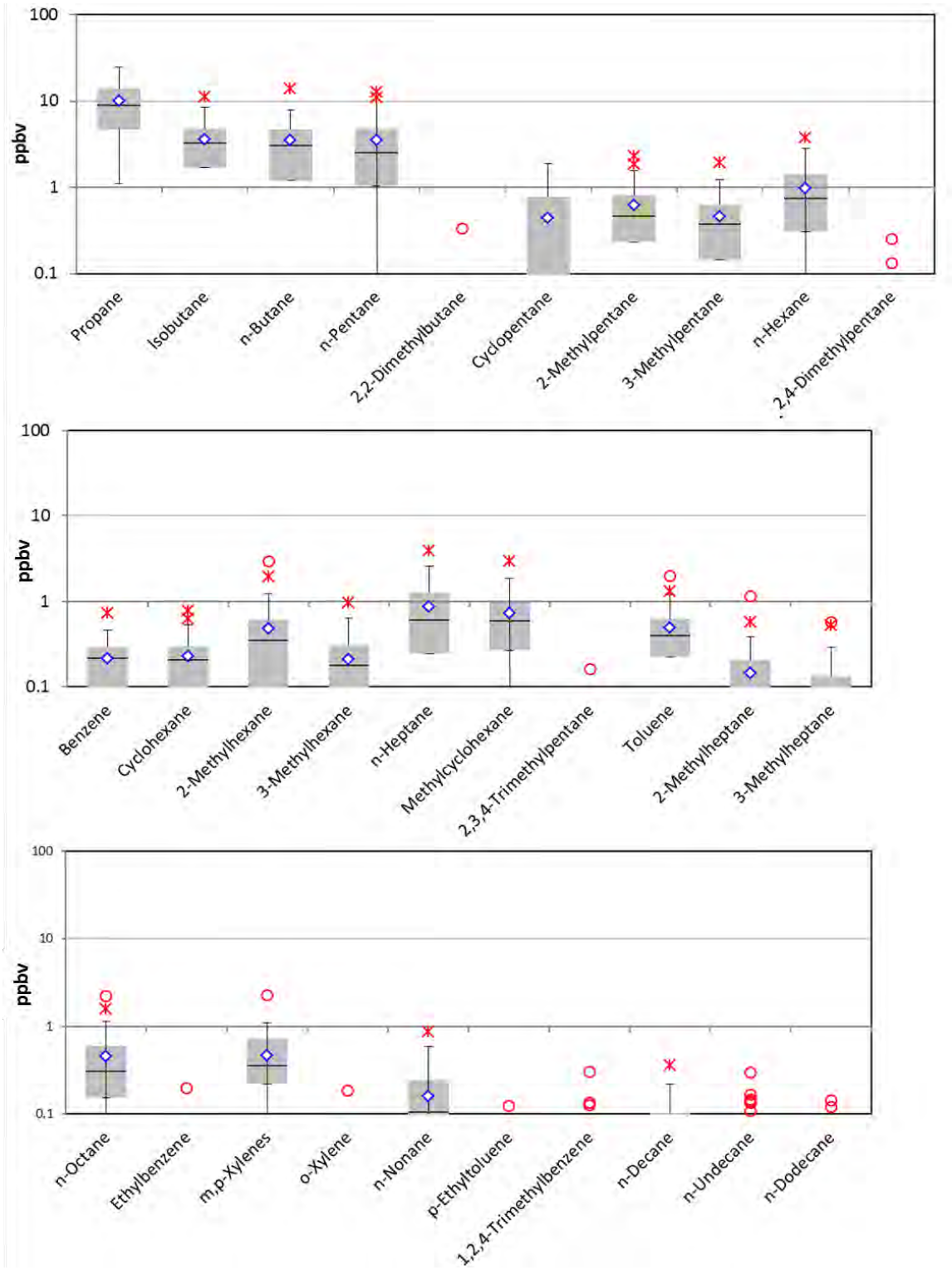

Figure 1-12. C3-C12 VOC compounds at Roosevelt, 14-24 Feb. 2012. Centerlines in grey boxes represent means, white diamonds represents medians, edges of grey boxes represent 25th and 75th percentiles, whiskers represent maximum and minimum concentrations, and circles or asterisks represent statistical outliers.

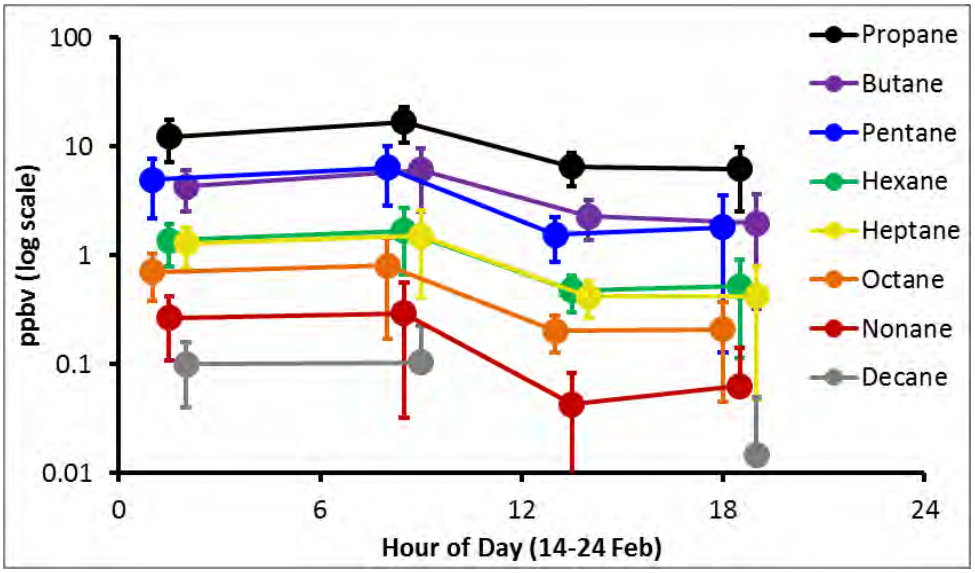

Figure 1-13. Average concentration of straight-chain alkanes at Roosevelt, 14-24 Feb. 2012, at different collection times.

Hydrocarbons at Roosevelt were 48% lower than at Horse Pool for the 14-24 February time period (Horse Pool data collected by NOAA; 15 compounds compared). Straight-chain alkanes were 45% lower, branched and cyclic alkanes were 68% lower, and aromatics were 38% lower. Of aromatics, m- and p-xylenes were 20% higher at Roosevelt than Horse Pool, while o-xylene, benzene, and toluene were 57%, 71%, and 43% lower, respectively.

Relative hydrocarbon concentrations were different at Roosevelt than at Horse Pool. Figure 1-14 shows linear regression relationships between select compound pairs at both sites. Slopes of regression lines are different for the two sites. A regression slope of the relationship between two compounds indicates that a unit increase in one compound is associated with a corresponding increase in the other compound. Assuming both compounds are emitted from the same source or source region, these regression relationships (also called enhancement ratios) can be used to characterize and identify sources based on known emissions characteristics (Weiss-Penzias et al., 2007). The distinct regression slopes at Roosevelt and Horse Pool indicate the existence of a different mix of sources at each site.

The benzene-toluene slope at Roosevelt was similar to published slopes for urban areas (e.g., 0.30 determined by Palmgren et al., 1999). The Benzene-o-xylene slope at Roosevelt closely matched published emission ratios from gasoline-powered motor vehicles (e.g., 2.99 mol mol^{-1} in Schauer et al., 2002). Butane-toluene slopes, however, were 49 and 99 times higher at Roosevelt and Horse Pool, respectively, than from gasoline engine emissions. These data indicate that gasoline engine exhaust was not the primary source of butane (or other alkanes) at these sites, and that alkane sources (including oil and gas extraction-related sources) were stronger at Horse Pool.

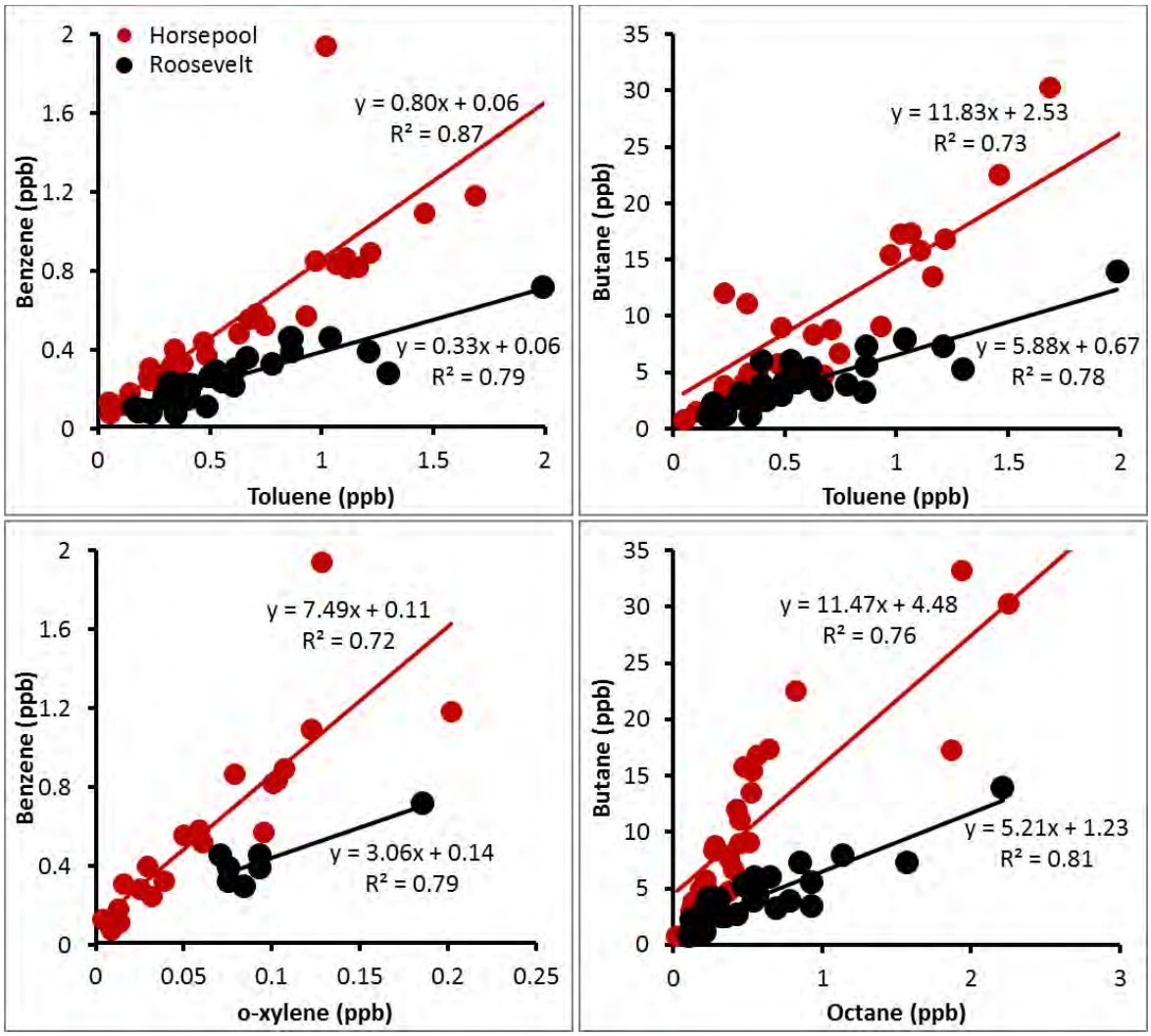

Figure 1-14. Relationships between hydrocarbon pairs at Horse Pool (red) and Roosevelt (black) for the same times of day, 14-24 Feb. 2012.

Carbonyl Compounds

Carbonyl compounds are reactive, and it is very likely that carbonyl concentrations measured from canister samples at Roosevelt were biased because of reactions that occurred in canisters after collection (Kelley and Holdren, 1995; Pate et al., 1992). Thus, carbonyl results from Roosevelt will not be considered here.

At Horse Pool, formaldehyde, acetaldehyde, and acetone were consistently detected, while larger carbonyl compounds were only occasionally detected. Formaldehyde (1.73 ± 0.13 ppb; mean ± 95% confidence interval) was the dominant carbonyl species, followed by acetone (0.67±0.10 ppb) and acetaldehyde (0.63 ± 0.17 ppb) (Figure 1-15). Among the targeted carbonyl species, only acrolein was never observed at Horse Pool.

Formaldehyde is both directly emitted (e.g., motor vehicles, building materials) and photochemically formed in the oxidation of various hydrocarbons, including methanol (methanol was observed in air at

Horse Pool by NOAA investigators). Finlayson-Pitts and Pitts (2000) summarize typical urban, rural/suburban, and remote concentrations of formaldehyde as 1-60 ppb, 0.1-10 ppb, and 0.3-2.0 ppb, respectively. Horse Pool formaldehyde concentrations are more consistent with rural or remote areas.

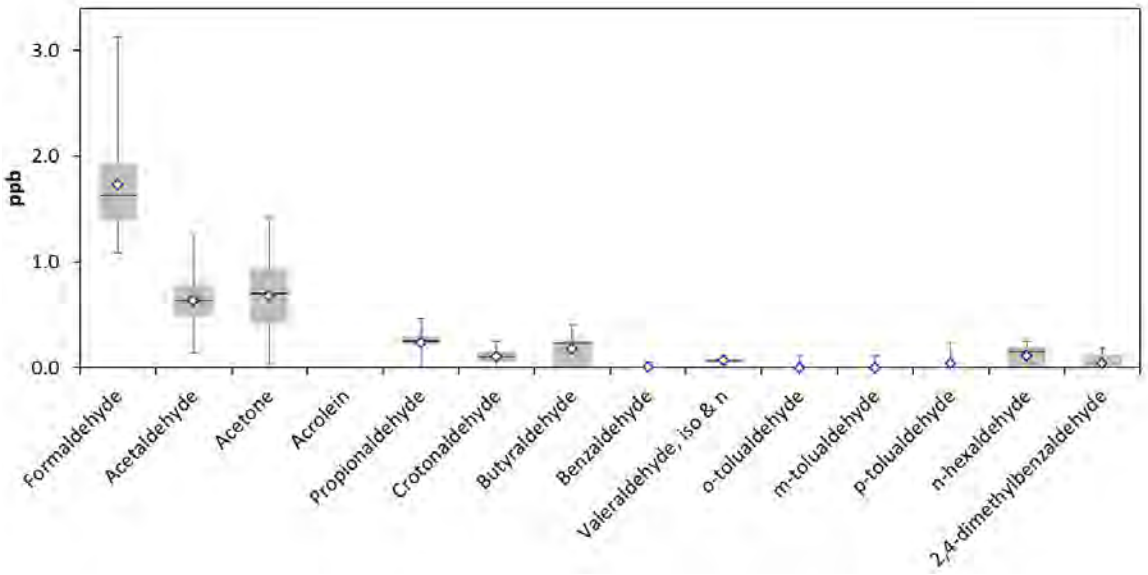

Figure 1-15. Carbonyl compounds at Horse Pool, 12-24 Feb. 2012. Centerlines in grey boxes represent means, white diamonds represent medians, edges of grey boxes represent 25th and 75th percentiles, and whiskers represent maximum and minimum concentrations.

Carbonyl compounds at Horse Pool peaked during midday and were lowest in the morning (Figure 1-16), though only formaldehyde showed a statistically significant morning-midday difference at the 95% confidence level. This profile indicates photochemical formation for some carbonyl species, in contrast with the diurnal profile of methane and NMHC at Horse Pool (Figure 1-8).

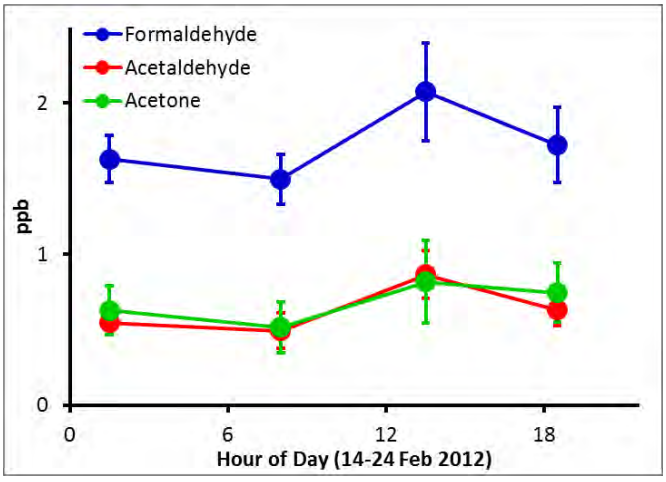

Figure 1-16. Diurnally averaged formaldehyde, acetaldehyde, and acetone as measured at Horse Pool (14-24 Feb. 2012). Circles indicate means, and whiskers represent 95% confidence intervals.

Particulate Matter

Figure 1-17 compares winter 2011-12 particulate data collected at Roosevelt and Horse Pool with 2010-11 data collected at Vernal and Red Wash. Measurements during 2011 were performed during an inversion event with snow-covered ground, while the 2012 measurements were performed without persistent inversion events or snow cover. The observed 2011 and 2012 concentrations did not exceed the 24-hr National Ambient Air Quality Standards (NAAQS) for $PM_{2.5}$ (35 µg/m^3) or PM_{10} (150 µg/m^3).

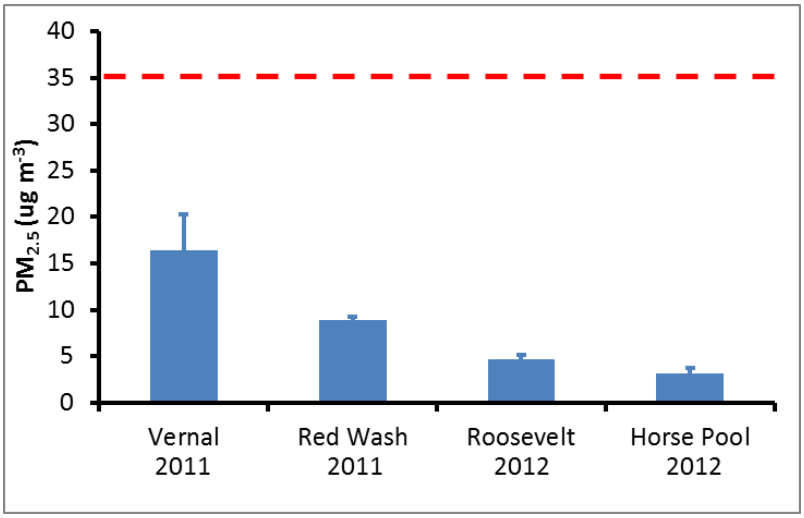

Figure 1-17. Average $PM_{2.5}$ concentrations for Feb. 2011 (Vernal and Red Wash) and 2012 (Roosevelt and Horse Pool). Whiskers represent standard deviations. The red dashed line represents the EPA NAAQS standard for $PM_{2.5}$ (24 hour average).

PM_{10} data at Horse Pool were characterized by frequent spikes, with some one-hour values greater than 150 µg/m^3 (Figure 1-18). Examination of the timing of these spikes shows the major peaks are associated with wind events and possibly vehicle traffic. This behavior is not unexpected as the lack of precipitation during the winter left much of the surrounding terrain and roads quite dry. $PM_{2.5}$ was only a small fraction of the airborne PM_{10} at the Horse Pool site, averaging 23.9 ± 4.3%. Furthermore, $PM_{2.5}$ was characterized by fewer spikes and rarely exceeded 20 µg/m^3.

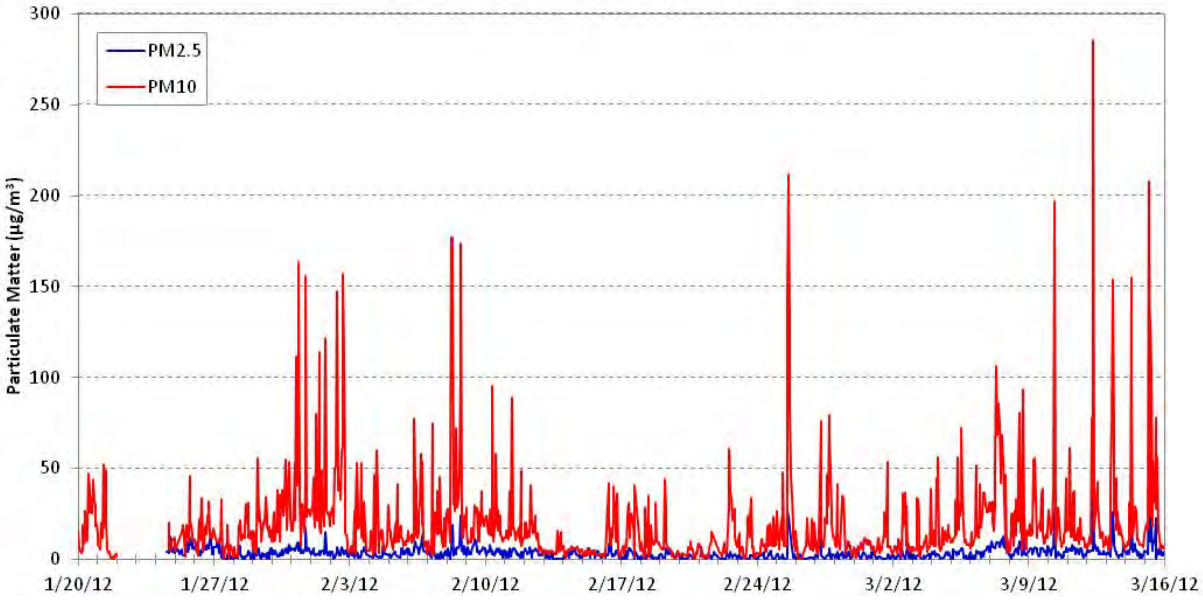

Figure 1-18. Hourly $PM_{2.5}$ and PM_{10} concentrations at Horse Pool, winter 2012.

Figure 1-19 shows 24-hour average $PM_{2.5}$ from Roosevelt, Horse Pool, and Vernal for January and February 2012. The more populated areas show slightly higher $PM_{2.5}$ concentrations, although the general trends are consistent between sites.

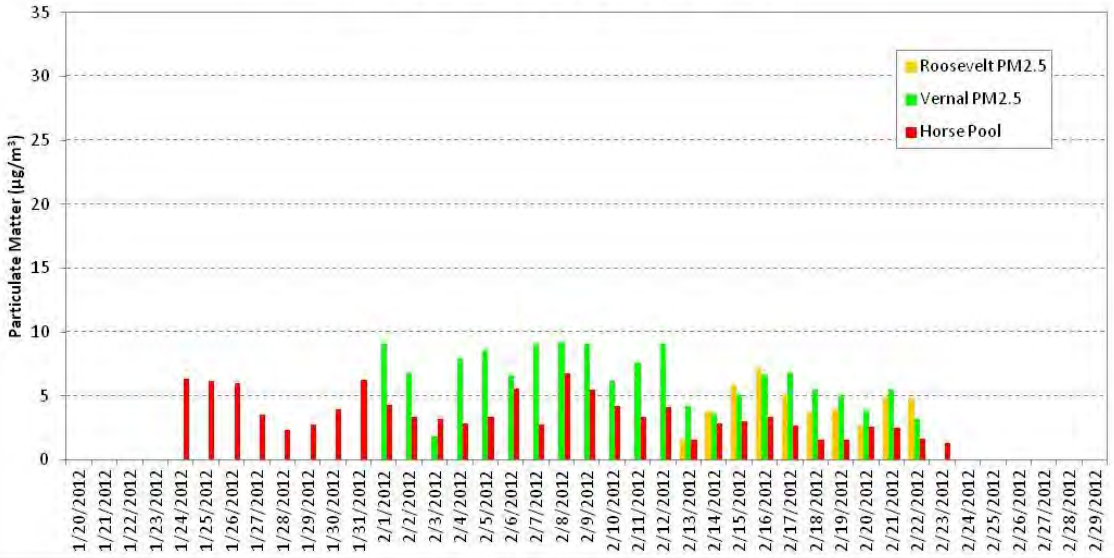

Figure 1-19. 24-hour $PM_{2.5}$ concentrations for Roosevelt, Vernal, and Horse Pool.

$PM_{2.5}$ mass at Roosevelt was dominated by organic and elemental carbon (Figure 1-20). The organic mass fraction accounted for an average of 69.8%, while the elemental carbon fraction averaged 3.3%. The remaining $PM_{2.5}$ mass fractions consisted of 10.2% soil (crustal) elements, 12.3% anions, and 8.0% cations. The 10.2% soil mass portion averaged 52% silicon-based materials, 18% aluminum based materials, 17% calcium-based materials, and 10% iron-based materials. The 12.3% anion mass fraction

consisted primarily of sulfate (64%), nitrate (33%), and chloride (3%). The bulk (97%) of the cationic mass fraction was made up of the ammonium ion.

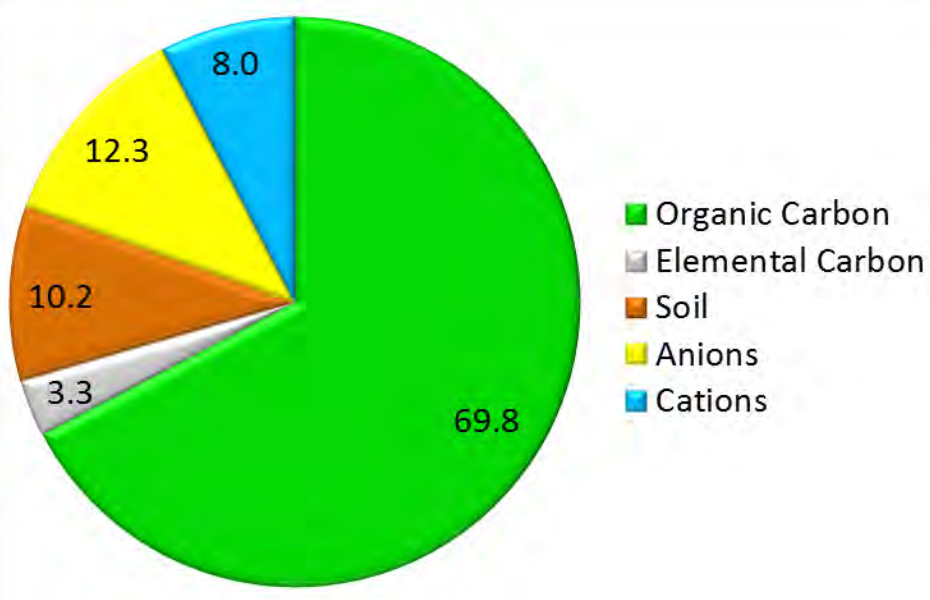

Figure 1-20. Average chemical composition of filter-collected $PM_{2.5}$ at Roosevelt, 13-25 Feb. 2012.

$PM_{2.5}$ compositional analysis from February 2011 was very similar to this study (Martin et al., 2011). Vernal $PM_{2.5}$ chemical speciation on 21-25 February 2011 was 64.1% organic mass, 13.4%, elemental carbon 0.4% crustal elements, 8.6% anions, and 9.5% cations. $PM_{2.5}$ at Red Wash during the same period was 69.6% organic mass, 12.8% elemental carbon, 3.5% crustal elements, 6.5% anions, and 7.7% cations.

These data contrast with observations made in other areas of Utah wherein photochemically-formed $PM_{2.5}$ is a wintertime non-attainment issue (especially in the Wasatch Front and Cache Valley) and ionic components, most notably ammonium (NH_4^+) and nitrate (NO_3^-), often account for mass percentages similar to that of the carbon component in the Uintah Basin (R. Martin, unpublished data). At sites in the Interagency Monitoring of Protected Visual Environments (IMPROVE) network, organic fine mass comprises 20-30% of total fine particle mass in the central Rocky Mountain region (Malm et al., 2004). The percent of organic carbon mass in Uintah Basin $PM_{2.5}$ samples, high relative to other locations in the region, indicates that local sources contribute to primary and/or secondary organic aerosol. Oil and gas extraction activity, shown in Chapter 2 to have a strong spatial relationship with elevated ambient hydrocarbon mixing ratios, is one likely source of this organic material.

Although USU chemical analysis at the Roosevelt site was very consistent with the 2011 compositional analysis, $PM_{2.5}$ measurements made by NOAA at Horse Pool showed a different composition, with crustal material comprising 42% and organic matter 31% of particle mass. The NOAA data also contrasts with University of Wyoming aerosol mass spectrometer measurements at the same site that observed organic material at 55% of sub-micron particle mass. The reason for this discrepancy is not known with certainty, but the NOAA $PM_{2.5}$ measurements at Horse Pool were about 10 meters from a dirt road, and it is likely that road dust contributed to their measurements, whereas the University of Wyoming measurements likely excluded road dust because of the targeted smaller particle size. Measurements

by USU in 2011 and 2012 were either not near well-traveled dirt roads or were performed in the presence of snow cover that limited the influence of dust.

Solar Radiation

Winter ozone formation is highly dependent on reflectance of sunlight by snow (Schnell et al., 2009). Due to snow surface reflectance (i.e., albedo), the amount of solar radiation available for ozone production can actually be greater in winter than in summer. Accurate measurements of solar radiation and surface reflectance are critical to understanding and modeling ozone formation in the Uintah Basin.

Snow cover was not present for an extended time in the Uintah Basin during the winter of 2012, but short periods of snowfall and snow cover did occur. One such period occurred 19-23 February. This snowfall period was not accompanied by inversion conditions or ozone concentrations above EPA standards, but it did show that snow cover dramatically increases reflectance of shortwave (300-2800 nm) and ultraviolet radiation. Figure 1-21 shows temperature and percent albedo of shortwave and ultraviolet radiation before, during, and after the short-lived snow event. On 19 February as snow accumulated during a storm, a rapid increase in albedo was observed. The next day, albedo rapidly decreased as temperature warmed and snow melted. Measurements like these improve estimates of chemical reaction rates that lead to ozone production and strengthen simulations of ozone production in numerical models.

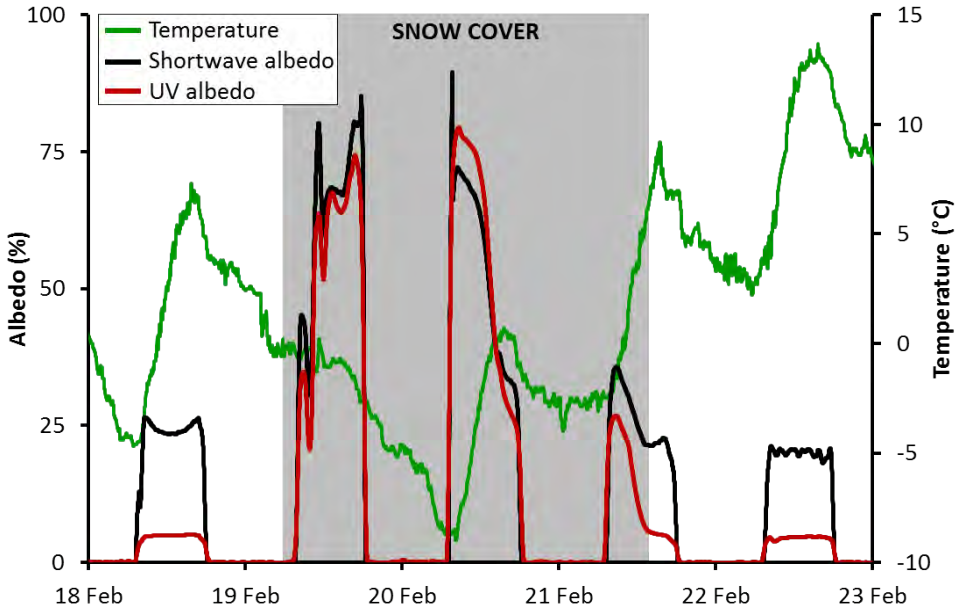

Figure 1-21. Temperature and percent albedo (i.e., surface reflectance) of shortwave (300-2800 nm) and ultraviolet radiation at Horse Pool, 18-23 Feb. 2012.

SUMMARY

The Horse Pool and Roosevelt study sites provide a sound, long-term infrastructure for understanding the meteorological and chemical processes involved in winter ozone production. Sustained site operation will provide data fundamental to the scientific understanding of winter ozone formation in the Basin and essential to the development and verification of ongoing mitigation strategies.

This study showed that ozone precursor concentrations around the Basin are associated primarily with known emission sources that exist in the Basin (further corroborated in Chapter 2). The study revealed a strong link between ambient NO_x and traffic and showed spatially diverse sources of methane and VOC. In fact, concentrations, diurnal behaviors, and sources of methane, VOC, and reactive nitrogen compounds are different at different locations around the Basin. This spatial heterogeneity not only underscores the importance of a Basin-wide approach to monitoring but also mandates a regularly updated, scientifically informed and validated mitigation strategy that addresses the unique characteristics of the Basin.

While relatively rich in organic matter, likely due to the abundance of VOC sources in the Basin, particulate matter concentrations were shown to be well within established EPA standards.

REFERENCES

Aneja, V.P., Kim, D.S., Das, M., Hartsell, B.E.: Measurements and analysis of reactive nitrogen species in the rural troposphere of Southeast United States: Southern Oxidant Study site Sonia. Atmos. Environ., 30, 649-659, 1996.

Birch, M.E., and R.A. Cary: Elemental carbon-based method for monitoring occupational exposures to particulate diesel exhaust. Aerosol. Sci. Tech., *25*, 221-241, 1996.

ENVIRON, Final Report: A Conceptual Model of Winter Ozone Episodes in Southwest Wyoming. Prepared for Air Quality Division, Wyoming Department of Environmental Quality. Available: http://deq.state.wy.us/aqd/Ozone%20Main.asp, 2010.

EPA: Compendium of Methods for the Determination of Toxic Organic Compounds in Ambient Air, 2nd Edition, Compendium Method TO-11A, Determination of Formaldehyde in Ambient Air Using Adsorbent Cartridge Followed by High Performance Liquid Chromatography (HPLC) - [Active Sampling Methodology]. EPA/625/R-96/010b, 1999.

Finlayson-Pitts, B. J. and J. N. Pitts, Jr.. Chemistry of the upper and lower atmosphere: theory, experiments, and applications. Academic Press, San Diego, California, 2000.

IMPROVE: http://vista.cira.colostate.edu/improve/tools/AerTypeEqs.htm Standard Aerosol-Type Equations, last access: April 2011.

Kelly, T.J.; Holdren, M.W.: Applicability of canisters for sample storage in the determination of hazardous air pollutants. Atmos. Environ., 29, 2595-2608, 1995.

Malm, W.C. and J.L. Hand: An examination of the physical and optical properties of aerosols collected in the IMPROVE program. Atmos. Environ., 41, 3407-3427, 2007.

Malm, W.C.; Schichtel, B.A.; Pitchford, M.L.; Ashbaugh, L.L.; and Eldred, R.A. J. Geophys. Res., 109, D03306, DOI: 10.1029/2003JD003739, 2004.

Martin, R.S., K. Moore, M. Mansfield, S. Hill, K. Harper, and H. Shorthill: Final Report: Uinta Basin Winter Ozone and Air Quality Study, EDL/11-039, June 14, 2011.

Palmgren, F.; Berkowicz, R.; Ziv, A.; Hertel, O.: Actual car fleet emissions estimated from urban air quality measurements and street pollution models. Sci. Total. Environ., 235, 101-109, 1999.

Pate, B.; Jayanty, R.K.M.; Peterson, M.R.; Evans, G.F. Temporal stability of polar organic compounds in stainless steel canisters. J Air. Waste. Manage., 42, 460-462, 1992.

Roussel, P.B., Lin, X., Camacho, F., Laszlo, F., Taylor, R., Melo, O.T., Shepson, P.B., Hastie, D.R., Niki, H. Observations of ozone and precursor levels at two sites around Toronto, Ontario, during SONTOS 92. Atmos. Environ., 30, 2145-2155, 1996.

Schauer, J.J.; Kleeman, M.J.; Cass, G.R.; Simoneit, B.R.T. Measurement of emissions from air pollution sources. 5. C1-C32 organic compounds from gasoline-powered motor vehicles. Environ. Sci. Technol., 36, 1169-1180, 2002.

Schnell, R.C; Oltmans, S.J.; Neely, R.R.; Endres, M.S.; Molenar, J.V.; White, A.B. Nature Geosci. DOI: 10.1038/NGEO415, 2009.

U.S. Census Bureau: http://www.google.com/publicdata/explore?ds=kf7tgg1uo9ude_&met_y=population&idim=place:4964670&dl=en&hl=en&q=roosevelt+utah+population, last access: June 2012.

Weiss-Penzias, P.; Jaffe, D.; Swartzendruber, P.; Hafner, W.; Chand, D.; Prestbo, E.: Quantifying Asian and biomass burning sources of mercury using the Hg/CO ratio in pollution plumes observed at the Mount Bachelor Observatory. Atmos. Environ., 41, 4366-4379, 2007.

CHAPTER II

DISTRIBUTED MONITORING OF OZONE, PRECURSORS, AND METEOROLOGY

Seth Lyman[1], Kori Moore[2], Randy Martin[3], Howard Shorthill[1], Scott Hill[4], and Chad Mangum[1]

[1]Bingham Entrepreneurship & Energy Research Center, Utah State University, Vernal, UT.

[2]Space Dynamics Laboratory, Utah State University Research Foundation, Logan, UT.

[3]Utah Water Research Laboratory, Utah State University, Logan, UT.

[4]Carbon Energy Innovations Center, Utah State University Eastern, Price, UT.

*Kiera Harper, Utah Department of Environmental Quality, participated in establishing sites and collecting and processing essential data.

INTRODUCTION

The distribution of ozone precursor concentrations and meteorology in the Uintah Basin ostensibly influences where and when elevated ozone occurs, but these parameters have not been measured with adequate spatial coverage or analyzed in sufficient detail to elucidate the relationship. During the winter months of 2010-11, measurements at 17 sites around the Uintah Basin provided a detailed account of the spatial distribution of ozone during several episodes of elevated ozone production. Ozone precursor concentrations in 2010-11, on the other hand, were monitored at just six sites, and vertical measurements of ozone and meteorology were collected for only four days at one site.

The 2011-12 study reported here (1) adds to existing datasets of spatial and temporal trends in ozone in the Basin and (2) shows spatial trends in oxides of nitrogen (NO_x), volatile organic compounds (VOC), and meteorological data in the Basin in 2011-12. The growing dataset will be critical for validation of air quality models developed for regulation and research, will improve understanding of the year-to-year variability and spatial distribution of ozone and precursor concentrations, and will help determine how changes in meteorology and emissions affect ozone concentrations.

For winter 2011-12, ten additional monitoring stations were distributed to supplement the 17 sites retained from the 2010-11 study. The additional sites covered areas on the periphery of the Basin, particularly areas of extensive oil and gas development. Data from sites under different authority are also included here. Most sites measured ozone from January 1 through March 15, minimally. NO_x and VOC sample deployment and collection occurred during February. Measurements at several of the sites have continued through summer 2012, but those data are not included here.

METHODS

Monitoring Sites

A total of 32 sites, including those established and maintained by other organizations, monitored ozone in and adjacent to the Uintah Basin. Locations are shown in Figure 2-1, and Table 2-1 provides information about each site. Monitors were sited and installed in accordance with guidelines given in 40 CFR 58 Appendix E, "Probe and Monitoring Path Siting for Ambient Air Quality Monitoring," including the stipulation to avoid proximity to potentially interfering air pollutant sources. Monitoring sites

established as part of this study were installed and maintained in cooperation with the Utah Department of Environmental Quality (UDEQ).

Passive samplers were also deployed at ten of the ozone monitoring sites to assess the spatial concentrations of NO_x and VOC. NO_x were also measured with active samplers at six sites operated by other organizations. Additional VOC measurements were made at Horse Pool and Roosevelt and are reported in Chapters 1 and 3.

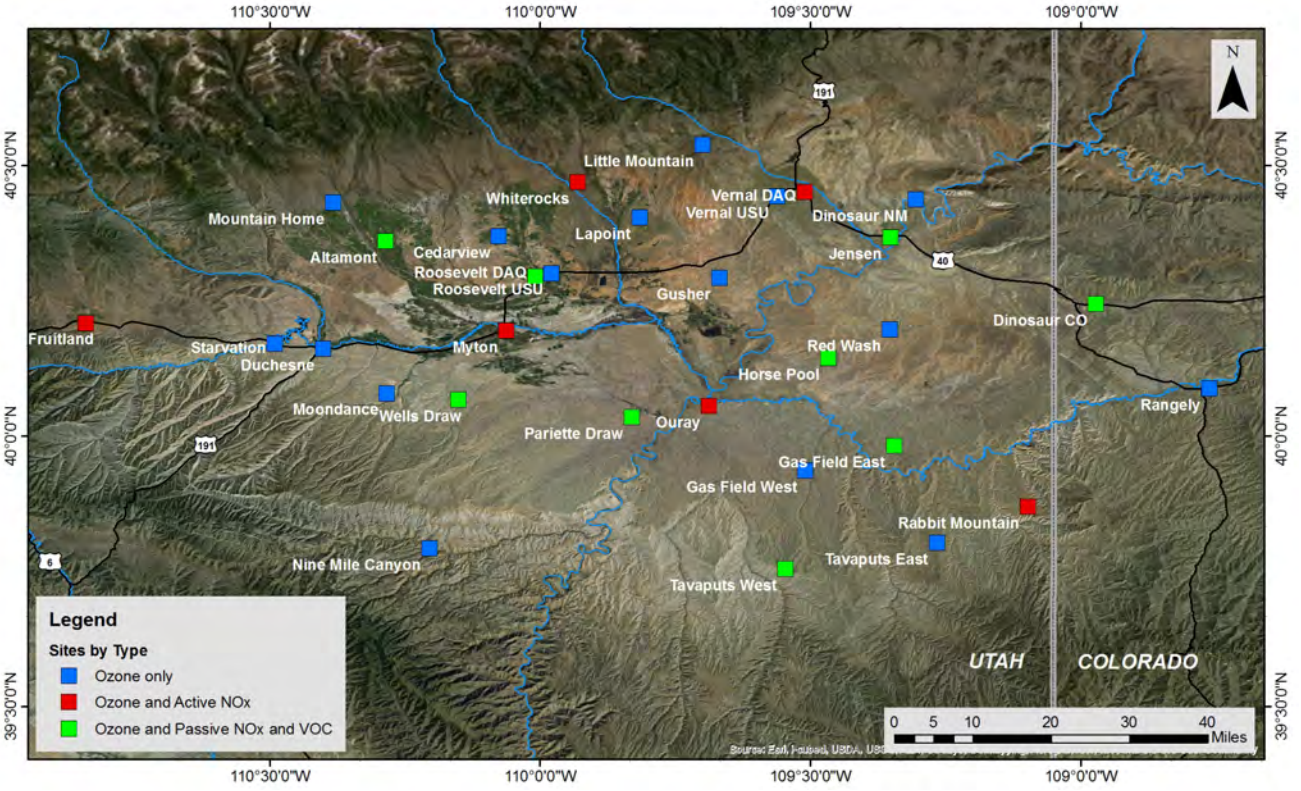

Figure 2-1. 2011-12 monitoring sites.

Table 2-1. Uintah Basin ozone monitoring site locations.

Location	Authority	Longitude	Latitude	Elevation (m)
Altamont	USU/UDEQ	40.3603	-110.2858	1950
Cedarview	USU/UDEQ	40.3835	-110.0726	1692
Dinosaur, CO	USU/UDEQ	40.2436	-108.9722	1814
Dinosaur NM	NPS/ARS	40.4371	-109.3047	1463
Duchesne	USU/UDEQ	40.1615	-110.4011	1682
Fruitland	UDEQ/AMC	40.2087	-110.8403	2021
Gas Field West	USU/UDEQ	39.9813	-109.3454	1608
Gas Field East	USU/UDEQ	40.3007	-109.9784	1618
Gusher	USU/UDEQ	39.9352	-109.5094	1557
Horse Pool	USU/UDEQ	40.2935	-109.6575	1569

Jensen	USU/UDEQ	40.1437	-109.4672	1451
Lapoint	USU/UDEQ	40.3671	-109.3522	1674
Little Mountain	NFS-EDL	40.4040	-109.8157	2624
Moondance	USU/UDEQ	40.5368	-109.7001	1978
Mountain Home	USU/UDEQ	40.0788	-110.2831	2234
Myton	Ute Tribe	40.4319	-110.3821	1550
Nine Mile Canyon	BLM	40.1948	-110.0622	1732
Ouray	Golder Assoc.	39.7919	-110.2035	1464
Pariette Draw	USU/UDEQ	40.0548	-109.6880	1467
Rabbit Mountain	Enefit	40.0346	-109.8301	1879
Rangely, CO	NPS/BLM	39.8687	-109.0973	1648
Red Wash	Golder Assoc.	40.0869	-108.7616	1689
Roosevelt (UDEQ)	USU/UDEQ	40.1972	-109.3525	1587
Roosevelt (USU)	USU/UDEQ	40.2942	-110.0090	1545
Starvation	USU/UDEQ	40.1706	-110.4905	1766
Tavaputs East	USU/UDEQ	39.8022	-109.2658	1880
Tavaputs West	USU/UDEQ	39.7539	-109.5460	1975
Vernal (UDEQ)	UDEQ	40.4531	-109.5097	1606
Vernal (USU)	USU/UDEQ	40.4433	-109.5610	1663
Wells Draw	USU/UDEQ	40.0670	-110.1510	1768
Whiterocks	Ute Tribe	40.4694	-109.9304	1841

Ozone Measurements

2B Technology Model 205 ozone monitors were used at most sites operated by USU and UDEQ. The sites at Wells Draw and Gusher used 2B Model 202 ozone monitors on loan from the Bureau of Land Management (BLM), and Ecotech Model 9810 and Teledyne-API Model 400 analyzers were used at the Horse Pool and Roosevelt (UDEQ) sites, respectively. Solar-powered stations, supplied by UDEQ and BLM, were deployed where electrical power was not available.

Quarter-inch diameter Teflon sample tubes (from three to ten meters in length) with Teflon funnel inlets and five-micron particulate filters were used upstream of ozone monitors. For solar-powered sites, sample inlets were at three meters. For sites in buildings, sample inlets were about one meter above roof level and from three to five meters above ground level, with the exception of the Vernal (USU) site where the inlet was two meters above roof level and 15 m above ground level.

Ozone monitor locations operated by USU and UDEQ were visited every two weeks during which service maintenance, data retrieval, three-point calibration checks, and, if necessary, monitor recalibrations were performed. Calibration checks were performed at 0, 90, and 140 ppb ozone using 2B Model 306 calibrators checked against NIST-traceable primary ozone standards. Calibration checks passed if monitors reported in the range of ±5 ppb when exposed to 0 ppb ozone, and if monitors were within ±7% deviation from expected values when exposed to 90 and 140 ppb ozone. If monitors failed checks, calibrations were performed at five points spaced linearly between 0 and 140 ppb. Data not bracketed by successful calibration checks were either adjusted via linear correction, when feasible, or withheld from the final dataset. The correction assumed a linear change in instrument response over the two-week period between calibration checks.

Geospatial Analysis

Geospatial analyses and map production were performed using ArcMAP 10 (ESRI). Geographic Information System data utilized in these operations were downloaded from the following sources:

> BLM Colorado. Available: http://www.blm.gov/co/st/en/BLM_Programs/geographical_sciences/gis.html. Last accessed: 28 Apr. 2011.
>
> Colorado Department of Transportation. Available: http://www.coloradodot.info/. Last accessed: 27 Apr. 2011.
>
> Colorado Oil and Gas Conservation Commission. Available: http://cogcc.state.co.us/. Last accessed: 7 June 2012.
>
> U.S. Geologic Survey National Elevation Dataset. Available: http://ned.usgs.gov. Last accessed: 22 Mar. 2011.
>
> Utah GIS Portal. Available: http://agrc.its.state.ut.us/. Last accessed: 19 July 2012.

Ozone concentrations were spatially interpolated using the Natural Neighbor interpolation tool in ArcMAP. The default option of a variable search radius that includes 12 data points was utilized in the interpolation process.

Oxides of Nitrogen

Ogawa passive samplers were used to measure NO_x at ten of sixteen NO_x measurement sites ($NO + NO_2$; Ogawa, 2012). Each sampler held one sorbent pad to collect NO_2 and one pad to collect NO_x. NO was determined as the difference between the pads. Gloves were worn during sample handling. Before deployment, samplers were rinsed thoroughly with distilled water, followed by 18.2 megaohm water, then covered and allowed to dry for at least 24 hours. No more than 24 hours before deployment, samplers were assembled and sealed in plastic bags within opaque plastic containers. Samplers were deployed in Radiello outdoor shelters at 2.5 m above ground level. After deployment, samplers were again sealed in plastic bags within opaque containers and were stored in a freezer until analysis.

All sampler deployments were for one week, and at least two field blanks were collected during each deployment. Three replicate samples were implemented at one or more sites during each deployment. Samples were analyzed using a Dionex ICS 3000 ion chromatograph.

NO_2 and NO_x were blank corrected using average field blank values for the entire study, 2.4 ± 1.4 and 2.7 ± 0.9 ppb, respectively (i.e., mean ± standard deviation). Since NO was derived as the difference between NO_x and NO_2, no NO-specific blank correction was applied (NO field blank values were 0.3 ± 1.3 ppb). Detection limits were calculated as two times the standard deviation of blanks, which resulted in detection limits of 2.6, 2.9, and 1.8 ppb for NO, NO_2, and NO_x, respectively. The relative standard deviation of replicate samples (100 × standard deviation/mean) was 89 ± 68%, 41± 55%, and 23 ± 9% for NO, NO_2, and NO_x, respectively.

Passive NO_x samplers were deployed alongside active NO_x samplers for six weeks at Horse Pool, four weeks at Fruitland, and two weeks at Roosevelt. Figure 2-2 shows passive NO_x measurements vs. weekly average active NO_x measurements for the three sites. Blank-corrected passive NO_x values were 155 ± 145% greater than weekly averaged active NO_x data. The cause of this bias is unclear. It is possible the Radiello outdoor shelters did not provide adequate protection from wind, but passive NO_x were not correlated with average wind speed ($R^2 = 0.01$). Passive NO_x data were corrected to match active measurements based on the reduced major axis regression relationship between the two

datasets. The correlation between passive and active data was low (R^2 = 0.04). Much of the variability between passive and active NO_x is likely due to both sampling methods being near their respective detection limits.

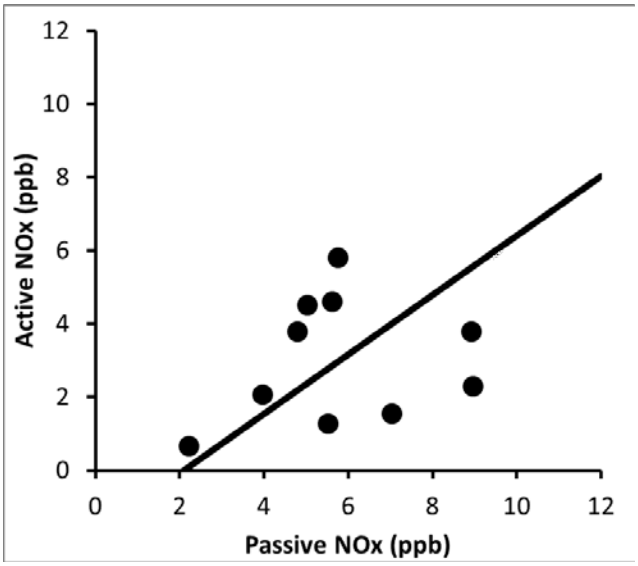

Figure 2-2. Passive NO_x measurements versus weekly average active NO_x measurements at Fruitland, Horse Pool, and Roosevelt. The line represents the reduced major axis regression relationship between active and passive measurements.

Volatile Organic Compounds

Radiello passive samplers (Model RAD120 diffusive body and Model RAD130 sorbent cartridge) were used to measure VOC (Radiello, 2012). New sorbent cartridges were placed in clean Radiello diffusive bodies, capped, and sealed in trace-clean 250 ml I-Chem glass jars with Teflon lids less than 24 hours before sampling. Samplers were deployed in Radiello outdoor shelters at 2.5 m above ground level. After deployment, samplers were returned to I-Chem jars for transport, and sorbent cartridges were placed in capped glass tubes for analysis.

All sampler deployments were for one week, and at least two field blanks were collected during each deployment. Three replicate samples were deployed at one or more sites during each deployment.

For VOC analysis, two ml of CS_2 was added to the tube containing the adsorbent cartridge. The cartridges were allowed to sit for 30 minutes. An aliquot of the CS_2 solution then was put in an autosampler and analyzed with a Shimadzu QP-2010 gas chromatograph with a flame ionization detector and mass spectrometer. The following standards were used for calibration: methyl-cyclopentane, benzene, cyclohexane, n-heptane, methyl-cyclohexane, toluene, ethyl-benzene, o-xylene, alpha-pinene, n-undecane. These standards were chosen because they represented a good distribution of retention times and were of interest to this study. Calibration curves from these compounds were used to quantify unknown peaks with similar retention times to the calibration compounds. Peaks were identified via retention time and mass spectra.

Data processing followed Radiello standard methods, and unknown peaks were quantified by assuming similarity to calibration compounds with similar retention times. Radiello Model 130 cartridges cannot quantify hydrocarbons with fewer than six carbons due to interference from the solvent peak and are

not effective for hydrocarbons larger than undecane. Mixing ratios for individual compounds are reported as ppbv of that compound. Mixing ratios for C6-C11 VOC (organic compounds with 6-11 carbon atoms, including unidentifiable peaks) were quantified as propane-equivalent ppb by (1) multiplying ppbv of each compound by the number of carbons in that compound to obtain ppbC, (2) dividing ppbC by three to obtain propane-equivalent ppb, and (3) summing the results of each peak for the entire sample.

Blanks for total C6-C11 VOC (including quantification of unidentifiable peaks) were 0.57 ± 0.42 ppb. Individual chromatographic peaks from field blanks were typically unidentifiable, and blank corrections for individual compounds were not applied. Relative standard deviations of replicates were 7.4 ± 5.1% for total C6-C11 VOC and averaged 22.9 ± 24.0% for individual compounds. Also, one deployment at Roosevelt and four deployments at Horse Pool overlapped with canister and real-time gas chromatograph data collection, respectively (Figure 2-3). The percent difference between passive and active measurements during these periods (100 × [passive-active]/active) was -38.7 ± 49.1%. Passive data were corrected using the reduced major axis regression relationship with active measurements.

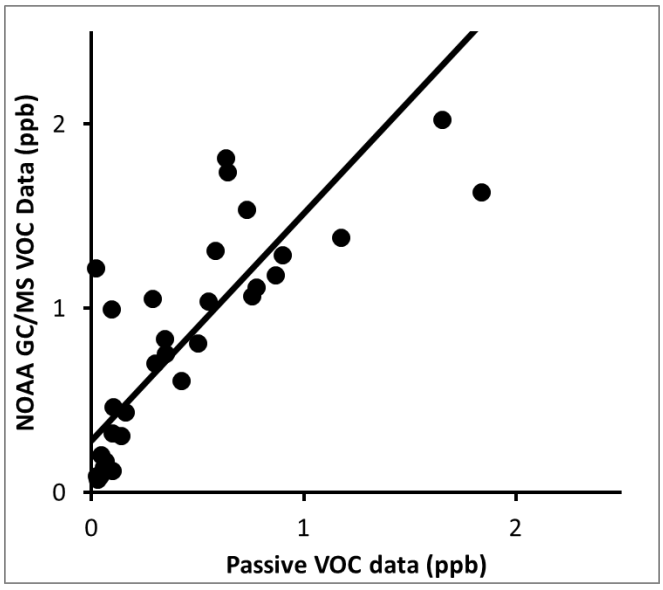

Figure 2-3. Values for individual VOC from weekly passive deployments at Horse Pool versus weeklong average VOC data from real-time samples collected by NOAA.

Meteorological Monitoring

Meteorological data were collected at 41 sites in and around the Uintah Basin (Figure 2-4). Parameters measured included temperature, relative humidity, pressure, wind speed, and wind direction at three meters above ground level.

Figure 2-4. Measurement locations of meteorological data in the Uintah Basin.

Vertical Measurements

Vertical measurements of ozone and meteorology were made using balloon-borne packages at Roosevelt, Red Wash, Ouray, Wells Draw, and Pariette Draw, 14-25 February. A modified 2B Technologies Model 205 analyzer was attached to the balloon and used to measure vertical ozone profiles. Two Anasphere SmartTether systems were used to concurrently measure temperature, relative humidity, pressure, and wind speed and direction profiles at different locations. Meteorological packages and the ozone analyzer were suspended about three meters below the balloons.

Ascent and descent of the balloon were manually controlled, with a standard initial height above ground of the package set at 2.0 m. Final heights of the package were between 100 and 500 m above ground and were determined by the lower of either the maximum altitude achievable based on the lifting capacity of the balloon or the maximum altitude allowed in the Federal Aviation Administration (FAA) waiver for each site. The descent usually was initiated less than three minutes after the maximum height was reached to reduce the time between the start of the ascent and end of the descent. A total time for the ascent and descent of 20-30 minutes was targeted. Vertical profile meteorological characterization was performed throughout the day, with special focus on the following time periods: shortly after sunrise, midday, mid-afternoon, and sunset. Digital compass calibration checks were performed with the differences in reported and actual wind direction recorded and then used to correct wind direction data.

RESULTS AND DISCUSSION

Ozone

A time series of hourly average ozone concentrations at all sites is shown in Figure 2-5. No exceedances of the EPA National Ambient Air Quality Standard (NAAQS) of 75 ppb were measured during the study period. Compliance with the NAAQS occurs if the three-year mean of the annual fourth highest daily maximum eight-hour average is lower than 75 ppb (NAAQS, 2012). The highest one-hour average, highest eight-hour average, and fourth highest eight-hour average values were recorded at Lapoint during this study (Table 2-2). The lowest values in each of these categories were measured at the Vernal UDEQ site.

The highest ozone levels recorded at most sites occurred on March 10 and 11, but were well below the EPA's 75 ppb standard. The highest recorded one-hour average was 65.8 ppb at Lapoint on March 10. In contrast, the highest one-hour average observed during the winter 2010-11 study was 149.0 ppb at Ouray. Daily maximum one-hour averages at all sites showed an increasing trend from December to March, which may be associated with the natural increase in incoming solar radiation as the days move further from the winter solstice. Average incoming solar radiation at the Ouray site from early January through early March is shown in Figure 2-6.

Nighttime ozone depletion greater than 20 ppb occurred almost daily at some sites throughout the Basin. Ozone removal may be due to surface deposition and reactions with other gas phase species, especially NO (Sillman, 1999). The strongest decreases in ozone concentrations were measured in the Duchesne, Roosevelt, and Vernal population centers. The location, regularity, and degree of depletion are evidence of strong impacts by local sources of ozone-removing compounds—probably mostly NO—associated with the population centers. The dominant anthropogenic source of NO is combustion, including automobiles, other engines, and heating systems.

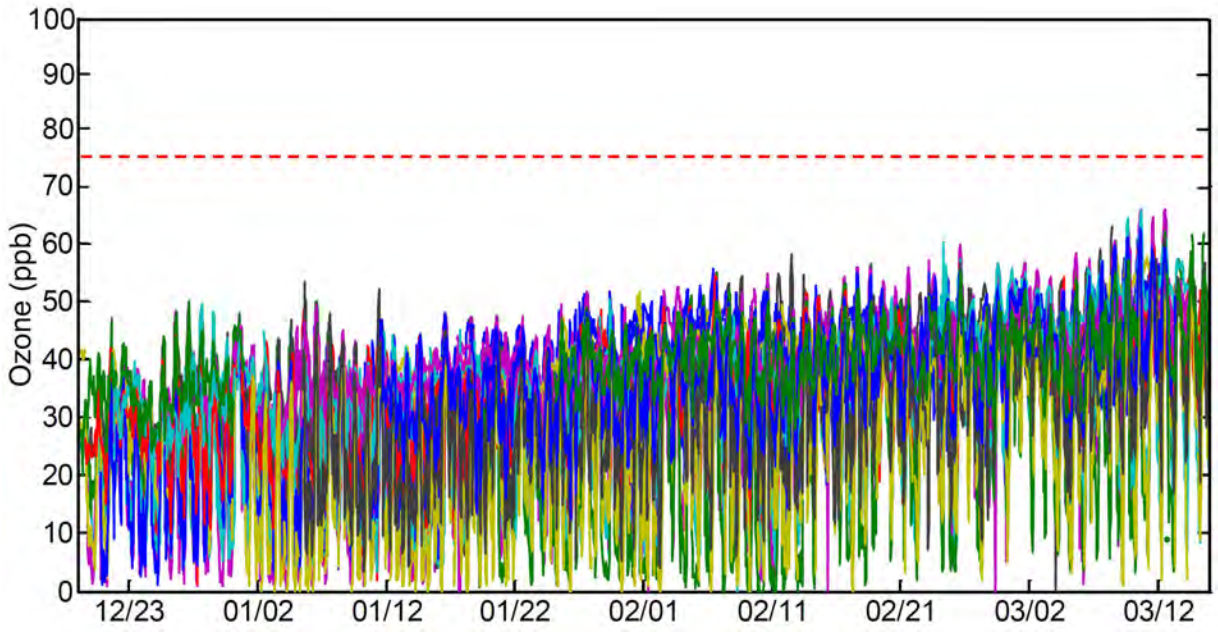

Figure 2-5. Time series of hourly average ozone concentrations observed at all monitoring locations in the Uintah Basin in winter 2011-12. Each colored trace indicates an individual monitoring station. The red dashed line shows 75 ppb.

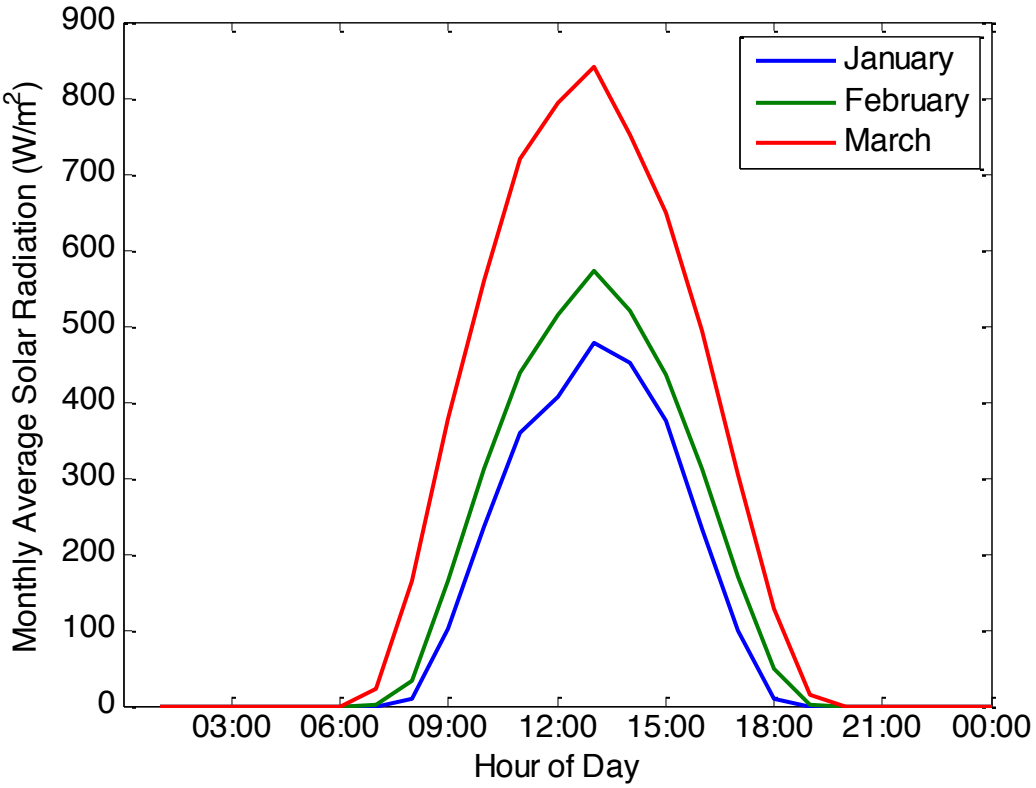

Figure 2-6. Averaged incoming solar radiation at Ouray for several time periods, winter 2012.

Table 2-2. Ozone concentrations recorded at each measurement site, winter 2011-12.

Site	Median of 1-hr Values	Highest 1-hr Average	Highest 8-hr Average	4th Highest 8-hr Average	Number of Exceedances
Altamont	41.1	60.7	56.4	54.3	0
Cedarview	39.8	62.9	58.8	58.1	0
Dinosaur, CO	39.2	58.8	56.3	55.2	0
Dinosaur NM	28.1	62.9	58.2	57.7	0
Duchesne	36.4	58.8	55.5	53.1	0
Fruitland	36.0	59.0	56.0	55.1	0
Gas Field East	35.7	63.1	59.0	55.0	0
Gas Field West	38.9	59.8	56.0	55.0	0
Gusher	42.8	65.0	61.1	59.9	0
Horse Pool	36.4	62.4	57.4	56.7	0
Jensen	33.0	59.9	55.6	54.7	0
Lapoint	44.7	65.8	62.9	62.0	0
Little Mountain	44.1	57.9	56.5	56.4	0
Moondance	39.5	60.3	55.5	54.2	0

Mountain Home	45.5	61.7	58.7	57.5	0
Myton	39.0	60.0	57.1	55.4	0
Ouray	33.0	59.0	55.4	52.5	0
Pariette Draw	35.6	61.4	57.1	55.7	0
Rabbit Mountain	40.8	59.4	56.8	55.0	0
Rangely	28.7	56.5	52.9	51.4	0
Red Wash	36.0	57.0	55.8	54.6	0
Roosevelt DEQ	30.0	60.0	55.4	54.6	0
Roosevelt USU	27.9	62.3	56.9	56.3	0
Starvation	41.4	61.7	58.7	57.8	0
Tavaputs East	42.3	65.6	62.4	60.6	0
Tavaputs West	40.9	57.0	54.1	53.6	0
Vernal DEQ	25.0	50.0	47.3	46.8	0
Vernal USU	32.4	60.9	56.6	55.7	0
Wells Draw	40.4	62.4	58.0	56.9	0
Whiterocks	42.0	57.0	54.4	53.5	0

Comparison of Winter 2011 and Winter 2012 Ozone Measurements

Figure 2-7 shows a time series of eight-hour average ozone concentrations in 2011 and 2012. No periods of ozone buildup above the NAAQS were observed in 2012. Monitoring stations in 2011, however, reported 25 NAAQS exceedances, with 14 of 17 sites affected (Martin et al., 2011).

Some similarities did exist between the 2011 and 2012 studies. The daily peak ozone values observed around the first of the year in 2011 (that is, before the first elevated ozone episode) were very similar to those observed in 2012 for the same time period, and values in mid-March were also similar for both years. Also, the Duchesne, Roosevelt, and Vernal population centers generally exhibited more ozone depletion during the nighttime hours in both 2011 and 2012 than other sites in less populated areas.

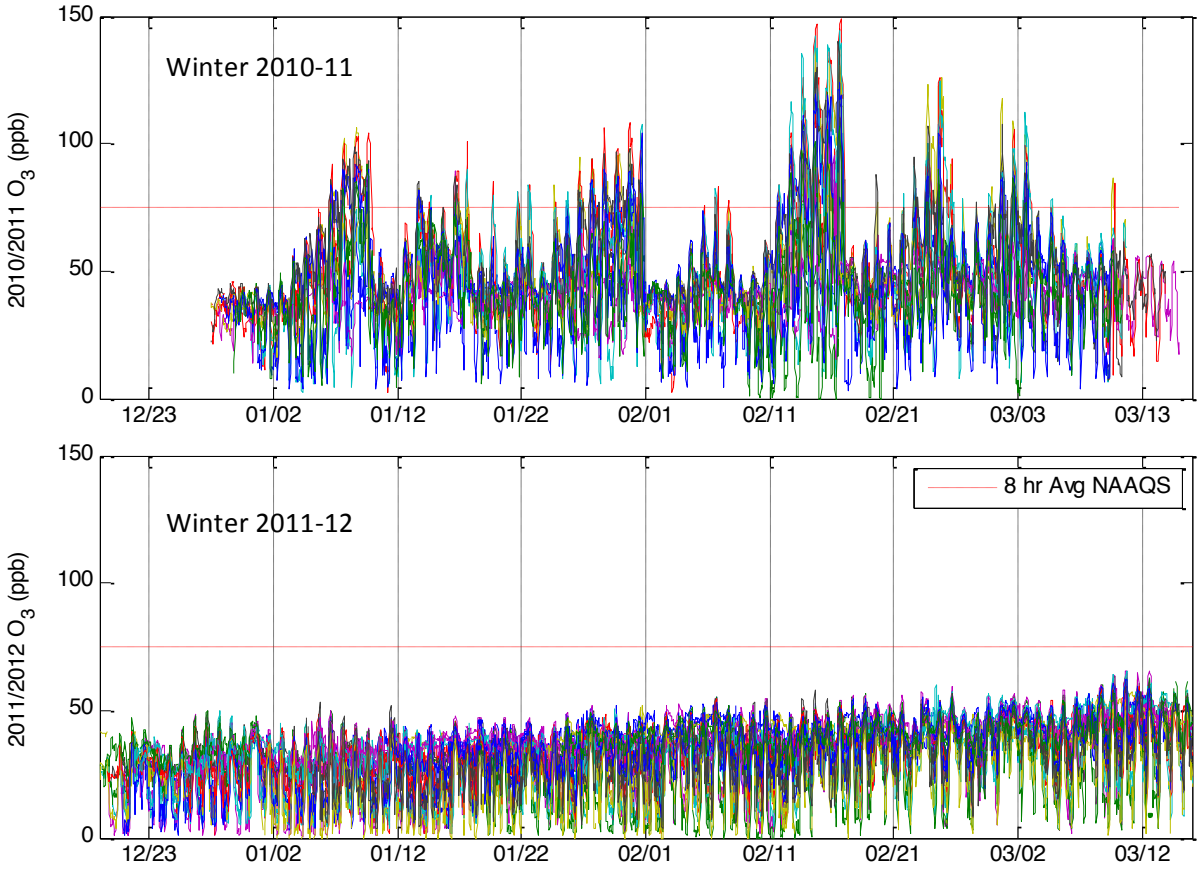

Figure 2-7. Hourly ozone concentrations in the Uintah Basin at all sites during winter 2010-11 and winter 2011-12 studies. Each colored line represents data from a different site. The horizontal red-dotted line marks the eight-hour average NAAQS value of 75 ppb.

Figure 2-8 shows contour maps of ozone distribution in the Basin. The first illustrates the highest hourly concentrations of the 2010-11 study (16 February 2011 at 15:00), and the second illustrates the highest hourly concentrations of the 2011-12 study (10 March 2012 at 15:00). The maps show very different ozone levels in the central area of the Basin, but concentrations in Fruitland, Altamont, Rabbit Mountain, and Rangely areas are similar for both years.

The contrast in ozone concentrations likely is due to the two winters' divergent meteorological and snow cover conditions. Winter 2011 had ample snow cover and multiple periods of persistent and stagnant temperature inversions, while winter 2012 experienced very limited snow cover and weak, short-lived temperature inversions. This year-to-year disparity highlights the role meteorology plays in producing wintertime ozone in the Uintah Basin. Elevated ozone values and a buildup of ozone over several days apparently occur only during periods of snow cover and temperature inversion. While snow cover was present throughout the winter in 2011, the buildup of ozone that led to concentrations above 75 ppb only occurred during multi-day calm periods between dynamic frontal systems. These same meteorological conditions were found to be necessary in producing elevated wintertime ozone levels in the Upper Green River Basin of Wyoming (Schnell et al., 2009; ENVIRON, 2010).

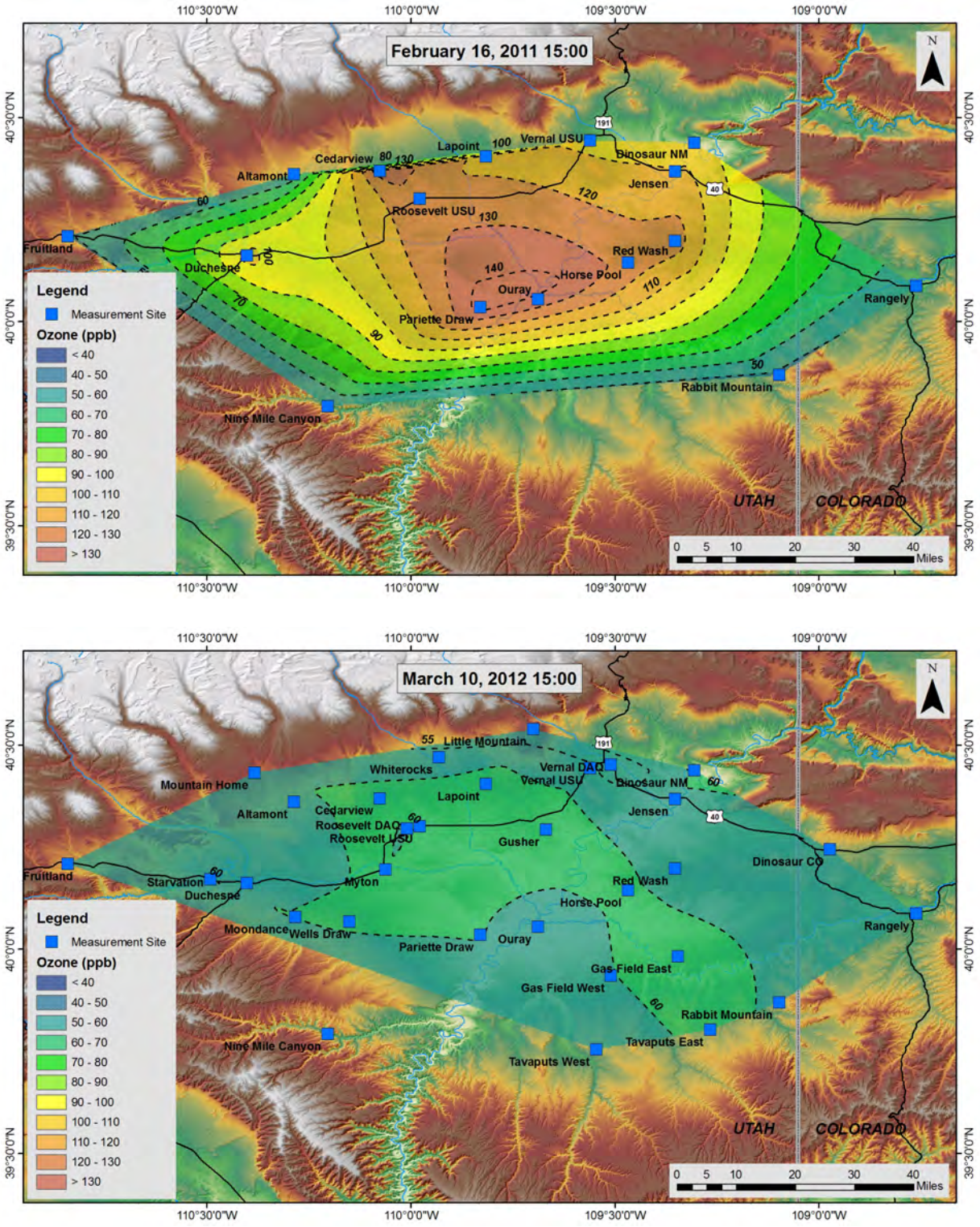

Figure 2-8. Highest one-hour average ozone concentrations in the Basin during the 2011 study on 16 Feb. at 15:00 (top) and the 2012 study on 10 Mar. at 15:00 (bottom). Color scales are on the same 10 ppb interval for both panels. The 2011 map uses 10 ppb contour lines; the 2012 map, 5 ppb.

Period of Highest Ozone: 8-11 March 2012

The highest ozone concentrations during winter 2011-12 were observed 8-11 March and are shown in Figure 2-9. Ozone concentrations and patterns were analyzed for this period and are discussed below.

A strong wind event occurred throughout the Basin around midnight on 8 March and lasted for several hours, resulting in a well-mixed atmosphere and uniform ozone concentrations at most sites. Most locations outside of the larger population centers did not see a decrease of ozone greater than 10-15 ppb in the early daylight hours on 8 March; however, large ozone decreases in population centers (Duchesne, Vernal, and Roosevelt) were observed shortly after the wind event ended. The time correlation with typical morning household activities and traffic patterns suggests that destruction of ozone by NO emitted from local combustion sources may have been responsible for this decrease. Other sites around the Basin exhibited less ozone reduction.

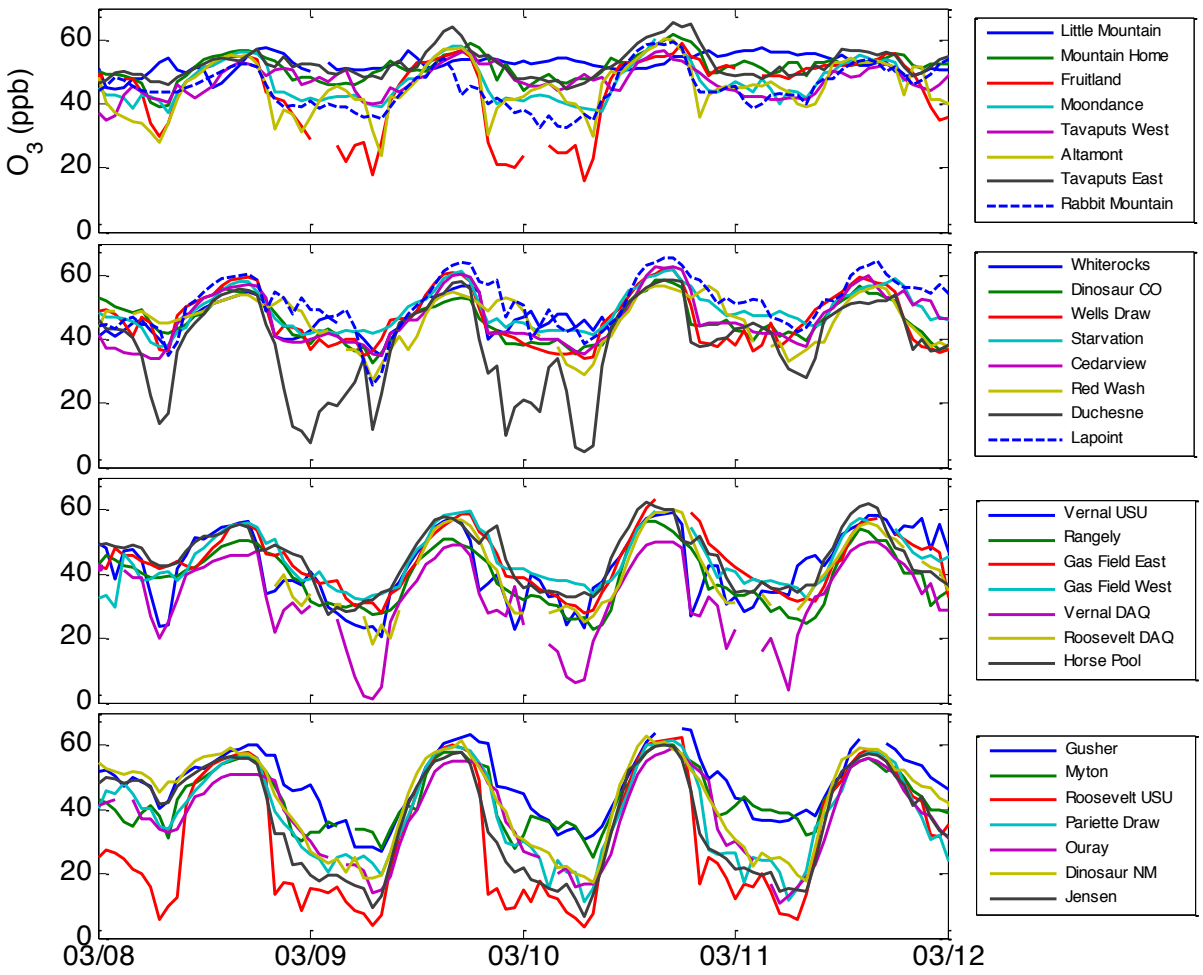

Figure 2-9. Ozone concentration time series at all sites during the highest recorded period of ozone levels, 8-11 Mar. 2012. In the legend, sites are ordered from highest to lowest elevation.

Very little diurnal variation in ozone concentrations was observed at Little Mountain, Mountain Home, Tavaputs East, and Tavaputs West (study sites of highest elevation) during the 8-11 March period and throughout the study. The patterns and ozone concentrations observed at these sites were consistent with wintertime measurements made at sites located in remote areas of the western US in normal (often snow-covered) conditions, such as Canyonlands or Yellowstone National Parks (ENVIRON, 2010; CASTNET, 2012).

Across the four days, as was generally observed throughout the study, midday ozone levels at all sites were within 10-12 ppb of one another. The homogeneity of daytime concentrations and patterns provides evidence of good daytime atmospheric mixing in the Basin compared to 2011.

Incoming solar radiation was greater in March than earlier in the winter, which may at least partly explain why 8-11 March had higher ozone than earlier in the winter. Also, Little Mountain and Mountain Home (two high elevation sites) experienced average increases in daily maximum ozone of 7.3 ppb and 6.3 ppb, respectively, during the 8-11 March period relative to the 4-7 March period. The average ozone increase for all monitors was similar (7.5 ppb), even though the sites were at different elevations and in varying proximity to ozone precursor sources. Because ozone increased at all sites during this event, it is likely that much of the event was dominated by an increase in concentrations of ozone transported from outside the Basin. However, since 13 sites recorded increases greater than the 7.3 ppb rise observed at Little Mountain, it is likely that local photochemical ozone production also played a role in the observed concentrations.

Hourly average ozone concentrations were calculated for 07:00 and 15:00, 8-11 March (times refer to the end of the averaging period). The difference between early morning and mid-afternoon ozone concentrations is indicative of the chemical reactions taking place to create and/or destroy ozone between those time periods. Spatial interpolations of the difference between 07:00 and 15:00 average concentrations are shown in Figure 2-10. The largest differences between morning and afternoon concentrations occurred in urban and lower elevation areas. These spatial trends in diurnal differences are likely driven mostly by ozone destruction at night (via chemical reactions and deposition to surfaces; Kley et al., 1994), since daytime concentrations at all sites were similar.

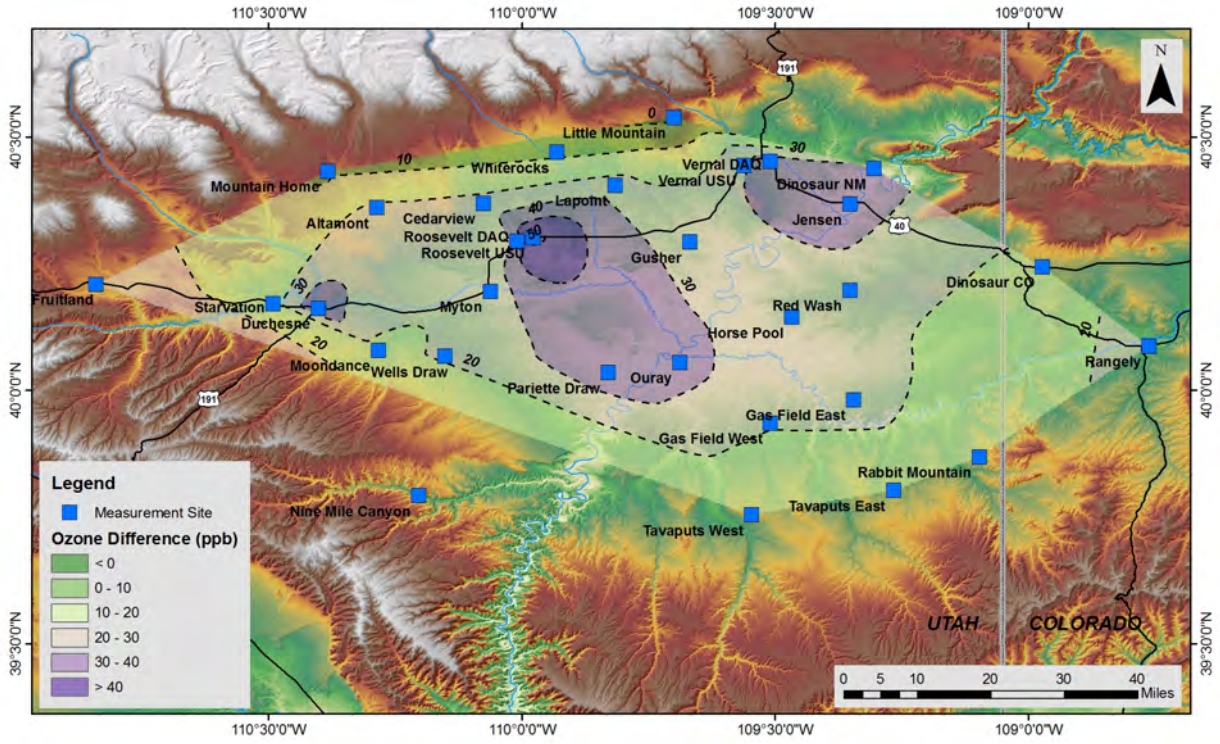

Figure 2-10. Differences between 07:00 and 15:00 ozone concentrations in the Uintah Basin, 8-11 Mar. 2012. Contour lines represent 10 ppb intervals.

Oxides of Nitrogen

NO_x were not evenly distributed in the Uintah Basin during winter 2012. Figure 2-11 shows the distribution of average NO_x concentrations at 16 sites during February 2012 (inclusive of passive and active NO_x measurements). Table 2-3 shows the average NO, NO_2, and NO_x for the same 16 sites during February 2012. An average for February was used to reduce the influence of day-to-day and week-to-week changes in meteorology on results. Vernal experienced the highest NO_x, likely due to emissions from urban and traffic sources. Vernal averaged a NO_2 concentration of 9.7 ppb, well under the 13.1 ppb average of 81 mostly urban locations around the United States in 2010 (EPA, 2012), and significantly lower than the 53 ppb EPA NAAQS annual average standard for NO_2 (NAAQS, 2012; No NAAQS standard exists for NO_x).

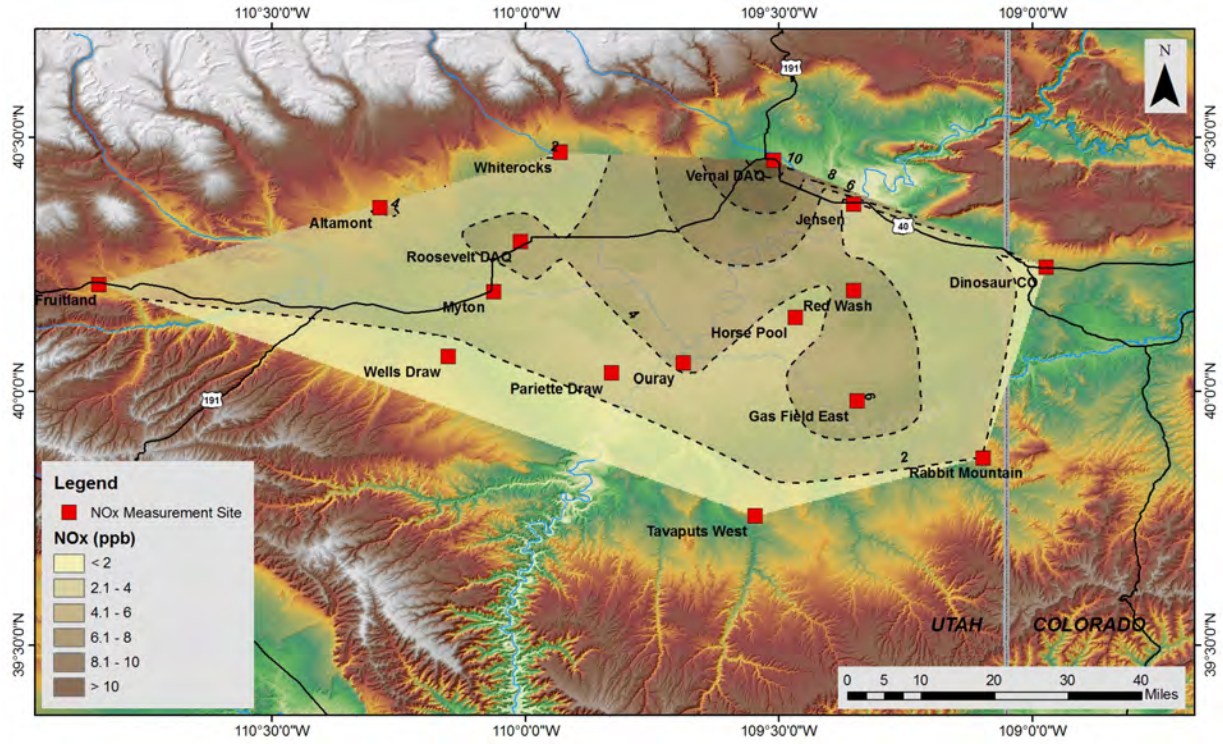

Figure 2-11. Average NO_x around the Uintah Basin, Feb. 2012.

Table 2-3. Average NO, NO_2, and NO_x at 16 sites around the Uintah Basin, Feb. 2012. (The sum of NO and NO_2 may not equal NO_x due to variability in and independent averaging of each parameter.)

Site Name	Latitude	Longitude	Type	NO (ppb)	NO_2 (ppb)	NO_x (ppb)
Tavaputs West	39.754	-109.546	Passive	1.1	0.0	0.6
Dinosaur	40.244	-108.972	Passive	0.7	0.0	1.6
Wells Draw	40.067	-110.151	Passive	0.3	0.0	1.6
Whiterocks	40.469	-109.930	Active	0.2	1.6	1.8
Rabbit Mountain	39.869	-109.097	Active	0.6	1.4	2.0
Fruitland	40.209	-110.840	Active	0.3	1.8	2.1
Pariette Draw	40.035	-109.830	Passive	0.0	1.3	2.7
Horse Pool	40.144	-109.467	Active	0.0	3.1	2.8
Jensen	40.367	-109.352	Passive	0.4	0.7	2.9
Myton	40.195	-110.062	Active	0.8	2.5	3.0
Altamont	40.360	-110.286	Passive	2.8	0.0	4.1
Ouray	40.055	-109.688	Active	0.5	3.6	4.3
Red Wash	40.197	-109.353	Active	0.9	4.3	4.9
Roosevelt	40.294	-110.009	Active	0.0	4.3	5.0
Gas Field East	39.981	-109.345	Passive	1.9	2.5	6.1
Vernal	40.453	-109.510	Active	1.7	9.7	11.2

The population of the Vernal metropolitan area was 9,089 in 2010 (Census, 2012), 1.5 times greater than Roosevelt (6,046). NO_x concentrations in Vernal were 2.3 times greater than in Roosevelt and four times greater than in Jensen (18 km east of Vernal). Gas Field East, situated in an area of multiple mobile and stationary NO_x sources and of greatest oil and gas well density in the Basin, experienced higher average NO_x than Roosevelt, but less than Vernal.

February average NO_x were 4.6 ppb for Horse Pool, Red Wash, and Gas Field East, three sites in the oil and gas production area of Uintah County. This value was 1.6 times higher than average NO_x for Wells Draw and Altamont (2.9 ppb), two sites in oil and gas production areas of Duchesne County. The WRAP III 2012 oil and gas emissions inventory (WRAP III, 2012) predicts 8849 tons per year of NO_x emissions associated with oil and gas production in Uintah County, 1.7 times greater than the NO_x emissions for Duchesne County (5352 tons per year). While measured NO_x concentrations aren't controlled solely by emission rates, and while the sites chosen may not provide ideal representation of oil and gas production in the two counties, the ratio of inventoried NO_x emissions in the two counties does appear to match the measured NO_x concentration ratio and suggests a first level of verification of existing inventories. These data, however, cannot be used to verify the absolute magnitude of emissions inventories (this can be best achieved by coupling inventories with 3D photochemical models to estimate ambient precursor concentrations). See Chapter 4 for a detailed discussion of emissions sources in the Basin.

The spatial distribution of NO_x in winter 2012 did not match the spatial distribution of ozone during elevated ozone episodes in winter 2011, during which the highest ozone concentrations were observed in Pariette Draw and Ouray (Figure 2-8). Additional measurements will be required to determine the relationship between NO_x and ozone spatial distributions during elevated ozone periods.

Volatile Organic Compounds

Figure 2-12 shows the average measured VOC concentrations around the Uintah Basin during February 2012, and Table 2-4 shows average concentrations of select VOC. Currently, no ambient environmental standard for VOC ambient air concentrations exists against which to weigh these data; however, concentrations of individual compounds reported in Table 2-4 are well below federal workplace exposure standards. The highest benzene concentration, for example, measured 0.1% of the Occupational Safety and Health Administration (OSHA) Permissible Exposure Limit (PEL; based on an eight-hour time-weighted average exposure; CDC, 2013) and 1.4% of the National Institute for Occupational Safety and Health (NIOSH) Recommended Exposure Limit (REL; based on lifetime occupational exposure; CDC, 2013). The highest toluene and methylcyclohexane concentrations measured were much less than 0.1% of the PEL and REL for those compounds.

VOC concentrations were highest in the areas of oil and gas production and were relatively low in urban areas. Average total VOC concentration for Horse Pool and Gas Field East, both in the oil and gas production area of Uintah County, was 48.8 ppb (as propane), 2.7 times higher than the average total VOC concentration at Wells Draw and Altamont (18.1 ppb as propane), which are in oil and gas production areas in Duchesne County. The WRAP III 2012 oil and gas emissions inventory predicts 46,637 tons per year of VOC emissions associated with oil and gas production in Uintah County, 2.4 times greater than Duchesne County (19,280 tons per year). As mentioned above, while concentration measurements are not controlled solely by emission rates, and while the sites chosen may not provide ideal representation of oil and gas production in the two counties, the ratio of inventoried VOC emissions in the two counties does appear to match the measured VOC concentration ratio reasonably well, suggesting again a first level of verification of existing inventories.

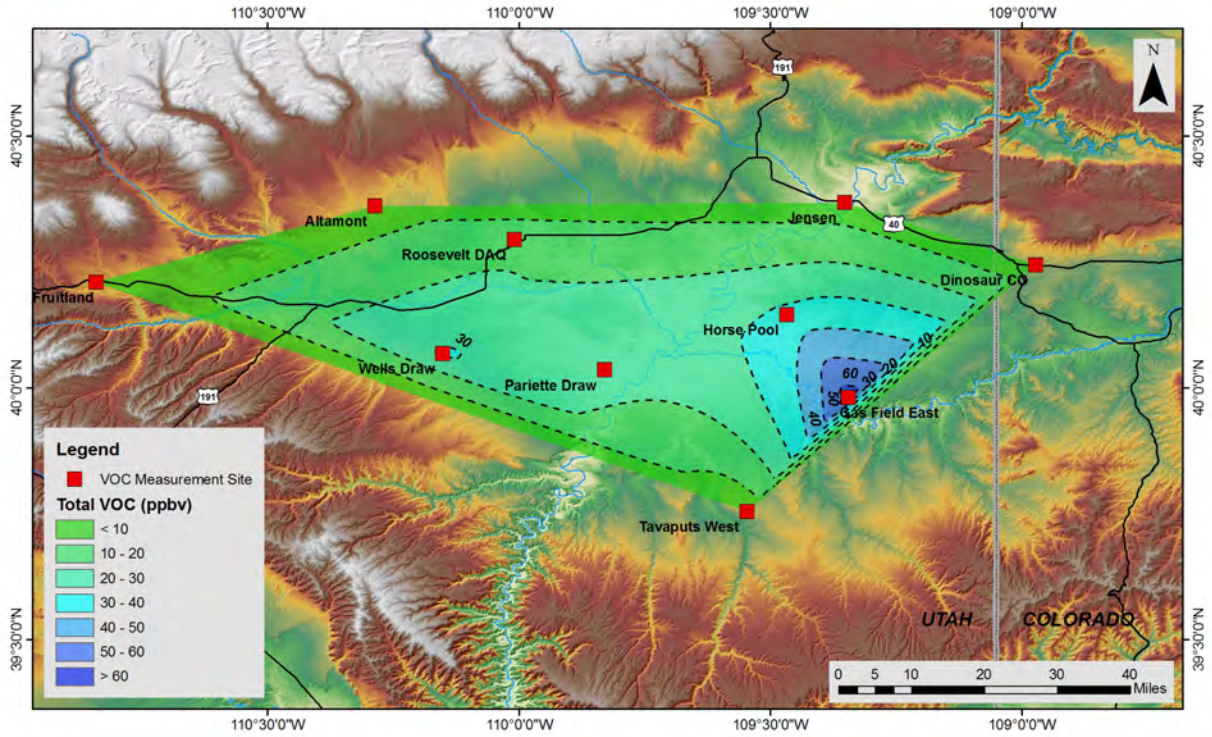

Figure 2-12. Average VOC concentrations in the Uintah Basin, Feb. 2012. Values shown are the sum of VOC with 6-11 carbon atoms, in units of ppb as propane.

Table 2-4. Average concentrations of select VOC in the Uintah Basin, Feb. 2012. Values are in ppb, except the sum of VOC with 6-11 carbon atoms, which is in ppb as propane. "N.D." signifies compounds not detected at a site.

Site	Methylcyclopentane	Benzene	Cyclohexane	3-Methylhexane	Heptane	Methylcyclohexane	Toluene	3-Methylheptane	Octane	Nonane	Sum of C6-C11 VOC
Altamont	0.5	0.5	0.5	0.4	0.4	0.5	0.4	N.D.	0.4	N.D.	5.2
Dinosaur	N.D.	0.5	0.4	N.D.	0.4	0.4	0.4	N.D.	N.D.	N.D.	2.9
Fruitland	N.D.	0.4	N.D.	N.D.	0.4	N.D.	N.D.	N.D.	N.D.	N.D.	1.7
Gas Field E	2.8	1.4	2.2	1	2.5	3.9	1.4	0.5	1	0.5	64.5
Horse Pool	1.4	0.9	1	0.7	1.6	2	0.9	0.4	0.7	0.4	33
Jensen	0.4	0.5	0.4	N.D.	0.4	0.5	0.4	N.D.	N.D.	N.D.	4.6
Pariette Draw	1	0.7	0.9	0.6	1.5	1.2	0.6	N.D.	0.6	0.4	24.3
Roosevelt	0.7	0.7	0.8	0.6	0.7	0.9	0.6	N.D.	0.6	0.4	17
Tavaputs W	0.4	0.4	0.4	N.D.	0.4	0.5	0.4	N.D.	N.D.	N.D.	3.4
Wells Draw	2.4	0.6	1	0.6	2	1.3	0.5	0.4	0.8	0.4	31

Figure 2-13 shows that the sum of VOC with 6-11 carbons at the different sampling sites has a strong correlation (R^2 = 0.92) with the number of oil and gas wells within 6 km of a site. Summed VOC concentrations were also shown to have a strong correlation with cumulative historical natural gas production within 6 km (R^2 = 0.84), but did not correlate well with cumulative historical oil production (R^2 = 0.01).

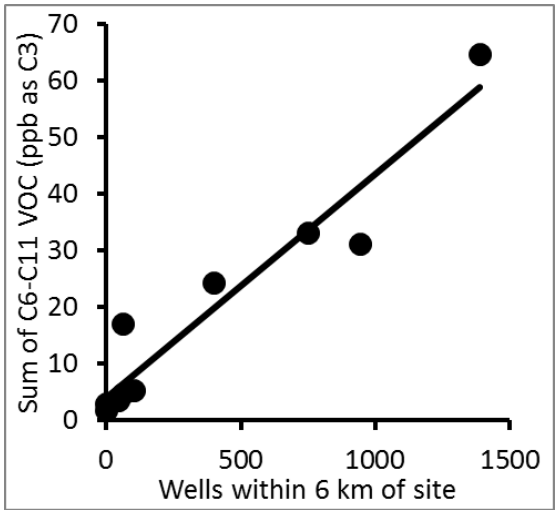

Figure 2-13. Average VOC concentration versus number of wells within 6 km of a site.

As with NO_x, the spatial distribution of VOC in winter 2012 did not match the spatial distribution of ozone during elevated ozone episodes in winter 2011. With the exception of Gas Field East, sites with higher VOC did not tend to have higher NO_x. Similar measurements during conditions with snow cover and elevated ozone concentrations will be required to determine the relationship between ozone and precursor spatial distributions during periods with elevated ozone.

VOC speciation (i.e., relative concentrations of individual VOC species) at sites in areas of concentrated gas production (Gas Field East and Horse Pool) differed from the speciation at sites in an area of concentrated oil production (Wells Draw). Figures 2-14, 2-15, and 2-16 show spatial distribution throughout the Uintah Basin of toluene, heptane, and cyclohexane, respectively. Concentrations of toluene and other aromatics were observed to be higher in gas-producing areas than in oil-producing areas. Higher concentrations of cycloalkanes were observed in gas-producing areas, but the contrast with oil producing areas was smaller than it was with toluene. Concentrations of heptane and other straight-chain alkanes were similar in both areas.

The heptane:toluene ratio in VOC samples across the Basin was strongly correlated with the number of oil wells within 6 km (R^2 = 0.85; Figure 2-17), indicating that these trends in VOC speciation are statistically meaningful. It may be possible to use the heptane:toluene ratio or other speciation ratios to determine the relative influence of oil vs. gas production on ambient VOC concentrations in the Basin.

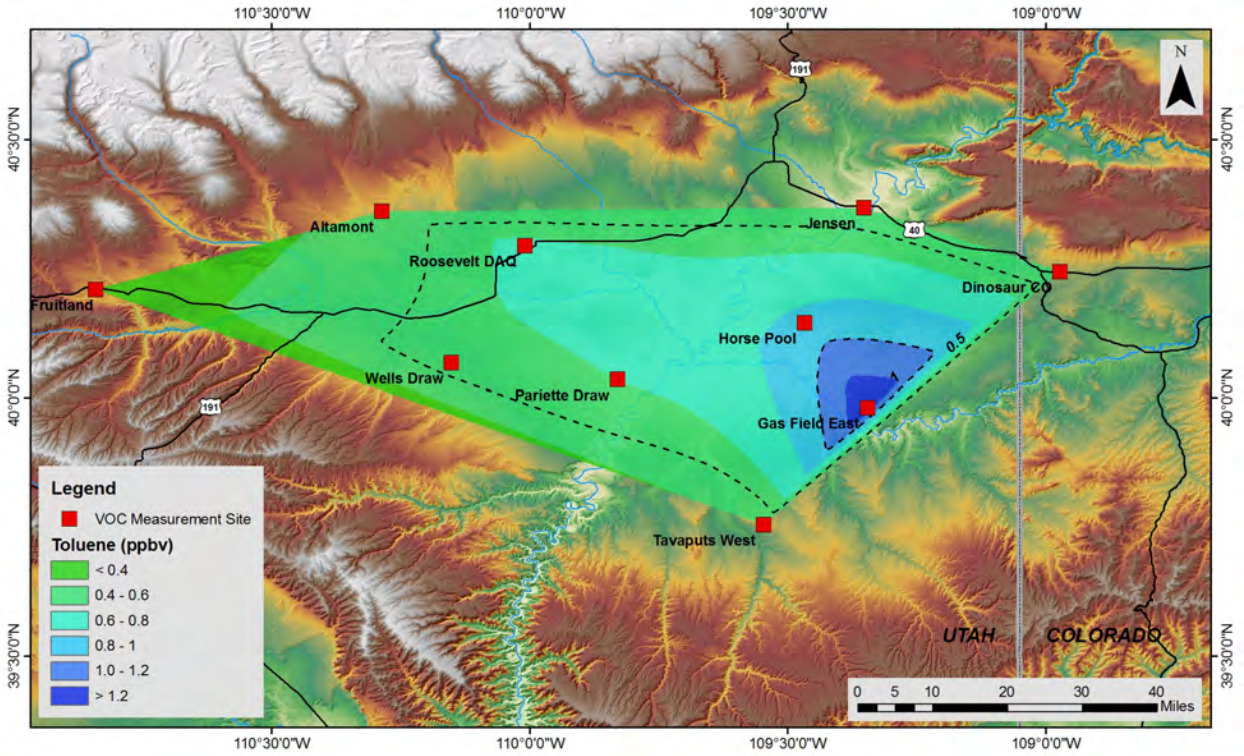

Figure 2-14. Average toluene concentrations in the Uintah Basin, Feb. 2012.

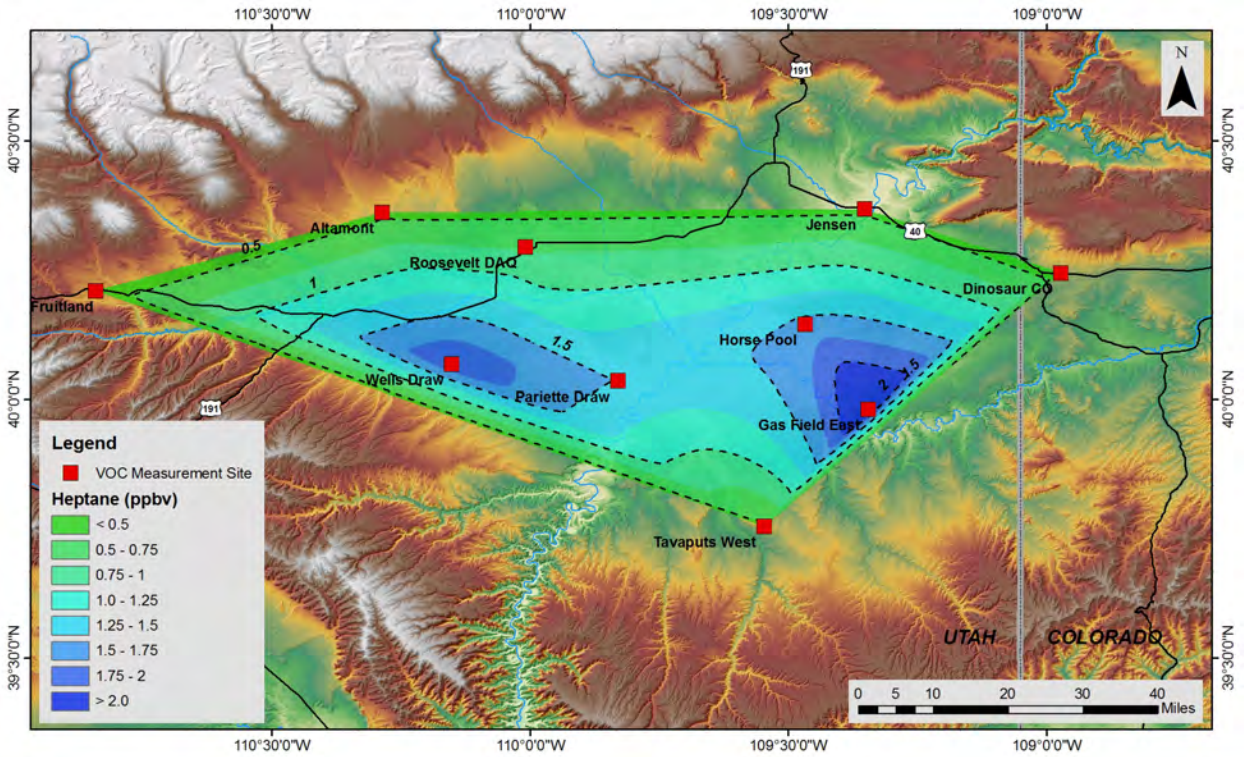

Figure 2-15. Average heptane concentrations in the Uintah Basin, Feb. 2012.

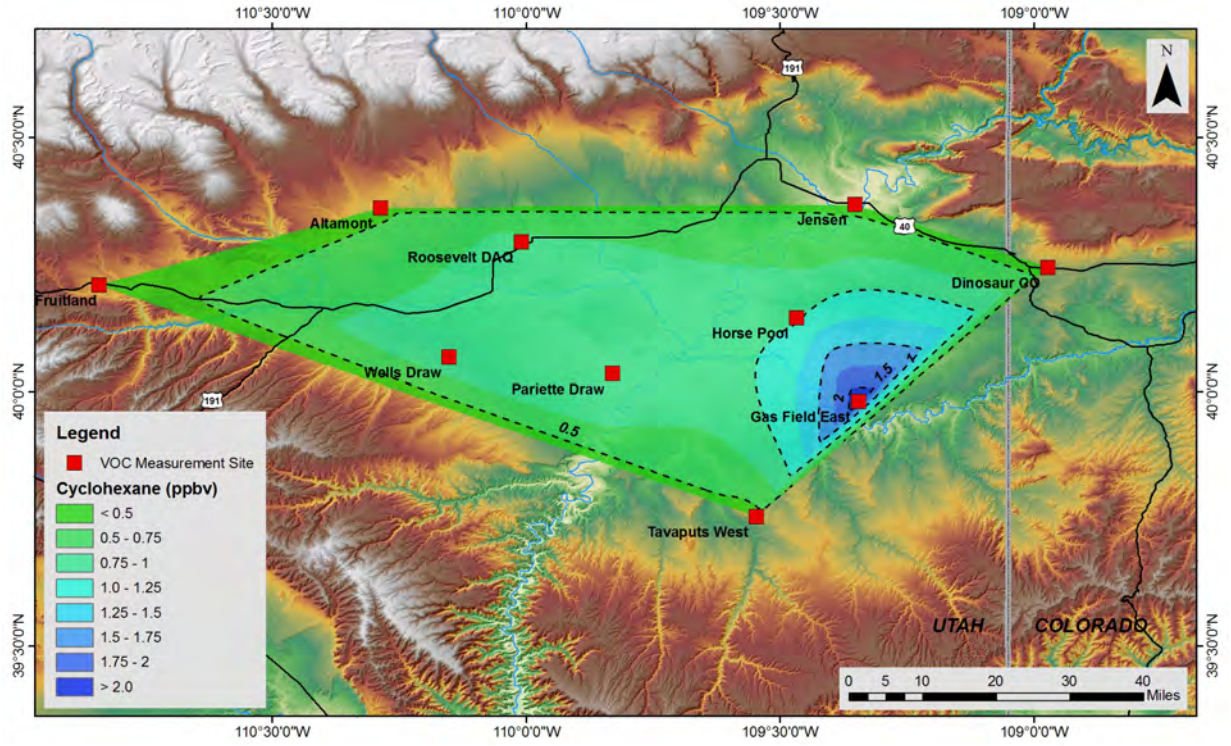

Figure 2-16. Average cyclohexane concentrations in the Uintah Basin, Feb. 2012.

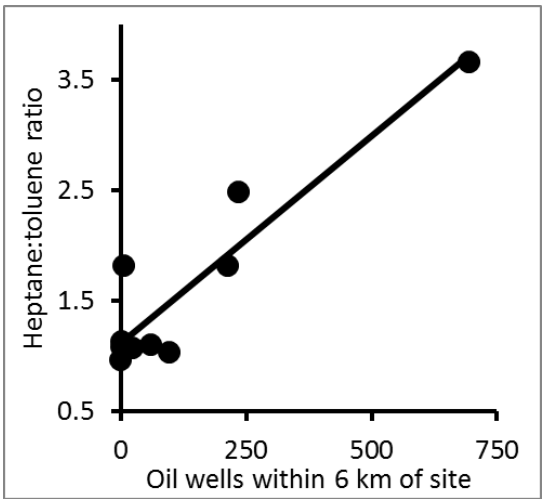

Figure 2-17. Ratio of heptane to toluene versus the number of oil wells within 6 km of a study site.

Maximum Incremental Reactivity is a photochemical model-derived metric used to quantify the ability of a given compound to produce ozone under a given set of conditions. Toluene has a maximum incremental reactivity of 4.00 g g^{-1} of ozone produced, compared to 1.07 g g^{-1} for heptane (Carter, 2009). These data indicate that a given mass of toluene is able to produce more ozone than the same mass of heptane. Though quantifying and identifying only a subset of VOC, 2012 passive measurements suggest that gas-producing areas of the Uintah Basin could influence ozone production more than the oil-

producing areas, if the total VOC concentrations are higher in gas-producing areas and the VOC mix associated with gas production is more reactive.

Meteorology

Temperature measurements across the Uintah Basin confirm that inversion conditions conducive to ozone formation were not present during winter 2012. Figure 2-18 shows average temperatures were highest in the lowest parts of the Basin during February 2012, contrary to what is expected during inversion conditions.

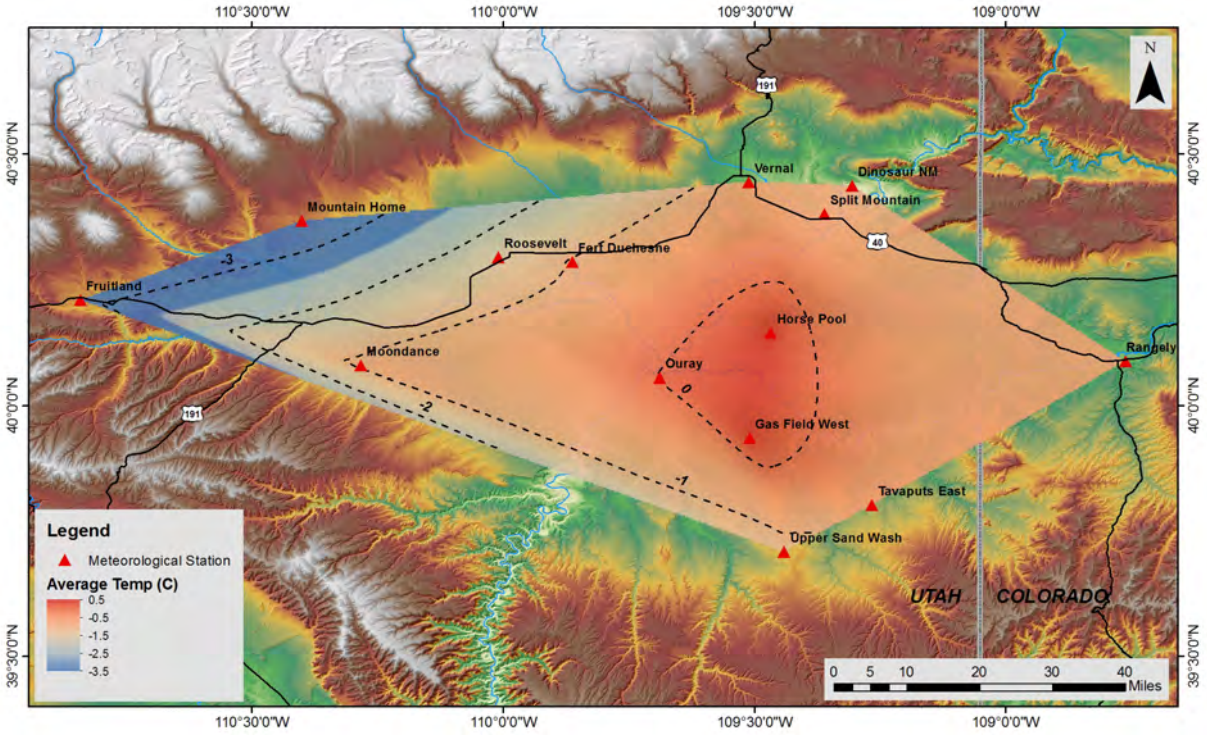

Figure 2-18. Average temperature in the Uintah Basin, Feb. 2012.

Figure 2-19 shows average day and night wind vectors at 14 meteorological stations around the Uintah Basin during February 2012. Day and night mean wind directions are not consistent across the Basin, even among some sites that are in relatively close proximity, and appear to be influenced by local terrain. Many of the sites exhibit upslope/downslope flow that leads to near 180° shifts in wind direction from night to day. The complex topography of the Basin likely leads to complex surface flows that transport ozone and its precursors around the Basin. This spatial heterogeneity may be magnified during inversion conditions conducive to ozone formation since temperature inversions are typically accompanied by light surface winds and variable wind directions. Surface winds were shown to be disconnected from the organized regional flows during the 2010-11 study (Martin et al., 2011).

Due to the Basin's complex topography and its influence on surface flow and accompanying pollutant transport, it is critical that future modeling of ozone formation include high-resolution simulations of topography and meteorology (e.g., Billings et al., 2006). The network of meteorological stations used in this work will inform and validate such an effort.

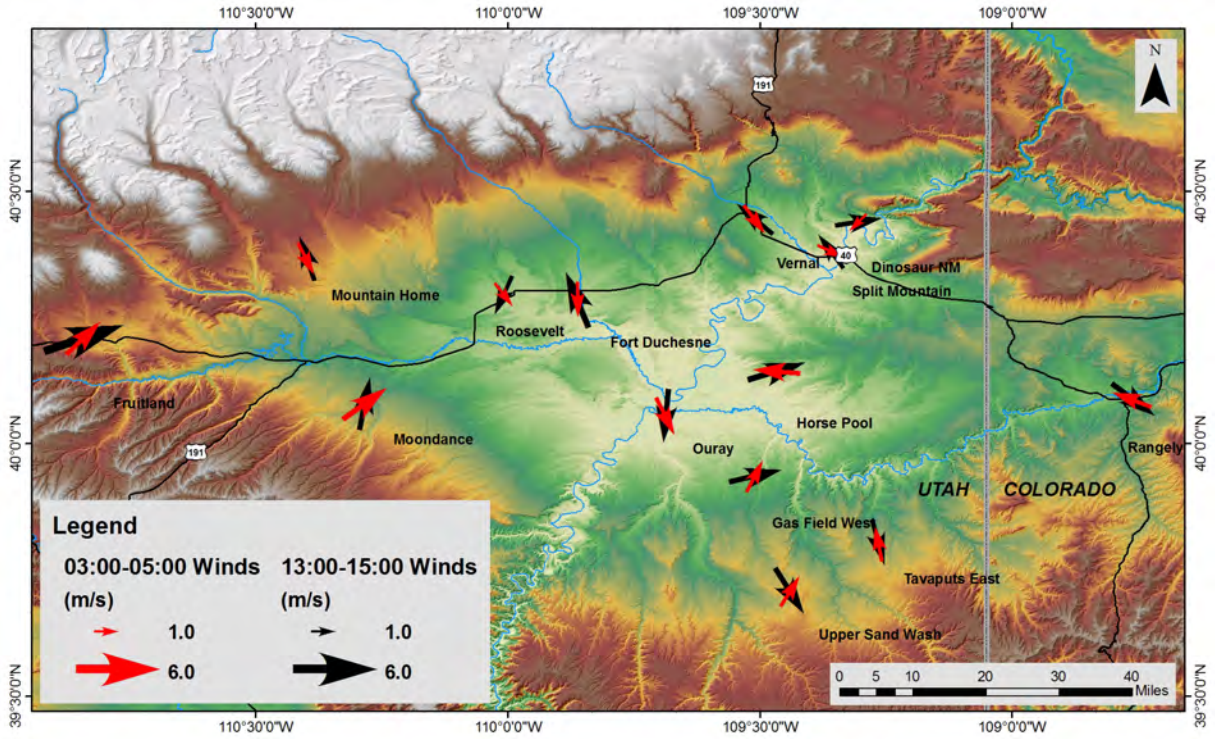

Figure 2-19. Mean day and night wind vectors at 14 meteorological stations in the Uintah Basin, Feb. 2012. The black arrows indicate monthly mean wind direction from 13:00 to 15:00 local time, and red arrows indicated monthly mean wind direction from 03:00 to 05:00 local time. The size of the arrow is proportional to the mean wind speed for each time period.

Vertical Ozone and Meteorology

Midday vertical measurements at Red Wash in February 2011 showed strong temperature inversions (i.e., increase in temperature with height) and maximum ozone near the surface (Martin et al., 2011). In contrast, measurements at Red Wash in February 2012 showed increasing ozone with increasing height and no temperature inversion (Figure 2-20). Without snow cover and accompanying inversions in 2011-12, ozone concentrations tended to stay low and were more uniform with height than during elevated ozone episodes in February 2011.

Early morning temperature inversions were observed consistently at all vertical profiling sites, and these inversions commonly dissipated by early afternoon (e.g., Figure 2-21). As discussed in previous sections, nighttime and morning ozone concentrations were lower at many sites around the Basin, likely due to inverted nighttime conditions that had trapped air close to the surface and allowed ozone in that surface layer to be depleted by chemical reactions and surface deposition. Figure 2-22 shows an example of this behavior at Roosevelt on February 15 when ozone concentrations were lower near the surface in the morning and increased to more closely match concentrations aloft as the depth of the surface layer increased by midday and afternoon.

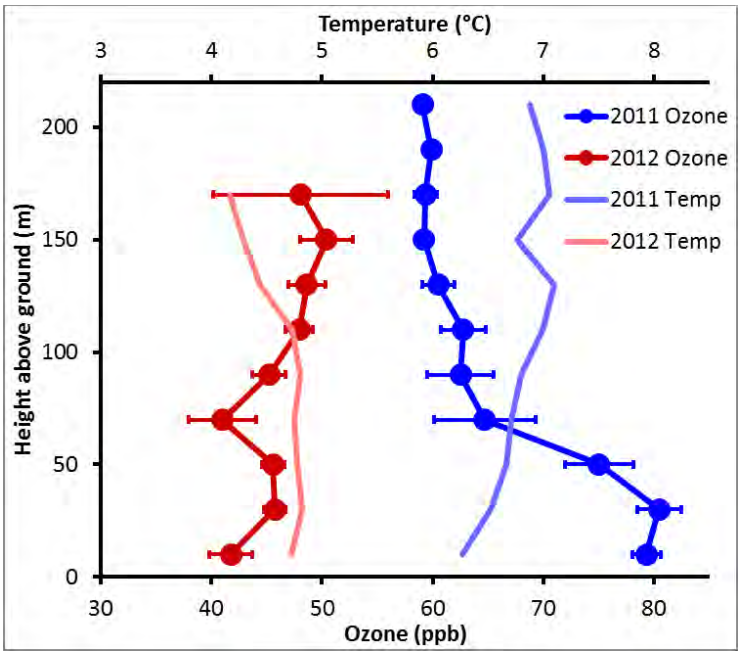

Figure 2-20. Comparison of vertical profiles of ozone and temperature at Red Wash from 12:30 to 14:30 on 24 Feb. 2011 and 21 Feb. 2012. For ozone, circles represent means for 20 m bins (i.e., 0-20 m above ground, 20-40 m above ground, etc.), and whiskers represent 95% confidence intervals. For temperature, lines represent the mean in 20 m bins.

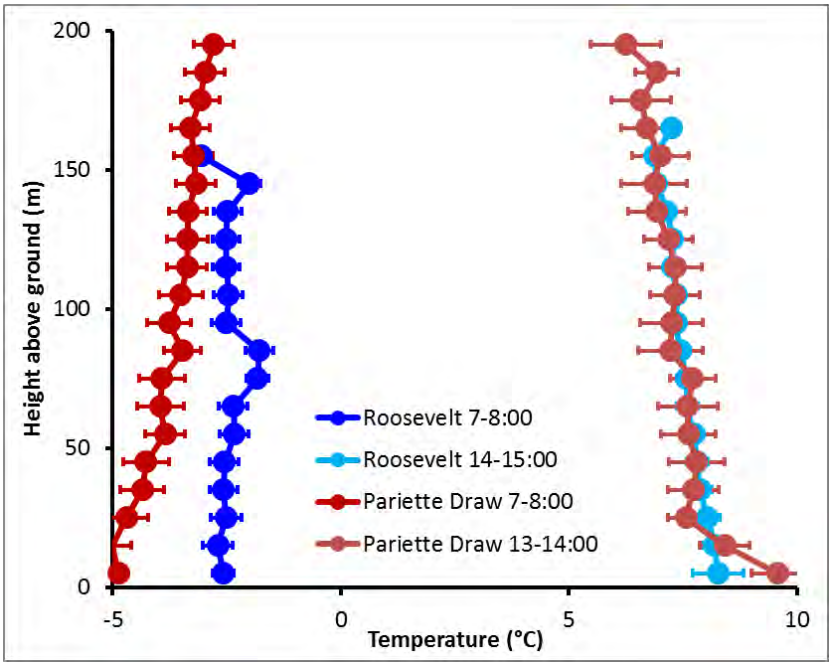

Figure 2-21. Morning and afternoon vertical temperature profiles at Roosevelt and Pariette Draw from 14-25 Feb. 2012 in 10 m bins (i.e., 0-10 m above ground, 10-20 m above ground, etc.). Circles represent means for each bin, and whiskers represent 95% confidence intervals. Measurements at other sites (Red Wash, Ouray, and Wells Draw) showed similar diurnal patterns.

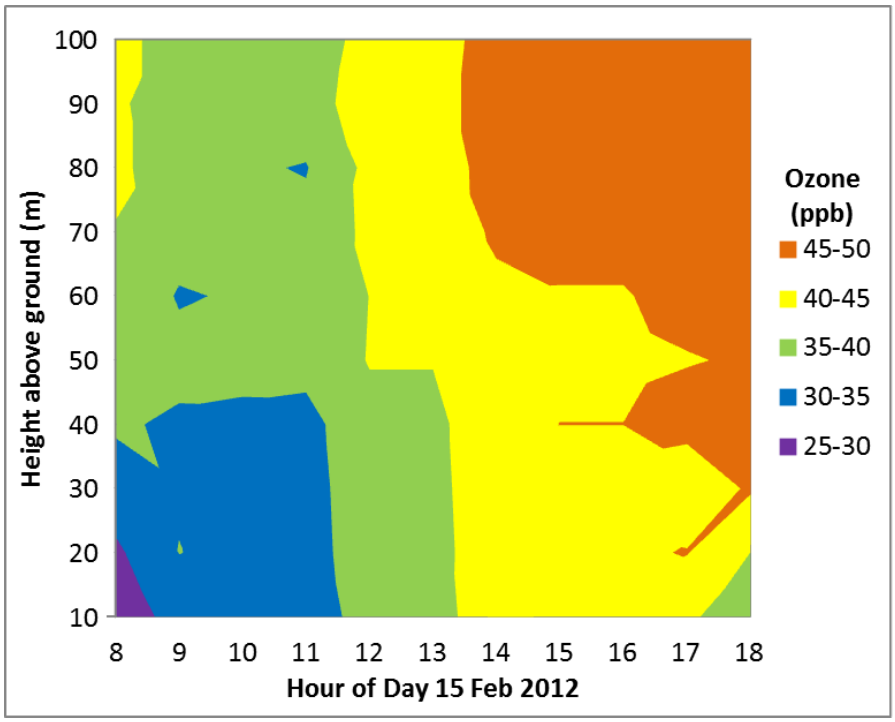

Figure 2-22. Time series of ozone vertical profiles at Roosevelt, 15 Feb. 2012.

SUMMARY

The most significant outcome of this work is the finding that ozone in the Uintah Basin is tightly coupled with meteorology. In the absence of snow cover and multiday temperature inversions, ozone concentrations stayed below EPA standards and were within the range of ozone concentrations measured at remote sites around the western United States. This study also shows that precursor (i.e., NO_x and VOC) concentrations are associated primarily with known emission sources of local origin and that, irrespective of source origin, elevated ozone does not form in the absence of specific meteorological conditions.

The complex and spatially varied topography of the Basin leads to strong spatial variability in surface airflow patterns. NO_x and VOC concentrations in the Basin are also spatially variable, with areas of higher NO_x concentrations distinct from areas of higher VOC concentrations (save for one area of intense gas development in Uintah County). VOC speciation is also spatially variable, leading to spatial variability in VOC reactivity (i.e., the ability of VOC to produce ozone). Areas of highest observed NO_x and VOC in 2012 are not the same areas of highest NO_x and VOC observed in 2011. No areas with NO_x or VOC exceeding health standards were found during the 2012 study.

It is likely that the spatial relationships between precursor emission sources and meteorology (including inversion characteristics and surface flow) control winter ozone formation in the Basin. Elucidating these relationships, particularly how they work to produce winter ozone, will be critical to (1) understanding the degree to which ozone precursors emitted in different areas contribute to ozone formation and (2) developing cost-effective mitigation strategies, since not only specific source types but also source locations and even heights may figure significantly.

REFERENCES

Billings, B.J.; Grubisic, V.; Borys, R.D. 2006. Maintenance of a mountain valley cold pool: a numerical study. Monthly Weather Review 134, 2266-2278.

Carter, W.P.L. 2009. Development of the SAPRC-07 chemical mechanism and updated ozone reactivity scales. Available at http://www.eos.ubc.ca/~bainslie/Carter_2009-SAPRC-07.pdf

CASTNET. 2012. CASTNET Ozone Data. Available: http://epa.gov/castnet/javaweb/index.html.
ENVIRON. 2010. Final Report: A Conceptual Model of Winter Ozone Episodes in Southwest Wyoming. Available: http://deq.state.wy.us/aqd/Ozone%20Main.asp.

CDC, 2013. Centers for Disease Control and Prevention: NIOSH Pocket Guide to Chemical Hazards. Available: http://www.cdc.gov/niosh/npg/.

Census, 2012. http://www.google.com/publicdata/explore?ds=kf7tgg1uo9ude_

EPA. 2012. http://www.epa.gov/airtrends/nitrogen.html

Kley, D., Geiss, H., and Mohnen, V.A. 1994. Tropospheric ozone at elevated sites and precursor emissions in the United States and Europe. Atmospheric Environment 28, 149-158.

Martin, R.S., K. Moore, M. Mansfield, S. Hill, K. Harper, and H. Shorthill: Final Report: Uinta Basin Winter Ozone and Air Quality Study, EDL/11-039, 14 June 2011.

NAAQS. 2012 http://www.epa.gov/air/criteria.html

Ogawa. 2012. http://www.ogawausa.com/pdfs/prono-noxno2so206.pdf). Radiello. 2012. http://www.radiello.it/english/cov_chim_en.htm.

Schnell, R.C; Oltmans, S.J.; Neely, R.R.; Endres, M.S.; Molenar, J.V.; White, A.B. Nature Geosci. DOI: 10.1038/NGEO415, 2009.

Sillman, S. 1999. The relation between ozone, NO_x, and hydrocarbons in urban and polluted rural environments. Atmos. Environ. 33, 1821-1845.

WRAP III, 2012. http://www.wrapair.org/forums/ogwg/PhaseIII_Inventory.html

CHAPTER III

INTENSIVE MEASUREMENTS AT THE HORSE POOL SITE

James M. Roberts[1], Eric J. Williams[1,2], Steven B. Brown[1], Lance Lee[3], Ronald Cohen[3], Shane Murphy[4], Jessica Gilman[1,2], Joost de Gouw[1,2], Carsten Warneke[1,2], Cora Young[1,2], Peter Edwards[1,2], Robert McLaren[5], James Kercher[6], Joel Thornton[6], Catalina Tsai[7], Jochen Stutz[7], and Robert Zamora[8]

[1]Chemical Sciences Division, NOAA Earth System Research Laboratory, Boulder, CO.

[2]Cooperative Institute for Research in the Environmental Sciences, U. of Colorado & NOAA, Boulder, CO.

[3]Department of Chemistry, University of California, Berkeley, CA.

[4]Department of Atmospheric Science, University of Wyoming, Laramie, WY.

[5]Centre for Atmospheric Chemistry, York University, Toronto, Canada.

[6]Department of Atmospheric Sciences, University of Washington, Seattle, WA.

[7]Department of Atmospheric and Oceanic Sciences, University of California, Los Angeles, CA.

[8]Physical Sciences Division, NOAA Earth System Research Laboratory, Boulder, CO.

INTRODUCTION AND BACKGROUND

The UBOS 2012 Study included an extensive set of chemical and meteorological measurements at the Horse Pool site. These experiments were assembled with the aim of understanding the chemistry behind ozone production at the process level, measuring the chemical and physical properties of aerosol particles and snow cover, and quantifying the vertical and horizontal distribution of winds and ozone at this central site. These goals involved detailed measurements of all the chemical and physical parameters that are either ingredients, radical sources, or co-factors in ozone photochemistry. The 2012 data do not provide a definitive answer to what causes elevated ozone in the Uintah Basin; however, much can be learned about sources and reactivity by looking at the absolute values of the oxides of nitrogen (NOx) and volatile organic compounds (VOCs), and about possible radical sources by comparing UBWOS 2012 to other sites at which similar measurements have been made.

Ozone is the only pollutant regulated by the Clean Air Act that does not come out of a tailpipe or smoke stack: it is made in the atmosphere itself. Moreover, as a simple three-atom compound of oxygen, measuring ozone by itself does not give many clues as to the source of the problem. As a result, photochemical ozone pollution has been a persistent air quality problem in the U.S. and around the World [*National Research Council and Chemistry*, 1992]. The production of ozone in the lower atmosphere requires several key ingredients: VOCs to act as fuel in the photooxidation process, NOx (= nitric oxide, NO, and nitrogen dioxide, NO_2) to act as catalysts, and radicals, chiefly hydroxyl radicals, OH, to initiate the chemistry. Detailed chemical measurements are required to understand what is contributing to ozone formation in a given air basin. These measurements include both primary (emitted from sources) and secondary (formed in the atmosphere) VOCs, NOx and the nitrogen-containing compounds that are produced from it (odd-nitrogen, NOy), sources of both OH radicals and Cl atoms.

The timing and circumstances of high wintertime ozone in the Uintah Basin have prompted an examination of factors that may contribute to this chemistry. Several elements of Study Component 3 were included with this requirement in mind. Measurements of 3-dimensional winds and 3-D O_3 distributions were conducted to define boundary layer structure. The analysis of aerosol particle

physical and chemical properties was included to assess the role of particles in radical initiation. There was also provision for chemical analysis of snow to explore possible radical sources arising from snow photochemistry.

This chapter describes the measurement techniques deployed during the intensive experiment at Horse Pool and summarizes the results of that work. The aspects of the results that bear on the summary of preliminary results will be noted. In addition, aspects of the findings that give guidance on how future projects should be conducted will also be discussed.

SITE DESCRIPTION AND DETAILS OF MEASUREMENT TECHNIQUES

The intensive measurement site was established at 40.1437 N lat, 109.4672 W long, at the same well pad that was designated 'Horse Pool' in the 2011 Uintah Basin Study. A satellite photo of the location and surroundings of the Horse Pool intensive site are shown in Figure 3-1, along with a diagram of the instrument trailers and sampling towers. The site consisted of 6 trailers, a recreational vehicle, one tent, and an instrument enclosure that was placed half way up the sampling tower. These are shown in a photograph of the site looking from south to north, Figure 3-2. Four of the trailers were clustered around the sampling tower, which consisted of a 20m walk up scaffold with a side platform at 10m. The measurement period ran from 00:00:00 on January 15, 2012 until February 29, 2012. Many instruments were run for this entire period, but some covered a shorter time period. Tables 3-1 through 3-3 below list and detail each set of measurements that were part of Study Component 3.

Table 3-1. Gas Phase Measurements.

Parameter(s)	Method	Detection Limit	Time Resolution	Organization
$NO/NO_2/NO_y$	Chemiluminescence w/ selective conversion	0.01-0.1 ppbv	1 sec-1 min	NOAA/CSD
O_3 in situ	UV Absorption	2 ppbv	1 min	NOAA/CSD
O_3 Lidar	UV Absorption			NOAA/CSD
$NO/NO_2/NO_3/N_2O_5/O_3$	Cavity ring-down spectroscopy	1-100 pptv	1 sec	NOAA/CSD
Acyl peroxynitrates Nitryl Chloride ($ClNO_2$)	Iodide ion chemical ionization mass spectrometry	5-25 pptv	1-5 sec	NOAA/CSD U. Wash.
Acyl peroxynitrates	Gas chromatography	10 pptv	5 min	NOAA/CSD
Carbon monoxide	Vacuum UV fluorescence	2 ppbv	1 min	NOAA/CSD
Methane, carbon dioxide	Cavity ring-down spectroscopy	N/A	1 min	NOAA/CSD
Sulfur Dioxide	UV fluorescence	0.1 ppbv	1 min	NOAA/CSD
VOCs: alkanes, alkenes, aromatics, aldehydes, ketones, alkyl nitrates	In situ gas chromatography/mass spectrometry	10 pptv	30 min	NOAA/CSD
Formaldehyde, OVOCs, Aromatics, acetonitrile	Proton-transfer reaction mass spectrometry	10 pptv	10 sec-1 min	NOAA/CSD
Acids	Negative ion proton transfer mass spectrometry	10 pptv	1-10 sec	NOAA/CSD
HONO, NO_2, NO_3, O_3	Differential optical absorption spectroscopy	0.03-1.5 ppbv		UCLA
NO_2, SPN, SAN	Thermal dissociation laser-induced fluorescence	24-34 pptv	1 sec-1min	UC Berkeley

Table 3-2. Aerosol Particle Phase Measurements.

Parameter(s)	Method	Time Resolution	Organization
Organic carbon/ Elemental carbon	Filter/denuder sampling, thermal/optical analyzer	5 – 12 hrs	NOAA/PMEL
Cations/anions	Impactor sampling/ion chromatography	5 – 12 hrs	NOAA/PMEL
Cations/anions	Particle-into-liquid-sampler/ion chromatography	30 min	NOAA/PMEL
Gravimetric mass	Cascade impactor/microbalance	5 – 12 hrs	NOAA/PMEL
Trace elements	Cascade impactor/x-ray emission spectrometry	5 – 12 hrs	NOAA/PMEL
Condensation Nuclei	Condensation nuclei counter		NOAA/PMEL
Light scattering and absorption	Nephelometer, absorption photometer		NOAA/PMEL
Aerosol number size distribution	Scanning mobility particle sizer, aerodynamic particle sizer	5 min	NOAA/PMEL
Aerosol Backscatter	Lidar		NOAA/CSD
Ammonium, nitrate, sulfate, total organics	Aerosol Mass Spectrometry	5 min	U of WY
SAN in particles	Thermal dissociation laser-induced fluorescence		UC Berkeley

Table 3-3. Study Component 3: Meteorological/Physical Measurements.

Parameter(s)	Method	Time Resolution	Organization
T, RH, Wind speed and direction at 19.5m and 13.5m on the walk-up tower	Standard commercial sensors, sonic anemometry at 13.5m	1 sec – 1 min	NOAA/CSD
Photolysis rates of NO_2, NO_3, and O_3 => O^1D	Filter radiometry	1 min	NOAA/cSD
Surface pressure, T, R.H. at 2, 10, and 20m	Commercial sensors		NOAA/PSD
Wind speed and direction 10, 20m	Commercial sensors		NOAA/PSD
Fast winds, temperature	Sonic anemometry		NOAA/PSD
Solar and IR irradiance	Eppley radiometers		NOAA/PSD
Boundary layer winds	Acoustic sounder		NOAA/PSD
Rain	Tipping bucket rain gauge	N/A	NOAA/PSD
Snow depth	Commercial sensor	N/A	NOAA/PSD
3-Dimensional winds	High-resolution Doppler Lidar	20 min	NOAA/CSD

Figure 3-1. Satellite photo of the Horse Pool site and surroundings.

Figure 3-2. Photo of the Horse Pool site looking north.

Priority Pollutants - NO, NO_2, NOy, O_3, SO_2, CO, local meteorological data

All measurements (except NO_y) were made through a common sampling manifold by instruments housed in a mobile field laboratory (modified shipping container). Complete descriptions of all the following measurements are available from [*E J Williams et al.*, 2009] and [*Lerner et al.*, 2009]. To avoid the ingestion of precipitation into the sampling manifold, a two-fold strategy was employed: (1) the inlet of a heated (30°C) 14-m perfluoralkoxy (PFA) polymer tube (9.5mm ID) was mounted approximately 10-m high on the walk-up tower, with the inlet tip inside an inverted funnel, and (2) a virtual impactor was placed just downstream of the inlet tip in a heated plastic box mounted at the top of the mast. This impactor is simply a coaxial pair of PFA tubes, with a sidearm sample flow of ~60 standard liters per minute (slpm) out of a total inlet flow of ~180 slpm. Assuming a fully turbulent flow through the impactor, particles greater than ~5-8 µm are excluded from the sample stream at these nominal flow rates, with a total residence time of less than 1 s for the sample manifold.

Ozone (O_3) was measured by UV-absorbance (TEII model 49c), with an accuracy of ± 2% and a precision of ± 1 ppbv for an integrated 1-minute sample. The field UV-absorbance instrument was calibrated against a lab reference UV-absorbance instrument (TEII model 49i-PS) before and after the study. Carbon monoxide (CO) was measured by a commercial vacuum-UV resonance fluorescence instrument (AeroLaser model 5002) with an accuracy of ± 4% and a precision of ± 0.5 ppbv. The sample stream used by the CO instrument passed through a Nafion dryer (PermaPure model PD-50T) before analysis, which reduces the water vapor mixing ratio in the sample stream to below 0.5 parts per thousand (ppth), and analyte mixing ratios are reported as measured (i.e., in dried air). Sulfur dioxide (SO_2) was measured with a commercial pulsed fluorescence instrument (TEII model 43s). Sample throughput was increased with the use of a large vacuum pump. Accuracy is estimated at ±5% and precision estimated to be ±0.15 ppbv. Carbon dioxide and water vapor were determined with a commercial non-dispersive infra-red instrument (LiCor model 7000) with accuracy estimated at ±2% and precision estimated at ±0.07 ppmv for CO_2 and ±1% and ±0.1 ppth, respectively, for H_2O.

Measurement of NO_x (NO_x=NO+NO_2) was performed with a pair of matched O_3-NO chemiluminescence detectors, one that continuously determined NO and another that continuously measured ambient NO plus a fraction of ambient NO_2 that had been converted to NO by a photolytic converter. Total uncertainty (random plus systematic errors) for NO is estimated at 4% with a detection limit (one minute average) of 6 pptv. Total uncertainty for NO_2 is estimated at less than 7% with a detection limit (one minute average) of 15 pptv.

Measurements of NO_y were made at 15.5 magl by conversion of the NO_y species on a heated (325°C) gold tube using H_2 as the reducing agent. Resulting NO was determined with an O_3-NO chemiluminescence instrument. Calibration with NO and NO_2 standard gases occurred every 5 hours, and the instrument background was checked hourly. Conversion of PAN was checked via addition of the standard gas into the inlet system. Checks for interference by acetonitrile were conducted similarly. Conversion of NO_2 and PAN was generally >90%. Uncertainty is estimated at ±(15% + 0.10) ppbv.

Photolysis rates for NO_2, NO_3 and O_3 (O^1D channel) were measured by commercially available (Metcon, Inc.) filter radiometers that were mounted on a separate tower (~10 magl) located ~15 meters south of the walk-up tower. The instruments use a combination of optical band pass filters to match the target molecule action spectrum (product of absorption spectrum and quantum yield) and photodiodes or photomultiplier tubes to measure the transmitted intensity, which ideally is directly proportional to the photolysis rate. Pairs of instruments were used to measure both down-welling and up-welling radiation

to acquire the full 4-pi-steradian photolysis rate for each molecule. Total uncertainties for 1-min averaged data are: jNO_2: +/- 15%; jNO_3: +/- 15%; $jO[^1D]$: +/- 25%. Photolysis rates were measured continuously at 1 Hz until 22 February 2012, when a strong wind gust toppled the tower holding the instruments, which did not survive the fall.

Standard meterological data were collected at two heights on the walk-up tower. Temperature and relative humidity (Vaisala, model HMP45AC) and wind direction and speed (RM Young, model 05103) were measured at the tower top (19.2 magl). Temperature and relative humidity (Vaisala model HMP45AC), pressure (Vaisala model PTB101B), and wind direction and speed (RM Young, 3-dimensional sonic anemometer, model 81000) were measured at about 13.5 magl).

Volatile Organic Compounds, Methane, and Carbon Dioxide

VOCs by GC/MS

A total of 65 volatile organic compounds (VOCs) were measured in-situ by a research-quality, two-channel, gas chromatograph-mass spectrometer (GC-MS). A detailed description of the instrument is described by [*Gilman et al.*, 2010] and [*Goldan et al.*, 2004]. A brief overview is provided here.

The inlet for the GC-MS consisted of a 50 m unheated Teflon line (0.25 inch o.d. standard wall), which was positioned on the southwest corner of the tower approximately 20 m above ground level. Ambient air was pulled continuously at a rate of approximately 7 L min^{-1} through the inlet line resulting in an inlet residence time of less than 5 s. From this high-flow sample stream, two separate ambient air samples were collected simultaneously at a flow rate of 70 mL min^{-1} for a total of 5 min via cryogenic trapping. The two sample channels have slightly different configurations designed to reduce water and carbon dioxide and remove O_3 from the sample stream prior to trapping at liquid nitrogen temperatures.

After the 5 min sample acquisition period, the two samples collected in parallel are then analyzed sequentially by holding each sample in separate cryofocus units until it is time for analysis. The analysis sequence begins by flash heating the cryofocus unit on channel one (CH1) from -165°C to 100°C in 0.2 s injecting the sample onto the CH1 column. Channel one utilizes 18 m Al_2O_3/KCl PLOT column that is ramped from 55°C to 150°C in 3.5 min in order to separate the C2-C5 hydrocarbons. The eluent is analyzed by a linear quadrupole mass spectrometer (Agilent 5973) operating in selected ion mode in order to increase the signal to noise ratio.

Once the analysis of CH1 is complete, the cryofocus unit on CH2 is flash heated and a 4-way pneumatic valve (Valco Instruments Co. Inc., Houston, TX) located upstream of the mass spectrometer switches so that the sample eluting from the CH2 column is directed to the MS. Channel two utilizes a semi-polar 20 m DB-624 capillary column that is ramped from 38°C to 130°C in 11 min in order to separate the C5-C11 hydrocarbons, oxygen-, nitrogen-, and other halogen-containing VOCs.

The entire sample collection (5 min) and analysis sequence (25 min) repeats automatically every 30 min beginning on the hour and half-hour. The limit of detection, precision, and accuracy are compound dependent, but are commonly better than 0.010 ppbv, 15%, and 25%, respectively.

VOCs by PTR-MS

During E&E-UBWOS 2012 two PTR-MS instruments (proton-transfer-reaction mass spectrometers) were deployed at the Horse Pool Intensive ground site for fast time response measurements of VOCs (Volatile Organic Compounds). The Chemical Sciences Division (CSD) of NOAA operated one instrument and the Karlsruhe Institute of Technology (KIT) the other one. The CSD instrument used in this study was described in detail by de Gouw and Warneke [J de Gouw and Warneke, 2007] and was used in similar configurations in multiple aircraft and ground based experiments. The KIT instrument was recently developed with the focus on optimizing the instrument for weight and it was deployed during E&E-UBWOS 2012 for the first time in the field.

In PTR-MS, H_3O^+ is produced in a hollow cathode ion source and allowed to react with VOCs that have a higher proton affinity (PA) than H_2O in a reaction chamber. The resulting $VOC{\bullet}H^+$ ions are detected together with the primary ions using a quadrupole mass spectrometer. The compounds that can be detected at a high sensitivity are oxygenates, aromatics, nitriles, alkenes and others like dimethyl sulfide. Alkanes are generally not detected or only at a very low sensitivity and selectivity. In PTR-MS only the mass of a compound is detected and for compounds with the same mass, such as the isomers of xylenes, only the sum of these compounds can be determined.

During E&E-UBWOS 2012 we used the KIT PTR-MS for parts of the study to measure full mass spectra to determine which masses show the largest signals, and the CSD PTR-MS to monitor the most important compounds at a higher time resolution and sensitivity. During another part of the study we sampled the two instruments from different heights of the tower to determine gradients in the mixing ratios.

Methane and Carbon Dioxide

CO_2 and CH_4 were measured and reported as dry air mole fractions at the Horse Pool ground site outside Vernal, Utah, using a commercial wavelength-scanned cavity ring-down analyzer (Picarro 1301-m) [Crosson, 2008]. Two CO_2 and CH_4 calibration gas standards known to within ±0.07 ppmv and ±1 ppbv, respectively, were regularly delivered to the inlet line to evaluate instrument sensitivity between 380 and 485 ppmv CO_2 and 1790 and 2500 ppbv CH_4. These secondary standards were calibrated in the Boulder laboratories before and after the field project using primary CO_2 and CH_4 standard tanks tied to the WMO standard from the Global Monitoring Division (GMD) at the NOAA Earth System Research Laboratory [Dlugokencky et al., 2005; Zhao and Tans, 2006]. Ambient water vapor corrections were made to calibration and ambient data using the built-in Picarro correction for CO_2 [Crosson, 2008] and following the work of [Chen et al., 2010] for CH_4; the uncertainty of these corrections is estimated at less than 0.05 ppmv and 0.5 ppbv, respectively, for the conditions encountered in Utah.

For the Horse Pool data set, we estimate a total inaccuracy of ±0.11 ppmv for all CO_2 measurements, and ±1.6 ppbv for CH_4 measurements between 1790 and 2500 ppbv. One-minute imprecision of the CO_2 and CH_4 measurements were ±0.02 ppmv and ±0.2 ppbv, respectively. After the field campaign, an additional GMD primary CH_4 gas standard of 5752.4 ppbv was used to evaluate CH_4 measurement accuracy at mixing ratios higher than the calibration range. From this, we estimate a total uncertainty of ±(0.2 ppbv + 0.5% of the reported CH_4 value) for CH_4 mixing ratios greater than 2500 ppbv.

Acid Species by Chemical Ionization Mass Spectrometry (Acid CIMS)

The measurement of atmospherically relevant inorganic and organic acids was accomplished by negative ion proton transfer chemical ionization mass spectrometry (NI-PT-CIMS), using acetate as the reagent ion. This method was developed by the NOAA/ESRL Chemical Sciences Division and is described in several publications from that laboratory [Roberts et al., 2010; Veres et al., 2008]. The NI-PT-CIMS method relies on the fact that acetic acid is the weakest gas-phase acid amongst the compounds that we typically think of as acids. As a result, acetate ion will exchange a proton with a large range of organic and inorganic acids, forming the corresponding anion, which is then detected by mass spectrometry.

Many acids are semi-volatile and soluble in water and, hence, can be quite absorptive on surfaces. The Acid CIMS was placed in the instrument enclosure at the 10m height on the tower in order to minimize the inlet length for the stickiest acids HNO_3, and HCl. The inlet consisted of a 1 m 1/8" OD PFA tube, thermostated at 65°C, through which a flow of 1.3 SLPM was pulled. The remainder of the inlet system - valves for zeros and calibrations, flow limiting orifice, ion flow tube - was temperature controlled at 65°C. Zero (instrument background) determinations were done every 3 hours for a period of 10 min by either switching a sodium carbonate denuder in line with the sample flow, or by overflowing the inlet with Zero Air. Calibrations were performed every 6 hrs by addition of a known amount of formic acid. Other gases were calibrated using relative response factors determined in the laboratory. Inlet effects are known to produce a slight interference in the HONO signal from NO_2 in the presence of humidity. Those effects, on the order of a few percent NO_2, were corrected using laboratory-determined responses. The uncertainties in acid measurements were ±(15% + 20 pptv) for formic acid, ±(20% + 25 pptv) for HONO and HNO_3, ±(20% + 10 pptv) for HNCO, and the sum of butyric and pyruvic acids.

Acyl Peroxynitrates and Nitryl Chloride

Acyl peroxynitrates ($RC(O)OONO_2$) were measured by both chemical ionization mass spectrometry (CIMS)[Slusher et al., 2004] and gas chromatography with electron capture detection GC/ECD[Flocke et al., 2005; J Williams et al., 2000]. The CIMS instrument also measured nitryl chloride, $ClNO_2$, an active chlorine compound that is a product of N_2O_5 reaction with chloride-containing particles [Osthoff et al., 2008]. GC inlet flow was tapped off of the main manifold flow used for the $CO/CO_2/SO_2/O_3$ instruments described above. The inlet for the CIMS instrument consisted of 3/8" O.D. PFA tubing as was place at approximately 11 m off the ground at the southern side of the sampling tower, right next to the VOC inlets (see below). Several modifications were made to minimize artifact formation due to N_2O_5 reacting with chloride deposited on the inside of the inlet from particles and dust; the main inlet was flushed with distilled water at least once every 2 days, and a 30cm length of ¼ O.D. stainless steel tube was place at the front of the PFA inlet and heated to 66°C. The heated inlet dissociated approximately 90% of the ambient N_2O_5, and the steel surface provided a sink for NO_3 radicals to prevent reformation.

The zero determinations for both systems were done the same way, by thermal decomposition of the sample air just previous to it entering the instrument. Calibrations of the acetyl peroxynitrates (PAN) signals were done in the field using acetone/NO photolysis sources described by Flocke et al.[Flocke et al., 2005], and Zheng et al[Zheng et al., 2011]. The PAN GC photosource used regular acetone, while the PAN CIMS used triply ^{13}C-labelled acetone (99%+), which permitted the system sensitivity to be measured continuously, thus accounting for any short-term changes due to high ambient NO or NO_2. The photosource efficiencies have been determined in the laboratory to be 93±6%, and measurements in the field during UBWOS 2012 were consistent with those results. The relative response of the systems to other PAN compounds, propionyl peroxynitrate (PPN) in this study, have been previously determined in the laboratory and found to be quite stable over time and a range of conditions, so those relative response factors are used here. The $ClNO_2$ zeroes were accomplished in the same way; however, $ClNO_2$

is only 95% decomposed at the temperature and residence time used (225°C). Nitryl chloride calibrations were accomplished by quantitative conversion of a known amount of N_2O_5 on a deliquesced NaCl slurry, the N_2O_5 being measured by the ARNOLD CaRDS system described below. The overall uncertainties of these measurements were ±(15% + 5 pptv) for PAN, ±(20% + 5pptv) for PPN, and ±(20% + 25pptv) for $ClNO_2$.

Cavity Rind-down Measurements of NO, NO_2, NO_3, N_2O_5, and O_3

The nighttime nitrogen oxides, NO_3 and N_2O_5, are measured using a custom-built cavity ring down spectrometer (CRDS)[Brown, 2003; Busch et al., 1999]. The nitrate radical, NO_3, has characteristic strong absorption bands in the red end of the visible spectrum with a maximum at 662 nm [Baynard et al., 2007; Yokelson et al., 1997]. The CRDS measures NO_3 directly by total gas-phase optical extinction at this wavelength [Brown et al., 2001; Brown et al., 2002]. The air sample is filtered to remove aerosol particles, which can lead to a large and variable optical extinction in the visible that significantly degrades instrument performance for gas phase measurements [Baynard et al., 2007; Pettersson et al., 2004]. The 25 μm thick Teflon membrane filters are changed every 1-3 hours using an automated device [Dube et al., 2006]. Loss of reactive trace gases on the filter surface is calibrated as described below.

The optical system consists of a temperature-tunable diode laser with 100 mW output that is aligned to the axis of a 93-cm stable optical resonator formed from two highly reflective (R > 99.9995%) reflective mirrors with 1 m radius of curvature [Wagner et al., 2011]. Light transmitted through the cavity is collected on an optical fiber and measured on a photomultiplier tube (PMT). The laser is tuned to the NO_3 maximum and square-wave amplitude modulated at a frequency of 500 Hz. The transient signal following the falling edge of the square wave is digitized and fit to a single exponential using custom software to determine the ring down time constant, τ, for decay of light from the optical cavity.

$$I(t) = I_0\, exp(-t/\tau) \qquad (1)$$

The time constant at 662 nm varies between 350 – 500 μs depending on the operating pressure, for an effective optical path length of 100 – 150 km. The zero time constant in the absence of NO_3 (τ_0) is acquired by adding sufficient NO to the inlet to chemically titrate NO_3.

$$NO + NO_3 \rightarrow 2NO_2 \qquad (R1)$$

Reaction (R1) is extremely rapid (k = 2.6×10^{-11} cm^3 $molecule^{-1}$ s^{-1} at 298 K [Sander et al., 2006]). The concentration of NO_3 is then determined absolutely from the two time constants using the standard equation for CRDS.

$$[NO_3] = \frac{R_L}{c\sigma}\left(\frac{1}{\tau} - \frac{1}{\tau_0}\right) \qquad (2)$$

Here, σ is the 662 nm absorption cross section of NO_3, c is the speed of light, and R_L is the ratio of the cavity length to the length over which the sample gas is present (1.21 in this instrument). The combination of 662 nm absorption and titration by NO is an extremely specific and sensitive method for

detection of NO_3 [Dube et al., 2006]. The sum of NO_3 and N_2O_5 is measured simultaneously in a second channel with a heated inlet and optical cavity to quantitatively convert N_2O_5 into NO_3 by thermal dissociation. A small correction factor (typically < 5%) is applied only at high NO_x (NO_2 > 20 ppbv) to account for incomplete conversion of N_2O_5 at the instrument operating temperature. The instrument sensitivity to NO_3 and N_2O_5 is 0.2 – 3 pptv, (2σ, 1s) depending on instrument operating conditions [Dube et al., 2006; Wagner et al., 2011].

The instrument simultaneously measures the concentration of NO_2 in a separate optical cavity at 405 nm, where NO_2 has its strongest visible absorption bands [Vandaele et al., 2002]. The detection principle is the same, except that the mirror reflectivity at 405 nm is 99.9965 % and the laser modulation frequency is more rapid (2 kHz) to compensate for the shorter (35-45µs) ring-down time constants. The instrument is zeroed by addition of either zero air from a cylinder or ambient air that has been scrubbed of NO_2 to the inlet. The sensitivity to NO_2 is 20-50 pptv (2σ, 1s) [Fuchs et al., 2009; Wagner et al., 2011]. The instrument also measures total NO_x (=NO + NO_2) and total O_x (=O_3+NO_2) simultaneously on two additional channels. In one channel, excess O_3, generated in a small flow of O_2 over a mercury pen-ray lamp, is added to convert NO into NO_2 [Fuchs et al., 2009].

$$NO + O_3 \rightarrow NO_2 + O_2 \qquad \text{(R2)}$$

The conversion is quantitative with addition of approximately 15-20 parts per million (ppm) O_3 to a converter with a 0.5 s residence time, but the measured NO_x concentration must be corrected (<2%) for the slow additional conversion of NO_2 to NO_3 and N_2O_5 in excess ozone. In the second channel, excess NO is added from a cylinder to measure O_x by quantitative conversion of O_3 to NO_2 by the same reaction [Washenfelder et al., 2011]. This channel does not require a correction factor since NO_2 does not undergo further oxidation in excess NO. The concentrations of NO and O_3 can then be determined by differencing each of these channels against the NO_2 channel. The sensitivity for NO and O_3 is ≤100 pptv (2σ, 1s) [Wagner et al., 2011; Washenfelder et al., 2011].

The NO_2 channels are calibrated via addition of a known concentration of NO_2, generated from measurement and conversion of a known concentration of O_3, to the inlet. The O_3 is generated and measured using a commercial ozone monitoring instrument and converted using the same chemistry described above. The resulting accuracy is ±3% for NO_2 and ±5% for NO and O_3 [Wagner et al., 2011; Washenfelder et al., 2011]. The NO_3 and N_2O_5 channels are calibrated by addition of N_2O_5 to the inlet from the vapor over a synthetic crystalline N_2O_5 sample stored on dry ice. The N_2O_5 (or NO_3 via thermal conversion) from this sample is measured at 662 nm, and the gas-phase sample is then quantitatively converted to NO_2 and measured on the 405 nm CRDS instrument. The accuracies for the NO_3 and N_2O_5 measurements are ±12 and ±11%, respectively [Fuchs et al., 2008]. The calibration procedure accounts for loss of these reactive trace gases on the inlet tubing and filter surfaces. All five trace gases (NO, NO_2, O_3, NO_3, N_2O_5) are thus ultimately calibrated against the same standard, which is the 254 nm UV absorption of O_3 from the commercial O_3 monitoring instrument (2% accuracy) [Wagner et al., 2011].

Aerosol Measurements – NOAA/PMEL

Sampling

Aerosol particles were sampled 12.6 m above the ground through a mast that extended 9.1 m above the aerosol measurement container. The mast was capped with an inverted-bowl rain

shield. Air was drawn down the 20 cm diameter mast at 1 m^3 min^{-1}. A 5 cm diameter 2.3 m long stainless-steel pipe extended into the base of the mast. The pipe was heated to 9.75 ± 0.68°C to dry the aerosol to a relative humidity (RH) of <25%. At the base of the mast, the flow through the stainless steel pipe was split into four 1.6 cm diameter stainless-steel tubes that were attached to four 2-stage multi-jet cascade impactors. A flow of 20 l min^{-1} provided 50% aerodynamic cutoff diameters, $D_{50,aero}$, at 2.5 and 12.5 um. One impactor (PM 2.5 only) was used for organic and elemental carbon analysis. The second impactor was used for anion and cation analysis. The third impactor was used for gravimetric and trace element (XRF) analysis. The fourth impactor was used to provide a PM 2.5 size cut for the particle-into-liquid sampler (PILS), the nephelometer, and the Particle Soot Absorption Photometer (PSAP). An additional 0.63 cm port in the flow splitter was used to provide aerosol to a Scanning Mobility Particle Sizer (SMPS), an Aerodynamic Particle Sizer (APS), and a water-based condensation nucleus (CN) counter. Impactor sampling times ranged from 5 to 12 hours. Generally one sample was collected during the day and one sample was collected between sunset and sunrise. The average temperature and RH in the sample line measured downstream of an impactor was 24.3 ± 1.9°C and 10.3 ± 3.9%, respectively.

OC/EC

A charcoal denuder was deployed upstream to the impactor used for organic carbon (OC) and elemental carbon (EC) sampling to remove gas phase organic species. The 32 cm long diffusion denuder contained 16 parallel strips (30 faces) of 20.3 cm x 3 cm carbon-impregnated glass fiber (CIG) filters (Whatman-10320163) separated by ~1.6 mm. The denuder cross-sectional area was 7.45 cm^2. Two 47mm quartz fiber filters (Pall Gelman Sciences, #7202, 9.62 cm^2 effective sample area) were used in series downstream of the 2.5 um impaction stage. The downstream filter was used as the sample blank. The analysis of the filter samples was done using a Sunset Laboratory thermal/optical analyzer (Bates et al., 2008).

Cations & Anions (impactor sampling)

One two-stage multi-jet cascade impactor was used to determine the sub 2.5 um and 2.5-12.5 um diameter concentrations of Cl^-, Br^-, NO_3^-, $SO_4^=$, oxalate (Ox^-), Na^+, NH_4^+, K^+, Mg^{+2}, and Ca^{+2}. The impaction stage at the inlet of the impactor was coated with silicone grease to prevent the bounce of larger particles onto the downstream stages. Tedlar films were used as the collection substrate in the impaction stage and a Millipore Fluoropore filter (1.0-um pore size) was used for the backup filter. The extracts were analyzed by ion chromatography [Quinn et al., 2000]. NH_4NO_3 is volatile and is not efficiently collected on filters in an impactor. The NO_3^- and NH_4+ concentrations reported here include the NO_3^- and NH_4^+ concentrations measured in the PILS samples averaged over the impactor sampling times.

Cations & Anions (PILS sampling)

A particle-into-liquid sampler (PILS) [Orsini et al., 2003; Weber et al., 2001]and fraction collector were used to collect PM 2.5 aerosols for cation and anion analysis. Fifteen l min^{-1} of sample flow were taken downstream of one of the two-stage impactors and routed through two URG denuders. One denuder was coated with sodium carbonate for the removal of gas phase acids and the other with citric acid to remove gas phase bases. The flow then entered the PILS to concentrate the aerosols particles. The impaction rinse flow was adjusted to obtain one sample vial (0.75 ml) every 30 minutes. The extracts were analyzed by ion chromatography [Quinn et al., 2000].

Gravimetric Mass and Trace Elements

One two-stage multi-jet cascade impactor was used to determine the sub 2.5 um and 2.5-12.5 um diameter gravimetric aerosol mass. The data are reported as PM 2.5 and PM 12.5 (sum of the two weights). Tedlar films and Teflo filters were used in the impactor. Films and filters were weighed at PMEL with a Cahn Model 29 and Mettler UMT2 microbalance, respectively. The balances are housed in a glove box kept at a humidity of 65 ± 4%. The resulting mass concentrations from the gravimetric analysis include the water mass that is associated with the aerosol at 65% RH. More details of the weighing procedure can be found in Quinn and Coffman [Quinn and Coffman, 1998]. After post-experiment weighing, the Teflo filter was used to determine the PM 2.5 mass of Al, Si, Ca, Ti, and Fe using thin-film x-ray primary and secondary emission spectrometry.

Condensation Nuclei (CN)

Total particle number concentration (CN) was measured with a water based CN counter (TSI 3785). This instrument counts all particles with diameters greater than 5 nm.

Aerosol In-situ Light Scattering and Absorption

A TSI integrating nephelometer (Model 3563) was used to measure integrated total aerosol light scattering at wavelengths of 450, 550, and 700nm. A Radiance Research Particle Soot Absorption Photometers were used to measure aerosol light absorption at 467, 530, and 660nm. Both instruments were downstream of a two-stage impactor that provided a 2.5 um diameter size cut.

Aerosol Number Size Distribution

The aerosol number size distribution was measured with a Scanning Mobility Particle Sizer (SMPS, TSI 3080 coupled to a TSI 3010 CN counter) and an Aerodynamic Particle Sizer (APS, TSI 3321). The SMPS was operated with a sheath air flow of 5 L/min and a sample flow of 1 L/min. The instrument counted particles between 20 and 500 nm geometric diameter. The APS was located directly below the mast. The inlet to the APS was vertical and its sample withdrawn isokinetically from the larger flow to the SMPS. The APS data were collected in 34 size bins with aerodynamic diameters ranging from 0.7 to 10.37 μm. Number size distributions were collected every 5 minutes. Further details can be found at http://saga.pmel.noaa.gov/data/. Contact persons: Tim Bates, tim.bates@noaa.gov; Trish Quinn, patricia.k.quinn@noaa.gov.

CSD Lidars

NOAA/ESRL/CSD deployed two of its lidar remote sensing instruments to the 2012 Uintah Basin Wintertime Ozone Study (UBWOS): the High Resolution Doppler Lidar (HRDL) and the Tunable Optical Profiler for Aerosol and oZone (TOPAZ) ozone lidar. Both instruments were situated at the Horse Pool Supersite.

The HRDL wind lidar was operated nearly continuously from 23 January until 1 March 2012 with only a few hours of downtime on two of the 39 days of measurements. Every 20 minutes, HRDL provided profiles of horizontal wind speed and direction, vertical wind speed and its variance, and un-calibrated aerosol backscatter. In this real time mode, the horizontal wind speed and direction profiles extend from about 10 m above ground level (AGL) to generally between 1 and 2 km AGL at a vertical resolution of 10 to 25 m with the highest resolution near the ground. The vertical velocity and backscatter profiles cover

altitudes from 250 m to about 3 km AGL with a 30-m vertical resolution. Preliminary HRDL data were posted in near real time (about 10 minutes after they were recorded) on a web site (http://www.esrl.noaa.gov/csd/groups/csd3/measurements/ubwos/hrdl/), where they were available for other study participant for use in the interpretation of their data and for planning the NOAA/ESRL/GMD-led flight operations at UBWOS 2012. In post analysis, vertically scanning data are used to estimate vertical profiles of horizontal wind speed and direction along with its variance and un-calibrated aerosol backscatter every twenty minutes to within 5 meters of the surface and with 5 meter vertical resolution.

The TOPAZ ozone lidar was operated on 14 days from 3 February to 29 February 2012, and it recorded 62 hours of ozone and aerosol backscatter profile data. In the absence of any high ozone events, our sampling strategy consisted of operating TOPAZ for several hours at a time and covering different segments of the diurnal cycle on different days. Prior to the UBWOS 2012, TOPAZ was converted from a downward-looking airborne system into a zenith-pointing instrument that was installed in a truck with a roof-mounted two-axis scanner. The scanner permits pointing the laser beam at several shallow elevation angles at a fixed but changeable azimuth angle. Zenith operation is achieved by moving the scanner mirror out of the laser beam path. During UBWOS 2012, repeated scans at 2, 10, and 90 degrees elevation angle were performed approximately every 5 minutes. The dwell time at each angle was 75 s. The ozone and aerosol backscatter profiles at these three angles were spliced together to create composite vertical profiles extending from 15 m to about 3 km AGL. The effective vertical resolution of the composite ozone profiles increases with altitude from 3 to 90 m. Occasional horizontal measurements were made to study the horizontal variability of ozone and aerosols. In addition, several comparisons were performed with NOAA/ESRL/GMD tethered and free-flying ozone sondes. Preliminary TOPAZ ozone and aerosol data will be posted at (http://www.esrl.noaa.gov/csd/groups/csd3/measurements/ubwos/topaz/).

Meteorological Measurements

The NOAA/ESRL Physical Sciences Division deployed an instrumented 20 m tower, ventilated broadband solar and IR Eppley radiometers, heated tipping bucket rain gage, snow depth sensor, and a bistatic acoustic sounder (3.4 m resolution, 6.0 m minimum range) at a site adjacent to the main Horse Pool site (see Figure 3-1). The tower instrumentation included surface pressure, air temperature and relative humidity (2, 10, and 20 m), fast response sonic anemometer/thermometer (6,16 m), wind speed and direction (10, 20 m).

Differential Optical Absorption Spectroscopy (DOAS)

UCLA's Long Path Differential Optical Absorption Spectrometer (LP-DOAS) measured vertical profiles of various trace gases at the Horse Pool site from January 22 to February 28, 2012. The LP-DOAS system consisted of a telescope that collimated and sent light from a Xe arc lamp onto a retroreflector array. The array folded back the light into the telescope, where it was fed through a fiber and into a spectrometer-detector system. The telescope was aimed consecutively at three retroreflector arrays (Figure 3-3) located at three different altitudes (1600, 1613, and 1637 m above sea level) and about 2.3 km northwest of the telescope (Figure 3-4).

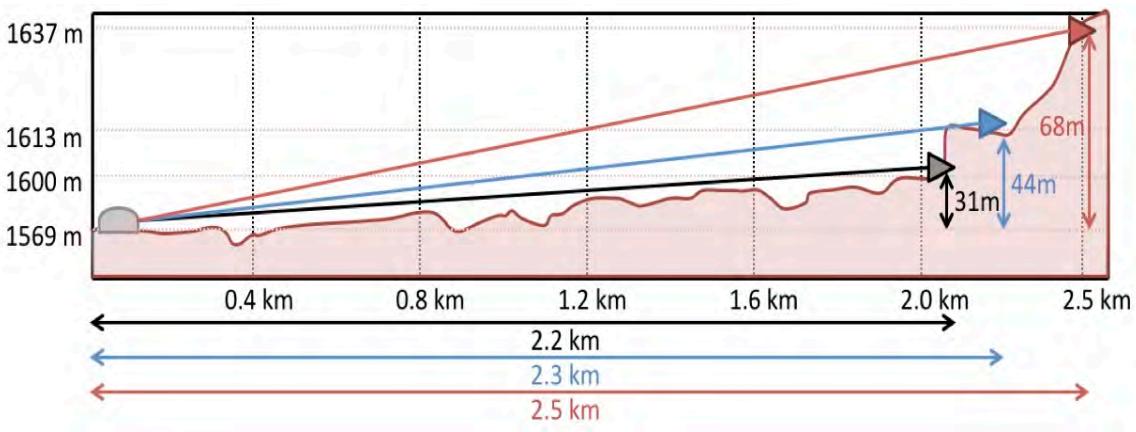

Figure 3-3. Side view of LP-DOAS system set up at the Horse Pool site.

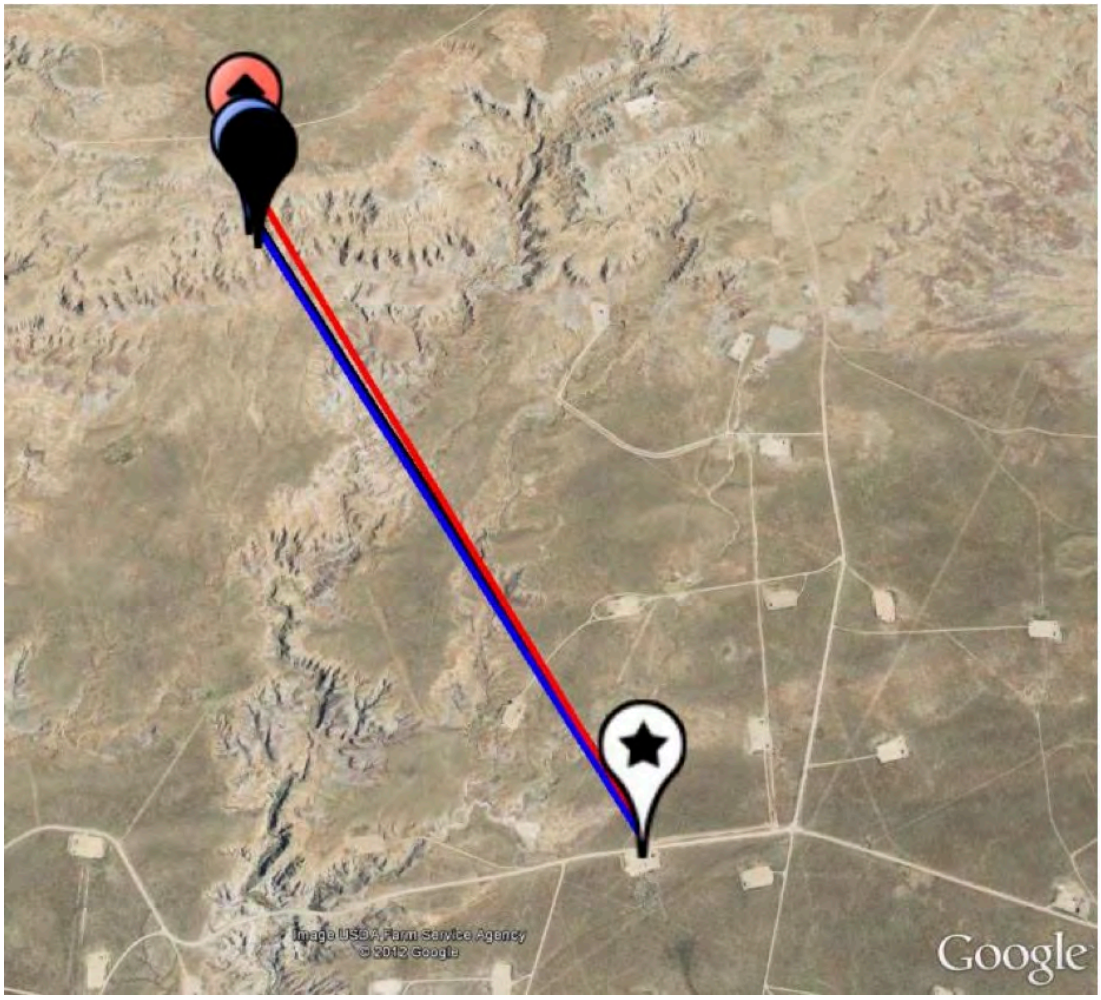

Figure 3-4. Top view of LP DOAS system.

The LP-DOAS instrument measured sequentially in two different wavelength ranges: 300-380 nm (for retrieval of O_3, SO_2, NO_2, HONO and HCHO), and 600-680 nm (for retrieval of NO_3) on all three light paths. For each wavelength range, information of the respective trace gases was recorded simultaneously.

Analysis of the atmospheric absorption spectra was achieved using a combination of a linear and non-linear least squares fit of the known trace gas absorption features [Platt and Stutz, 2008]. Spectral absorption structures were incorporated in the fitting procedure using the literature absorption cross sections of O_3 [Serdyuchenko et al., 2011], NO_2 [Voigt et al., 2002], HONO [Stutz et al., 2000], HCHO [HITRAN, 2008], SO_2 [Vandaele et al., 1994]. Errors of reported mixing ratios were calculated as 1σ statistical uncertainties by the analysis procedure for each individual spectrum and trace gas. The systematic error of the reported trace gas mixing ratios were dominated by the uncertainties of the absorption cross sections of the respective trace gases which were in the range of 3 – 8%. The systematic error of the DOAS spectrometer was <3% [Platt and Stutz, 2008]. Table 3-4 shows the average detection limits of the LP-DOAS for NO_2, HONO, HCHO, O_3 and SO_2 during UBWOS 2012.

Table 3-4. Detection limits of the LP-DOAS instrument during UBOS 2012.

	TRACE GASES AVERAGE DETECTION LIMITS				
Light Path	**NO_2 (ppb)**	**HONO (ppb)**	**HCHO (ppb)**	**O_3 (ppb)**	**SO_2 (ppb)**
Lower	0.066	0.034	0.31	1.46	0.05
Middle	0.065	0.033	0.29	1.38	0.05
Upper	0.065	0.033	0.28	1.33	0.05

University of Wyoming Aerosol Mass Spectrometer

The University of Wyoming deployed an Aerodyne quadropole aerosol mass spectrometer (AMS) during E&E UBWOS 2012 [Jayne et al., 2000]. The AMS generated size-resolved mass loadings of non-refractory aerosol species (predominantly organic, sulfate, nitrate and ammonium). The instrument also recorded the full mass spectrum of the aerosol from 0-300 amu. Data was measured continuously during the project and averaged into 5-minute intervals. The inlet for the AMS was located on the main sampling tower, approximately 30 feet above ground level. Aerosol particles were transported from the inlet through copper tubing to the instrument. Relative humidity and temperature of the air stream were constantly monitored. Other than a few minor stoppages for calibration and repair, the AMS ran successfully during the entire 6-week project.

Data from the AMS are currently being analyzed and corrected based on calibrations during the study [Middlebrook et al., 2011]. After this basic analysis, the data will be analyzed with positive matrix factorization (PMF) to aid in determining the various sources of organic aerosol and their magnitudes [Ulbrich et al., 2009]. Measurements of AMS organic aerosol and VOC will be compared to determine the yield of secondary organic aerosol from emissions in the Uintah Basin [J A de Gouw et al., 2005]. Measurements of inorganic mass from the AMS will be integrated with gas-phase measurements to close the NO_y budget.

UC Berkley TD-LIF In-situ Measurement of NO_2 and Higher Oxides of Nitrogen

Two thermal dissociation laser-induced fluorescence (TD-LIF) instruments [Day et al., 2002; Thornton et al., 2000; Wooldridge et al., 2010] were installed at the Horse Pool site and used to measure NO_2; the

sum of PAN and other peroxynitrates (ΣPN); the sum of alkyl and other organic nitrates (ΣAN), both gas and aerosol; and total particulate organic nitrates. One instrument (laser excitation wavelength 408 nm) had its inlet roughly coincident in height with other aerosol measurements (9 m). This instrument measured NO_2, Σ(AN+PN), and particulate-phase organic nitrates based on the design of Rollins et al. (2010). In this design, gas phase compounds are removed with a charcoal denuder while aerosol particles are transmitted. A PM2.5 cyclone was used to reject dust and other large particles. A second instrument (laser excitation wavelength 530 nm) had its inlet at the height of the majority of the gas phase measurements (16 m). This instrument measured NO_2, ΣPN and ΣANs. In both instruments, higher oxides of nitrogen were converted to NO_2 at the inlet by thermal dissociation, and then the pressure was reduced for transit to the detection cells at the base of the tower. Residence time in the transfer line was ~1 second. Measurements were recorded at 1Hz and then averaged to 1 minute. Hourly calibrations were performed using a 5 ppm NO_2 standard diluted with zero air. Zeros (baseline determinations) were recorded every 30 minutes. Both routines overflowed the sampling inlet to ensure identical instrumental condition as during normal sampling. The detection limit for the 408 nm system at 1 minute averaging time was 24 ppt (1σ) for NO_2 and 34 ppt (1σ) for organic nitrates. The 530 nm system had 1 minute detection limit of 51 ppt (1σ) and 72 ppt (1σ) for NO_2 and organic nitrates. The accuracy of the instruments is estimated to be ±10% for NO_2 and ±20% for the higher nitrates.

RESULTS AND DISCUSSION

Priority Pollutant Measurements

Overview

Measurements of NO, NO_2, NO_y (total reactive nitrogen), O_3, CO, CO_2, SO_2, photolysis rates of NO_2, NO_3, and O_3, and standard meteorological parameters were made by NOAA/CIRES personnel at the Horse Pool site during the UBWOS 2012. Data were recorded at one-second intervals and averaged to one-minute values. These data are available for UBWOS 2012 PIs at the ESRL/CSD website. In this section we provide summary data for NO_x ($NO+NO_2$), CO, SO_2, and O_3. These are compared to data from two other locations for context: the NOAA tall tower (at ~24 meters agl) near Erie, CO, during Feb-Mar of 2011 and the ground supersite at Pasadena, CA, during the CalNex study during May-Jun of 2010. The former location is at the edge of the Wattenberg field of the Denver-Julesberg basin, and the latter location is an urban area in the South Coast Air Quality Basin of California. Figures 3-5 through 3-8 show the distributions of the three directly emitted species (NO_x, CO, SO_2) and for O_3 at the sites. These plots contain all data; that is, there has not been any filtering, for example by wind. For NO_x, the Pasadena location has the highest mode of the three distributions followed by the Erie site. This reflects the intensity and proximity of sources, principally motor vehicle traffic. The Horse Pool site distribution appears to have two modes - one very peaked at ~0.4 ppbv NO_x and another more broad at ~3 ppbv. The lower mode is due to those periods of high winds more representative of background levels. The higher, more broad mode in the Horse Pool data is more representative of those low wind speeds that would be expected for the high-ozone events. This mode level is similar to that for the Erie site which has a much higher population density than the Horse Pool site. Evidently, the oil and gas operations in the Uinta Basin produce similar levels of NO_x to those found in rural/suburban areas. For CO, shown in Figure 3-6, the Pasadena data again have the highest mode (~300 ppbv), reflecting the higher source intensity, while the Horse Pool and

Erie data virtually superimpose with a mode at ~150 ppbv. This latter point is a little surprising given the proximity of the tall tower to higher population density, heavily traveled rural roads, and a major interstate highway where a large fraction of traffic is from gasoline-powered vehicles (i.e., CO sources). In contrast, the majority of vehicles in the Uinta Basin were diesel-powered which produce very little CO emissions. Thus, there must be sources in the Basin that emit non-negligible quantities of CO. In Figure 3-7 the SO_2 distributions for Horse Pool and Pasadena (no data for the Erie site) have similar modes at ~0.2 ppbv, which is near the detection limit. However, the Horse Pool distribution drops off very sharply at 0.4-0.5 ppbv where the Pasadena data have a long tail to higher levels. Again, this reflects the greater intensity and distribution of SO_2 sources in the urban area compared to the Uinta Basin. The ozone distributions in Figure 3-8 are quite interesting. While the mode for the Pasadena data would be expected to be the highest, the CalNex 2010 study occurred at the early part of the Los Angeles ozone season, and the highest value recorded was 108 ppbv. Nevertheless, the distribution does show the expected broad shape with titration and deposition dominating the low end (i.e., significant fraction of near-zero values) and photochemistry producing the tail to higher levels. Contrast that with the Erie and Horse Pool data which both show a sharp cutoff at the higher levels, reflecting a dearth of photochemical production during the wintertime. Moreover, the Horse Pool data have a mode about 20 ppbv lower than Erie, doubtless due to less intense photochemistry in the Basin despite similar levels of NO_x.

Emissions in the Uinta Basin

There are many different sources of emissions in the Uinta Basin. Most of these are associated with oil and gas operations, but the single largest point source is the Bonanza power plant. On February 4, 2012, at the Horse Pool site, a large plume event was observed. Figure 3-9 shows three plots that provide information about the composition of this plume to possibly suggest its source. The correlation between SO_2 and NO_y (left plot) shows that the source produces both NO_x and SO_2, although the ratio of S to N is lower than the average from the Bonanza stack monitors. The middle plot shows the correlation between CO and CO_2 and indicates that the level of CO (~4%) in the plume is very high for a coal-fired power plant (electric generating unit - EGU). The right-hand plot shows that almost all of the reactive nitrogen in the plume is NO_x; that is, the plume has not significantly aged. Initially, these combined data (especially the CO/CO_2 plot) suggested that the plume was from a source other than the Bonanza power plant. However, subsequent aircraft flights by colleagues at GMD conclusively showed that the emission of CO (at 3-5%) from this EGU was much higher than expected for a power plant. Plus, since there are no other significant sources of SO_2 in the Basin, we conclude that this plume did come from the Bonanza EGU, and that emissions from this source will be mixed to the surface and must be included in emissions inventories for this region.

The data collected at the Horse Pool site also will provide information about other sources of emission in the Basin. During the intensive, numerous smaller plume events were observed that can be analyzed in a manner similar to that shown in Figure 3-9. These analyses can provide mass-based emission factors for these different sources (both point and mobile) that can be used in emission inventory modeling.

Photochemistry at the Horse Pool Site

The above measurements made at Horse Pool provide an indication of the intensity of photochemistry during the 2012 intensive. Figure 3-10 shows a plot of O_3 versus the difference quantity NO_y - NO_x, sometimes called NO_z. This quantity is a measure of the conversion of the

emitted species, NO_x, to other reactive nitrogen species, where a value of 0 (all NO_y is NO_x) indicates fresh emissions and larger values show the level (in ppbv) of NO_x converted to more oxidized nitrogen species, such as PANs or HNO_3. A relationship should exist between O_3 and NO_z if both are produced via atmospheric photochemistry. Looking first at the active photochemical environment shown by the Pasadena data in Figure 3-11, it is clear that as NO_z increases so does O_3 above about 40 ppbv, which could be considered the background O_3 level. On the other hand, there seems to be no relationship whatsoever in the Horse Pool data, shown in Figure 3-10. If anything, NO_z increases when O_3 drops below about 25 ppbv. This is consistent with nighttime chemical conversion of NO_x to NO_3, N_2O_5, and $ClNO_2$ at the expense of O_3 (plus O_3 deposition). There is very little in these data to suggest any substantial photochemical activity resulting in O_3 production at the Horse Pool site, even though the levels of precursor species (NO_x and VOCs) were sufficient to maintain photochemical production.

Photolysis rates for O_3 and NO_2 were similar at the Horse Pool site and at Pasadena. Figure 3-12 shows both the upward-looking and down-looking photolysis rates for NO_2 measured at Horse Pool in mid-February. The sum of these rates on a sunny day gives total photolysis of about 0.007 Hz at midday. For comparison the total NO_2 photolysis rate for Pasadena was about 0.008 Hz under similar conditions. Also of significance in Figure 3-12 are the data for 20 Feb. There was a small snow event that occurred on 19 Feb which left about an inch of snow on the ground. The next day was sunny, and the increase in the ground albedo is clearly seen in the downward-looking data on 20 Feb. For this day the total photolysis rate for NO_2 equals or exceeds 0.01 Hz, and confirms the expectation that snow-cover can be a contributing factor to high ozone events in the Uinta Basin during winter.

Summary

This brief overview of only some of the interesting priority pollutant observations made at the Horse Pool site can be summarized as follows:

A. The levels of NO_x observed under the low speed wind conditions were about 3-4 ppbv and are comparable to those seen at a rural/suburban site in Colorado. For high wind conditions, NO_x levels dropped by about an order of magnitude.

B. Levels of CO in the Basin were typically around 150 ppbv, which, surprisingly, are comparable to the more populated Colorado site.

C. Except for a few events, SO_2 was generally observed near the detection limit of the instrument which indicates almost no local sources of this compound.

D. Snow on the ground significantly enhances surface albedo in the UV range, which increases photolysis rates. The photolysis rates for NO_2, when there was snow on the ground, were similar to those at the more photochemically active Pasadena site. For most of the 2012 study, however, the ground was bare and NO_2 photolysis was much reduced.

E. There was very little indication of significant photochemistry during the intensive. Levels of O_3 never exceeded ~60 ppbv, and the conversion of NO_x to higher oxidized species was less than 50% of that seen in the more active photochemical environment of Pasadena, CA.

Priority Pollutant Figures:

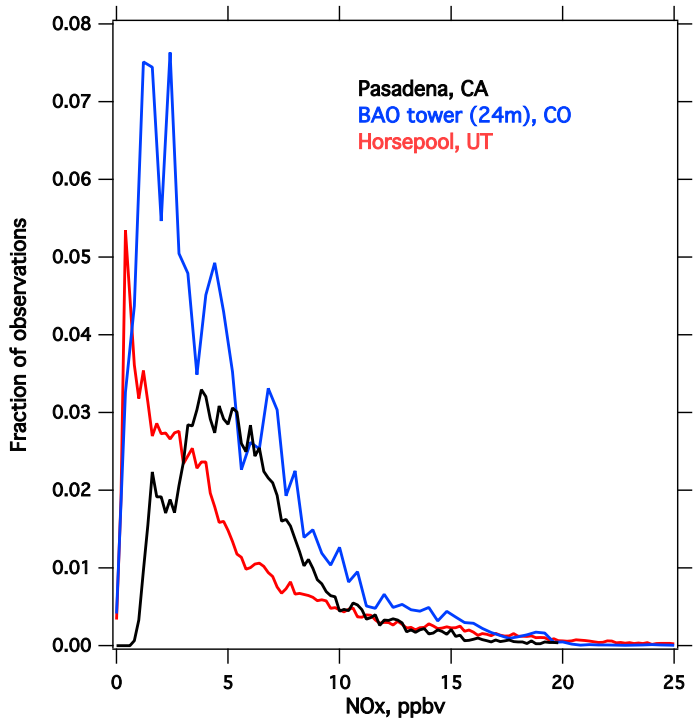

Figure 3-5. Distributions of NOx.

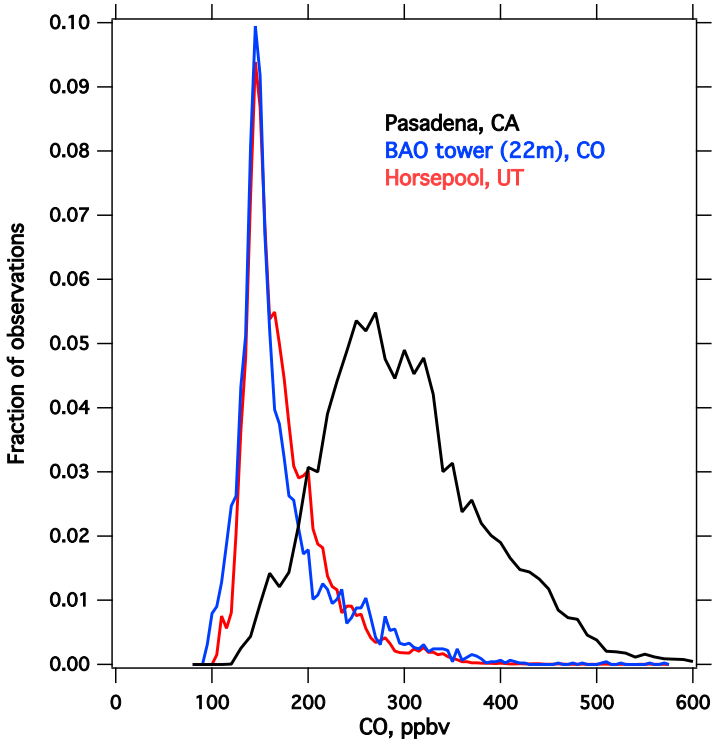

Figure 3-6. Distributions of CO.

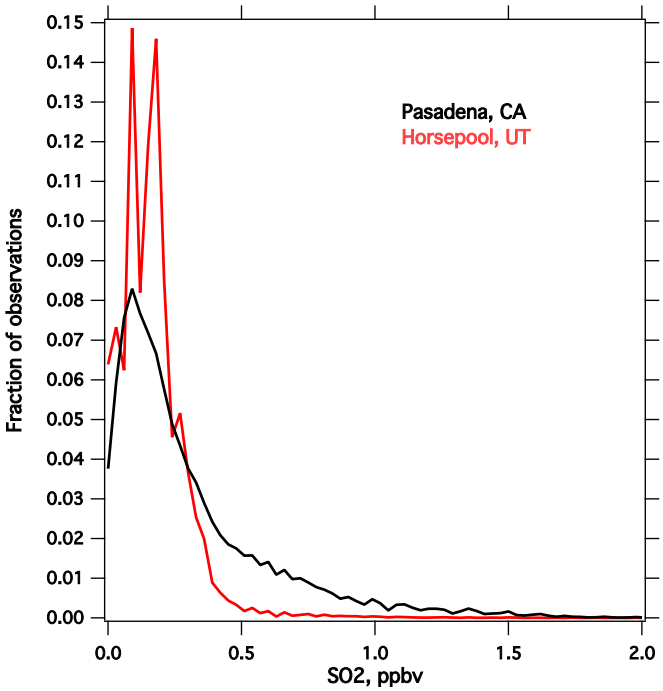

Figure 3-7. Distributions of SO_2.

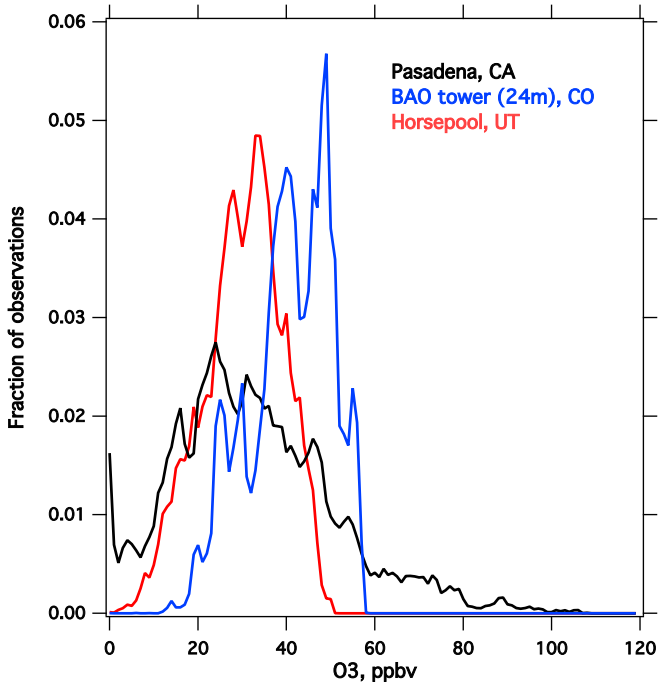

Figure 3-8. Distributions of O_3.

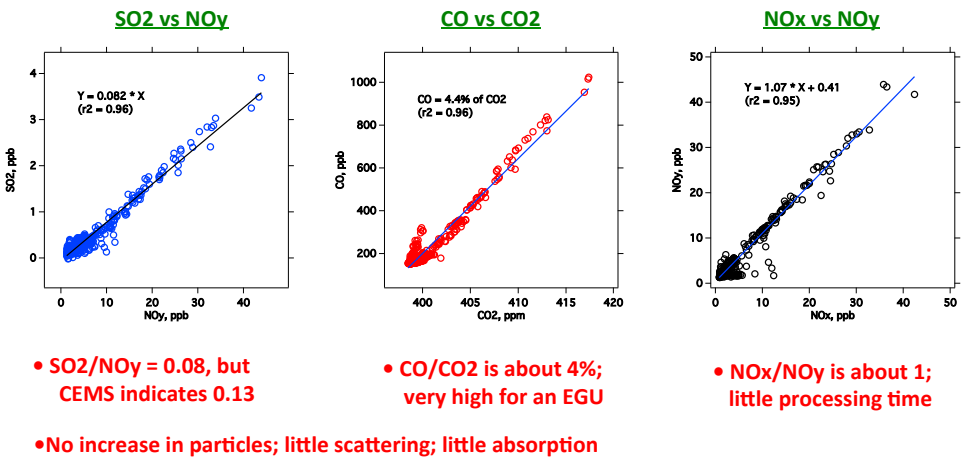

Figure 3-9. Correlation plots from a plume event at Horse Pool on 04 Feb 2012.

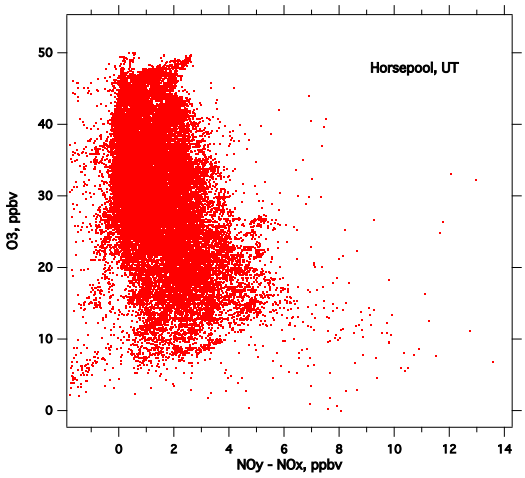

Figure 3-10. O_3 vs NO_z at Horse Pool

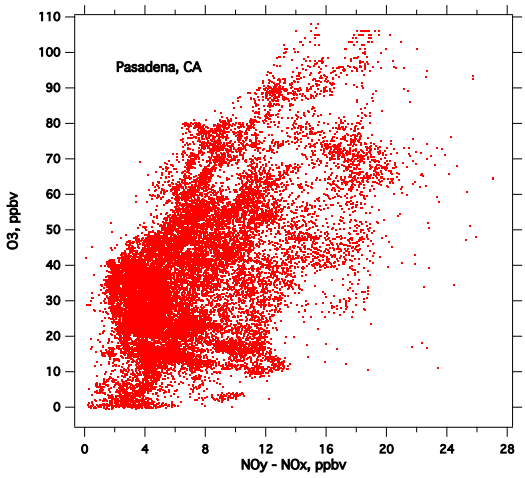

Figure 3-11. O_3 vs NO_z at Pasadena, CA.

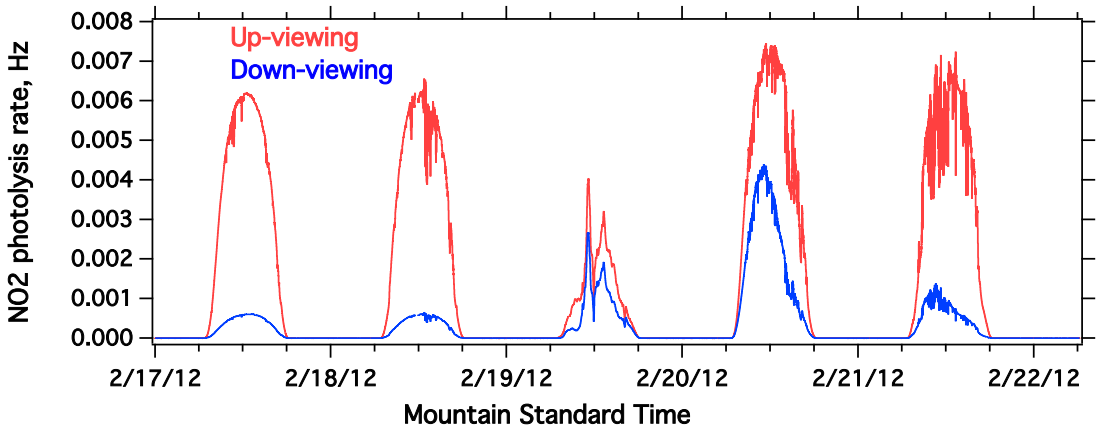

Figure 3-12. Photolysis of NO_2 at Horse Pool.

Volatile Organic Compounds

GC/MS Measurements

A full suite of volatile organic compounds (VOCs), including alkanes, alkenes, cycloalkanes (napthenes), aromatics, oxygentated VOCs (OVOCs), nitrogen- and halogen-containing species, were measured in-situ via a gas chromatograph-mass spectrometer instrument (GC-MS) at the Horse Pool site. This high-level of chemical speciation allows for a detailed analysis of the primary emissions of VOCs from oil and natural gas operations and the key reactive species in potential photochemical ozone formation.

During UBWOS 2012, very high levels of several hydrocarbons and methanol were routinely observed. First, we compare the average mixing ratios observed during UBWOS 2012 to previous measurements conducted at the Red Wash site in winter 2011 (Figure 3-13). In general, the Horse Pool site observed larger average mixing ratios for the C_3-C_9 alkanes, cycloalkanes, and the C_6-C_8 aromatics. The relative composition of these species is comparable between the two sites. The largest differences in the observed mixing ratios occur for the C_9 aromatics and the alkenes, where much larger values were reported for the Red Wash site. Ethyne, a common tracer for combustion, was 70 times greater in 2011 compared to 2012. Isoprene, a temperature-dependent biogenic emission, was routinely measured near the detection limit (<0.01 ppbv) at Horse Pool; however, the average mixing ratio for Red Wash was reported as 2.91 ppb. Other biogenic species, such as monoterpenes, were not observed at the Horse Pool site. The source for the anomalously high levels of the alkenes remains unknown. During UBWOS 2012, the observed mixing ratios were 3.8 (range 60-0.15) times higher than the Red Wash site for the alkane, cycloalkane, and aromatic VOCs.

Next, we compare the average mixing ratios observed during UBWOS 2012 to previous measurements collected near active areas of oil and natural gas operations in northeastern Colorado in winter 2011. These measurements were conducted at NOAA's Boulder Atmospheric Observatory (40.05°N and 105.00°W) situated in Weld County, Colorado in the southwestern sector of Wattenberg Gas Field of the greater Denver-Julesburg Basin (DJB). At the time of these measurements, there were 17,000 active oil and gas wells in Weld County compared to the 8,000 wells in Uintah County. As shown in Figure 3-14, the average observed mixing ratios were larger for many of the VOCs measured in Uintah compared to Weld County, Colorado. The higher alkenes observed in Weld County are consistent with urban combustion sources in the vicinity. Methanol is 3.6 times higher in Uintah than in Weld County. Methanol is added to the raw natural gas stream by certain operators as anti-freeze. The reasons for the differences in methanol levels between the two areas are not clear at this time. The higher ethanol in Weld County is consistent with numerous sources in the vicinity, including agriculture, breweries, and the use of E10 fuel (10% Ethanol) for gasoline-powered vehicles. During UBWOS 2012, the observed mixing ratios were 6.5 (range 26-1.6) times higher than the Weld County site for the alkane, cycloalkane, and aromatic VOCs.

The final comparison is between the wintertime measurements in Uintah near oil and natural gas operations and summertime measurements in Pasadena, California, as part of the CalNex 2010 field campaign. Pasadena is a large urban area situated 15 km northwest of Los Angeles. The greater Los Angeles area is well known for its air quality issues that are attributed to a dense population (>10 million people) in a large geologic basin that is inadequately ventilated. We include the Pasadena dataset here in order to 1) identify the primary source of alkanes in the

Uintah Basin and 2) compare the VOC composition between Uintah in the wintertime and an urban area during the more typical summertime "ozone season."

In order to identify the primary source of alkanes in the Uintah Basin, we compare the observed enhancement ratios of the pentane isomers for the Uintah and Pasadena datasets (Figure 3-15). The iso- to n-pentane ratio for Pasadena is a factor of 2.7 times higher than that observed in Uintah. The observed iso- to n-pentane ratio in Pasadena is consistent with published values for tailpipe emissions from gasoline powered vehicles [Schauer et al., 2002]. The observed enhancement ratios for UBWOS 2012, Red Wash 2011, and Weld 2011 are comparable, and they are consistent with the composition of raw natural gas in Wattenberg Field as reported by the Colorado Oil and Natural Gas Conservation Commission [COGCC, 2007]. This analysis shows that the hydrocarbon signature from oil and natural gas operations can be clearly differentiated from urban emissions dominated by on-road sources.

As shown in Figure 3-16, the alkanes are greatly enhanced in Uintah (22-1.9 times greater) compared to the urban site, while the aromatics were relatively comparable (5-0.6 times greater). Cycloalkanes were not reported for the CalNex dataset. During UBWOS 2012, the observed mixing ratios were 7.7 (range 22-0.58) times higher than the Pasadena site for the alkanes and aromatics. For UBWOS 2012, the C_2-C_8 alkanes and C_6-C_8 aromatics are 18 (range of 40-1.3) times higher than the average mixing ratios reported for 25 U.S. cities by Baker et al. [Baker et al., 2008]. The alkenes are higher for the CalNex dataset due to the prevalence of on-road combustion sources in the LA Basin; however, these elevated mixing ratios are well below the reported values for the 2011 Red Wash site. Biogenics, such as isoprene, are larger for the Pasadena dataset as it was a summertime experiment conducted near isoprene emitting vegetation. On average, the Pasadena site observed mixing ratios 22 (range of 86-1.5) times higher for the alkenes. The average mixing ratio of the oxygenated VOCs were 6.6 (range of 29-0.36) times greater in Pasadena than Uintah. This large enhancement in the OVOC in Pasadena is related to primary emissions of ethanol and the secondary production of aldehydes and ketones.

Here we investigate the relative contribution of VOCs, methane (CH_4), carbon monoxide (CO), and nitrogen dioxide (NO_2) to potential ozone formation by comparing the various sinks of the hydroxyl radical (OH). OH reactivity is a simple metric determined by the product of the abundance of a particular species and its reaction rate coefficient with OH (k_{OH+VOC}). This method identifies the key reactive species that may contribute to potential ozone formation. Figure 3-17 shows a time series of the total OH reactivity (top panel). During UBWOS 2012, the average total OH reactivity was 9.8 ± 8.4 s^{-1}. This is comparable to the average OH reactivity calculated for Pasadena (11 ± 4 s^{-1}).

During UBWOS 2012, the VOCs contributed 71% of the total OH reactivity. Figure 3-17 (bottom panel) shows the factional contribution of the VOC compound classes to the VOC-OH reactivity. On average, the alkanes accounted for 58% of the VOC-OH reactivity, followed by the OVOCs (17%), cycloalkanes (14%), aromatics (8%), and the alkenes (3%). This is a very different mixture of VOCs than observed in Pasadena, where the VOC-OH reactivity was dominated by OVOCs (46%), alkenes (19%), biogenics (16%), and aromatics (10%). Even though the mixture of VOCs is completely different between the two measurement sites, the magnitude was comparable. This is the direct consequence of the very high mixing ratios of the alkanes, cycloalkanes, and methanol that were observed during UBWOS 2012.

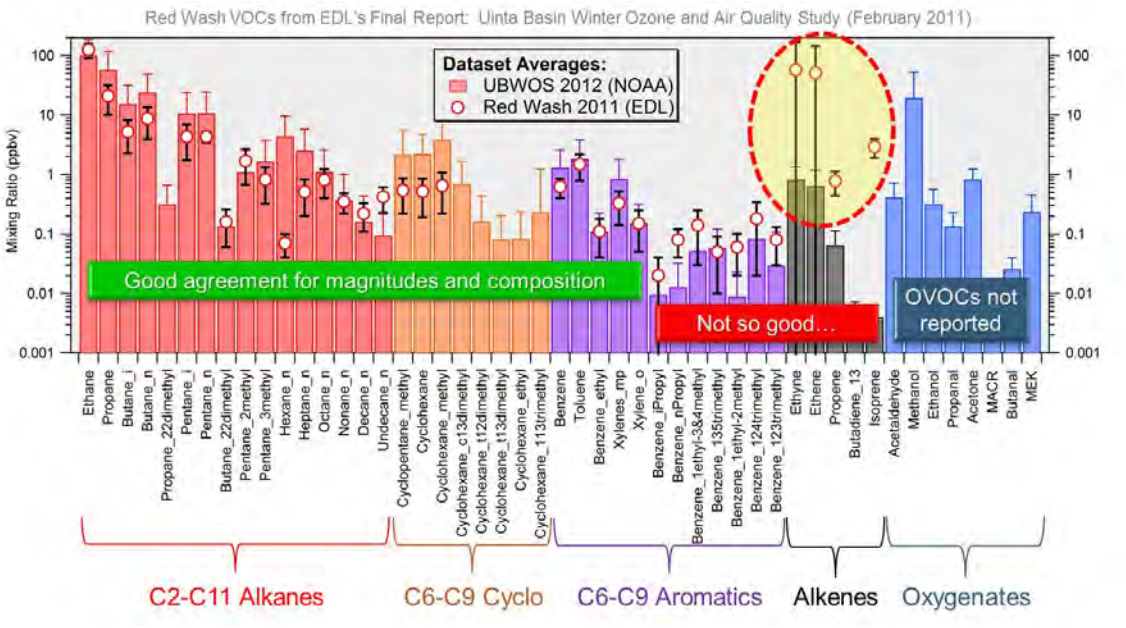

Figure 3-13. Average mixing ratios for UBWOS 2012 and Red Wash 2011.

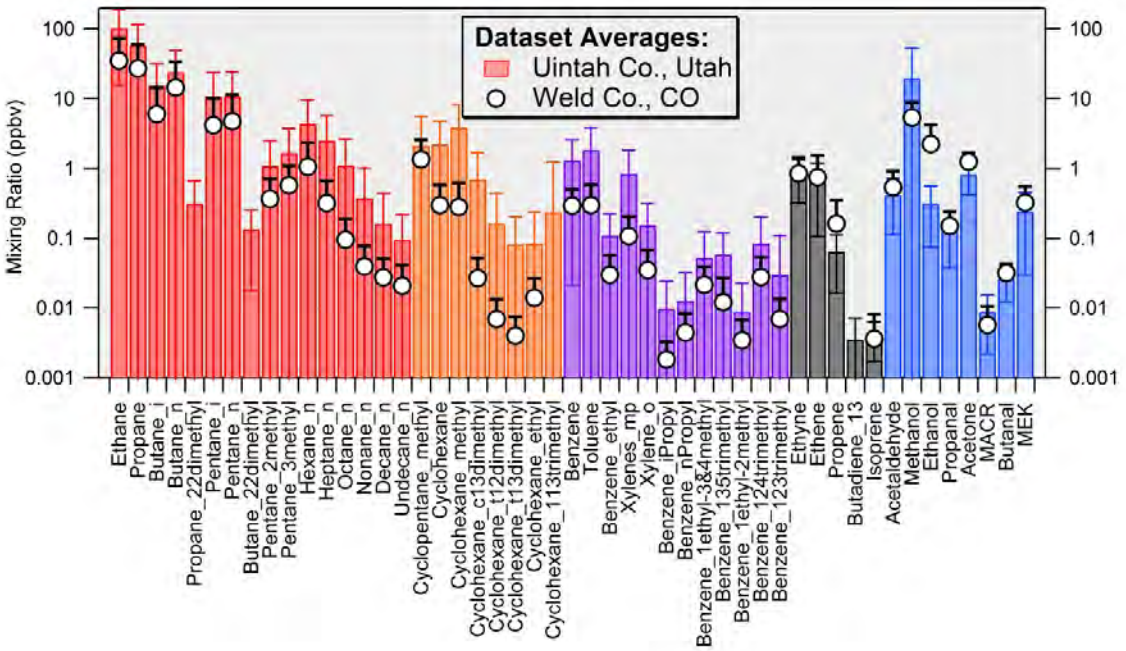

Figure 3-14. Average mixing ratios for Uintah County, Utah (UBWOS 2012) and Weld County, Colorado (2011 BAO site).

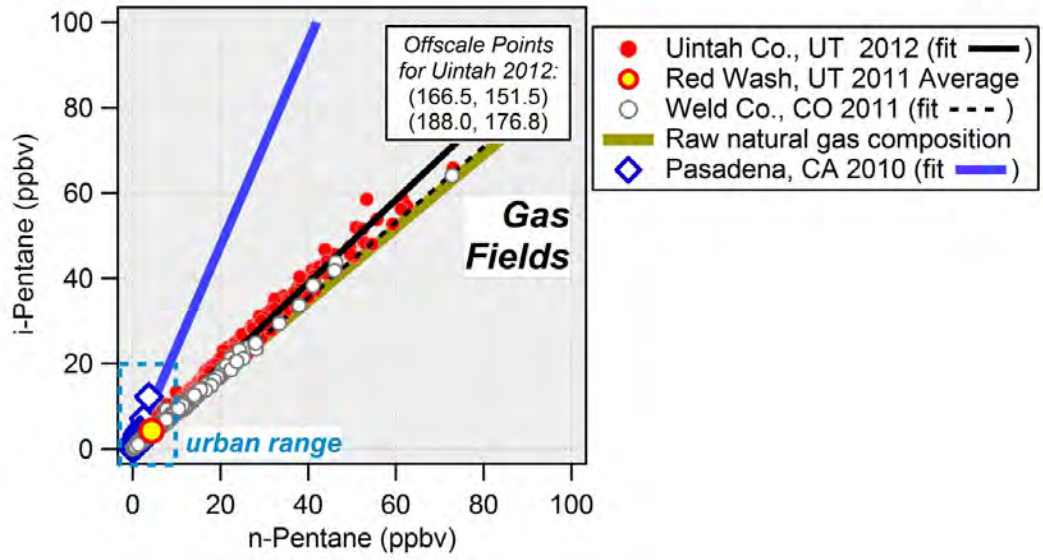

Figure 3-15. Iso-pentane to n-pentane enhancement ratios.

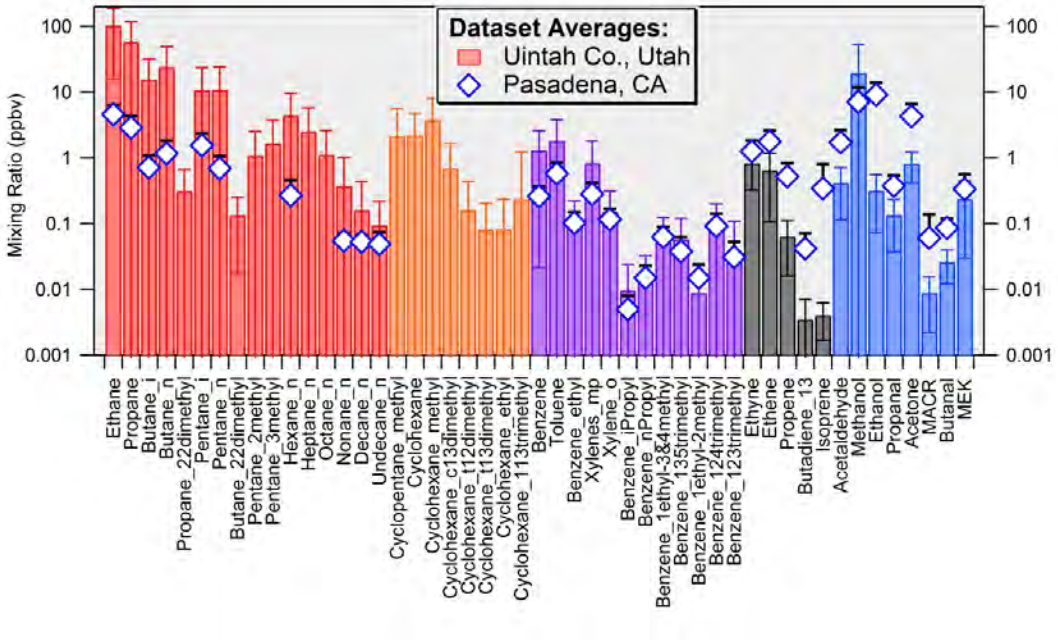

Figure 3-16. Average mixing ratios for Uintah County, Utah (UBWOS 2012) and Pasadena, California (CalNex 2010).

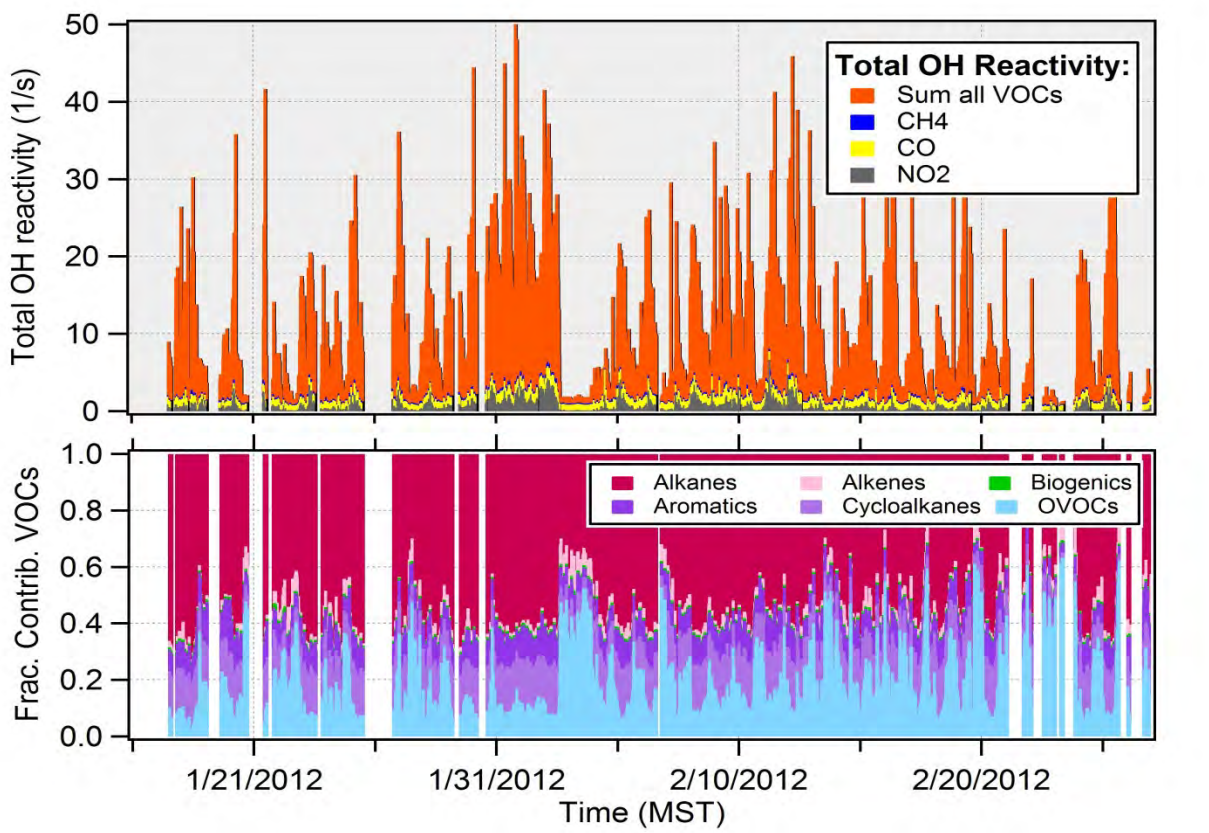

Figure 3-17. Time series of total OH reactivity (top panel) and the fractional contribution of the VOCs to the VOC-OH reactivity (bottom panel).

Formaldehyde

Formaldehyde is a VOC of particular interest to the Uintah Basin because it can have a variety of combustion-related sources, and is a potent radical source. The measured formaldehyde levels are shown in Figure 3-18 for the entire intensive period, and ranged from below detection limit up to 15 ppbv. The distribution of CH_2O in UBWOS 2012 is shown in Figure 3-19 and compared to several other data sets from summertime polluted areas, Houston-Galveston, and Pasadena, CA. The median and average levels of CH_2O in the Uintah Basin were lower than the corresponding numbers from the other two data sets. The implications of measured CH_2O for the radical budget of the Basin are discussed below.

The UBWOS 2012 measurements show a number of short-term peaks in CH_2O, most of which were correlated with methanol, as shown for example in Figure 3-20. The close correlation of CH_2O and methanol, which was independent of time of day (i.e., not photochemical in origin), implies that the observed formaldehyde is present as an impurity in the liquid methanol that is stored and used at numerous sites in the basin. The overall correlation of formaldehyde and methanol, shown in Figure 3-21, confirms that much of the observed formaldehyde comes from methanol. However, there are several instances of short-term plumes of CH_2O that did not correspond to elevated methanol that deserve closer examination, as shown in Figure 3-22. The first instance on Feb. 3, at about 12:50PM, there were no corresponding plumes of other materials that might indicate the origin. In contrast, the plume on Feb 16 at 6:50PM was

associated with carbon monoxide and so appears to be related to a near-by combustion source, possibly a motor vehicle.

The 2012 measurements indicate that on average CH_2O is not unusually high in the Uintah Basin compared to other sites that experience photochemical ozone pollution. Most of the high CH_2O values that were observed were due to methanol use in the Basin. The absence of snow and cold pool conditions did not allow an assessment of snow pack sources of CH_2O. There were infrequent observations of CH_2O plumes that did not correspond to methanol levels and are likely due to combustion sources.

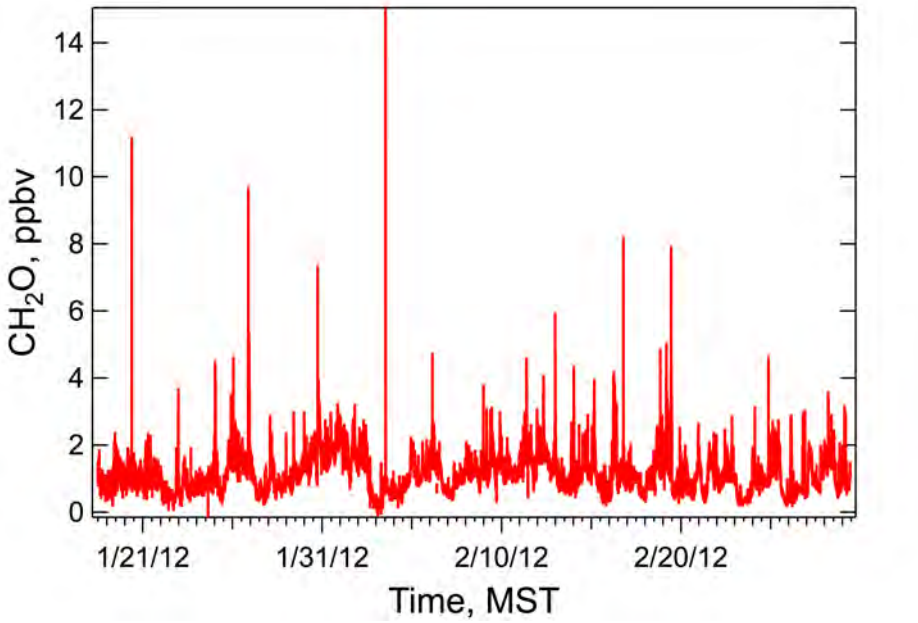

Figure 3-18. Measurements of formaldehyde at the Horse Pool site.

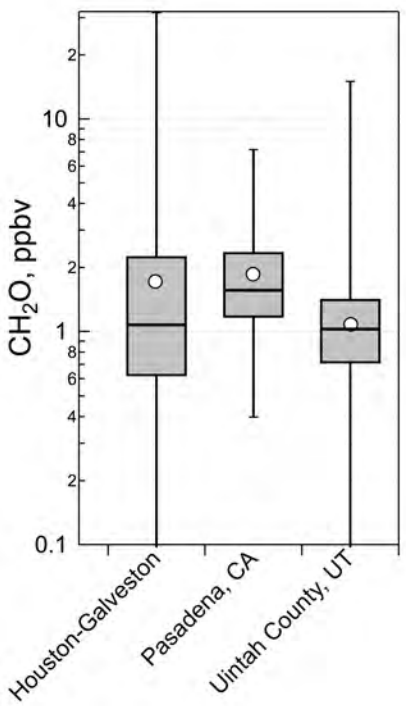

Figure 3-19. Distributions of formaldehyde at 3 different sites. The bars span the maximum and minimum of the data; the box denotes the central 50% of the data; the central bar is the median; and the open circle is the mean.

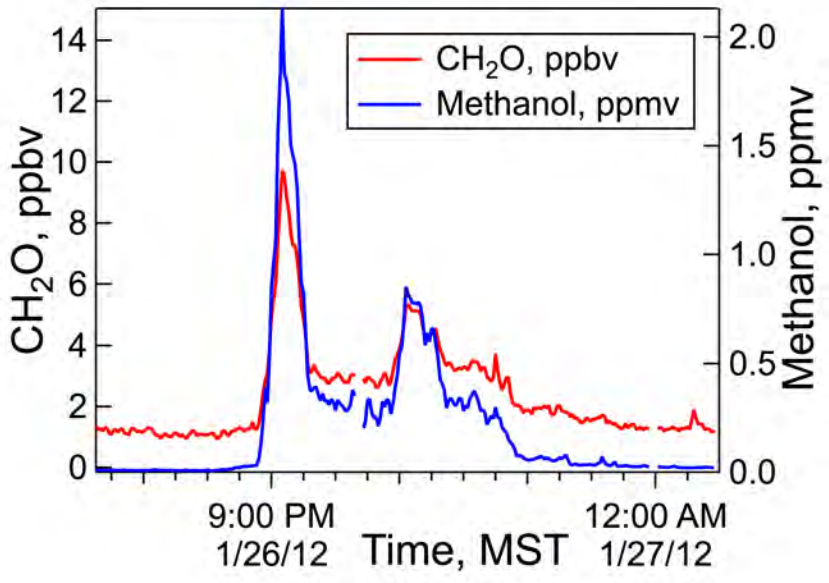

Figure 3-20. Detailed timeline of formaldehyde (red) and methanol (blue) at the Horse Pool site.

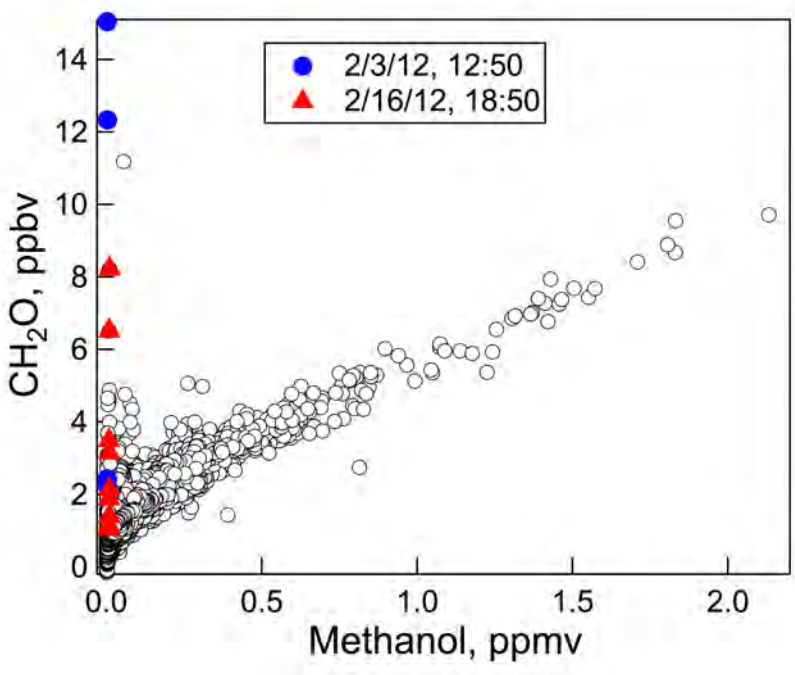

Figure 3-21. The correlation of formaldehyde and methanol, with 2 unusual plumes denoted in blue (2/3 12:50) and red (2/16, 18:50).

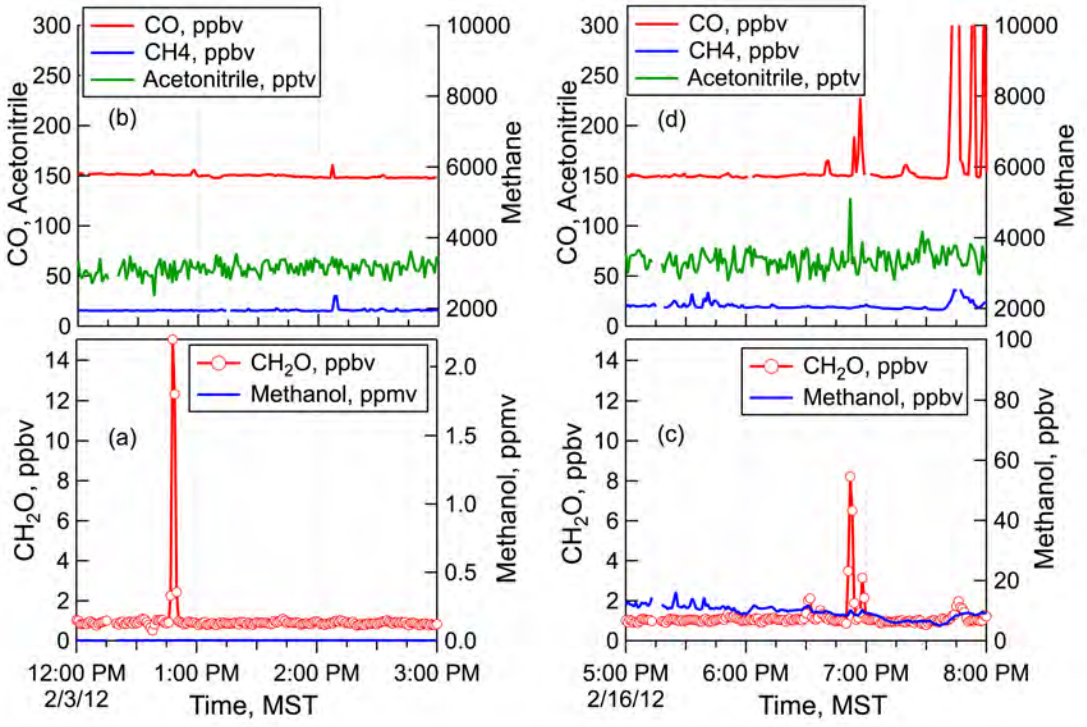

Figure 3-22. Detailed timelines for the periods identified in Figure 3-21.

Measurements of Acids by NI-PT-CIMS

The Acid CIMS has the capability to measure a wide range of both inorganic and organic acids in the gas phase. Only a few acids of each type were found to be important in the UBWOS 2012 campaign; the inorganic acids- hydrochloric acid (HCl), nitrous acid (HONO), nitric acid (HNO_3), and isocyanic acid (HNCO); and the organic acids- formic acid, (HC(O)OH), and butyric/pyruvic acids ($C_3H_7C(O)OH$, $CH_3C(O)C(O)OH$), Each acid can potentially play a unique role in the chemistry of the atmosphere of the Uintah Basin as will be discussed below.

Inorganic Acids

Hydrochloric acid is a strong acid that has a number of sources; some coal-fired power plants; biomass burning; and volatilization of chloride from particles, either sea salt or soil. The liberation of HCl from particles requires another strong acid, either sulfuric or nitric acid, hence is closely associated with low particle pH conditions. The HCl observations by acid CIMS during UBWOS 2012 were somewhat compromised by high system backgrounds and sensitivity to inlet pressure fluctuations. These factors combined to raise the detection limit of the method to between 0.15 and 0.2 ppbv. No significant HCl was observed during UBWOS 2012 above these detection limits under these conditions.

Nitric Acid is another strong acid that is a product of NOx oxidation either through the reaction of NO_2 with OH in the daytime or the reactions of N_2O_5 with particles, or reaction of NO_3 with certain VOCs at nighttime. Daytime HNO_3 is a useful indicator relative to other NOx products such PANs and alkyl nitrates since HNO_3 is radical-chain terminating, and the organic nitrates indicate chain-propagating chemistry. HNO_3 is highly soluble and semi-volatile, so it partitions to aerosol particles depending on their pH and will readily deposit on ground surfaces. Both photochemistry and deposition affect the diurnal profile of HNO_3. The diurnal profile of HNO_3 measurements during UBWOS 2012 is shown in Figure 3-23. Individual values ranged up to 4.2 ppbv on a single day (Feb. 9) but in general the values were much lower than that. The distribution of HNO_3 during UBWOS 2012 is shown in Figure 3-24, which also provides a comparison with the CalNex 2010 measurements made at the Pasadena ground site. There are substantial differences in the two data sets, consistent with the lower photochemical activity during UBWOS 2012.

Nitrous acid has a number of sources in the lower atmosphere: the reaction of NO_2 on particles and ground surfaces, the photolysis of nitrate on surfaces or in snow pack, and the photo-assisted reduction of NO_2 via an organic chromophore. HONO is a potentially important radical source as its photolysis is relatively rapid and yields OH radicals directly. This effect is most important for daytime, when any HONO formed at this time would have an impact on the local radical balance and hence ozone formation. A summary of the HONO distribution measured by both the Acid CIMS and the DOAS long-path instrument (lowest light path) are shown in Figure 3-25, and compared to 2 other data sets, the CalNex 2010 Pasadena measurements and the 2011 Weld County, CO. measurements. The Uintah Basin values were lower than the other 2 data sets, a feature mainly reflective of the lower NOx values compared to CalNex 2010 and the fact that the Weld County measurements were made at heights as low as 2 meters above ground, which sampled the ground source more effectively than either UBWOS 2012 measurement. The diurnal profile of HONO measurements during UBWOS 2012 is shown in Figure 3-26, for both the DOAS (individual points and averages) and the Acid CIMS (averages). There is a distinct decrease in HONO at sunrise due to its relatively efficient photolysis (lifetimes at local noon 10-15 minutes), but both instruments report measureable HONO in the daytime.

The contribution of daytime HONO to the radical budget during UBWOS 2012 is discussed in a subsequent section. There was no attempt to measure vertical profiles of HONO with the Acid CIMS with a long inlet because of the absence of snow, however, there was evidence of local photochemical production of HONO on surfaces adjacent to the short Acid CIMS inlet. An example of these short-term HONO pulses is shown in Figure 3-27 for several days during the study. This effect was apparent only at low winds speeds (<3 m/s), which is consistent with a local surface source. This HONO production is a real phenomenon and is consistent with previous daytime HONO measurements; however, a local (tower) surface source is not representative of the UBWOS 2012 environment, so these periods were edited out of the final data file and were not include in the summaries shown in the above Figures.

Isocyanic acid is a relatively obscure compound that is a product of biomass burning and also a photooxidation product of reduced nitrogen species, amines and amides [Roberts et al., 2011]. In addition, there is a potential for HNCO emissions from Urea-SCR (selective catalytic reduction) NOx control systems. While there does not appear to be any of these SCR systems deployed in this basin, it is useful to have baseline measurements of HNCO should this become a future control strategy. HNCO levels during UBWOS 2012 ranged up to approximately 0.12 ppbv on a few occasions, and averaged 0.011ppbv. This was lower than the average level observed at the Pasadena site during CalNex, 0.025 ppbv. The most significant correlation of HNCO was found to be with formic acid as shown in Figure 3-28, and there was no correlation of HNCO with acetonitrile, a well-known biomass burning marker. These features imply that HNCO is a photochemical product in this basin since formic acid is known to be photoproduct in VOC-NOx impacted air masses [Veres et al., 2011]. Both compounds deposit to ground surfaces, giving an additional reason for this correlation.

Organic Acids

Formic acid is often the most abundant carboxylic acid in VOC-NOx impacted air basins. The distribution of HC(O)OH observations from UBWOS 2012 and 2 previous studies are shown in Figure A3.29. The mean and median Uintah Basin values were more than a factor 3 lower than the values found at the Pasadena site during CalNex 2010, and higher than the values found in Weld County, CO., during NACHTT. The diurnal profile of formic acid, plotted in Figure 3-30, shows the highest levels were found in the mid-morning through noon, and in the evening. The average levels increased in the morning when the boundary layer started to mix, and were higher into the early afternoon. This implies a boundary layer source of HC(O)OH and perhaps some depositional losses at the surface. Two other organic acids were measured, butyric and pyruvic acids (detected at the same mass), and were low, with a maximum of 0.06 ppbv, and well correlated with formic acid. This implies a similar source for these three acids.

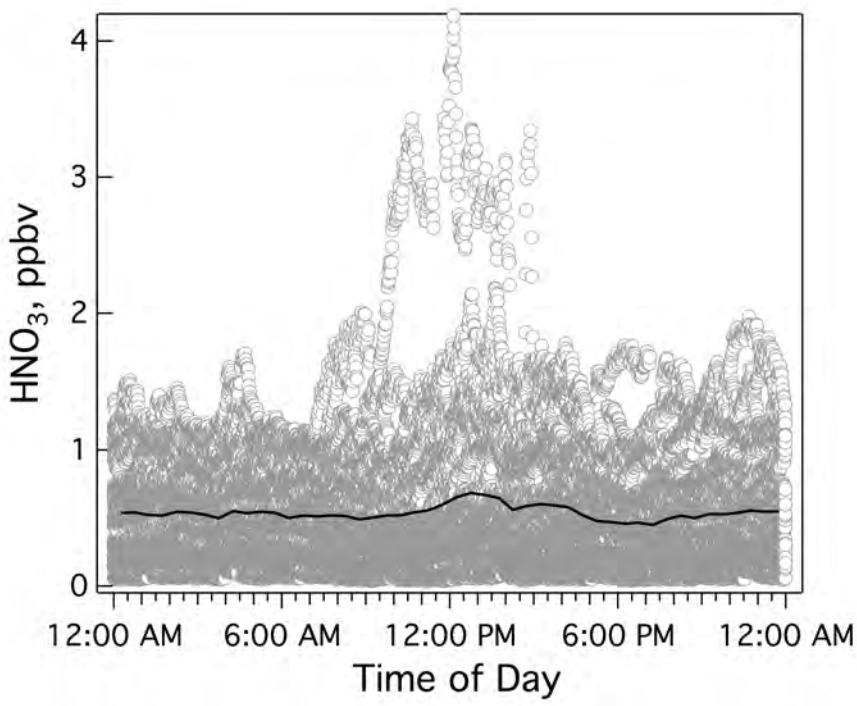

Figure 3-23. The diurnal profile of HNO_3 measurements during UBWOS 2012.

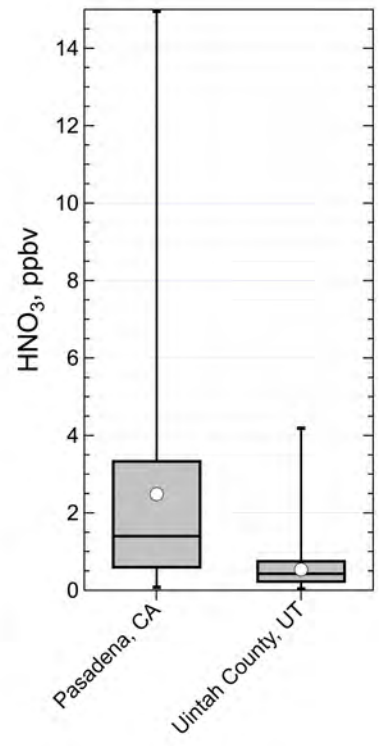

Figure 3-24. The distribution of HNO_3 from both the UBWOS 2012 and CalNex 2010 studies.

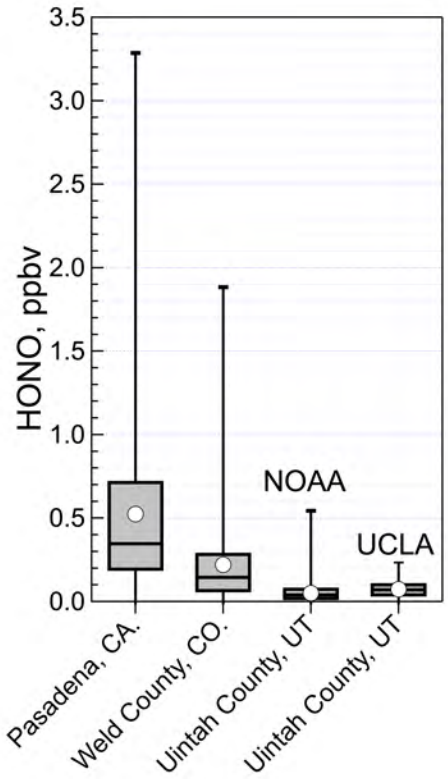

Figure 3-25. A summary of the HONO distributions from UBWOS 2012, for both NOAA and UCLA DOAS measurements (lowest light path), and the CalNex and NACHTT data sets.

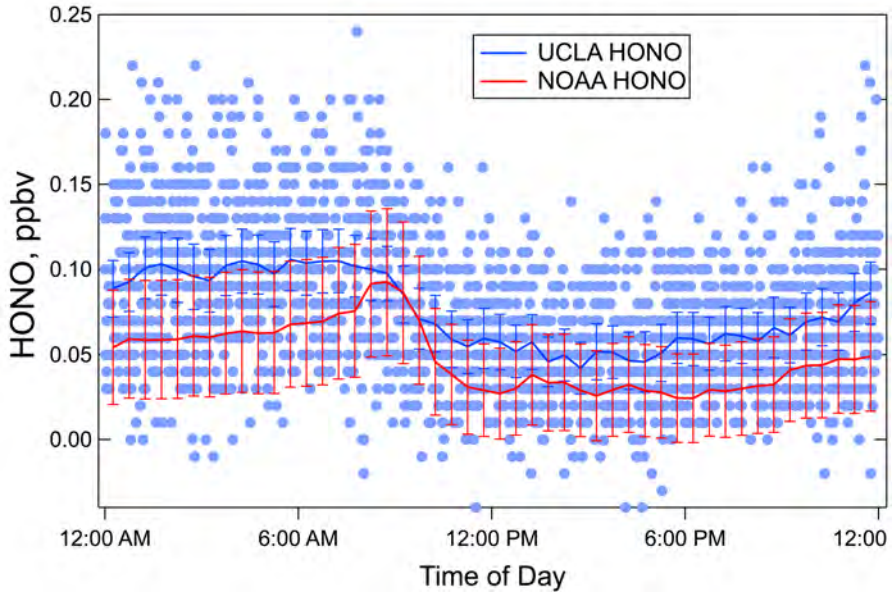

Figure 3-26. The diurnal profile of HONO measurements during UBWOS 2012.

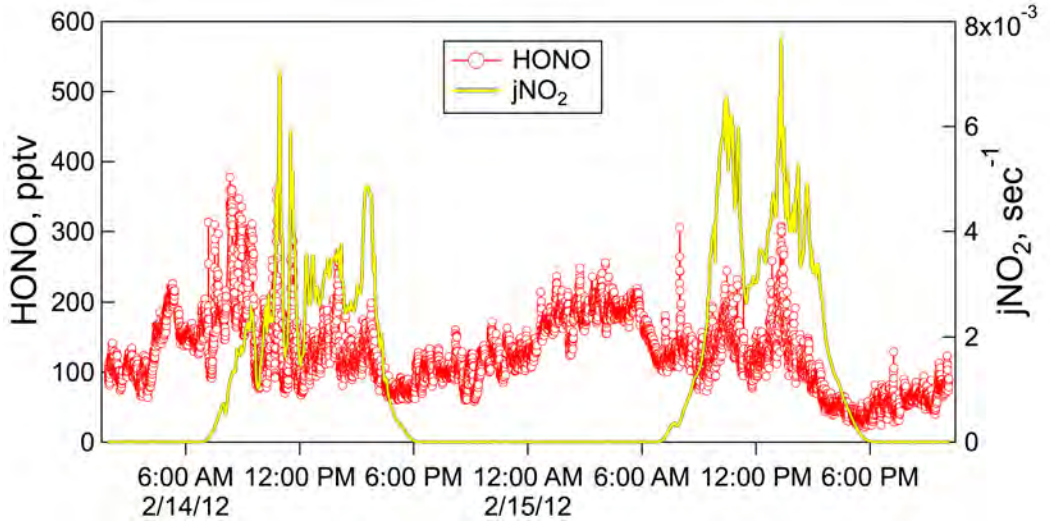

Figure 3-27. A timeline of HONO and NO_2 photolysis rate showing short-term HONO pulses correlated with sunlight.

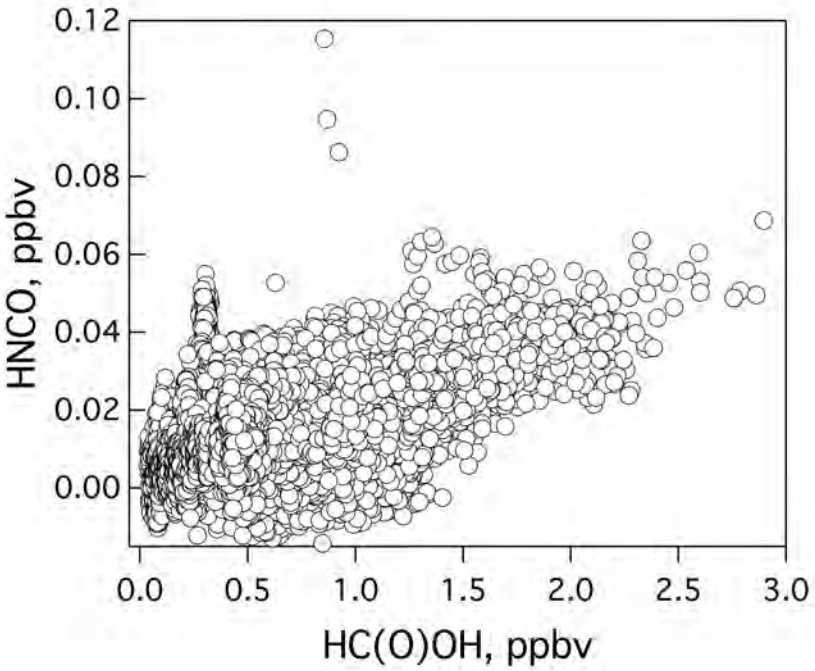

Figure 3-28. The correlation of HNCO with formic acid during UBWOS 2012.

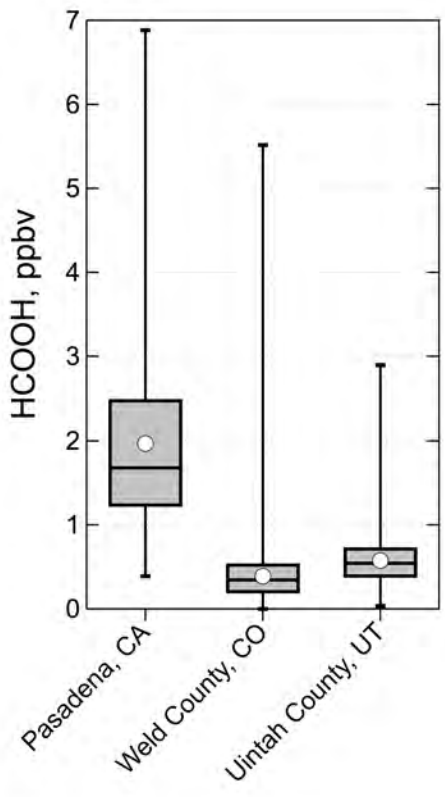

Figure 3-29. A comparison of the distribution of HC(O)OH observations UBWOS 2012 with those from 2 other sites.

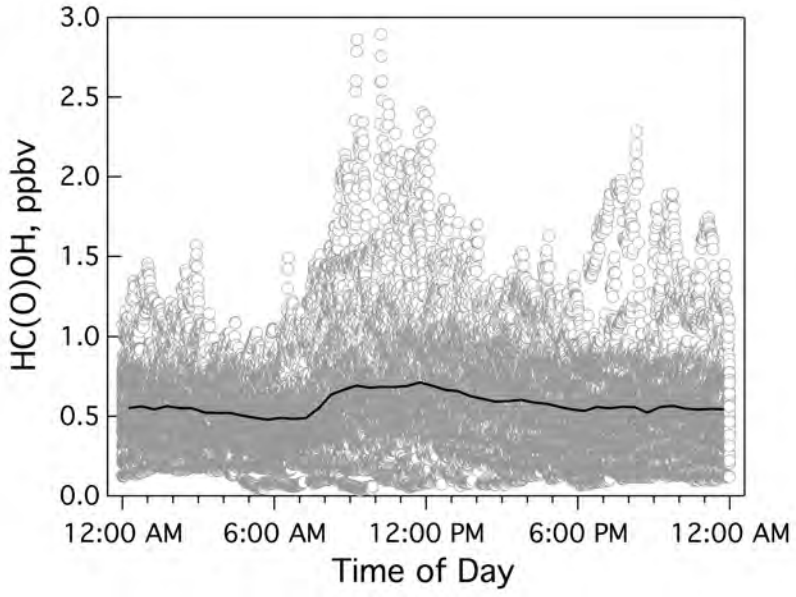

Figure 3-30. The diurnal profile of formic acid measured at Horse Pool during UBWOS 2012. The open circles are individual one-minute averages and the line shows averages for each half-hour.

Acylperoxynitrates (PANS) and Nitryl Chloride ($ClNO_2$)

The chemistry of nitrogen oxides in the troposphere produces several unique products that have significant diagnostic value (PANs), and can provide a source of radicals to the photochemical system ($ClNO_2$). This section presents the results of these measurements and some comparisons to other site that are more representative of urban pollution. The contributions of PANs to the daytime odd-nitrogen budget, and $ClNO_2$ to the nighttime odd-nitrogen budget are discussed in other sections. Likewise, the extent of $ClNO_2$ participation in the radical budget is discussed in the section devoted to that subject.

PAN compounds are produced by the same VOC-NOx photochemistry that produces O_3. For a number of reasons, the formation of the C_2 PAN compound acetyl peroxynitrates ($CH_3C(O)OONO_2$) is favored by the photochemistry that occurs in the typical mixture of VOCs found in urban and continental pollution [Roberts, 1990]. This was also true during UBWOS 2012 where PAN represented 90% of the total PAN-type compounds. This section focuses exclusively on PAN since it is the major compound observed.

The key feature of PAN chemistry is that its formation is intimately linked to photochemical oxidation of many VOCs, which results in production of peroxyacetyl radical;

$$VOC + Radicals + O_2 \Rightarrow CH_3C(O)OO \quad (1)$$

Peroxyacetyl radicals take part in reversible reaction with NO_2 to form PAN;

$$CH_3C(O)OO + NO_2 \; <=> \; CH_3C(O)OONO_2 \quad (2)$$

The equilibrium for this reaction has a strong temperature that has been studied extensively and lies far in favor of PAN in the temperature range observed during UBWOS 2012. As a result, the loss of PAN in the UBWOS 2012 environment will be due mostly to deposition to the surface.

The range of PAN concentrations measured during UBWOS 2012 was quite modest when compared to other urban and continental polluted sites, as shown in Figure 3-31. The data sets being compared are all from urban/suburban sites and were all acquired in the summer. The Nashville site was in the middle of a suburban area surrounded by high biogenic VOC sources, and the results of this study can be found in [Roberts et al., 2002]. The Houston 2000 measurements were conducted in the suburban Houston area adjacent to the Ship Channel petrochemical complex and are discussed in several publications [Roberts et al., 2001a; Roberts et al., 2001b; Roberts et al., 2003]. The CalNex 2010 measurements were conducted in Pasadena, CA., an area primarily impacted by motor vehicle sources with minor contributions from biogenic VOCs. The CalNex data have not yet been published. The highest PAN observations in the summertime data sets were all highly correlated with high O_3 values.

The features of PAN chemistry noted above can be seen in the average diurnal profile that was observed during UBWOS 2012 as shown in Figure 3-32. The average profile ranged from 0.22 to 0.35 ppbv, and shows a slight increase through the morning to mid-afternoon time period (0900-1500 local time). Also, there is a slow decrease in average PAN from about 2100 to 0600 local time. These features are consistent with slow deposition of PAN during the night, increased PAN in the morning due to mixing of

slightly higher PAN down from aloft as the boundary layer develops, and a slight production of PAN in the noon to afternoon time period.

Production of PAN is always accompanied by O_3 production due to the close coupling of both species to VOC-NOx photochemistry. This results in the broad correlation of O_3 with PAN that has been observed in numerous urban and continental data sets [Roberts et al., 1995]. The correlation of PAN with O_3 in UBWOS 2012 is shown in Figure 3-33 along with the correlation observed during the CalNex 2010 Pasadena measurements. The range of observations during UBWOS 2012 is quite a bit smaller than CalNex, and the UBWOS 2012 data do not show a clear positive correlation. However, there maybe correlations on individual days that may be related to photochemistry, which will be a subject for further investigation.

Nitryl chloride is a product of the nighttime reaction of N_2O_5 with chloride on particle [Finlayson-Pitts et al., 1989; Osthoff et al., 2008] or ground surfaces;

$$N_2O_5 + Cl^-_{(surface)} \Rightarrow ClNO_2 + NO_3^- \quad (3)$$

The formation rate of $ClNO_2$ can have a number of limited factors: the production of N_2O_5, the availability of chloride, and the presence of sufficient surface area. There are not very many $ClNO_2$ measurements to date, but typically sea salt chloride and its re-distribution through acid displacement is the main source of soluble chloride in the lower atmosphere. The presence of oil and gas production and its unique sources may provide other sources of chloride such as HCl and brine, potentially making $ClNO_2$ an important component in the Uintah Basin.

The N_2O_5 and $ClNO_2$ observations from UBWOS 2012 are shown in Figure 3-34 for the entire time period. There are no $ClNO_2$ data available before 1/22/2012 due to inlet interferences. There is a general correspondence between N_2O_5 and $ClNO_2$ with similar concentration ranges, with the highest levels just over 2 ppbv. Detailed analysis of individual nights along with aerosol surface and composition data will be an on-going part of our investigation.

The composite plot of $ClNO_2$ versus time of day in shown in Figure 3-35 and illustrates several interesting points. $ClNO_2$, while formed exclusively at night, persists into the morning hours and is available to serve as a radical source during this time. The timing of this $ClNO_2$ persistence is due to a photolysis rate that is moderate compared to other photo-labile species such as NO_3, and somewhat temperature dependent [Ghosh et al., 2012]. The noon to afternoon ClNO2 levels were usually at or below detection limit (0.025ppbv).

It is useful to compare the UBWOS 2012 $ClNO_2$ values with measurements for other sites. Figure 3-36 shows summaries of data sets from the CalNex 2010 Pasadena site, and the Weld County, CO measurements, which were made in February and March 2011. In a broad sense, the chloride sources at each site appear to have the largest influence over the magnitudes of the average and maximum $ClNO_2$ levels that were observed. Pasadena, being in the LA basin, is impacted by sea salt chloride, which is readily redistributed to all particle size ranges through acid displacement. The Weld County site is in the middle of the continent, not far from the site used by Thornton et al.,[Thornton et al., 2010]. In this case, chloride sources are smaller and more diverse, ranging from soils, to point source of HCl (power plants), with some evidence of long-range transport of sea salt. Understanding the chloride sources

operating in the Uintah Basin will be an important aspect of assessing the impact of $ClNO_2$ formation, particularly if this chemistry ends up being an important radical source in the winter ozone formation.

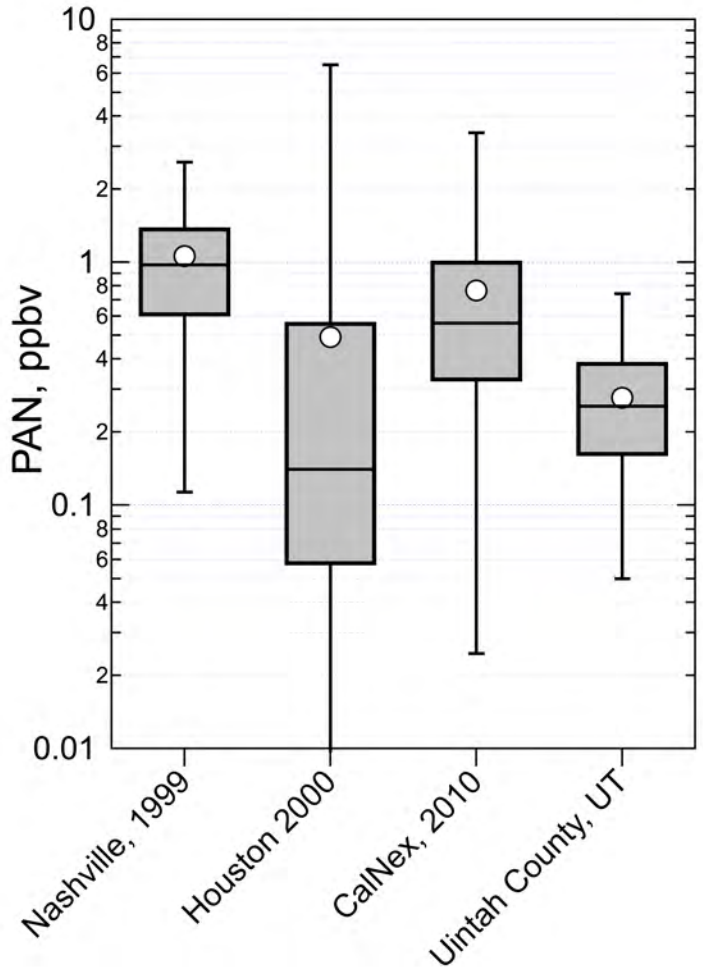

Figure 3-31. Summary distributions of PAN measured at four different sites in the U.S. including the UBWOS 2012 data. The bars show the max and min, the box shows the central 50%, the center bar shows the median, and the open circle shows the average of the each data set.

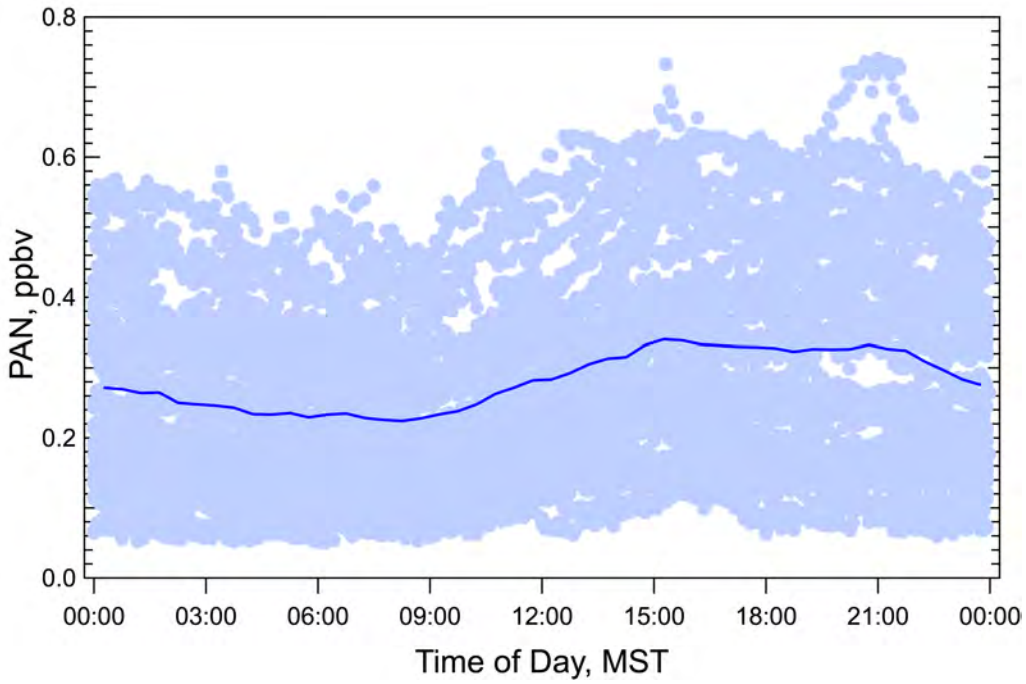

Figure 3-32. A composite of measured PAN versus time of day (local time) for the entire UBWOS 2012 data set. The dots are individual 5-minute determinations, and the line is the average for each half-hour.

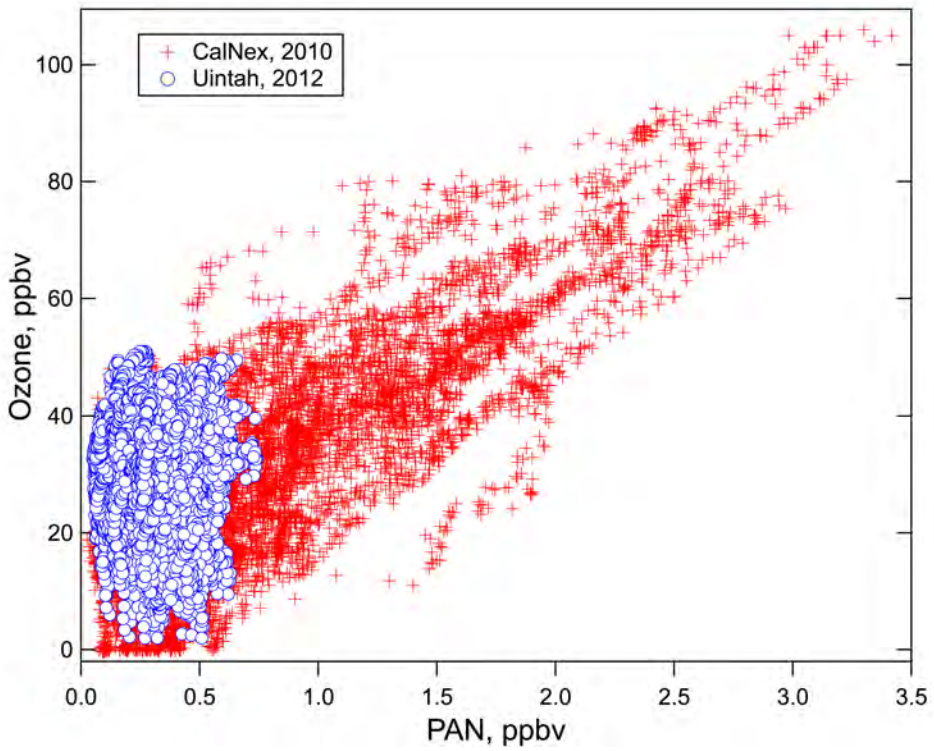

Figure 3-33. The correlation of O_3 and PAN observed during the CalNex Pasadena project (red crosses), and during the UBWOS 2012 experiment (blue circles). The CalNex O_3 data are from Barry Lefer. All other data are from NOAA/ESRL/CSD.

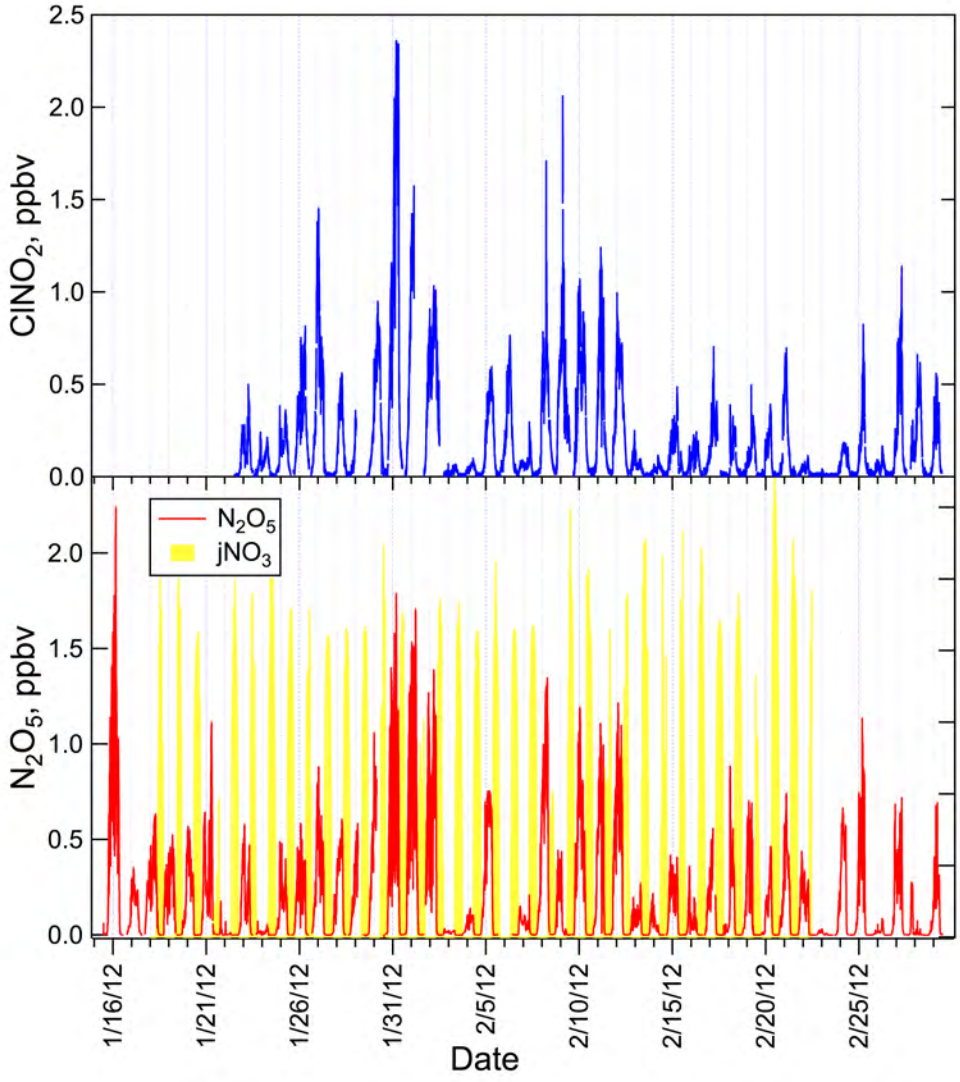

Figure 3-34. Timelines of measured $ClNO_2$, N_2O_5, and NO_3 photolysis rate (jNO_3 shown to indicate daylight) for the entire UBWOS 2012 intensive period.

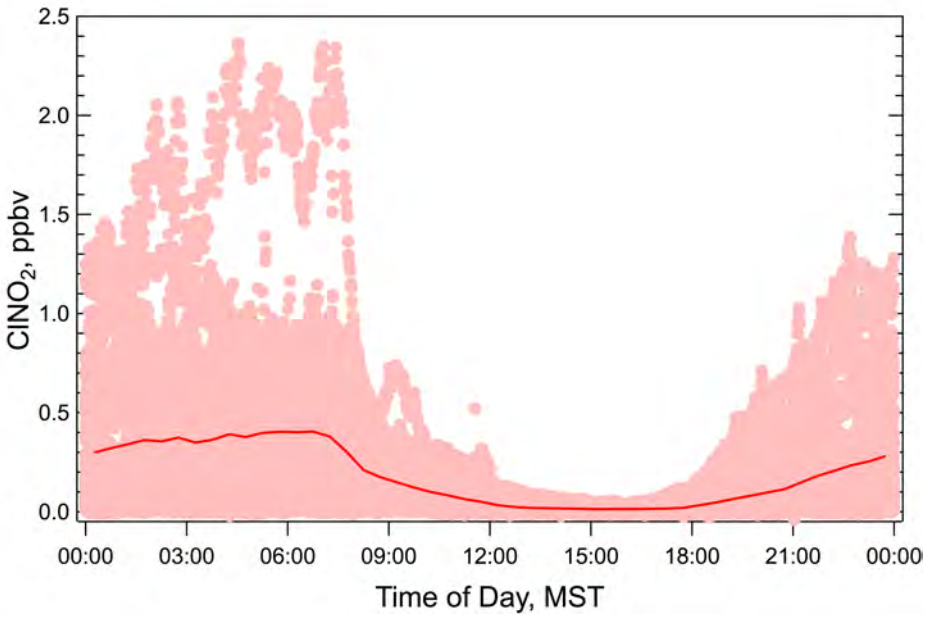

Figure 3-35. A composite of measured $ClNO_2$ versus time of day (local time). The individual dots are 1-minute averages, and the line is the average for each half hour.

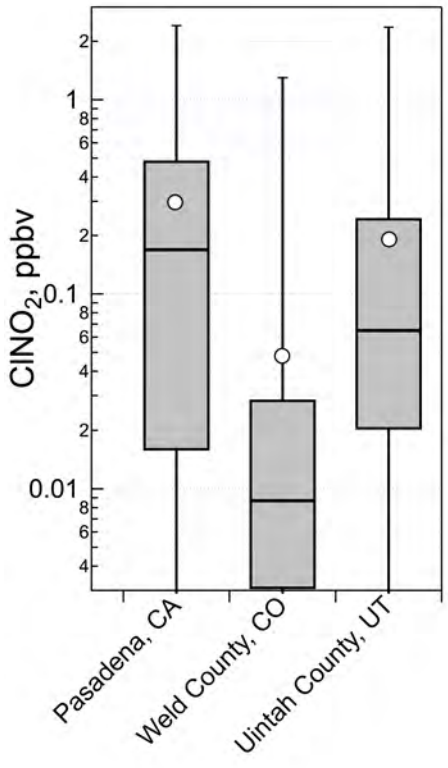

Figure 3-36. Comparison of measured $ClNO_2$ distributions from three different field projects, including UBWOS 2012. The CalNex data are from Osthoff and Mielke (manuscript in preparation), and the Weld County data were taken during the NACHTT 2011 study (Reidel and Thornton, un-published data).

Nightime Chemistry

The nighttime chemistry of nitrogen oxides is relevant in several respects to the wintertime ozone problem in western oil and gas producing basins.

First, dark oxidation of NO_x (=NO+NO_2) to the nighttime nitrogen oxides, NO_3 and N_2O_5, is one of the principal mechanisms by which NO_x is chemically removed from ambient air.

$$NO + O_3 \rightarrow NO_2 + O_2 \quad \text{(R1)}$$

$$NO_2 + O_3 \rightarrow NO_3 + O_2 \quad \text{(R2)}$$

$$NO_3 + NO_2 \leftrightarrows N_2O_5 \quad \text{(R3)}$$

Since NO_x is one of the key ingredients for daytime photochemical ozone production, the magnitude of its nighttime removal, which does not lead to ozone formation, is important to the NO_x budget. Furthermore, during short winter days with low sun angle, photochemical NO_x removal via reaction of NO_2 with OH is much slower than it is during summertime. The oxidation of NO_2 by O_3 (R2) is also slower in winter but is capable of converting 30-80% of the NO_x present at sunset to NO_3 and N_2O_5 within a given air mass over the course of a single night. The reaction sequence also consumes ozone, with three O_3 molecules required to produce one N_2O_5 molecule. Thus, it can represent a significant ozone sink if the ratio of NO_x emissions to background ozone is substantial. The subsequent reactions of NO_3 and N_2O_5 determine the overnight fate of NO_x and O_x (=O_3 + NO_2). This mechanism is generally unimportant during daylight due to the photochemical instability of NO_3, which photolyzes rapidly and reacts with photochemically generated NO. Reaction of NO_3 with VOCs is important during summer but generally unimportant during winter because the equilibrium in (R3) is strongly temperature dependent, such that the concentration of NO_3 is normally quite small at cold temperatures. Heterogeneous uptake of N_2O_5 on aerosol is important during wintertime and can represent a permanent sink for nitrogen oxides if the principle reaction product is HNO_3.

$$N_2O_5\,(g) + H_2O\,(l) \rightarrow 2HNO_3\,(g) \quad \text{(R4)}$$

Reaction (R4) is written with liquid phase water, where the liquid water is presumed present in the aerosol phase. The efficiency of the reaction sequence (R1-R4) in removing nitrogen oxides overnight depends on the ambient ozone concentration and temperature, which determine the rate of (R2), and on the available aerosol surface area, S_a, and the N_2O_5 uptake coefficient, $\gamma(N_2O_5)$, which determine the first order loss rate coefficient for N_2O_5, $k(N_2O_5)$ (s^{-1}), in (R4).

$$k(N_2O_5) = \frac{1}{4} c S_a \gamma(N_2O_5) \quad (1)$$

Here c is the mean molecular speed of N_2O_5.

A second aspect of nighttime nitrogen oxide chemistry relevant to daytime ozone formation is the formation of radical reservoirs that are photochemically active on the following day. Radical reservoirs are any species that form chemically or are directly emitted at night, and that undergo photolysis in sunlight to produce free radicals that initiate the degradation of VOCs. Nighttime radical reservoirs can be a particularly important radical source during wintertime, when photochemical OH radical production through ozone photolysis is greatly reduced. There are two nighttime nitrogen oxide reactions the produce radical reservoirs, and both are heterogeneous. The first is the reaction of N_2O_5 with aerosol phase chloride to produce nitryl chloride, $ClNO_2$, which photolyzes in sunlight to produce Cl atoms and regenerate NO_2.

$$N_2O_5\,(g) + Cl^-\,(aq) \rightarrow NO_3^-\,(aq) + ClNO_2\,(g) \qquad (R5)$$

Reaction (R5) competes with (R4) and depends upon the relative concentrations of liquid water and chloride in the aerosol phase. The NO_3^- produced in this reaction may be released to the gas phase as HNO_3 depending on the thermodynamic stability of aerosol phase nitrate. The yield of $ClNO_2$, $\Phi(ClNO_2)$, is defined as the first order rate coefficients for the two reactions.

$$\Phi(ClNO_2) = k_4/(k_4 + k_5) = k_4/k(N_2O_5) \qquad (2)$$

The other reaction of importance is the heterogeneous reaction of NO_2 to produce nitrous acid, HONO, which also photolyzes in sunlight to release OH radicals and regenerate NO_x. This is thought to be a disproportionation reaction of NO_2 with liquid water that occurs more readily on ground surfaces than on aerosol surfaces.

$$2NO_2\,(g) + H_2O\,(l) \rightarrow HNO_3\,(g) + HONO\,(g) \qquad (R6)$$

Nitrous acid may also be directly emitted from combustion processes as part of the total NO_x emissions. Some studies have also indicated a much more rapid conversion of NO_2 to HONO during daylight hours, though the mechanism for rapid photochemical HONO production remains uncertain. This analysis will only consider the nighttime produced HONO.

Figure 3-37 shows the diurnally averaged data from the Horse Pool site for ozone (O_3) and odd oxygen ($O_x = O_3 + NO_2 + 3N_2O_5$) in panel A, NO_2, NO_x and total reactive nitrogen (NO_y) in panel B, and N_2O_5, $ClNO_2$ and HONO in panel C. Data for all species other than HONO are from in-situ instruments located at Horse Pool, while HONO is from the lowest path of the long-path DOAS instrument. All data are shown at 1-minute time resolution except for $ClNO_2$ (5 min) and HONO (30 min). The color code on the background of the figure indicates the average length of night (grey) and day (yellow) during the January 15 - February 29, 2012 period of the Horse Pool intensive study. The average day length (solar zenith angle < 90°) was 10.2 hours, varying from 9.45 hours on January 15 to 11.05 hours on February 29. All of the diurnally average data in Figure 3-37 excludes periods of higher winds in order to capture the quiescent periods in the Uintah Basin. Figure 3-38 shows the time series of wind data (panel A) and the

distribution (panel B). Data for diurnal averages were filtered at the 2σ wind speed from a Gaussian fit to the peak of the low wind speed distribution in Figure 3-38B. The dashed line in Figure 3-38A shows this 4.4 m s^{-1} threshold. Exclusion of the higher wind data removes approximately 10% of the data for the six-week period.

The diurnal cycle in O_3 in Figure 3-37A is relatively typical, varying from 22 ppbv near dawn to 38 ppbv in late afternoon. The daytime increase is consistent with either photochemistry or mixing of ozone rich air from aloft during the breakup of the boundary layer, while the nighttime decrease is consistent with both depositional loss to the surface and titration by NO_x emissions. The diurnal cycle in O_x is less pronounced, varying from 30 – 40 ppbv from early morning to late afternoon. The nighttime decay in O_x indicates that not all of the ozone loss is due to chemical reaction with NO_x emissions, but must also include a depositional term. This model described below quantifies this depositional loss.

The majority of NO_y in Figure 3-37B is made up of NO_x, indicating that NO_x oxidation proceeds slowly in this environment. The average NO_x/NO_y ratio was 0.82 ± 0.06 and was on average slightly less oxidized during daytime (NO_x/NO_y = 0.84) relative to nighttime (NO_x/NO_y = 0.81). The nighttime buildup of reactive nitrogen species is consistent with continuous emission into a shallow nocturnal boundary layer, while the late afternoon decrease is consistent with dilution during boundary layer growth. The diurnal pattern of reactive nitrogen is similar to that of stable gases, such as CO_2, CH_4 and CO, which also show nighttime buildup and late afternoon dilution. The model below quantifies the NO_x emissions consistent with the nighttime buildup.

Figure 3-37C shows $ClNO_2$, N_2O_5 and HONO. The $ClNO_2$ and N_2O_5 are quite comparable in magnitude and have a clear diurnal cycle, with nighttime production and daytime loss. The loss of N_2O_5 after sunrise results from its thermal lifetime (reverse reaction in (R3)), which is approximately 23 minutes at the average morning temperature of -3.5 °C. The loss of $ClNO_2$ is slower and is determined by photolysis, mixing and surface deposition. The diurnal cycle in HONO is less distinct, with a nightly maximum and daytime minimum of 0.1 and 0.05 ppbv, respectively.

Figure 3-39 shows the diurnally averaged ratio of NO_x to NO_y (panel A) and the partitioning among the species that make up oxidized nitrogen ($NO_z = NO_y - NO_x$, panel B). As described above, the ratio of NO_x to NO_y was generally smaller at night, although it was also at a minimum in late afternoon during the period when the boundary layer was well mixed. It was higher in early morning, following the decay of N_2O_5, and again in early evening after the collapse of the daytime boundary layer. During nighttime, the dominant component of NO_z was N_2O_5, which contains two nitrogen atoms, followed by $ClNO_2$. PAN showed weak photochemical production in late afternoon and a small, steady level during nighttime hours. HONO is not shown on this plot but would be a small component of NO_z. At the time of this analysis, there is not a sufficient time series of HNO_3 for comparison of its contribution to NO_y or NO_z. The combination of N_2O_5, $ClNO_2$, PAN and HONO accounts for the majority of NO_z at night, even though the production of $ClNO_2$ implies at least as much HNO_3 production as $ClNO_2$. However, HNO_3 may be readily lost to dry deposition (see model description below). Nitric acid may also be a large component of the unaccounted NO_z during daytime in Figure 3-39B.

To understand the nighttime budget for nitrogen oxides and its potential to remove reactive nitrogen from the system or to act as a source for radical reservoirs, the averaged nighttime trends in reactive nitrogen species are compared to a chemical box model. A box model is appropriate for the quiescent periods at the Horse Pool site if the average horizontal distribution of pollutions and their transport is uniform, and if the average nighttime boundary layer depth is constant over the night. The box model provides a quantitative interpretation of the chemical transformations within the air mass. It includes

the reactions described above, as well as NO_x emission and O_3 deposition. The model does not include temperature variations over the course of the night, holding all reaction rate coefficients constant at the average nighttime temperature of -1 °C. The model runs for 13 hours from sunset in order to model only the periods that were dark during the entire duration of the campaign. Parameters in the model are initialized by the observations at sunset and tuned to match the observations 13 hours later.

Figure 3-40 shows the comparison between model and measured NO_2 (panel A) and ozone (panel B). The NO_2 mixing ratio (equivalent to total NO_x during darkness) rose from 4.3 to 6.9 ppbv during 13 hours. This rise together with the nighttime chemistry is reproduced by a NO_x emission rate equivalent to 0.42 ppbv hr^{-1}, as shown in the figure. This rate would be equivalent to an emission of 0.071 kg NO_x km^{-2} hr^{-1} for an assumed nocturnal boundary layer depth of 100 m. Average O_3 decreased from 35.7 to 22.8 ppbv in 13 hours and was best fit by the NO_x emission rate described above (where NO_x is assumed to be emitted exclusively as NO) together with a first-order depositional loss rate coefficient of 4.4×10^{-6} s^{-1} (lifetime with respect to deposition of 63 hours). This loss rate coefficient is equivalent to a deposition velocity of 0.2 cm s^{-1} for an assumed 100 m nocturnal boundary layer depth. The model predicts that approximately half of the ozone loss is due to chemical reactions of nitrogen oxides, and the other half is lost to deposition. Of the amount lost to chemical reactions overnight, approximately 2/3 is retained at sunrise in the form of the odd oxygen containing species NO_2, N_2O_5 and $ClNO_2$.

Figure 3-41 shows model-to-measurement comparison for nighttime N_2O_5 (panel A), the N_2O_5 lifetime, $\tau(N_2O_5)$ (panel B), and $ClNO_2$ (panel C). The model reproduces the averaged N_2O_5 nicely with a lifetime for heterogeneous uptake of 4.2 hours. Aerosol surface area was not available at the time of this analysis, but this lifetime would be equivalent to an uptake coefficient of 0.0045 for a typical aerosol surface area of 250 μm^2 cm^{-3}. This uptake coefficient is relatively small but not inconsistent with the range of relative humidity, which varied from 45% at sunset to 70% at sunrise. Figure 3-41B shows the evolution of the steady state N_2O_5 lifetime over 13 hours. The actual lifetime used as a model input is shown as the dotted-dash line at the top of the figure, and is constant at 4.2 hours. The steady state lifetime is defined as the ratio of the observed N_2O_5 mixing ratio to its production rate from the reaction of NO_2 with O_3.

$$\tau_{SS}(N_2O_5) = N_2O_5/k_2NO_2O_3 \qquad (3)$$

The steady state lifetime in both the model and the observations approaches the actual lifetime but does not reach it in the course of 13 hours, indicating that N_2O_5 never reaches steady state between its production and loss. This behavior is typical for cold, high NO_x conditions. The $ClNO_2$ in the lower panel of Figure 3-41 rises from a slightly non-zero value (a result of the averaging here, where the zero time captures varying times since sunset over the course of the six week period) to 0.44 ppbv. The model captures the magnitude of this rise with a $ClNO_2$ yield of 45%. The model does not, however, capture the observed time dependence of $ClNO_2$, which rises faster at early times and more slowly at later times. This discrepancy may indicate that there is a chemical process not captured in the model. For example, the yield of $ClNO_2$ may vary systematically with time if aerosol uptake of N_2O_5 via reaction (R5) depletes the reservoir of aerosol phase chloride over the course of a night. Alternatively, a depositional loss process for $ClNO_2$ such as soil uptake would alter its time dependence and lead to an under-estimate for its yield. The reasons for the model-measurement discrepancy in the temporal profile of $ClNO_2$ are currently being investigated. A $ClNO_2$ yield of 45%, however, is a surprising result and indicates that a

large fraction of the produced N_2O_5 reacts to form this radical reservoir. The source of the required chloride is an area of current investigation.

Finally, Figure 3-42 shows the model prediction of NO_z and its speciation compared to the measurements. The mixing ratio of PAN, shown in Figure 3-39, is not included here since the nighttime model does not produce PAN. The observed NO_z is offset to an average of zero at sunset for comparison to this model, such that the lack of an offset for PAN should not affect the simulation of the production of oxidized nitrogen at night. Modeled NO_z over-predicts measured NO_z over the course of the simulation, consistent with the loss of HNO_3 to deposition. By the end of the night, HNO_3 is the largest single component of modeled NO_z, but HNO_3 is not likely conserved in the gas phase. Dry depositional loss with a deposition velocity of 1 cm s^{-1} in a 100 m boundary layer would result in a 2.8-hour lifetime for HNO_3, which would consume a large fraction of the predicted HNO_3 production. The growth in NO_z approximately follows the sum of $2\times N_2O_5$ + $ClNO_2$, with only a small offset attributable to HNO_3 not lost to deposition. Growth of HONO from 0.05 to 0.1 ppbv (less a 0.05 ppbv offset at sunset), equivalent to an first order loss rate coefficient of NO_2 of 2×10^{-7} s^{-1}, is also included in the model but does not significantly contribute to oxidized nitrogen in this simulation. It is possible that the actual loss of NO_2 is more rapid and that there is a depositional sink for HONO to the soil as well. The potential for this NO_2 heterogeneous process to act as a larger nighttime radical reservoir source under snow-covered conditions is also currently under investigation.

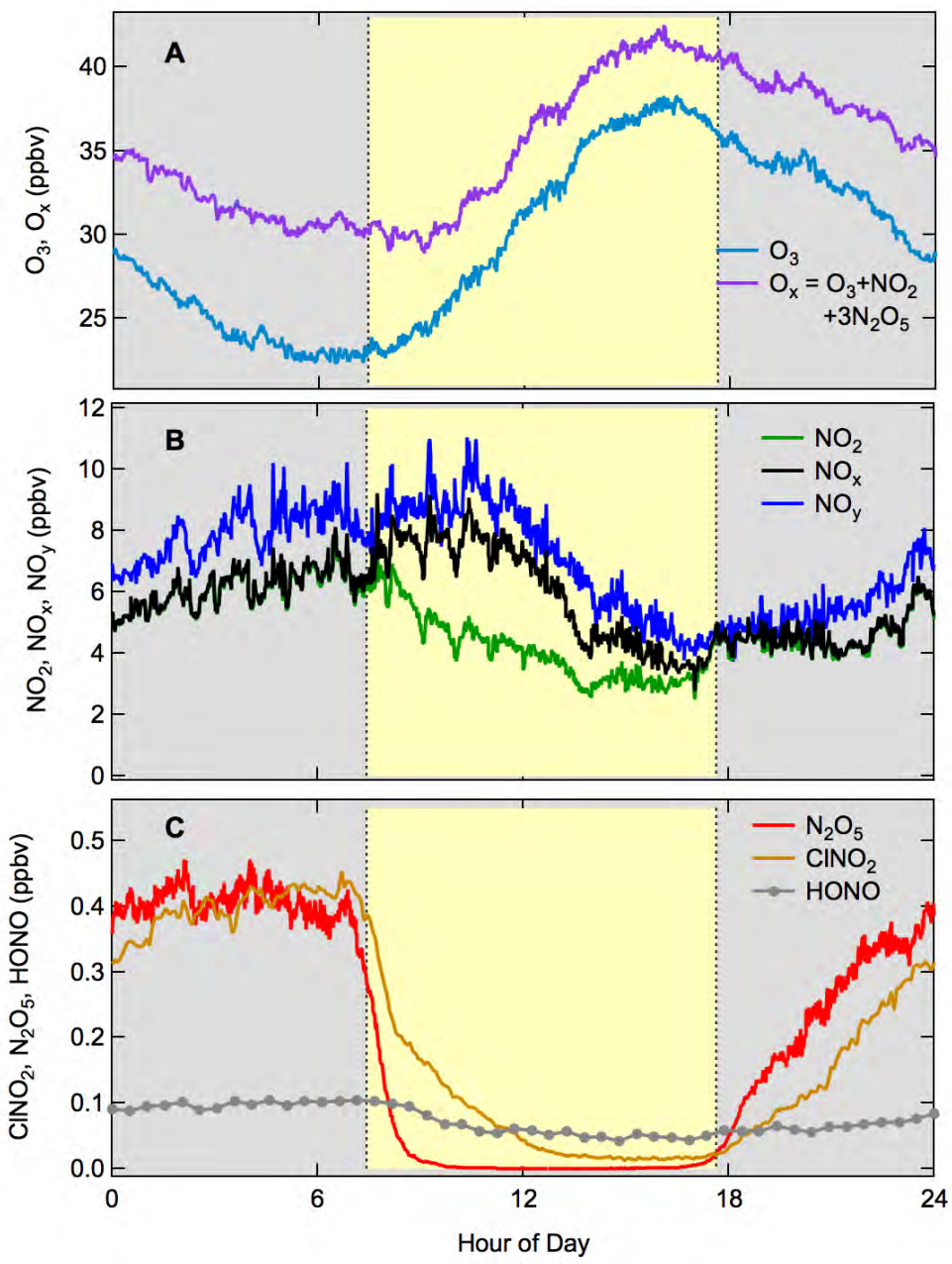

Figure 3-37. Diurnally averaged data for A. O_3 and O_x, B. NO_2, NO_x and NO_y and C. N_2O_5, $ClNO_2$ and HONO for the Horse Pool site. Data are filtered as described in the text and shown in Figure 3-38.

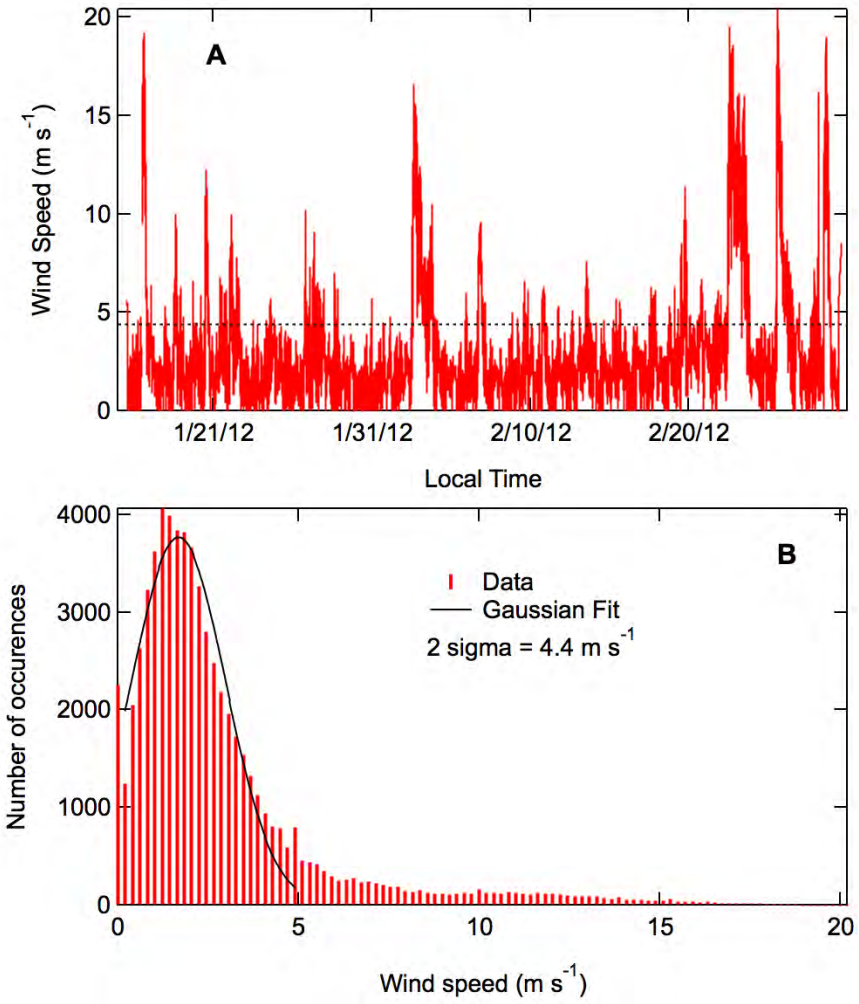

Figure 3-38. Time series (A) and distribution (B) of wind speeds during the Horse Pool intensive. Diurnally averaged data have been filtered to include only data within 2σ of the low wind speed peak, or 90% of the data.

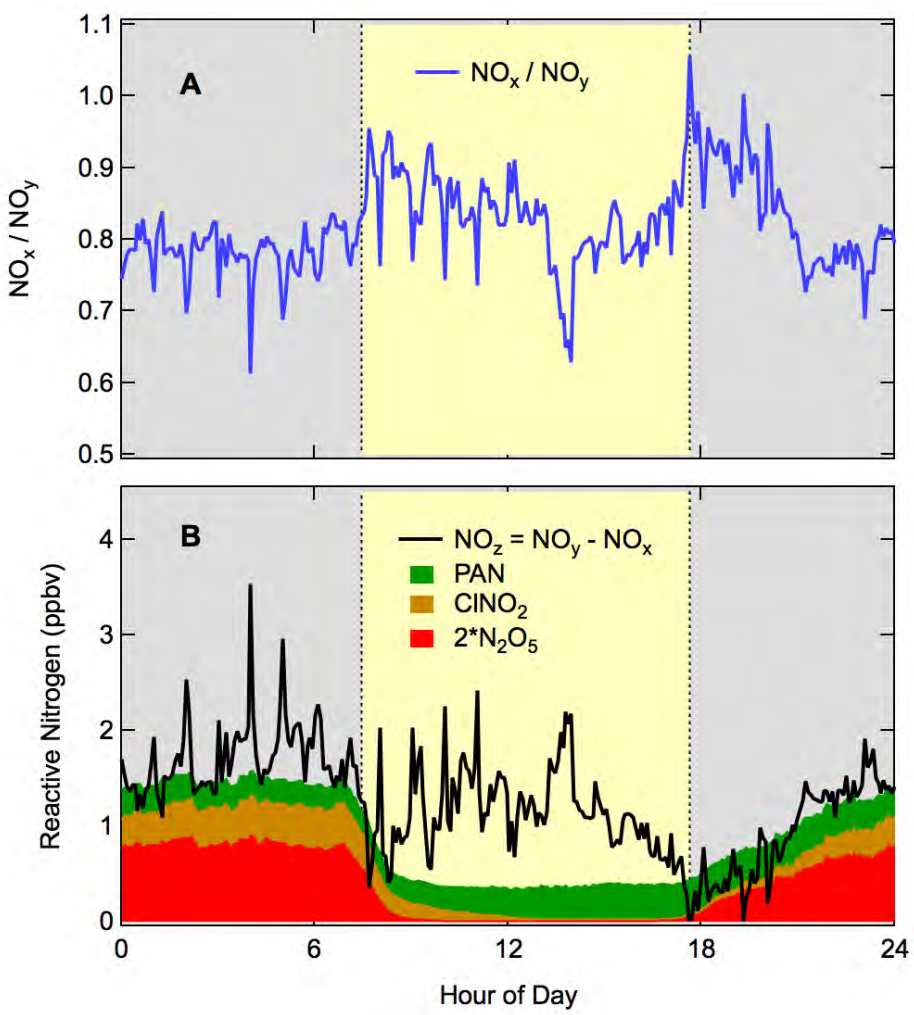

Figure 3-39. Diurnal average of the ratio of NO_x / NO_y (A) and NO_z = NO_x – NO_y, together with PAN, $ClNO_2$ and 2×N_2O_5 (B).

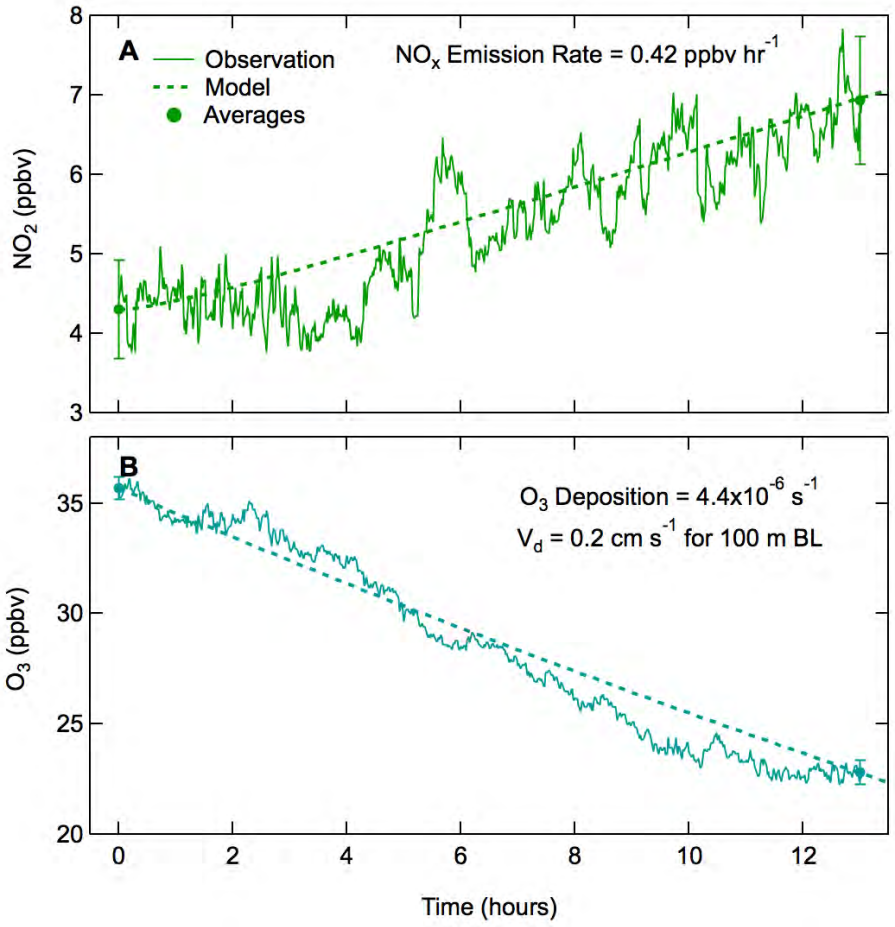

Figure 3-40. Comparison of a nighttime nitrogen oxide box model (dashed lines) to the nighttime diurnal average data (solid lines) for NO_2 (A) and O_3 (B). Time zero is sunset.

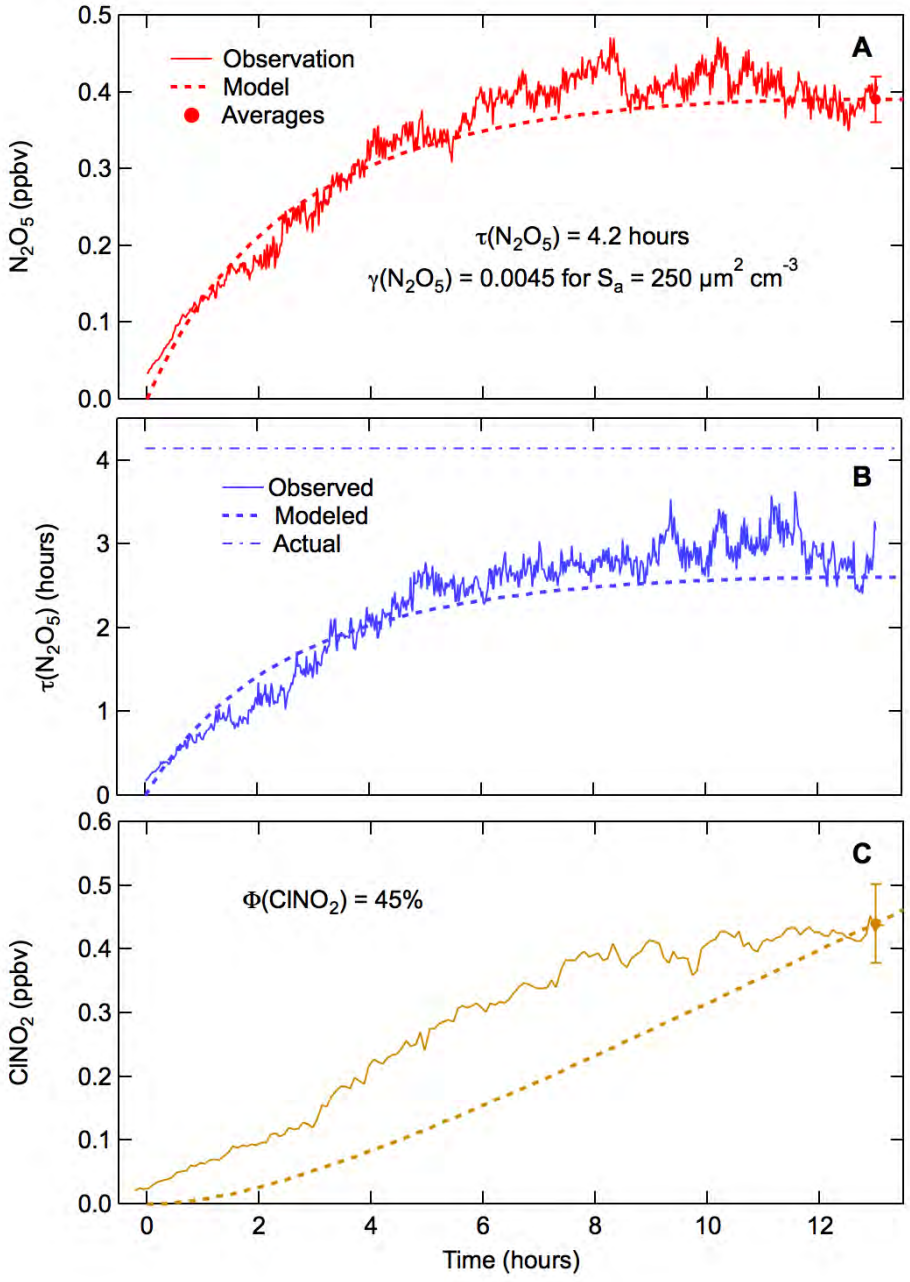

Figure 3-41. Comparison of a nighttime nitrogen oxide box model (dashed lines) to the nighttime diurnal average data (solid lines) for N_2O_5 (A), $\tau(N_2O_5)$ (B) and $ClNO_2$ (C). Dotted dashed line in panel B is the constant, actual lifetime of N_2O_5 in the model, as described in the text.

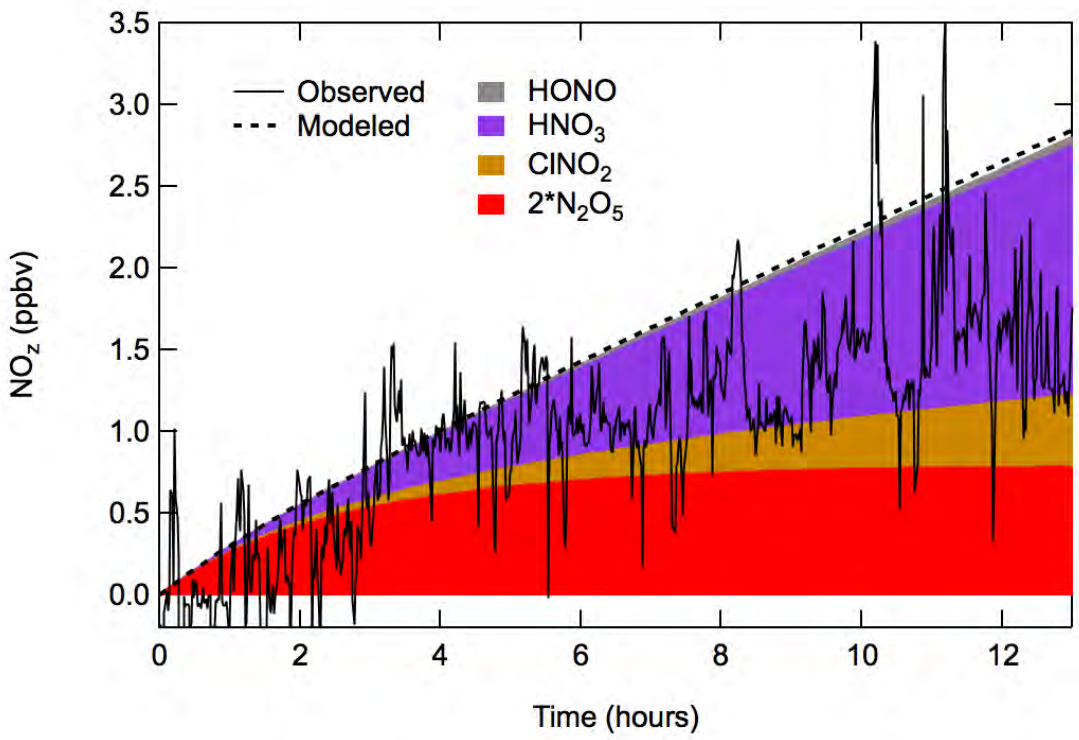

Figure 3-42. Comparison of a nighttime nitrogen oxide box model (dashed line) to the nighttime diurnal average data (solid lines) for NO_z. Solid areas show the model predicted components of NO_z as indicated in the legend.

Radical Sources

The oxidant chemistry of the troposphere is driven primarily by the photolysis of a select few chemical species that act as radical sources. Photolysis of O_3 to form OH radicals is typically thought to be the dominant radical source in the lower atmosphere. Recent work has shown that other compounds; formaldehyde (CH_2O), nitrous acid (HONO), and nitryl chloride ($ClNO_2$) can also constitute substantial sources of radicals under some circumstances. The appearance of high O_3 in oil and gas production areas during the winter, a season when photochemical activity is normally low, leads to the hypothesis that there may be unusual radical sources occurring in these areas. Consequently, an assessment of radical sources was a major goal for Study Component 3 during the UBWOS 2012. The contribution of each of the above radical sources is estimated below, and while meteorological conditions prevent a definitive answer concerning high ozone production, these data provide a useful baseline for comparison.

The photolysis of ozone has been recognized as the major source of tropospheric OH radicals for about 40 years [Levy II, 1971]. This process starts when O_3 absorbs a photon at or below about 300nm wavelength, resulting in an excited state oxygen atom (O^1D);

$$O_3 + hn \Rightarrow O^1D + O_2 \qquad (1)$$

Most of the time, O^1D collides with either N_2, or O_2 and is deactivated to O^3P, which reforms O_3, but a fraction of the time O^1D reacts with $H_2O_{(g)}$ and produces 2 OH radicals;

$$O^1D + M\ (N_2, O_2) \Rightarrow O^3P + M \quad (2)$$

$$O^3P + O_2 + M \Rightarrow O_3 + M \quad (3)$$

$$O^1D + H_2O \Rightarrow 2\ OH \quad (4)$$

The absorption cross-sections and reaction rate constants for these processes are all well known [Sander et al., 2006; Wallington et al., 2012] and, along with O_3, H_2O and actinic flux measurements, can be used to calculate the OH formation rate from this process from the following simple expression;

$$p(OH)_{O3} = 2k_4 jO_3[O_3][H_2O]/k_2[M] \quad (5)$$

It should be noted here that actinic fluxes were either measured with filter radiometers or calculated from several filter radiometers. The actinic flux was folded into the absorption spectrum and quantum yield for the process being measured. For example, the jO_3 measurement has an optical filter combination to match the O_3 absorption spectrum. The jHONO values are derived from measured jNO_2 with a scaling factor included to account for the different in absorption cross-sections. The uncertainties in the calculated j values (jHONO, jCH_2O, and $jClNO_2$) are estimated to be ±30%.

The photolysis of nitrous acid (HONO) is a direct source of OH radicals that has been considered in a number of urban and polluted air masses [Young et al., 2012]. This reaction is a direct photolysis that is very efficient at wavelengths below approximately 410nm.

$$HONO + hn \Rightarrow OH + NO \quad (6)$$

The corresponding production rate then depends on HONO concentration and the actinic flux.

$$p(OH)_{HONO} = jHONO[HONO] \quad (7)$$

The photolysis of formaldehyde takes place at wavelengths below about 340nm via two channels;

$$CH_2O + hn \Rightarrow H + CHO \quad (8a)$$

$$\Rightarrow H_2 + CO \quad (8b)$$

The products (H atoms and CHO radicals) react rapidly with O_2 to form HO_2 radicals;

$$H + O_2 + M \Rightarrow HO_2 + M \quad (9)$$

$$CHO + O_2 \Rightarrow HO_2 + CO \quad (10)$$

The rapid reaction of HO_2 with NO in high NOx environments leads to the formation of OH radical;

$$HO_2 + NO \Rightarrow NO_2 + OH \quad (11)$$

making CH_2O an indirect, but potentially significant, source of HO radicals. The HOx source from CH2O is calculated similarly to that of HONO, assuming that Reactions (9-11) are the only pathways operating and jCH2O is based on the photolysis Reaction 8a;

$$p(OH)CH_2O = 2jCH_2O[CH_2O] \quad (12)$$

The photolysis of nitryl chloride takes place at wavelengths below about 450nm and is categorically different from the above radical sources in that it produces chlorine atoms;

$$ClNO_2 + hn \Rightarrow Cl + NO_2 \quad (13)$$

The calculation of production rate is done as before:

$$p(Cl) = jClNO_2[ClNO_2] \quad (14)$$

It should be noted, however, that the actinic flux used in this calculation is based on the old absorption cross-section that were assumed constant with temperature and not the new temperature-dependent cross sections of Ghosh et al. [Ghosh et al., 2012]. This makes the current calculation about 25% higher than it would be if temperature dependence had been included.

The absolute amount of actinic flux available during the UBWOS 2012 study is the first point of comparison with other more photochemically active environments. The time series of jO_3 for the UBWOS 2012 and CalNex studies are shown in Figures 3-43, along with two typical clear days during those projects. It is clear that jO_3 alone is more than a factor of 3 different between the two studies.

Calculated radical production rates for the four sources listed above are summarized in Figure 3-44 for the UBWOS 2012 project. Perhaps surprisingly, the photolysis of O_3 is a minor contributor to the radical budget during UBWOS 2012. In addition to the lower actinic flux noted above, water vapor and ozone concentrations were also low during this study. The other OH sources were more important, and the Cl atom source from $ClNO_2$ was similar in magnitude to O_3 photolysis. It should be noted that Cl atoms are several hundred times more reactive towards some compounds, notably alkanes and methanol, amplifying the effect of this source.

The UBWOS 2012 results can be put in context through comparison with the same calculations that have been done for the CalNex Pasadena 2010 study [Young et al., 2012], shown in Figure 3-45. The CalNex radical sources were substantially larger than those estimated for the UBWOS 2012 data set. The major difference was in the photolysis of O_3, but the other two sources calculated for CalNex were also higher. The lack of radical production is the root cause of the absence of elevated O_3 during UBWOS 2012. This type of radical budget analysis is a crucial tool in future investigations of O_3 production in the Uintah Basin.

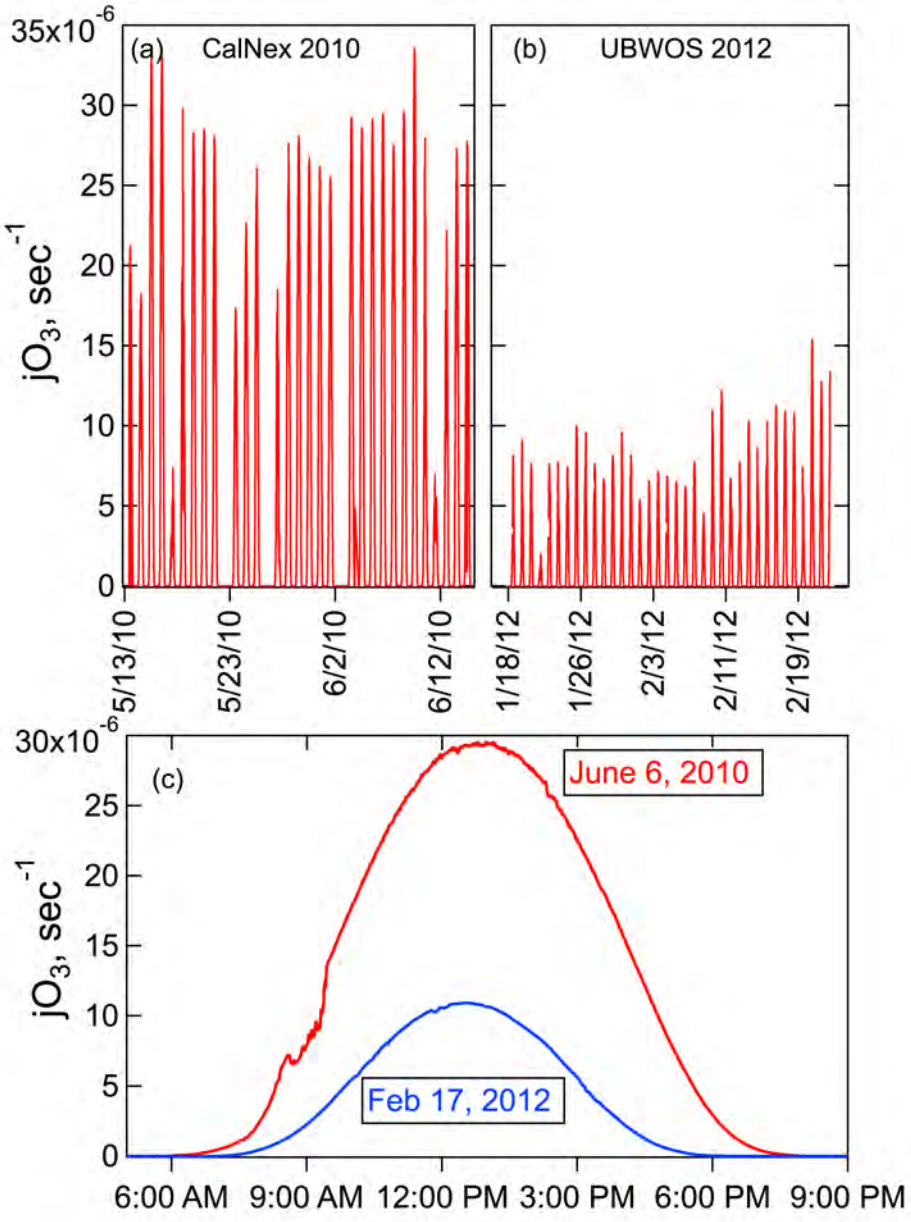

Figure 3-43. Summary of jO_3 measurements during (a) CalNex and (b) UBWOS 2012, and (c) a close up of typical clear days during those projects.

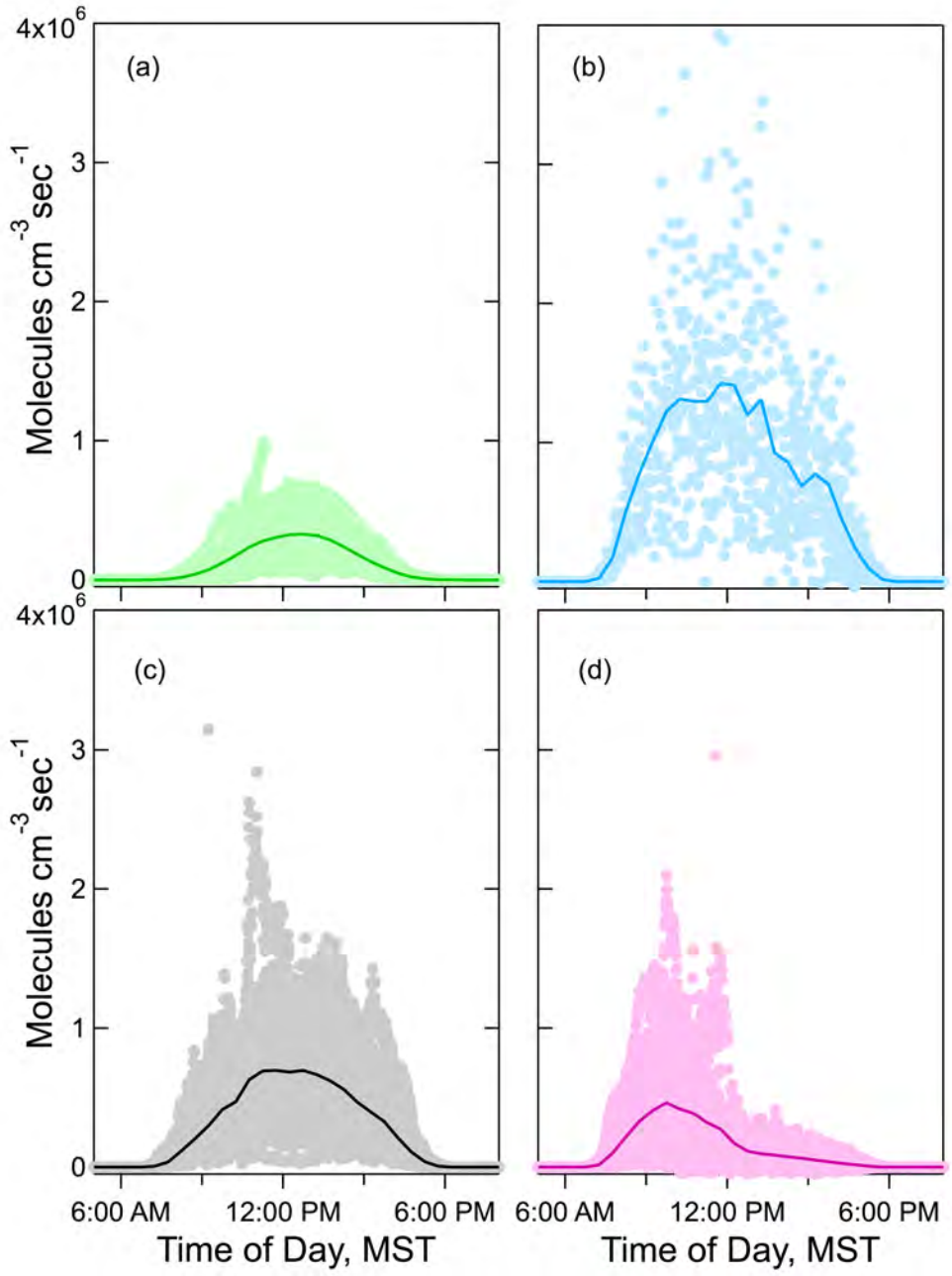

Figure 3-44. A summary of the radical production rates from (a) O_3, (b) HONO, (c) CH_2O, and (d), $ClNO_2$, versus time of day (local time).

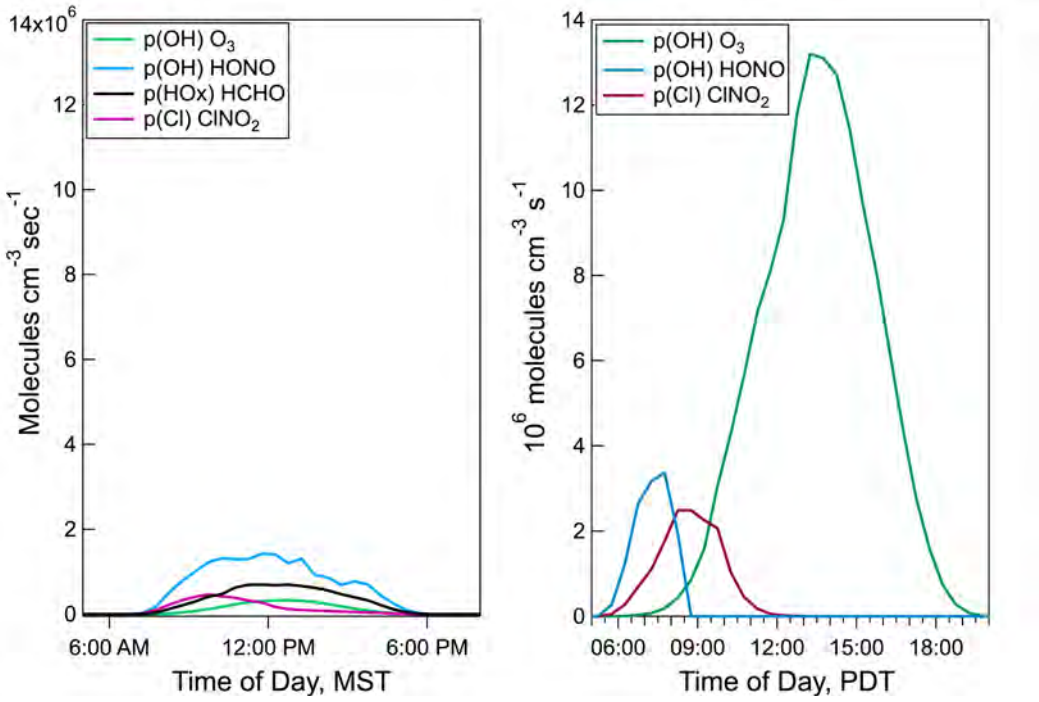

Figure 3-45. A comparison of radical sources calculated from (a) the UBWOS 2012 study and (b) the CalNex 2010 Pasadena site.

Aerosols

The PM 2.5 dry mass during UBWOS 2012 (January 16- February 27, 2012) varied from 1 to 27 ug m^{-3} with an average during the study of 7.5 ± 6.8 ug m^{-3}. The PM 2.5 gravimetric dry mass was well correlated with the sum of the chemically analyzed mass (slope = 0.97, r^2=0.89), indicating that the chemically measured species accounted for all of the aerosol mass. The ionic, elemental, and organic measurements were summed into six components: ammonium sulfate [AS -$(NH_4)_2SO_4$], ammonium nitrate [AN - NH_4NO_3], particulate organic matter [POM = organic carbon x 1.8], light absorbing carbon [LAC], soil [the common oxides of Al, Si, Ca, Fe, and Ti], and sea salt [SS = Na x 1.47 + Cl] [IMPROVE, 2011; Quinn et al., 2004].

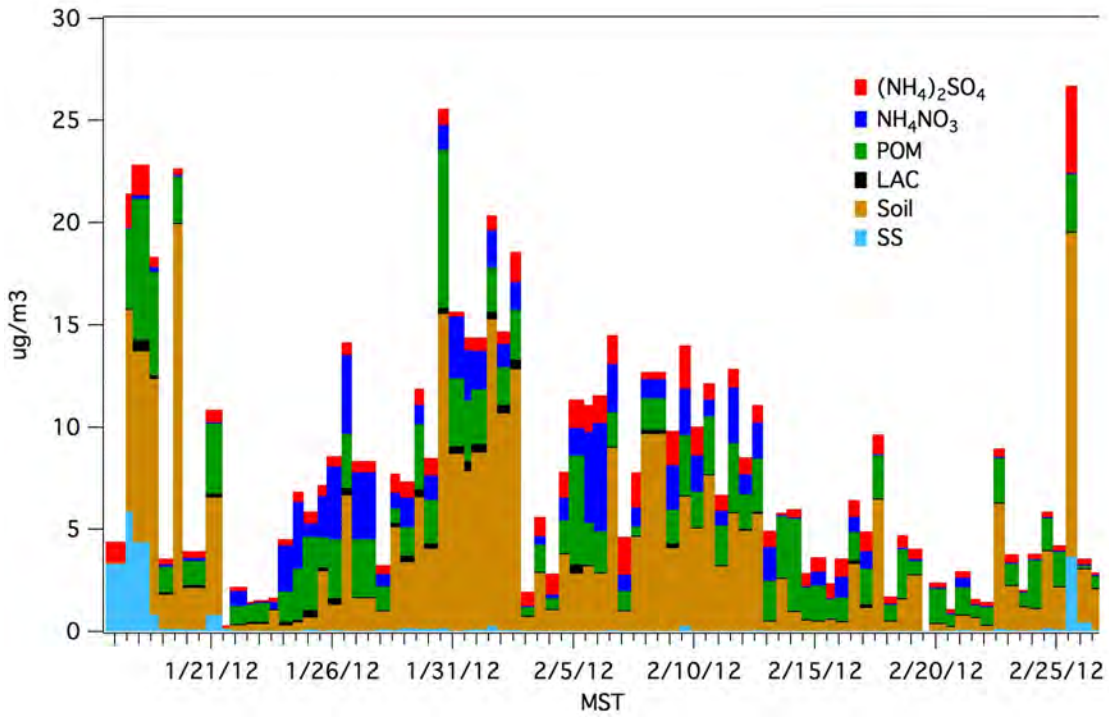

Figure 3-46. The time series of aerosol chemical composition (<2.5um) measured during UBWOS 2012.

With the lack of snow, soil was the dominant aerosol component (42 ± 20%) followed by POM (31 ± 16%), AS (12 ± 9%), AN (12 ± 13%), SS (1.8 ± 2.6%), and LAC (1.3 ± 1.7%).

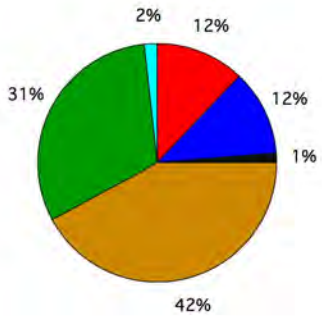

Figure 3-47. Average fractional composition of PM 2.5 measured during UBWOS 2012.

The average PM 2.5 aerosol mass measured at the Horse Pool Site in 2012 was very similar to that measured at Red Wash in 2011 (9.5 ug m^{-3};[EDL, 2011]) and the annual mean concentration reported by the IMPROVE network (7.6 ug m^{-3};[IMPROVE, 2011]). The POM mass fraction, however, is much less than that measured at Red Wash in 2011 (65%). This may be due to the lack of snow cover and SOA production or could be a measurement artifact. With the high VOC concentrations in the region, it is quite easy to capture VOCs on the particulate filter.

The PM 2.5 aerosol surface area and volume were dominated by the accumulation mode centered at 200 nm dry diameter. The average PM 2.5 aerosol surface area was 45 ± 55 $um^2\ cm^{-3}$. The aerosol number distribution was dominated by the Aitken mode (< 100 nm dry diameter). The total CN averaged 3700 ± 2000 cm^{-3}.

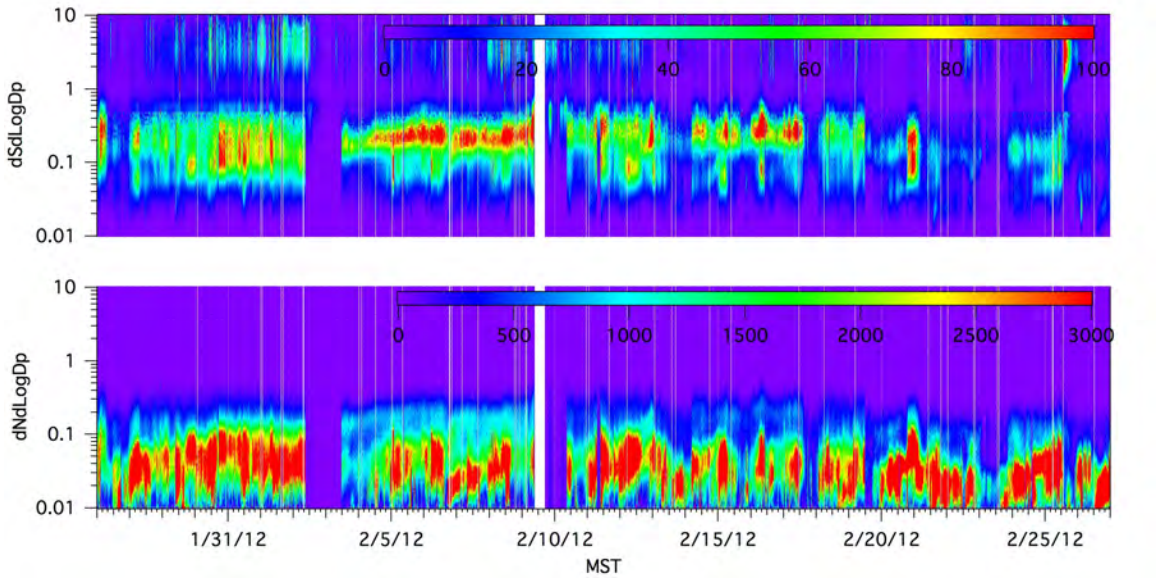

Figure 3-48. The time series of size distributions of aerosol surface area (top) and number (bottom).

The average PM 2.5 aerosol light scattering coefficient was 15.5 ± 18.8 Mm^{-1} with a mass scattering efficiency of 2.0 $m^2\ g^{-1}$. The single scattering albedo was 0.88 ± 0.08.

Ozone Lidar

Introduction

NOAA/ESRL/CSD deployed the Tunable Optical Profiler for Aerosol and oZone (TOPAZ) lidar to the 2012 Uintah Basin Wintertime Ozone Study (UBWOS 2012). The TOPAZ lidar was situated at the Horse Pool Supersite. The primary objective of deploying TOPAZ was to characterize the vertical structure of ozone from near the surface to several kilometers above ground level (AGL). Below about 300 m AGL, the TOPAZ ozone profiles complemented the ozone tether sonde measurements at Horse Pool by providing temporal continuity between tether sonde launches. The lidar ozone profile measurements above 300 m AGL provided information about the ozone structure beyond the maximum altitude reachable with the tether sondes. This was critical for detecting ozone layers aloft, which may be associated with long-range transport of ozone in the lower free troposphere or downward mixing of stratospheric ozone. Under the right conditions, these ozone layers aloft can be mixed down to the surface and can impact surface ozone concentrations.

TOPAZ Lidar Description and Deployment Strategy

The TOPAZ ozone and aerosol lidar is based on a state-of-the-art, solid state, tunable laser that emits laser pulses in the ultraviolet spectrum at three wavelengths between 285 and 300 nm [Alvarez et al., 2011]. The TOPAZ lidar measures ozone and aerosol backscatter profiles along the laser beam path with high spatial and temporal resolution. Prior to UBWOS 2012, TOPAZ was converted from a downward-looking airborne system into a zenith-pointing instrument that was installed into a truck with a roof-mounted two-axis scanner. The airborne version has been used in several air quality field campaigns since 2006 and has been extensively tested and compared with collocated in situ ozone sensors [Langford et al., 2011; Senff et al., 2010]. Details about the new truck-mounted version of the TOPAZ lidar can be found in Alvarez et al. [Alvarez et al., 2012].

The TOPAZ ozone lidar was operated on 14 days between 3 and 29 February, 2012, and recorded 62 hours of ozone and aerosol backscatter profile data. In the absence of any high ozone events, the sampling strategy consisted of operating TOPAZ for several hours at a time and covering different segments of the diurnal cycle on different days. Figure 3-49 shows the truck-based TOPAZ lidar with roof-mounted two-axis scanner. The scanner permits pointing the laser beam at several shallow elevation angles at a fixed, but changeable azimuth angle. Zenith operation is achieved by moving the scanner mirror out of the laser beam path. During UBWOS 2012, repeated scans at 2, 10, and 90 degrees elevation angle were performed approximately every 5 minutes. The dwell time at each angle was 75 s. The ozone and aerosol backscatter profiles at these three angles were spliced together to create composite vertical profiles extending from 15 m to about 3 km AGL (Figure 3-50). The effective vertical resolution of the composite ozone profiles increases with altitude from 3 to 90 m. Occasional horizontal measurements were made to study the horizontal variability of ozone and aerosols. Preliminary TOPAZ ozone data are posted at

http://www.esrl.noaa.gov/csd/groups/csd3/measurements/ubwos/topaz/.

Several comparisons were performed with tethered and free-flying ozone sondes as well as with scaffold-mounted in situ ozone sensors. Generally, the lidar measurements compared well with the other ozone measurements, and the observed discrepancies were within the stated instrument accuracies of the lidar and the in situ sensors.

Preliminary Findings

Figure 3-51 shows all ozone lidar measurements displayed as normalized probability distribution functions (PDFs) for three altitude ranges: 15-200 m AGL, 200-1000 m AGL, and 1000-3000 m AGL. The mean ozone values for these altitude ranges were approximately 46 ppbv, 48 ppbv, and 52 ppbv, respectively. Figure 3-51 shows that no ozone values above about 75 ppbv were measured with the lidar at any altitude below 3000 m AGL. In particular, no exceedances of the 8-hour National Ambient Air Quality Standard were observed. This lack of high ozone episodes was likely due to the fact that the boundary layer was generally rather deep and well-mixed, which prevented a buildup of high concentrations of ozone and its precursors. The almost complete absence of any snow cover during UBWOS 2012 prevented the formation of a shallow cold-air pool and the development of strong temperature inversions. As a result, the boundary layer was much deeper and much better ventilated than during typical wintertime conditions in the Uintah Basin. Figure 3-51 also reveals that on average ozone concentrations were increasing slightly with altitude during UBWOS 2012. The mean ozone value of about 52 ppbv in the upper

altitude bin is typical for background ozone conditions in the lower free troposphere for the western US. The slightly lower ozone values in the two altitude ranges below 1000 m are probably due to titration and surface deposition of ozone. The slight vertical gradient of ozone and the similarity of the ozone PDFs for the three altitude ranges are consistent with the generally well-mixed conditions observed during UBWOS 2012.

Figure 3-49. Truck-mounted TOPAZ ozone lidar with roof-top, two-axis scanner.

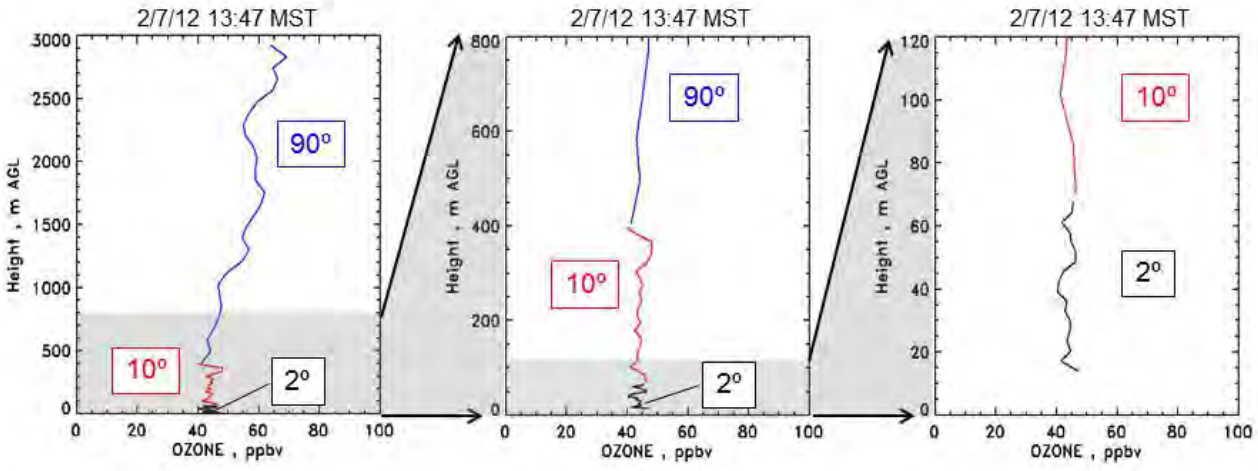

Figure 3-50. Lidar ozone profiles at elevations angles of 2°, 10°, and 90°, projected vertically and blended together. The entire profile is shown on the lefthand plot and the righthand plots show sucessive expansions of the profile.

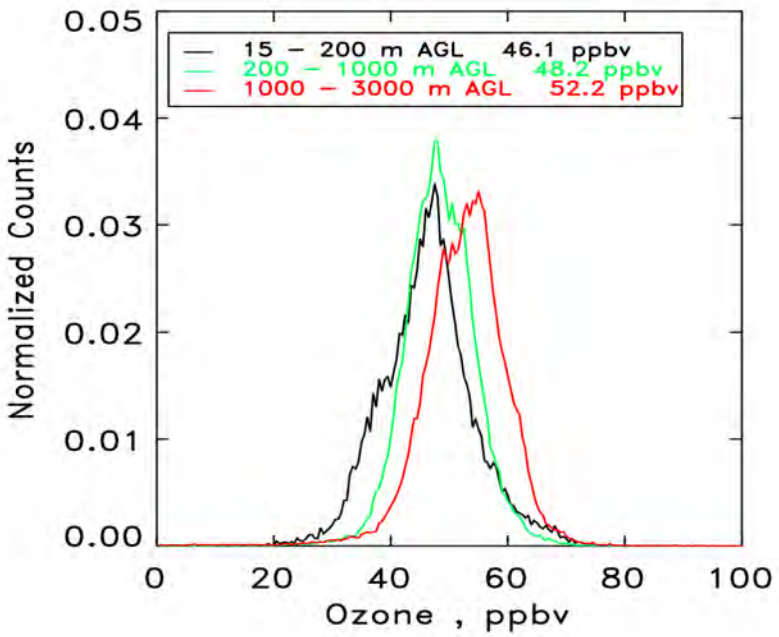

Figure 3-51. Normalized PDFs of all UBWOS 2012 ozone lidar measurements for three altitude ranges. Mean ozone values for the different altitude bins are indicated in the legend.

High Resolution Doppler Lidar

Measurement of wind direction and speed profiles is important for quantifying emission source strengths (as described elsewhere in this report) and for assessing the impact of atmospheric transport. Net transport when winds are light, as they had been during O_3 episodes in the 2011 Uintah Basin campaign, may be negligible if the wind direction is highly variable, but can cover tens of kilometers if the wind direction persists for several hours.

Often light wind periods in mountainous terrain feature thermally driven wind systems, due to the diurnal heating and cooling cycle at the earth surface. These wind systems, often referred to as local wind systems because of the local nature of the forcing mechanisms, blow upvalley or upslope during daylight and downslope or downvalley (drainage flows) at night. At a given time of day, in other words, the local winds blow from a preferred direction for several hours, so that the winds and their effects (e.g., transport) show up in multiday averages or composites of the data.

The daytime component of the local winds in winter often may not be well developed due to low solar angles and short day lengths, resulting in weak surface heating, weak forcing, and local winds that may be difficult to detect. So important questions are: Is there a discernible diurnal signature to the low-level winds in the Uintah Basin in wintertime conditions, and could the daytime slope flows contribute to the daytime transport of pollutants?

During the 2011 measurement campaign, the concentrations of O_3 had been found to vary considerably in the horizontal, meaning either that the sources were unevenly located over the basin or that atmospheric transport over the complex terrain had an important role in determining the concentrations. But precursor sources were distributed over the basin, so the horizontal variability of wintertime O_3 concentrations indicated that horizontal transport was occurring and influencing the O_3

concentrations. Highest concentrations were measured at the lowest-elevation sites in the Green River valley, which could be explained by drainage flows, but high concentrations were also seen at higher-elevation sites to the east of the river-valley sites.

Weak winds require a precise measurement system to detect. NOAA/ESRL's High-Resolution Doppler Lidar (HRDL) has been shown to be such a precise system. Although a scanning system, HRDL is able to produce accurate profiles of the mean wind at vertical resolutions of less than 5 m through the lowest several hundred meters of the atmosphere, extending up to 2 km. HRDL was located at the Horse Pool site, so it sampled the wind conditions in the eastern portion of the basin.

Different types of wind conditions were observed by HRDL during January-February 2012. Strong-wind periods are generally dominated by large-scale meteorological systems, as typical of wintertime conditions in mid-latitude locations such as Utah. In such conditions the near-surface winds reflect the stronger winds aloft, as illustrated in Figure 3-52. In weak-wind periods the effects of local forcing of the winds become evident if the forcing is strong enough. Figure 3-53 shows the evolution of wind profiles on a day when such forcing is clear. On this day, the near-surface winds were light, but the nighttime winds had a distinct easterly component, and daytime winds were from the west up to several hundred meters. Although many light-wind days exhibited variability in the winds superimposed on the local winds by traveling disturbances, the diurnal pattern was observable in HRDL profiles on most light-wind days of the 2012 project, and in composites of all days when the winds aloft were light (< 4 m/s). Thus HRDL was able to detect a diurnal pattern in the near-surface winds in the Horse Pool vicinity, with light easterly flow draining toward the Green River valley at night and light westerly upslope flow during daytime hours. The easterly flow accounts for the appearance of high concentrations in the lowest areas of the basin, and the daytime westerlies can explain the secondary appearances of high concentrations on higher ground to the east of the river bottom. Characterizing meteorological controls on the pollutant concentrations is important to assessing the transferability of the findings in the Uintah basin to other gas and oil drilling locations.

HRDL information was also useful in attributing longer-range transport. Trajectories calculated from the 20-min winds identified the source of several bursts of pollutants observed in Horse Pool chemistry measurements as being the power plant to the northeast.

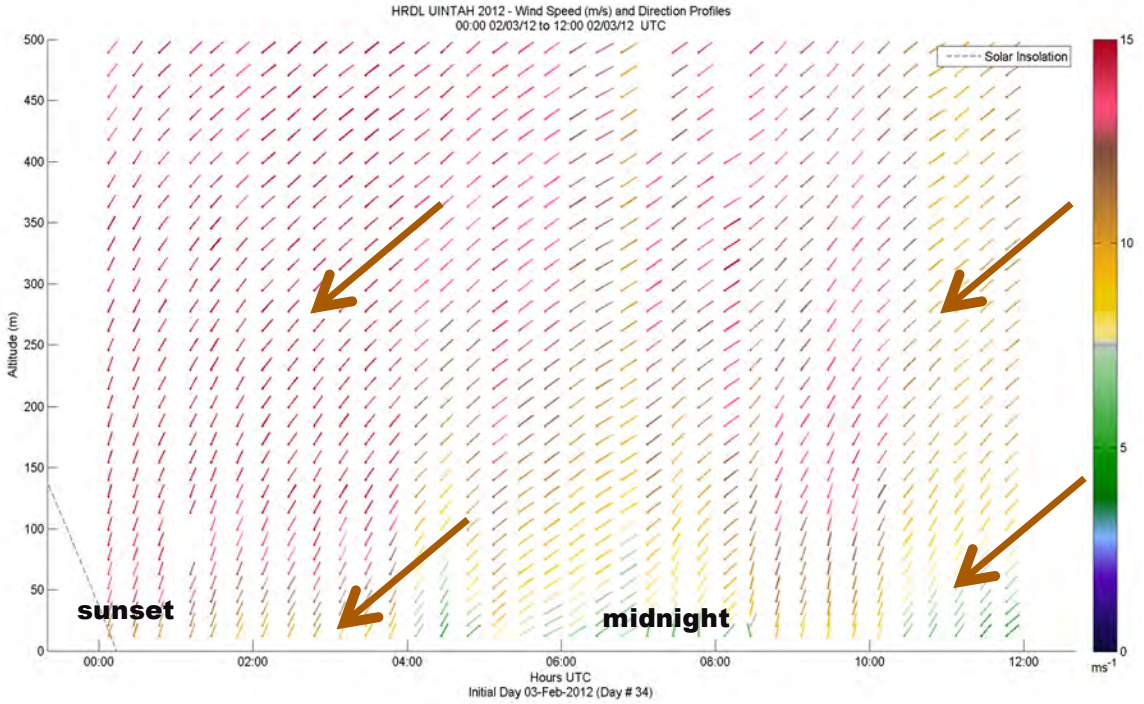

Figure 3-52. Profiles of 20-min wind speed and direction for 0000-1200 UTC on 3 Feb. 2012, showing strong northeasterly flow at 500 m agl, extending down to the surface. Wind barbs indicate direction from which winds were blowing, and color coding of barbs indicates wind speed as shown on color bar. Horizontal axis is time (UTC, which is 7 hr ahead of MST), and vertical axis is height above ground (m).

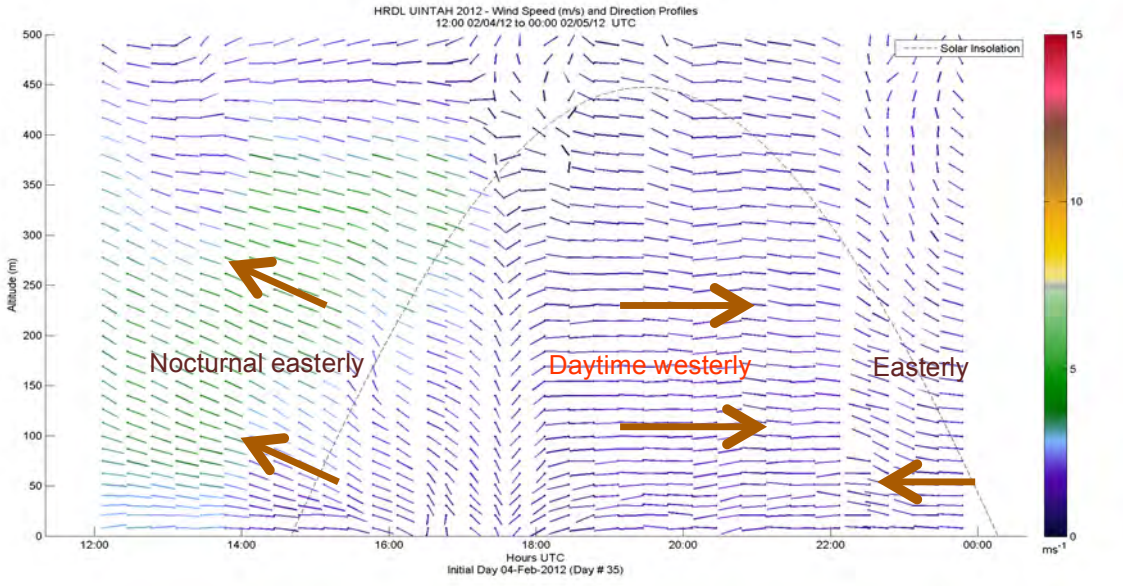

Figure 3-53. Profiles of 20-min wind speed and direction for 1200 UTC, 4 Feb. to 0000 UTC, 5 Feb. 2012, showing diurnal cycle of winds below 500 m. Dotted black curve is clear-sky solar flux, indicating time of day. Wind barbs and axes as in Figure 3-52.

Meteorological Measurements

Data from the standard meteorological instrumentation and radiometers were archived at 1.0 min intervals. The fast response anemometer/thermometers were sampled at 10.0 Hz. The raw 10.0 Hz samples were archived. Net radiative fluxes, turbulent heat fluxes, and turbulent momentum fluxes were estimated using the radiometric and sonic anemometer/thermometer data sets. Jpeg images of the backscattered power measured by the sodar were generated at 30-minute intervals.

Preliminary analysis of the meteorological data show that the lack of snow cover and subsequent strong radiative heating of the surface produced anomalously deep convective boundary layers. The sodar data helped document the establishment and evolution of these boundary layers. A strong diurnal cooling/heating cycle was observed using the radiometric data set. Analysis of the turbulent heat flux observations shows that peak surface heat fluxes over 200 W m^{-2} at solar noon were not uncommon in February.

Snow cover was observed on 19 and 29 February. During those time periods the observed surface albedos exceeded 0.3. The average surface albedo measured at Horse Pool during the experiment was 0.25.

Questions concerning data access, data quality and the preliminary analyses should be directed to Robert Zamora (robert.j.zamora@noaa.gov) or Allen White (allen.b.white@noaa.gov).

DOAS

The LP-DOAS instrument measured sequentially in two different wavelength ranges: 300-380 nm (for retrieval of O_3, SO_2, NO_2, HONO and HCHO); and 600-680 nm (for retrieval of NO_3) on all three light paths. For each wavelength range, information of the respective trace gases was recorded simultaneously.

In order to study the vertical distribution of the observed trace gases, the measured path averaged mixing ratios were converted to height interval averaged mixing ratios through a two-step process. First, all mixing ratios were linearly interpolated onto the time grid of the lowest light path observations to account for the temporal variations originated by taking the measurements sequentially. The interpolations were made under the assumption that the change of trace gas mixing ratios between the times of the scans could be approximated using a linear function. Second, the path averaged mixing ratios for the upper three light paths were converted to height interval averaged mixing ratios by using equation 1.

$$c_i = \frac{(h_i - H)}{(h_i - h_{i-1})} S_i - \frac{(h_{i-1} - H)}{(h_i - h_{i-1})} S_{i-1} \qquad (1)$$

Where H is the base height of the lowest light path (31 m), c is the retrieved mixing ratio, h is the top height (m), and S is the average mixing ratio of the i^{th} (middle, upper, highest) light path. The mixing ratio along the lowest light path is the average mixing ratio for the lowest height interval (0-31 m). The middle (31-44 m) and upper (44-68 m) height interval mixing ratios were calculated using equation 1. The original measurement errors were propagated to derive the uncertainties of the retrieved mixing ratios for each data point.

In order to study the diurnal behavior of the trace gases, the one-hour average diurnal mixing ratio of the measured trace gases were calculated using the retrieved height intervals mixing ratios (Figure 3-

54). Figure 3-54 shows that the diurnal average of NO_2, O_3, HONO, HCHO and SO_2 were between 2-8ppb, 25-42ppb, 25-125ppt, 0.8-1.2ppb and 100-200 ppt respectively.

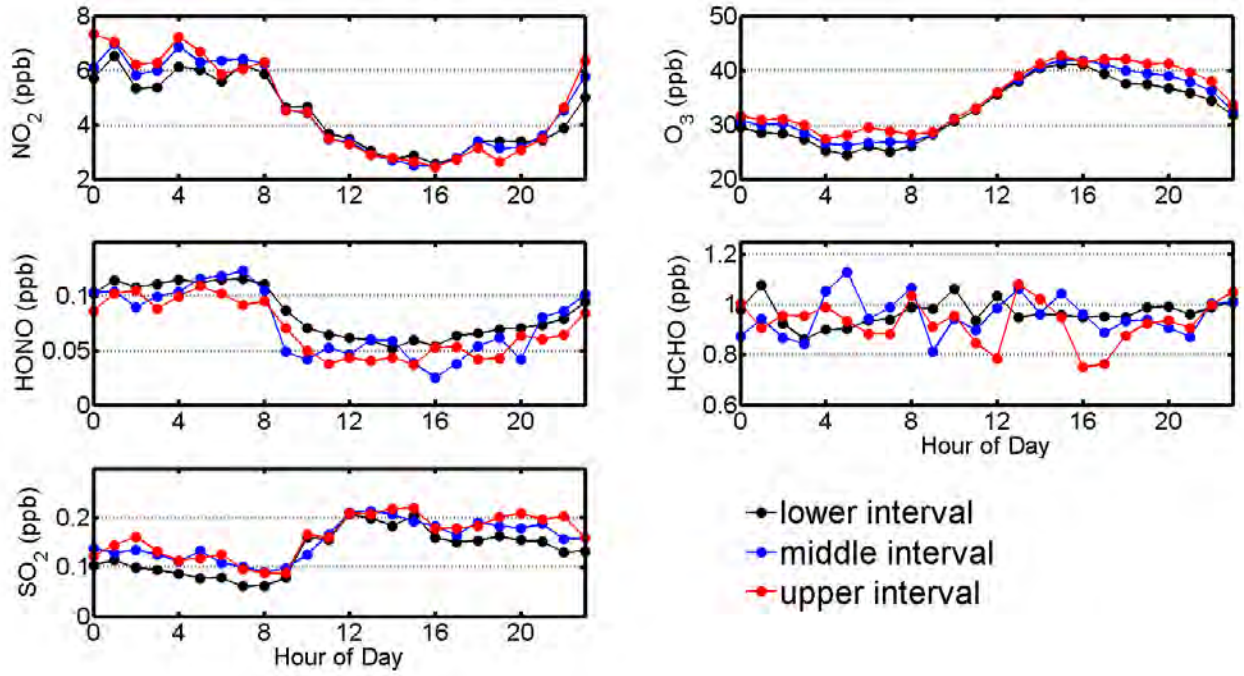

Figure 3-54. One hour average diurnal profile of a) NO_2, b) O_3, c) HONO, d) HCHO and e) SO_2.

Figure 3-54 also shows vertical profiles for NO_2, O_3, HONO and SO_2. The calculated vertical gradients for NO_2, O_3 and HONO are shown in Figure 3-55.

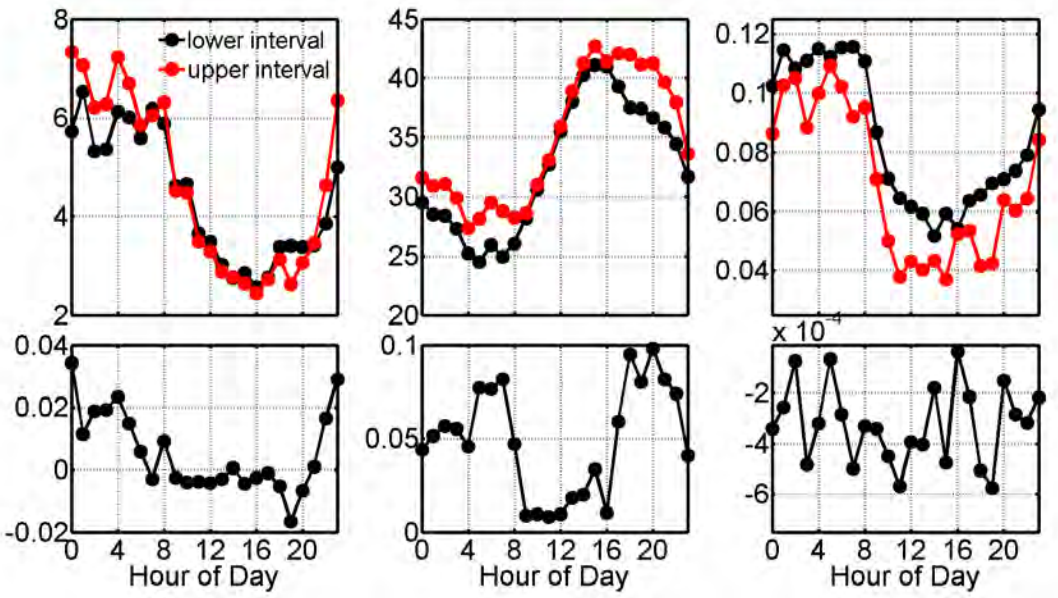

Figure 3-55. Upper and lower diurnal average for a) NO_2, b) O_3 and c) HONO and calculated vertical gradients of d) NO_2, e) O_3 and f) HONO.

Figures 3-54 and 3-55 show that NO_2 and O_3 gradients occur only at night and that these nocturnal gradients are positive. The positive gradients of NO_2 and O_3 suggest that there were NO_2 and O_3 deposition during the night. In contrast, HONO gradients (shown in Figure 3-54 and 3-55) persisted both during the day and night and were negative both during the day and the night. The HONO negative gradients indicate that there was a surface source of HONO during the project. The idea that both the deposition of NO_2 and O_3 and surface flux of HONO occurred during UBWOS 2012 will be further studied by calculating HONO and NO_2 surface fluxes and NO_2 and O_3 deposition velocities.

Aerosol Mass Spectrometer

Dr. Shane Murphy's group from the Department of Atmospheric Science at the University of Wyoming deployed an Aerodyne Aerosol Mass Spectrometer (AMS) [Jayne et al., 2000] to the Uintah Basin Winter Ozone Study (UBWOS 2012) from January 15 to March 1, 2012. The AMS collected continuous data for over 95% of the study period, and data were averaged into 5-minute intervals. Data consist of the size-averaged and size-resolved non-refractory composition of the sub-micron aerosol, are currently available to all scientists who participated in the project, and will be made available to the public in March 2013. Non-refractory, as used here, means any chemical species that is volatile at or below the 600 ^{o}C operating temperature of the vaporizer on the instrument. The major particulate species measured were organics, nitrate, ammonium, and sulfate.

Data from the AMS were corrected for instrumental collection efficiency. The instrument collects roughly half of the particles because of particle bounce off the vaporizer. While a more detailed analysis of the collection efficiency following the method of Middlebrook et al. [Middlebrook et al., 2011] is currently underway, preliminary data has been corrected assuming a collection efficiency of 55%, consistent with previous field measurements [Middlebrook et al., 2011]. The preliminary data for the mass and composition of non-volatile sub-micron aerosol measured during UBWOS 2012 is shown in Figure 3-56. Also shown in Figure 3-56 is the volume of sub-500 nm aerosol measured by a scanning

mobility particle sizer (SMPS) operated by NOAA PMEL. Figure 3-56 shows that there is a tight correlation between non-refractory mass and particulate volume. This tight correlation suggests that the mass of refractory species, such as dust or black carbon, present in the sub-micron aerosol is fairly small. If refractory material constituted a significant fraction of sub-micron mass during certain periods, we would see significant differences between the AMS and SMPS traces during these periods. We cannot rule out the possibility that the fraction of refractory material is constant throughout the field campaign, but given that the sources of refractory material (diesel engineers, wind speed) are transient in time and space this seems highly unlikely.

Figure 3-57 shows the composition of the non-refractory sub-micron aerosol during the UBWOS 2012 period. Organic material is typically the most abundant, followed by nitrate and ammonium. Ammonium is present in sufficient quantity to be the sole counter-ion for nitrate during the experiment. There is not sufficient sulfate mass present to comment with confidence on its neutralization state. The average fraction of sub-micron aerosol mass that is organic was 0.55 ± 0.18.

Figure 3-58 shows the mass of sub-micron organic aerosol along with the gas-phase concentration of formaldehyde and acetone measured by the NOAA Chemical Sciences Division proton transfer reaction mass spectrometer and gas chromatograph mass spectrometer (CSD). Acetone and formaldehyde are, in most cases, formed from the gas-phase oxidation of volatile organic compounds (VOCs) and are not primary emissions. The strong correlation between acetone and formaldehyde and the mass of organic aerosol is highly suggestive that the organic aerosol is being formed from the condensation of oxidized organics into the particle phase, a process known as secondary organic aerosol (SOA) formation. The fact that much of the particulate organic mass appears to be secondary is significant because it suggests that it is being formed locally when high concentrations of VOC are oxidized. This means that the mass of organic aerosol will increase if VOC concentrations increase or if there is an increased rate of oxidation.

Figure 3-59 shows a typical size distribution for the various chemical components observed during the field project. A large fraction of the organics is present in a smaller mode that is almost entirely composed of organic material. The relative fraction of the organic mass present in this mode increases during periods when the fraction of total aerosol mass that is organic is high and during periods of high concentrations of secondary gas-phase species such as acetone and formaldehyde. Interestingly, the oxidation level of the organic aerosol is quite low. Typical ambient SOA has an oxygen to carbon (O:C) ratio ranging from 0.2 to 0.9 [Aiken et al., 2008]. The O:C ratio observed during events with high organic mass fraction and a large amount of mass found in the smaller mode of Figure 3-59 was typically around 0.25. This low oxidation level suggests that VOCs require less oxidation to condense in this environment than in most typical cities and that there is a large reservoir of VOCs that will condense with more atmospheric oxidation.

All of the measurements made here suggest a secondary source of organic aerosol. While high ozone conditions were not observed during the study, it is expected that the mass and mass-fraction of organic aerosol will increase significantly during high ozone events. While not currently exceeding national air quality standards, the sub-micron aerosol mass needs to be carefully monitored and its formation understood to avoid future health and visibility issues.

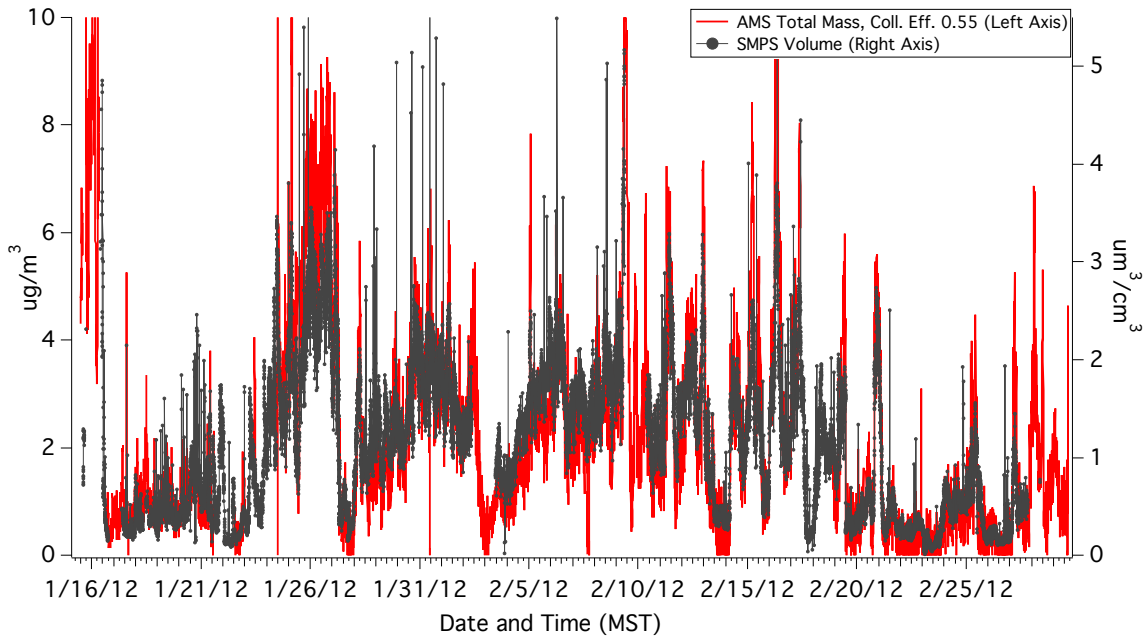

Figure 3-56. Total non-refractory mass (measured by the AMS) and total volume (measured by the SMPS) of sub-micron aerosol during UBWOS 2012.

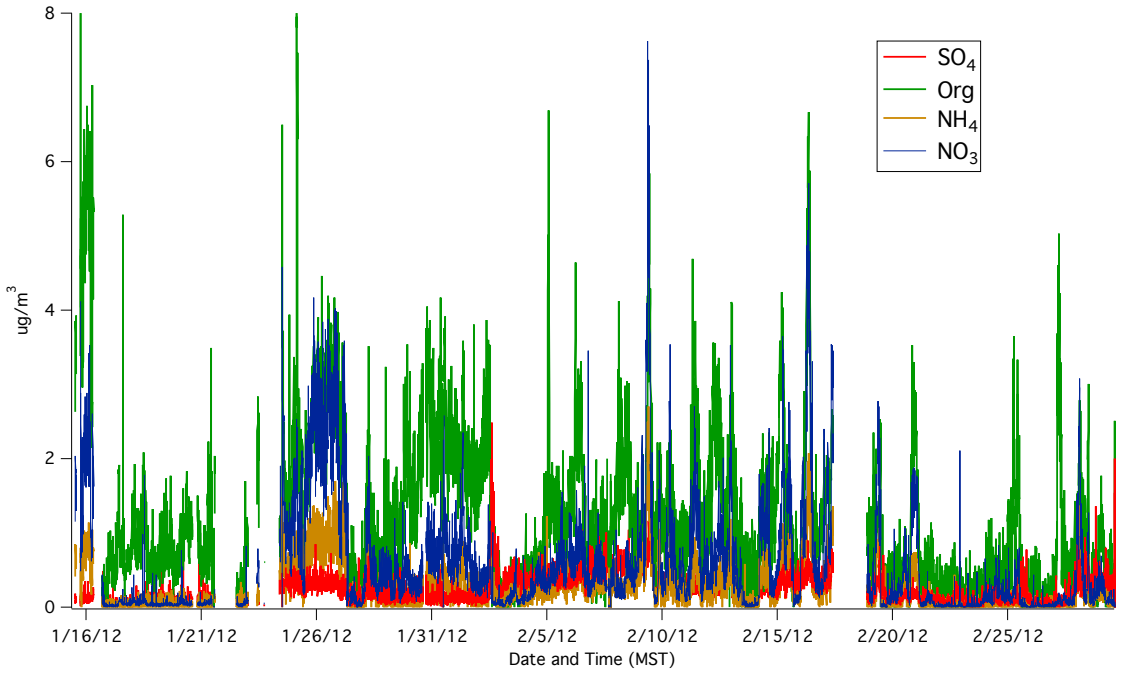

Figure 3-57. Mass of sulfate, organics, nitrate and ammonium measured by the U. of Wyoming AMS.

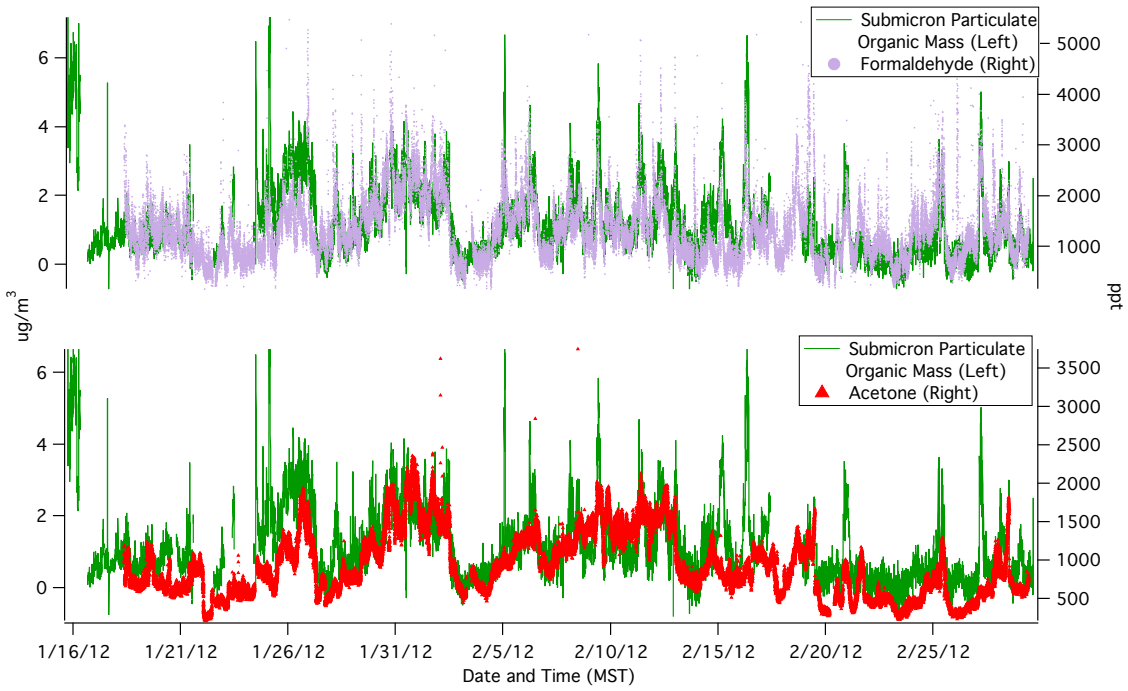

Figure 3-58. Time-series of particulate organic mass and the gas-phase species acetone and formaldehyde.

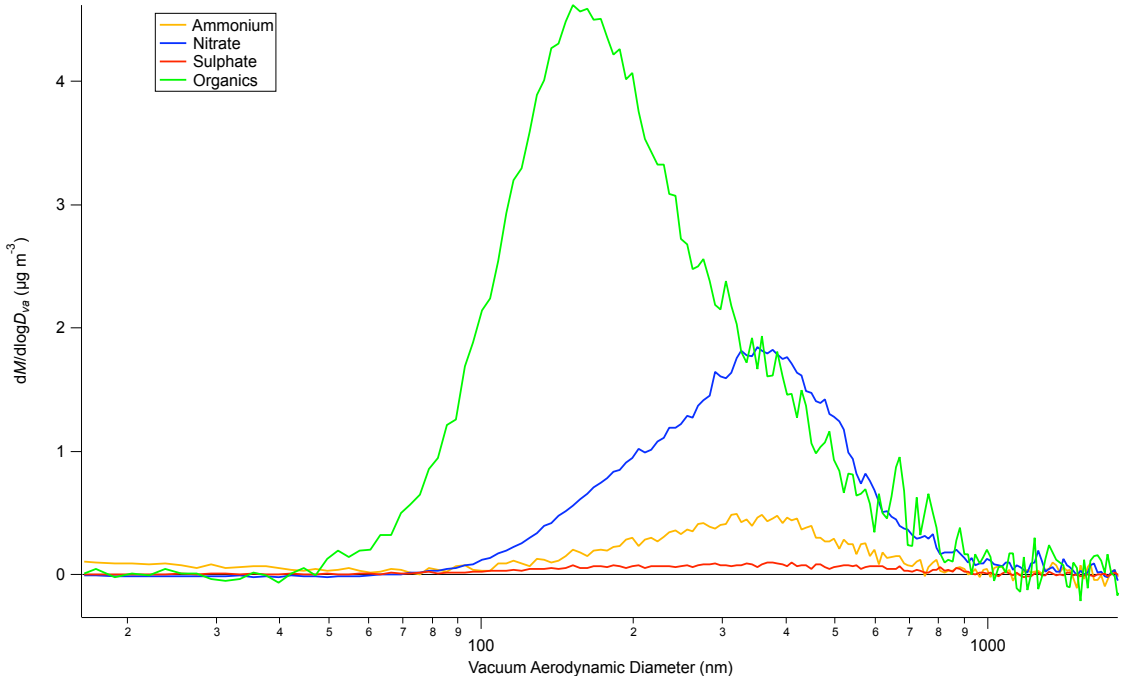

Figure 3-59. Size distribution of sub-micron non-refractory aerosol mass during a period of high organic mass concentration.

Nitrogen Species by TD-LIF (Data Description)

Figure 3-60 shows data from 408 nm system from January 18 to February 29. Generally, NO_x built up inside the basin during periods of mild winds, such as the period from January 28 to February 2. Occasionally, high wind episodes flushed out pollutants in the basin, and a significant drop in NO_x concentration was observed, e.g., starting at noon-time on February 2. Due to the proximity of sampling tower to existing truck route, early morning and afternoon NO_2 spikes were prominent features of the dataset. During the measurement period, NO_2 concentration spanned a range from ~100 ppt to 40 ppb with a diurnal pattern inversely correlated to boundary layer height. When compared with the cavity ring down system (ARNOLD) also measuring NO_2 at similar height, excellent correlation (R^2 =0.99) was obtained, with our system reporting values 8% higher than from ARNOLD. ∑(ANs+PNs) signal had a more consistent time-of-day variation than NO_2 signal, generally peaking at noon time when photochemical processes were fastest. We observed ∑(ANs+PNs) concentration ranging from ~150 ppt to 6 ppb during the campaign. It is noted that small alkyl nitrates (propyl nitrate and below) were also measured by GC-MS method during the campaign. They account for less than 10% of the total measured by TD-LIF, suggesting the importance of larger organic nitrate compounds. Particulate nitrate measurements spanned a concentration range from 0 to ~170 ppt, representing less than 15% of ∑(ANs+PNs) signal. When compared with other aerosol measurements, particulate nitrate correlates very well with aerosol volume calculated from SMPS data covering size range of 10 nm to 500 nm. Correlation is weakened if compared to measurements of larger size particles such as aerodynamic particle sizer (APS) or PM2.5 filter gravimetric data. Particulate organic nitrate did not exhibit a regular time-of day variation.

For 530 nm system, the time series of measured species are shown in Figure 3-61. Data were reported for NO_2 from January 20, for ∑PNs from January 24, and for ∑ANs from January 25 to February 28. NO_2 measured at 16 m was similar to NO_2 at 9 m, especially during the day. During the night, we observed slightly higher NO_2 concentration further from the ground and significant variations in NO_x spikes at the two heights. Comparison of other NO_2 measurements at 16 m (MABEL) gave very good correlation (R^2=0.97) and a slope of 0.993 (MABEL v.s. 530 nm system). ∑ANs data at 16 m had similar pattern as the ∑(PNs+ANs) measurements at 9 m, peaking during mid-day. ∑PNs showed a weak time-of-day variation with higher concentration during the night due to N_2O_5. Subtracting N_2O_5 measured by ARNOLD, the remainder of ∑PNs have a daytime peak.

An extensive suite of speciated VOC reported by GC-MS provides one way of calculating ∑ANs production rates and correlations with related chemical products such as O_3. We intend to pursue a deeper and more quantitative understanding of the ∑ANs chemistry and its gas-aerosol partitioning.

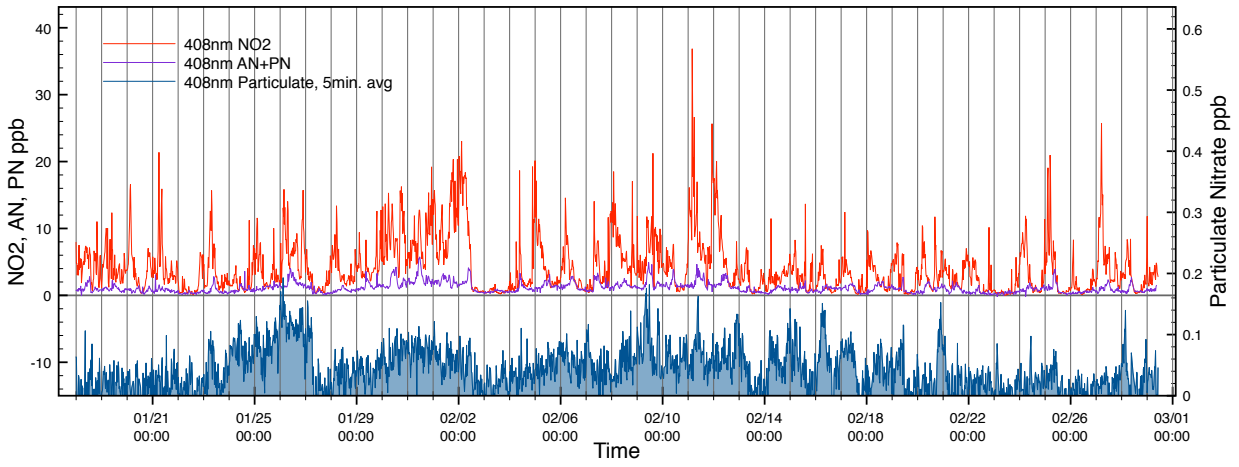

Figure 3-60. The time series of the data from the 408nm system.

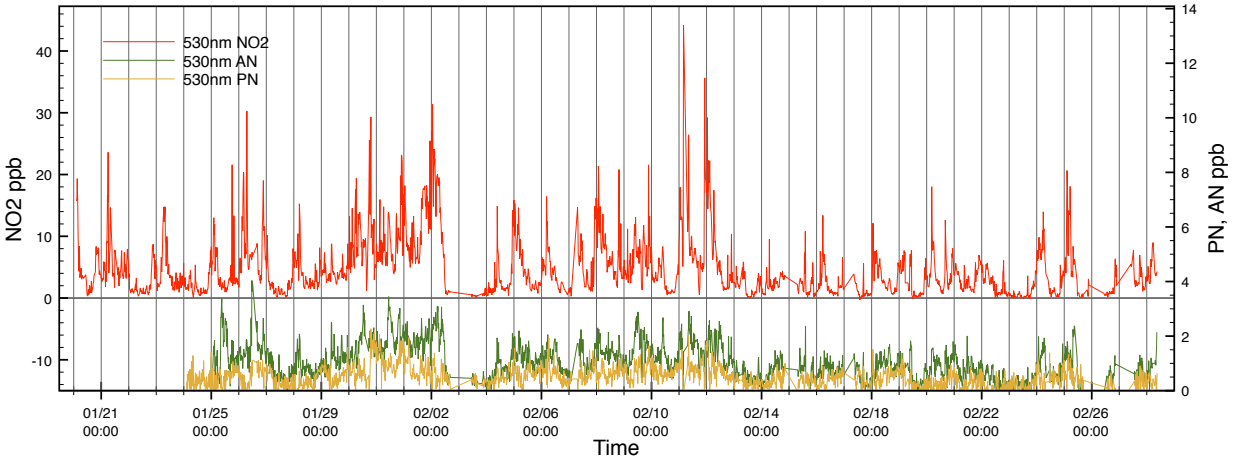

Figure 3-61. The time series of the data from the 530nm system.

Acknowledgements

We thank Questar Energy Products for site preparation and support. Robert McLaren acknowledges receipt of a York University Sabbatical Leave Fellowship, which partially funded his participation in the study. Shane Murphy acknowledges NSF Grant No. 1215926. Joel Thornton acknowledges NSF-AGS CAREER Grant No. 0846183.

The scientific results and conclusions, as well as any views or opinions expressed herein, are those of the author(s) and do not necessarily reflect the views of NOAA or the Department of Commerce.

REFERENCES

Aiken, A. C., et al. (2008), O/C and OM/OC ratios of primary, secondary, and ambient organic aerosols with high-resolution time-of-flight aerosol mass spectrometry., Environ. Sci Technol., 42, 4478-4485.

Alvarez, R. J., C. J. Senff, A. M. Weickmann, S. P. Sandberg, A. O. Langford, R. D. Marchbanks, W. A. Brewer, and R. M. Hardesty (2012), Reconfiguration of the NOAA TOPAZ Lidar for Ground-based Measurement of Ozone and Aerosol Backscatter, in Proceedings of the 26th International Laser Radar Conference, edited, pp. pp. 249 – 252, Porto Heli, Greece.

Alvarez, R. J., et al. (2011), Development and Application of a Compact, Tunable, Solid-State Airborne Ozone Lidar System for Boundary Layer Profiling, J. Atmos. Oceanic Technol., 28, 1258-1272.

Baker, A. K., A. J. Beyersdorf, L. A. Doezema, A. Katzenstein, S. Meinardi, I. J. Simpson, D. R. Blake, and F. S. Rowland (2008), Measurements of nonmethane hydrocarbons in 28 United States cities., Atmos Environ, 42, 170-182.

Baynard, T., E. R. Lovejoy, A. Petterson, S. S. Brown, D. Lack, H. D. Osthoff, P. Massoli, S. Ciciora, W. P. Dube, and A. R. Ravishankara (2007), Design and application of a pulsed cavity ring-down aerosol extinction spectrometer for field measurements, Aerosol Sci. Technol., 41, 447-462.

Brown, S. S. (2003), Absorption Spectroscopy in High-Finesse Cavities for Atmospheric Studies, Chem. Rev., 103, 5219-5238.

Brown, S. S., H. Stark, S. Ciciora, and A. R. Ravishankara (2001), In-situ measurement of atmospheric NO_3 and N_2O_5 via cavity ring-down spectroscopy, Geophys. Res. Lett., 28, 3227-3230.

Brown, S. S., H. Stark, S. Ciciora, R. J. McLaughlin, and A. R. Ravishankara (2002), Simultaneous in-situ detection of atmospheric NO_3 and N_2O_5 via cavity ring-down spectroscopy, Rev. Sci. Instr., 73, 3291-3301.

Busch, K. W., M. A. Busch, and Eds. (1999), Cavity-Ringdown Spectroscopy, American Chemical Society, Washington, DC.

Chen, H., et al. (2010), High-accuracy continuous airborne measurements of greenhouse gases (CO_2 and CH_4) using the cavity ring-down spectroscopy (CRDS) technique, Atmos. Meas. Tech., 3, 375-386.

COGCC (2007), Greater Wattenberg Area Baseline Study; Colorado Oil and Gas Conservation Commission (COGCC): Rep., Denver.

Crosson, E. R. (2008), A cavity ring-down analyzer for measuring atmospheric levels of methane, carbon dioxide, and water vapor, Appl. Phys. B, 92, 403–408.

Day, D. A., P. J. Wooldridge, M. B. Dillon, J. A. Thornton, and R. C. Cohen (2002), A thermal dissociation laser-induced fluorescence instrument for in situ detection of NO_2, peroxy nitrates, alkyl nitrates, and HNO_3, J. Geophys. Res., 107, 4046.

de Gouw, J., and C. Warneke (2007), Measurements of volatile organic compounds in the Earth's atmosphere using proton-transfer-reaction mass spectrometry, Mass Spectrom. Rev., 26, 223-257.

de Gouw, J. A., et al. (2005), The budget of organic carbon in a polluted atmosphere: Results from the New England Air Quality Study in 2002, J. Geophys. Res., 110, D16305.

Dlugokencky, E. J., R. C. Myers, P. M. Lang, K. A. Masarie, A. M. Crotwell, K. W. Thoning, B. D. Hall, J. W. Elkins, and L. P. Steele (2005), Conversion of NOAA atmospheric dry air CH_4 mole fractions to a gravimetrically prepared standard scale, J. Geophys. Res., 110, D18306.

Dube, W. P., S. S. Brown, H. D. Osthoff, M. R. Nunley, S. J. Ciciora, M. W. Paris, R. J. McLaughlin, and A. R. Ravishankara (2006), Aircraft instrument for simultaneous, in-situ measurements of NO_3 and N_2O_5 via cavity ring-down spectroscopy, Rev. Sci. Intr., 77, 034101.

EDL (2011), EDL Final Report: Uinta Basin Winter Ozone and Air Quality Study, December 2010 - March 2011Rep.

Finlayson-Pitts, B. J., M. J. Ezell, and J. N. J. Pitts (1989), Formation of chemically active chlorine compounds by reactions of atmospheric NaCl particles with gaseous N_2O_5 and $ClONO_2$, Nature, 337(6204), 241-244.

Flocke, F. M., A. J. Weinheimer, A. L. Swanson, J. M. Roberts, R. Schmitt, and S. Shertz (2005), On the measurement of PANs by gas chromatography and electron capture detection, J. Atmos. Chem., 52(1), 19-43.

Fuchs, H., W. P. Dube, S. Ciciora, and S. S. Brown (2008), Determination of Inlet Transmission and Conversion Efficiencies for in Situ Measurements of the Nocturnal Nitrogen Oxides, NO_3, N_2O_5 and NO_2, via Pulsed Cavity Ring-Down Spectroscopy, Anal. Chem., 80, 6010-6017.

Fuchs, H., W. P. Dube, B. M. Lerner, N. L. Wagner, E. J. Williams, and S. S. Brown (2009), A sensitive and versatile detector for atmospheric NO_2 and NO_x based on blue diode laser cavity ring-down spectroscopy, Environ. Sci Technol., 43, 7831-7836.

Ghosh, B., D. K. Papanastasiou, R. K. Talukdar, J. M. Roberts, and J. B. Burkholder (2012), Nitryl chloride (ClNO2): UV-Vis absorption spectrum between 210 and 296K and O(3P) quantum yield at 193 and 248 nm, J. Phys. Chem. A., 116, 5796-5805.

Gilman, J. B., et al. (2010), Ozone variability and halogen oxidation within the Arctic and sub-Arctic springtime boundary layer, Atmos. Chem. Phys., 10, 10223-10236.

Goldan, P. D., W. C. Kuster, E. Williams, P. C. Murphy, F. C. Fehsenfeld, and J. Meagher (2004), Nonmethane hydrocarbon and oxy hydrocarbon measurements during the 2002 New England Air Quality Study, J. Geophys. Res., 109, D21309.

HITRAN (2008), http://www.cfa.Harvard.edu/HITRAN/HITRAN2008/ edited.

IMPROVE (2011), IMPROVE report, Spatial and Seasonal Patterns and Temporal Variability of Haze and its Constituents in the United States: Report Rep.

Jayne, J. T., D. C. Leard, X. Zhang, P. Davidovits, K. A. Smith, C. E. Kolb, and D. R. Worsnop (2000), Development of an aerosol mass spectrometer for size and composition. Analysis of submicron particles, Aerosol Sci. Technol., 33, 49-70.

Langford, A. O., C. J. Senff, R. J. Alvarez, R. M. Banta, R. M. Hardesty, D. D. Parrish, and T. B. Ryerson (2011), Comparison between the TOPAZ airborne ozone lidar and in situ measurements during TexAQS 2006, J. Atmos. Oceanic Technol., 28, 1243-1257.

Lerner, B. M., P. C. Murphy, and E. J. Williams (2009), Field measurements of small marine craft gaseous emission factors during NEAQS 2004 and TexAQS 2006, Environ. Sci Technol., 43, 8213-8219.

Levy II, H. (1971), Normal atmosphere: Large radical and formaldehyde concentrations predicted, Science, 173, 141-143.

Middlebrook, A. M., R. Bahreini, J. L. Jimenenz, and M. R. Canagaratna (2011), Evaluation of composition-dependent collection efficiencies for the Aerodyne Aerosol Mass Spectrometer using field data, Aerosol Sci. Technol., 46, 258-271.

National Research Council, and C. o. T. O. F. a. Chemistry (1992), Rethinking the Ozone Problem in Urban and Regional Air Pollution National Academy Press Washington, D.C.

Orsini, D., Y. Ma, A. Sullivan, B. Sierau, K. Baumann, and R. J. Weber (2003), Refinements to the particle-into-liquid sampler (PILS) for ground and airborne measurements of water soluble aerosol composition, Atmos Environ, 37, 1243-1259.

Osthoff, H. D., et al. (2008), High levels of nitryl chloride in the polluted subtropical marine boundary layer, Nature Geoscience, 1, 324-328.

Pettersson, A., E. R. Lovejoy, C. A. Brock, S. S. Brown, and A. R. Ravishankara (2004), Measurement of aerosol optical extinction at 532 nm with pulsed cavity ring down spectroscopy, J. Aerosol Sci., 35, 995-1011.

Platt, U., and J. Stutz (2008), Differential Optical Absorption Spectroscopy: Principles and Applications, 597 pp., Springer Verlag, Heidelberg.

Quinn, P. K., and D. Coffman (1998), Local closure during the First Aerosol Characterization Experiment (ACE 1): Aerosol mass concentration and scattering and backscattering coefficients, J. Geophys. Res., 103, 16,575-516,596.

Quinn, P. K., et al. (2000), Surface submicron aerosol chemical composition: What fraction is not sulfate?, J. Geophys. Res., 105, 6785-6805.

Quinn, P. K., et al. (2004), Aerosol optical properties measured on board the Ronald H. Brown during ACE-Asia as a function of aerosol chemical composition and source region, J. Geophys. Res., 109, D19S01.

Roberts, J. M. (1990), The atmospheric chemistry of organic nitrates, Atmos Environ, 24A, 243-287.

Roberts, J. M., H. Tanimoto, F. Flocke, A. Weinheimer, B. T. Jobson, D. Riemer, E. Atlas, E. J. Williams, and F. C. Fehsenfeld (2001a), Observations of APAN during TexAQS 2000, Geophys. Res. Lett, 28, 4195-4198.

Roberts, J. M., F. Flocke, C. A. Stroud, D. Hereid, E. J. Williams, F. C. Fehsenfeld, W. Brune, M. Martinez, and H. Harder (2002), Ground-based measurements of PANs during the 1999 Southern Oxidants Study Nashville intensive, J. Geophys. Res., 107.

Roberts, J. M., C. A. Stroud, B. T. Jobson, M. Trainer, D. Hereid, E. J. Williams, F. C. Fehsenfeld, W. Brune, M. Martinez, and H. Harder (2001b), Application of a sequential reaction model to PAN and aldehyde measurements in two urban areas, Geophys. Res. Lett, 28, 4583-4586.

Roberts, J. M., et al. (2010), Measurement of HONO, HNCO, and other inorganic acids by negative-ion proton-transfer chemical-ionization mass spectrometry (NI-PT-CIMS): Application to biomass burning emissions., Atmos. Meas. Tech., 3, 981-990.

Roberts, J. M., et al. (2011), Isocyanic acid in the atmosphere and its possible link to smoke-related health effects, PNAS, 108, 8966-8971.

Roberts, J. M., et al. (1995), Relationships between PAN and ozone at sites in eastern North America, J. Geophys. Res., 100, 22821-22830.

Roberts, J. M., et al. (2003), An examination of the chemistry of peroxycarboxylic nitric anhydrides (PANs) and related VOC chemistry during TexAQS 2000 using ground-based measurements, J. Geophys. Res., 108.

Sander, S. P., et al. (2006), Chemical Kinetics and Photochemical Data for Use in Atmospheric Studies, Evaluation Number 15, NASA/JPL, Pasadena, CA.

Schauer, J. J., M. J. Kleeman, G. R. Cass, and B. R. T. Simoneit (2002), Measurement of Emissions from Air Pollution Sources. 5. C_1–C_{32} Organic Compounds from Gasoline-Powered Motor Vehicles, Environ. Sci Technol., 36, 1169-1180.

Senff, C. J., R. J. Alvarez, R. M. Hardesty, R. M. Banta, and A. O. Langford (2010), Airborne lidar measurements of ozone flux downwind of Houston and Dallas, J. Geophys. Res., 115, D20307.

Serdyuchenko, A., V. Gorshelev, M. Weber, and J. P. Burrows (2011), New broadband high-resolution ozone absorption cross-sections, Spectroscopy Europe, http://www.spectroscopyeurope.com/articles/55-articles/3082-new-broadband-high- resolution-ozone-absorption-cross-sections.

Slusher, D. L., L. G. Huey, D. J. Tanner, F. M. Flocke, and J. M. Roberts (2004), A thermal dissociation-chemical ionization mass spectrometry (TD-CIMS) technique for the simultaneous measurement of peroxyacyl nitrates and dinitrogen pentoxide, J. Geophys. Res., 109(D19), D19315, doi:19310.11029/12004JD004670.

Stutz, J., E. S. Kim, U. Platt, P. Bruno, C. Perrino, and A. Febo (2000), UV-Visible absorption cross section of nitrous acid, J. Geophys. Res., 105, 14585–14592.

Thornton, J. A., P. J. Wooldridge, and R. C. Cohen (2000), Atmospheric NO_2: In situ laser-induced fluorescence detection at parts per trillion mixing ratios, Anal. Chem., 72, 528-539.

Thornton, J. A., et al. (2010), A large atomic chlorine source inferred from mid-continental reactive nitrogen chemistry, Nature, 464, 271-274.

Ulbrich, I. M., M. R. Canagaratna, Q. Zhang, D. R. Worsnop, and J. L. Jimenenz (2009), Interpretation of organic components from Positive Matrix Factorization of aerosol mass spectrometric data, Atmos. Chem. Phys., 9, 2891-2918.

Vandaele, A. C., S. P.C., J. M. Guilmot, M. Carleer, and R. Colin (1994), SO_2 absorption cross section measurement in the UV using a Fourier transform spectrometer, J. Geophys. Res., 99, 25,599–525,605.

Vandaele, A. C., C. Hermans, S. Fally, M. Carleer, R. Colin, M. F. Merienne, A. Jenouvrier, and B. Coquart (2002), High-resolution Fourier transform measurement of the NO_2 visible and near-infrared absorption cross sections: Temperature and pressure effects, J. Geophys. Res., 107, 4348.

Veres, P. R., et al. (2011), Evidence of rapid production of organic acids in an urban air mass, Geophys. Res. Lett, 38, L17087.

Veres, P., J. M. Roberts, C. Warneke, D. Welsh-Bon, M. Zahniser, S. Herndon, R. Fall, and J. de Gouw (2008), Development of negative-ion proton-transfer chemical-ionization mass spectrometry (NI-PT-CIMS) for the measurement of gas-phase organic acids in the atmosphere, Int. J. Mass Spectrom., 274, 48-55.

Voigt, S., J. Orphal, and J. P. Burrows (2002), The temperature and pressure dependence of the absorption cross-sections of NO_2 in the 250-800 nm region measured by Fourier-transform spectroscopy, J. Photochem. Photobiol. A: Chem. , 149, 1-7.

Wagner, N. L., W. P. Dube, R. A. Washenfelder, C. J. Young, I. B. Pollack, T. B. Ryerson, and S. S. Brown (2011), Diode laser-based cavity ring-down instrument for NO_3, N_2O_5, NO, NO_2 and O_3 from aircraft, Atmos. Meas. Technol., 4, 1227-1240.

Wallington, T., M. Ammann, R. Atkinson, R. A. Cox, C. J., R. Hynes, M. E. Jenkin, W. Mellouki, M. J. Rossi, and J. Troe (2012), Evaluated kinetic and photochemical data, IUPAC Subcommittee for Gas Kinetic Data Evaluation, http://www.iupac-kinetic.ch.cam.ac.uk/index.html.

Washenfelder, R. A., W. P. Dube, N. L. Wagner, and S. S. Brown (2011), Measurement of atmospheric ozone by cavity ring-down spectroscopy, Environ. Sci Technol., 45, 2938-2944.

Weber, R. J., D. Orsini, Y. Daun, Y.-N. Lee, P. J. Klotz, and F. Brechtel (2001), A particle-into-liquid collector for rapid measurement of aerosol bulk chemical composition, Aerosol Sci. Technol., 35, 718-727.

Williams, E. J., B. M. Lerner, P. C. Murphy, S. C. Herndon, and M. S. Zahniser (2009), Emissions of NO_x, SO_2, CO, and HCHO from commercial marine shipping during the Texas Air Quality Study (TexAQS) 2006, J. Geophys. Res., 114, D21306.

Williams, J., et al. (2000), A method for the airborne measurement of PAN, PPN, and MPAN, J. Geophys. Res., 105, 28,943-928,960.

Wooldridge, P. J., et al. (2010), Total Peroxy Nitrates (SPNs) in the atmosphere: the Thermal Dissociation-Laser Induced Fluorescence (TD-LIF) technique and comparisons to speciated PAN measurements, Atmos. Meas. Tech., 3, 593-607.

Yokelson, R. J., J. B. Burkholder, R. W. Fox, and A. R. Ravishankara (1997), UV photodissociation of $ClONO_2$: Time-resolved absorption studies of product quantum yields, 101, 6667-6678.

Young, C. J., et al. (2012), Vertically resolved measurements of nighttime radical reservoirs in Los Angeles and their contribution to the urban radical budget, Environ. Sci Technol., submitted.

Zhao, C. L., and P. P. Tans (2006), Estimating uncertainty of the WMO mole fraction scale for carbon dioxide in air, J. Geophys. Res., 111, D08S09.

Zheng, W., F. M. Flocke, G. S. Tyndall, A. Swanson, J. J. Orlando, J. M. Roberts, L. G. Huey, and D. J. Tanner (2011), Characterization of a thermal dissociation chemical ionization mass spectrometer for the measurement of peroxy acyl nitrates (PANs) in the atmosphere, Atmos. Chem. Phys., 11, 6529-6547.

CHAPTER IV

EMISSIONS INVENTORY REPORT

Marc Mansfield, Devin Moss, Courtney Hall, Emily Smith, and Howard Shorthill
Bingham Entrepreneurship & Energy Research Center, Utah State University, Vernal, UT.

INTRODUCTION

This document reports the results of an emissions inventory conducted during the first quarter of 2012 in conjunction with the 2012 Uintah Basin Winter Ozone Study (see Table 4-1 for inventory summary). Unless otherwise stated, all results are for February 2012, the peak season for ozone production in the Basin and the focus of this inventory. All assumptions involved in arriving at these numbers are explained in the main body of the text. Some estimates are not well constrained, so a careful examination of provided assumptions and caveats is recommended.

Several different classifications of hydrocarbons are used. VOC stands for "volatile organic compounds," but in the context of ozone chemistry, the term usually designates all volatile organics except methane and ethane, since these have relatively limited ozone reactivity. At sufficient concentrations, however, methane and ethane do contribute to ozone formation and, therefore, is included in this inventory. NMHC designates "non-methane hydrocarbons," so this category is equivalent to VOC plus ethane. It is sometimes possible to estimate the contribution of methane and ethane when only VOC values are given, to estimate ethane and VOC when only methane is given, or to estimate methane when only NMHC are given.

Table 4-1. Uintah Basin emissions estimates by category for Feb. 2012, in tons per month. Surrogate column is explained below. PS (point source) indicates that actual coordinates of the source are known or will be known, rendering surrogate representation unnecessary.

SOURCE CATEGORY	VOC	METHANE	NMHC	NO_X	SURROGATE[1]
OIL & GAS EMISSIONS					
• **Glycol dehydrators**	2200†			13†	GP
• **Heaters**				110†	W
• **Drill rigs**		0.39•	4.0•	330† or 156•	W† or PS•
• **Workover rigs**		0.018•	0.18•	13† or 6.9•	W† or PS•
• **Fracking processes**		0.055•	0.56•	22•	W
• **Pneumatic devices**	1850†				W
• **Fugitives**	240†				W
• **Venting processes**	180†				GP
• **Condensate tanks**	1700†				CP
• **Oil tanks**	1600†				OP
• **Pneumatic pumps**	1000†				W
• **Compressor engines**◈	9†			47†	GP
• **Artificial lift engines**	75†			240†	OP
• **Other**	240†			13†	W
• **Compressor stations**	130			390	PS
• **Gas plants**	25			14	PS
• **Evap. ponds, land farms**[2]	0			0	PS
• **Pipeline fugitive emissions**[5]		72	3.8		GP
TOTAL OIL & GAS	**9200**	**72**	**8.5**	**1000 to 1200**[3]	
NON OIL & GAS EMISSIONS					
• **Bonanza Power Plant**				610	PS
• **Mobile sources**[6]		4.4	68	106	P
• **Biogenic/Agricultural**		420			P (?)
• **Home Heating**		49	22	2.2	P
• **Land Fills**		37			PS
• **Natural Hydrocarbon Seeps**[5]		500*	25*		W
TOTAL NON OIL & GAS		**510 to 1000**[4]	**90 to 120**[4]	**720**	
GRAND TOTAL	**9200**	**580 to 1100**[4]	**98 to 130**[4]	**1700 to 1900**[3]	

◈ Non-centralized.
† Estimates taken directly from WRAP 2012 projections.
• Estimates based on 2012 industry survey.
* Poorly constrained estimate (tightest bounds at this time put value between 30 and 30,000 tons/month).
[1] Surrogate: CP=condensate production, GP=gas production, OP=oil production, P=population, PS=point source(s), W=wells
[2] Data insufficient to estimate emissions for all ponds in winter conditions.
[3] Lower value results if the 2012 industry survey replaces WRAP projections.
[4] Lower value results if the contribution of natural seepage is omitted.
[5] Assumes 95/5 split in CH_4/NMHC percentages (Rice, et al, 1992).
[6] Likely does not include a complete accounting of mobile sources related to the oil and gas industry.

RELATED WORK

The only other region in the world known to produce winter ozone above Environmental Protection Agency (EPA) National Ambient Air Quality Standards (NAAQS) is the Upper Green River Basin (UGRB) in Wyoming. Ozone was detected there several years before the Uintah Basin, and Sublette County has already moved into non-attainment with respect to the ozone NAAQS. An emissions inventory was assembled for the Upper Green, (WDEQ, 2011), and there are some indications that it underestimates emissions (Stoeckenius and Ma, 2010). Another telling point is that the Wyoming Division of Air Quality (WDAQ) conducted surprise spot-tests of a number of engines throughout the state and found a significant number to be emitting higher than reported AP-42 factors (Dietrich, 2011).

PREVIOUS EMISSIONS INVENTORIES AND SURVEYS

2006 WRAP-III and 2012 WRAP-III Projections

Working under the auspices of the Western Regional Air Partnership (WRAP), ENVIRON International Corporation has been contracted to perform emissions inventories throughout the Western United States. These inventories have had an important impact on air quality studies and on permitting of new facilities. They have gone through multi-year iterations, the third of which—usually referred to as WRAP-III—covers the year 2006. ENVIRON has also prepared a document that projects the 2006 WRAP-III estimates to the year 2012 (Friesen, et al 2009; Bar-Ilan, et al 2009).

Many of the WRAP-III estimates are based on self-reporting by the oil and gas industry. WRAP operationally defines the Uintah Basin as Wasatch, Duchesne, Uintah, Carbon, Grand, and Emery counties. Although combining these counties for the purposes of organization and reporting is understood, the Uintah Basin airshed only includes Duchesne and Uintah counties; therefore, only those two counties are included in this report. (Wasatch County has no oil or gas industry and its only population center is separated from the Uintah Basin by an 8000-foot pass, and the coal bed methane wells of Carbon, Grand, and Emery counties are separated from the Uintah Basin by a 9000-foot pass.)

Unless stated otherwise, each emission category in the WRAP III is assumed to have a uniform annual temporal distribution, meaning that survey numbers for annual emissions are multiplied by a factor 29/366 (7.92%) to achieve a February 2012 basis. This assumption is based on the observation that the Uintah Basin petroleum industry operates at about the same magnitude year-round.

BLM 2010 Inventory

The Bureau of Land Management (BLM) has contracted with outside consultants to develop its own projection of the WRAP-III inventory. This inventory has yet to be released publicly and is not available for comparison in this document. When available, the BLM projection will be coordinated with this and the WRAP studies to inform future USU inventory and modeling efforts.

WEA 2012 Survey

In conjunction with the current study, Western Energy Alliance (WEA) submitted surveys to oil and gas operators that sought information on well drilling and fracking activity during the first quarter of 2012. As of this writing, five companies—Anadarko, Newfield, Gasco, EOG, and XTO—have responded, a 72% response rate. The Utah Division of Oil, Gas, and Mining (UDOGM) also collects data on well drilling and completions. Data from both sources will help compensate for under-reporting.

SURROGATE DISTRIBUTIONS

Computer models require spatial and temporal resolution of emissions data. Typical resolutions might be two to four km spatially and seconds or minutes temporally. Inventories, however, lack such resolution. WRAP-III, for example, gives annual emissions broken down by county. In such situations, it is customary to use "surrogate" distributions, i.e., spatial or temporal distributions that are already known and that provide a reasonable approximation of the actual distribution. For example, below we assume that the distribution of wood stoves follows the population distribution.

For the oil and gas industry, adequate surrogate distributions are available from the UDOGM database (UDOGM, 2012), which reports monthly the oil and gas production of each well in the state, including the number of days during which any given well was actually producing. Longitude and latitude for each well are also given. The maps in Figures 4-1 through 4-4 display data for the entire quarter, but actual modeling resolution is monthly. The last column of Table 4-1 indicates which surrogate distribution will be applied in any given situation.

The maps indicate three broad regions of oil and gas industry. First is the broad swath arching across the northwest part of the Basin from an area east of Bluebell to the Cedar Rim area west of Duchesne. Second is the region near the Pleasant Valley/Pariette Ridge/Monument Butte area. Third is the region near the Red Wash/Ouray/Bonanza triangle. The first two regions, lying mostly in Duchesne County, produce mostly oil, while the third, located in Uintah County, produces mostly gas.

Oil and Gas Production

Figures 4-1 and 4-2 display the spatial distribution of oil and gas production, respectively, for the three months of January-March 2012 and will be used as surrogate distributions as specified in Table 4-1. Total oil and gas production figures for this time period are given in Table 4-2.

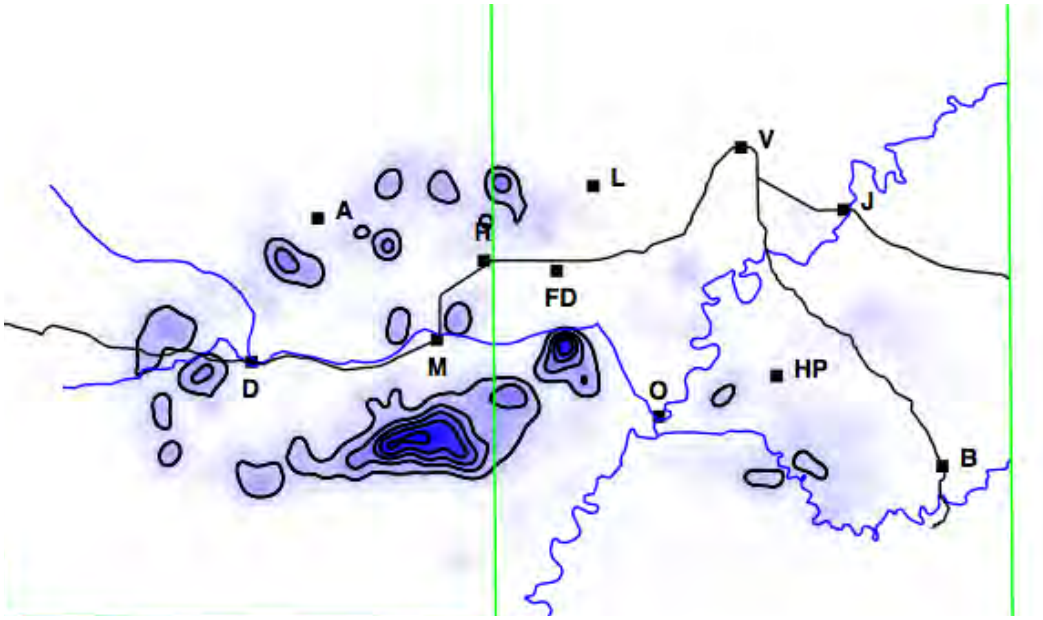

Figure 4-1. Spatial distribution of oil production, Q1 2012. Location symbols here and in subsequent maps: A=Altamont, B=Bonanza, D=Duchesne, FD=Fort Duchesne, HP=Horse Pool, J=Jensen, L=Lapoint, M=Myton, O=Ouray, R=Roosevelt, V=Vernal. County boundaries are in green, major highways in black, and rivers in blue. Contours are at intervals of 2000 bbl/km^2 up to 10000 bbl/km^2.

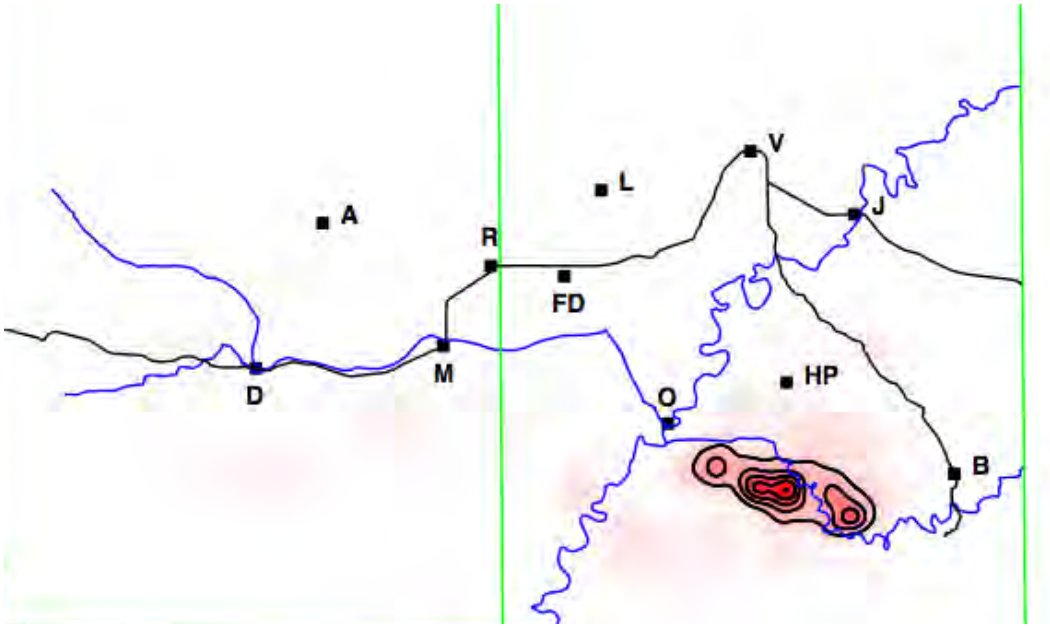

Figure 4-2. Spatial distribution of gas production, Q1 2012. Contours are at intervals of 10^8 cf/km^2 up to 5×10^8 cf/km^2.

Table 4-2. Oil and gas production in Uintah and Duchesne Counties.

Report Month	Oil (10^6 bbl)	Gas (10^9 cf)	Gas Condensate (10^6 bbl)	Full-Time Equivalent Wells
Jan. 2012	1.72	29.0	0.217	7824
Feb. 2012	1.65	28.3	0.202	7971
Mar. 2012	1.81	30.7	0.229	8175
Quarter Total	**5.18**	**88.0**	**0.648**	**7991**

Gas Condensate Production

Gas condensate refers to a petroleum product that is in the gas phase at underground temperatures and pressures but which condenses to a liquid at the surface. Unfortunately, the UDOGM database does not differentiate between gas condensate and produced oil. It does, however, differentiate between "oil" and "gas" wells, the distinction being one of degree, as most gas wells produce some oil, and most oil wells produce some gas. For the purposes of constructing a gas condensate surrogate distribution from the UDOGM database, "gas condensate" will be defined operationally as oil produced from any well designated by UDOGM as a gas well. The resulting distribution appears as Figure 4-3. See Table 4-2 for a summary of gas condensate production according to this definition.

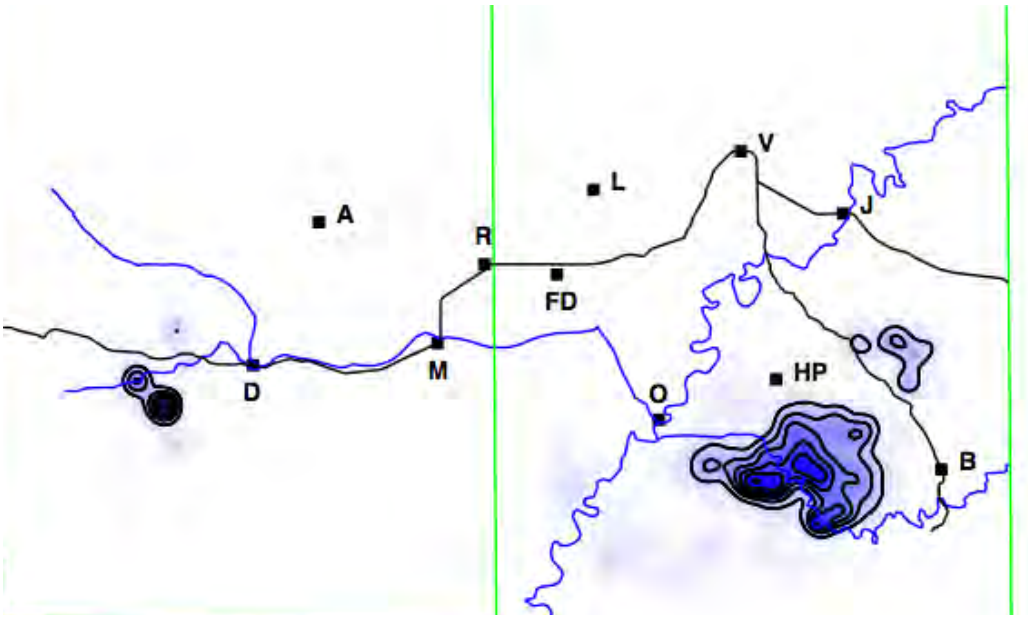

Figure 4-3. Spatial distribution of gas condensate production for the first quarter of 2012. Contours are at intervals of 400 bbl/km^2 up to 2400 bbl/km^2.

Well Density

The density of active oil and gas wells for the period January-March 2012 appears in Figure 4-4. The figure only includes wells that actually produced during the time period. To qualify as one full-time equivalent, a well had to be operational for the entire time period. Otherwise, the contribution of a well was apportioned according to the actual number of days of operation. The number of full-time-equivalent active wells is given in Table 4-2.

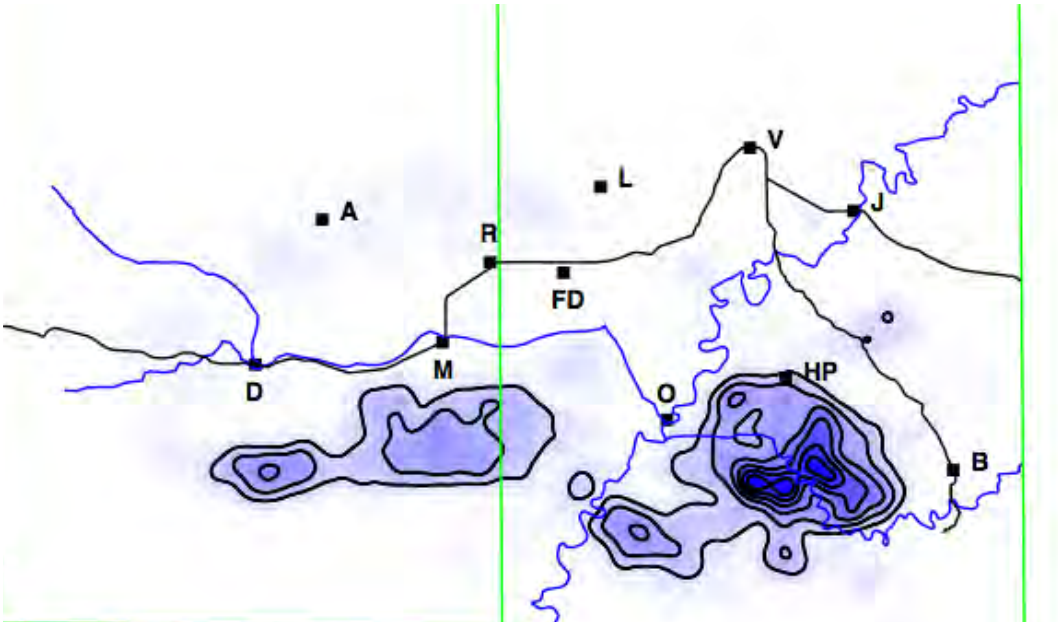

Figure 4-4. Spatial distribution of active wells, Q1 2012. Contours are at intervals of two full-time-equivalent wells per km^2 up to 12 wells/km^2.

Population Density

Population figures were obtained from the 2010 U.S. Census. The resulting distribution map appears in Figure 4-5.

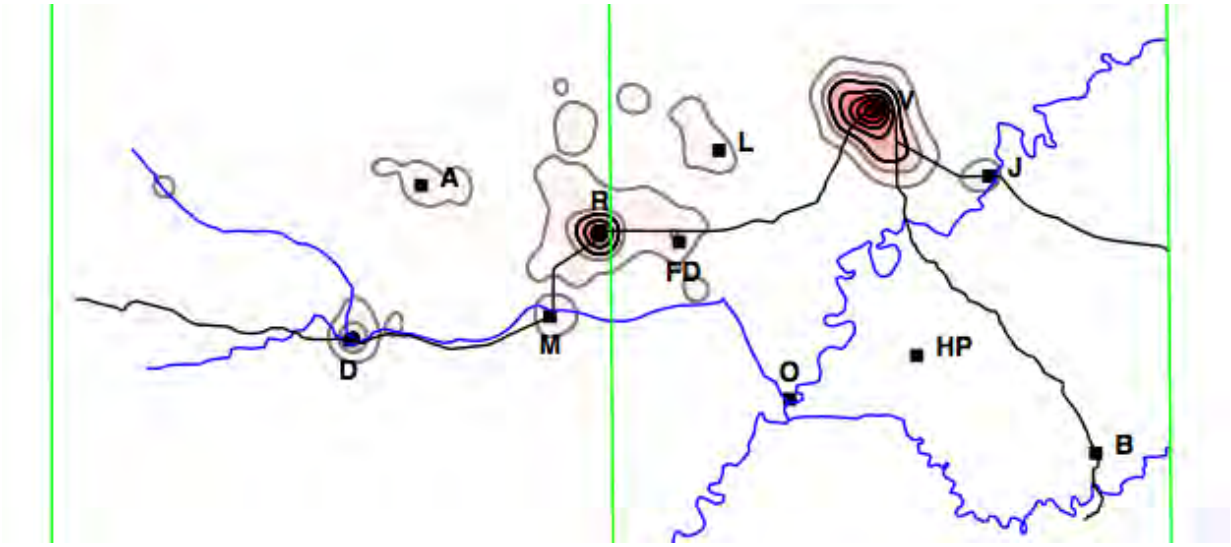

Figure 4-5. Population density in the Uintah Basin. Total population is 51,182. Light gray contours are at 10 and 50 individuals/km^2. Solid contours are at intervals of 100 individuals km^{-2} up to 500.

OIL & GAS EMISSIONS

For convenience in categorizing, this section considers emissions from the oil and gas industry. Emissions from all other sources are covered below in the section, "Non Oil and Gas Emissions."

WRAP-III does not include any non oil-and-gas emissions, and several oil-and-gas categories are also omitted. For those emissions categories covered by WRAP-III, the emissions quantities provided by the WRAP-III 2012 projection have been adopted, as indicated in Table 4-1. The original WRAP-III documents (Friesen, et al, 2009; Bar-Ilan, et al, 2009) are available, and review of methodologies and assumptions is encouraged. Estimates are provided for all remaining significant source categories. All additions or alterations to the WRAP-III numbers are explained below, and also appear in Table 4-1.

Emissions categories unavailable at the time of the WRAP-III inventory or that have become obsolete because of newer data can be summarized as follows:

1. The WEA industry survey gives a detailed picture of the drilling and fracking activity during an eight-week period from mid-January to mid-March 2012.
2. Probably because they have come on line since 2006, several major point source emitters (compressor stations, gas plants) are not documented by WRAP-III.
3. Due to minor source classification and absent report requirement, none of the 90 or so smaller compressor stations and gas plants was included in WRAP-III. It was observed, however, that these sources collectively emit about as much as the *ca.* 20 major sources.

4. Produced water disposal sites (evaporation ponds, land farms) were not included in WRAP-III.
5. Fugitive emissions from pipelines that transport natural gas from wellheads to compressor stations were not integrated in WRAP-III estimates.

This study attempts to estimate the emissions contributions of sources not included in WRAP III.

Drilling and Fracking Activity: Results of Industry Survey

Drill Rigs, New Wells (Spuds)

Drilling activities are an important source of emissions because of the large diesel engines powering the drill rigs. Uintah Basin operators were asked to submit reports on drilling activity for the eight-week period from 15 January to 10 March 2012. Five companies responded, and results are summarized in Table 4-3. One hundred three new wells were drilled by these companies over the eight-week reporting period, and drilling operations consumed 977,000 gallons of diesel fuel. According to the UDOGM database, 1074 new wells were completed in all of 2011, 777 of which were drilled by the five respondent companies. In other words, these five companies accounted for 72.3% of all new wells drilled in 2011.

To compensate for non-responses to the survey, the same ratio over the reporting period is assumed. It is estimated, therefore, that non-reporting companies consumed 373,000 gallons of diesel fuel during the same eight-week period. While accurate spatial and temporal distributions of diesel consumed by the five reporting companies exist (daily fuel consumption and longitude and latitude are reported for each well drilled), it is assumed that the additional 373,000 gallons are distributed uniformly in time (6669 gal/day), and well density as a surrogate is used for spatial distribution. Figure 4-6 displays the daily diesel consumption according to these assumptions.

Table 4-3. Statistics on new well drilling and completions. RIS = Reported in Survey.

COMPANY	Number of New Wells RIS	2011 Completions Reported to State	Fuel Consumption (10^3 gal of diesel) RIS
Anadarko	56	394	555
Newfield	43	313	330
EOG	2	44	75
XTO	2	25	17
Gasco	0	1	0
SUB-TOTAL	**103**	**777**	**977**
All others	not reported	297	373 (estimated)

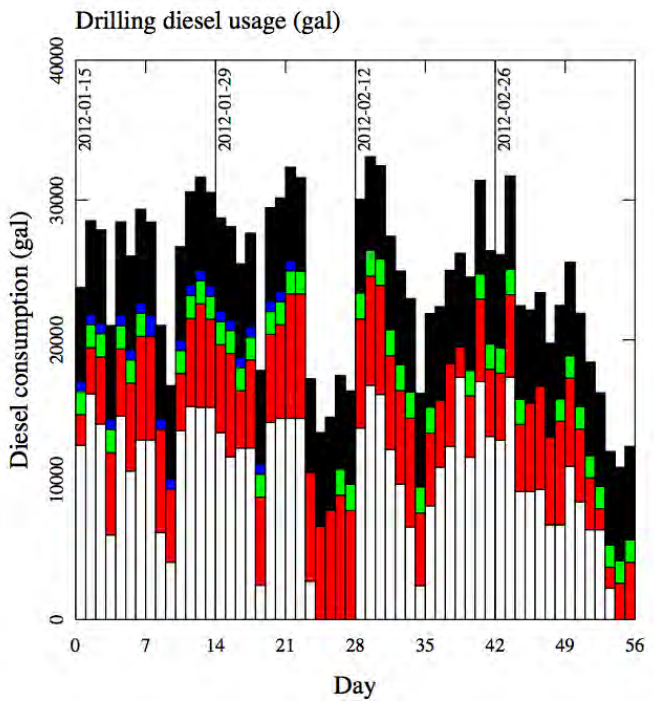

Figure 4-6. Daily consumption of diesel fuel for the drilling of new wells, 15 Jan. - 10 Mar. 2012. Contributions for Anadarko, Newfield, EOG, and XTO are shown respectively in white, red, green, and blue. Estimated contributions for non-responding companies are shown in black.

AP-42 emissions factors for the large diesel engines used in these activities permit the following emissions estimates (AP-42, 2012): (0.219 ton NO_x)/(1000 gal diesel), (5.5×10^{-4} ton CH_4)/(1000 gal diesel), and (5.6×10^{-3} ton NMHC)/(1000 gal diesel). From 1-29 February 2012, it is estimated that 711,000 gallons of diesel were consumed during new well drilling. Resulting values appear in Table 4-1.

Workover Rigs and Fracking

Over the eight-week reporting period, the four companies above reported fuel consumption by workover rigs and by fracking activities at 51,000 gal and 207,000 gal, respectively. Over the period 1-29 February 2012, the companies reported the use of 29,000 gal for workover drilling and 100,000 gal for fracking. The same adjustment for under-reporting and the same emissions factors are applied to arrive at the entries shown in Table 4-1.

Fracking Flowback Estimates

As part of the survey, operators were asked to report volumes of gas vented and flared as a result of fracking flowback during the reporting period. Due to the employment of green completions, Anadarko and EOG reported zero for both categories. Newfield reported that it had flared 4.1×10^3 cf of gas. Flaring of a few thousand cf should produce only negligible amounts of NO_x. (The appropriate emission factor is 76 lb $NO_x/10^6$ cf [EPA-AP42].) XTO did not complete this part of the survey, whether because it employs green completions or because it does not frack is not clear. In either case, since XTO's contribution would have been much smaller than Newfield's, further analysis of this category was not performed.

Major and Minor Oil-and-Gas Point Sources

Depending on location, either the State of Utah or the Ute Tribe has jurisdiction over air quality permitting and report collection, with the Tribe receiving technical assistance from EPA. Since no single jurisdiction had a complete list of point sources, emissions and location data were compiled from:

1. EPA Region 8 reports of ~20 "Title V" (major source) gas plants and compressor stations,
2. Utah Division of Air Quality permit information,
3. Uintah and Duchesne County governments GIS shape files and/or paper maps,
4. State and County tax assessors lists, and
5. Anadarko gas plant and compressor station maps and gas collection data, (Anadarko, 2012).

Since no industry standard exists for the naming of stations, and since station names are not always distinctive (e.g., "East Compressor Station") or are taken from geographical landmarks, stations occasionally shared the same or similar name. In this context, it was necessary to assume that such stations were distinct if (1) they had different operators, (2) were reported to be in different locations (different latitude/longitude, section/township, county), or (3) were listed separately by some governmental entity (seemingly, Anadarko and Mustang Fuel operate distinct Willow Creek stations).

Operators are required to submit an annual emissions report (AER) for each major (i.e., "Title V") emissions source, but not for minor sources. In the Uintah Basin, about 20 compressor stations and gas plants fall under the former category, and about 90 fall under the latter. Of the major sources, the latest available AER typically was from 2011, at times from 2010. For this study, 2012 Q1 emissions have been extrapolated from the latest AERs. Furthermore, as part of the permitting process for a construction application, a potential-to-emit statement (PTES) is required, which then becomes public record. Several PTESs were obtained, both for major and minor sources, and were used in this study to estimate emissions in the absence of AERs. It was found, however, that when both a PTES and an AER were available, the PTES was an over-estimate. When both were available, the "over-estimation rate" (OER) was applied to rescale emissions reported by the PTES. Finally, any minor source with neither a PTES nor an AER was assumed to emit at the same average rate as a minor source with a rescaled PTES.

Compressor Stations

A compressor station collects gas from individual wellheads through a network of pipelines and compresses the gas for transmission at higher density. These stations emit both VOC and NO_x. Gas compression activities are reported in the WRAP-III projection as either "centralized" (i.e., occurring at compressor stations) or "non-centralized" (i.e., occurring at the well head or during lateral transmission). WRAP-III projects non-centralized compressor emissions to be 9 tons/month of VOC and 47 tons/month of NO_x. These values also appear in Table 4-1. WRAP-III estimates centralized compressor emissions to be 31 tons/month of VOC and 130 tons/month of NO_x. However, based on the updated survey of compressor stations, as summarized in Table 4-4, centralized compressor emissions are estimated to be 130 tons/month of VOC and 390 tons/month of NO_x, values appearing in Table 4-1 under the "compressor stations" category. A complete list of stations with location and emissions data is available upon request.

Table 4-4. Emissions from Uintah Basin compressor stations. OER = over-estimation rate of PTES.

		#	VOC (ton/yr)	NO_x (ton/yr)
1	Number of Title V stations found.	19		
2	Number of stations in Line 1 with available PTESs.	3		
3	Average VOC and NO_x emissions of stations in Line 1.		43.5	69.1
4	OER of stations in Line 2.		3.6	3.4
5	Number of non Title V stations found.	88		
6	Number of stations in Line 5 with available PTESs.	14		
7	Average VOC and NO_x emissions of stations in Line 6, PTES reported		35.4	140.1
8	Adjustment (rescale) for over-estimation (Line 7 ÷ Line 4).		9.8	41.2
9	Total emissions estimate for Title V stations (Line 1 × Line 3).		826.5	1312.9
10	Total emissions estimate for non Title V stations (Line 5 × Line 8).		862.4	3625.6
11	**Total annual emissions** (Line 9 + Line 10).		**1688.9**	**4938.5**

Gas Plants

Gas plants play a role in purification of raw natural gas. Table 4-5 presents estimates for plant emissions of VOC and NO_x. Tables 4-4 and 4-5 confirm that, collectively, non-permitted stations emit about as much as permitted ones.

Table 4-5. Emissions from Uintah Basin gas plants. OER = over-estimation rate of PTES.

		#	VOC (ton/yr)	NO_x (ton/yr)
1	Number of Title V plants found.	3		
2	Number of plants in Line 1 with available PTESs.	2		
3	Average VOC and NO_x emissions of plants in Line 1.		51.1	35.8
4	OER of plants in Line 2.		2.5	4.2
5	Number of non Title V plants found.	6		
6	Number of plants in Line 5 with available PTESs.	2		
7	Average VOC and NO_x emissions of plants in Line 6, PTES reported		67.62	49.9
8	Adjustment (rescale) for over-estimation (Line 7 ÷ Line 4).		27.00	11.9
9	Total emissions estimate for Title V plants (Line 1 × Line 3).		153.3	107.4
10	Total emissions estimate for non Title V plants (Line 5 × Line 8).		162.0	71.4
11	**Total annual emissions** (Line 9 + Line 10).		**315.3**	**178.8**

Land Farms

A land farm is a type of disposal facility similar to a landfill. Unrecoverable petroleum or contaminated soil is discharged into a lined pit and blended with additional soil. Microbes in the soil break down the petroleum, and the liner prevents environmental contamination. When retired from service, the farm is covered over. While only two or three currently are in

operation in the Basin, emissions from such facilities are not at all characterized. At this time, no effort has been made to account for land farm emissions.

Evaporation Ponds

Produced water is brought to the surface along with oil and gas during production. It is too fouled with hydrocarbons to be discharged directly into the environment. One technology for its disposal is to discharge it into evaporation ponds. These are typically on the order of one- or two-meters deep and have surface areas of about an acre or two. A single disposal facility might contain only one or as many as a dozen separate ponds. The ponds are lined with thick polyethylene to sequester its contents from the environment. These ponds are assumed to be sources of VOC emissions. The hydrocarbons that find their way into the ponds either evaporate directly, are converted by bacteria to CO_2 or to lighter hydrocarbons which then vent, or they remain as sludge. At the end of their life cycle, the ponds are covered with soil, liner and all, raising the possibility that emissions can continue even from decommissioned, buried ponds.

Accounting for emissions from the evaporation ponds is problematic on three counts. First, as with compressor stations, simply assembling a complete list has proven to be a challenge, but combining data from several sources has led to some success. (A spreadsheet of all located facilities will be made available upon request.) Second, estimating emissions from facilities that have not been well characterized or studied has been uncertain. Third, gaining access to ponds has been complicated, often requiring extensive negotiations not only with management but also with legal representatives and environmental consultants. While USU has initiated emissions measurements at a few ponds, only preliminary data is available at this time. Additionally, it has been observed that evaporation ponds can freeze over during intense wintertime inversions, but data adequate to quantitatively assess the effects of temperature and state changes on hydrocarbon emissions from ponds is not yet available.

At this time, data are insufficient to estimate wintertime pond emissions for the entire Basin. Measurements must be obtained during all seasons and over both active and decommissioned ponds to provide better emissions characterization.

Fugitive Pipeline Emissions

The WRAP-III inventory omitted estimates for fugitive pipeline emissions from the wellheads to the compressor stations ("gathering" pipelines) because it lacked data on the relevant pipeline mileage. For this study, however, gathering pipeline mileage figures were found for both Anadarko and QEP at their respective websites (Anadarko, 2012; QEP, 2012). These companies are the major gas producers in the area, and as a coarse approximation it is assumed that these figures account for the bulk of gas transmission losses. Table 4-6 summarizes the emissions factor that has been applied to gathering pipeline (Shires et al., 2009).

Table 4-6. Estimate of fugitive pipeline emissions.

Anadarko mileage	1300 mi
QEP mileage	1030 mi
Total mileage	2330
Emissions factor	826 lb CH_4/(mi × yr)
Total annual emission	962 tons/year
Total monthly emissions	76 tons/month

Use of a "one-size-fits-all" emissions factor is probably a gross oversimplification. A more accurate calculation would count the number of fittings, flanges, etc. At this time, however, this is the best estimate that can be made given the available data.

NON OIL & GAS EMISSIONS

Bonanza Power Plant

The Bonanza Power Plant is the only PSD (Prevention of Significant Deterioration) facility in the Basin, and is also its single largest source of NO_x. The effects of emissions are mitigated by the use of a 600-ft stack, so wintertime emissions may often be injected above the mixing layer and may not contribute significantly to ozone formation. Modeling will provide better understanding of these effects.

The plant sends quarterly reports to the EPA with detailed hourly emissions data, which then become part of the public record. The Q1 2012 report was obtained from EPA's website (AMPD, 2012). Total emissions for February 2012 were 610 ton NO_x and 98 ton SO_2. Figure 4-7 plots daily emissions for the quarter. Most power plants do not emit a significant amount of VOC (Garcia et al., 1992).

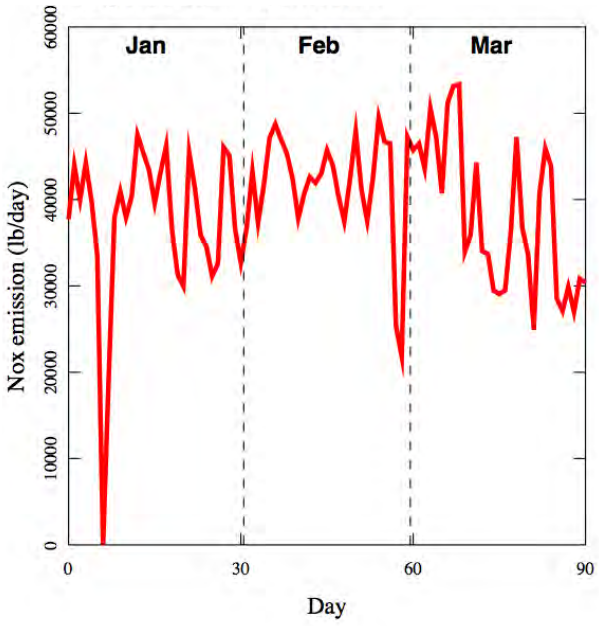

Figure 4-7. Daily NO_x emission from the Bonanza Power Plant, Q1 2012.

Other Point Sources

The only other significant point-source emitters of which we are aware are the Simplot Phosphate Mine, 10 mi north of Vernal, and the American Gilsonite Mine, near Bonanza. Both qualify as minor sources, so emissions data are not readily available. Futhermore, the phosphate mine is situated on the southern flank of the Uinta Mountains and typically remains above the inversion layer during periods of winter ozone production.

Mobile Sources

The dominant contribution in this source category is emissions by vehicles. The calculation reported here used the EPA-approved MOVES computer program and was performed by Patrick Barickman, Richard McKeague, and Peter Verschoor of the Utah Division of Air Quality. MOVES uses meteorological variables such as relative humidity and temperature, which were obtained from the MesoWest database (Mesowest, 2012), and data on the number and types of registered vehicles and the number of vehicle miles traveled, which were supplied to the Division by the Utah Department of Transportation. MOVES estimates hourly emissions based on these data. The extent to which these data accurately represent mobile source emissions in oil and gas producing areas in the Uintah Basin is unclear since the Department of Transportation does not routinely collect traffic data on rural or dirt roads (Virgen, 2012). Runs performed for six separate days during February 2012 included four weekdays and two weekends. Table 4-7 summarizes the results of these calculations.

Table 4-7. Mobile non oil-and-gas emissions: summary of MOVES runs. All units are tons/day.

	Duchesne County			Uintah County			TOTAL		
Date	**CH_4**	**NMHC**	**NO_x**	**CH_4**	**NMHC**	**NO_x**	**CH_4**	**NMHC**	**NO_x**
02/01/2012, Wed	0.07	1.02	1.51	0.10	1.52	2.25	0.17	2.54	3.76
02/07/2012, Tue	0.08	1.09	1.52	0.11	1.60	2.26	0.19	2.69	3.78
02/13/2012, Mon	0.06	0.89	1.49	0.08	1.35	2.22	0.14	2.24	3.71
02/16/2012, Thu	0.06	0.93	1.50	0.09	1.40	2.24	0.15	2.33	3.74
02/19/2012, Sun	0.05	0.82	1.39	0.08	1.28	2.00	0.13	2.10	3.39
02/25/2012, Sat	0.05	0.79	1.40	0.07	1.16	2.00	0.12	1.95	3.40

Weekdays generally are expected to have higher emissions than weekends due to differences in usage patterns. Table 4-8 gives averages for weekends and weekdays.

Table 4-8. Mobile non oil-and-gas emissions averages of different usage patterns. All units are tons/day.

	CH_4	**NMHC**	**NO_x**
Weekdays	0.160	2.45	3.750
Weekends	0.125	2.02	3.395

The above averages, however, can be used to estimate emissions for the entire month of February 2012 (8 weekends and 21 weekdays): CH_4 = 4.4 tons/mo; NMHC = 68 ton/mo; NO_x = 106 ton/mo. Spatial distribution for the emissions will use population as a surrogate (Figure 4-6).

Biogenic and Agricultural

Cellulose-digesting animals (e.g., ruminants) are expected to be the only wintertime biogenic or agricultural source of emissions. They generate and belch methane during the digestive process. Estimates (in units of kg/yr/head) of the methane production of several common animals include 60 for beef cattle, 120 for dairy cattle, 8 for sheep, 5 for goats, and 18 for horses, with smaller emissions for immature animals (EPA, 1993; Johnson and Johnson, 1995).

The single largest ruminant population in the Uintah Basin is beef cattle, estimated at 80,000 head (Kitchen, 2012). Calving occurs in early spring, so by the following February, there are no immature individuals; even the youngest cattle emit methane essentially at the adult rate. Some dairy farming also occurs but is less extensive and has not yet been estimated. Sheep ranching also occurs but is not given high priority due to the much smaller emissions factor. Horses in the Basin are either privately owned or part of wild herds on BLM land. BLM was unable to estimate wild herd numbers, so the total horse population remains unknown, and emissions have not been estimated. The 80,000 head beef cattle population monthly emits 420 tons/mo.

The correct spatial distribution of cattle emissions is not known. Ranchers usually winter their herds in the valleys just south of the Uinta Range. Human population density might prove one possible, though perhaps imperfect, surrogate for cattle population density.

Home Heating (Wood Burning Stoves)

Residential and commercial heating emissions are assumed to be dominated by wood-stove usage. Two separate approaches, agreeing to within 24%, were used to estimate annual cordage of wood burned for home heating. The average of the two approaches was then used in all subsequent computations.

Cordage of Wood Consumed in Winter 2011-12, Approach 1

The Vernal offices of the US Forest Service and the BLM were asked to supply data on wood permit purchases (Simons and Palmer, 2012). Many uncertainties associated with these data have compelled the decision to use two separate approximations. These uncertainties are informed by the understanding that,

1. Not all permitted wood is actually harvested;
2. Not all harvesters buy permits;
3. Some harvesters, presumably, exceed their permitted limit;
4. The relatively mild 2011-12 winter likely resulted in less wood used than was harvested;
5. BLM sells both residential and commercial permits and estimates that much of the commercial wood is resold outside the Uintah Basin (e.g., at least two sawmills buy wood through timber permits and resell it as firewood).

The following table summarizes the results of these interviews. Permits sold by Forest Service and BLM are for fiscal year 2011. (The Forest Service also sells permits through their Dutch John office, but that contribution is being omitted under the assumption that the Dutch John wood is burned north of the Uinta Mountain crest line.)

Table 4-9. Wood harvested during FY 2011.

USFS, Vernal Office	2612 cords
USFS, Roosevelt Office	1345 cords
USFS, Duchesne Office	1022 cords
BLM, residential permits	309 cords
BLM, commercial permits	162 cords
TOTAL	**5500 cords**

Cordage of Wood Consumed in Winter 2011-12, Approach 2

The US Census Bureau conducts surveys to determine the number of households that heat with the following three fuels: gas, electric, and fuel oil (Census Bureau, 2012). The results for Uintah and Duchesne counties (as well as the entire State of Utah, included for comparison) appear in Table 4-10. Totals do not add up to 100%, but it is assumed we can assume that the remainders, 7.2% and 11.9%, heat with wood or propane. Propane is a clean-burning fuel whose emissions will be neglected here. We do not have usage estimates for propane, so as an upper-limit estimate it is assumed that the 7.2% or 11.9% can be attributed to wood burning. Population figures are from the 2010 census (Onlineutah, 2012). According to the 2010 Economic Report to the Governor, the statewide 2008 household size is 3.15 persons (Governor, 2010). This ratio leads to the estimates shown of numbers of households and numbers of households heating with wood.

Table 4-10. Estimates of households heating with wood.

Home Heating Source	Uintah Co.	Duchesne Co.	State of Utah
• **Gas**	77.7%	71.2%	88.1%
• **Electric**	15.0%	16.1%	9.8%
• **Fuel oil**	0.1%	0.8%	0.3%
TOTAL	**92.8%**	**88.1%**	**98.2%**
• **Remainder attributed to wood**	**7.2%**	**11.9%**	**1.8%**
Population	32588	18607	
Households	10000	5900	
Households heating w/ wood	**720**	**700**	

While approximately 1400 households in the Uintah Basin are estimated to heat with wood, the number of cords of wood consumed by the typical household depends on the size of house, number of residents, quality of insulation, air circulation patterns in the house, comfort level of occupants, etc. Based on an informal survey, the amount of wood consumed by the average household is estimated to be five cords/yr, which extrapolates to 7000 cords/year for the entire basin (five cords times 1400 households).

Cordage of Wood Consumed, Winter 2011-12, Average of Approaches 1 & 2

The rounded average of the two approaches, 5500 cords/yr and 7000 cords/yr, is set at 6000 cords/yr, and was used for all subsequent calculations.

Tonnage of Wood Consumed, Winter 2011-12

The EPA's AP-42 emissions factors for wood stoves are on a tonnage basis. Most woods have a specific gravity of around 0.48 g/cm^3, while one cord of wood is 128 ft^3 (USFS, 2010). The product of these two factors is 1.9 tons/cord. That figure does not account for air space in a cord of split wood, which we estimate at 25%, so the conversion used is 1.4 tons/cord, yielding 8400 tons/yr of wood consumed.

Emissions Estimates

Wood stoves differ in the amount of emissions that they produce. The EPA lists AP-42 emissions factors for conventional stoves, stoves with secondary burning chambers, and catalytic stoves (Wood Stoves, 2012). Of the three, conventional stoves produce the most emissions. Here emissions factors for the conventional stoves are used, with the understanding that the result overestimates emissions to the extent that cleaner stoves are actually being used.

Natural Gas Consumption as Surrogate for Temporal Distribution

Table 4-11 gives natural gas usage for a typical household for one 12-month period. Contributions for the five warmest months (May-September) are assumed to be attributable entirely to cooking and average to 2.2 decatherms. The cooking contribution is then deducted from each month, and the final value is reported in the last column on a percentage basis.

Table 4-11. Monthly natural gas consumption in a typical household.

Month	**Usage** (decatherms)	Less Cooking	Percentage
06/11	2.1	-0.1	0%
07/11	2.1	-0.1	0%
08/11	2.2	0	0%
09/11	1.8	-0.4	0%
10/11	3.8	1.6	4%
11/11	7.8	6.6	13%
12/11	11.8	9.6	22%
01/12	13.2	11.0	25%
02/12	10.2	8.0	18%
03/12	8.1	5.9	13%
04/12	4.4	2.2	5%
05/12	2.9	0.7	0%

Given this basis, 18% of the annual wood stove emissions will be attributed to Feb. 2012. Table 4-12 shows completed calculations for wood stove emissions. As a best estimate, these emissions are distributed according to population distributions (Figure 4-6).

Table 4-12. Estimate of wood stove emissions

Pollutant	Emissions Factor†	Wood Stove Emissions*	02/12 Wood Stove Emissions●
PM-10	30.6	130	23
CO	230.8	1200	220
NOx	2.8	12	2.2
Sox	0.4	1.7	0.31
TOC (CH_4)	64.0	270	49
TOC (non-CH_4)	28.0	120	22
PAH	0.730	3.1	0.56

† given in lb/ton, * in ton/year, ● in ton/month

Landfills

The Uintah County Landfill lies on the northeast edge of Ashley Valley (40.47, –109.47) and covers a total area of 230 acres. Emissions factors applied here are 536 mg methane/m^2/day for summer emissions, and 1290 mg methane/m^2/day for winter (Klusman and Dick, 2000). These emissions factors were determined for a landfill in the Denver, Colorado, area and were selected for use because of the climatic similarities to the Uintah Basin. Emissions factors for summer are lower because colder temperatures suppress methanotrophic bacterial action in the soil. Emissions for February 2012 are estimated to be 37 ton/mo.

Natural Hydrocarbon Seeps

There is evidence that hydrocarbons, primarily in the form of natural gas, seep to the surface from underground petroleum reservoirs. This seepage occurs because there is a natural limit to the carrying capacity of any gas reservoir, and whenever the pore pressure of the reservoir exceeds this limit, the reservoir leaks. As long as gas generation continues, and as long as the pressure is not relieved in other ways (such as through production from the reservoir), the pressure in such reservoirs is expected to hover near the limit and all new gas entering the reservoir is balanced by an equal amount of leakage. A conceptual model for the process is presented below, and a more extensive document is in preparation (Mansfield, 2012).

Just how many Uintah Basin gas reservoirs have pressures that hover near their natural limits is not known, and actual measurements of these emissions are practically non-existent. Emissions attributable to this source, consequently, are very difficult to quantify. Klusman (2003a; 2003b) has performed flux measurements at the oil field in Rangely, Colorado, and reports wintertime and summertime fluxes, respectively, of 25 and 4.2 mg methane/m^2/day. Wintertime fluxes are presumably larger because of temperature-induced suppression of methanotrophic bacterial action. Because of the obvious similarities between the geology, terrain, and climate of the Uintah and Rangely basins, the Rangely measurements provide strong evidence for the occurrence of such emissions in the Uintah Basin, although other indirect evidence also exists (Mansfield, 2012). Applying Klusman's wintertime rate to the Uintah Basin and assuming a total effective area of 700 to 1000 km^2 (roughly equivalent to the area of intensive oil and gas operations) lead to an estimate of 500 to 800 tons methane/mo for February 2012 (Table 4-1).

Klusman's sample size is likely too small to be representative, and this estimate could easily change, up or down, by an order of magnitude or more. Two other estimates based on sound reasoning, but which only give rough upper and lower bounds, put the monthly emission due to natural seepage at somewhere between 30 and 30,000 tons methane/mo, a range of three orders of magnitude (Mansfield, 2012). Klusman (2003a) detected light hydrocarbons along with methane in soil gas but did not make quantitative measurements of NMHC emissions from hydrocarbon seepage.

Over a period of several years, the LeRoy Gas Storage Facility is known to have leaked about 100 million cf/yr (see below). The surface footprint of the reservoir is approximately 9 mi^2. Assuming that the entire leakage emerges at the surface and is distributed uniformly over these 9 mi^2 and uniformly over an entire year implies a flux of about 230 mg methane/m^2/day, or about 9 times more than the average wintertime flux observed over the Rangely field. Both the LeRoy storage facility and the Rangely oil field are artificially pressurized, but so also are some of the petroleum-bearing formations of the Uintah Basin. The significance of the LeRoy case study is that the surface flux can be estimated accurately and is found to lie within the rather broad bounds presented above.

Natural Hydrocarbon Seepage: A Conceptual Model

Natural gas is found underground in natural traps. Because of the buoyancy of the gas, the pore pressure in the gas traps is higher than in surrounding formations. However, capillary barriers prevent the gas from escaping until the buoyancy pressure, a function of the amount of gas in the trap, exceeds the capillary pressure, which is a function of the aperture size of the fractures through which the gas eventually escapes. In other words, a gas trap has a limited capacity and leaks gas whenever it fills beyond this limit. Evidence for this behavior is two-fold. First, a very common pattern for gas traps is that seepage evidence is observed over a virgin reservoir and stops as soon as gas is produced from the reservoir. Seepage only recurs when the reservoir is subsequently re-pressurized by injection. Second, the Leroy gas storage facility in Uinta County, Wyoming, has been reported to leak, with total annual losses of about 100 million cf, whenever it is pressurized above about 110 bar (Araktingi et al., 1984).

Natural gas is formed by thermal cracking of kerogen, the organic component of oil shale and liquid petroleum, and it occurs when the source rock formations are found in the appropriate temperature window. Furthermore, formation of gas is ongoing in the source rocks beneath the Uintah Basin. If traps have a limited capacity, and if they are already filled to capacity, then all ongoing gas generation spills over. Such traps are in a steady-state condition and probably have been for a very long time. As already mentioned, modern-day production (removing fluid from traps) and injection (adding fluids) disturbs the steady state.

There are two separate processes by which gas escapes from a trap. One process involves "gas-phase invasion," as an intact gas phase invades the water column. Gas-phase invasion is opposed by the capillary barrier mentioned above. (While the details have been disputed—e.g., many sub-micron spherical bubbles vs. a single gas-phase plug conforming to the shape of the fracture—there is, nevertheless, no disputing the fact that the trap will leak whenever internal pressure overcomes the capillary barrier.) The second process involves "gas solvation." Under the assumption that water circulates in the water column above the trap, then natural gas dissolves into the water at a high partial pressure at the gas-water interface and leaves solution at the low partial pressure at the water table. Even in the absence of water circulation, dissolved natural gas will move diffusively through the water column. In this diffusion limit, the known diffusivity of methane in water indicates that evaporation of the trap occurs over a time scale of mega-years. With circulation of the water column, the evaporation rate is determined by the rate of circulation.

For traps at or above the capillary barrier, and that are constantly being replenished, the primary mechanism of gas loss is gas-phase invasion, and the rate of loss equals the rate of replenishment. Gas loss by solvation is much slower than gas-phase invasion and only dominates at pressures below the capillary threshold. Unless a trap is being actively replenished by the formation of new gas, it will de-gas over a time scale of mega-years.

Natural gas in the soil, and presumably also dissolved in the water column, is subject to bacterial degradation (i.e., methanotrophy); therefore, some unknown fraction of hydrocarbons is degraded to CO_2 prior to venting to the atmosphere.

Seepage is detected at the surface in a number of ways, many of which are only indirect. Indirect measurements include modifications of soil chemistry and of biochemical processes in vegetation. Another is presence of methanotrophic bacteria in the soil. Direct techniques include soil gas and flux measurements. Only the latter, however, gives a direct indication of atmospheric emissions.

ONGOING AND FUTURE WORK

Emissions inventories are like road repair – the job is never finished. The current inventory is regarded as a living, evolving product. Improved estimates and more complete surveys will permit us to refine the inventory over time. Furthermore, economic growth from year to year implies that emissions are never static.

Updated Projections

The 2012 WRAP inventory [Bar-Ilan et al., 2009] projects across six years, five of which have now passed. Actual production data is available to replace projected data, and these will be applied to the estimates shown in Table 4-1.

Evaporation Ponds and Land Farms

As mentioned above, emissions from evaporation ponds and land farms are poorly characterized. USU personnel are engaged in measuring pond emissions and plan to collect data under a number of seasonal and climatic conditions. It is currently estimated that *winter* pond and land farm emissions are small, so measurements will be performed in winter to quantify pond emissions and add estimates to Table 4-1 accordingly. Decommissioned ponds and land farms also should be studied, as these likely emit VOC over the course of at least a few years as the buried heavy hydrocarbons degrade.

Emissions from Rio Blanco County, Colorado

Based on ozone-altitude correlations from the winter of 2011, it was believed that emissions occurring above about 6000 ft do not become entrapped in the stagnant air layer and, therefore, probably do not contribute significantly to Uintah Basin ozone. The Rangely oil field in Rio Blanco County, Colorado, lies at an elevation of about 5300 ft (similar to the town of Vernal), and is separated from the Uintah Basin proper by a ridge of about 6000 ft. Yet, while initial estimates implied the barrier's efficacy, ozone measurements in Rangely and modeling of the spatial extent of the wintertime inversions will determine whether Rio Blanco County needs to be included in the next phase of the emissions inventory.

Modeling Studies

The winter ozone studies will not be entirely complete until a detailed photochemical grid model (e.g., CAMx or CMAQ) is developed and verified to successfully link the predictions of the emissions inventory with the measurements of atmospheric concentrations. These photochemical grid models will be based on accurate, high-resolution WRF models of the terrain and meteorology, to which Basin emissions data will be added and on which sensitivity and source apportionment studies will be performed and verified.

SUMMARY, CONCLUSIONS, RECOMMENDATIONS

Our current emissions estimates for the Uintah Basin for February 2012 are summarized in Table 4-1. It should be remembered, however, that these are only estimates, and readers are encouraged to examine the assumptions and approximations described in the body of the text. The current WRAP-III series of estimates are all based on a survey reporting activities from 2006, six years ago. The response rate from that survey was reported to be 71% of well ownership, 82% of gas production, and 78% of oil production (Friesen, et al, 2009). The WRAP-III 2012 projection (Bar-Ilan et al., 2009) is based ultimately on the same survey. As mentioned above, a survey covering only drilling and fracking operations was conducted as part of the current study, but at this writing, the response rate is about 72% of well

completions. A completely new survey covering all aspects of the oil and gas industry, with focus on winter activities, would prove extremely useful.

A new and updated inventory and survey will allow for the development of mitigation strategies for winter ozone that are more accurate, equitable, and efficient than is possible with current knowledge. Extensive industry involvement and cooperation will be an essential part of this process.

REFERENCES

AMPD: http://ampd.epa.gov/ampd/, last access: September 2012.

Anadarko: http://www.anadarko.com/Midstream/Pages/Overview.aspx, last access: August 2012.

Shires, T., Loughran, C., Jones, S. and Hopkins, E.: Compendium of greenhouse gas emissions methodologies for the oil and natural gas industry, American Petroleum Institute, available at http://www.api.org/ehs/climate/new/upload/ 2009_ghg_compendium.pdf, 2009.

Araktingi R., Benefield, M., Bessenyei, Z., Coats, K., and Tek, M., Leroy Storage Facility, Uinta County, Wyoming: A case history of attempted gas-migration control, J. Petroleum Tech., 34, 132-140, 1984.

Bar-Ilan, A., Friesen, R., Parikh, R., Grant, J., Pollack, A. K., Henderer, D., Pring, D., Sgamma, K., Development of 2012 Oil and Gas Emissions Projections for the Uinta Basin, Environ, Novato, California, USA, available at http://wrapair.org/forums/ogwg/documents/2009-03_12_Projection_Emissions_Uinta_Basin_Technical_Memo_03-25.pdf, 2009.

Census Bureau, American Community Survey: census.gov/acs/www/, last access: August 2012.

Dietrich, S. A.: Special purpose studies: Air Quality Division: Wyoming Department of Environmental Quality: http://deq.state.wy.us/aqd/Special%20Purpose%20Studies/WDEQ.AQD_2011_Engine_Emissions_Study.pdf, last access: August 2012.

Environmental Protection Agency: Anthropogenic methane emissions in the United States: estimates for 1990, Report to Congress. Environmental Protection Agency. EPA 430-R-93-003, 1993.

Environmental Protection Agency: AP-42, Fifth Edition: epa.gov/ttn/chief/ap42/, last access: September 2012.

Friesen, R., Parikh, R., Grant, J., Bar-Ilan, A., Pollack, A. K., Henderer, D., Pring, D., Sgamma, K., Schlagel, P.: Development of Baseline 2006 Emissions from Oil and Gas Activity in the Uinta Basin, Environ, Novato, California, USA, available at http://wrapair.org/forums/ogwg/documents/2009-03_06_Baseline_Emissions_Uinta_Basin_Technical_Memo_03-25.pdf, 2009.

Governor: Economic report to the governor: http://governor.utah.gov/DEA/ERG/2010ERG.pdf, last access: August 2012.

Garcia, J. P., Beyne-Masclet, S., Mouvier, G.: Emissions of volatile organic compounds by coal-fired power stations, Atmos. Environ., 26A, 1589-1597, 1992.

Johnson, K. A., Johnson, D. E.: Methane Emissions from Cattle, J. Animal Science, 73, 2483-2492, 1995.

Kitchen, B.: Uintah County Extension, private communication, 2012.

Klusman, R. W.: Rate measurements and detection of gas microseepage to the atmosphere from an enhanced oil recovery/squestration project, Rangely, Colorado, USA, Appl. Geochem., 18, 1825-1838, 2003a.

Klusman, R. W.: A geochemical perspective and assessment of leakage potential for a mature carbon dioxide–enhanced oil recovery project and as a prototype for carbon dioxide sequestration; Rangely field, Colorado, AAPG Bulletin, 87, 1485-1507, 2003b.

Klusman, R. W. and Dick, C. J.: Seasonal variability in CH_4 emissions from a landfill in a cool, semiarid climate," J. Air Waste Manage., 50, 1632-1636, 2000.

Mansfield, M.: Natural hydrocarbon seeps in the Uintah Basin: literature review and potential for atmospheric emissions, in preparation, 2012.

Mesowest: http://mesowest.utah.edu, last access: August 2012.

Onlineutah: http://onlineutah.com/countypopulation.shtml, last access: August 2012.

QEP: Field services assets are concentrated in QEP producing areas: http://qepres.com/pdf_docs/Field%20Services.pdf, last access: September 2012.

Rice, D. D., Fouch, T. D., Johnson, R. C., Influence of source rock type, thermal maturity, and migration on composition and distribution of natural gases, Uinta Basin, Utah, in: Hydrocarbon and Mineral Resources of the Uinta Basin, Utah and Colorado, Utah, USA, 1992.

Simons, D., Palmer, D.: Bureau of Land Management Vernal Office, private communication, 2012.

Stoeckenius, T., Ma, L.: Final Report: A Conceptual Model of Winter Ozone Episodes in Southwest Wyoming," Environ, Novato, CA, USA, available at http://deq.state.wy.us/aqd/Ozone/WDEQ_ 03conceptModel_Report.pdf, 2010.

Utah Division of Oil, Gas, and Mining: http://oilgas.ogm.utah.gov/Data_Center, last access: September 2012.

United States Forest Service: Wood Handbook—Wood as and Engineering material, Department of Agriculture, Forest Service, Forest Products Laboratory, Madison, Wisconsin, USA, General Technical Report FPL-GTR-190, 2010.

Virgen, N.: Utah Department of Transportation, private communication, 2012.

Wyoming Department of Environmental Quality Air Quality Division: http://deq.state.wy.us/aqd/ Actual%20Emissions.asp, last access: August 2012.

CHAPTER V (PART A)

SOURCE CHARACTERIZATION, ATTRIBUTION, AND OZONE DISTRIBUTION IN THE UINTAH BASIN USING THE NOAA MOBILE LABORATORY

Gabrielle Pétron[1,3], Peter Edwards[2,3], Jonathan Kofler[1,3], Benjamin Miller[1,3], William Dubé[2,3], Detlev Helmig[4], Jacques Hueber[4], Colm Sweeney[1,3], Steven Brown[2], Ed Dlugokencky[1], Stephen Montzka[1], Laura Patrick[1,3], Felix Geiger[5], Carsten Warneke[2,3], and Ken Aikin[2,3]

[1]NOAA Earth System Research Laboratory, Global Monitoring Division.
[2]NOAA Earth System Research Laboratory, Chemical Sciences Division.
[3]University of Colorado, Cooperative Institute for Research in Environmental Sciences.
[4]University of Colorado, Institute for Arctic and Alpine Research.
[5]Karlsruhe Institute of Technology.

OBJECTIVE

The goal of the NOx and VOC Mobile Lab surveys in the Uintah Basin was to characterize important source processes for ozone precursors and to document the chemical composition and patterns of the emissions in space and time. The Multi-Species Mobile Lab was deployed for three weeks in February 2012. There were no temperature inversions with high ozone pollution during the 2011-12 winter; therefore, we were not able to document the air composition during such events. The Mobile Lab sampled NOx, VOCs, CH_4 , CO_2 and CO plumes from various sources (well pads, compressor stations, processing plants, evaporation ponds, flowback pond, pipeline leaks) and mapped the ambient levels of NO, NO_2, O_3, CO, CO_2 and CH_4.

INSTRUMENTATION

The Multi-Species Mobile Lab (ML) is a NOAA Earth System Research Laboratory unit built to deploy in-situ trace gas analysis, GPS and meteorological instrumentation as well as a discrete air sampling system in the field, close to known sources of air pollutants and/or greenhouse gases.

The ML is a retrofitted van with a custom-built power system and air sampling module. The instrumentation can draw its power from the engine or from a set of batteries, allowing the unit to collect measurements for 8-10 hours when the engine is turned off.

Figure 5A-1. NOAA Multi-Species Mobile Lab near a compressor station in the Uintah Basin.

In-Situ Analyzers

The in-situ measurements are displayed on a screen in real-time to inform the operators about changes in the ambient levels of the trace gases mixing ratios and to detect plumes of point sources for targeted discrete flask sample collection. The in-situ fast response instruments on-board the ML include:

- two 2B O_3 commercial instruments at 1 second frequency
- a NO_x diode laser cavity ring down instrument (NOxCaRD, NOAA Chemical Sciences Division): NO, NO_2 at 1 second frequency
- a four species cavity ring down instrument (Picarro): CO_2, CH_4, H_2O vapor, CO (all at 2.5 second frequency)
- T, wind speed and direction, RH met box (10 sec frequency)
- GPS units for plotting positions of ML and the discrete air sampler, 1 second frequency

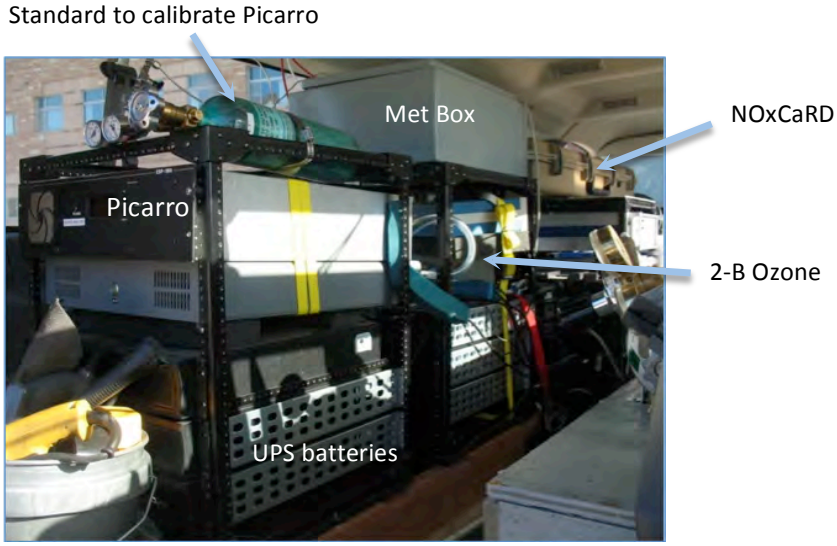

Figure 5A-2. In-situ analyzers installed in the Mobile Lab, November 2011. A similar configuration was used in February 2012.

Table 5A-1. In-situ measurements onboard the Mobile Lab

Analysis System	Species	Output Frequency	Total uncertainty	Reference
2B UV absorption	O_3	10 s	1 ppb or 2%	
NOxCaRD	NO	1 s	See text below	Fuchs et al. [2009]
	NO_2	1 s		
	O_3	1 s		
Picarro WS-CRDS	CO_2	2.5 s	0.1 ppm on 1sec	Sweeney et al. [in prep]
	CH_4	2.5 s	2 ppb on 1 sec	
	CO	2.5 s	2 ppb on 30 sec	
	H_2O	2.5 s	10 ppm on 30 sec	

The 2-B ozone instruments were calibrated by the NOAA Global Monitoring Division (GMD) Ozone group in the Boulder lab and in the ML prior to each field campaign. The inlet module was conditioned prior to deployment with high ozone levels (500 ppb) for 3 hours to prevent ozone losses on surfaces during the campaign.

The air going to the Picarro analyzer is not dried. We apply a water correction to the CH_4, CO_2 and CO data based on the H_2O mixing ratio measured by the instrument and water tests performed on the Picarro unit in the NOAA GMD Boulder lab. The Picarro measurements are calibrated before and after each drive with a cylinder of reference gas prepared in the NOAA/WMO GHG calibration lab in Boulder. The instrument was also calibrated in the field. A null test was done while driving with standard gas running through the instrument to determine if motion or other environmental factors impacted the noise and drift of the instrument. Past experiments with this same instrument in aircraft have indicated that motion and environmental factors were not a concern.

The NO_2 and NO instrument is based on measurement of total gas-phase optical extinction at 405 nm, which in most environments is specific to NO_2 [Fuchs *et al*., 2009]. The instrument has a second channel in which excess ozone is added to quantitatively convert NO to NO_2 for a measurement of total NO_x. The concentration of NO is then determined by difference. For operation during the winter study, the instrument was configured to measure either total NO_x or total O_x (= O_3 + NO_2). The O_x measurement is analogous to that of NO_x, except that excess NO is added to the second channel for quantitative conversion of O_3 to NO_2. The O_3 concentration is then determined by difference [Washenfelder, 2011]. The instrument measured either NO_2 and NOx, or NO_2 and O_x for any given drive, but it did not measure all three species simultaneously. The calibration was based on the absorption cross section of NO_2, which should not vary with sampling conditions. Calibrations were performed once per drive using a commercial O_3 monitor to generate and measure a known O_3 concentration, which is quantitatively converted to NO_2 as described above and added to the instrument. The NO_2 precision is 22 pptv (2σ, 1 s), with an accuracy of ±3%. The precision is similar for NOx and O_x, but is somewhat worse for the individual species determined by difference (NO, O_3 <50 pptv, 1s). Accuracy for NO is ±5%, while accuracy for O_3 is ±3%.asdfasdf.

Discrete Air Sampling

The discrete air sampling module (Figures 5A-3 and 5A-4) is a NOAA GMD custom built system which includes a 12 flask package, a compressor package, a temperature and humidity probe, a GPS unit and a pilot display to allow the operator to choose when to collect an air sample. Flask sample collection

typically takes 10 to 20 seconds after 1.5 to 2 min of flushing time. The discrete air samples are analyzed for over 60 species in the NOAA GMD and University of Colorado (INSTAAR) laboratories in Boulder, CO.

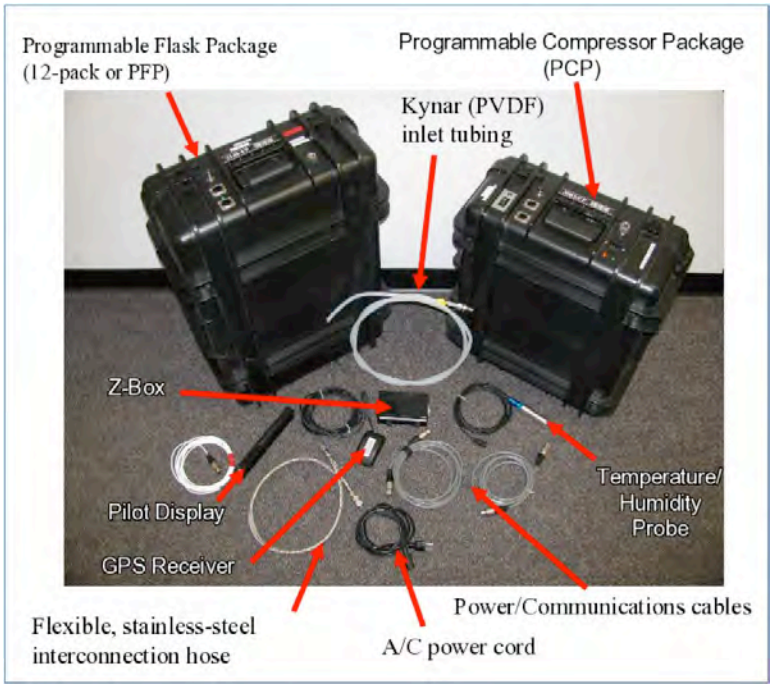

Figure 5A-3. NOAA discrete air sampling system. While this system was initially designed specifically for use on small aircraft, it is now also being used at unattended tall towers, surface sites, and in the NOAA and DOE Mobile Labs.

Figure 5A-4. NOAA discrete air sampling system close-up. On the left is the Programmable Flask Package (also called 12-pack or PFP), which contains 12 glass flasks (0.7L each). On the right is the Programmable Compressor Package (PCP), which contains pumps for flushing the manifold and flask prior to pressurizing the flask to approximately 40 psia.

First, the discrete air samples collected in the Uintah Basin in November 2011 and February 2012 went to the Carbon Cycle and Greenhouse Gas (CCGG) measurement group at NOAA GMD to be analyzed for six compounds: CO_2, CH_4, N_2O, CO, H_2 and SF_6. NOAA CCGG is the World Meteorological Organization Central Calibration Laboratory for CO_2, CH_4 and CO, and is responsible for maintaining and distributing the WMO Mole Fraction scale for these gases.

Figure 5A-5. NOAA MAGICC flask analysis system. Every year, the MAGICC lab analyses over 20,000 air samples collected by scientists and volunteers at a global network of surface sites and a North American network of tall towers, aircraft vertical profile and intensive study sites (http://www.esrl.noaa.gov/gmd/dv/iadv/).

Table 5A-2. Components of the NOAA MAGICC analysis system and specs for the six species measured.

Analysis System	Species	Instrument	Repeatability 1σ	Reference
MAGICC NOAA Carbon Cycle and Greenhouse Gases group	N_2O SF_6	GC/ECD	0.4 ppb 0.03 ppt	[Dlugokencky et al., in preparation, 2011]
	H_2	GC/HePPD	0.4 ppb	[Novelli et al., 2009]
	CO	Resonance fluorescence	1 ppb	[Novelli et al., 1998]
	CH_4	GC/FID	1.2 ppb	[Dlugokencky et al., 1994]
	CO_2	NDIR analyzer	0.03 ppm	[Conway et al., 1994]

Every year, over 20,000 air samples from around the world are analyzed on the NOAA GMD MAGICC system. The Cooperative Global Air Sampling Network (see North American sampling sites in Figure 5A-6) has been gathering information on the background levels of CO_2 since 1967 and CH_4 since 1983. The analysis of a small number of Volatile Organic Compounds (ethane, propane, i-butane, n-butane, n-pentane, n-hexane) in a number of the air samples coming from remote sites started in 2005 and is performed by Detlev Helmig's group at the University of Colorado Institute for Arctic and Alpine

Research (INSTAAR). The surface network provides valuable information on the background levels of several of the trace gases of interest for the Uintah Basin study.

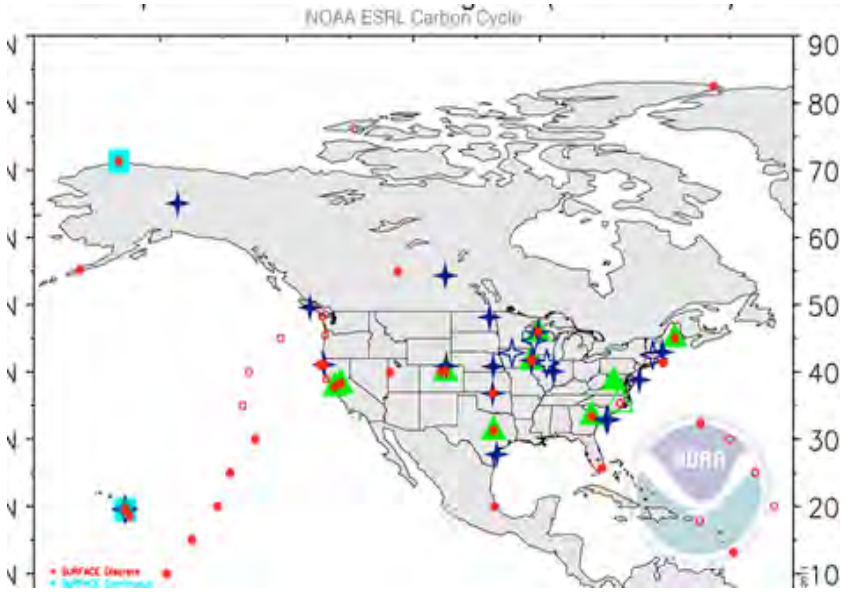

Figure 5A-6. Cooperative Air Sampling Programs in North America. Note the different symbols use for the surface (red), tall tower (green), and aircraft (dark blue) networks.

Methane is long-lived greenhouse gas (GHG). With a global lifetime of approximately 9 years, it is the second most important anthropogenic GHG in terms of radiative forcing. The background level of CH_4 at 40^{o}N latitude is around 1.85 to 1.86 ppm in the wintertime. The MAGICC methane, CH_4, analysis of the discrete air samples collected in the field provides a first indication on whether a particular sample has been influenced by local or regional CH_4 sources such as leaks from oil and gas operations or a landfill, for example.

Next, the Uintah Basin discrete air samples were analyzed on a GC/MS by the NOAA GMD Halocarbons and other Atmospheric Trace Species (HATS) group. The 38 species measured on this system are listed in Table 5A-3 below. The uncertainty on the measurements for VOC mixing ratios going from a few ppt to a few hundreds of ppb is around 2 to 5%. Depending on the expected levels of contamination, a standard gas is run on the system after every “unknown” air sample or after a set of four “unknown” air samples to track potential changes in the detector sensitivity.

To access the storage stability of the VOCs of interest in the discrete flasks, we have conducted storage tests of typically 30 days duration, which is greater than the actual storage time of the samples used in this study (typically < 7days). Results for C_2H_2 and C_3H_8 show no statistically significant enhancement or degradation with respect to our "control" (the original test gas tank results) within our analytical uncertainty. For the remaining species, enhancements or losses average less than 3% for the 30 day tests.

Table 5A-3. Species analyzed on the NOAA HATS GC/MS. The species highlighted in red are the ones most likely to be elevated in an oil and gas-producing basin.

acetylene	CFC-12	bromoform	HCFC-22	HFC-365mfc
propane	CFC-13	chloroform	HFC-227ea	n-butane
benzene	dibromomethane	carbon disulfide	HFC-125	i-pentane
carbon tetrachloride	dichloromethane	Halon-1211	HFC-134a	n-pentane
CFC-113	methyl bromide	Halon-1301	HFC-143a	carbonyl sulfide
CFC-114	methyl chloroform	Halon-2402	HFC-152a	perfluoropropane
CFC-115	methyl chloride	HCFC-141b	HFC-23	
CFC-11	methyl iodide	HCFC-142b	HFC-32	

Finally, the discrete air samples were analyzed on a GC/ FID by Detlev Helmig's group at the University of Colorado INSTAAR to measure a longer suite of VOCs. Table 5A-4 lists targeted species. We will only report mixing ratios for those species that can be well identified and quantified by the INSTAAR VOC system. Work is undergoing on samples collected in November 2011 in the Uintah Basin, and results from the analysis will inform the sampling strategy and analysis for the wintertime campaign.

Table 5A-4. Targeted species.

Acetylene	1-Pentene	n-Hexane	2,3,4-Trimethylpentane	n-Propylbenzene
Ethylene	n-Pentane	Methylcyclopentane	Toluene	1,2,4-Trimethylbenzene
Ethane	Isoprene	2,4-Dimethylpentane	2-Methylheptane	1,3,5-Trimethylbenzene
Propylene	trans-2-Pentene	Benzene	3-Methylheptane	o-Ethyltoluene
Propane	cis-2-Pentene	Cyclohexane	n-Octane	m-Ethyltoluene
Isobutane	2,2-Dimethylbutane	2-Methylhexane	Ethylbenzene	p-Ethyltoluene
1-Butene	Cyclopentane	2,3-Dimethylpentane	m/p-Xylene	m-Diethylbenzene
n-Butane	2,3-Dimethylbutane	3-Methylhexane	Styrene	p-Diethylbenzene
trans-2-Butene	2-Methylpentane	2,2,4-Trimethylpentane	o-Xylene	1,2,3-Trimethylbenzene
cis-2-Butene	3-Methylpentane	n-Heptane	n-Nonane	n-Decane
Isopentane	2-Methyl-1-Pentene	Methylcyclohexane	Isopropylbenzene	n-Undecane

SAMPLING STRATEGIES

Ambient Levels Mapping

The NOAA Mobile Lab was deployed in the Uintah Basin for 4 days in November 2011 and over 3 weeks in February 2012. The van was ready to be deployed by January 15, 2012; however, the lack of snow in the Basin in January led to the later start. The van was operated for several hours on different days, mostly during day light hours to help with the source attribution of observed plumes. Since there was no high surface O_3 event during the campaign, the Mobile Lab team decided to focus more on identifying important point sources of O3 precursors and in collecting air samples in plumes to identify the mix of VOCs present.

Point Source Characterization

The fast response analyses and visualization for O_3, NO, NO_2, CO, and CH_4 in the Mobile Lab guided the collection of discrete air samples. Flasks were filled in well-identified point sources plumes as well as when interesting gradients were recorded by the fast response instruments. Special efforts were made to also collect air samples to characterize the regional and local background air compositions.

Occasionally, the Mobile Lab was parked with the engine turned off downwind of some point sources to collect a representative set of measurements.

ANALYSIS CHALLENGES

The in-situ analytical instruments encountered some challenges during the February campaign in the Uintah Basin, specifically localized interferences (downwind of produced water ponds for the Picarro CO measurement, downwind of a flowback site for the 2B O_3 measurement) or saturation (downwind of new well pad and downwind of a flowback site for the Picarro CH_4 measurement). These will be covered in more details in instrumentation manuscripts.

The flask analysis on the GC/MS, and to a lesser extent on the GC/FID, was also challenged when air samples had VOC levels beyond the linear range of the instrument. Here we only present flask data for which the analysis did not encounter any of these problems.

AREA OF STUDY

The Uintah Basin experienced very high O_3 events in past winters (2009/2010 and 2010/2011) during cold temperature inversions. Vernal in the northern part of the Basin is the largest town (~ 9,000 inhabitants) in the region. Utah State University hosted the Mobile Lab at the Bingham Research Center in Vernal during the two campaigns in November 2011 and February 2012.

The main economical activities in the region are natural resources extraction, including oil and natural gas in Duchesne County and Uintah County, as well as phosphate and gilsonite. Put together, both Counties have close to 5000 gas wells and 3300 oil wells. In 2011, the Uintah Basin represented close to 80% of Utah's gas production and 87.4% of the oil production.

Co-located with the well pads where oil and gas extraction occurs are a fair amount of centralized compressing and/or processing facilities. The midstream network of pipelines, which transports the natural gas from the well pads to processing facilities, is mostly located above ground in the Uintah Basin. Most pipelines have some kind of insulation around them. However, to help prevent hydrates formation, methanol is commonly injected in the oil and gas field at wellheads and in the midstream pipelines.

Another large point source of NOx in the region is the Bonanza power plant, located 33 miles SE of Vernal on State route 45. It is a coal-fired 500 MW capacity plant owned and operated by the Deseret Power Electric Cooperative.

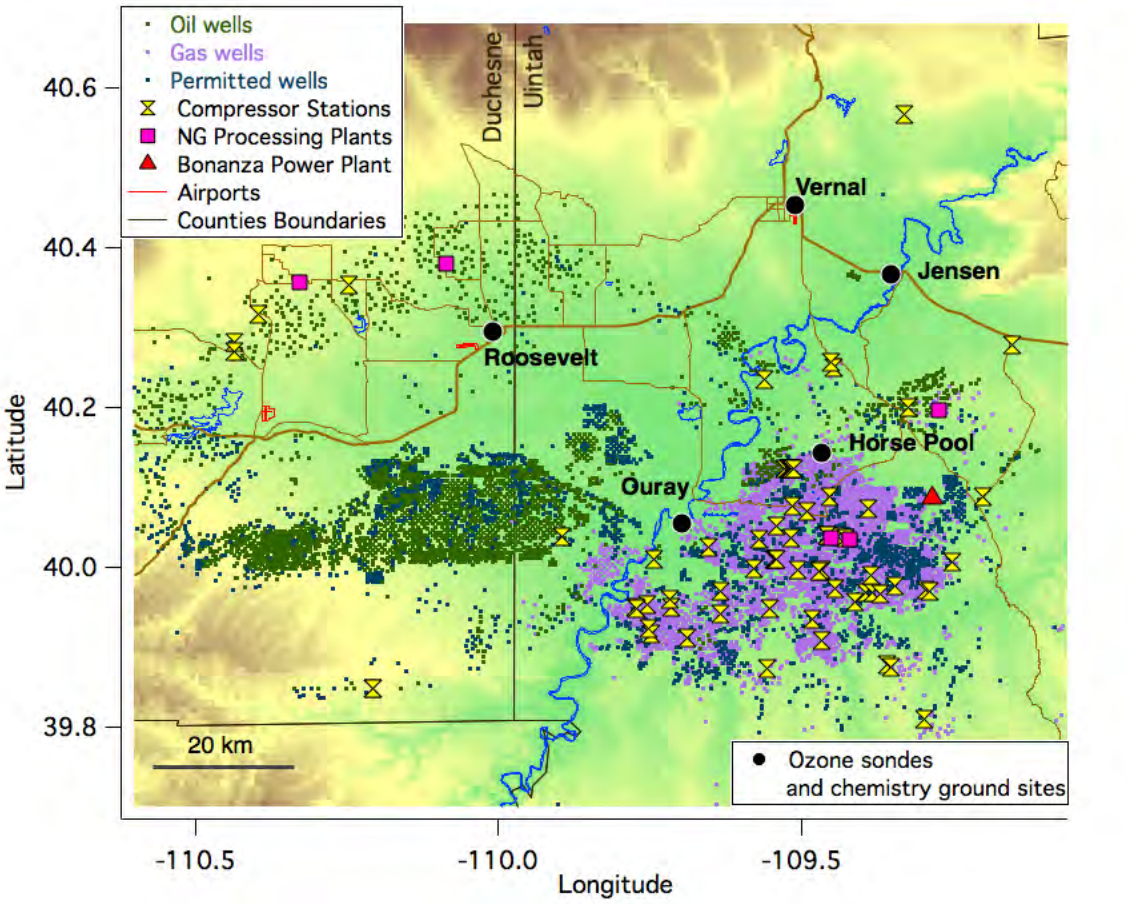

Figure 5A-7. Map of the Uintah Basin in northeastern Utah showing the oil and gas fields, the location of known large point sources of O_3 precursors, and the four sites with vertical O_3 measurements operating in February 2012.

RESULTS FOR HYDROCARBON MEASUREMENTS

The Mobile Lab conducted 17 surveys between February 2 and February 21. The GMD Mobile Lab team left on February 22 and left the Mobile Lab to NOAA CSD collaborators who did 6 more surveys.

The goals of the Mobile Lab surveys were twofold:

1. Identify large point sources of ozone precursors, i.e., VOCs and NOx.
2. Collect air samples in plumes to characterize different sources' VOC emission profiles.

The primary constituent of natural gas is methane. A previous Mobile Lab study in the Denver-Julesburg Basin has shown strong correlation between methane and other light alkanes in air samples influenced by emissions in the gas field [Pétron et al., 2012]. The in-situ methane (Picarro) measurements onboard the Mobile Lab were used to identify fugitive emissions of natural gas. The photo on the right side shows the near real time display of the methane and carbon monoxide measurements (~ 10 sec delay) on a screen in the front of the van (Figure 5A-8).

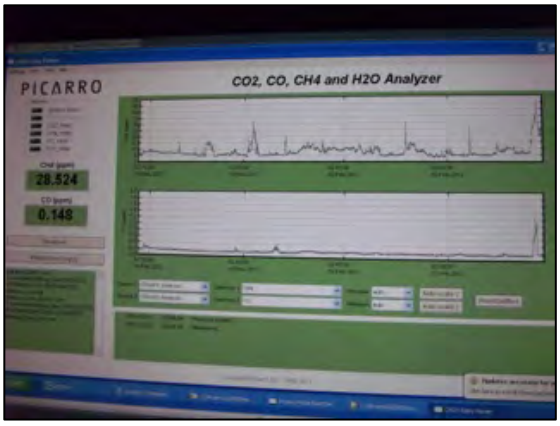

Figure 5A-8. Photograph of Picarro in situ measurements display.

The NO/NO_2 (NOAA NOxCaRD) measurements in the Mobile Lab were used to study NOx sources. These measurements are presented in another section of this report.

Example of Drive in the Gas Field

Figures 5A-9 through 5A-11 below show the methane surface levels measured by the Mobile Lab during the survey conducted on February 5, 2012. This survey's main objective was to look at emissions of methane and VOCs from a few (centralized) compressor stations. As mentioned earlier, wintertime methane levels at the surface in the background atmosphere at the same latitude as the Basin are currently around 1.85 ppm. Most of the methane mixing ratio variability at background surface sites is related to synoptic weather events (bringing air from different latitudes), and it is less than 100 ppb or 0.1 ppm.

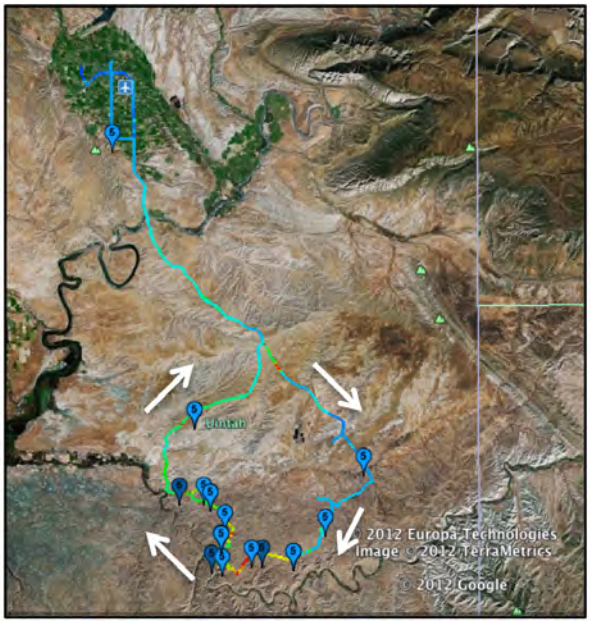

Figure 5A-9. Map of February 5, 2012 survey track, color coded with methane mixing ratio (from 1.8 ppm in blue to 4ppm and beyond in red). Blue balloons show the discrete flasks sampling locations.

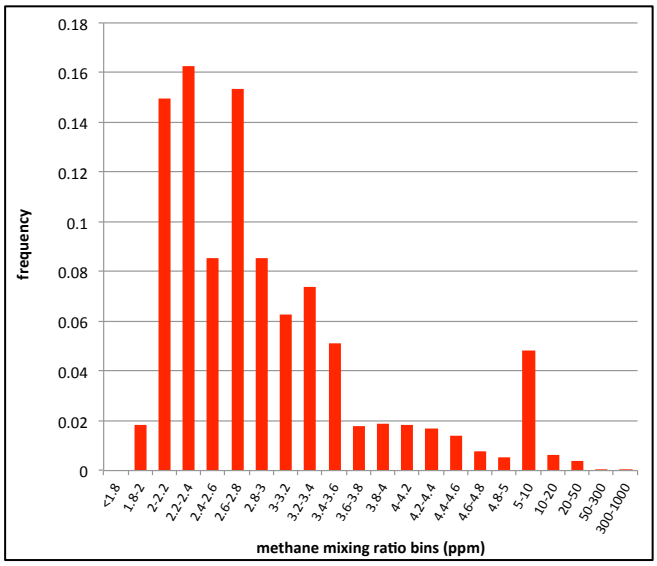

Figure 5A-10. Frequency distribution of the methane mixing ratios measured in-situ by the Mobile Lab on February 5, 2012.

The frequency distribution plot on Figure 5A-10 shows that the methane ambient levels in the Basin on February 5, 2012 were almost all enhanced by several hundreds of ppbs compared to the wintertime background value of 1.85ppm. These enhancements are well beyond the synoptic variability observed at the NOAA cooperative sampling surface network background sites. 35% of the methane in-situ readings on February 5, 2012 are above 3 ppm. The methane ambient levels measured in the Uintah Basin can reflect not only the proximity to large point sources (see for examples methane plumes in time series plot in Figure 5A-11) but also local to regional scale enhancements related to the accumulation of emissions from an area source (i.e., here juxtaposition of small or large point sources of methane).

The plumes we sampled downwind of large point sources such as compressors almost certainly do not reflect the absolute emissions coming out of each site. We stayed on the main roads and tried to detect potential plumes for each facility to collect flask samples. The absolute methane levels measured in-situ and in the flasks reflect not only emission levels but also wind and dispersion conditions. Also for some facilities or uncooperative wind conditions, we could not always sample downwind of different pieces of equipment or operations.

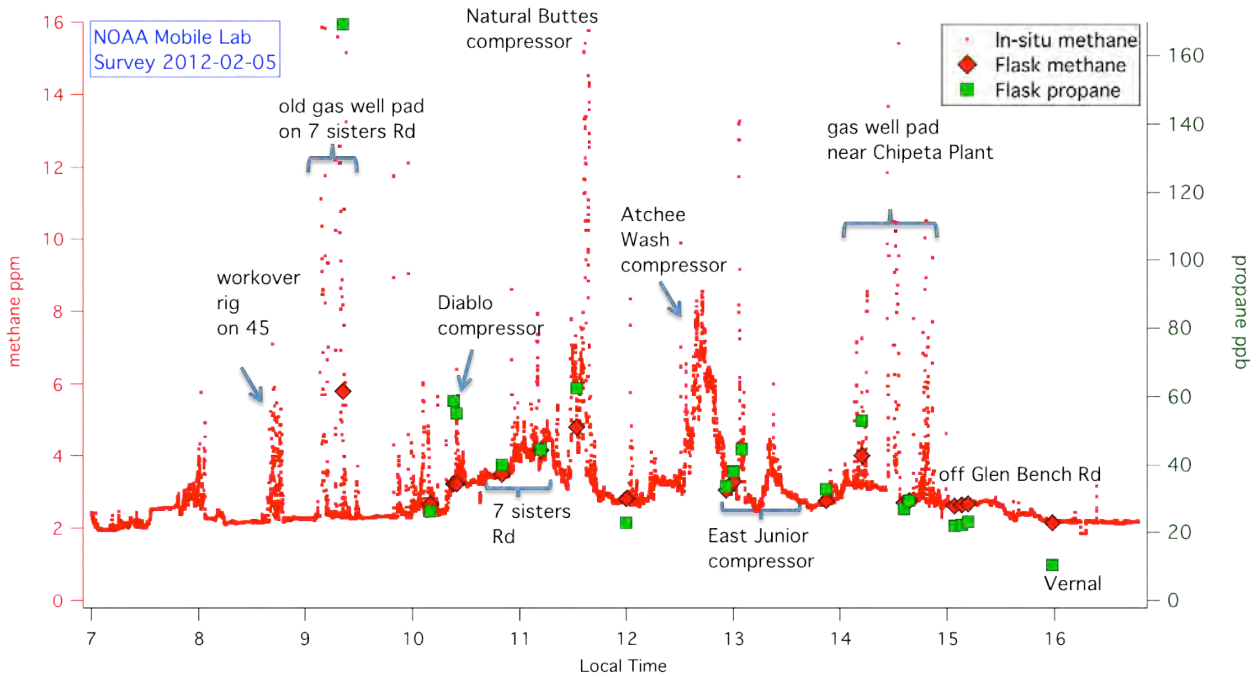

Figure 5A-11. Time series of methane ambient levels measured during the NOAA Mobile Lab survey of February 5, 2012. Also shown are the methane and propane mixing ratios measured in flasks collected during the drive in and out of plumes.

The Uintah Basin did not experience any high ozone pollution events during the 2011-2012 winter. Ozone levels measured with the NOAA Mobile Lab across the Basin between February 4 and February 20, 2012 were below 60 ppb, most often below 50 ppb. Figure 5A-12 below shows the Mobile Lab ozone data (purple symbols) measured with a commercial 2B UV absorption instrument as well as the methane level time series shown above in Figure 5A-11.

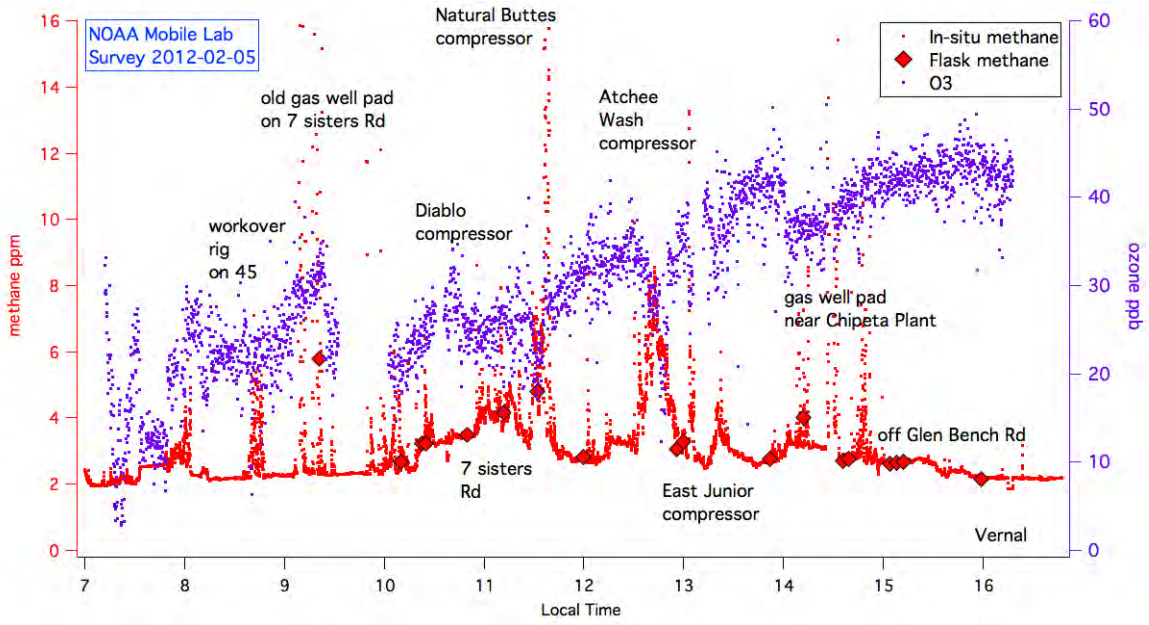

Figure 5A-12. Time series of methane and ozone ambient levels measured during the NOAA Mobile Lab survey of February 5, 2012. Note the titration (destruction) of ozone in some of the plumes intercepted during the survey.

Example of Drive in the Oil Field

Figures 5A-14 and 5A-15 below show the methane and carbon monoxide (CO) surface levels measured in-situ by the Mobile Lab during the survey conducted on February 11, 2012 in the Gilsonite Draw oil field, south of US 40 and west of Ouray. This survey's main objective was to look at emissions of methane, CO, NOx and VOCs from a few oil well pads. The field is mostly off the electrical grid. At all the pads sampled, the pumpjack engine was running on the casing natural gas associated with the oil.

Figure 5A-13. Pumpjack in Duchesne County.

The four oil well pads surveyed during the February 11, 2012 Mobile Lab drive all showed significant emissions of unburned raw gas as well as combustion products such as CO_2, CO, and NOx. Figure 5A-16 shows that the O_3 levels measured with the 2B instrument were between 35 and 45 ppb for most of the drive in the oil field. Some of the discrete flask data is plotted in Figure 5A-17. The samples collected downwind of the Ashley compressor show a different chemical signature compared to the samples collected downwind of the oil well pads. For the nine samples collected downwind of the oil well pads, the light non-methane hydrocarbons correlate very well (R^2 ~ 0.9 for C3-C5 alkanes).

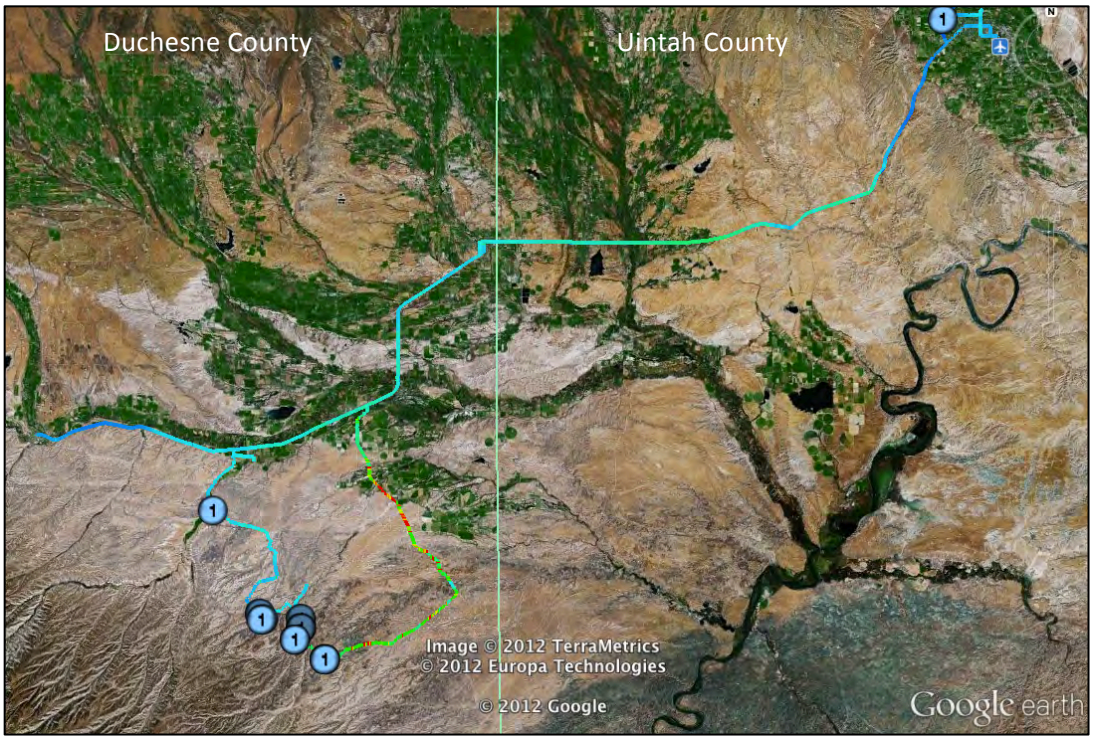

Figure 5A-14. Map of February 11, 2012 survey track, color coded with methane mixing ratio (from 1.8 ppm in blue to 3.8ppm and beyond in red). Blue balloons show the discrete flasks sampling locations.

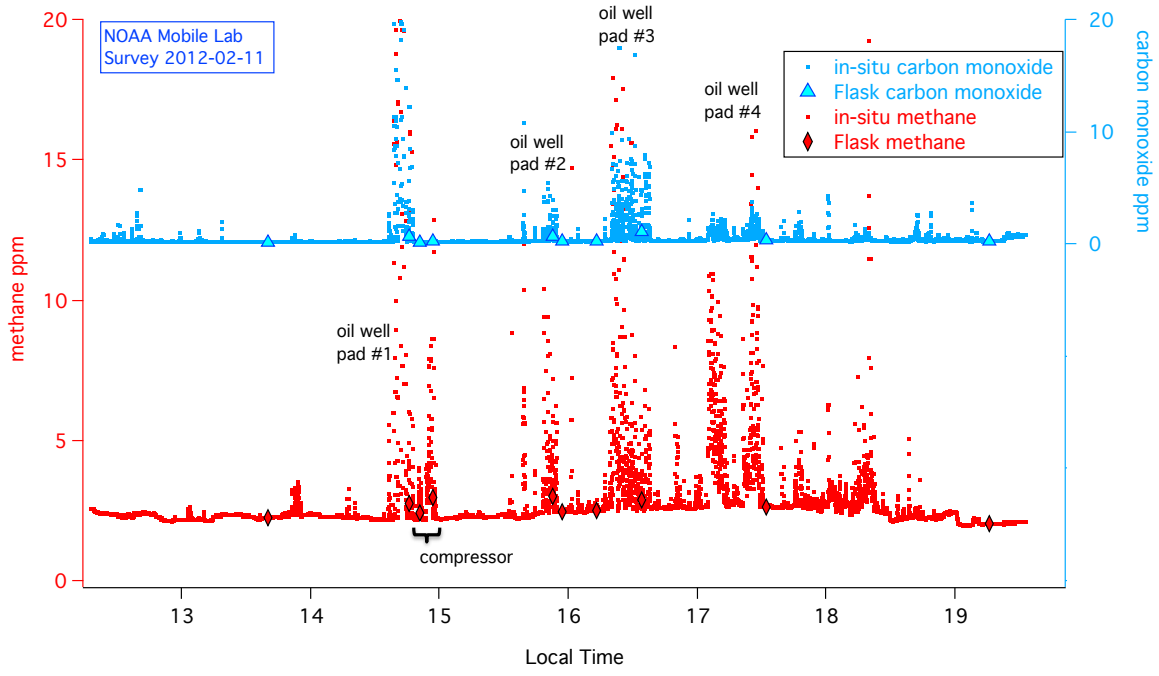

Figure 5A-15. Time series of methane and carbon monoxide ambient levels measured during the NOAA Mobile Lab survey of February 11, 2012. Also shown are the methane and carbon monoxide mixing ratios measured in flasks collected during the drive in and out of plumes.

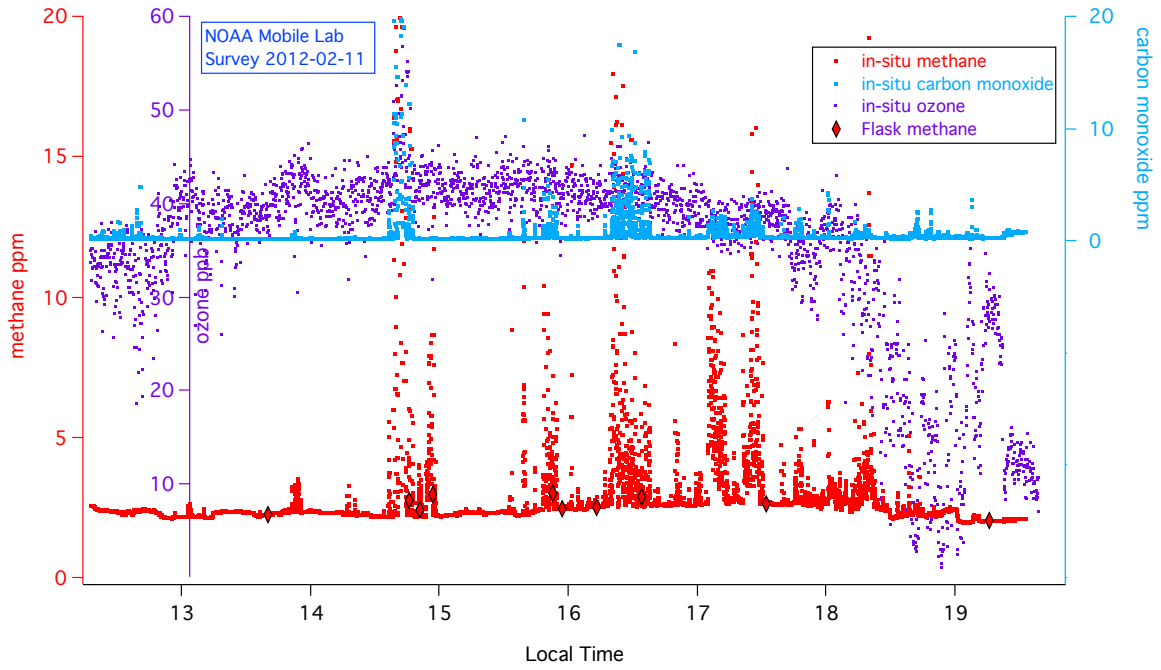

Figure 5A-16. Time series of ozone ambient levels measured during the NOAA Mobile Lab survey of February 11, 2012 together with some of the data shown above in Figure 5A-15.

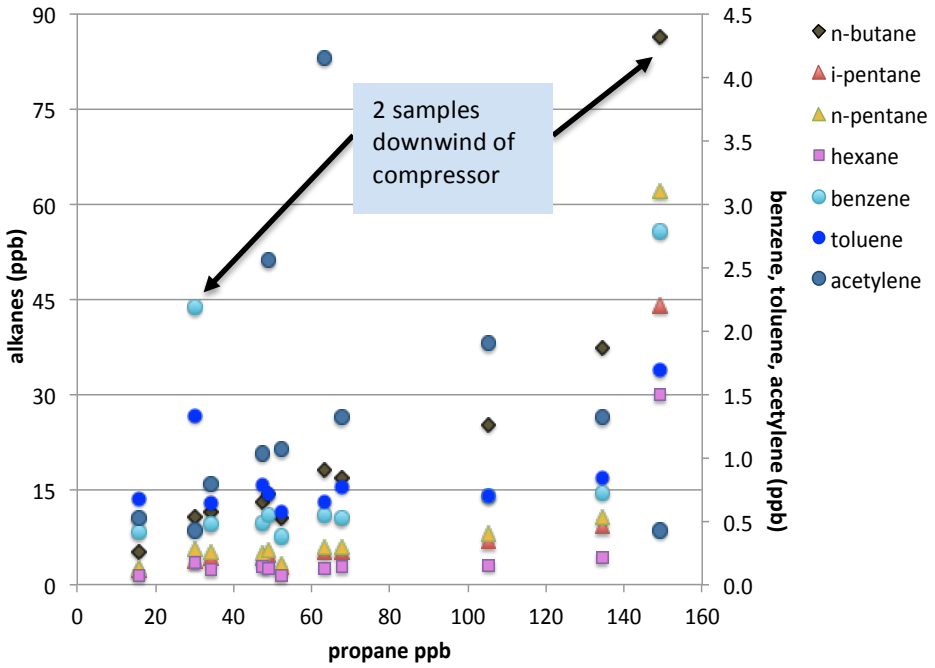

Figure 5A-17. Flask composition data for 11 samples collected during the February 11, 2012 survey.

Point Sources Composition Characterization

In November 2011, NOAA GMD conducted a quick 3-day survey in the Uintah Basin, following the November 2, 2011 planning meeting in Vernal, UT. 58 flasks were collected during that time in NOAA GMD flask packages (see photos of PFP and PCP in Figures 5A-3 and 5A-4).

In February 2012, air samples were collected in similar flask packages by both instrumented platforms: the Mobile Lab (shown in yellow symbols on Figure 5A-17 below) and the light Aircraft (shown by blue symbols on Figure 5A-17). These air samples were collected in capture mode to document specific source plumes, characterize local gradients (sometimes with unknown source origin) and regional or local background levels. The flask packages were brought back to Boulder, CO, for chemical analysis by NOAA GMD and CU INSTAAR ARL.

The Mobile Lab flask samples chemical analysis data set is available on the NOAA GMD ftp server: ftp://ftp.cmdl.noaa.gov/ccg/campaign/mls/Utah2012/. Note that we are still in the process of evaluating the analytical instruments response for high VOC levels and not all data is available at this time.

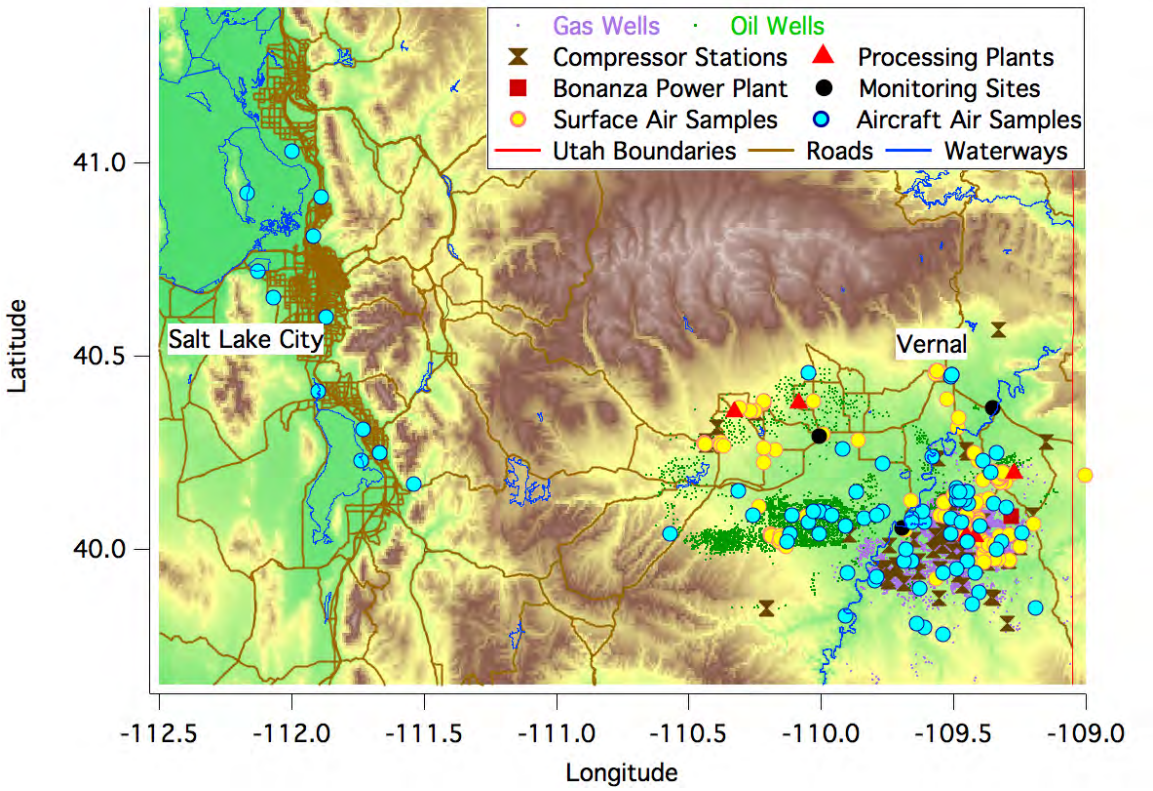

Figure 5A-18. Map showing the location of the discrete air samples collected with the NOAA Mobile Lab (yellow circles) and the NOAA contracted light aircraft (blue circles) during the November 2011 and February 2012 surveys. Also shown in the colored background is surface elevation.

Only light alkane data for which the NOAA GC/MS and CU INSTAAR ARL VOC analysis results agree well are shown in the following plots. As expected, VOC levels in the discrete air samples correlate well with the methane enhancement levels above the 1.85 ppm background. Figures 5A-19 through 5A-22 below display the correlation plots for various VOC measurements done in the Mobile Lab flasks collected in November 2011 and February 2012. For some species, there is a clear distinction in the correlation slopes depending on the source type, but for many others there is some correlation between the various VOCs enhancements, yet there is too much spread within an individual source type, suggesting that some tracers are just emitted in varying relative amounts compared to each other. The Glen Bench site refers to a newly completed gas well close to US 45 and the entrance of Glen Bench Rd. Simulation at the well occurred on February 8 and 9, and a flowback pond was located next to the public road.

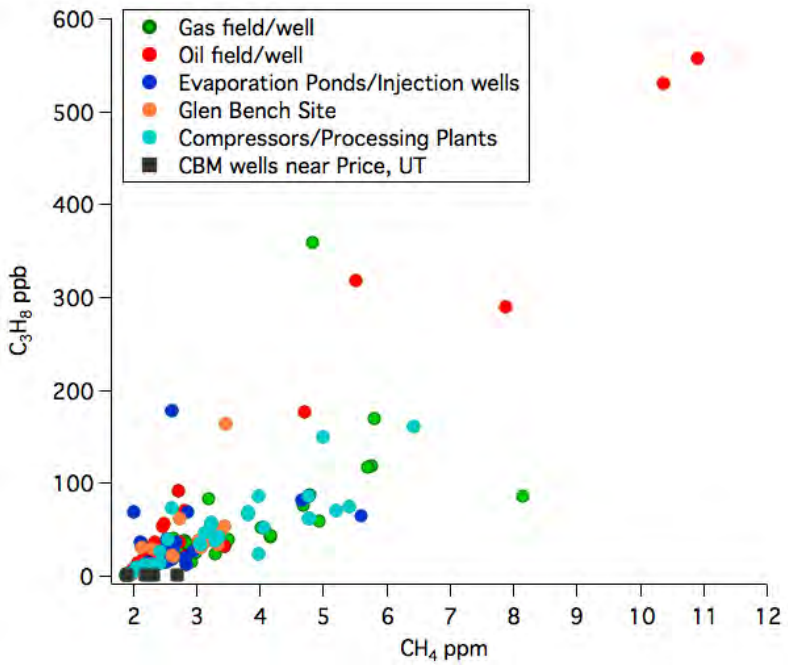

Figure 5A-19. Propane versus methane in the discrete air samples collected with the NOAA Mobile Lab (for both November 2011 and February 2012 campaigns). Color indicates where the sample was taken, in the oil or gas fields or in the plume of an identified large point source.

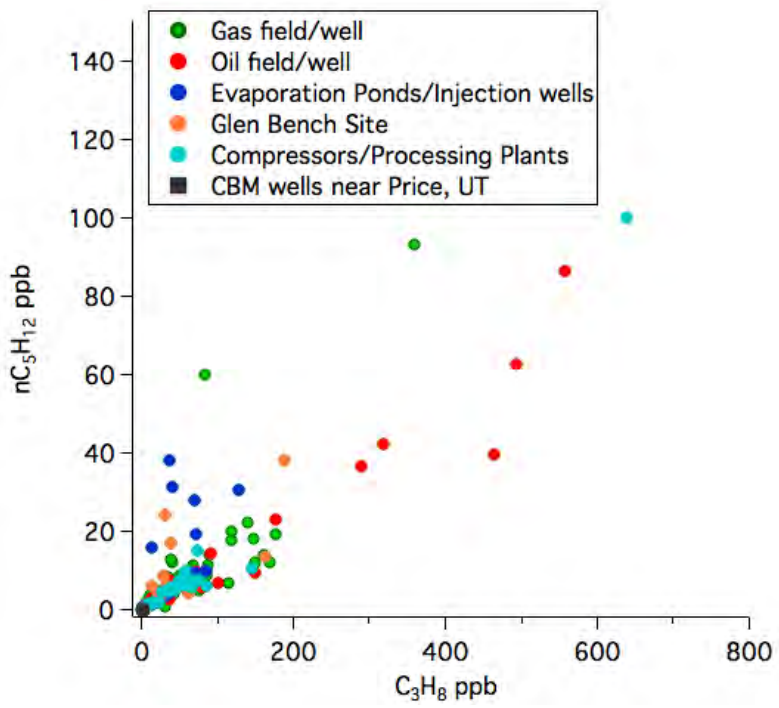

Figure 5A-20. Similarly to Figure 5A-19, n-pentane versus propane in the discrete air samples collected with the NOAA Mobile Lab (for both November 2011 and February 2012 campaigns).

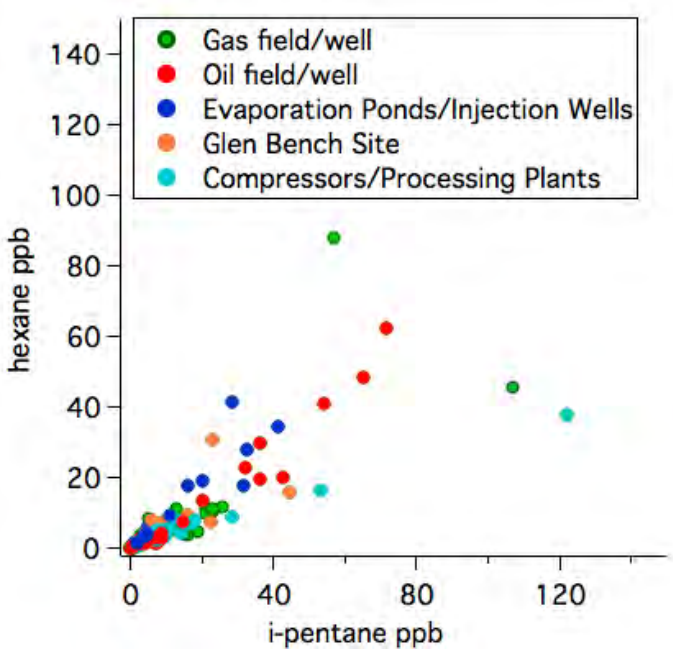

Figure 5A-21. Similarly to Figures 5A-19 and 5A-20, hexane versus i-pentane in the discrete air samples collected with the NOAA Mobile Lab (for both November 2011 and February 2012 campaigns).

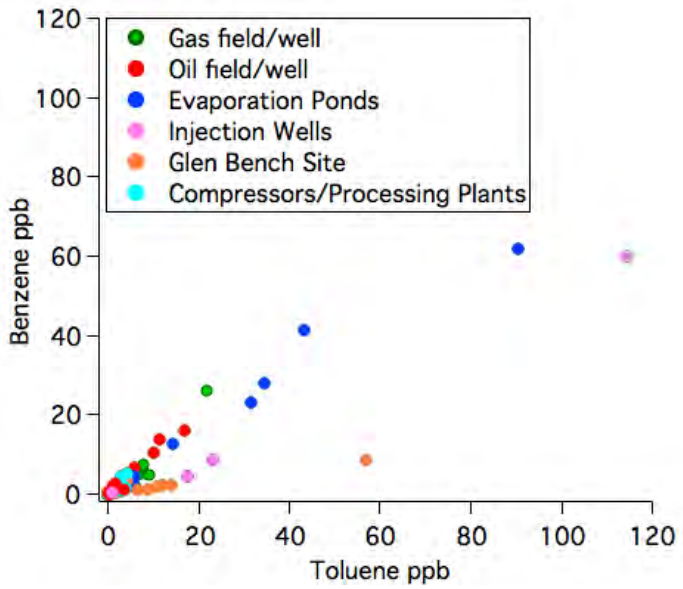

Figure 5A-22. Similarly to Figures 5A-19 and 5A-21, benzene versus toluene in the discrete air samples collected with the NOAA Mobile Lab (for both November 2011 and February 2012 campaigns).

As the Mobile Lab sampled mostly individual point sources plumes, the relative enhancements of various hydrocarbons are showing some substantial spread. Some of the spread is likely due to the non-uniform composition of the gas, condensate and oil produced in the region. Processing of the raw gas and leaks or emissions from various pieces of processing equipment may also explain some of the variability observed.

Figure 5A-23 below presents the range of levels measured by NOAA GMD and CU INSTAAR ARL for a large suite of hydrocarbons. Note the logarithmic scale used to display the results. The flasks hydrocarbon data set is still preliminary at this point, and numbers may be slightly adjusted in the coming months to reflect further tests and scale adjustments.

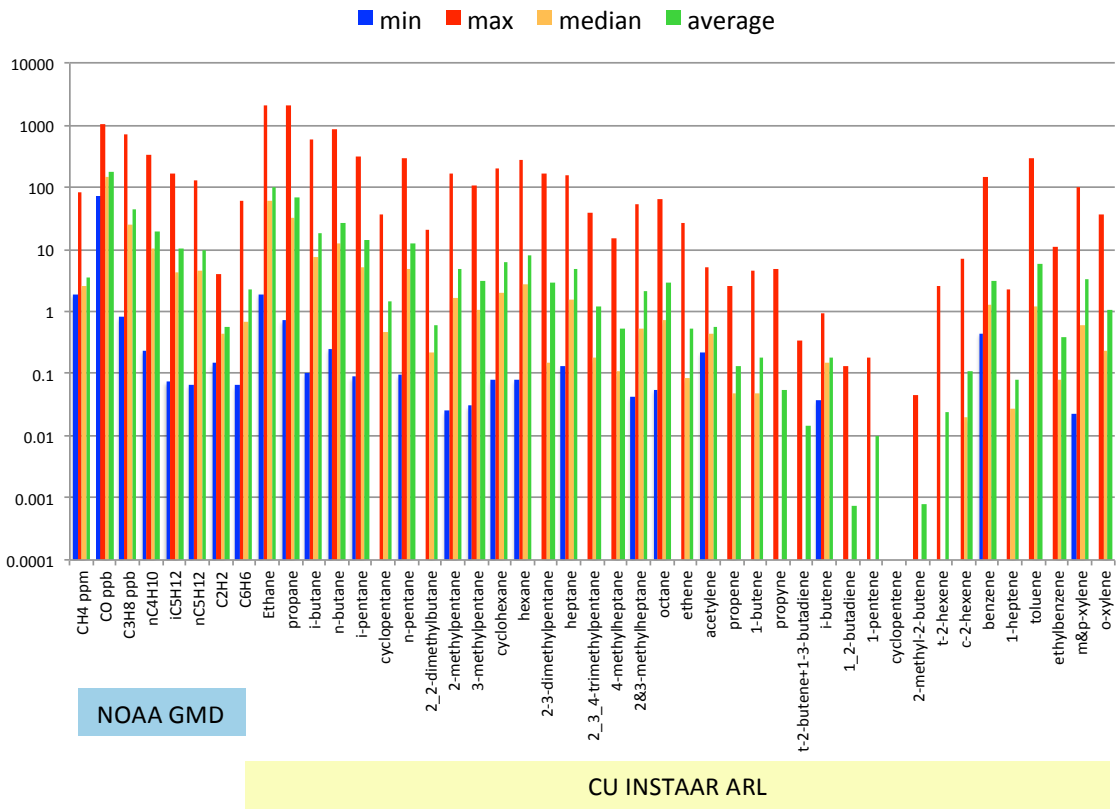

Figure 5A-23. Summary of the minimum, maximum, median and average levels measured in the flasks by NOAA GMD and CU INSTAAR ARL. Note that the subset of flasks analyzed for both labs are not exactly the same. The unit used for the non-methane hydrocarbons mixing ratios is ppb.

CONCLUSIONS

Based on our limited but high quality data set representing air influenced by different sources in the oil and gas fields, we can summarize our preliminary findings by the following statements:

- Targeted sampling of regional enhancements and specific point sources plumes show that alkanes are the most enhanced hydrocarbons. C2+ alkanes during most drives correlate well with methane.
- Aromatics levels are also elevated (> 2 ppb) downwind of certain sources.
- We did not measure significant levels of alkenes in the air samples.
- Measured levels depend on the proximity of the Mobile Lab sampling to the center of the emission plume and on the dispersion conditions when the sample was collected. Therefore, measured absolute atmospheric mixing ratios (or concentrations) should not be considered to be representative of the actual magnitude of a source.

The NOAA Mobile Lab proved to be a very versatile and dependable platform, which allowed the research team to conduct targeted air sampling downwind of specific point sources. The Mobile Lab in-

situ data also provides a valuable record of spatial gradients across the oil and gas fields. A more detailed analysis is underway. It will take into account meteorological conditions and present a synthesis for the data collected during the November 2011 and February 2012 measurement campaigns.

RESULTS FOR NITROGEN OXIDES MEASUREMENTS

The two-channel cavity ring-down spectrometer (CRDS) instrument NOxCaRD (Nitrogen Oxide Cavity Ring Down) was deployed in the mobile laboratory for 17 drives in the Uintah Basin in February 2012. As described in section 1 of this report, the first of these channels directly measures NO_2 by optical extinction at 405 nm and the second measures either NO_x (= NO_2 + NO) or O_x (= NO_2 + O_3) after chemical conversion to NO_2. As both NO_x and O_x cannot be measured simultaneously with the current version of this instrument, 8 of the 17 drives were made in NO_x mode and 9 in O_x mode. The initial findings from these two phases of observations are summarized in the following sections.

NO^2 and NO_x Observations

Simultaneous NO_2 and NO_x observations, at a 1 Hz measurement frequency, were made down wind of gas and oil well pad equipment, compressor stations, and trucks operating within the Uintah Basin. A map showing an example drive when NO_x concentrations were being measured is shown in Figure 5A-24. These measurements were made with concurrent observations of CO, CO_2 and CH_4 (Figure 5A-25), with the aim of characterizing the multiple small NO_x sources within the Basin. This data set has enabled the identification of approximately 100 plume intercepts, with 62 of these being from stationary NO_x sources at oil and gas well pads. Although there is insufficient data to conduct a full test of the regional NO_x emissions inventory, these observations of small sources are to be used in conjunction with the continuous NO_x observations made at the Horse Pool site to better understand the processes controlling NO_x concentrations within the Basin.

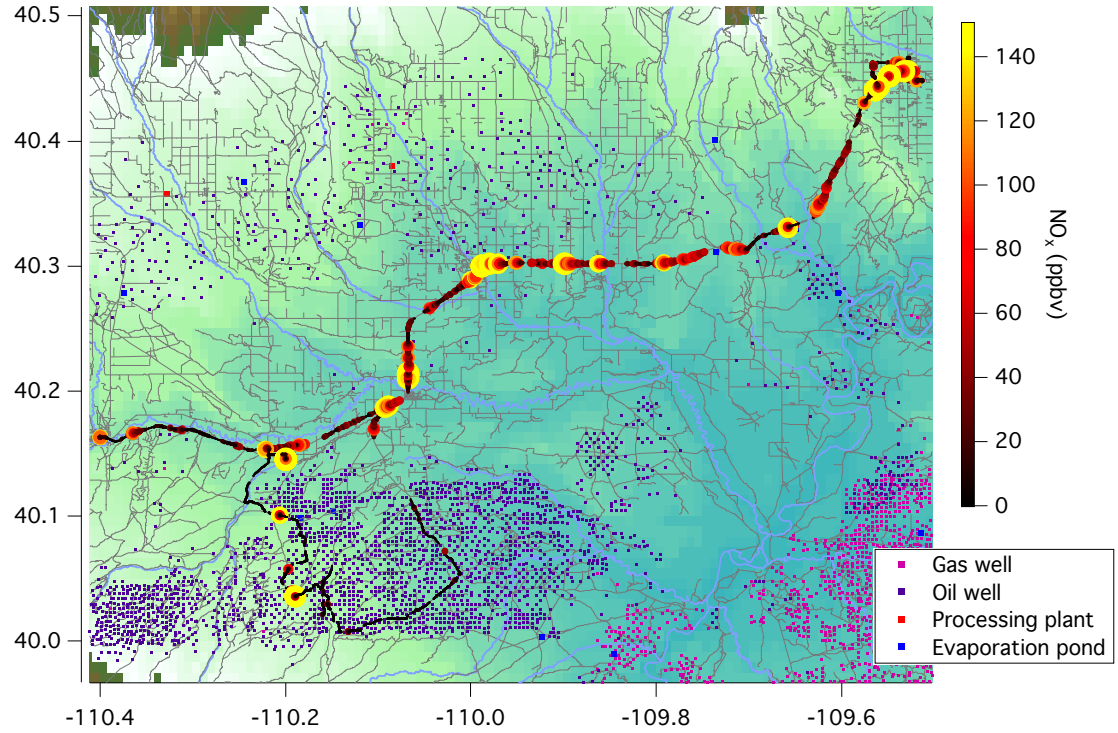

Figure 5A-24. GPS track of a sample drive colored for NO_x concentration. This drive on 11 February 2012 was focused on the emissions from oil well-pads in the west of the Uintah Basin.

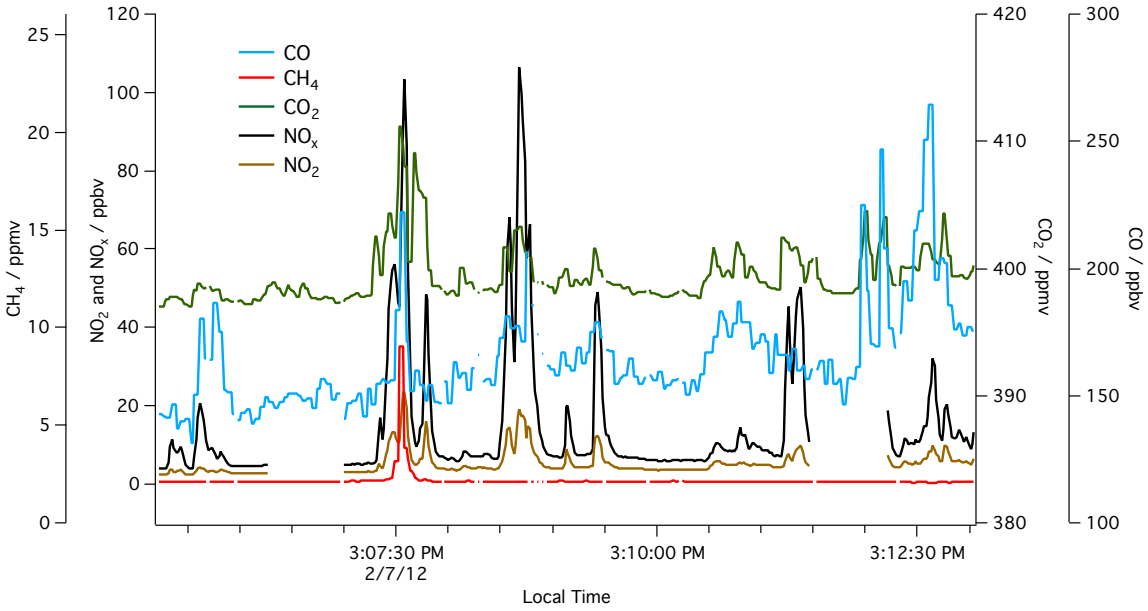

Figure 5A-25. Time series data from the Mobile Laboratory during the intercept of emissions from equipment running at a gas well in the East Uintah Basin. Increases in NO_x and NO_2 are seen to correlate with the combustion tracers CO and CO_2, whilst elevated CH_4 is seen in one of the plume intercepts but not all of them, indicating a potentially different source located on the well pad.

Initial analysis of plumes from equipment at multiple oil/gas well-pads throughout the Uintah Basin finds a large degree of variability in the emission ratios of NO_x to other tracers. Figures 5A-26 and 5A-27 show correlation plots for NO_x with the combustion tracers CO and CO_2 as well as with CH_4, the raw natural gas and the fuel used in the pump motors, and NO_2 in the emission plumes from two different oil well pads. Correlations between NO_x and CO, CO_2, CH_4 and NO_2 are excellent (>0.8) for both sources. The emission ratios of these species, however, are significantly different between the two different oil well pads. This large variability in emissions from seemingly similar sources means that the number of facilities sampled during our study is insufficient to be able to derive an emissions inventory for the entire Basin. These data do, however, provide important information on the magnitude and variability of NO_x emissions from these small sources, of which there are >8000 distributed throughout the Basin (~5000 gas wells and ~3300 oil wells).

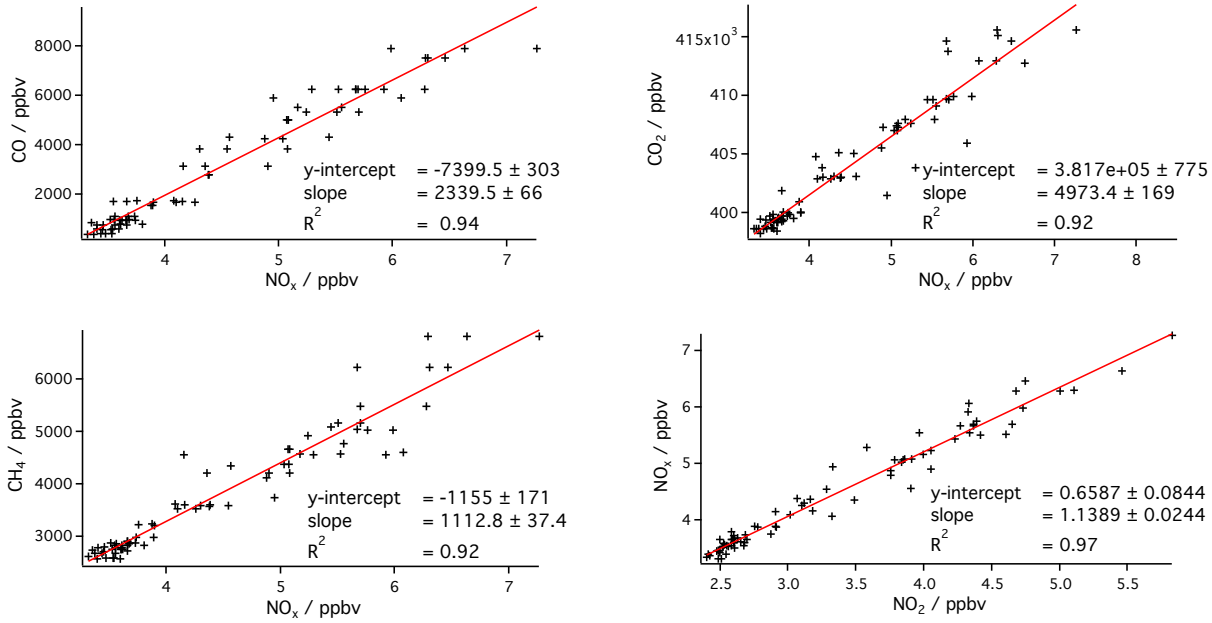

Figure 5A-26. Correlation plots for emissions from oil well pad 1 in Duchesne County. Note the low NO_x:NO_2 ratio of 1.14, implying significant direct NO_2 emissions from this combustion source.

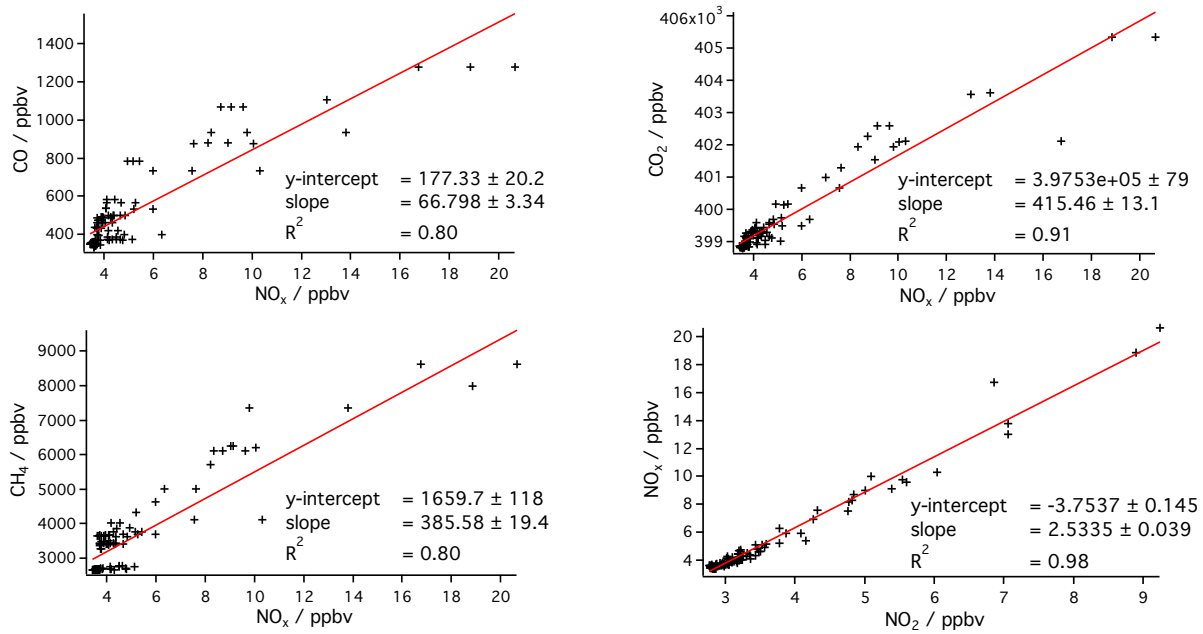

Figure 5A-27. Correlation plots for emissions from oil well pad 2 in Duchesne County.

Continued analysis of the Mobile Lab NO_x data in conjunction with data collected at the Horse Pool site, where continuous observations of NO_x and NO_y were made between 16 January and 1 March 2012, should enable the estimation of the relative importance to basin-wide NO_x of the individual sources identified. This data will then be available to help inform future decisions regarding NO_x emission controls within the Uintah basin.

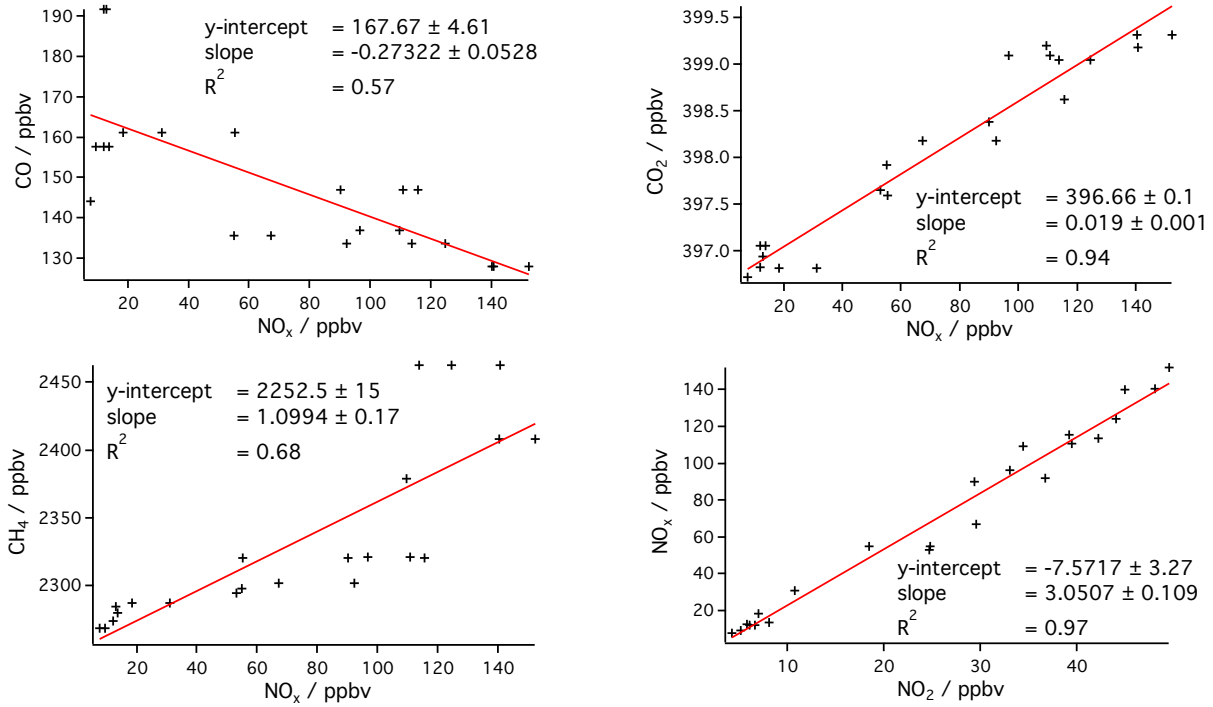

Figure 5A-28. Compressor station.

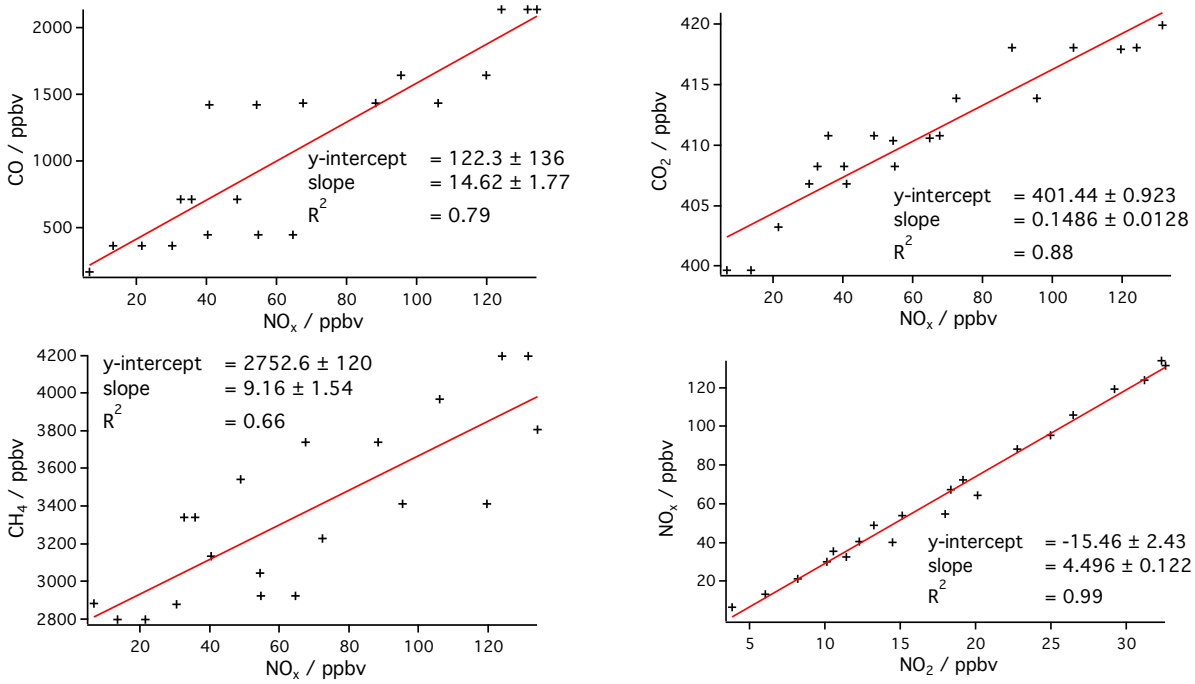

Figure 5A-29. Gas well pad.

Ozone Observations

The O_x (or O_3) mode of the NOxCaRD instrument was intended for characterization of the distribution of ozone across the Uintah Basin during high ozone events. The instrument successfully characterized O_3 distributions, but since there were no events during the 2012 campaign, the instrument demonstrated a relatively uniform background O_3 level within the Basin, similar to what had been observed at the Horse Pool intensive site. The fast-response O_3 instrument did run alongside two more conventional UV absorption O_3 monitors in the mobile lab. The direct comparison between these measurements identified the presence of large, transient interference signals on the UV absorption instruments due to absorption of UV light by aromatic hydrocarbons.

Figure 5A-30 shows O_3 data for the drive on February 19, 2012. The map in the upper left hand corner shows the Uintah Basin, Vernal, the oil and gas wells locations, and the location of the Horse Pool site and the Bonanza power plant. The heavy line is the van drive track, color and size coded by the mixing ratio of O_3 measured by one of the UV instruments (color code shown below the map, size code scaled to color code). The data show UV O_3 mixing ratios in excess of 500 ppbv near the site marked Glen Bench on the map. The time series shows the O_3 data for all three instruments (CRDS O_3 and the two UV instruments). The two UV instruments show similar, large, transient peaks near the end of the drive when the van was in the vicinity of the Glen Bench site. The CRDS O_3, by contrast, shows no apparent deviation from the background level in the area around Glen Bench.

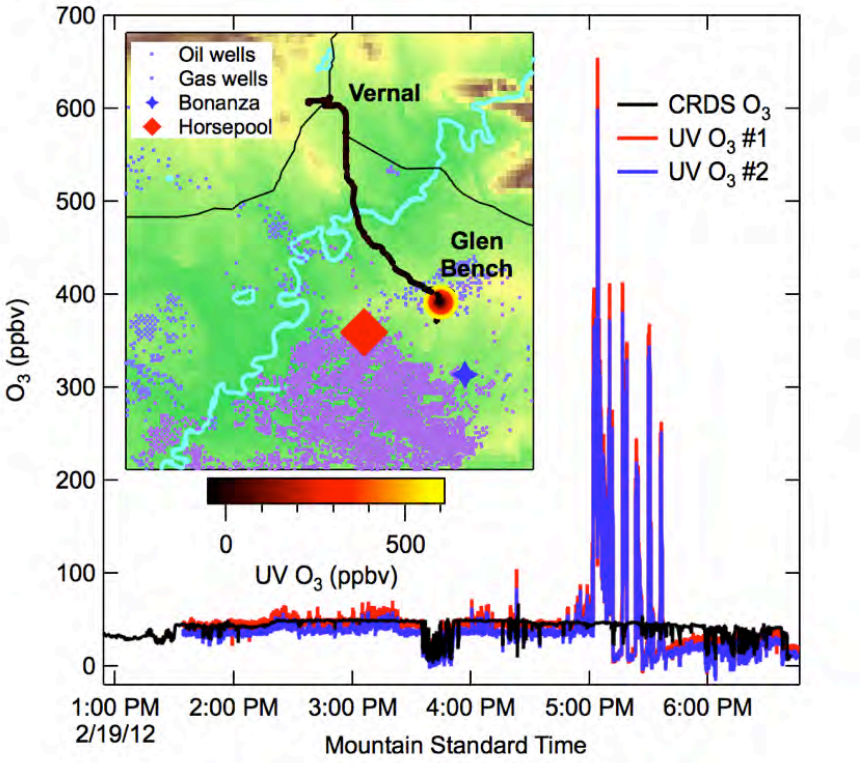

Figure 5A-30. Ozone data for 19 February van drive.

The Glen Bench site was at the intersection of Utah state highway 45 and Glen Bench Road. During the time of the UBWOS 2012 study, there was a well under development at this site that included a flowback pond. Aromatic hydrocarbon concentrations at this site were substantial, and were measured on several different days using a proton-transfer reaction mass spectrometer (PTR-MS) that was mounted on the van for the last half of the campaign. Figure 5A-31 shows an expanded time series of the data from Figure 5A-30 for the time period when the van sampled downwind of the Glen Bench site. The upper graph shows measured concentrations of a variety of different aromatic hydrocarbons, which were well in excess of 1 part per million (ppm) for C6 – C9 aromatics, with peak mixing ratios approaching 10 ppm for C8 aromatics.

The lower graph of Figure 5A-31 shows the calculated interference signal for 254 nm absorption, assuming quantitative transmission of the aromatic VOCs through the UV ozone instrument and no loss of the VOC during instrument zeros. Since the PTR measures only classes of compounds rather than individual ones, the 254 nm absorption cross sections for each class of VOCs was taken as the average of the cross section for the compounds within the class. For example, C8 aromatics consist of ethyl benzene and 1,2-, 1,3- and 1,4-dimethylbenzene. The calculated interference exceeds the measured interference, but the calculated and measured interference signals correlated well, as shown in Figure 5A-32. The measured interference was approximately 60% of the calculated for both instruments.

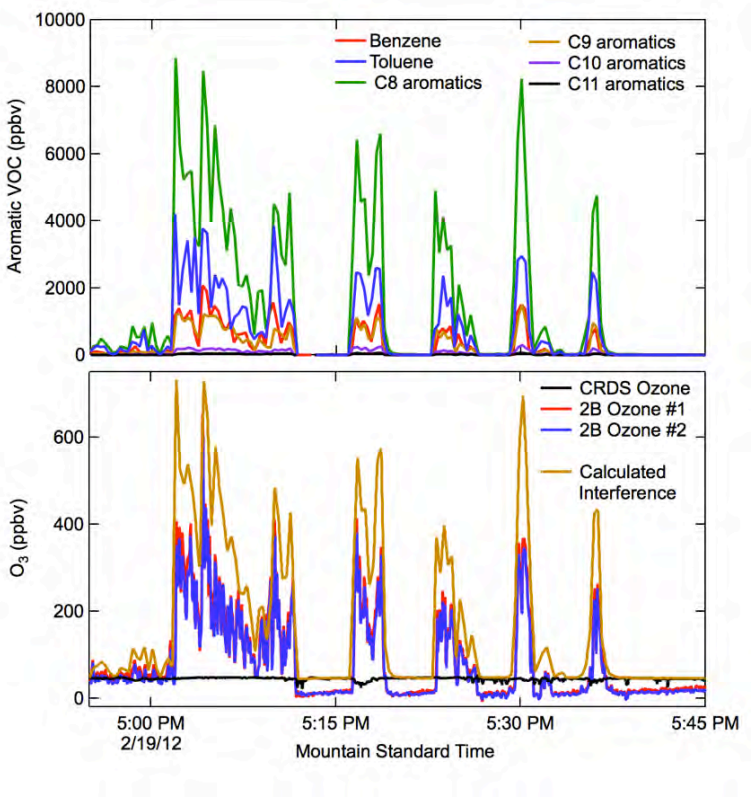

Figure 5A-31. Expanded time series of aromatic VOCs (top) and comparison of measured O_3 signal to the calculated interference (bottom) for the measured aromatics.

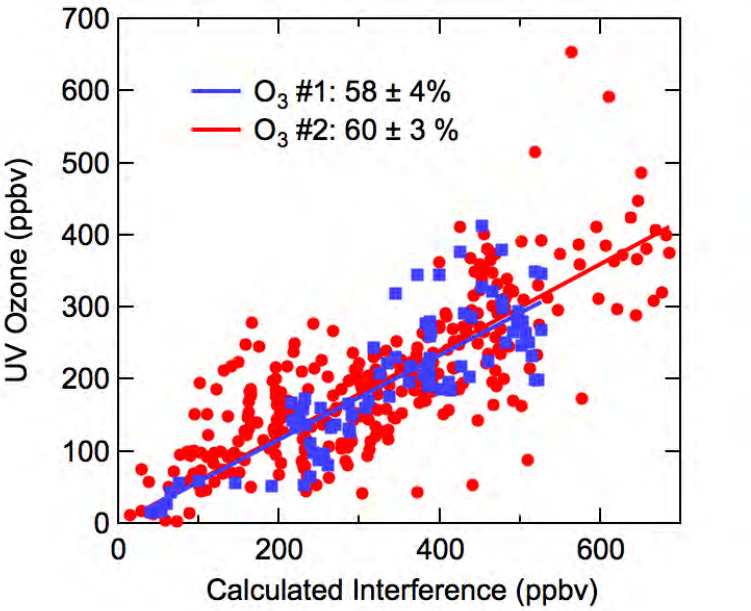

Figure 5A-32. Correlation of measured UV O_3 to calculated interference from Figure 5A-31 for the two UV O_3 monitors.

The discrepancy between the calculated and measured interference signals is most likely due to an impartial zeroing of the aromatic VOCs on the scrubber in the 2B O_3 monitors. These monitors use a metal catalyst to scrub O_3 from ambient air. If the catalyst were also to scrub all of the aromatic VOCs from air, the monitor would register the entire aromatic VOC absorption as an O_3 signal. If the catalyst only partially scrubs the aromatics, it will register a signal smaller than the maximum possible interference. The comparison in Figure 5A-32 suggests that the scrubbers in these monitors remove aromatic VOCs with approximately 40% efficiency.

Observations of interferences on the UV O_3 monitors were observed frequently and with the largest intensity at the Glen Bench flowback pond site. However, it was also observed with regularity, albeit at smaller levels, throughout the Uintah Basin. Figure 5A-33 shows the van drive for February 27. The map inset shows the track of the drive, in this case color and size coded by the difference between the UV and CRDS O_3 instruments. The time series also shows this difference (left axis) and the measured mixing ratio of benzene (right axis). Although the Glen Bench site showed the largest measured interference signal (up to 100 ppbv on this drive), there were numerous other transient interferences correlated with large mixing ratios of benzene at other locations with in the basin, especially within the area with a large number of gas wells.

An immediate question raised by these observations is the potential for aromatic VOC emissions to bias the O_3 measurements and associated O_3 exceedances observed from stationary monitors within the Uintah Basin. Both UV and CRDS based O_3 measurements were made at the Horse Pool site. The UV O_3 monitor at Horse Pool was made by Thermo Electric Corporation ("TECO") and uses a different scrubber material that should make it less sensitive to such an interference. The observed levels of benzene at Horse Pool also did not reach the levels observed immediately downwind of point sources that were sampled by the mobile laboratory. Calculated, transient interferences at Horse Pool never exceeded 10 ppbv O_3, and the campaign average calculated O_3 interference there was less than 0.2 ppbv. Although there were transient differences between the two O_3 instruments at Horse Pool that were on the order of a few ppbv, none correlated with the presence of aromatic VOC in a manner that was systematic enough to suggest interference on the TECO O_3 monitor. Thus, although there were clear, large, transient interferences associated with large point sources sampled by the mobile lab, they are unlikely to bias the conclusions from prior measurements that large exceedances of O_3 occurred within the Uintah Basin in winter under cold temperature inversions.

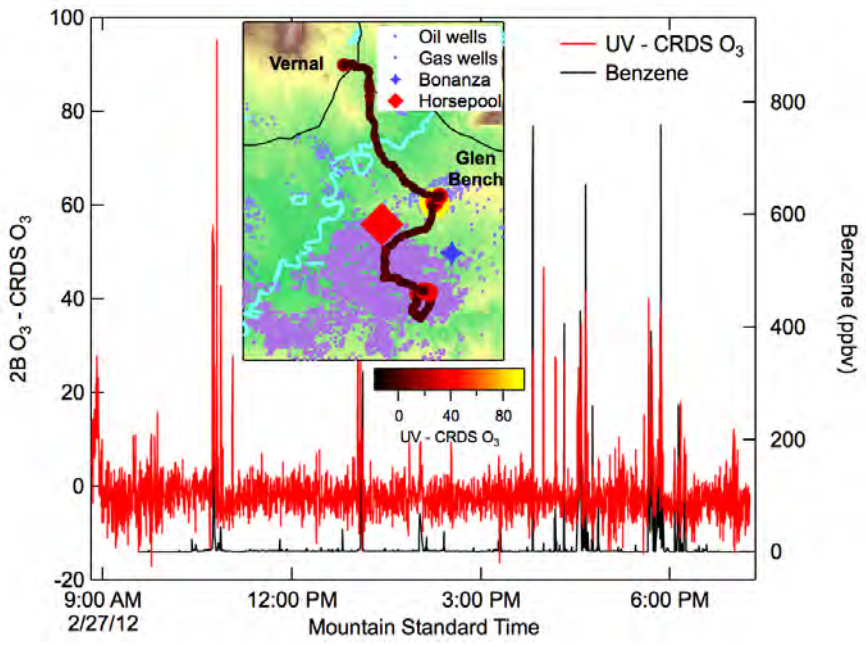

Figure 5A-33. Data from the February 27th mobile lab drive plotted as the difference between the two O_3 monitors (left axis) and the benzene mixing ratio from the PTR-MS (right axis). The map at inset shows the track of the drive in the Uintah Basin, color and size coded by the O_3 difference in the time series.

DATA ACCESS

- Mobile Lab data collected by NOAA GMD is available at:

  ftp://ftp.cmdl.noaa.gov/ccg/campaign/mls/Utah2012/

  As data is being reprocessed, new folders and files will be uploaded on the ftp site.

- Mobile Lab data collected by NOAA CSD is available at (password required):

  http://www.esrl.noaa.gov/csd/groups/csd7/measurements/2012ubwos/Ground/DataDownload/mobilelab.php

Please contact the study PIs if you would like to use the data or have questions about the data. Gabrielle.Petron@noaa.gov and Peter.M.Edwards@noaa.gov

REFERENCES

Conway T., P.P. Tans, L.S. Waterman, K.W. Thoning, D.R. Kitzis, K.A. Masarie, and N. Zhang, Evidence of interannual variability of the carbon cycle from the NOAA/CMDL global air sampling network, J. Geophys. Research, vol. 99, 22831-22855, 1994.

Dlugokencky E.J., L.P. Steele, P. M. Lang and K.A. Masarie, The growth rate and distribution of atmospheric methane. *J. Geophys. Res.*, vol. 99, 17021-17043, 1994.

Dlugokencky E.J., K.A. Masarie, P. M. Lang & P.P. Tans, Continuing decline in the growth rate of the atmospheric methane burden. Nature, vol. 393, p. 447–450, 1998.

Fuchs, H., W. P. Dubé, B. M. Lerner, N. L. Wagner, E. J. Williams, and S. S. Brown, A sensitive and versatile detector for atmospheric NO2 and NOx based on blue diode laser cavity ring-down spectroscopy, *Environ. Sci. Technol.*, 43(20), 7831-7836, doi:10.1021/es902067h, 2009.

Novelli P.C., V.S. Connors, H.G. Reichle, Jr., B.E. Anderson, C.A.M. Brenninkmeijer, E.G. Brunke, B.G. Doddridge, V.W.J.H. Kirchhoff, K.S. Lam, K.A. Masarie, T. Matsuo, D.D. Parrish, H.E. Scheel, and L.P. Steele, An internally consistent set of globally distributed atmospheric carbon monoxide mixing ratios developed using results from an intercomparison of measurements, J. Geophys. Res., Vol. 103, No.D15, p. 19,285-19,293. 1998.

Novelli P. C., A. M. Crotwell and B. D. Hall (2009), Application of Gas Chromatography with a Pulsed Discharge Helium Ionization Detector for Measurements of Molecular Hydrogen in the Atmosphere, *Environmental Science & Technology*, *43*(7), 2431-2436, 10.1021/es803180g.

Pétron, G., et al. (2012), Hydrocarbon emissions characterization in the Colorado Front Range: A pilot study, J. Geophys. Res., 117, D04304, doi:10.1029/2011JD016360.

Washenfelder, R. A., W. P. Dubé, N. L. Wagner, and S. S. Brown, Measurement of atmospheric ozone by cavity ring-down spectroscopy, *Environ. Sci. Technol.*, *45*, 2938-2944, 2011.

CHAPTER V (PART B)

TETHERED OZONESONDE MEASUREMENTS IN THE UINTAH BASIN

Bryan Johnson[1], Russ Schnell[1], Patrick Cullis[2], Emrys Hall[2], Rob Albee[3], Allen Jordan[2], Jim Wendell[1], and Sam Oltmans[2]

[1]NOAA Earth System Research Laboratory, Boulder, CO.
[2]CIRES, University of Colorado, Boulder, CO.
[3]Science and Technology Corporation, http://www.stcnet.com.

INTRODUCTION

Ozone and temperature profiles were measured by tethered ozonesondes at 4 different sites within the Uintah Basin during a three-week period in February 2012. Ozonesondes have been used at NOAA for more than 25 years for monitoring stratospheric ozone at long-term sites and on numerous intensive campaigns. The ozonesondes are typically released on free-flying balloons that reach 30-35 km altitude in less than 2 hours. However, for the Uintah Basin campaign, the relatively fast rising balloon (~ 300 meters per minute rise rate) on a typical ozonesonde flight would travel too quickly through the layer of interest near the surface. Therefore, a new custom built tether system, shown in Figure 5B-1, was designed by NOAA GMD to carry an ozonesonde from ground level to a height of 320 meters and back down in about 60-70 minutes. Based on the 2011 ozone study (Martin et al., 2011) within the Uintah basin this height would extend above the top of a localized wintertime inversion. Therefore, running several profiles per day would track the vertical development of high ozone and provide high-resolution measurements during the inversion period. Ozone levels well above the tether height were important to check fro transport into the basin so full tropospheric and stratospheric profiles were measured from balloon-borne ozonesonde launches within the basin on 2 occasions.

Figure 5B-1a. The portable automated ozonesonde tether setup at Horse Pool.

Figure 5B-1b. The portable automated ozonesonde tether setup at Jensen, Utah.

In addition to the tethered ozonesondes, a continuous UV Photometric surface ozone analyzer (TEI) was operating full time at the Ouray National Wildlife Refuge to measure the diurnal surface ozone concentration range and for ozonesonde data checks prior to each tethered profile measurement. A dual ozonesonde package was also set up to sample from the ozonesonde group's van during five 1-2 hour drives primarily between Ouray, Horse Pool, Jensen and Vernal near the end of the February campaign. The Ouray TEI UV monitor was added on two of the drives to compare with the ozonesondes. One additional comparison involved driving the dual ozonesonde van behind the NOAA full-time mobile van that was using 2B UV ozone monitors.

Figure 5B-2. UV photometric surface ozone analyzer TEI operated full time at the Ouray site during the February campaign.

METHODS AND OBSERVATIONS

Ozonesondes are ideal for vertical ambient and mobile measurements since they are stable under a wide range of temperatures and pressures. The measurement principle is based on the on the iodometric method, the fast reaction of ozone and iodide (I^-) in an aqueous 1% potassium iodide solution. The ozonesonde sensor described by Komhyr et al. [1969, 1995] uses a platinum electrode electrochemical cell. The sensor's output current is linearly proportional to the rate at which ozone is bubbled into the KI solution. Precision is better than ± (3–5)% with an accuracy of about ± (5–10)% up to 30 km altitude based on environmental chamber simulation tests reported by Smit et al. (2007), and from a field ozonesonde intercomparison campaign [Deshler et al., 2008]. The Appendix shows the specifications for the instruments used during the Uintah campaign.

The sensor is interfaced with an Imet radiosonde that measures and transmits ambient pressure, temperature, relative humidity, and GPS altitude and location along with the ozone data.

The Uintah ozonesondes were conditioned and prepared according to NOAA standard operating procedures then compared to a NIST-standardized Thermo Environmental UV ozone calibrator model 49C at 0, 40, and 100 ppbv at the Bingham Research Center Laboratory in Vernal. Final data was QA/QCd using NOAA viewing and editing software.

Figure 5B-3. Ozonesonde preparation and testing location in Bingham Research Center Laboratory. Every ozonesonde used in the Uintah Basin program was tested and calibrated before use.

Tether Ozonesonde Measurements

Two months prior to the start of the Uintah measurements project in February, the tether system was developed and tested by the NOAA Global Monitoring Division. The system is based upon a motorized deep-sea fishing rod and reel with 50-pound line. The fishing rod provided tension relief on the line allowing lower weight line to be used. The lightweight system was shown to be rugged and reliable during operation. The design also included communication software and data loggers to continuously monitor the radiosonde pressure allowing control of the ascent and descent rates. The system can operate unmanned during ascent, descent, and holding at an altitude level as controlled from a laptop computer located up to 30 m distant. Four systems were used during the campaign.

The tethered balloon sites shown on the map in Figure 5B-4 are also listed in Table 5B-1 along with the maximum ozone levels (46.5 to 58.5 ppbv) observed at each site during the February 6-28, 2012 study period. The Horse Pool tether sonde was operated by the University of Colorado group alongside their Sky Doc tether balloon system. Figure 5B-4 shows height above ground level versus average ozone (± 1 standard deviation) for all of the sites, while Figure 5B-5 shows altitude (elevation above sea level) versus average ozone (± 1 standard deviation) for each individual site. Both plots show typical lower morning ozone levels increasing to 40-50 ppbv range by afternoon. Peak values of 50-58 ppbv were observed around 3 PM local time. The Roosevelt site only had 8 profiles measured in the afternoon which makes it appear higher but was not significantly different from other sites when comparing similar times.

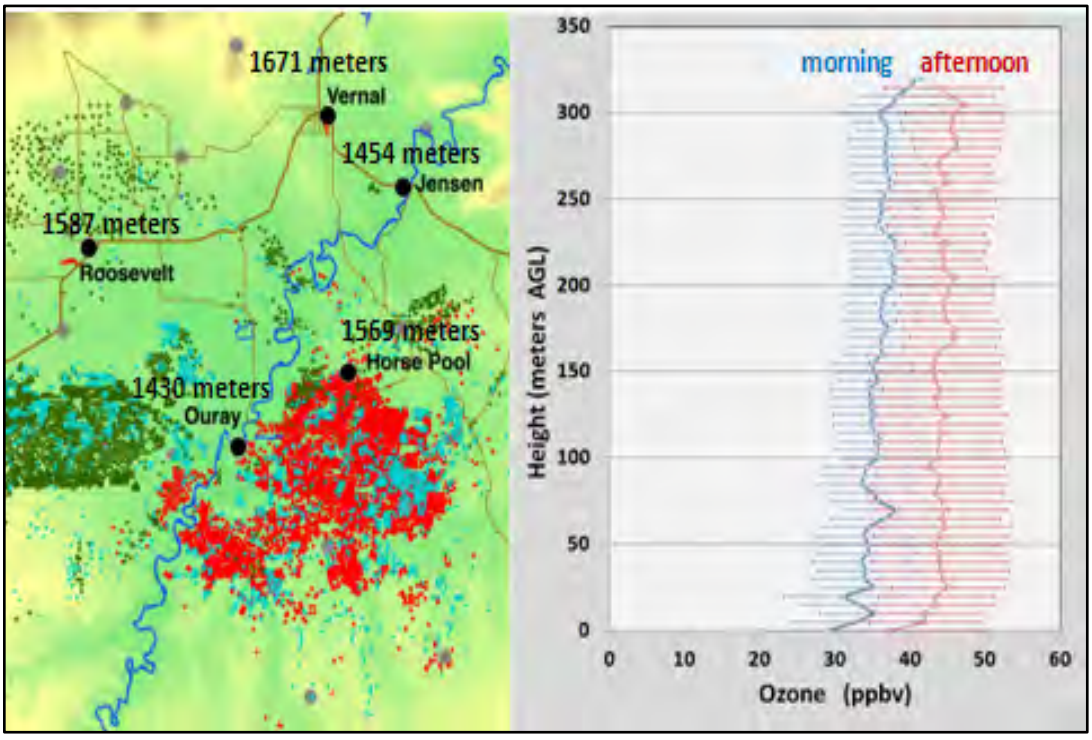

Figure 5B-4. The Uintah Basin tethered ozonesonde site locations with a summary plot of the average ozone mixing ratio and standard deviations measured at all sites during morning (between sunrise and local noon) and afternoon (noon to sunset). The tethersonde systems conducted 135 profiles in February, 2012 in the Uintah Basin plus 16 demonstration profiles in Vernal and Fort Duchesne.

Table 5B-1. Uintah Basin primary tethered ozonesonde site locations, number of profiles measured and maximum ozone mixing ratios measured during February 2012.

Location	Longitude (°W)	Latitude (°N)	Elevation (m)	# of tether profiles/dates	[O3]max (ppbv)
Ouray	109.64459	40.13470	1430	42 Feb 6-27	53.4
Horse Pool	109.46743	40.14309	1569	62 Feb 7-26	58.5
Jensen	109.35191	40.36872	1454	33 Feb 6-28	46.5
Roosevelt	110.00819	40.29425	1587	8 Feb 16	51.1

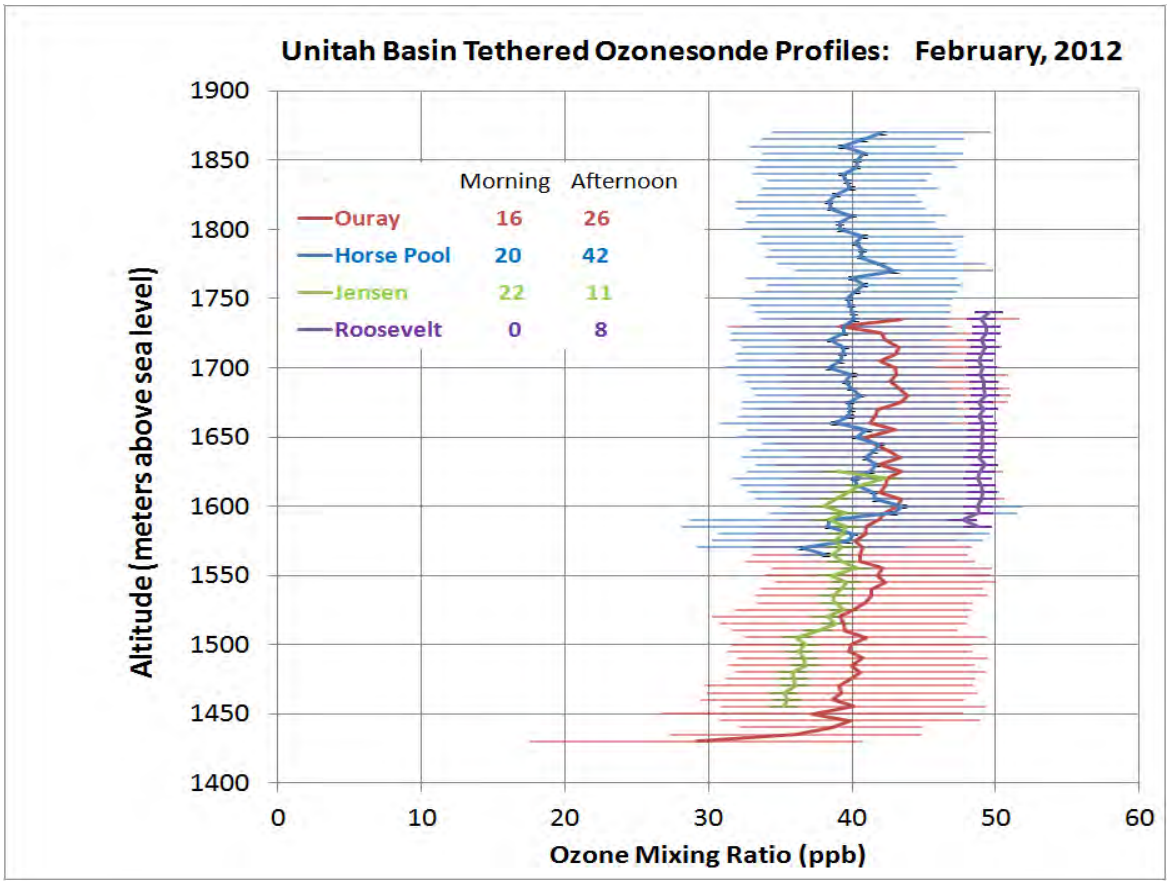

Figure 5B-5. Vertical profiles of ozone ranging from 30-50 ppbv measured by tethered ECC ozonesondes with one standard deviation bars. The vertical axis displays altitude above sea level (meters) rather than height above ground level in order to show matching altitude levels between the color-coded sites in the graph. The peak ozone values were measured between 2 and 4 PM local time. The Roosevelt site only shows afternoon measurements.

The progression of ozone mixing ratio and temperature throughout the first 300 meters in a single day was measured from 20 profiles at Ouray on February 17 from 6:35 AM to 5:46 PM local time. Figures 5B-6 and 5B-7 show two of the individual ozone and temperature profiles during ascent (up) and descent (down) along with height versus time in the shaded region directly below each plot. During the morning (Fig. 6), ozone was very low at 12 ppbv at 2 meters above ground level and increased to 28 ppbv at 50 meters above the surface. The morning up and down profiles from ground to 310 meters showed differences of 5 to 8 ppbv. However, Figure 5B-7 shows that by the afternoon (15:38 – 16:47)

the ozone mixing ratios were nearly identical and well mixed at 51-52 ppbv throughout ascent and descent. The contour plots in Figure 5B-8 summarize the transition in ozone and temperature throughout the day from all 20 profiles. At all times during the campaign, 8hr average surface levels were well below the 75 ppb ozone National Ambient Air Quality Standard.

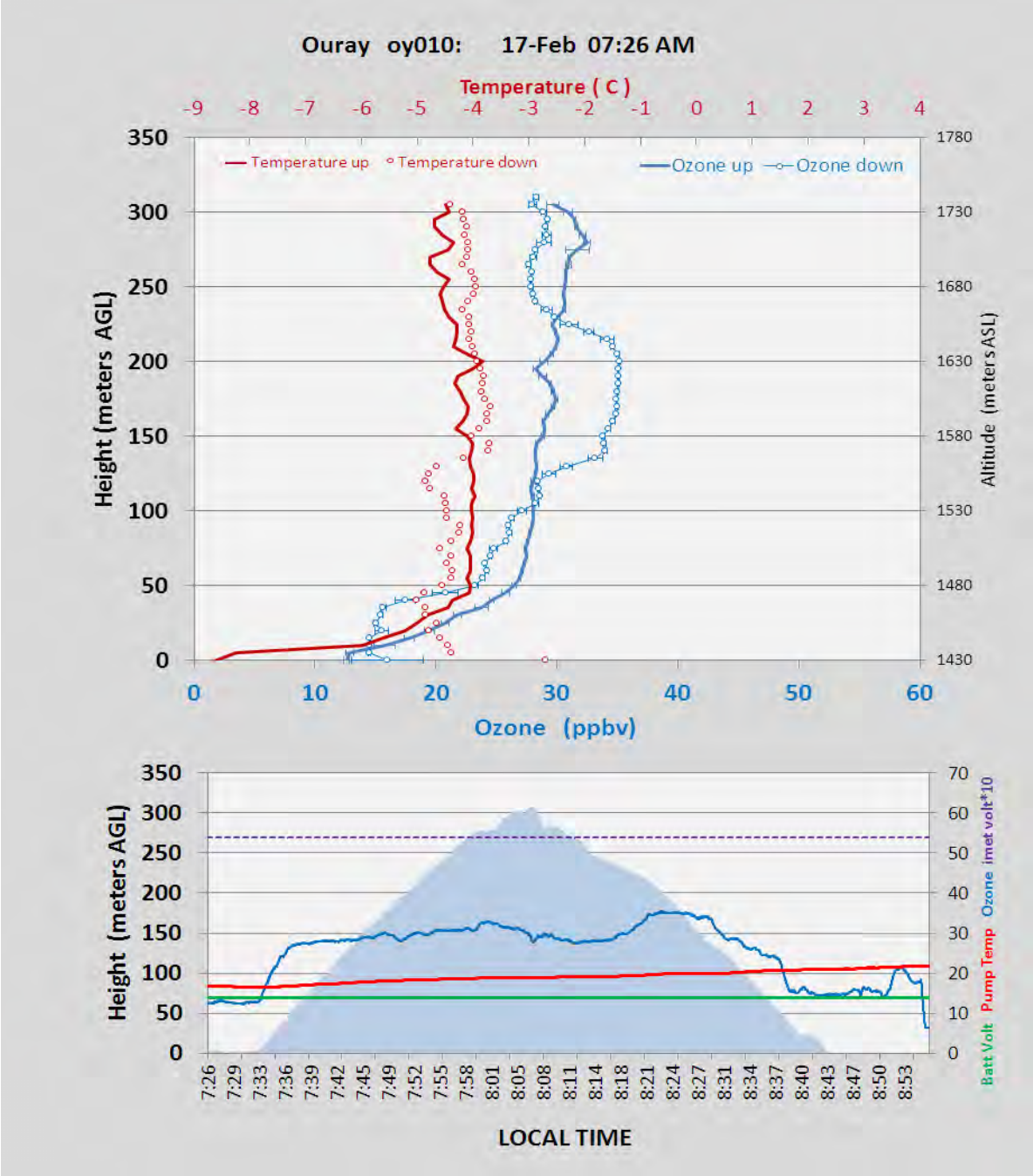

Figure 5B-6. Morning ozonesonde profile at the Ouray site on February 17 from 7:33 to 8:43 local time showing the low ozone levels near the ground. The lower chart shows the altitude in blue shading along with ozone and various ozonesonde instrument-operating parameters on the right vertical axis. It is important to monitor the ozonesonde operating parameters to ensure accurate measurements that are consistent between successive ozone soundings.

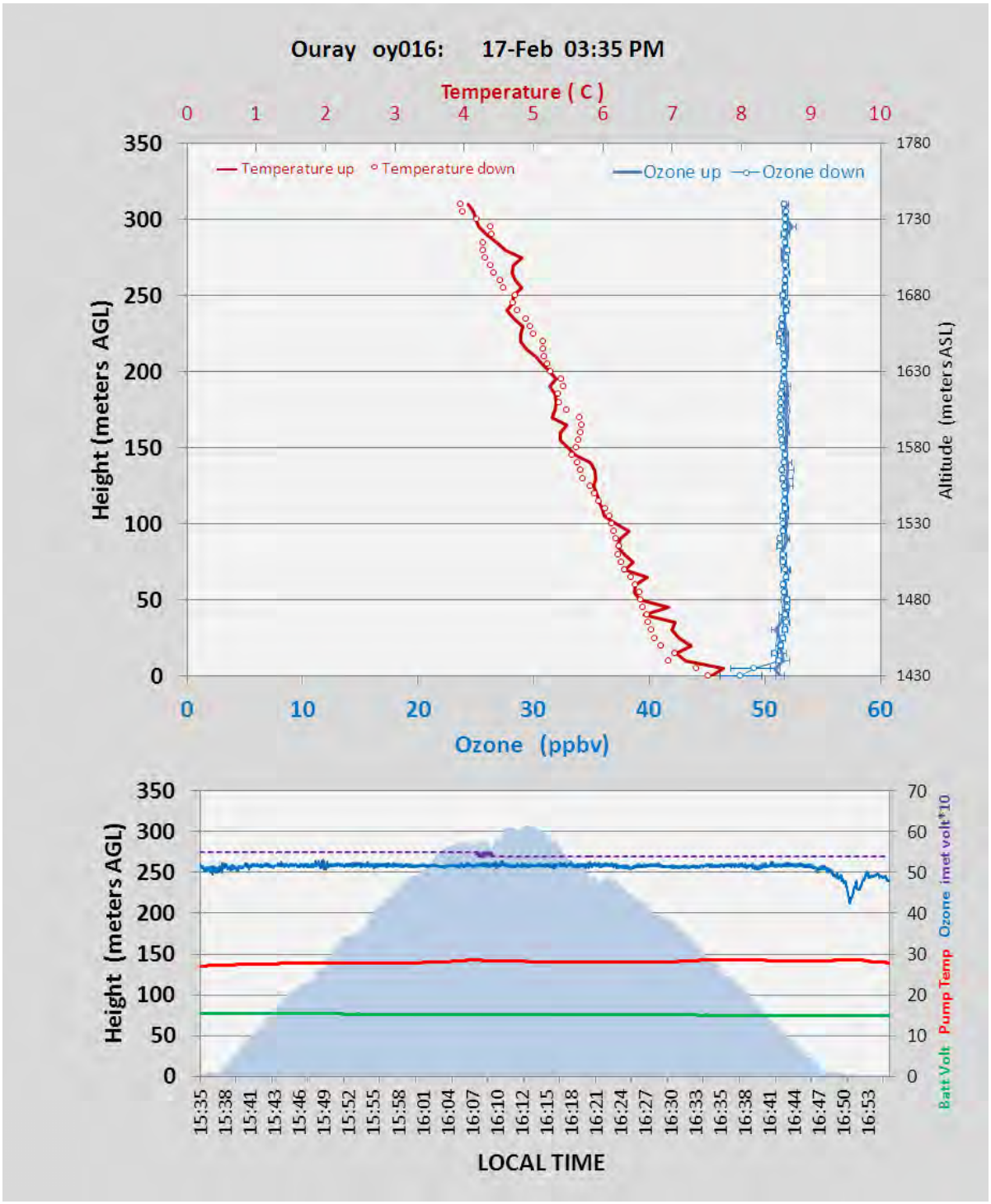

Figure 5B-7. Afternoon ozonesonde profile at Ouray site on February 17 from 15:38 to 16:50 local time showing a well-mixed layer up to 310 meters above ground level and the excellent agreement with ascent and descent ozone mixing ratios.

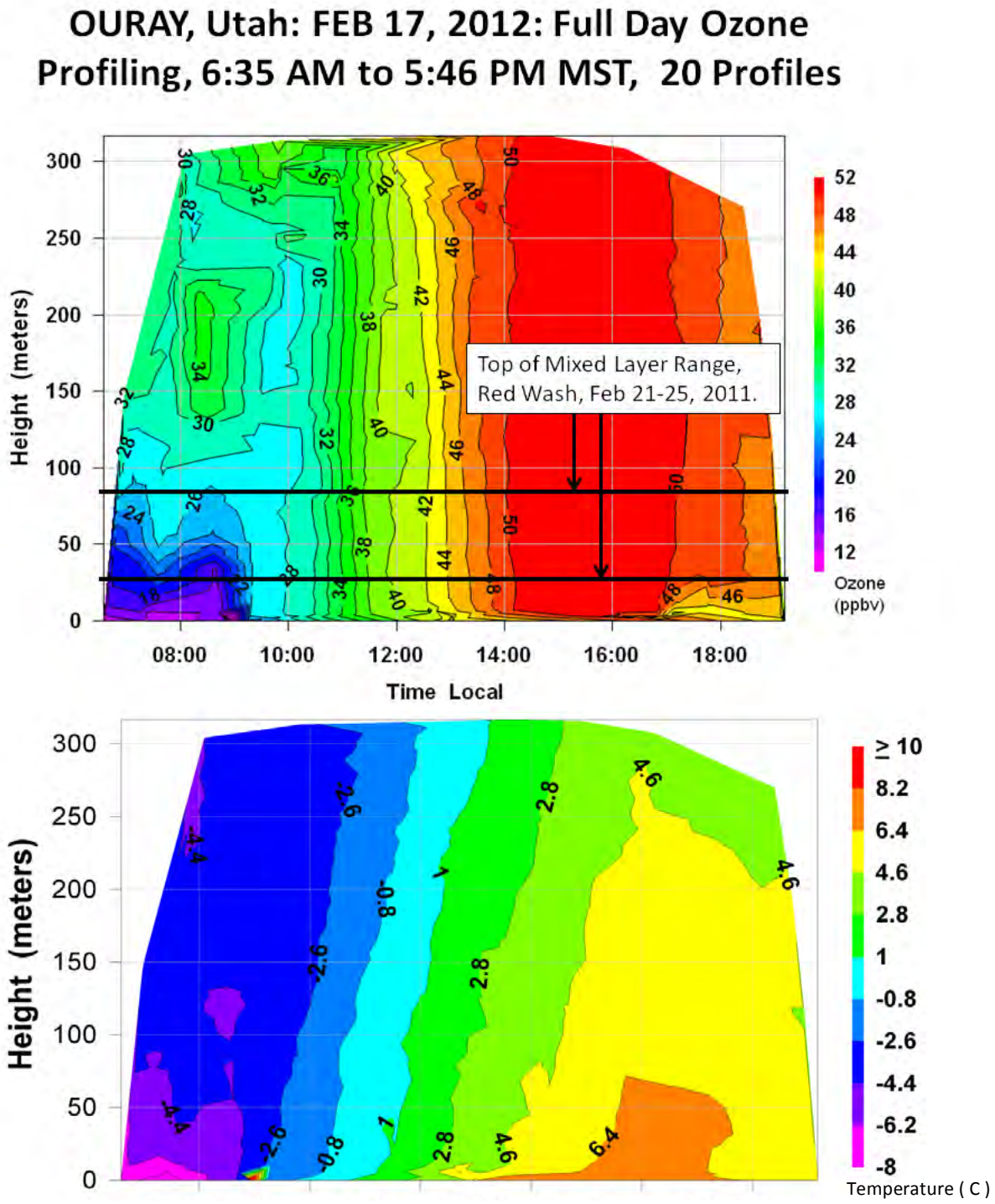

Figure 5B-8. Contours of ozone ppb (top) and temperature (bottom) measured from sunrise to sunset at the Ouray, Utah tethered ozonesonde site on February 17, 2012. The dark horizontal lines shows the typical range for the top of the mixed layer based on 2011 measurements from the Red Wash site. In 2013 we propose to operate four such sites in the Uintah Basin.

TEI Surface Ozone Monitor

The TEI continuous surface ozone monitor at Ouray ran from February 6 until February 27. Figure 5B-9 shows the ozone mixing ratio data averaged in one-minute intervals. The diurnal minimum occurred near 7:00 local time while the ozone-mixing ratio peaked in the afternoon at 15:00 as shown in the lower graph of Figure 5B-9. The one-hour maximum ozone of 50.1 ppb was measured on Feb 18 from 15:00-16:00 local time.

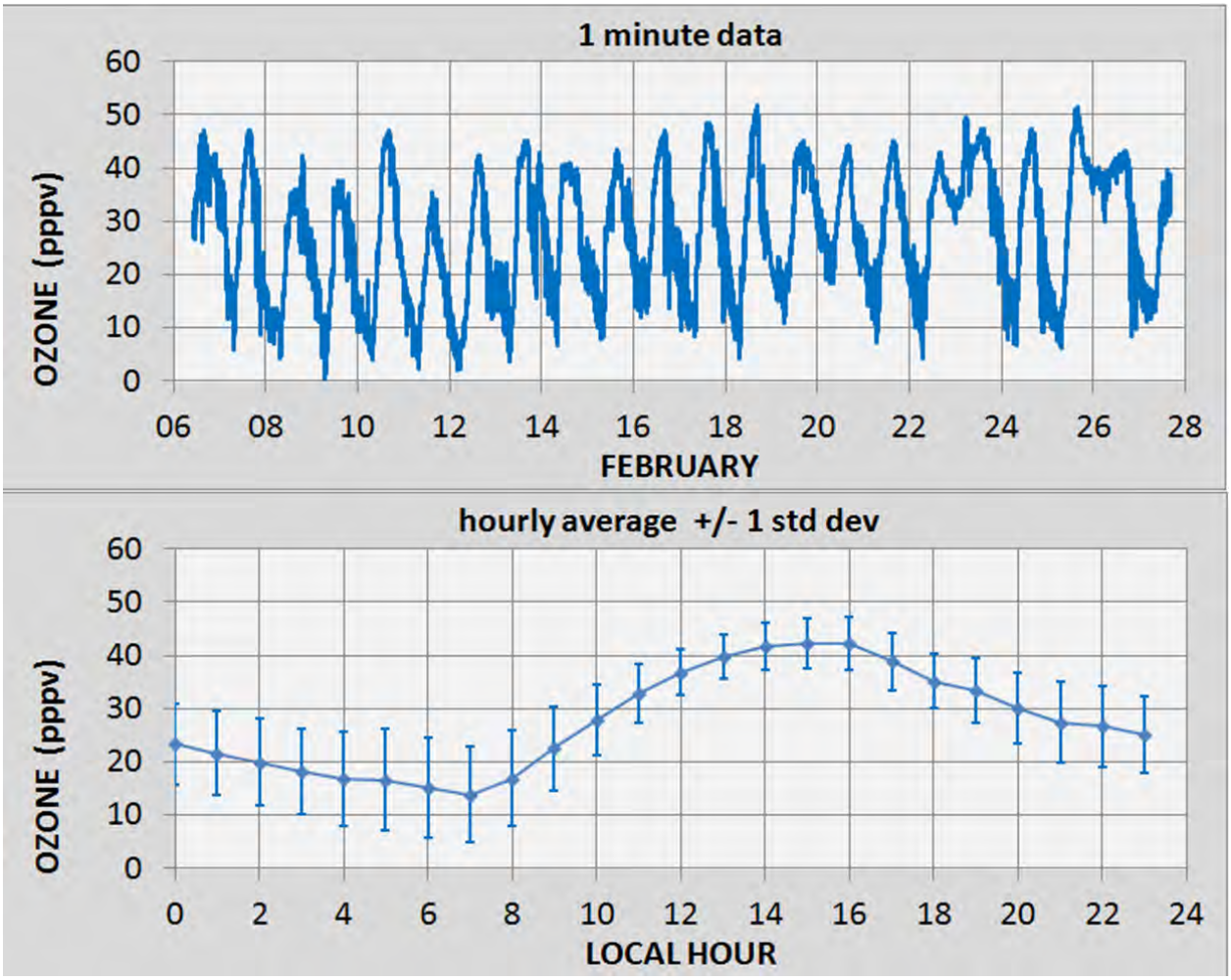

Figure 5B-9. Ouray site TEI surface ozone monitor one-minute data (top) and hourly average with standard deviations for the February 6-27, 2012 period.

Free Flying Ozonesondes

One of the two complete tropospheric and stratospheric ozone profiles measured during the project is shown in Figure 5B-10. The ozonesondes were launched in the afternoon and showed tropospheric ozone remaining below 62 ppbv (right graph) up to 10.2 kilometers above sea level when ozone increased sharply as the sonde entered the stratosphere. The free flying ozonesonde ascent rate was approximately 300 meters per minute, reaching balloon burst altitude in 110 minutes. The receiver and 403 MHz antenna setup at Ouray was able to track the ozonesonde data transmission after burst - the descent was slowed by a small plastic parachute. The ozonesonde data transmission weakened and was

finally lost once the ozonesonde had floated back down to 8 km altitude. The GPS location showed the sonde was then approximately 150 miles to the northeast of Ouray.

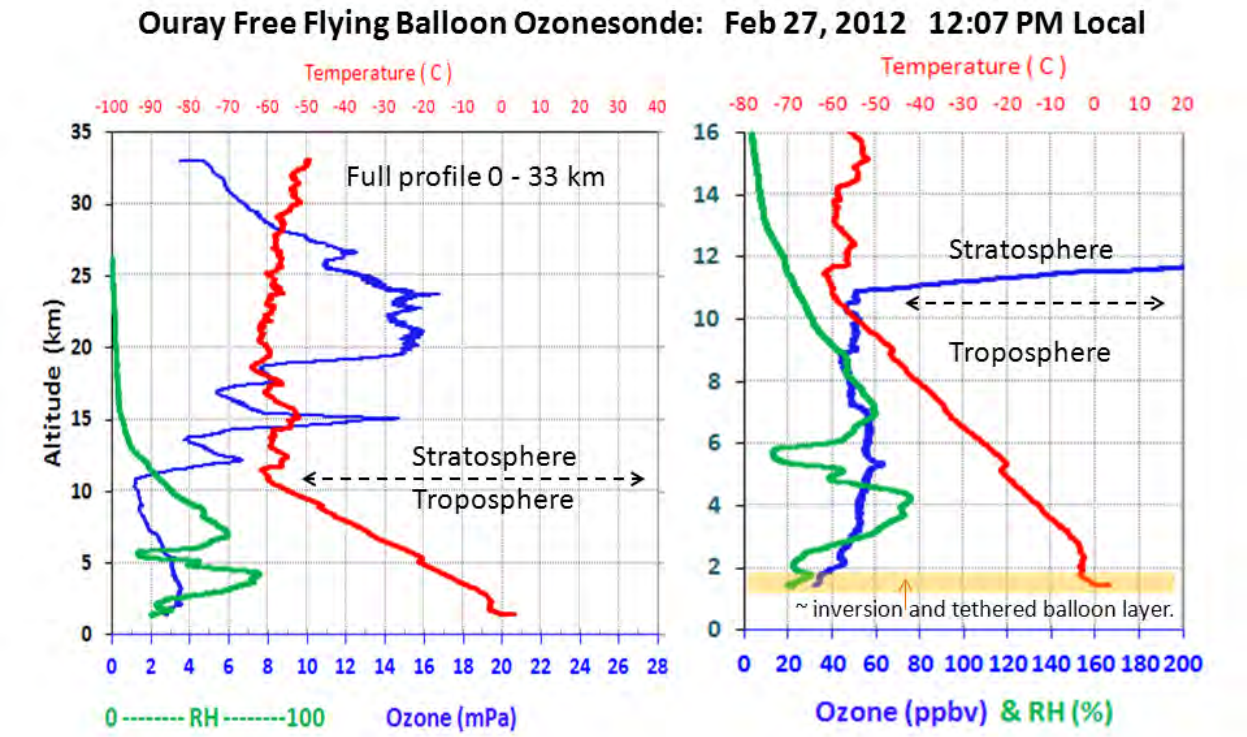

Figure 5B-10. Free flying balloon ozonesonde launched from Ouray on February 27, 2012 showing the sharp temperature and ozone transition from the troposphere to the stratosphere layer at 10.2 kilometers above sea level (33,000 feet). The left graph shows the full ozone profile (partial pressure millipascals) and temperature up to balloon burst height at 33.4 km (110,000 feet).

Dual Ozonesonde Surface Measurements from a Moving Van

The versatility of the ECC ozonesonde allowed for additional surface mobile ozone measurements by mounting a dual ECC ozonesonde (which includes a standard GPS radiosonde) in the rear passenger side window of the NOAA van. Five of the ~ 1.5 to 2 hour drives are summarized in Table 5B-2. Two of the drives included the TEI ozone monitor sampling line directly next to the ozonesonde intake tubes. Power for the receiver and laptop for the ozonesonde system and the TEI ozone monitor was supplied by a 600 watt pure sine wave inverter and 12 volt deep cycle marine battery inside the van.

One of the ECC ozonesondes also included a filter on the air intake to scrub sulfur dioxide. SO_2 interferes with the standard ECC ozonesonde measurement by decreasing the ozone signal by 1 ppb for each ppb of SO_2 in the sampled air. This is typically not a problem for ozonesonde observations since SO_2 natural background concentrations are low, less than 2 ppb. However, in regions where there may be an SO_2 plume, the concentration could be high enough so a difference between the filtered and unfiltered ozonesonde would infer a measurable SO_2 concentration with a detection limit of 3 ppb (Morris et al., 2010).

Figure 5B-11. NOAA dual ozonesonde instrument mounted for mobile measurements.

The ECC ozonesondes and TEI ozone monitor compared very well within rural areas of the sampling drives, usually within 1 ppb. The instruments showed the most variation on February 27, while driving through Vernal city limits during calm, nighttime conditions when differences in the ozonesonde and TEI sampling response times and possibly not well mixed air gave noisy results. The vertical bar in Figure 5B-12 shows when the van entered Vernal city limits. The differences between the SO_2 filtered and unfiltered ECC sondes showed only a few spikes close to 5 ppbv with most average differences below the estimated detection limit of the SO_2 inference method.

Table 5B-2. Summary of dual ozonesonde drives with average, minimum, maximum ozone in parts per billion by volume (ppbv) measured by the dual ozonesondes (#1 = no filter, #2 = SO_2 filter).

Date	From	To	[O3] avg #1 / #2	[O3]min #1 / #2	[O3]max #1 / #2 (ppbv)
Feb 26 17:00	Ouray	Vernal	36.9 / 37.5	20.2 / 18.4	46.9 / 44.7
Feb 27 09:00	Vernal	Ouray	31.4 / 30.9	24.8 / 24.1	35.5 / 35.8
Feb 27 17:00	Ouray	Vernal	33.6 / 34.3	27.7 / 28.2	38.0 / 38.4
Feb 28 09:30	Vernal	Glen Bench	36.6 / 37.2	14.0 / 15.7	46.6 / 47.9
Feb 29 08:15	Vernal	Rangely CO	36.1 / 36.6	21.2 / 21.8	43.6 / 45.5

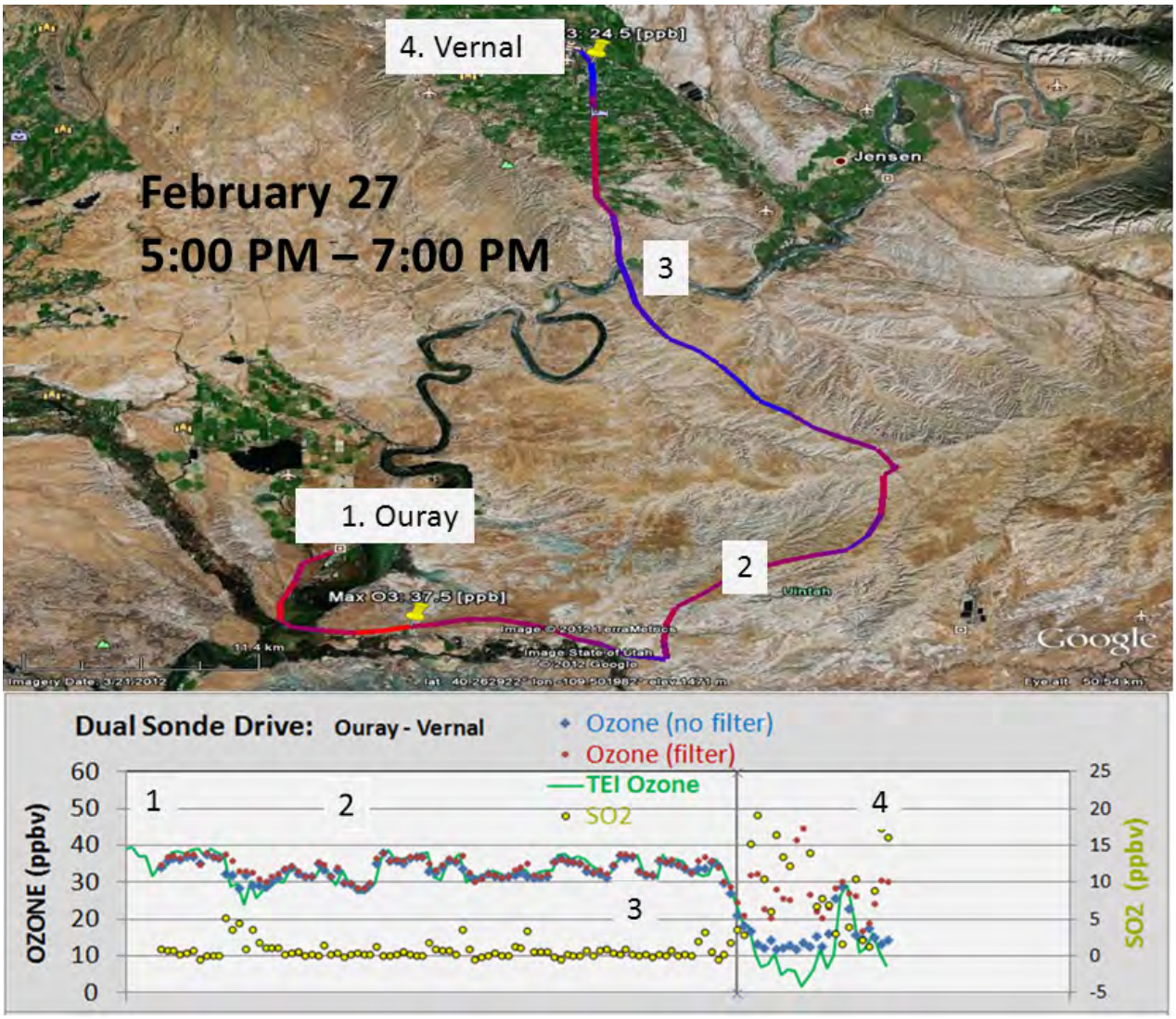

Figure 5B-12. Map of route travelled and measured ozone from the dual ozonesonde and TEI ozone monitor on February 27. The ~ SO_2 scale (ppbv) on the right represents the difference between sonde #1 (no filter) and sonde #2 (SO_2 filter). The vertical bar shows when the van entered Vernal.

OUTREACH AND EDUCATION

The tethered balloon ozonesonde system was set up for 3 different public relation events for demonstration purposes. Along with talks and slideshows the balloon worked very well as a visual aid showing actual scientific measurements of ozone from the balloon-tethered ozonesonde. Presentations were done during the Winter Ozone Study Kickoff Event at the Bingham research center press conference and two local schools: Uintah River High School in Fort Duchesne and Vernal Middle School.

Figure 5B-13. Presentation and balloon demonstration at Uintah River High School in Fort Duchesne, Utah.

Figure 5B-14. Presentation and balloon demonstration at Vernal Middle School.

SUMMARY

Vertical profiles of ozone were measured by tethered ozonesondes at four different sites within the Uintah Basin during the February 2012 air quality study. The primary goal was to set up in early February in preparation for a wintertime inversion forecast, then begin intensive measurements from sunrise to sunset for several days at the sites. However, the conditions never developed as the winter remained mild with very little snow and no winter temperature inversions. Nonetheless, 145 profiles were measured at various times throughout the study period to provide good background ozone measurements typically in the 30-50 ppb range from surface up to 310 meters (1000 feet) above ground level. Peak values were in the 50-58 ppbv range between 2 PM and 4 PM local time. The tethered ECC ozonesonde system was shown to be very mobile and easy to setup to measure ozone profiles under low-wind conditions. In addition to tethered ozonesonde measurements, 2 free flying sondes were released which showed that ozone levels were below 62 ppb throughout the troposphere from surface to nearly 11,000 meters (36,000 feet) altitude, then increased sharply once entering the stratosphere. Mobile van measurements from a dual ozonesonde package and a TEI ozone monitor agreed very well, all measurements showing ozone in the 15–48 ppbv range.

All tethered, free flying balloon, and dual ozonesonde van drive data is available at:
ftp://ftp.cmdl.noaa.gov/ozwv/ozone/Uintah/DATA_NOAA_Balloon/

ACKNOWLEDGEMENTS

The NOAA Global Monitoring Division greatly appreciated the permission, access to power, and assistance for setting up at two excellent locations for the tether ozonesonde system at:

- Ouray National Wildlife Refuge Site (Wildlife Refuge Rd.)
  Thanks to Dan Schaad (Refuge Manager).

- Split Mountain Nursery, 9122 E Highway 40, Jensen, Utah
  Thanks to Heather and Day.

Thanks to the personnel at Bingham Research Center in Vernal for always-available cheerful assistance and for plenty of modern laboratory space to properly check out and calibrate the ozonesondes.

REFERENCES

Deshler, T., et al., Atmospheric comparison of electrochemical cell ozonesondes from different manufacturers, and with different cathode solution strengths: The Balloon Experiment on Standards for Ozonesondes, *J Geophys Res-Atmos*, 113(D4), 2008.

Komhyr, W.D.: Electrochemical concentration cells for gas analysis, *Ann. Geophys., 25*, 203-210, 1969.

Komhyr, W.D., R.A. Barnes, G.B. Brothers, J.A. Lathrop,, and D.P. Opperman: Electrochemical concentration cell ozonesonde performance evaluation during STOIC 1989, *J. Geophys. Res*., 100, 9231-9244, 1995.

Martin, R., K. Moore, M. Mansfield, S. Hill, K. Harper, and H. Shorthill, Final Report: Uintah Basin Winter Ozone and Air Quality Study, December 2010 – March 2011., *Energy Dynamics Laboratory, Utah State University Research Foundation Report,* Document Ndo appumber EDL/11-039, June 14, 2011.

Morris, Gary A., Walter D. Komhyr, Jun Hirokawa, James Flynn, Barry Lefer, Nicholay Krotkov, Fong Ngan: A balloon sounding technique for measuring SO_2 plumes. *J. Atmos. Oceanic Technol*., 27, 1318–1330. doi: 10.1175/2010JTECHA1436.1, 2010.

Smit, H. G. J., et al.: Assessment of the performance of ECC-ozonesondes under quasi-flight conditions in the environmental simulation chamber: Insights from the Juelich Ozone Sonde Intercomparison Experiment (JOSIE), *J Geophys Res-Atmos*, 112(D19), 2007.

APPENDIX: INSTRUMENT SPECIFICATIONS

ECC (electrochemical concentration cell) Ozonesonde

The ozonesonde sensor described by Komhyr et al. [1969, 1995] uses a platinum electrode electrochemical cell. The sensor's output current is linearly proportional to the rate at which ozone is bubbled into the KI solution. Ozone mixing ratio can then be computed from Equation (1).

$$PO_3 = 4.30 \bullet (I - I_{BG}) \bullet Tp \bullet PF / P \qquad (1)$$

Where:
PO_3 = Ozone mixing ratio (parts per billion by volume)
I = Cell output current (~ 0-5.0 microamperes)
I_{BG} = Cell background current (typically 0-0.03 microamperes)
Tp = Temperature of sonde pump (K)
PF = Flow rate in seconds per 100 ml of air flow
Measured by a standard soap bubble flow meter with small correction (+2.5% to +3.5%) applied to account for evaporation of the soap bubble solution.
P = Ambient Air Pressure (hectopascals or millibars)

Accuracy Troposphere: ± 2 ppbv (parts per billion by volume) ± 3-5% of reading
Accuracy Stratosphere: ± (5–10)% up to 30 km altitude.
Precision: ± 3-5%
Data frequency: 1 hz
Calibration: The electrochemical method for measuring ozone is an absolute method. However, ECC ozonesondes are screened before use in the field by checking against the laboratory NIST-standardized Thermo Environmental UV ozone calibrator model 49C at zero, 40 ppbv and 100 ppbv. The ozonesonde must read within 2% of the calibrator before use in the field.

	Free flying release ozonesonde:	Tethered ozonesonde:
Altitude Range:	surface to 98,000 feet	surface to 1,000 feet
Balloon Rise Rate:	800 feet/ minute	35 feet/minute
Vertical Resolution:	160 feet	7 feet

Intermet Radiosonde

Temperature accuracy/precision: ± 0.2 C / 0.2 C
Humidity accuracy/precision: ± <3% / 2%
Pressure accuracy/precision: ±0.5hPa (millibars) / 0.5 hPa
GPS Altitude: +/- 5 meters (16 feet)

Thermo Scientific 49i Ozone Monitor (TEI)

Principle: Dual path UV Absorption
Accuracy Troposphere: ± 1 ppbv (parts per billion by volume)
Precision: ± 3%
Range: 1-250 ppbv Calibration: NIST Traceable Data frequency: 1 minute averages

Contact:

Bryan Johnson
U.S. Department of Commerce
NOAA/ESRL, 325 Broadway, R/GMD1
Ozone & Water Vapor Group
Boulder, CO 80305-3328
phone: (303) 497-6842
email: bryan.johnson@noaa.gov

DATA FTP site: ftp://ftp.cmdl.noaa.gov/ozwv/ozone/Uintah/DATA_NOAA_Balloon

CHAPTER VI

CONTINUOUS VERTICAL PROFILING OF METEOROLOGICAL VARIABLES, OZONE, NITROGEN OXIDES, METHANE, AND TOTAL HYDROCARBONS

Detlev Helmig
Institute of Arctic and Alpine Research, University of Colorado, Boulder

STUDY OBJECTIVES

The objective of this project was to study the sources, sinks, and distribution of ozone, nitrogen oxides, and hydrocarbons in the Uintah Basin by continuous vertical profiling of these gases using the CU Boulder/INSTAAR tethered balloon vertical profiling platform. Meteorological variables were monitored in concert with the chemical observations for linking the chemical behavior of these gas species to synoptic, micrometeorological, and boundary layer conditions and upwind source regions.

STUDY PERIOD & PARTICIPATING SCIENTISTS

The study by the CU Boulder/INSTAAR group was conducted at the Horsepool site from January 28-February 29, 2012. Two to four scientists were at the site at any given time. An RV was rented and kept at the site throughout the study, allowing researchers to spend the night at the site and attend the experiment on a 24/7 schedule. Field personnel included Detlev Helmig (P.I.), Lee Mauldin (senior scientist), Jacques Hueber (engineers), Patrick Boylan (graduate student), Brie vanDam (graduate student), Jorrel Torres (undergraduate researcher). In addition, Brian Seok (graduate student) and Jason Evans (undergraduate student) helped with the field experiment preparation and data handling and processing at CU.

EXPERIMENTAL DETAILS

A SkyDoc tethered balloon was used as a vertical profiling platform. A photograph of the deployment at the site is shown In Figure 6-1. The launch site was approximately 100 meters south of the NOAA CSD instrument trailers and scaffolding. An instrument trailer was placed adjacent to the balloon launch site. A 2 m tower was installed 10 m south of the trailer. Three 650-foot Teflon sampling lines were raised by the balloon, and air was continuously drawn day and night through to the surface. One inlet was placed on the tower at 2 m, and one inlet was placed on the ground to prepare for sample air being drawn from below the snow. Meteorological sensors were mounted at fixed heights on the balloon for measurement of vertical profiles of temperature, wind speed, wind direction, and humidity. A sketch of the experimental setup is shown in Figure 6-2. Gas measurements from the five inlet locations included ozone, nitrogen oxides, methane, and volatile organic compounds (VOC).

Figure 6-1. Setup of the CU Boulder experiment at the Horsepool site. The photograph depicts the 20-foot diameter SkyDoc tethered balloon, the balloon winch (inside wooden box), and the CU instrument trailer. At the time of the picture, the balloon was lowered to the surface (here at approximately 30 feet) for instrument maintenance. During regular operation, the balloon was raised to 500 feet and served as a "sky dock" for raising instruments and sampling-line inlets.

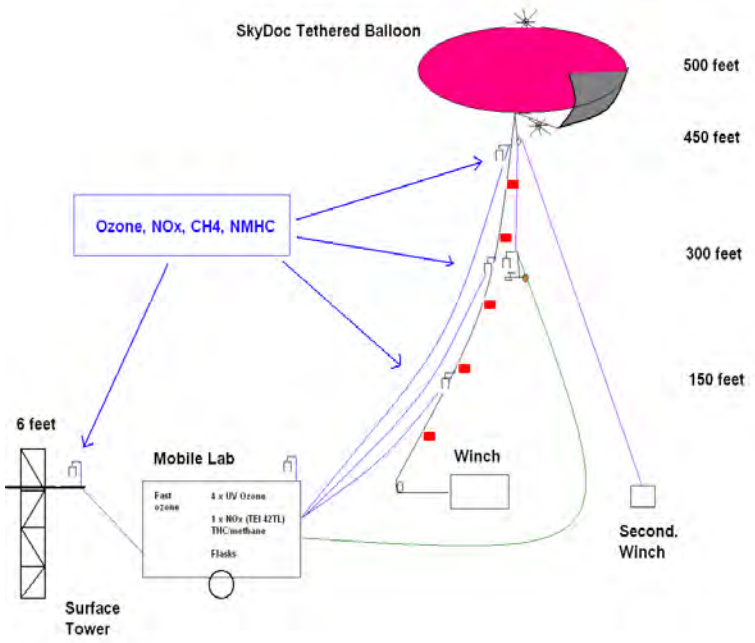

Figure 6-2. Schematic of the CU Boulder balloon experiment.

RESULTS

The experiment provided continuous, 100% data coverage from the ground observations February 1-29. The tethered balloon vertical profiling observations covered approximately 75% (~ 500 hours) of that time, which reflects a remarkably successful operation of the balloon system. Gaps in the balloon data resulted from the regular ground level intercomparison measurements of balloon sampling line inlets and meteorological sensors, from several periods with high winds when the balloon had to be kept near the surface for safety reasons, and from two occasions when the balloon had to undergo repairs of damages suffered during high wind conditions.

Summary of Ozone Measurement Results

Ozone was measured in the range of 10-60 ppbv during the study period. Ozone showed a very dynamic behavior, typically increasing during the day and declining at night. The daytime/nighttime amplitude was on the order of 20-40 ppbv. At night, the lowest 500 feet of the atmosphere that were probed with the balloon showed a distinct stratification, with stronger ozone removal/destruction observed near the surface. During daytime hours, a homogeneous vertical distribution was observed. The example in Figure 6-3 shows a typical diurnal cycle of ozone measured at four heights.

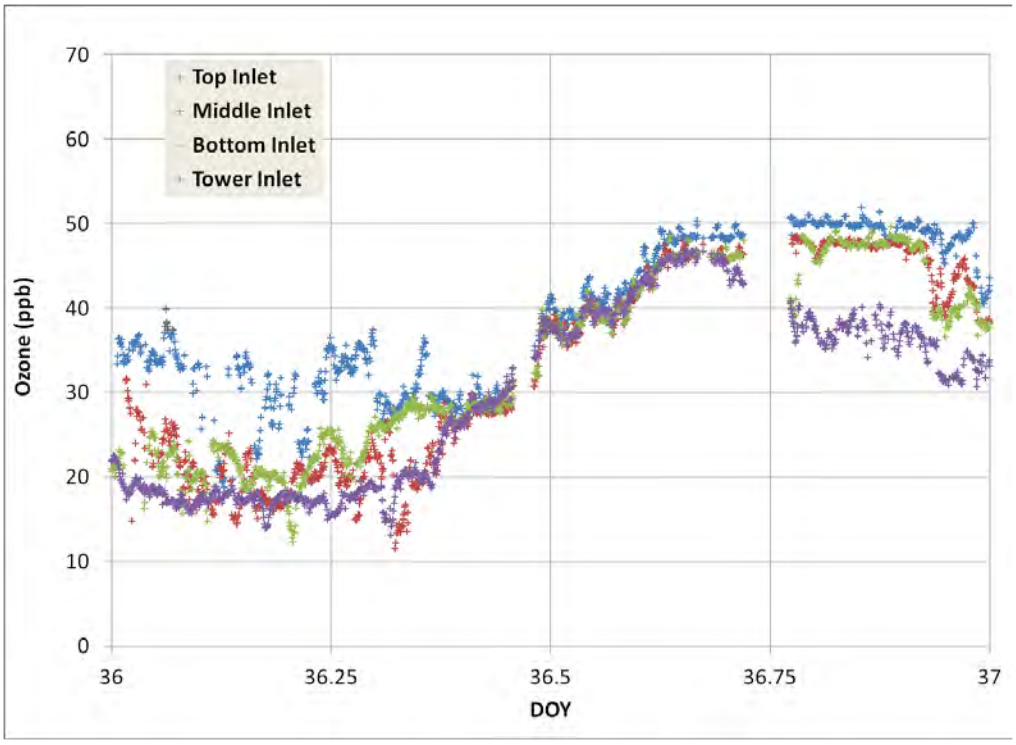

Figure 6-3. Example of a full day of ozone measurements from the three balloon inlets (top = 450 feet, middle = 300 feet, bottom = 150 feet) and tower inlet (6 feet) on 5 Feb. 2012 (DOY 36).

Summary of Nitrogen Oxides Measurement Results

Total nitrogen oxides (NOx) were generally in the range 1-30 ppbv. NOx were quite variable, with large enhancements occurring both during day and at night. Stronger enhancements were at times seen at the lower sampling heights, and at other times in air drawn from higher aloft. The observed NOx levels and their dynamic concentration behavior point towards a multitude of significant NOx sources in the

immediate surroundings of the site. The NOx seen at Horsepool resembles an urban/inner city behavior. A NOx data example is shown in Figure 6-4.

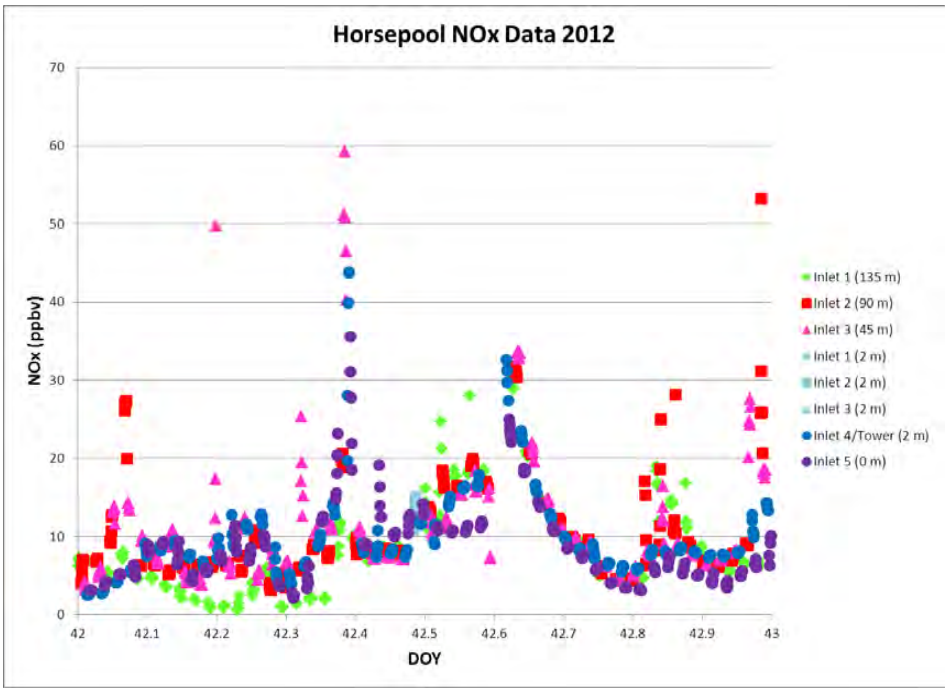

Figure 6-4. Example of one day of NOx measurements from the balloon inlets, and surface tower, and ground inlets from 11 Feb. 2012 (DOY 42).

Nitrogen monoxide (NO) showed strong diurnal cycles, with maxima of 1-5 ppbv during the daytime and levels dropping well below 1 ppbv at night. The low nighttime NO levels illustrate that natural NO soil emissions at the site are an insignificant source, and that most NO originates from the photolysis of NO_2 that is transported to the site.

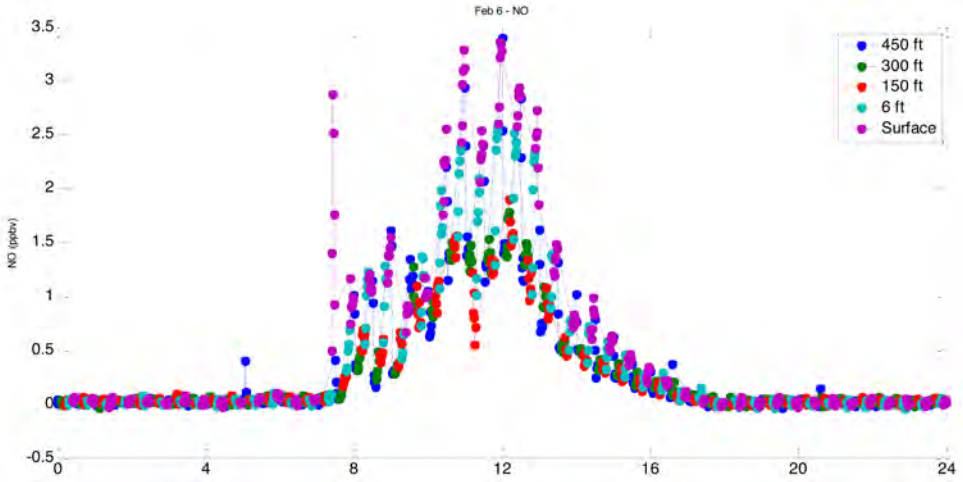

Figure 6-5. Example of one day of NO measurements from the balloon inlets, surface tower, and ground inlet from 6 Feb. 2012. Please note that the data from the long balloon line have not been corrected (yet) for possible NO -> NO2 conversion that can occur during the ~ 1 min residence time in the tubing.

Summary of Methane Results

Methane showed remarkable enhancements over background concentrations. Observed methane levels were in the range of 2-20 ppmv. Methane showed accumulation in the surface layer during night and lower levels during daytime hours. Higher methane concentrations were seen near the surface at night compared to aloft. A relatively homogeneous distribution with height was seen during the day. The methane data point towards a multitude of strong sources in the region. An example of a diurnal methane cycle and diurnal profile is shown in Figure 6-6.

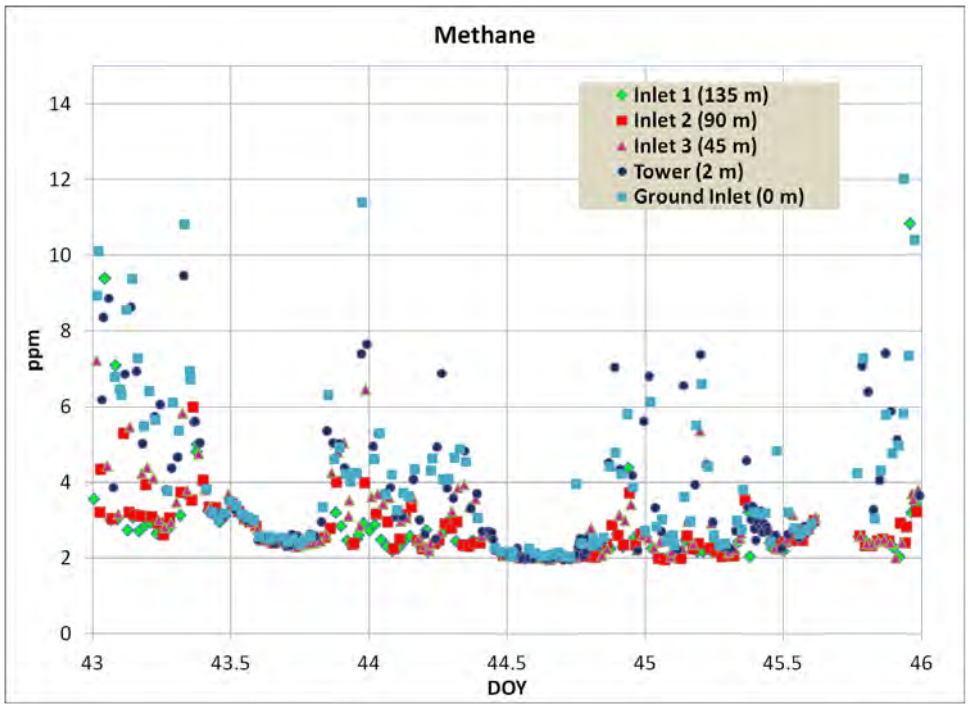

Figure 6-6. Methane in air drawn from the balloon inlets, surface tower, and ground inlet from 12-15 Feb. 2012 (DOY 43-46).

Summary of Volatile Organic Compounds Results

VOC were determined at the site in-situ with a gas chromatography system operated in the CU instrument trailer and in flask samples that were collected at the site and then brought back to CU for analysis on a laboratory system. Results from these two independent procedures were very consistent. VOC were dominated by light non-methane hydrocarbons, with the largest mass fraction constituted by alkanes, i.e., ethane, propane, iso-butane, n-butane. There were many more higher carbon number alkanes identified, with generally their mass contribution declining with increasing molecule size. NMHC showed distinct diurnal cycles, with similar patterns as observed for methane. Concentration maxima were observed at night, and minima during midday to evening hours. Figure 6-6 shows this pattern for three days of ethane data. Concentrations of NMHC were highly elevated over background levels. For instance, the background for ethane for 40 deg N latitude and the month of February is on the order of 2 ppbv. The data in Figure 6-6 show that ethane levels measured at Horsepool ranged between 2-350 ppbv, with maxima exceeding the hemispheric background by up to 150 times. NMHC showed similar concentration patters from the ground to the highest balloon inlet, with near-surface concentrations in general being 10-50% higher than aloft. Observed NMHC concentrations are by far the highest ethane levels we have observed in 20+ years of ambient air ethane monitoring, including observations from

inner city sites. Similar conclusions can be drawn for the other NMHC that were quantified. There were strong correlations between individual NMHC species (Figure 6-7). NMHC also correlated with methane (Figure 6-8). The high correlation seen between NMHC and methane makes it plausible that these compounds share common sources. The slopes of the NMHC to methane relationships can consequently be used to estimate the mass of NMHC released in relation to methane. This analysis suggests that ethane constitutes 6-10% of the mass of methane emitted. Pooling all identified NMHC results over methane results in a total NMHC mass ratio of approximately 30%. In Figure 6-9, the ethane-methane data pairs are color-coded by surface wind direction during the time of sampling. Furthermore, the size of the data point is an indication of wind speed, with larger data points resulting from high wind conditions. This analysis illustrates that higher methane and ethane concentrations were observed when winds came from the east to southwest sector. Furthermore, higher concentration occurred during low wind speeds. At higher winds, NMHC were consistently at the lower threshold of observed concentrations.

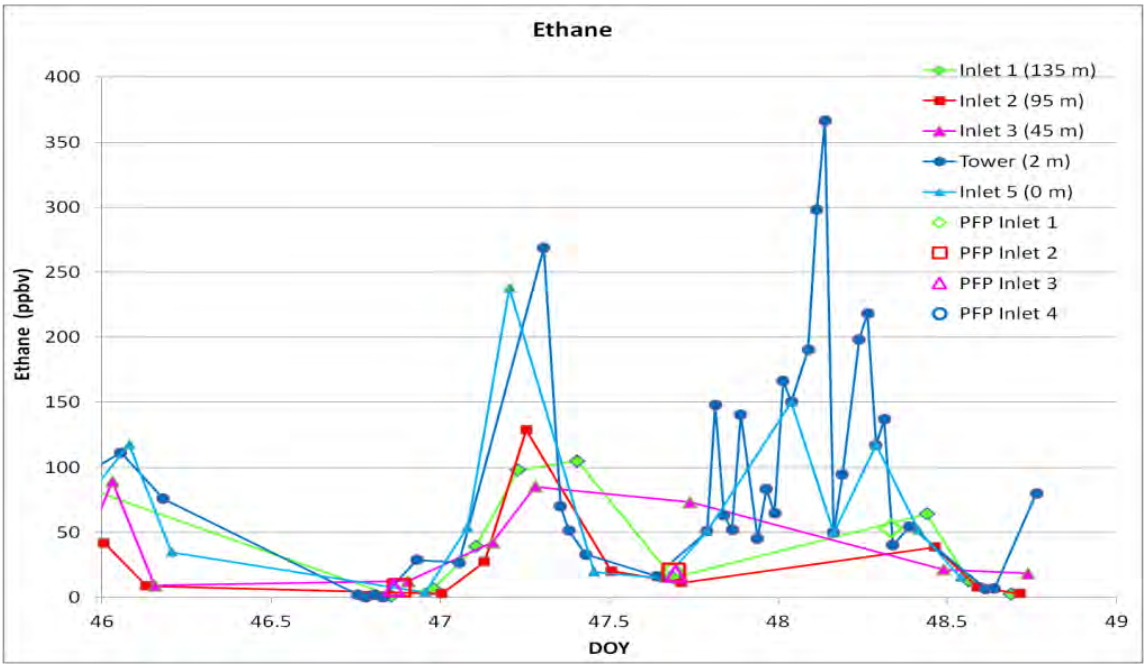

Figure 6-7. Ethane in air drawn from the balloon inlets, surface tower, and ground inlet 15-18 Feb. 2012 (DOY 46-49).

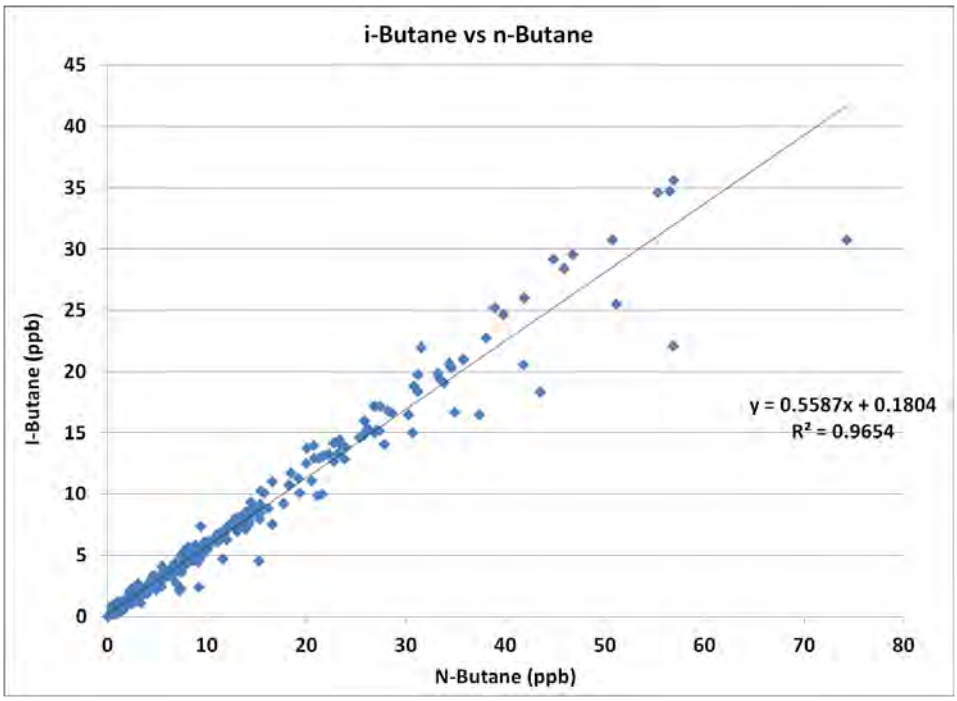

Figure 6-8. Relationship between two NMHC, in this case i-butane and n-butane, in samples collected at the ground and from balloon sampling-line inlets.

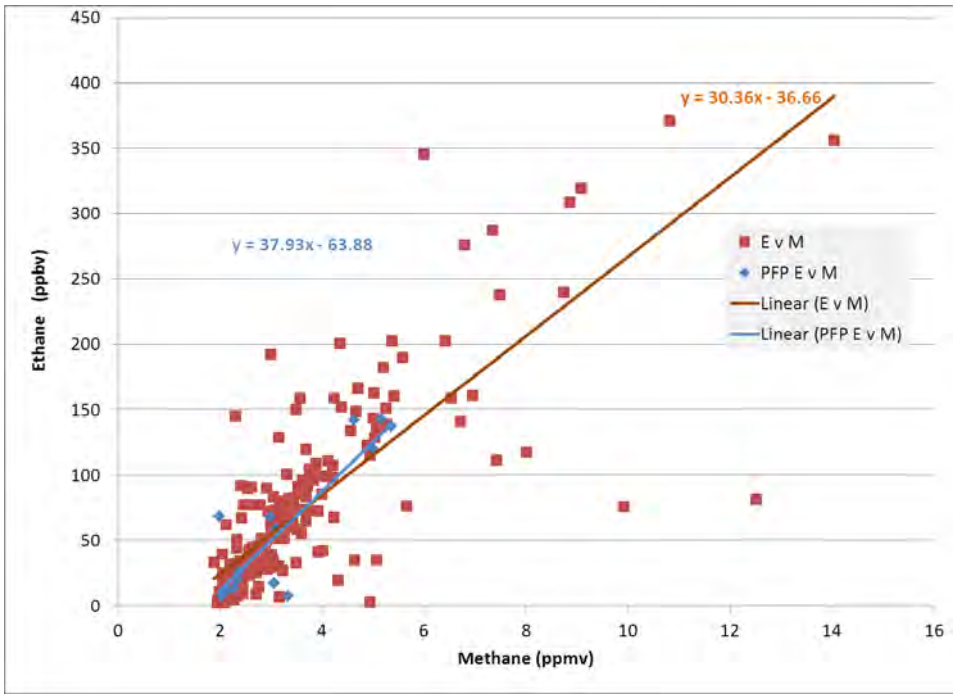

Figure 6-9. Ethane versus methane correlation in samples collected from the balloon and surface tower inlets with the instrument operated at the site as well as in samples that were brought back to the Boulder laboratory system for analysis. The slope value of this relationship (added to the graph in color) for the in-situ data (red) and programmable flask package (PFP) data (blue) suggests an ethane to methane mass emission ration of 6-10%.

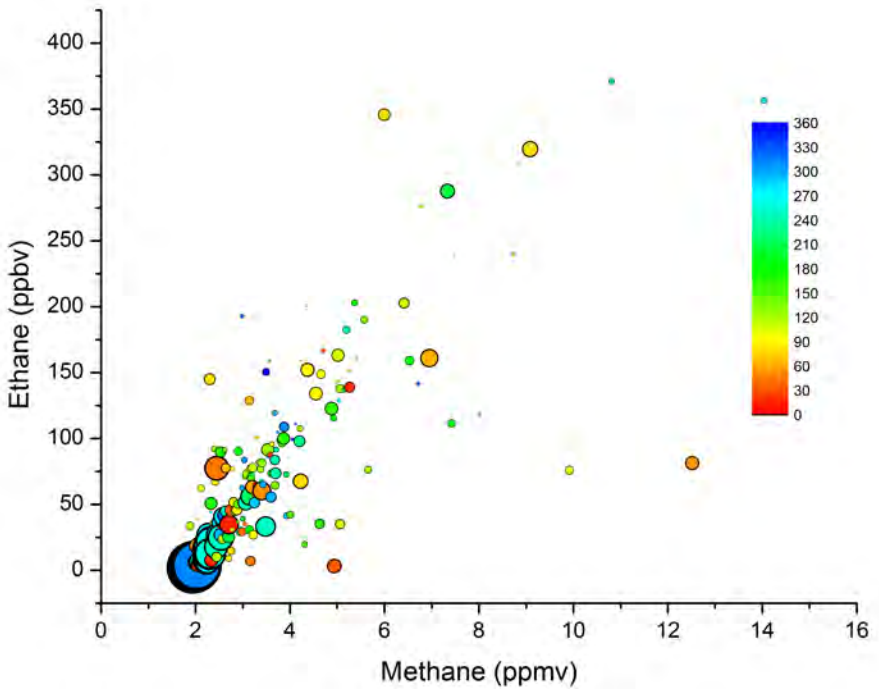

Figure 6-10. Ethane to methane relationship with data points color coded by wind direction (see color bar inside the figure for wind direction scale) and marker size being indicative of wind speed.

SUMMARY

The surface and vertical tethered balloon data collected at Horsepool illustrate a strong case of the effect of the diurnal cycling between nighttime stable conditions and daytime convective mixing on ozone and ozone precursor compounds. Concentration enhancements seen from the ground to 500 feet height for methane, NMHC, and NOx point towards strong sources of these gases in the immediate surroundings of the site. NOx levels were measured at significantly higher concentrations than what would be expected for an environment this far away from urban areas. Furthermore, VOC, in particular light NMHC, were highly elevated. Ozone behavior indicates nighttime destruction from deposition and NO titration, and moderate ozone production during daytime hours. Due to the lack of snow during the study period, no data under snow-cover conditions could be collected. It appears likely that the increased atmospheric stability expected over snow and the strongly suppressed mixing during daytime (compared to non-snow covered conditions) will result in further enhancements of ozone precursor concentrations (NOx and VOC) and that their concentrations will likely build up over consecutive days to levels that exceed the February 2012 observations, which, under the expected increased solar irradiance over snow, would result in increased ozone production.

CHAPTER VII

THE POTENTIAL FOR OZONE PRODUCTION IN THE UINTAH BASIN: A CLIMATOLOGICAL ANALYSIS

Marc Mansfield and Courtney Hall
Bingham Entrepreneurship & Energy Research Center, Utah State University, Vernal, UT.

SUMMARY

Winter ozone events have been observed in the Upper Green River Basin (UGRB) of Wyoming and in the Uintah Basin (Basin) in eastern Utah. However, since extensive ozone monitoring in the Basin has occurred during three winter seasons only, our understanding of the Basin's ozone production in any given winter is incomplete. We do know that some winters are worse for ozone than others. Multiple exceedances of the 75-ppb eight-hour-average National Ambient Air Quality Standard (NAAQS) were observed in the winters of 2009-10 and 2010-11, but none in 2011-12. This document reports an analysis of historical climate patterns intended to predict the likelihood that any given winter in the Basin will exhibit either low or high ozone.

A conceptual model of the UGRB [Stoickenius & Ma, 2010] indicates that the following "ingredients" are required to produce winter ozone events:

- ozone precursors (VOC and NO_x) in the atmosphere,
- solar radiation,
- intense thermal inversions, and
- snow cover.

Solar radiation and ozone precursors are the "basic ingredients," while thermal inversions and snow cover are "intensifiers" of the basic ingredients. Persistent (i.e., multi-day) inversions trap precursors within a surface layer and permit them to build, while snow cover reflects rather than absorbs solar radiation hitting the surface. Three years of ozone monitoring in the Basin are consistent with this conceptual model: Snow cover and inversions were plentiful during 2009-10 and 2010-11, but were scarce during 2011-12.

In this study, we have examined climate data for a total of 63 winter seasons covering the time period from January 1950 to February 2012. Normally, thermal inversions are detected directly through balloon-borne sonde measurements, which of course are not generally available day in and day out. However, we developed a technique based on the daily surface temperature recorded at various elevations throughout the Basin. We find that as long as the input temperature data are accurate and as long as we have a representative sampling of surface temperatures from throughout the Basin, we are able to identify and characterize the strength of thermal inversions on any given day since 1950. Using snow depth measurements from throughout the Basin, we have also determined the average snow depth on any given day (with occasional gaps in the data) since 1950.

Using ozone data from three winter seasons (2009-10, 2010-11, 2011-12), we have developed a mathematical model (in the form of a quadratic regression) that predicts the daily maximum ozone concentration. The independent variables in the model are (1) daily lapse rate (a measure of the strength of thermal inversions), (2) snow depth, (3) temperature, (4) solar zenith angle, and (5) number of consecutive days since the beginning of a multi-day inversion event. Although imperfect, the model is reasonably accurate. Given values of the above five variables, we can estimate the maximum ozone concentration on any given day with a standard error of about 13 ppb. As explained below, our greatest confidence in the model is in the prediction of (1) ozone levels when actual ozone is low, and (2) the relative ranking of ozone production in any two given years.

Because we only have three winter seasons of actual ozone measurements from which to draw, and because the emissions of ozone precursors probably did not vary much over these three winters, there is no way at present to design a predictive model that includes dependence on precursor emissions. (It remains to be seen whether this can be done for the UGRB, where ozone monitoring has extended now over six winters.) Nevertheless, we can apply our predictive model to any given winter day for which the values of the above five dependent variables are available, and estimate the potential for ozone production on that day under the assumption that precursor emissions are at the levels typical of the period 2009 to 2012. While the model does not tell us anything about past ozone levels, it does let us estimate the probability for ozone production in the Basin in any typical winter over the next few years, essentially for as long as precursor emissions remain approximately at their current level.

Interestingly, there appears to be a lag of about one month between peak inversion season (January) and peak ozone season (February). The likely explanation for the lag is the changing solar angle. The sun is lowest in the sky at the winter solstice, December 21, and climbs steadily throughout the remainder of the winter season. Therefore, we find that inversions occurring before the end of January are less ozone-productive than those occurring from the beginning of February until the snow cover melts. Indeed, the data seem to indicate that after mid-February, even weak inversions can generate high ozone levels, if there is also adequate snow cover.

We also find that multi-day inversion events, because they lead to build-up of precursors, produce more ozone than isolated, single-day inversions. We also find that inversions occurring without snow cover are ineffective for ozone.

Based on climate data since the 1950s, we find 44% odds that any given winter will be compliant with the NAAQS standard, assuming current precursor emission levels. We also find 27% odds that a winter will be as bad or worse for ozone than the most recent heavy ozone season, 2010-11, and 40% odds that a winter will be as good or better than the most recent light ozone season, 2011-12. The remaining 33% falls somewhere between these extremes.

The model does not include the effects of cloud cover. Occasionally, the Basin experiences extended periods of inversions combined with fog or a low ceiling. No ozone measurements have ever been made under such conditions, but it is quite plausible that cloud cover blocks enough sunlight to prevent significant ozone production, which would mean that the estimates for ozone production cited in the previous paragraph may be high. Once we obtain ozone data during such conditions we can adjust the predictions of the model.

One important question is the occurrence of multi-year trends. In other words, if one season is either bad or good for inversions, snow cover, or ozone, is there a heightened probability that the succeeding

year will follow suit? The data indicate that if multi-year trends occur, the effect is not strong. We find that the distribution of high and low years is consistent with a random sequence.

The model also indicates that ozone levels are temperature-sensitive. With deep snow cover and with all other variables being equal, the model indicates that ozone concentration drops by about 1 ppb for every 1 °C drop in the temperature. This indicates a potential problem with modeling of winter ozone events that we first raised last year [Martin, et al, 2011; pp. 81-95]. Existing chemistry models, which were designed with summer ozone in mind, may not have the proper temperature dependence to adequately represent winter ozone formation.

INTRODUCTION

Tropospheric ozone is produced by the action of solar radiation on ozone precursors. These conditions occur during the wintertime in the UGRB and the Uintah Basin because of (1) multi-day wintertime thermal inversions that facilitate the build-up of precursor concentrations, and (2) snow cover whose reflectivity intensifies the available solar radiation.

A thermal inversion is defined as the condition in which the air temperature increases with elevation. In most temperate regions worldwide, inversions are established over night when a layer of cold air forms at the surface. During the day, however, the sun warms the earth's surface, which then warms the atmosphere from the bottom up, leading to a non-inverted condition with temperature decreasing with elevation [Seinfeld & Pandis, 2006]. This diurnal pattern is often disrupted in the winter in many intermountain basins and valleys because solar heating is inadequate to warm the surface layer [Whiteman, et al, 2001]. Several effects contribute to this inefficient heating: (1) the low solar elevation, (2) snow cover that reflects solar radiation back into space, (3) the basin topography which allows cold air to pool, and (4) cloud cover. As we show below, the Basin shows a strong correlation between the presence of inversions and of snow cover, although we sometimes see inversion conditions with little or no snow.

The standard diurnal pattern in which inversions set up overnight and dissipate during the day provides for good mixing of the atmosphere. When the air warms from the bottom up, convection cells are established that lead to vertical mixing. On the other hand, when the surface air fails to warm adequately, such as occurs during multi-day wintertime inversions, this mixing does not occur, and a pool of cold air ("cold pooling") sets up close to the surface that persists throughout the duration of the inversion. Any pollutants emitted during such inversions tend to remain in the cold pool and build up from one day to the next. Often, these persistent inversions remain in place until a storm front moves through.

The atmosphere either absorbs or reflects much solar radiation, decreasing the amount reaching the earth's surface. The attenuation of radiation is most pronounced in winter because of the longer path length through the atmosphere. However, surface snow cover causes much of the radiation reaching the surface to be reflected rather than absorbed, nearly doubling the amount of radiation available to drive ozone formation. Calculations indicate that with snow cover, there is about as much solar energy available in the Basin in January as there is in Los Angeles in July [Schnell, et al, 2009]. There is little surprise, then, if ozone precursors are also present, that ozone concentrations reach values comparable to Los Angeles.

Conditions were favorable for ozone formation during winters 2009-10 and 2010-11 but not during 2011-12. 2011-12 was distinguished by the absence of thermal inversions and of snow cover. We therefore performed a historical study examining the past 63 winter seasons to see how they compare, in terms of thermal inversions and snow cover, with these three base years. This document presents our results.

METEOROLOGICAL STATIONS

We accessed daily temperature and snow depth data from 19 stations, listed in Table 7-1 with latitude, longitude and elevation and shown in Figure 7-1. Temperature and snow cover data for each station were obtained from the Utah Climate Center [Utah Climate Center, 2012]. Each station has a descriptive name, usually derived from the name of a nearby town. For example "MAESER 9NW" is located nine miles northwest of the town of Maeser. Not every station was in operation or reported a temperature or a snow depth for every single day during the study period, but usually on any given date, there were around a half-dozen to a dozen reporting stations. The stations range in elevation from about 1400 m (Ouray and Jensen) to over 1900 m (Altamont). Sites were selected to achieve a broad distribution both geographically and by altitude. Each date between January 01, 1950 and February 29, 2012 was included.

Table 7-1. Meteorological stations providing data for the study.

	Station Name	Latitude	Longitude	Elevation (m)
01	ALTAMONT	40.356	–110.288	1942
02	DINOSAUR QUARRY AREA	40.438	–109.304	1464
03	DUCHESNE	40.168	–110.395	1682
04	FT DUCHESNE	40.284	–109.861	1540
05	JENSEN	40.364	–109.345	1449
06	MAESER 9NW	40.560	–109.664	1963
07	MYTON	40.194	–110.062	1548
08	NAPLES 0.8 N	40.441	–109.491	1583
09	NEOLA	40.418	–110.051	1814
10	OURAY 4 NE	40.134	–109.642	1422
11	ROOSEVELT 0.2 WSW	40.295	–110.004	1575
12	ROOSEVELT 1.1 SE	40.286	–109.983	1532
13	ROOSEVELT RADIO	40.288	–109.959	1528
14	VERNAL 1.5 WSW	40.446	–109.563	1662
15	VERNAL 2SW	40.427	–109.553	1667
16	VERNAL 3.7 WNW	40.480	–109.596	1726
17	VERNAL MUNICIPAL AP	40.442	–109.514	1603
18	VERNAL	40.430	–109.510	1608
19	DINOSAUR NATIONAL MONUMENT	40.244	–108.972	1804

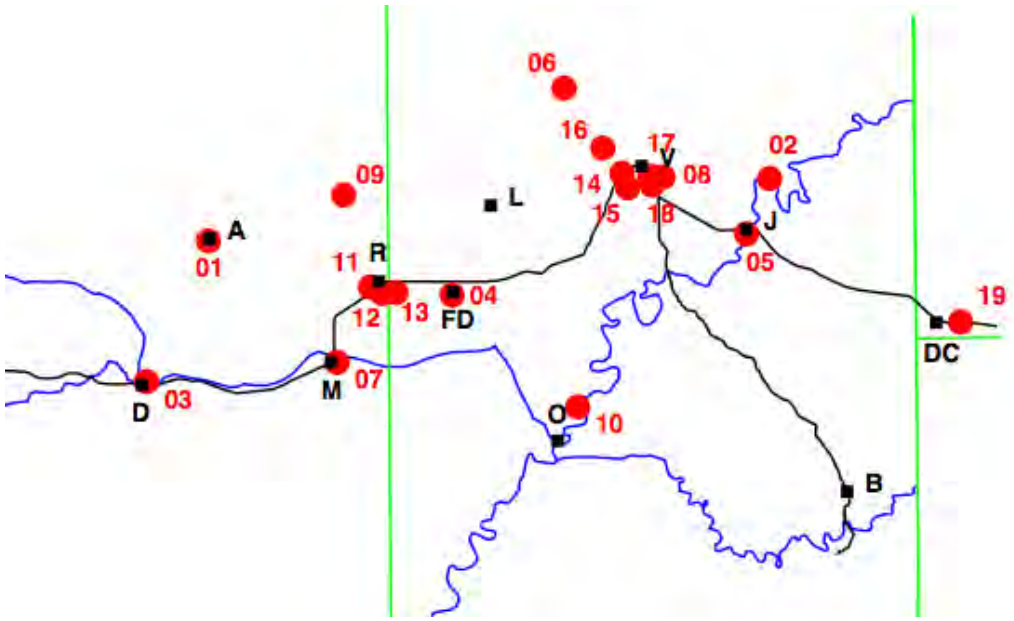

Figure 7-1. Map showing distribution of meteorological stations. Black squares are towns (D=Duchesne, M=Myton, R=Roosevelt, V=Vernal, J=Jensen, A=Altamont, O=Ouray, FD=Fort Duchesne, B=Bonanza, L=Lapoint, DC=Dinosaur, CO). The Green, White, and Duchesne rivers are shown in blue. Green lines are county or state boundaries. Red dots are met stations number-coded according to Table 7-1.

INVERSION AND SNOW COVER

A temperature inversion is indicated when the temperature of the atmosphere increases with altitude, and is measured by the so-called lapse rate: [Seinfeld and Pandis, 2006]

$$\Lambda = -\frac{dT}{dz} \qquad (1)$$

where T represents temperature and z altitude. By this definition, a negative lapse rate indicates a temperature inversion. Lapse rates are usually determined by sonde measurements, which are not available for the time period of this study. Therefore, we developed the following approach to arrive at a daily lapse rate for the Basin as a whole. For any given date, we construct a least-squares linear correlation between maximum daily temperature and altitude, employing data from all stations reporting a maximum temperature for the day. The lapse rate for any given day is defined operationally as the negative of the slope of the correlation line. Figure 7-2 shows the linear correlations for four selected days.

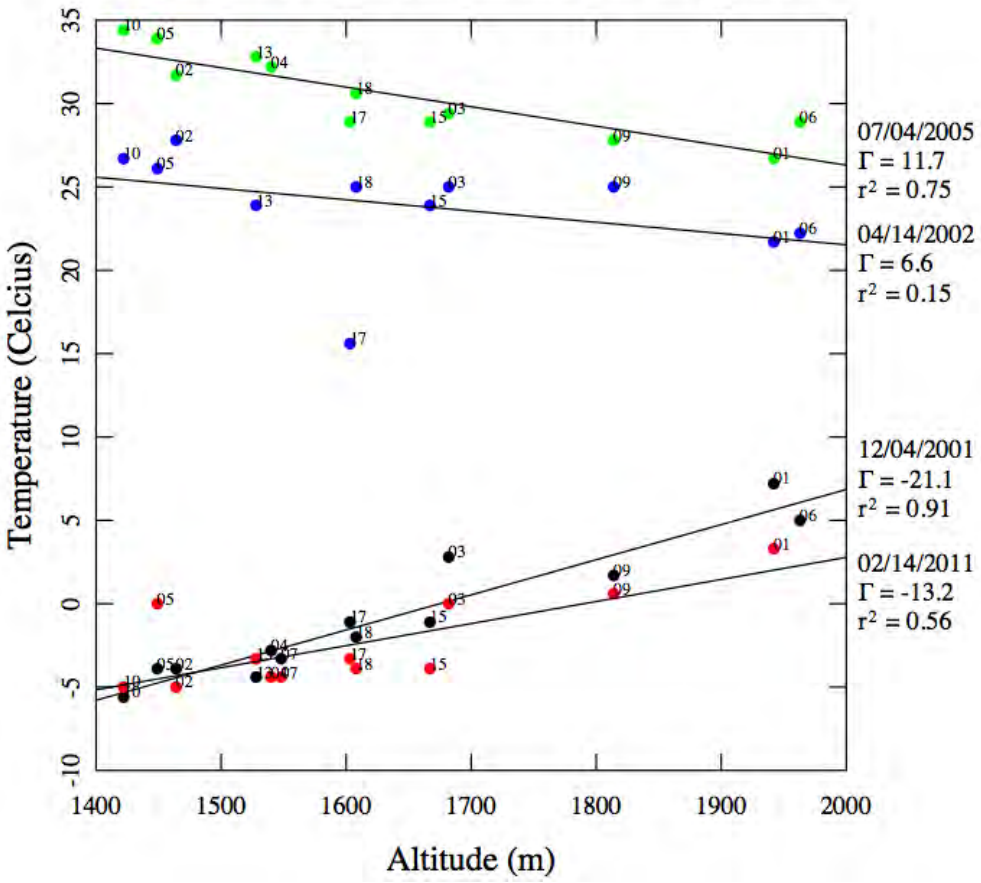

Figure 7-2. Temperature vs. altitude for four sample days. Each point in the figure is labeled with the number of the station. The slope is negative on typical summer days, but positive for winter days with inversions. The numerical value of the daily lapse rate determined in this way (Γ; units are K/km) and the r^2 correlation coefficients are also displayed.

Figure 7-3 illustrates seasonal trends in the lapse rate for a few selected years. Each one shows the daily lapse rate from July 1 to June 30. Inversions are indicated whenever the lapse rate goes negative, which occurs almost exclusively in winter. Winter 2005-06 is typical of a low-inversion season, while the other three seasons displayed more inversion events. Lapse rate data for all 63 years of the study will be provided upon request. Figure 7-4 shows the average lapse rate for all days of the year. The seasonal trend in lapse rate is obvious, and we also observe that the standard deviation in the lapse rate is larger in winter.

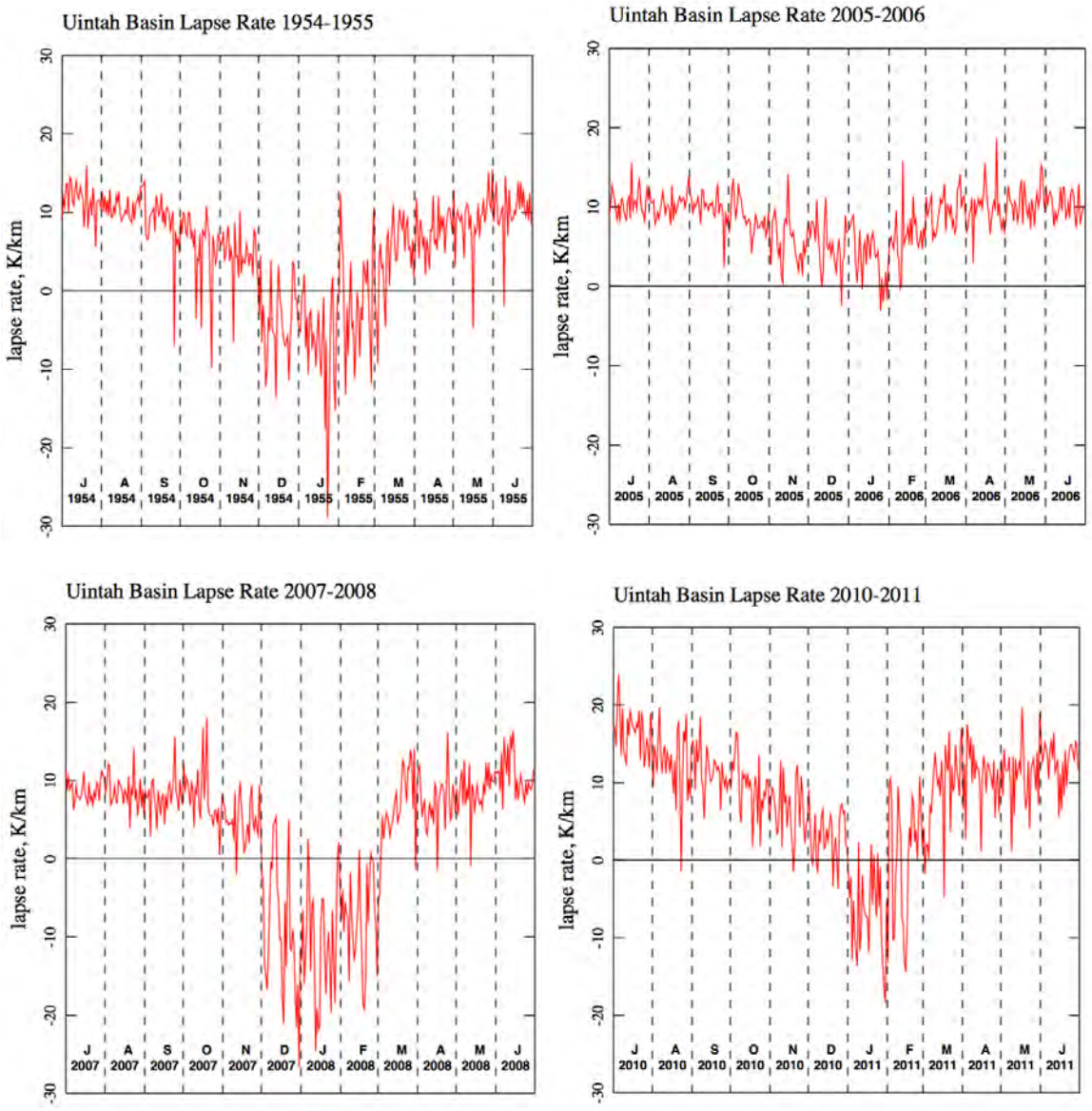

Figure 7-3. Time series of lapse rates for selected years. Negative lapse rates indicate inversions.

Figure 7-4 shows, for any given date throughout the calendar year, the average lapse rate in red and the average plus or minus one standard deviation in green. The seasonal trend in lapse rate is obvious, and we also observe that the standard deviation in the lapse rate is larger in winter. The black curve is a low-pass filtered Fourier representation of the lapse rate data (see note 1).

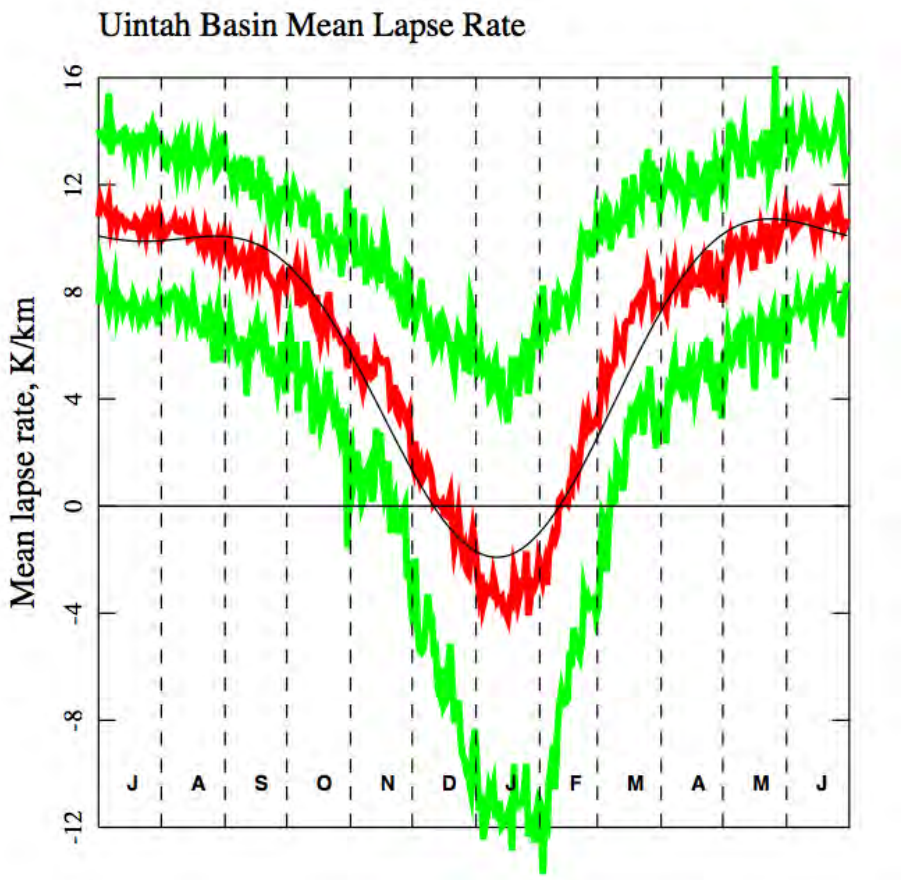

Figure 7-4. Average lapse rate for all days of the year. The average lapse rate is in red and the average plus or minus one standard deviation is in green. The black curve is a low-pass filtered Fourier representation of the lapse rate data (see Note 1).

The 19 stations mentioned above also report snow depths. For the most part, all entries are rounded to the nearest inch. This is true even when the station reports depths in mm. For example, we find entries of 25 mm (= 1 inch) or of 51 mm (= 2 inches), but usually nothing in between. Other common entries are "M," (missing) and "T" (trace).

There are questions about the quality of the snow depth data. For example, we find days for which one station reports a snow depth of 0 while all others report ample snow. For over 600 consecutive days (summer and winter) in 2005 and 2006, the Vernal station reports depths of exactly 1000 in. (We interpret that as equivalent to "missing.")

For every day in the study period (01/01/1950 - 02/29/2012) we calculated an average snow depth by averaging over all stations reporting a depth, interpreting "T" (trace) as 10 mm. However, because of the uncertainties mentioned above in the quality of the data, we also rejected any measurement that fell more than 2 standard deviations away from the mean for the day. After that rejection, a new mean was calculated. In what follows, we apply the operational definition that a day with snow cover means a day for which the mean snow depth is greater than 50 mm.

Figure 7-5 gives snow depth results obtained in this way for four selected years, and Figure 7-6 shows average snow depth for any given day of the year. 1972-73 is one of the heavier snow seasons, while 1962-63 and 2011-12 are among the lightest. Almost one quarter of winters have snow as light as 2011-12. Figure 7-6 shows the mean snow depth for each day of the year.

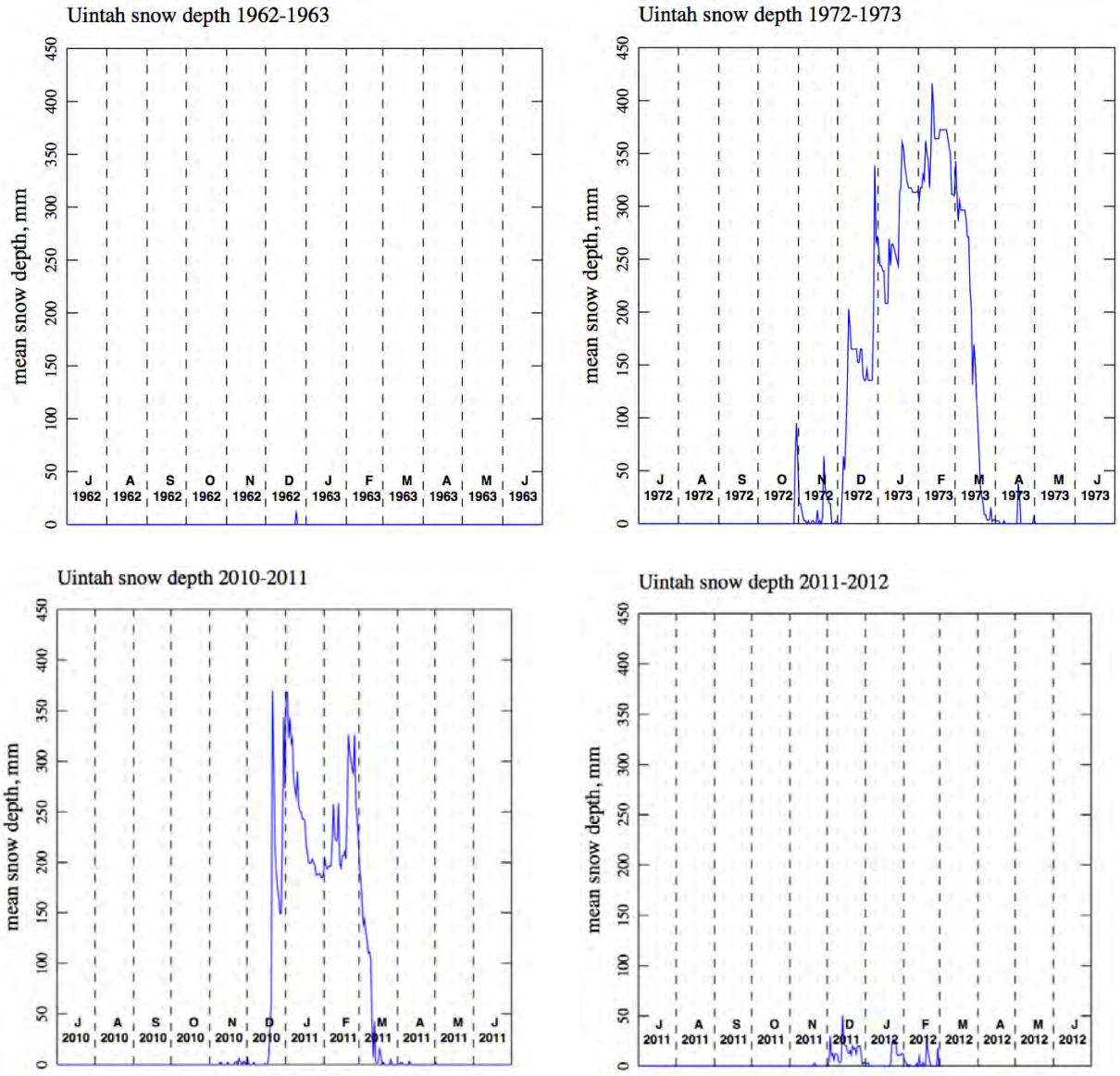

Figure 7-5. Time series of average snow depth in the Basin for selected years.

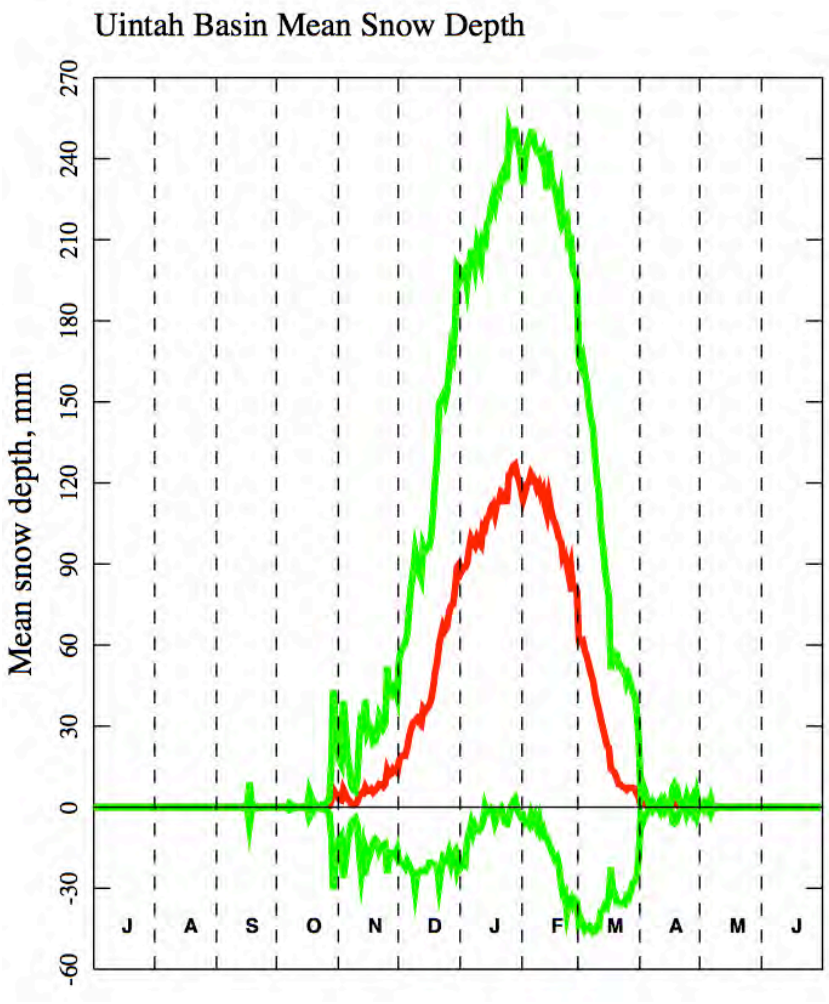

Figure 7-6. Average snow depth for each day of the year. The red curve represents the average snow depth and the green curves display the average plus or minus one standard deviation.

Figure 7-7 shows the overlap in probability that a given day of the year will have snow cover or inversions. Interestingly, the data can be well represented by Gaussian distributions. The distributions all peak in January at probabilities of approximately 50% or 60% and have standard deviations of about 30 days. These curves indicate that the odds approach 50% of finding a day in mid-January that has both a negative lapse rate and for which the mean snow depth is greater than 50 mm (See also note 1).

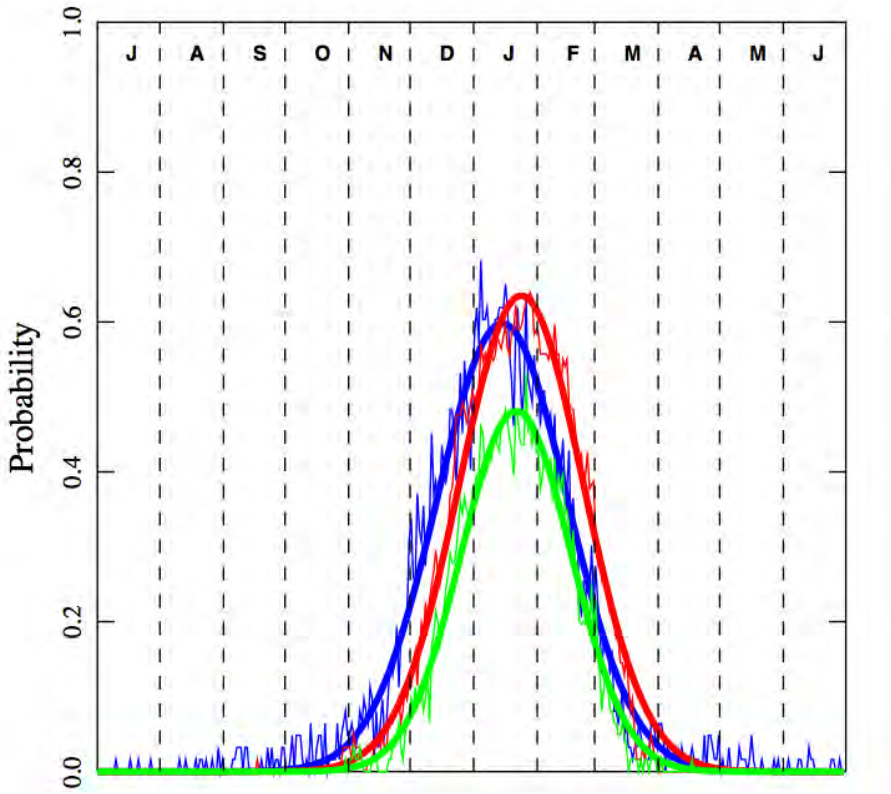

Figure 7-7. Probability that a given day of the year will display an inversion (blue), have snow cover (red), or have both an inversion and snow cover (green). The jagged lines represent actual values, and the thick, smoothed lines represent Gaussian distributions.

SNOW COVER/INVERSION CORRELATIONS AND LONG-RANGE TRENDS

Column 2 of Table 7-2 gives the total number of days with inversions in each of 54 consecutive winter seasons, where we have included contributions from all days between December 1 and March 31. (Gaps in the data prevent us from compiling a list of consecutive seasons that includes all 63 years.) Column 4 gives the total number of days for which the average snow depth exceeded 50 mm. The average number of days per year with inversions is 41.2 days, while the average number of days with 50 mm or more of snow cover is 47.6. The third column reports whether the number of days with inversions in any given season is higher (1) or lower (0) than the median of 38.5 days. The fifth column reports whether the number of days with snow cover is higher or lower than the median of 51.5 days.

Table 7-2 indicates a strong correlation between inversions and snow cover. With only six exceptions, a high or low inversion year is also a high or low snow year. (We are in the process of studying snow cover/inversion correlations in a number of other intermountain basins. Although this study is incomplete, we find that snow cover/inversion correlations are exceptionally strong in the Basin.)

The trends in Table 7-2 suggest that the occurrence of high and low years might be non-random. For example, we observe a grouping of low years from 1993 to 2000, and of high years from 2006 to 2010. However, such trends can be misleading. The sequence of highs and lows may in fact be random. (Athletes in a “winning streak” tend to believe the outcome of the next game is biased in their favor,

when in fact, random sequences also produce streaks.) We applied the following test for non-randomness in the sequence of high and low inversion and snow years. In each sequence there are 27 zeros and 27 ones. The inversion sequence displays 21 reversals, i.e., a pair of consecutive seasons when the sequence switches from 0 to 1 or from 1 to 0. The snow sequence displays 25 reversals. A highly non-random process in which the outcome of one season influences the outcome of the following season would produce a very small number of reversals. So one way of framing the question of randomness is to consider a thought experiment: Place 27 tiles labeled 0 and 27 labeled 1 in a bag, and draw them out of the bag at random. What is the probability that the resulting sequence will have either 21 or fewer reversals or 25 or fewer? One way to obtain the probability is through Monte Carlo computer simulation; we effectively simulate millions of independent instances of the tiles-in-a-bag experiment. The result is that the odds of drawing 21 or fewer reversals are 6.5%, while the odds of producing 25 or fewer reversals are 34.1%. 6.5% might be considered borderline for weak non-randomness, but not 34.1%. And because the two sequences are correlated, we must weigh both results in making our determination. The long sequence of low years in the 1990s notwithstanding, the sequence of high and low inversion years is probably random. The outcome of one season has at most only a weak influence on the outcome of the following season.

It has been suggested that the pattern of inversions in the Basin is influenced by the North Atlantic Oscillation, or some other global oscillation. Our results do not entirely preclude such a possibility, as long as the typical oscillation time is not much longer than a single year.

Table 7-2. Statistics on days with inversions and snow cover.

Season	Days with LR < 0	Higher (1) or lower (0) than median	Days with SD > 50 mm	Higher (1) or lower (0) than median
1957-58	10	0	2	0
1958-59	20	0	10	0
1959-60	58	1	77	1
1960-61	6	0	1	0
1961-62	37	0	38	0
1962-63	22	0	0	0
1963-64	22	0	0	0
1964-65	61	1	109	1
1965-66	31	0	4	0
1966-67	85	1	86	1
1967-68	68	1	91	1
1968-69	57	1	67	1
1969-70	38	0	34	0
1970-71	19	0	16	0
1971-72	17	0	16	0
1972-73	79	1	105	1
1973-74	70	1	68	1
1974-75	27	0	50	0

1975-76	62	1	58	1
1976-77	15	0	2	0
1977-78	51	1	62	1
1978-79	98	1	106	1
1979-80	39	1	63	1
1980-81	13	0	0	0
1981-82	29	0	53	1
1982-83	56	1	71	1
1983-84	94	1	111	1
1984-85	91	1	99	1
1985-86	60	1	76	1
1986-87	11	0	8	0
1987-88	60	1	69	1
1988-89	42	1	74	1
1989-90	22	0	17	0
1990-91	55	1	59	1
1991-92	42	1	40	0
1992-93	60	1	90	1
1993-94	9	0	1	0
1994-95	10	0	2	0
1995-96	16	0	23	0
1996-97	38	0	63	1
1997-98	17	0	40	0
1998-99	32	0	14	0
1999-00	18	0	0	0
2000-01	6	0	17	0
2001-02	40	1	30	0
2002-03	56	1	48	0
2003-04	34	0	64	1
2004-05	15	0	27	0
2005-06	8	0	9	0
2006-07	51	1	56	1
2007-08	85	1	105	1
2008-09	46	1	63	1
2009-10	74	1	94	1
2010-11	44	1	81	1
MEAN	**41.2**	**MEAN**	**47.6**	
MEDIAN	**38.5**	**MEDIAN**	**51.5**	

ACTINIC FLUX

Figure 7-7 indicates that, when averaged over many years, there are as many inversions before mid-January as after. This is somewhat surprising because our experience, both in the UGRB and the Basin, is that ozone events are more likely from about mid-January until the snow melts than they are before mid-January. The most likely explanation becomes obvious from Figure 7-8, which shows the actinic flux (the amount of solar energy available to power photochemistry) as a function of time of year.

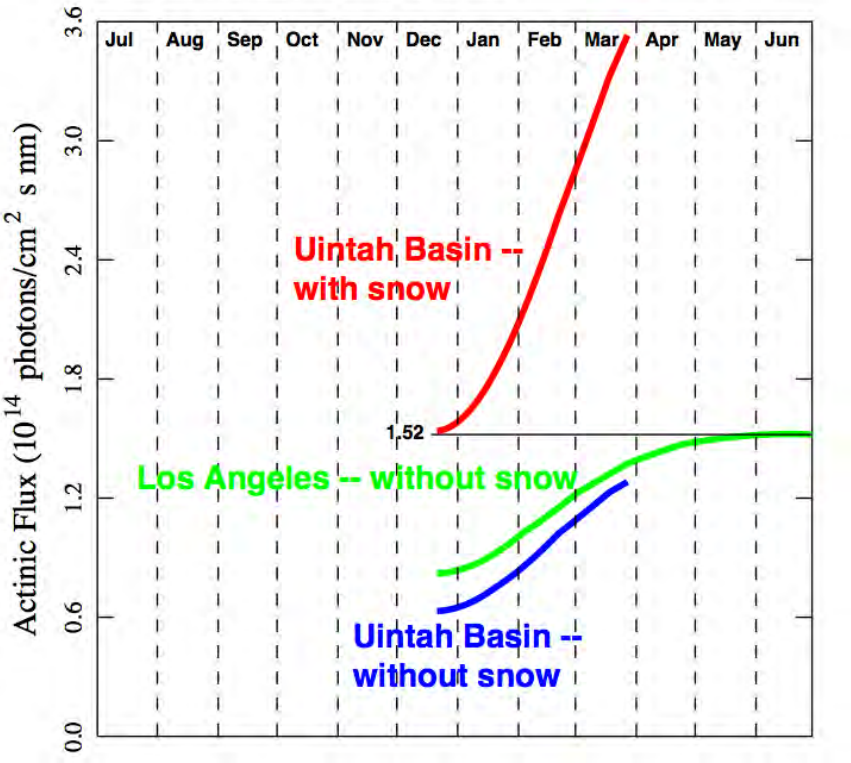

Figure 7-8. Midday actinic flux at wavelength of 325 nm. The grey line labeled with an actinic flux of 1.52 shows that the flux during the summer solstice in Los Angeles is similar to the flux during the winter solstice in the Basin with snow cover.

These curves were adapted from the actinic flux tables and solar zenith angle formulas published in Finlayson-Pitts and Pitts [2000] (see their Tables 3.7 and 3.11, and discussion on page 65), in which it is assumed that the albedo is 80% (Table 3.11) with snow, and 5% (Table 3.7) without. Of course, the actinic flux depends on wavelength, and ozone production responds to wavelength in a complex way. Because Figure 7-8 only shows the flux at 325 nm, it does not give a complete picture of the energy available for ozone production. Nevertheless, note that the actinic flux is at its lowest at the winter solstice, December 21, and increases steadily until the snow melts. Because the sun continues to climb higher in the sky, inversions occurring near the peak of the bell-curve in Figure 7-7, that is in mid-January, have less available solar energy than in February, and therefore are less effective ozone-producers. This diagram also highlights the role of snow cover: Note that the actinic flux in the Basin at the winter solstice with snow cover is very nearly the same as that in Los Angeles at the summer solstice without snow cover.

OZONE/LAPSE RATE CORRELATION

Figures 7-9 through 7-11 give daily ozone concentrations at Ouray and daily lapse rate values for three winters for which ozone concentration data are available. Immediately obvious is the lack of significant ozone or inversion events in 2012. Ozone stayed near 40 or 50 ppb for the entire winter. Correlations between lapse rate and ozone can be seen for the other two winters, but we also note that inversions in December are less likely to produce significant ozone than those in February. The probable explanation, as mentioned above, is that solar intensity is too weak in early winter to stimulate much ozone. February and March of both years show several ozone events although the lapse rate is already trending positive. Lapse rates based on potential temperature (Note 2), since they are stronger indicators of actual atmospheric stability, would probably be a better predictor of ozone formation. Positive lapse rates, below about 10 K/km, still indicate stable atmospheric conditions [Seinfeld and Pandis, p. 730].

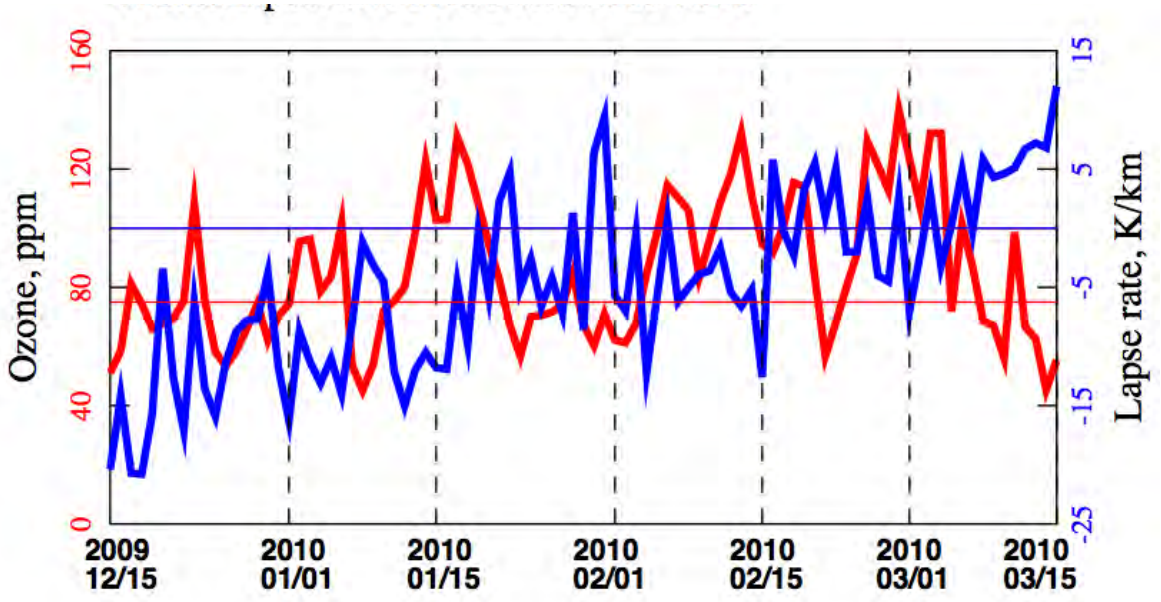

Figure 7-9. Time series of daily ozone concentrations at Ouray (the daily maximum of the hourly average) and daily lapse rate values for 2009-10. Ozone concentrations appear in red and lapse rates in blue. The red horizontal line marks the 75 ppb ozone level. The horizontal blue line marks the zero lapse rate level, so it divides inverted from non-inverted days.

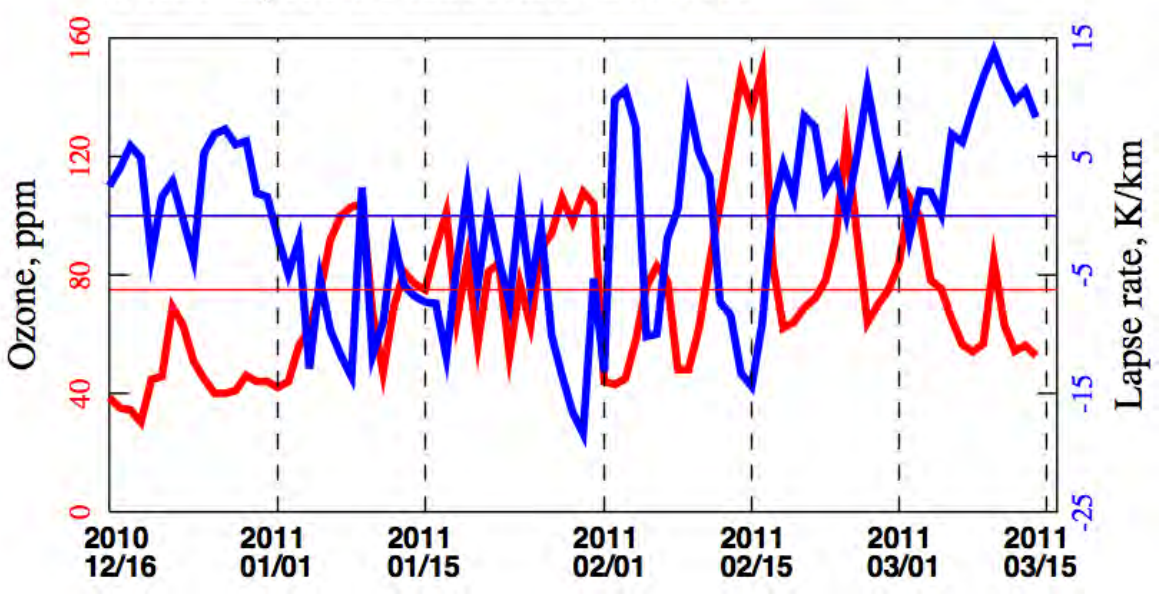

Figure 7-10. Time series of daily ozone concentrations at Ouray (the daily maximum of the hourly average) and daily lapse rate values for 2010-11.

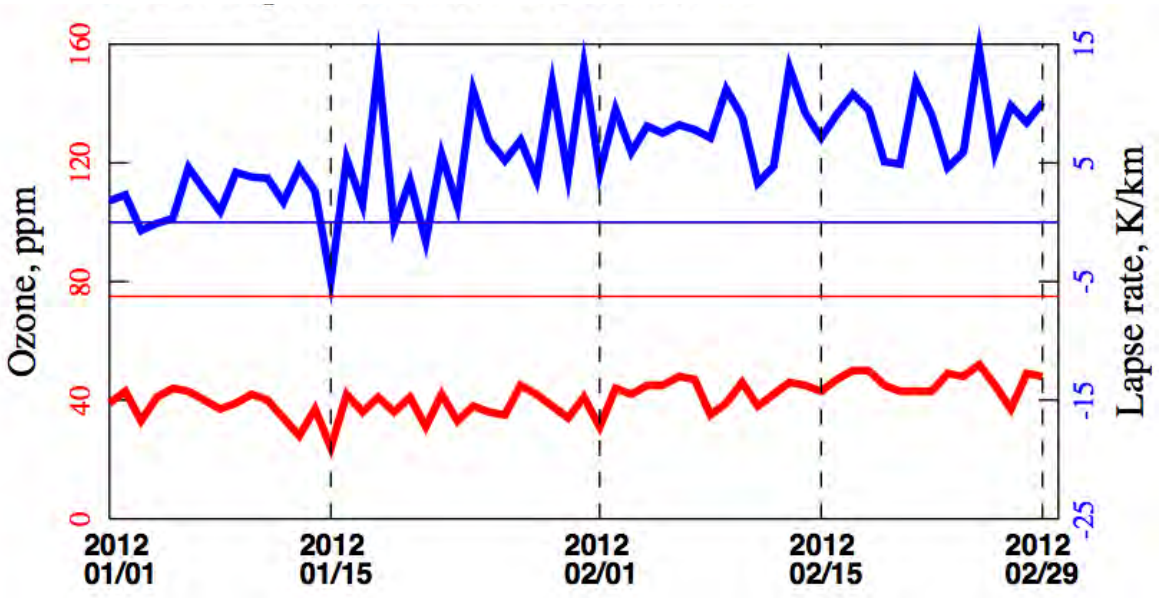

Figure 7-11. Time series of daily ozone concentrations at Ouray (the daily maximum of the hourly average) and daily lapse rate values for 2011-12.

MULTIVARIATE REGRESSION ANALYSIS (PREDICTION OF OZONE POTENTIAL)

Monitoring of winter ozone began only recently in the Basin. One of the goals of the study reported here is to estimate ozone production in years prior to the beginning of measurements as well as to project future ozone trends. We developed a quadratic least-squares regression model in order to estimate the ozone potential for any given winter day. The model was first "calibrated" with the three winters for which ozone data are available and then used to predict ozone levels on any other day. The current version of the model employs five independent variables:

- **x_{1j}** Daily lapse rate (LR), calculated as explained above from the least-squares fit to the temperature-elevation plot. Units are K/km. With this and all subsequent variables, the second subscript, "j," denotes the j-th day in the time series.

- **x_{2j}** Daily mean snow depth (SD), in mm, averaged over all reporting stations as explained above.

- **x_{3j}** The "basin temperature" or "temperature at 1400 m" (T1400). Figure 7-2 introduced the least-squares fit to the daily temperature-elevation plot. The variable x_{3j} is defined as the intercept of the least-squares fit at 1400 m. Units are °C.

- **x_{4j}** Daily noon-day solar zenith angle (SA). Units are degrees, with 0° for the sun at the zenith, and 90° for the sun at the horizon. It is calculated for any given day using formulas in Finlayson-Pitts and Pitts. [2000]

- **x_{5j}** Number of days since the beginning of a multi-day inversion event, or consecutive days in an inversion (CDI). The precise definition is: $x_{5j} = 0$ for any day that the lapse rate (x_{3j}) is positive. $x_{5j} = 1$ if today's lapse rate is negative while yesterday's is positive. If both days have negative lapse rate, then $x_{5j} = x_{5,j-1} + 1$. Units are days. x_{5j} is used by the model to account for the build-up of precursors in a multi-day inversion. Typical values range from 0 to about 10, although one extremely persistent inversion drove x_{5j} up to 43 days on 20 Jan 2010.

The model has one dependent variable:

- y_j Daily maximum in the eight-hour average ozone concentration (acronym: O8O, 8-hr ozone at Ouray). Ozone data from the EPA station at Ouray was selected for this study since these data will probably be used in future regulation or policy decisions. Units are ppb. In what follows, we let y_j represent the ozone concentration as actually measured at the site, and we let $\overline{y}_j$ represent the prediction of the model for ozone concentration.

The predictive model includes polynomial terms through quadratic:

$$\overline{y}_j = A + \sum_{\alpha=1}^{5} B_\alpha x_{\alpha j} + \sum_{\alpha=1}^{5}\sum_{\beta=\alpha}^{5} C_{\alpha\beta} x_{\alpha j} x_{\beta j} \qquad (2)$$

It is very common in statistical studies to do *linear* regressions, i.e., models in which the $C_{\alpha\beta}$ terms are absent. This model is a *quadratic* regression. Inclusion of quadratic terms should increase the effectiveness of the model. For example, quadratic terms allow two variables to exercise a synergistic effect.

In the above as well as in what follows, we use Greek indexes as labels to represent one of the five independent variables, and Roman indexes to represent a particular day. The coefficients A, B_α, and $C_{\alpha\beta}$ were selected to minimize

$$\sum_j \left(y_j - \overline{y}_j\right)^2 \qquad (3)$$

where the sum extends over all days in the "calibration set," or the set of days for which ozone data were procured and used to calibrate the model. It consists of the following 239 days in three consecutive winter seasons: 16 Dec 2009 to 15 Mar 2010, 16 Dec 2010 to 14 Mar 2011, and 01 Jan 2012 to 29 Feb 2012. It is fortunate that the calibration set contains both heavy and light ozone seasons, as that increases the likelihood that the final model can adequately represent each extreme.

Table 7-3 displays means, standard deviations, minima, and maxima taken over the 239 days in the calibration set for each of the variables.

Table 7-3. Statistics of the input variables.

VARIABLE	Mean ± Std. Dev.	Min, Max	Units
x_1, LR	–0.46 ± 7.8	–20.85, 14.45	K/km
x_2, SD	149 ± 105	0, 370	mm
x_3, T1400	–0.7 ± 7.2	–18.1, 14.1	°C
x_4, SA	56.5 ± 6.2	42.3, 63.7	°
x_5, CDI	4.9 ± 9.8	0, 43	days
y, O8O	63.8 ± 25.5	21.0, 139.1	ppb

Because the model is linear in the 21 coefficients A, B_α, $C_{\alpha\beta}$, optimal values of the coefficients can be determined by solving a system of 21 linear equations. Table 7-4 displays the model parameters so obtained.

Table 7-4. Coefficients of the predictive model.

A	202	ppb
B1	–9.21	ppb km/K
B2	0.609	ppb/mm
B3	2.81	ppb/(°C)
B4	–4.62	ppb/(°)
B5	9.96	ppb/day
C11	–0.00405	ppb km^2/K^2
C12	–0.00324	ppb km/mm K
C13	0.0857	ppb km/(°C) K
C14	0.157	ppb km/(°) K
C15	–0.0291	ppb km/day K
C22	–0.000491	ppb/mm^2
C23	–0.00975	ppb/mm (°C)
C24	–0.00586	ppb/(°) mm
C25	–0.00830	ppb/mm day
C33	–0.131	ppb/$(°C)^2$
C34	–0.0229	ppb/(°)(°C)
C35	0.0850	ppb/(°C) day
C44	0.0291	ppb/$(°)^2$
C45	–0.106	ppb/(°) day
C55	–0.0176	ppb/day^2

Figure 7-12 summarizes the agreement between actual ozone measurements y_j and modeled ozone values $\overline{y}_j$ for each day in the calibration set. The daily predictions of the model fall within 10 ppb of the actual ozone measurement about 60% of the time. It would certainly have been nice to see better agreement between measurements and modeled values, but nevertheless, the agreement is good enough to generate a useful model. We note that the best agreement occurs for low ozone measurements, below about 50 ppb. We also note that for measurements above 90 ppb, the actual measurement is usually higher than the modeled value. In other words, the model underestimates ozone concentration when the concentration is large.

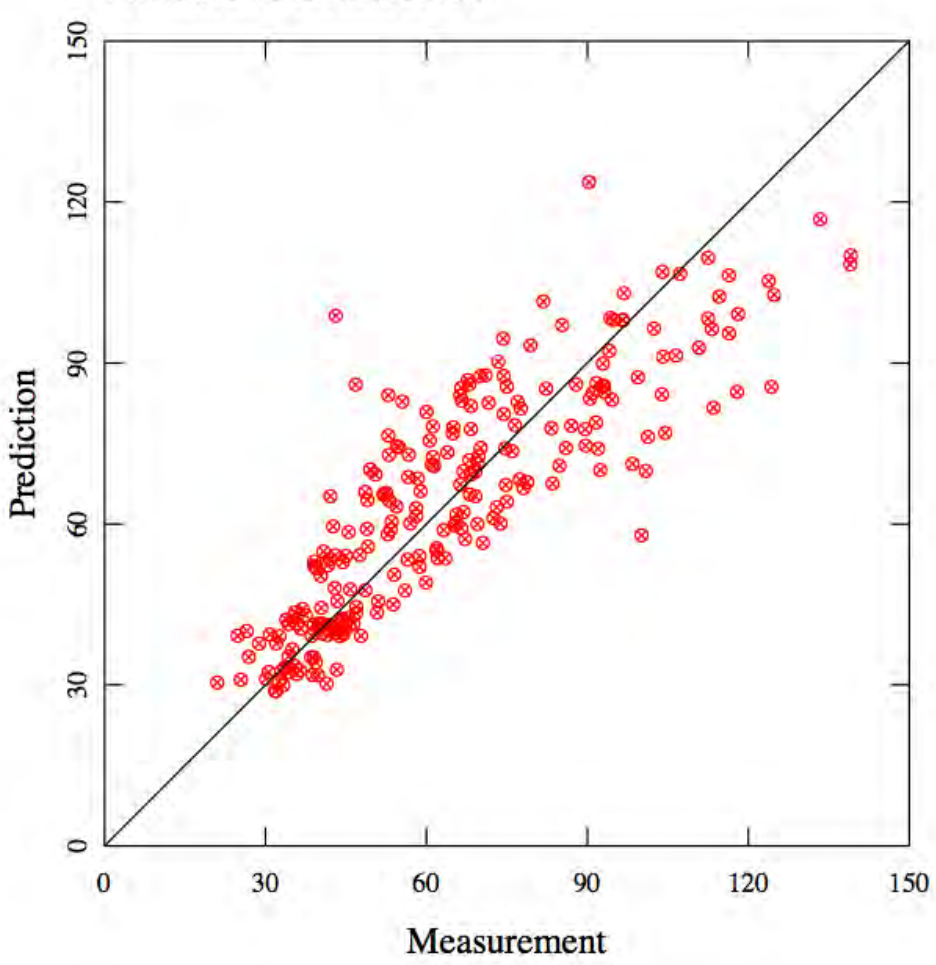

Figure 7-12. Comparison between measured and modeled ozone concentrations at Ouray (in ppb).

Because the model works best at lower ozone levels, we can have confidence when it predicts a low value. We have less confidence in absolute predictions at higher levels, but because much of the error is systematic, we can still be confident when it ranks the relative ozone severity of any two given years.

With the model calibrated using the winters for which data are available, we can then use it to estimate ozone production on any other winter day. Figure 7-13 displays the average daily ozone, as predicted by the model and averaged over the 63 winters of the study . According to the model, peak ozone production occurs in February.

An interesting feature of Figure 7-13 is the peak appearing at the end of February. Upon close inspection, we have found that the model occasionally predicts very high ozone concentrations. There were about thirty days throughout the 63 years of the study when the predicted ozone was 180 ppb or higher, with a maximum of 258 ppb on 28 February 1952. These high predictions occur when at least three of the following four variables assume extreme values: lapse rate (LR), snow depth (SD), solar angle (SA), and number of consecutive days under inversions (CDI). No such extreme combinations of the independent variables occurred during the three seasons of the calibration set, meaning that these exceptionally high estimates are extrapolations of the existing data, and might easily be overestimated. Most such days appear at or around March 1 when the sun is only a few weeks away from the vernal

equinox, but only in years when deep snow cover persists until then. Enough of these days appear in the dataset to cause the peak seen in Figure 7-13. These may be overestimates, but we can probably anticipate, under rare circumstances, significant ozone events even into early March.

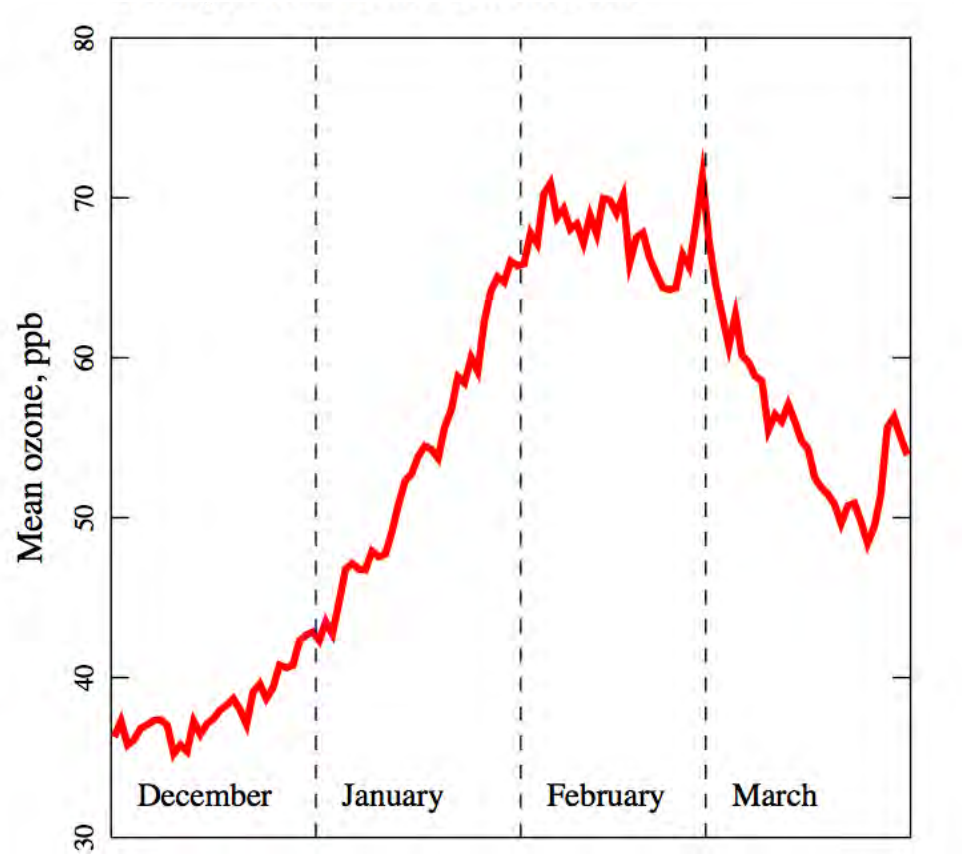

Figure 7-13. Time series of average predicted ozone concentrations at Ouray. Because of the smaller sample size contributed by Feb. 29, its results have been combined with Feb. 28.

Table 7-5 compares model and measurement results for 2-month periods (January and February) in each of the three winters for which ozone data are available. It reports the number of days found in each of several different ozone categories:

- Category A, $[O_3] \leq 25$ ppb;
- Category B, 25 ppb $\leq [O_3] < 50$ ppb;
- Category C, 50 ppb $\leq [O_3] < 75$ ppb;
- Category D, 75 ppb $\leq [O_3] < 100$ ppb;
- Category E, $[O_3] \geq 100$ ppb;

Table 7-5. Comparison between measurements and model predictions of ozone concentrations at Ouray for the three winters for which ozone measurements are available.

		OZONE CATEGORY						
TIME PERIOD	**MEASUREMENT**	**A**	**B**	**C**	**D**	**E**	**A+B+C**	**D+E**
Jan, Feb 2010	Prediction	0	0	18	33	8	18	41
	Actual	0	3	20	21	15	23	36
Jan, Feb 2011	Prediction	0	3	32	21	3	35	24
	Actual	0	9	28	15	7	37	22
Jan, Feb 2012	Prediction	0	60	0	0	0	60	0
	Actual	2	58	0	0	0	60	0

For categories D+E, days with ozone over 75 ppb, the model errs by five, two, and zero days, respectively, in each of the three time periods.

Table 7-5 also highlights a point made above. Even though the model is only moderately accurate in predicting absolute ozone production each winter, especially given a high-ozone winter, it correctly ranks the three winters for ozone production. In general, we expect the model to be accurate for determining relative ozone production between any two given years.

This predictive model lets us estimate the ozone severity for each of the 55 winters for which estimates are possible. (Gaps in the data prevented estimates for the following seasons: 1952, 1953, 1955, 1956, 1957, 1963, 1968.) Table 7-6 gives the predictions by ozone category. It ranks each winter for ozone production, with lighter years appearing at the top. (As already mentioned, we have confidence in the ability of the model to determine relative rankings and are therefore confident in the ranking order as it appears in Table 7-6.) Each winter season analyzed in Table 7-6 includes three consecutive months, December, January, and February. Although Decembers are included in the statistics of this table, they are almost never predicted to produce ozone above 75 ppb.

Table 7-6. Historical predictions of ozone production.

SEASON	**CATEGORY**						
	A	**B**	**C**	**D**	**E**	**A+B+C**	**D+E**
1950-51	20	69	1	0	0	90	0
1953-54	1	83	6	0	0	90	0
1957-58	1	89	0	0	0	90	0
1960-61	0	89	1	0	0	90	0
1963-64	9	80	2	0	0	91	0
1965-66	8	79	3	0	0	90	0
1970-71	5	83	2	0	0	90	0
1971-72	4	86	1	0	0	91	0
1974-75	8	46	36	0	0	90	0
1976-77	0	88	2	0	0	90	0

1980-81	0	90	0	0	0	90	0
1981-82	0	48	42	0	0	90	0
1986-87	2	84	4	0	0	90	0
1993-94	0	87	3	0	0	90	0
1994-95	3	85	2	0	0	90	0
1997-98	0	83	7	0	0	90	0
1999-00	1	89	1	0	0	91	0
2000-01	0	76	14	0	0	90	0
2001-02	0	75	15	0	0	90	0
2004-05	0	77	13	0	0	90	0
2005-06	3	83	4	0	0	90	0
2011-12	**2**	**89**	**0**	**0**	**0**	**91**	**0**
1958-59	6	72	10	2	0	88	2
1975-76	3	59	26	3	0	88	3
1995-96	0	69	17	5	0	86	5
1998-99	3	72	9	4	2	84	6
1969-70	0	74	7	7	2	81	9
1989-90	0	71	10	2	7	81	9
2002-03	0	39	42	9	0	81	9
1968-69	0	47	33	10	0	80	10
2003-04	0	33	48	10	0	81	10
1961-62	10	54	15	7	4	79	11
2008-09	0	37	42	8	3	79	11
1982-83	0	34	43	13	0	77	13
1991-92	6	54	16	8	7	76	15
1964-65	0	14	59	17	0	73	17
1979-80	1	50	21	10	9	72	19
1988-89	2	30	38	17	3	70	20
1996-97	0	44	26	17	3	70	20
2006-07	0	64	6	11	9	70	20
1985-86	0	31	35	9	15	66	24
1990-91	5	42	19	6	18	66	24
1992-93	1	32	33	17	7	66	24
2010-11	**0**	**25**	**41**	**21**	**3**	**66**	**24**
1977-78	4	37	23	13	13	64	26
1959-60	0	41	18	28	4	59	32
1972-73	0	20	33	22	15	53	37
1978-79	3	20	28	11	28	51	39

1987-88	0	28	22	31	10	50	41
2009-10	3	9	37	33	8	49	41
1973-74	3	31	11	26	19	45	45
1966-67	0	12	31	23	24	43	47
2007-08	0	0	44	28	19	44	47
1983-84	0	2	40	14	35	42	49
1984-85	0	18	23	23	26	41	49

We take the 2010-11 (in red) and 2011-12 (in blue) seasons to be typical of bad and good ozone years, respectively. Note that 24/55 = 44% of the seasons are predicted to have 3 or fewer exceedancesof the 75-ppb NAAQS standard. Because the model is most accurate at low ozone values, we have good confidence in its predictions for good ozone years. Also note that 22/55 = 40% are predicted to be no worse (zero exceedancesof the 75-ppb standard) than 2011-12, while 15/55 = 27% are predicted to be as bad or worse (24 or more exceedences) than 2010-11. Figure 7-14 shows the predicted number of exceedancesyear by year.

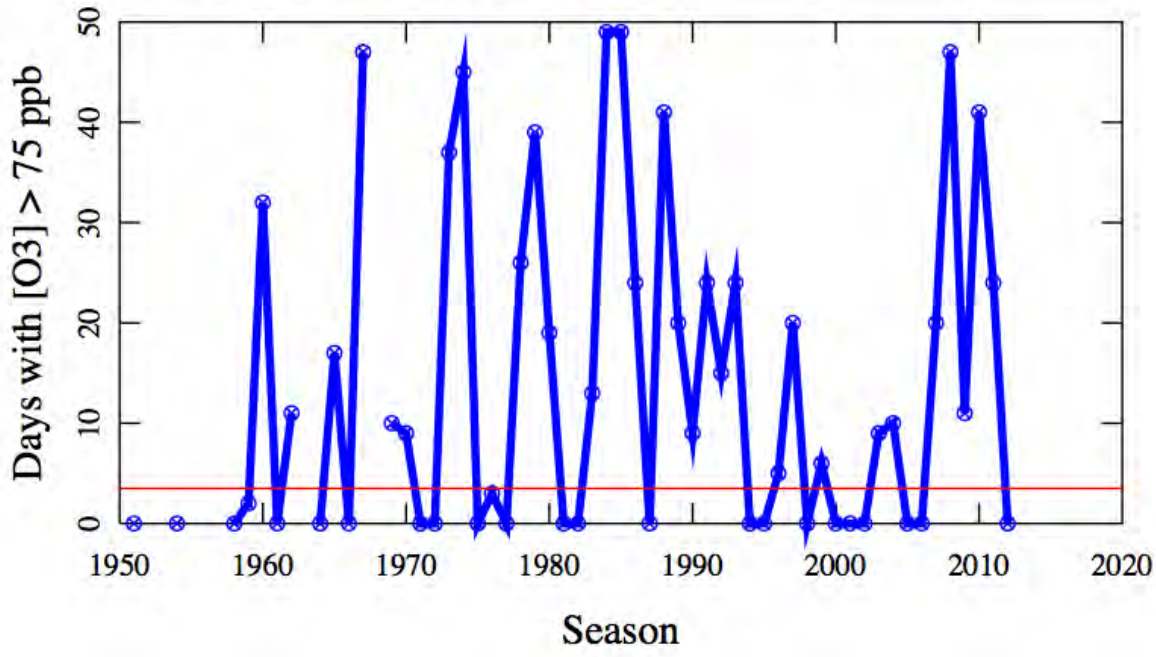

Figure 7-14. Predicted number of days with eight-hour ozone concentrations > 75 ppb in each winter season. Horizontal red line shows the 4-day regulatory threshold. Gaps in the data prevented estimates for the following seasons: 1952, 1953, 1955, 1956, 1957, 1963, 1968.

SENSITIVITY ANALYSIS OF THE PREDICTIVE MODEL

In this section, we present a sensitivity analysis of the predictive model. This involves determining how predictions of the model respond to changes in the independent variables. For example, does the model exhibit a temperature effect? Does it respond as expected to changes in independent variables? Of the various independent variables, which ones exert the greatest influence in driving up ozone concentrations? The reader should bear in mind that we are asking about sensitivities of the *model*, not of the actual ozone concentrations in the Basin. However, because the model at least approximates the actual physical system, it gives us some notion of the behavior of the latter.

To measure sensitivity we will examine the derivatives $\partial\overline{y}/\partial x_\alpha$. The derivative gives the change in ozone concentration for a unit increase in the independent variable. We only consider these derivatives for physically realistic values of the independent variables. Therefore, we will examine statistics of the derivatives when evaluated at any of the 239 points in the calibration set. We have also found that these sensitivities behave somewhat differently depending on snow depth. Therefore, we consider the range of sensitivities under three different cases: Case A, little to no snow, or $x_2 < 100$ mm (≈ 4 in); Case B, moderate snow, or 100 mm < x_2 < 200 mm (≈ 4 to 8 in); and Case C, deep snow, or $x_2 > 200$ mm (≈ 8 in). We have calculated the derivatives $\partial\overline{y}/\partial x_\alpha$ at each point in the calibration set, and then considered the distribution of $\partial\overline{y}/\partial x_\alpha$ in each of the three cases. Histograms of these distributions appear in Figures 7-15 through 7-19.

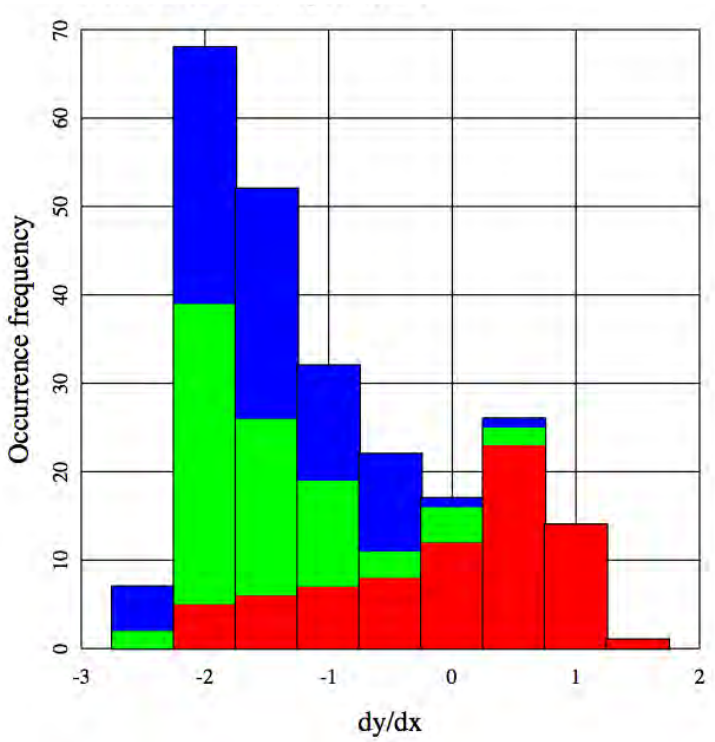

Figure 7-15. Histogram of derivatives $\partial\overline{y}/\partial x_\alpha$ showing the change in ozone concentration per unit change in lapse rate. Red indicates derivatives for snow depth less than 100 mm, green for snow depth between 100 and 200 mm, and blue for snow depth greater than 200 mm.

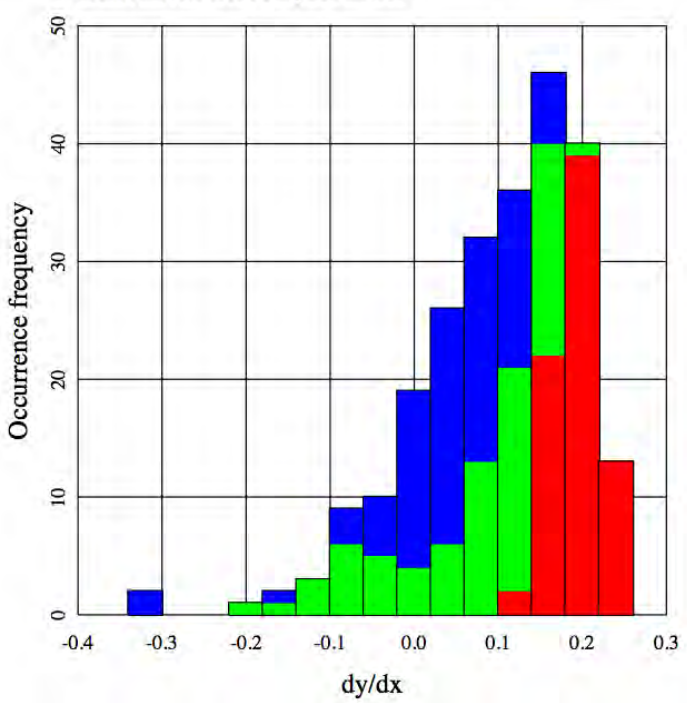

Figure 7-16. Histogram of derivatives $\partial\overline{y}/\partial x_\alpha$ showing the change in ozone concentration per unit change in snow depth. Red indicates derivatives for snow depth less than 100 mm, green for snow depth between 100 and 200 mm, and blue for snow depth greater than 200 mm.

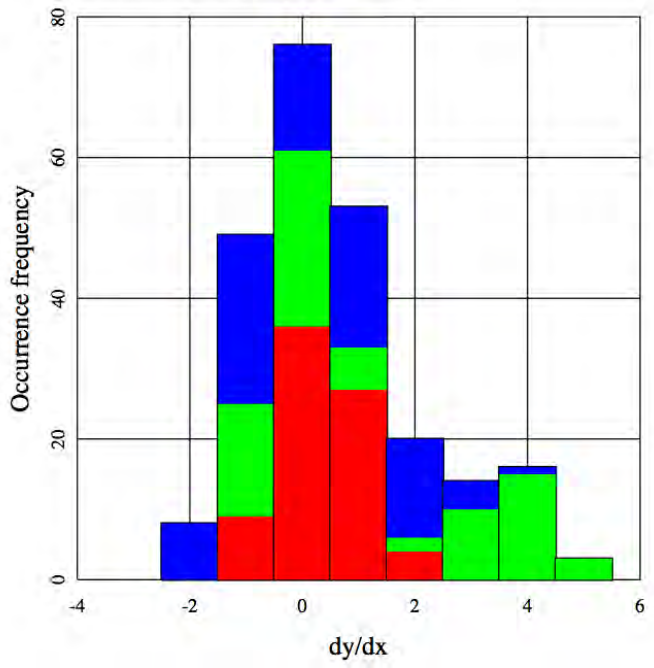

Figure 7-17. Histogram of derivatives $\partial\overline{y}/\partial x_\alpha$ showing the change in ozone concentration per unit change in temperature. Red indicates derivatives for snow depth less than 100 mm, green for snow depth between 100 and 200 mm, and blue for snow depth greater than 200 mm.

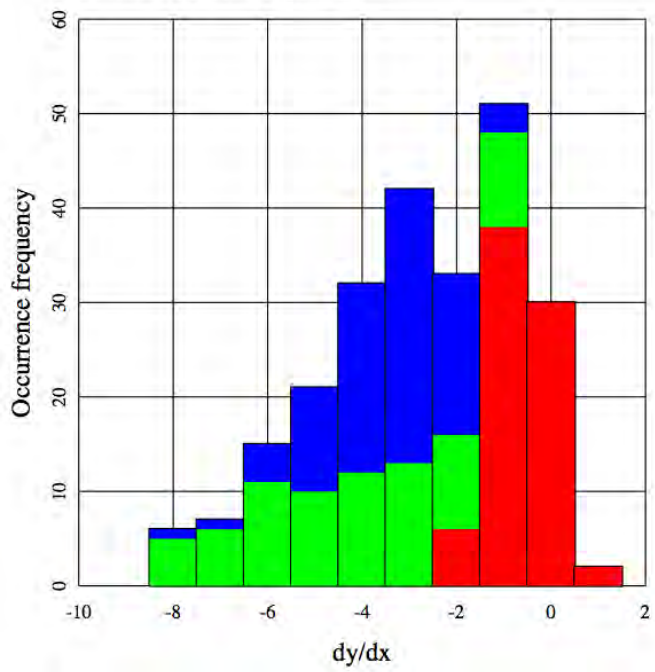

Figure 7-18. Histogram of derivatives $\partial\overline{y}/\partial x_\alpha$ showing the change in ozone concentration per unit change in solar angle. Red indicates derivatives for snow depth less than 100 mm, green for snow depth between 100 and 200 mm, and blue for snow depth greater than 200 mm.

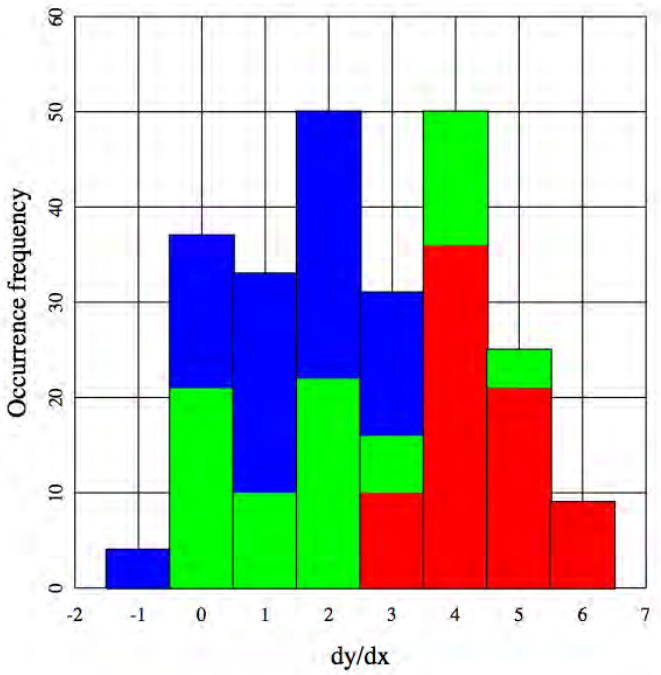

Figure 7-19. Histogram of derivatives $\partial\overline{y}/\partial x_\alpha$ showing the change in ozone concentration per unit change in consecutive days with inversions. Red indicates derivatives for snow depth less than 100 mm, green for snow depth between 100 and 200 mm, and blue for snow depth greater than 200 mm.

Results for the sensitivities are also shown in Table 7-7. The mean and standard deviation for each derivative is shown for each variable and for each of the three snowdepth cases. Table 7-7 also displays σ(dy/dx) for each variable in each of the three snowdepth cases, where σ is the standard deviation for the variable as given in Table 7-3. This product indicates how much the ozone concentration is influenced by the given variable as that variable changes over its typical range. For example, in deep snow conditions, σ(dy/dx) is about –20 ppb for the solar zenith angle, implying that as the solar angle changes from typical low to typical high values, the ozone concentration is impacted by about 20 ppb.

Table 7-7. Derivatives $\partial\bar{y}/\partial x_\alpha$ showing the change in ozone concentration per unit change in each independent variable, and σ(dy/dx), the standard deviation for each variable (mean ± standard deviation).

VARIABLE	DERIVATIVE	SNOW <100 mm	SNOW 100-200 mm	SNOW >200 mm	UNITS
x_1 Lapse Rate	$d\bar{y}/dx_j$	–0.040 ± 0.90	–1.5 ± 0.6	–1.5 ± 0.6	ppb km/K
	$\sigma_j\left(d\bar{y}/dx_j\right)$	–0.30 ± 7	–11 ± 5	–11 ± 5	ppb
x_2 Snow Depth	$d\bar{y}/dx_j$	0.19 ± 0.03	0.07 ± 0.1	0.045 ± 0.083	ppb/mm
	$\sigma_j\left(d\bar{y}/dx_j\right)$	20 ± 3	7 ± 10	5 ± 9	ppb
x_3 Temperature	$d\bar{y}/dx_j$	0.33 ± 0.69	1.28 ± 1.97	0.28 ± 1.38	ppb/(°C)
	$\sigma_j\left(d\bar{y}/dx_j\right)$	2.3 ± 5.0	9.2 ± 14	2.0 ± 10	ppb
x_4 Solar Angle	$d\bar{y}/dx_j$	–0.66 ± 0.57	–4.1 ± 2.1	–3.5 ± 1.3	ppb/(°)
	$\sigma_j\left(d\bar{y}/dx_j\right)$	–4.1 ± 3.6	–25 ± 12	–21 ± 8	ppb
x_5 Consecutive Days with Inversion	$d\bar{y}/dx_j$	4.4 ± 0.9	1.95 ± 1.52	1.39 ± 1.06	ppb/day
	$\sigma_j\left(d\bar{y}/dx_j\right)$	43 ± 8	19 ± 15	14 ± 10	ppb

Much useful information is found in these sensitivities. We can make all of the following observations:

1. The sensitivity to snowdepth decreases as the snow becomes deeper, varying from 20 to 7 to 5 ppb. This is probably a saturation effect. When the snow is deep, adding more has less of an effect than when the snow is shallow.

2. The sensitivity to lapse rate is low in the shallow snow case, and larger for deeper snow. Without snow, inversions have little effect on ozone production.

3. The temperature sensitivity is about 9 ppb in Case B (moderate snow cover), indicating that the ozone concentration falls by more than 1 ppb for every 1°C drop in temperature. This is probably the combined result of the temperature dependence of each individual chemical reaction in the ozone chemistry mechanism. The fact that ozone concentrations are sensitive to temperature highlights a potential problem for modeling winter ozone events that we have already pointed out elsewhere [Martin, et al, 2011, p. 81-95]. The standard photochemical smog modeling mechanisms were all developed at or near room temperature for summertime applications and are probably not entirely accurate for winter ozone.

4. The sensitivity to solar zenith angle appears with the proper sign: Recall that the angle is 0° at the zenith and 90° at the horizon. These sensitivities, around –20, confirm our assertion that late-season inversions are more ozone-productive because of the higher solar elevation.

5. Sensitivities to lapse rate are also of the anticipated sign. However, it is interesting to note that their magnitudes are smaller than those observed for the solar zenith angle. This also seems to be consistent with observations made above: Late winter ozone events draw their strength more from the intensity of solar radiation than from the intensity of inversions.

6. Sensitivities to the number of days since the beginning of a multi-day inversion (CDI) are large, around 20 to 40 ppb. This probably reflects the accumulation of precursors during multi-day inversion events. It implies that ozone levels increase around 2 to 4 ppb per day as we proceed through a multi-day inversion.

FUTURE WORK

Because the UGRB has had a longer history of winter ozone monitoring, a similar analysis there would also be very informative. The quality of the regression analysis should improve as more years are added to the calibration dataset. And with ozone data extending over more years, a regression analysis might tease out dependence on the levels of oil or gas production. Such a study would also indicate similarities and differences between the ozone systems of the two basins. Likewise, assuming that ozone monitoring at Ouray will continue into the foreseeable future, each passing year will permit us to refine the predictive model presented here.

It has been suggested that inversion events in the Basin are related to the North Atlantic Oscillation, or some other global climate pattern. We will compare the historical climate data with historical NAO indexes to test this hypothesis.

The predictive model employed a quadratic regression, i.e., it employs linear and quadratic basis functions of the independent variables. However, as more years of ozone data accumulate, we may be able to develop more accurate regression models, involving either more sophisticated basis functions or more independent variables.

MAJOR CONCLUSIONS

- Thermal inversions and snow cover in the Basin are most likely in January. The frequency of days that simultaneously have inversions and snow cover is at a maximum of about 50% in mid-January, and conforms very well to a Gaussian distribution with a standard deviation of about 30 days, meaning that such days are considerably less prevalent either in December or February.

- Based on experience in both the Uintah Basin and UGRB, as well as on the results of the predictive model, we conclude that ozone events are most intense in February, i.e, they lag behind the most intense inversions by about one month. The most reasonable explanation for this lag is that solar radiation intensifies as the winter progresses.

- Based on climate patterns from the past 50 or 60 years , we predict 44% odds that any given winter is compliant with the National Ambient Air Quality Standard. We predict 27% odds that any given winter will be as bad or worse for ozone as 2010-11, and 40% odds that any given winter will be as good or better than 2011-12. The remaining 33% lie somewhere in between.

- A naïve examination of the data suggests multi-year trends, with several years in succession of either high or low inversion frequency or high or low snow cover. However, the sequences of high and low years are not inconsistent with an entirely random process. Any actual multi-year trends, if present, are weak.

REFERENCES

B.J. Finlayson-Pitts & J.N. Pitts, *Chemistry of the Upper and Lower Atmosphere*, Academic Press, San Diego, 2000.

R. Martin, K. Moore, M. Mansfield, S. Hill, K. Harper, H. Shorthill; *Final Report: Uinta Basin Winter Ozone and Air Quality Study: December 2010 – March 2011*, Energy Dynamics Laboratory, Utah State University Research Foundation, Document Number EDL/11-039, June 14, 2011. Available at rd.usu.edu/files/uploads/edl_2010-11_report_ozone_final.pdf

R.C. Schnell, S.J. Oltmans, R.R. Neeley, M.S. Endres, J.V. Molenar, A.B. White "Rapid photochemical production at high concentrations in a rural site during winter," Nature Geoscience, 2, 120-122 (2009).

J.H. Seinfeld & S.N. Pandis, *Atmospheric Chemistry and Physics*, 2nd edition, Wiley-Interscience, Hoboken, N.J., 2006.

T. Stoeckenius & L. Ma, "*Final Report: A Conceptual Model of Winter Ozone Episodes in Southwest Wyoming*," Environ, Novato, CA, 2010.

Utah Climate Center: climate.usurf.usu.edu

C.D. Whiteman, S. Zhong, W.J. Shaw, J.M. Hubbe, X. Bian, J. Mittelstadt, "Cold Pools in the Columbia Basin," Weather and Forcasting, 16, 432-447 (2001).

NOTES

Note 1

Equation for the filtered curve in Figure 7-7:

$$\left[6.20 + 5.93\cos\left[2\pi\nu_1\left(t-\delta_1\right)\right] + 2.19\cos\left[2\pi\nu_2\left(t-\delta_2\right)\right]\right]\ \frac{K}{km}$$

taking the zero of *t* to be July 1, and with

$$\nu_1 = 1\ yr^{-1}, \nu_2 = 2\ yr^{-1}, \delta_1 = 0.0235\ yr, \delta_2 = -0.215\ yr$$

Equations for the Gaussian distributions in Fig. 13:

$$A\exp\left[-\frac{\left(t-t_0\right)^2}{2\sigma^2}\right]$$ (again taking the zero of *t* to be July 1)

Inversions only:	A = 0.598,	t_0 = 197 days (Jan 14),	σ = 32 days.
Snow cover only:	A = 0.635,	t_0 = 207 days (Jan 24),	σ = 30 days.
Inversions + snow:	A = 0.481,	t_0 = 204 days (Jan 21),	σ = 27 days.

Note 2

The so-called "potential temperature" reflects the fact that a parcel of air cools when expanded adiabatically, i.e., without the transfer of heat. Therefore, a column of air in stable equilibrium is expected to be cooler aloft where the pressure is lower. The potential temperature involves an adjustment for the ambient pressure in such a way that it will be constant throughout a column of air at equilibrium. Therefore, the potential temperature is a better indicator of atmospheric stability than the actual temperature. See, for example, Seinfeld & Pandis [2006].